The 0.7 anomaly in quantum point contacts
A microscopic model for the first conductance step

Jan Heyder

SIGILL. UNIVERSITAT. LUDOVIC. MAXIM.

München 2014

The 0.7 anomaly in quantum point contacts
A microscopic model for the first conductance step

Jan Heyder

Doktorarbeit
an der Fakultät für Physik
der Ludwig–Maximilians–Universität
München

vorgelegt von
Jan Heyder
aus Frankfurt am Main

München, den 8.12.2014

Erstgutachter: Professor Jan von Delft
Zweitgutachter: Privatdozent Dr. Stefan Ludwig
Tag der mündlichen Prüfung: 8.12.2014

Contents

Contents v

Zusammenfassung 1

Abstract 3

1 Introduction 5

2 Electronic transport in one-dimensional systems 9
- 2.1 Noninteracting transport in 1D . . . 9
  - 2.1.1 The relation between the electron's velocity and the LDOS in 1D . . . 10
  - 2.1.2 The current through a 1D system . . . 10
  - 2.1.3 The quantized conductance of a 1D system . . . 11
- 2.2 Quasi 1D systems . . . 12
  - 2.2.1 The effective potential of quasi 1D systems . . . 12
  - 2.2.2 The conductance of quasi 1D systems . . . 13
- 2.3 Experimental realization of low-dimensional systems . . . 14
  - 2.3.1 The 2-dimensional electron system (2DES) . . . 14
  - 2.3.2 The quantum point contact (QPC) . . . 14
- 2.4 The 0.7 anomaly . . . 16
  - 2.4.1 Evolution of the 0.7 anomaly with magnetic field . . . 17
  - 2.4.2 Evolution of the 0.7 anomaly with temperature . . . 17
  - 2.4.3 The zero-bias anomaly (ZBA) . . . 19
  - 2.4.4 Additional features . . . 20
- 2.5 Conclusion and outlook . . . 20

3 The origin of the 0.7 anomaly 23
- 3.1 Shape of the 1D effective barrier . . . 24
  - 3.1.1 Experimental setup . . . 24
  - 3.1.2 The parabolic 1D barrier . . . 24
  - 3.1.3 The distinctiveness of the sub-open regime . . . 26
- 3.2 Non-interacting physics of a parabolic barrier . . . 26
  - 3.2.1 The non-interacting transmission and conductance of a parabolic barrier 27
  - 3.2.2 The noninteracting LDOS of a parabolic barrier . . . 30

3.2.3 Buildung a bridge to interactions 32
3.3 Physics of a parabolic barrier in the presence of interactions 32
3.3.1 Interacting Model 32
3.3.2 Treatment of interactions 33
3.3.3 The effective interaction strength - a simple Hartree argument 36
3.4 Interacting conductance of a parabolic barrier - the 0.7 anomaly 38
3.4.1 Conclusion 40

4 Microscopic origin of the *0.7 anomaly* in quantum point contacts 41

5 On the relation between the *0.7 anomaly* and the Kondo effect 79

6 fRG Approach for Inhomogeneous Interacting Fermi Systems 101

7 The effect of spin-orbit interactions on the *0.7 anomaly* in quantum point contacts 115

8 Conductance Formula for Interacting Fermi Systems in Keldysh Formalism 129

9 Towards combined transport and optical studies of the *0.7 anomaly* in a QPC 155

Bibliography 164

List of Publications 169

Curriculum Vitae 171

Danksagung 173

List of Figures

2.1 *1D system:* The semi-infinite and homogeneous leads L and R are connected via a central scattering region C, where traversing electrons are scattered at a spin-dependent potential barrier $V^{\sigma}(x)$. A finite voltage V_{sd} drives a current J through the system, which features a quantized conductance $G = dJ/dV_{sd}$. . . . 10

2.2 *1D constriction and effective 1D potential:* **(a)** Illustration of the constriction seen by an incoming right-moving electron with wave vector k_x. The grey-shaded areas mark regions that cannot be entered by the charge carrier due to an applied electrostatic potential $V(x, y)$, leaving only a narrow adiabatic transport channel centered at $y = 0$. **(b)** In addition to the electrostatic potential $V(x, y = 0)$ (red line) an electron experiences a potential energy $\varepsilon_n(x)$ when entering the constriction via the n-th transversal mode. This leads to a 1D effective barrier $V_n(x) = V(x) + \varepsilon_n(x)$ (black lines). In order to traverse the bottleneck via the transport channel n the charge carrier's energy must exceed the height of the corresponding effective barrier, $\varepsilon(k_x) > V_n(x = 0)$. In the scenario depicted here the electron will overcome the barrier when entering the constriction via the $n=1$ mode, but is reflected at the classical turning point x_t, when entering it via the $n=2$ mode. 13

2.3 *Quantum point contact and the 0.7 anomaly:* **(a)** Split-gate geometry: A negative voltage V_g, applied to two adjacent metallic gates, depletes the 2DES underneath and restricts electronic transport between the leads to the QPC. **(b)** A sketch of the electrostatic potential $V(x, y)$ of a QPC, including discrete eigenstates due to the small extension in transverse direction. In the vicinity of the QPC's center, $x = y = 0$, the potential can be approximated by a saddle point form with curvatures in transport and tranverse given by the two energy scales Ω_x and Ω_y, see Eq. (2.14). **(c)** The linear conductance of a QPC as function of gate voltage features a staircase in units of the conductance quantum G_Q, the hallmark of transport in quasi 1D systems. The data was taken from van Wees et al. (1988). **(inset)** The additional shoulder-like step in the linear conductance of the lowest subband - the *0.7 anomaly* - is interaction-induced and its origin still subject to controversal discussions. The figure is taken from Thomas et al. (1996). 15

2.4 *Magnetic field dependence of the first conductance step:* **(a)** The noninteracting conductance of a parabolic barrier as function of barrier height V_c (corresponding to gate voltage V_g, see Eq. (2.15)) for several values of magnetic field B. Upon increasing the magnetic field, spin degeneracy of the system is lifted, resulting in a symmetric double step of width B (the conversion factor $\mathrm{g} \cdot \mu_B$ is absorbed in the magnetic field). **(b)** Measurement of the linear conductance of a QPC embedded in a GaAs-AlGaAs heterostructure performed by Koop et al. (2007). Upon increasing the magnetic field, the *0.7 anomaly* develops from above into the spin-resolved conductance steps. Analysis of the sub-band splitting reveals an interaction-induced enhancement of the g-factor. 18

2.5 *Temperature dependence of the first conductance step:* **(a)** The noninteracting conductance of a parabolic barrier as function of barrier height V_c (corresponding to gate voltage V_g, see Eq. (2.15)) for several values of temperature T. Upon increasing the temperature, the conductance step is smeared out symmetrically on a scale set by T. **(b)** Measurement of the linear conductance of a QPC embedded in a GaAs-AlGaAs heterostructure performed by Thomas et al. (1996). In the region of the *0.7 anomaly* the conductance is anomalously strong suppressed by temperature. This invokes a pronounced shoulder-like step at intermediate temperatures of ~1K, which represents the most prominent distinctive feature of the *0.7 anomaly*. Note that the step is even more emphasized due to an unexpectedly weak reaction of the pinch-off conductance on temperature. 19

2.6 *Source-drain voltage dependence of the first conductance step:* **(a)** The noninteracting differential conductance of a parabolic barrier as function of bias voltage V_{sd} for several barrier heights V_c (corresponding to gate voltage V_g, see Eq. (2.15)). The differential conductance features a peak/dip in the sup-open/pinch-off regime at zero bias, $V_{sd} = 0$. For large bias voltages it saturates at $g(V_{sd}) = 0.5$. **(b)** Measurement of the differential conductance by Cronenwett et al. (2002), realized within a GaAs-AlGaAs heterostructure QPC. A narrow zero bias peak shows up over the whole range of gate voltages that correspond to the first conductance step. It is usually accompanied by finite-bias side peaks (here around $|V_{sd}| \simeq 0.7$mV). For large voltages, the differential conductance tends to saturate at values $g(V_{sd}) \simeq 0.25$. 20

3.1 *Shape of conductance step and sub-open regime:* **(a)** Measurement of the linear conductance by the Ludwig group. The data features both the typical linear conductance staircase as well as a weak *0.7 anomaly* in the conductance of the first subband. The lower inset shows the gate structure of the probe, defining the QPC. Six pairwise adjacent gates allow for a particularly high tunability of the electrostatic potential. An additional global top-gate can be used to manipulate the chemical potential in the QPC region. The upper inset shows a comparison between the $n = 1$ and $n = 3$ step, highlighting the interaction-induced modulation of conductance in the sub-open regime. **(b)** A zoom-in on the smooth $n = 3$ linear conductance step. **(c)** Linear conductance as function of barrier height V_c, calculated for several potentials defined via Eq. (3.2). Comparison with **(b)** corroborates the picture, that the effective 1D potential features a parabolic ($p = 2$) barrier top. 25

3.2 *Noninteracting transport through a quadratic barrier.* **(a)** Scheme of scattering at a quadratic potential barrier. The solution of the Schrödinger equation (Eq. (3.7)) can be decomposed into an incident, a reflected and a transmitted wave (Eq. (3.9)). **(b)** Energy-dependent transmission through the parabolic barrier (Eq. (3.10)). Quantum effects smear out the classical transmission function (dashed line) in symmetric fashion on a scale set by the potential curvature Ω_x. **(c)** The evolution of the noninteracting conductance of a parabolic barrier as function of gate voltage $\tilde{V}_c = V_c/\Omega_x$ with magnetic field $\tilde{B} = B/\Omega_x$, temperature $\tilde{T} = T/\Omega_x$ and source drain voltage $\tilde{V}_{sd} = V_{sd}/\Omega_x$, calculated via Eqs. (2.8)-(2.11). For a detailed discussion see Sec. 2.4. 29

3.3 *Local properties of a parabolic barrier.* **(a)** The local density of states as function of position and energy. The distinct "van Hove ridge" (black) is located just above the potential barrier. **(b)** The LDOS, $A^{\mu}(\tilde{V}_c)$, as function of barrier height shows a maximum in the sub-open regime corresponding to $g \approx 0.8$. This structure causes the anomalous conductance features at finite interaction strength, known as 0.7 anomaly (see Sec. 3.3). The black dashed line shows for comparison the corresponding classical time an electron spends in the vicinity of the barrier center (in arbitrary units). **(c)** An illustration of the modification of the LDOS by the inhomogeneity. In the QPC's center the LDOS is shifted and smeared by the potential barrier. 31

3.4 *The Hartree barrier:* **(a)** Illustration of the bare ($U = 0$) potential $V(\tilde{x})$ and the Hartree potential $V^h(\tilde{x})$ in the vicinity of the barrier top. The combination of finite density $n_0(\tilde{x})$ and finite interaction strength U causes an enhancement w. r. t. the bare barrier given by the Hartree self-energy $\Sigma^h(\tilde{x}) = n_0(\tilde{x})U$. **(b)** The barrier height V_c^h of the effective Hartree potential depends nonlinear on the original barrier height V_c: Beyond pinch-off ($\tilde{V}_c \gg 0$), where all density is pushed away from the QPCs center, both coincide independent from the value of U. Yet, in the sub-open regime the dependence of V_c^h on V_c descreases with increasing U. The plot shows exemplary calculations for several values of the interaction parameter U. 37

3.5 *Formation of the 0.7 anomaly with increasing interactions:* **(a)** The evolution of the linear conductance g as function of barrier height V_c for increasing interaction parameter U, calculated using fRG. The data features a weak 0.7 shoulder at intermediate interaction strength. **(b)** Its origin can be associated with a maximum in $A^{\mu}(\tilde{V}_c)$ in the sub-open regime, which indicates slow electrons in the barrier center at the chemical potential. These are subject to an enhanced backscattering probability as a consequence of strong local interactions at the barrier top. **(c)**,**(d)** Comparison between "noninteracting" and "interacting" conductance. The data were shifted in V_c for clarity. Note the remarkable similarity between theory and experiment. 39

Zusammenfassung

Diese Arbeit hat zum Ziel den mikroskopischen Ursprung eines Phänomens im Bereich der Halbleiter Nanostrukturen zu beleuchten, das beim elektronischem Transport durch kurze eindimensionale Verengungen, sogenannte Quantenpunktkontakte (QPCe), auftritt: Während das stufenhafte Ansteigen des linearen Leitwerts eines QPCs als Funktion seiner Breite in Einheiten des Leitwertquantums G_Q eine wohlverstandene Eigenschaft quasi eindimensionaler Systeme ist [Landauer (1957)], bereitet eine zusätzliche schulterartige Zwischenstufe bei $0.7 \times G_Q$ seit nunmehr beinahe 20 Jahren Kopfzerbrechen - die *0.7 Anomalie*. Seit ihrer ersten Erwähnung im Jahre 1996 [Thomas et al. (1996)] gab es eine Vielzahl von experimentellen Arbeiten [Micolich (2011)], die immer neue Facetten dieses faszinierenden Effekts aufdeckten. Besonders hervorzuheben ist hierbei die anormal starke Reduktion des Leitwerts im sogenannten *sub-offenen Regime* als Funktion von externen Parametern wie Magnetfeld, Temperatur oder angelegter Spannung. Während Einigkeit darüber herrscht, dass der zugrundeliegende Mechanismus der *0.7 Anomalie* in der gegenseitigen Beeinflussung (= Wechselwirkung) der Elektronen beim Durchqueren des QPC zu finden ist, zeigt die außerordentlich hohe und ständig wachsende Anzahl an vorhandenen Erklärungsversuchen, dass ein Konsens über das detaillierte Zustandekommen dieser ungewöhnlichen Schulter bislang nicht erlangt wurde. Insbesondere scheint keine Theorie eine umfassende Erklärung für die *0.7 Anomalie* und all ihre Begleiterscheinungen liefern zu können. Hier präsentieren wir ein mikroskopisches Model, das versucht, genau diesem Anspruch zu genügen.

Wir beschreiben die effektive Barriere der untersten Transportmode des QPC durch ein eindimensionales parabolisches Potential. Dass eine parabolische Barriere die Realität ausreichend approximiert, lässt sich durch detaillierte Analyse der experimentellen Leitwert-Stufenform überzeugend begründen. Um ein möglichst genaues Bild von der Physik eines QPCs zu erhalten legen wir besonderen Wert auf die Herausarbeitung seiner Einteilchen-Physik; in der Umgebung des Barrierenzentrums finden wir ein ausgeprägtes Maximum in der lokalen Zustandsdichte bei Energien knapp oberhalb des Potentials. Dieses "*van Hove Maximum*", der in einem semiklassischen Bild mit langsamen Elektronen über der Barriere assoziiert werden kann, fällt im *sub-offenen Regime* mit der Fermikante zusammen. Hier führt er, bei endlicher Wechselwirkungstärke, zu einer stark erhöhten Rückstreuwahrscheinlichkeit für einlaufende Elektronen, resultierend in einer starken Reduktion des Leitwerts; in einem äußeren Magnetfeld liegt dieser Reduktion eine wechselwirkungsinduzierte Verstärkung der lokalen Verarmung des Subbandes der energetisch benachteiligen Spinspezies zugrunde (vergleichbar dem ferromagnetischen Stonermodell), im Falle endlicher Anregungsenergien resultiert sie aus einer erhöhten inelastischen Rückstreuung. Damit liefert das Wechselspiel aus *van Hove ridge* und Elektron-Elektron Wechselwirkung in einem QPC eine natürliche Erklärung für das Auftreten der *0.7 Anomalie* und ihrer mannigfaltigen Ausprägungen.

Für die Berechnung der wechselwirkenden Physik unseres eindimensionalen QPC Modells verwenden wir zwei unterschiedliche Methoden: Eine eigens entwickelte Näherung innerhalb der funktionalen Renormierungsgruppe (fRG) liefert verlässliche Resultate für die Magnetfeldabhängigkeit der *0.7 Anomalie*. Für endliche Temperaturen und Spannungen greifen wir auf Störungstheorie in zweiter Ordnung in der Wechselwirkung (SOPT) zurück. Da deren Validität auf geringere Wechselwirkungsstärken beschränkt ist, ist eine Erweiterung der fRG-Anwendbarkeit auf endliche Anregungsenergien derzeit in Arbeit.

Abstract

This thesis aims at shedding light on the microscopic origin of a phenomenon in the field of semiconductor nanostructures, which occurs in transport through a short and narrow quasi one-dimensional constriction, the quantum point contact (QPC). Unlike the stepwise increase of linear conductance of a QPC as function of its width in units of the quantum G_Q, which is well understood and was predicted already in the 1950s [Landauer (1957)], an additional shoulder-like step at $0.7 \times G_Q$ raises questions since its discovery in 1996 [Thomas et al. (1996)]: the *0.7 anomaly*. Subsequent experimental investigations [for a review see Micolich (2011)] revealed a plethora of accompanying features of this fascinating structure. Most famously these include a strong reduction of conductance in the *sub-open regime* of a QPC as function of external parameters such as magnetic field, temperature or bias voltage. While it is agreed upon that the *0.7 anomaly* arises from electron-electron interactions, the high number of theoretical attempts at an explanation indicates that the detailed microscopic origin of the peculiar shoulder is still subject to controversal discussions. In particular no theory seems to describe the whole variety of signatures of the *0.7 anomaly* sufficiently. Here, we present a microscopic model that qualifies to meet this requirement.

We model the effective barrier of the lowest transport mode of a QPC by a one-dimensional parabolic potential with short-ranged Coulomb interactions. By systematic analysis of experimental data we show that a parabolic barrier approximates the actual barrier shape of the QPC adequately well. In order to understand the physics of a QPC in detail, we put emphasis on the noninteracting properties of our model; we find a pronounced maximum in the local density of states in the vicinity of the barrier center at energies just above the potential. Importantly, this "*van Hove ridge*", which can be associated with slow electrons above the barrier coincides with the chemical potential if the QPC is tuned to be *sub-open*. Here, it causes an enhancement of backscattering at finite interactions and a subsequent anomalous reduction of conductance. In case of a magnetic field the underlying mechanism for this reduction is an interaction-enhanced local depopulation of the disfavoured spin species' subband; at finite excitation energies the reduction is a consequence of an interaction-enhanced inelastic backstattering probability. Hence, the interplay of *van Hove ridge* and electron-electron interactions provides a natural explanation for the appearance of the *0.7 anomaly* and its various features.

We calculate properties of our interacting one-dimensional QPC model using two methods: A specially developed approximation scheme within the functional renormalization group (fRG) provides reliable results for the magnetic field dependence of the *0.7 anomaly* at zero temperature. At finite temperature and finite bias voltage we rely on second order perturbation theory in the interaction (SOPT). Since SOPT's validity is restricted to weaker interaction strength, where calculations clearly show the right trend but not yet the full manifestation of the *0.7 anomaly*, we are currently setting up an extension of our fRG approach within the Keldysh formalism, which will allow us to also explore finite excitation energies.

Chapter 1

Introduction

Mesoscopic systems are systems on intermediate length scales where quantum effects start to matter. Understanding their physics is not only of conceptual relevance, but also gains increasing importance due to the ongoing miniaturization of technical devices. As local thermodynamic observables are mostly difficult to access experimentally in mesoscopic systems, transport measurements often serve as the main diagnostic tool to investigate a system's microscopic properties. Theoretical understanding is essential to draw conclusions from the measured data about the detailed microscopic structure of a probe. This demands a thorough theoretical analysis of the transport properties of such systems. Starting in the mid 50s with Landauers conductance formula in one dimension [Landauer (1957)] transport theory has thenceforth consistently proven its ability to explain and predict basic phenomena of coherent transport in mesoscopic systems: Amongst others this famously includes the Aharonov-Bohm effect [Aharonov and Bohm (1959)], the quantum hall effect [Laughlin (1981)], weak localization [Altshuler et al. (1980)] and weak anti-localization [Hikami et al. (1980)] as well as ongoing successes in the theory of transport through one-, and zero-dimensional structures. Despite this success story there are, naturally, still some blank spots, where theory is in search for the microscopic origin of an observed phenomenon. One of these appears in transport through an elementary building block of semiconductor nanostructures: The *0.7 anomaly* in the conductance of a quantum point contact (QPC).

The validation of Landauers 1D transport theory took some time, as the experimental realization of a system where electronic movement is restricted to only one dimension requires fine-tuning of the system's geometry on the scale of nanometers. But technical progress was catching up eventually and in the late 80s van Wees et al. (1988) finally succeeded: By applying negative voltage to metallic gates located above a two-dimensional electron system (2DES), where electrons are restricted to two dimensions by an electrostatic potential, they had managed to define a short and narrow quasi one-dimensional constriction, the quantum point contact (QPC). Its small extension in transverse direction causes a quantization condition on its eigenstates, such that they form a discrete spectrum of one-dimensional transport modes. Upon increasing the width of the QPC by increasing the gate voltage one after another of those modes is shifted from above through the chemical potential, resulting in the famous step-wise increase of linear conductance in units of the conductance quantum $G_Q = 2e^2/h$, where e is the electron charge and h is Planck's constant. While this staircase, which is considered one of the hallmarks of low-dimensional systems, proves the validity of Landauers transport theory it also harbors one of the biggest conundrums of mesoscopic systems: The first linear conductance step of a QPC features an additional shoulder-like structure in the sub-open regime around $0.7G_Q$. Unlike the staircase this *0.7 anomaly* cannot be explained by noninteracting theory, but is commonly attributed to electron-electron interactions. Much effort has been devoted to understand the mechanism behind this unusual and striking physical characteristic of a sub-open QPC; since its first mentioning by Thomas et al. (1996) the *0.7* *anomaly* was subject of hundreds of experimental studies [Micolich (2011)], which brought a plethora of subsequental features to light: Most impressive is the anomalous reduction of conductance as function of magnetic field [Koop et al. (2007)], temperature [Thomas et al. (1996)] and bias voltage [Cronenwett et al. (2002)]. Further anomalous signatures arise in shot-noise [Koop et al. (2007)], compressibility [Smith et al. (2011)], thermopower [Appleyard et al. (2000)] and almost every additional measurable quantity of a sub-open QPC.

The high number of experimental studies of the *0.7 anomaly* is accompanied by comparably many theoretical models that aim at explaining the remarkable interaction-induced features of a sub-open QPC. Thomas et al. (1996) attributed the appearance of a 0.7 shoulder at zero magnetic field to spontaneous spin-polarization in the QPC. A theoretical model promoting this picture was presented by Wang and Berggren (1998). The similarity between the behavior of the conductance as function of external parameters in a sub-open QPC and a quantum dot in the Kondo regime motivated the picture of a quasi-localized spin-$1/2$ state forming in the vicinity of the QPC's center [Cronenwett et al. (2002), Meir et al. (2002), Rejec and Meir (2006), Iqbal et al. (2013)]. The possible localization of electrons in a QPC by Wigner crystallization was suggested by Matveev (2004) and Güçlü et al. (2009). Strong ferromagnetic spin coupling was stated as origin of the *0.7 anomaly* by Aryanpour and Han (2009). Inelastic scattering and momentum non-conserving processes were discussed by Sloggett et al. (2008) and Lunde et al. (2009). The diversity of theoretical models as well as their still increasing number demonstrate that consensus about the microscopic origin of the *0.7 anomaly* is not reached yet. Often, a theory seems taylor-made to explain a certain sub-group of features of the *0.7 anomaly*, only to fail in other aspects. While the large number of features naturally brings about all kinds of theories, it appears to also complicate the discovery of a microscopic mechanism that provides an overall explanation for the various characteristics of the *0.7 anomaly*.

This thesis is devoted to a thorough theoretical analysis of a sub-open QPC. We argue that its essential physics is captured by a one-dimensional model with a parabolic potential barrier and short-ranged electron-electron interactions (EEI), thereby following the footsteps of previous works [e.g. Büttiker (1990), Sloggett et al. (2008)]. Special emphasis is put on the interplay between geometry-induced and interaction-induced physics, which allows for a clear interpretation of all calculated features. In order to provide reliable results we calculate the influence of interactions using two perturbative approaches: A taylor-made approximation scheme within the framework of the functional renormalization group (fRG) is used for calculations at zero temperature and zero source-drain voltage, whereas finite excitation energies are covered by second order perturbation theory (SOPT). Both schemes were tested extensively upon their qualitative reliability. In order to sharpen the physical intuition of the reader for the underlying microscopic mechanisms, we lay special focus on a semi-classical interpretation of our results. Our calculations provide ample evidence that the chosen model is indeed capable of reproducing all major conductance features of the *0.7 anomaly*.

Outline of this thesis

In chapter 2 we discuss electronic transport in one-dimensional systems. We present a derivation of Landauers conductance formula, which highlights the inverse proportionality between the local density of states and the semi-classical velocity of electrons in 1D. We introduce the QPC, one of the elementary building blocks of electronic nanostructure devices. We show experimental measurements of the conductance of a QPC, including the staircase data of linear conductance and the evolution of the first conductance step as function of external parameters. In the latter case the features of the *0.7 anomaly* are emphasized by comparison to predictions of noninteracting theory.

Chapter 3 introduces our 1D model of a QPC. We present analytic calculations for both the noninteracting transmission through the QPC and the noninteracting local density of states (LDOS) of the QPC. We then discuss the influence of short-ranged electron-electron interactions (EEI) on the physics of our model; we give an overview of the ideas of fRG and SOPT, the methods we use to treat interactions. Finally, we present fRG calculations that show the evolution of the first conductance step with increasing interaction strength.

All subsequent chapters contain papers, that are either published, submitted to a journal or will be submitted in the near future:

Chapter 4 provides a reprint of the NATURE-publication "*Microscopic origin of the 0.7 anomaly in quantum point contacts*" [Bauer et al. (2013)], where we present the main findings of our work; we argue that an interplay between the *van-Hove ridge*, a local maximum in the LDOS in the vicinity of the barrier center just above the potential barrier, and EEI causes an interaction-induced enhancement of backscattering in a sub-open QPC. This provides a natural explanation for the emergence of the *0.7 anomaly*. The paper features the comparison of our theoretical data with experimental measurements, that were performed in the group of Stefan Ludwig. The qualitative agreement of theory and experiment provides further evidence for the validity of our "*van-Hove ridge scenario*".

Chapter 5 contains the paper Heyder et al. (2014), where we discuss the geometric crossover from a QPC to a quantum dot with Kondo effect (KQD). We emphasize the similarities of the physics of both geometries at low energies, which originate from strong spin-fluctuations, and the differences at high energies, where the unscreened local moment of the KQD does not have a counterpart in the open structure of a QPC.

In chapter 6 we present the paper Bauer et al. (2014), where we give a detailed description of the fRG approach we used to calculate physical properties of the 1D model at zero temperature and zero source-drain voltage - the coupled ladder approximation (CLA). In order to treat the inhomogeneity of the potential at intermediate interaction strength with due accuracy we have to include the flow of the two-particle vertex γ_2. The CLA reduces the independent variables of γ_2 to a manageable amount, while including the leading second order frequency-, and space-dependence of the vertex.

Chapter 7 is based on the manuscript Goulko et al. (2014), where we extend the 1D model of a QPC by a term modelling the effect of (Rashba) spin-orbit interactions (SOI). We investigate the influence of intermediate and strong SOI both in the absence and presence of EEI. We find striking features caused by an interplay of SOI and EEI that predict the outcome of future experiments.

In the article Heyder (2014), reprinted in chapter 8, we present a detailed discussion of the SOPT approach, which we use to calculate conductance of the 1D model at finite excitations. Additionally, we present a Keldysh-based derivation of the linear conductance formula formerly derived by Oguri (2001) in Matsubara formalism.

In chapter 9 we present an experiment in order to measure the magnetization of a QPC with the help of Faraday rotation technique. The future results will be used to shed further light on the *van-Hove ridge scenario*.

Chapter 2

Electronic transport in one-dimensional systems

In this chapter we provide the necessary background for an understanding of electronic transport in one-dimensional (1D) systems.

We highlight the derivation of the conductance formula of 1D and quasi 1D fermionic systems by Landauer (1957), with special focus on the relation between the velocity of the electrons and the local density of states (LDOS). In order to facilitate the interpretation of subsequent experimental results we present explicit formulas for the conductance of 1D systems as function of magnetic field B, temperature T and voltage V_{sd}.

We discuss properties of quasi low-dimensional systems, where the movement of electrons is severely restricted in some directions, invoking discrete transverse modes, that act as transport channels. We introduce two of the main experimental realizations of quasi low-dimensional systems: The two-dimensional electron system (2DES), a quasi 2D system forming at the heterojunction between two semiconducting materials, and the one-dimensional quantum point contact (QPC), a narrow 1D constriction manufactured by applying negative voltage V_g to metallic gates above the 2DES. As function of increasing V_g, corresponding to increasing constriction width, one after another transport channel opens up and the QPC famously features a linear conductance staircase in units of the conductance quantum $G_Q = 2e^2/h$, with electron charge e and Planck's constant $h = 2\pi\hbar$.

Experiments show an additional shoulder-like structure at around $0.7G_Q$ in the so called *sub-open* regime. This famous *0.7 anomaly* is induced by mutual interactions between the electrons in a narrow QPC. Its origin has been subject to controversial discussions for almost twenty years now. We show key features of this conductance anomaly and compare experimental data to noninteracting predictions.

2.1 Noninteracting transport in 1D

Throughout this section we consider an infinite one-dimensional spinful noninteracting fermionic system in thermal equilibrium with temperature T. A scheme can be found in Fig. 2.1. The system is composed of three parts: Two semi-infinite homogeneous regions, the left lead L and the right lead R, are coupled via a central region C, where we allow for single particle scattering at an arbitrary spin-dependent ($\sigma \in \{\uparrow,\downarrow\} = \{+,-\}$) potential landscape $V^\sigma(x)$. This introduces an energy-, and spin-dependent transmission $\mathcal{T}^\sigma(\varepsilon)$, which describes the probability that an electron with energy ε and spin σ traverses the central region (as a textbook example consider the transmission through a 1D square well potential). The occupation of the lead $s \in \{L, R\}$ is given by the Fermi function

$f_s(\varepsilon) = [1 + \exp((\varepsilon - \mu_s)/(k_B T))]^{-1}$, with Boltzman constant k_B and chemical potential μ_s. The homogeneous leads harbor plane wave eigenstates with kinetic energy $\varepsilon = \hbar^2 k^2/(2m)$, where k is the wave number and m the electron's mass.

2.1.1 The relation between the electron's velocity and the LDOS in 1D

An electron traverses a lead with semiclassical velocity

$$v(\varepsilon) = 1/\hbar \cdot d\varepsilon/dk. \tag{2.1}$$

Once it enters the central region it is either reflected at the potential barrier or overcomes the obstacle and leaves into the other lead. According to its direction of motion we refer to an electron as a right mover ($k > 0$) or left mover ($k < 0$). Since the leads are one-dimensional they feature an inverse proportionality between the LDOS per spin species and the velocity of the electrons:

$$\mathrm{LDOS}(\varepsilon) = 1/\pi \cdot dk/d\varepsilon = \frac{1}{\pi\hbar v(\varepsilon)}. \tag{2.2}$$

In other words, the LDOS is proportional to the time an electron with energy ε spends in the vicinity of a given position. With the energy dependence of velocity and LDOS cancelling each other, note that the number of particles that traverse a lead s at given energy ε is proportional to the Fermi distribution $f_s(\varepsilon)$.

2.1.2 The current through a 1D system

In order to calculate transport properties of the system, we consider the out-of-equilibrium situation $\mu_L \neq \mu_R$, which amounts to a finite source-drain voltage $V_{sd} = (\mu_L - \mu_R)/e$. Here, the occupation of the left lead differs from the occupation of the right lead and the resulting imbalance in the number of right and left movers generates a current J through the system. The number of right/left movers that leave the left/right lead via the central region at given energy ε per time unit is given by

$$\dot{n}_s(\varepsilon) = f_s(\varepsilon) \cdot \mathrm{LDOS}(\varepsilon)/2 \cdot v(\varepsilon) = \frac{f_s(\varepsilon)}{2\pi\hbar} = \frac{f_s(\varepsilon)}{h}, \tag{2.3}$$

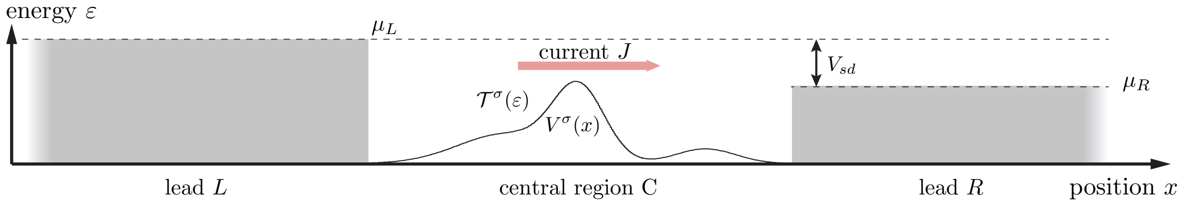

Figure 2.1: *1D system:* The semi-infinite and homogeneous leads L and R are connected via a central scattering region C, where traversing electrons are scattered at a spin-dependent potential barrier $V^\sigma(x)$. A finite voltage V_{sd} drives a current J through the system, which features a quantized conductance $G = dJ/dV_{sd}$.

where we accounted for the definite direction of the electrons by dividing the LDOS by a factor of 2. Since charge current is defined as the net particle transfer between the two leads per time unit, i.e. the net particle transfer through the central region per time unit, we have to account for the scattering processes at the potential landscape (via $\mathcal{T}^\sigma(\varepsilon)$) and integrate over all energies. This yields the simple current formula

$$J = e\sum_\sigma \int_{-\infty}^{\infty} d\varepsilon[\dot{n}_L(\varepsilon) - \dot{n}_R(\varepsilon)]\mathcal{T}^\sigma(\varepsilon) = \frac{e}{h}\sum_\sigma \int_{-\infty}^{\infty} d\varepsilon[f_L(\varepsilon) - f_R(\varepsilon)]\mathcal{T}^\sigma(\varepsilon). \tag{2.4}$$

Note that J vanishes trivially in equilibrium.

2.1.3 The quantized conductance of a 1D system

We define the conductance G as the derivative of the current w. r. t. the bias voltage, $G = dJ/dV_{sd}$, and apply the voltage in a symmetric fashion, $\mu_L = \mu + eV_{sd}/2$ and $\mu_R = \mu - eV_{sd}/2$. Since the transmission probability is an intrinsic property of the central region (hence not dependent on the chemical potentials in the leads) the voltage derivative acts on the Fermi functions only and the conductance of the system reads

$$G = dJ/dV_{sd} = -\frac{e^2}{2h}\sum_\sigma \int_{-\infty}^{\infty} d\varepsilon\; [f_L'(\varepsilon) + f_R'(\varepsilon)]\mathcal{T}^\sigma(\varepsilon), \tag{2.5}$$

where we introduced frequency derivatives $f_s'(\varepsilon) = df_s(\varepsilon)/d\varepsilon$. For fixed potential landscape the conductance $G(V_{sd}, B, T)$ is a function of magnetic field B, temperature T and voltage V_{sd}. Let us briefly discuss its properties when varying one parameter, while setting the other two to zero. In order to keep notation compact we use $G(B) = G(V_{sd} = 0, B, T = 0)$. Furthermore, we introduce the conductance quantum,

$$G_Q = 2e^2/h, \tag{2.6}$$

and the dimensionless conductance $g = G/G_Q$. In equilibrium, $V_{sd} = 0 \Rightarrow f' := f_L' = f_R'$, the linear conductance is given by

$$g(B,T) = -\frac{1}{2}\sum_\sigma \int_{-\infty}^{\infty} d\varepsilon\; f'(\varepsilon)\mathcal{T}^\sigma(\varepsilon). \tag{2.7}$$

Contributions to the conductance are limited to an energy-window of width of the temperature around the chemical potential μ, where the derivative of the fermi function is non-zero. In absence of a magnetic field, the spin degrees of freedom are degenerate, $\mathcal{T}^\uparrow(\varepsilon) = \mathcal{T}^\downarrow(\varepsilon)$, and the temperature-dependent conductance reads

$$g(T) = -\int_{-\infty}^{\infty} d\varepsilon\; f'(\varepsilon)\mathcal{T}(\varepsilon). \tag{2.8}$$

At zero temperature the Fermi function is a step function and its derivative the negative of the Dirac delta function, $\lim_{T\to 0} f'(\varepsilon) = -\delta(\varepsilon - \mu)$. This implies the remarkable fact, that the linear conductance of a noninteracting 1D system at $B = T = 0$ is identical to the transmission at the chemical potential,

$$g = \mathcal{T}(\mu). \tag{2.9}$$

Note that this is in direct consequence of the relation in Eq. (2.2). In case of perfect transmission the conductance is just given by the conductance quantum, $g = 1$.

A finite magnetic field lifts the spin degeneracy of the system. The field couples to the spin degree of freedom of the particles and shifts their energy by the Zeeman term $\sigma B/2$. Note, that in this definition spin-up is energetically favoured. It proves useful to absorb the Zeeman shift in the potential, $V^\sigma(x)=V(x-\sigma B/2)$. This implies, that a spin-down electron sees an increased and a spin-up electron a descreased potential. Hence, the transmission, $\mathcal{T}^\sigma(\varepsilon)=\mathcal{T}(\varepsilon+\sigma B/2)$, aquires a spin dependence, too, and we can write the linear conductance in presence of a finite magnetic field as

$$g(B)=\frac{1}{2}\sum_\sigma \mathcal{T}^\sigma(\mu)=\frac{1}{2}\left[\mathcal{T}(\mu-B/2)+\mathcal{T}(\mu+B/2)\right]. \tag{2.10}$$

Finally, at finite bias voltage but zero temperature and field, the conductance is given by the sum over the transmission through the central region evaluated at the chemical potentials of the two leads. In fact, the conductance is identical to the case of finite magnetic field with $B=V_{sd}$,

$$g(V_{sd})=\frac{1}{2}\left[\mathcal{T}(\mu_L)+\mathcal{T}(\mu_R)\right]=\frac{1}{2}\left[\mathcal{T}(\mu+V_{sd}/2)+\mathcal{T}(\mu-V_{sd}/2)\right]. \tag{2.11}$$

Throughout this thesis we will repeatedly refer to Eqs. (2.8)-(2.11) when discussing transport properties of our 1D quantum point contact model. The system is always assumed to be extended along the x-axis with the central region being centered at $x=0$. Whenever additional spatial dimensions are important they will be referred to as transversal and denoted by y and z.

Let us briefly summarize the main point of this section: The quantization of linear conductance is a fundamental property of 1D systems and direct consequence of the inverse proportionality between velocity and LDOS, Eq. (2.2). This involves, in particular, that the linear conductance at $B=T=V_{sd}=0$ is purely given by the transmission probability through the system at the chemical potential, Eq. (2.9).

2.2 Quasi 1D systems

In our world a system can never be purely one-dimensional. In order to design structures that test the predictions of 1D theory (such as the transport formulas Eqs. (2.8)-(2.11)), one has to minimize or preferably even eliminate the influence of the two other spatial dimensions y and z. This can be done by confining the particles with the help of an electrostatic potential, thereby considerably limiting their movement in the directions in question; upon narrowing down the size of a system, its boundaries become of increasing importance for its physical properties by imposing quantization conditions on eigenstates and eigenenergies. If the confinement is small enough, then the energy spectrum of the system along y and z can no longer be described by a continuum, as in the extended dimension x, but is rather given by a set of discrete quantum states, whose energy level spacing increases with further narrowing of the system (consider the standard example of a particle in a 1D box, where the distance between successive eigenenergies depends inversely quadratic on the width of the box). Time evolution is now nontrivial in x-direction only, which limits transport to 1D. There is simply no room for movement in any other direction. Such systems are called "quasi one-dimensional" (quasi 1D).

2.2.1 The effective potential of quasi 1D systems

The confined transverse world in a quasi 1D system has striking influences on its transport properties. Let us consider the following situation (for clarity we only consider one transverse dimension y): A right-moving electron, coming from an extended and homogeneous region with kinetic energy $\varepsilon(k_x)$ is about to enter a constriction C that is confined in all but the x-direction in consequence of an electrostatic potential $V(x,y)$ (see Fig. 2.2(a)). The narrowing happens adiabatically, i.e. the size of the system in transverse direction is a smooth and continuous function of x, with smallest width at $x=0$, and centered at $y=0$. Hence, the constriction hosts discrete transverse modes with position-dependent eigenenergies $\varepsilon_n(x)$, which increase with decreasing $|x|$ towards their maximum value at $x=0$. Upon approaching the constriction the electron starts to "feel" the influence of the boundaries: Unlike in the extended region, where its energy was purely kinetic and determined by the wave vector k_x, the electron now populates a quantum state, which divides its energy between a (with x slowly increasing) transverse energy $\varepsilon_n(x)$ and a (with x slowly decreasing) kinetic energy $\varepsilon(k(x)) = \varepsilon(k_x) - \varepsilon_n(x)$. In other words, the electron continuously slows down as it travels towards the center of the constriction, since the nearby boundaries act as an effective potential energy barrier, adding to the electrostatic potential $V(x) = V(x, y = 0)$. Hence, an electron that enters the constriction by population of the n-th transverse mode experiences an effective 1D potential barrier given by

$$V_n(x) = V(x) + \varepsilon_n(x), \tag{2.12}$$

involving a mode-dependent transmission probability $\mathcal{T}_n(\varepsilon)$. If the electron has enough energy to overcome the effective barrier, i.e. $\varepsilon(k_x) > V_n(0)$, then the transmission is close to one. Otherwise the electron is reflected in the vicinity of the classical turning point x_t, where $\varepsilon(k_x) = V_n(x_t)$, and the transmission is close to zero. This situation is depicted in Fig. 2.2(b), where the electron's energy is chosen such, that it can transverse the constriction only via the mode $n=1$, while being reflected in $n=2$.

2.2.2 The conductance of quasi 1D systems

We are now in a position to write down an extension of the 1D conductance formula (Eq. (2.5)) to quasi 1D systems. Since every transverse mode provides a 1D transport channel with potential barrier $V_n(x)$

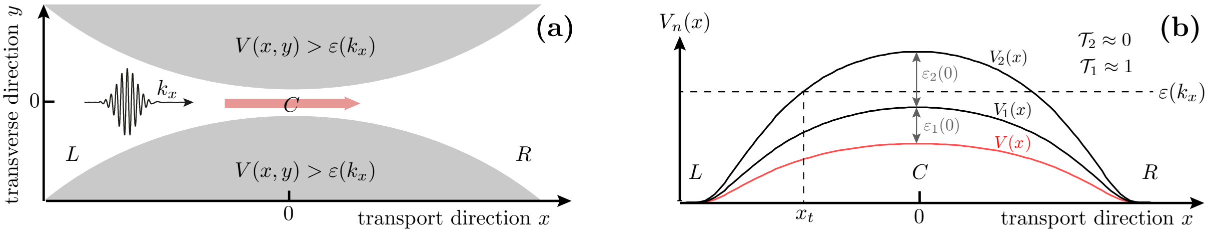

Figure 2.2: *1D constriction and effective 1D potential:* **(a)** Illustration of the constriction seen by an incoming right-moving electron with wave vector k_x. The grey-shaded areas mark regions that cannot be entered by the charge carrier due to an applied electrostatic potential $V(x, y)$, leaving only a narrow adiabatic transport channel centered at $y = 0$. **(b)** In addition to the electrostatic potential $V(x, y = 0)$ (red line) an electron experiences a potential energy $\varepsilon_n(x)$ when entering the constriction via the n-th transversal mode. This leads to a 1D effective barrier $V_n(x) = V(x) + \varepsilon_n(x)$ (black lines). In order to traverse the bottleneck via the transport channel n the charge carrier's energy must exceed the height of the corresponding effective barrier, $\varepsilon(k_x) > V_n(x = 0)$. In the scenario depicted here the electron will overcome the barrier when entering the constriction via the $n = 1$ mode, but is reflected at the classical turning point x_t, when entering it via the $n=2$ mode.

and transmission probability $\mathcal{T}_n(\varepsilon)$, the total conductance (for simplicity evaluated at $B = T = V_{sd} = 0$, see Eq. (2.9)) is given by the sum of all channel's contributions,

$$g = \sum_n \mathcal{T}_n(\mu). \tag{2.13}$$

Let us emphasize the peculiarity of this formula: The total number of electrons that enter the 1D constriction in a time unit is equally distributed among all transverse modes.

2.3 Experimental realization of low-dimensional systems

2.3.1 The 2-dimensional electron system (2DES)

Experimentally, the basis for the investigation of 1D properties is the so called two-dimensional electron system (2DES). Here, electrons are free to move in two dimensions (x and y) but are trapped in the third one (z), where they occupy the localized ground state mode only. 2DES can be realized in different ways: A metal-oxide-semiconductor field-effect transistor (MOSFET) in inversion mode has a strongly confined layer of electrons at the semiconductor-oxide junction [Pierret (1983)], some materials and liquids (most prominent liquid helium) can confine electrons at their surface [Sommer (1964)], graphene is facricated to be only one or few atomic layers thick [Geim (2009)]. In our nature publication [Bauer et al. (2013)] the group of Stefan Ludwig uses a high-electron-mobility transistor (HEMT) to form a 2DES of high mobility. The probe includes a heterostructure, i.e. adjacent layers of two semi-conductor materials with different band gaps, here undoped gallium arsenide (GaAs) and n-doped aluminum gallium arsenide (AlGaAs). The small intermediate region (heterojunction) at the interface between the two materials is characterized by a rectangular shaped potential minimum (on the GaAs side) - a so called quantum well - , that hosts a discrete spectrum in the direction perpendicular to the layers. Electrons drop from the AlGaAs layer into the quantum well and subsequently form a 2DES which features a high electronic density of $1.9 \times 10^{11}\mathrm{cm}^{-1}$.

The electronic movement in a 2DES is naturally subject to constraints due to lattice properties and will be hindered by several factors: While electron-phonon scattering can be somewhat limited by cooling the system, impurity scattering (e.g. at dopant atoms or imperfections) naturally sets a limit to the mean free path of the electrons and thus on the mobility of the charge carriers. In order to guarantee a systematic investigation of fundamental transport properties of low dimensional systems one has to ensure quasi-ballistic transport by restricting the system size to below the mean free path. In 2DESs formed within a GaAs/AlGaAs heterostructures the mean free path of the electrons is usually of the order of several microns.

2.3.2 The quantum point contact (QPC)

Adding metallic gates on top of the heterostructure enables further restriction to the movement of electrons within the 2DES. Applying negative voltage to these gates generates repulsive electrical force on the charge carriers and leads to a local depletion of the 2DES underneath the gates. Electronic movement in the 2DES is now constrained by an electrostatic potential landscape $V(x, y)$, that is governed by the shape of the gates and the strength of the voltage. The control of this potential via these external metallic gates allows for a fine-tuning of the geometry of the resulting low-dimensional system.

The split-gate geometry

A particular simple arrangement is the split-gate structure, which is illustrated in Fig. 2.3(a). Two gates (oriented along y) face each other some hundred nanometers apart. Applying the negative gate voltage

$V_g \approx -1$V (volt) to them devides the 2DES into two electron reservoirs, usually referred to as the leads. Electronic transport between these is now restricted to a short and narrow constriction in between the gates - the quantum point contact (QPC) -, which harbors a discrete spectrum of transverse modes due to its small extension in y direction (see Fig. 2.3(b) for an illustration of the electrostatic potential and the transverse modes within the QPC).

Linear conductance of a QPC

Fig. 2.3(c) shows the first measurement of the linear conductance of a QPC as function of gate voltage performed by van Wees et al. (1988). Increasing the gate voltage (in other words make it less negative) widens the QPC as the influence of the gates on the 2DES weakens. This causes a decrease of the transverse eigenenergies, such that one after another 1D effective barrier top $V_n(0)$ is shifted from above through the chemical potential, leading to a stepwise increase in linear conductance by G_Q. Thus, the measurement corroborates the prediction of Eq. (2.13) and is an impressive confirmation of Laudauers transport theory in quasi 1D.

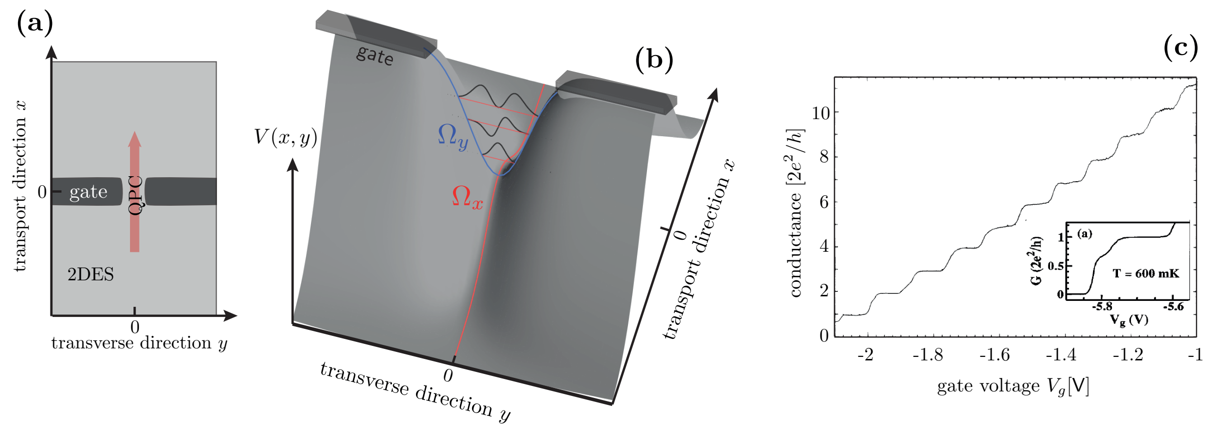

Figure 2.3: *Quantum point contact and the 0.7 anomaly:* **(a)** Split-gate geometry: A negative voltage V_g, applied to two adjacent metallic gates, depletes the 2DES underneath and restricts electronic transport between the leads to the QPC. **(b)** A sketch of the electrostatic potential $V(x,y)$ of a QPC, including discrete eigenstates due to the small extension in transverse direction. In the vicinity of the QPC's center, $x = y = 0$, the potential can be approximated by a saddle point form with curvatures in transport and tranverse given by the two energy scales Ω_x and Ω_y, see Eq. (2.14). **(c)** The linear conductance of a QPC as function of gate voltage features a staircase in units of the conductance quantum G_Q, the hallmark of transport in quasi 1D systems. The data was taken from van Wees et al. (1988). **(inset)** The additional shoulder-like step in the linear conductance of the lowest subband - the *0.7 anomaly* - is interaction-induced and its origin still subject to controversal discussions. The figure is taken from Thomas et al. (1996).

The electrostatic and effective potential of a QPC

The electrostatic potential in the vicinity of the QPC's center ($x = y = 0$) can be approximated by the parabolic saddle point form

$$V(x,y) = V_0 + \frac{m}{2\hbar^2}\Omega_y^2 y^2 - \frac{m}{2\hbar^2}\Omega_x^2 x^2, \tag{2.14}$$

where the height V_0 is roughly linear in gate voltage V_g, while the curvatures Ω_x and Ω_y show only weak dependence on V_g. This can be deduced from the almost constant step width and plateau length (the former determined by Ω_x, the latter by Ω_y, see Sec. 3.1) over a significant range of gate voltage in the staircase data of Fig. 2.3(c). In fact this form comes not as a surprise: The gates are usually far enough above the 2DES (typically $\sim 100\text{nm}$) to form a smooth potential landscape. As illustrated in Fig. 2.3(b), their symmetric arrangement naturally causes a potential maximum in transport direction and a potential minimum in transverse direction at the QPC's center, $x = y = 0$, and a leading order expansion directly yields Eq. (2.14). Its validity is guaranteed if higher orders contribute for $|x| \gtrsim \hbar/\sqrt{m\Omega_x}$ and $|y| \gtrsim \hbar/\sqrt{m\Omega_y}$ only. We note, that the saddle point ansatz for the electrostatic potential of a QPC is widely established and was used in a variety of theoretical works [e.g. Büttiker (1990), Sloggett et al. (2008), Lunde et al. (2009)].

The transmission through a QPC

As a consequence of the separation of the space variables x and y in Eq. (2.14), the 1D effective barriers of the transport modes of the QPC can be approximated by parabolic potentials

$$V_n(x) = V_{c,n} + \mu - \frac{m}{2\hbar^2}\Omega_x^2 x^2, \tag{2.15}$$

where the actual height, $V_{c,n} = V_0 + \varepsilon_n - \mu$ (here measured w.r.t. the chemical potential μ), is determined by the transverse quantum harmonic oscillator eigenenergy $\varepsilon_n = \Omega_y(n + 1/2)$. In Sec. 3 we present detailed calculations for transport through such a quadratic geometry both in the absence and presence of electron-electron interactions. In particular, one finds (Sec. 3.2.1 and e.g. Büttiker (1990)) that the transmission through a parabolic barrier is given by a smooth step function, whose width is determined by the curvature of the potential,

$$\mathcal{T}_n(\varepsilon) = \frac{1}{1 + \exp\left(2\pi(-\varepsilon + V_{c,n} + \mu)/\Omega_x\right)}. \tag{2.16}$$

By plugging this expression into the conductance formulas, Eqs. (2.8)-(2.11), we make noninteracting predictions for the conductance of the lowest subband ($n = 1$) of a QPC below (Sec. 2.4) and compare these to experimental data. This facilitates the identification of interaction-induced features and provides further insight into the physics of a QPC.

2.4 The 0.7 anomaly

In addition to the (by noninteracting theory predicted) quantized conductance plateaus at integer values of G_Q the data held a surprise for van Wees et al: The onset of the first plateau featured an additional shoulder-like step around $g \simeq 0.7$. At that time they attributed this unexpected and anomalous linear conductance behavior to an impurity effect and decided to show the data for the second and higher subbands [Kouwenhoven (2002)]. Nevertheless one can see an intermediate plateau forming at the left edge of Fig. 2.3(c).

It took eight years to fully realize that the occurence of this feature had not just been coincidence. One of the first works addressing the peculiar shoulder directly is Thomas et al. (1996); after "having observed this feature in many 1D constrictions" they concluded that it is an "intrinsic property" of narrow QPCs and worth further study. The inset of Fig. 2.3(c) shows a zoom-in on the first conductance step at intermediate temperatures. The linear conductance shows a distinctive shoulder-like step - the *0.7 anomaly*.

As a result of this remarkable finding experimentalists started to investigate the transport properties of narrow QPCs, tuned into the regime of the first conductance step, in more detail. They found a plethora of subsequent features, all of which seem to have a common interaction-induced origin and are collectively referred to as *0.7 anomaly*. Here, we present some of the most prominent characteristics of this anomaly. In order to illustrate what is commonly meant by the phrase "anomalous", we compare measurements to noninteracting predictions, where the electrostatic QPC potential is assumed to be of saddle point form (Eq. (2.14)), so that the lowest subband features an effective 1D parabolic potential of height $V_c = V_{c,1}$ (Eq. (2.15)). For a further in-depth topical review of experimental results and theoretical attempts at an explanation for the *0.7 anomaly* we refer to Micolich (2011).

2.4.1 Evolution of the 0.7 anomaly with magnetic field

One of the key features of the *0.7 anomaly* is its evolution with an increasing magnetic field $\vec{B}$. In order to avoid coupling to the orbital motion of the electrons, which would involve orbital effects, the field is oriented in the plane of the 2DES, $B_z = 0$. Hence, it couples to the spin degree of freedom of the charge carriers only and can be described by a Zeeman term. The noninteracting conductance at finite field, but $T = V_{sd} = 0$, can be calculated with Eq. (2.10), which predicts a symmetric splitting of the conductance step into two spin resolved sub-steps, see Fig. 2.4(a), separated by the Zeeman energy $\Delta E = \mathrm{g}\mu_B B$, where g is the material dependent bulk g-factor and μ_B the Bohr magneton. The physical mechanism for this behavior is quite simple: A finite magnetic field lifts the spin degeneracy of the transverse modes; each two modes that formerly (at $B = 0$) belonged to the same energy level are now spin-polarized, separated by ΔE and successively populated/depopulated upon increasing/decreasing the gate voltage. This causes a doubling of steps in the staircase.

A typical measurement of the magnetic field dependence of the lowest linear conductance step (Fig. 2.4(b) presents conductance measurements of a QPC embedded in a GaAs-AlGaAs heterostructure performed by Koop et al. (2007)) shows several trends that cannot be explained by noninteracting theory: While the step indeed develops into two sub-steps with increasing B it does so in striking asymmetric fashion: On the one hand the shape of the conductance in the *pinch-off* regime ($g < 0.5$) is hardly affected by the field. On the other hand, the *sub-open* regime ($0.5 < g < 1$) features a strong negative magnetoconductance, which conveys the impression that the *0.7 anomaly* develops "from above" into the spin-resolved conductance steps. In addition, the energetic splitting of the transverse modes is found to be much larger than expected. In fact, the literature shows several mentionings of g-factor enhancements of up to a factor of 6 [Thomas et al. (1998), Koop et al. (2007)]. Since the *0.7 anomaly* at zero magnetic field looks like a remnant of the spin-split scenario at large fields Thomas et. al. speculated that it might be attributed to spontaneous spin polarization which exists in the QPC even in absence of an applied magnetic field. An experimental study that argues to have found further evidence for spin polarization at zero field is given by Rokhinson et al. (2006), a theoretical model promoting this picture is presented by Wang and Berggren (1998).

2.4.2 Evolution of the 0.7 anomaly with temperature

The most prominent manifestation of many-body physics in a QPC is revealed by measurements of the temperature dependence of the lowest conductance step. As in the case of magnetic field we consider the

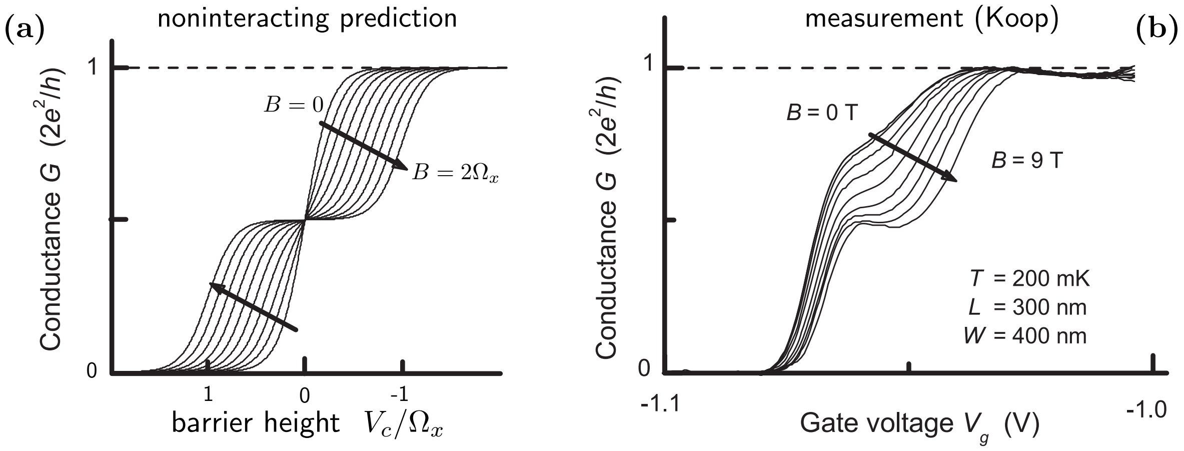

Figure 2.4: *Magnetic field dependence of the first conductance step:* **(a)** The noninteracting conductance of a parabolic barrier as function of barrier height V_c (corresponding to gate voltage V_g, see Eq. (2.15)) for several values of magnetic field B. Upon increasing the magnetic field, spin degeneracy of the system is lifted, resulting in a symmetric double step of width B (the conversion factor $g\cdot\mu_B$ is absorbed in the magnetic field). **(b)** Measurement of the linear conductance of a QPC embedded in a GaAs-AlGaAs heterostructure performed by Koop et al. (2007). Upon increasing the magnetic field, the *0.7 anomaly* develops from above into the spin-resolved conductance steps. Analysis of the sub-band splitting reveals an interaction-induced enhancement of the g-factor.

single particle situation first, see Fig. 2.5(a): According to Eq. (2.8) we expect finite temperature to smear out the conductance step by convolution of the transmission with the derivative of the Fermi function; at nonzero temperature a fraction of the charge carriers is excited to energies above the chemical potential, which in turn leaves some states below μ unoccupied. This predicts an increase of conductance in the pinch-off regime ($g < 0.5$) and a decrease of conductance in the sub-open regime ($g > 0.5$). This smearing of the conductance step should happen in symmetric fashion, i.e. the increase and decrease of conductance below and above the inflection point, $V_{c,1} = \mu$, should be identical.

Fig. 2.5(b) presents a typical measurement of the evolution of the first conductance step with increasing temperature. The experiment was performed in a QPC defined by split-gates within a GaAs-AlGaAs heterostructure by Thomas et al. (1996) and reveals striking discrepancies from the noninteracting prediction: While the conductance indeed decreases in the sub-open regime (and in fact much stronger than expected in absence of interactions), the pinch-off regime hardly reacts on the finite temperature. This feature is certainly very surprising and seems to counteract common physical intuition about what temperature usually does (namely to broaden structures, see above). While the anomalously strong reduction of conductance with temperature in the sub-open regime is considered the main feature of the *0.7 anomaly*, we want to emphasize, that the unusual lethargy of the step's onset concerning temperature is not less spectacular.

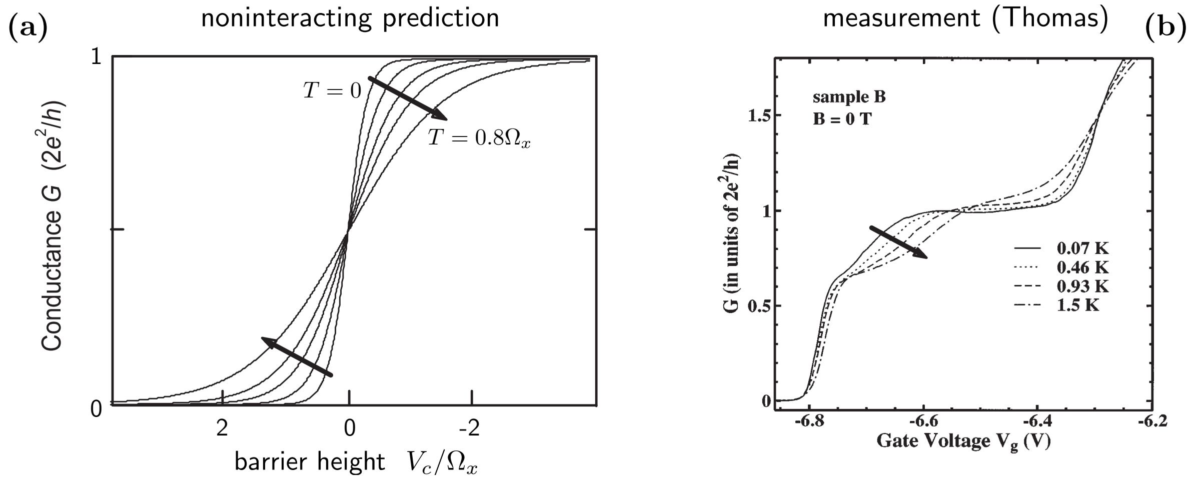

Figure 2.5: *Temperature dependence of the first conductance step:* **(a)** The noninteracting conductance of a parabolic barrier as function of barrier height V_c (corresponding to gate voltage V_g, see Eq. (2.15)) for several values of temperature T. Upon increasing the temperature, the conductance step is smeared out symmetrically on a scale set by T. **(b)** Measurement of the linear conductance of a QPC embedded in a GaAs-AlGaAs heterostructure performed by Thomas et al. (1996). In the region of the *0.7 anomaly* the conductance is anomalously strong suppressed by temperature. This invokes a pronounced shoulder-like step at intermediate temperatures of ~1K, which represents the most prominent distinctive feature of the *0.7 anomaly*. Note that the step is even more emphasized due to an unexpectedly weak reaction of the pinch-off conductance on temperature.

2.4.3 The zero-bias anomaly (ZBA)

Another famous feature of a narrow QPC appears in its differential conductance $g(V_{sd}) = dJ/dV_{sd}$. Fig. 2.6(a) shows the noninteracting differential conductance for several gate voltages corresponding to different positions within the first linear conductance step. According to Eq. (2.11) noninteracting theory predicts a peak at zero bias, $V_{sd}=0$, for the differential conductance in the sup-open regime and a dip for the differential conductance in the pinch-off regime. For large bias voltages the differential conductance is expected to saturate at $g(V_{sd})=0.5$.

Fig. 2.6(b) shows the corresponding experimental data from a measurement performed by Cronenwett et al. (2002). In contrast to the single-particle prediction the differential conductance features a narrow zero-bias peak (ZBP) throughout the whole spectrum of linear conductance, $0<g<1$, which can be subject to splitting in a magnetic field [Sarkozy et al. (2009), Ren et al. (2010)]. In addition, a saturation at large bias is usually observed at $g(V_{sd})\simeq 0.25$ [Chen et al. (2008)]. Since a ZBP is one of the key features of a quantum dot in the Kondo regime [van der Wiel et al. (2000)], the *0.7 anomaly* was associated with the formation of a local moment in the QPC [Rejec and Meir (2006)].

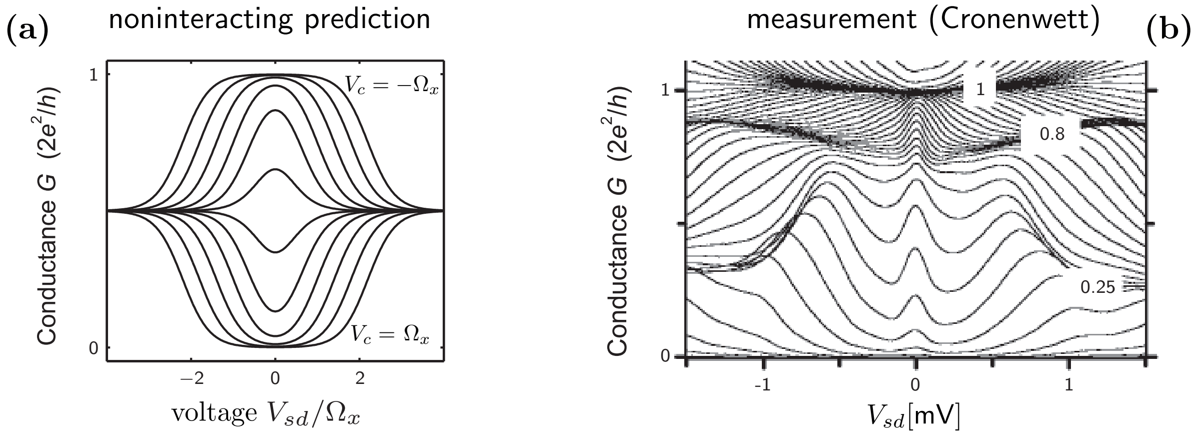

Figure 2.6: *Source-drain voltage dependence of the first conductance step:* **(a)** The noninteracting differential conductance of a parabolic barrier as function of bias voltage V_{sd} for several barrier heights V_c (corresponding to gate voltage V_g, see Eq. (2.15)). The differential conductance features a peak/dip in the sup-open/pinch-off regime at zero bias, $V_{sd} = 0$. For large bias voltages it saturates at $g(V_{sd}) = 0.5$. **(b)** Measurement of the differential conductance by Cronenwett et al. (2002), realized within a GaAs-AlGaAs heterostructure QPC. A narrow zero bias peak shows up over the whole range of gate voltages that correspond to the first conductance step. It is usually accompanied by finite-bias side peaks (here around $|V_{sd}| \simeq 0.7$mV). For large voltages, the differential conductance tends to saturate at values $g(V_{sd}) \simeq 0.25$.

2.4.4 Additional features

The presence of a many-body interactions in a narrow QPC manifests itself in various other transport and local thermodynamic properties. We list some notable measurements here, but make no claim of completeness. DiCarlo et al. (2006) report an asymmetric shot noise factor, that is anomalously reduced relative to its noninteracting value when a QPC is tuned in the regime of the 0.7 anomaly. They attribute their finding to a spin-gap, i.e. an energetic splitting of spin-up and spin-down states that grows linearly with the density in the constriction. Compressibility measurements by Smith et al. (2011) show minima associated with the 0.7 anomaly, indicating that the shoulder-like 0.7 anomaly might be accompanied by a plateau-like feature in the density of a QPC as function of gate voltage. Appleyard et al. (2000) report that the thermopower, i.e. the voltage induced by a finite temperature gradient between source and drain, is almost constant in the regime of the 0.7 anomaly.

2.5 Conclusion and outlook

In this chapter we discussed general properties of fermionic transport through 1D systems. We saw that the inverse proportionality between the electron's velocity and the $LDOS$ involves a quantized linear conductance. This peculiar property of 1D (and quasi 1D) systems is highlighted by the linear conductance staircase of a QPC. We introduced the *0.7 anomaly*, an additional shoulder-like step in the sub-open regime of the first subband linear conductance. Its existance at $B = T = V_{sd} = 0$, as well as its anomalous evolution with those external parameters strongly suggests an interaction-induced mechanism as its origin, which is, to date, still subject to controversial discussion. In order to investigate a QPC in the regime of the *0.7 anomaly*, we will continue this thesis by establishing a 1D model of a QPC in the next section.

Chapter 3

The origin of the 0.7 anomaly

In Sec. 2.3.2 we argue that the electrostatic potential of a typical QPC can be approximated by a saddle-point form. As a result, the effective 1D barrier of a given subband features a parabolic barrier top

$$V(x) = V_c + \mu - \frac{m}{2\hbar^2}\Omega_x^2 x^2, \tag{3.1}$$

where the barrier height V_c is measured w. r. t. the chemical potential μ. In order to further validate this conjecture we analyze linear conductance data from the group of Stefan Ludwig (Sec. 3.1): We introduce the experimental setup (Sec. 3.1.1), which features a particularly high tunability of the QPC potential. In Sec. 3.1.2 we investigate the shape of the conductance step of a higher QPC subband ($n = 3$), which, as we argue, can be explained predominantly within noninteracting theory. This allows for a direct comparison with exact numerical calculations. We show that the absence of Fabri-Perot oscillations in the plateau and the smooth shape of the step are strong indications for the applicability of Eq. (3.1). A subsequent comparison between the $n = 1$ and $n = 3$ conductance step in Sec. 3.1.3 reveals that the influence of interactions on the shape of the lowest subband step (at $B = V_{sd} = 0$ and a temperature T below all relevant energy scales) is mostly limited to the so-called "sub-open regime", defined by linear conductance values of $0.5 \lesssim g \lesssim 0.9$.

In order to provide a detailed understanding for the physics of a parabolic barrier we discuss its noninteracting properties in Sec. 3.2. We calculate transport through the barrier in Sec. 3.2.1. As introduced in Eq. 2.16 the transmission features a smooth, symmetric step, centered at the barrier height $V_c + \mu$ [Büttiker (1990)]. This explains the noninteracting conductance data shown in Sec. 2.4. A calculation of the local density of states of the barrier (Sec. 3.2.2) reveals a maximum just above the potential barrier (which we term "van Hove ridge"), which is a remnant of the 1D van Hove singularity in a homogeneous 1D system, smeared and shifted by the potential.

In Sec. 3.3 we introduce our interacting 1D model of a QPC (Sec. 3.3.1). We argue that many-body effects in a QPC are described sufficiently well by short-ranged interactions in the vicinity of the barrier center. In Sec. 3.3.2 we briefly introduce main concepts of the functional renormalization group (fRG) and second order perturbation theory (SOPT), the two methods we use to treat those interactions. We discuss advantages and disadvantages of both approaches and state their range of validity. In order to illustrate why the effective strength of interactions in a QPC is governed by the $LDOS$ at the chemical potential in the barrier center we present a simple Hartree argument in Sec. 3.3.3. Finally, we show results for the conductance of our interacting model of a QPC, that are in striking qualitative agreement with experimental data by Stefan Ludwigs group. We argue that the *0.7-anomaly* is due to the van Hove ridge, which brings about an enhanced possibility of backscattering and a subsequent reduction of conductance in the sub-open regime in the presence of interactions.

3.1 Shape of the 1D effective barrier

In this section we analyze linear conductance data from an experiment performed by David Borowsky and Enrico Schubert in the group of Stefan Ludwig. Here, this data serves as representative of general properties of transport through a QPC. While some minor details might differ in other QPC geometries, the major conclusions in that section still express universal properties of QPCs.

3.1.1 Experimental setup

Fig. 3.1(a) shows a linear conductance staircase from the Ludwig experiment. Their QPC is defined by a gate structure of particular high tunability (see lower inset): Unlike in the usual split-gate setup (Sec. 2.3.2), here a total of three pairwise adjacent gates manipulate the electrostatic potential in the 2DES via voltages V_c and V_s. An additional large global top-gate controls the chemical potential in the vicinity of the gates and hence in the QPC. This setup is taylor-made to vary both the length and the width of the constriction independently. In particular, it can be used for a fine-tuning of the electrostatic potential, in order to exclude spurious effects of geometry or impurities. All experimental results for a QPC presented in our publications were measured within this setup. In the publication Heyder et al. (2014) this probe was additionally used to study the crossover from a QPC with *0.7 anomaly* to a quantum dot featuring Kondo physics.

3.1.2 The parabolic 1D barrier

As we discuss in Sec. 2.2.2 the staircase can be explained within Landauer's transport theory, i.e. without considering interactions. This is particularly true for a wide QPC, where the charge carriers can somewhat avoid coming too close within the constriction and where screening, i.e. the rearrangement of charge in order to counteract interactions, is strong due to the population of several transport modes. Here, traversing electrons are mostly unhampered by the presence of other electrons in the QPC (interaction effects will mostly manifest in an overall Hartree shift of the higher conductance steps). Hence, the shape of the linear conductance of higher subbands (unlike the first step, which features strong electron-electron interactions in the form of the *0.7 anomaly*) is reasonably well approximated by noninteracting theory [1]. Since single-particle transport through an arbitrary shaped 1D potential barrier can be calculated exactly using numerically, this provides an opportunity to learn more about the geometry of the 1D effective barrier in a QPC: Fig. 3.1(b) shows the linear conductance step of the $n = 3$ subband. It exhibits a smooth step and a flat plateau as function of gate voltage V_g. Since the temperature of the electrons in the 2DES is extremely low ($T \sim 30mK$), this curve is basically identical to the hypothetical zero temperature case. In Fig. 3.1(c) we show the noninteracting conductance of various 1D potential geometries, defined via their leading order p around the barrier top,

$$V(x) = V_c + \mu - \Omega_x \left(\frac{x}{l_x}\right)^p, \tag{3.2}$$

with characteristic length $l_x = \hbar/\sqrt{2m\Omega_x}$. Note, that the potential broadens with increasing p, corresponding to a flattening of the barrier top. While a parabolic barrier features a symmetric and smooth conductance step - in beautiful agreement with the experimental measurement - all other geometries exhibit conductance curves with Fabri-Perot type resonances in the plateau and somewhat skewed step shapes. This simple analysis adds evidence to the assumption that the electrostatic potential of "our"

---

[1] We note, that weaker manifestations of the 0.7 anomaly have been observed in higher subbands also. Still, they are observed somewhat less frequently, thus not contradicting with our general argument.

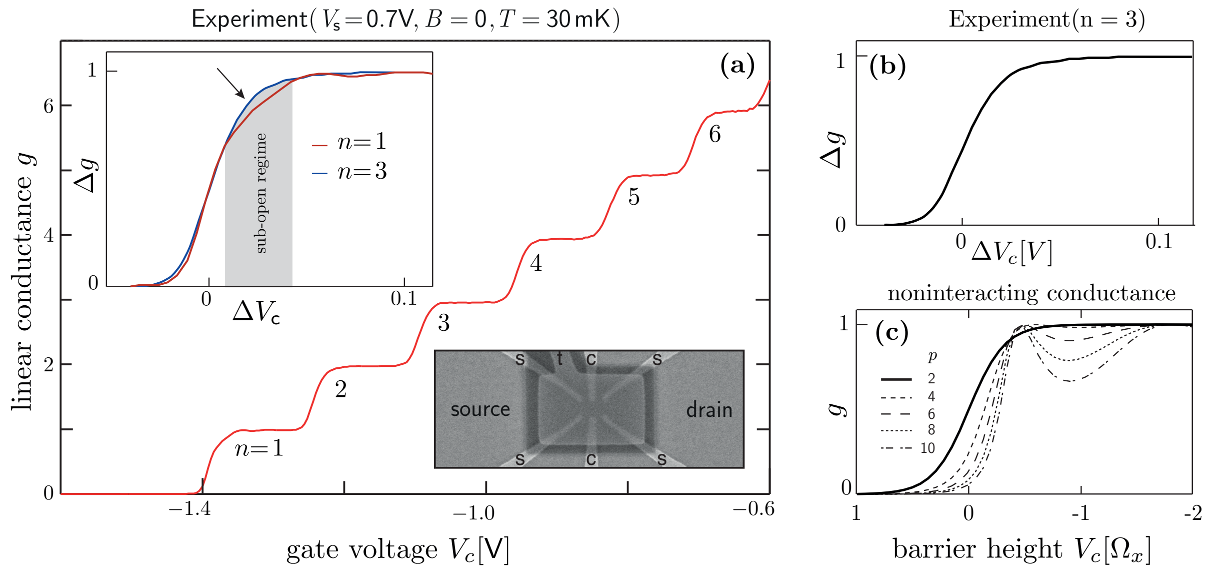

Figure 3.1: *Shape of conductance step and sub-open regime:* **(a)** Measurement of the linear conductance by the Ludwig group. The data features both the typical linear conductance staircase as well as a weak *0.7 anomaly* in the conductance of the first subband. The lower inset shows the gate structure of the probe, defining the QPC. Six pairwise adjacent gates allow for a particularly high tunability of the electrostatic potential. An additional global top-gate can be used to manipulate the chemical potential in the QPC region. The upper inset shows a comparison between the $n=1$ and $n=3$ step, highlighting the interaction-induced modulation of conductance in the sub-open regime. **(b)** A zoom-in on the smooth $n=3$ linear conductance step. **(c)** Linear conductance as function of barrier height V_c, calculated for several potentials defined via Eq. (3.2). Comparison with **(b)** corroborates the picture, that the effective 1D potential features a parabolic ($p=2$) barrier top.

QPC is of saddle-point form and, in particular, supports the subsequent picture that its 1D barrier is parabolic near the center.

Let us close this section with some conclusive remarks: Under certain circumstances QPCs can feature non-parabolic 1D barrier tops aswell. This can happen both in very short and very long QPCs (detailed discussion can be found in Heyder et al. (2014)) or in consequence of a nearby impurity, which influences the shape of the electrostatic potential beyond control. We argue, though, that properties of interaction-induced signatures should be investigated preferably in QPCs that are tuned to feature a parabolic barrier top, where the noninteracting linear conductance is a smooth function of gate voltage without any resonances. This allows for a clear distinction between single-particle and many-body physics and facilitates the search for the underlying mechanisms. Measurements in different geometries, where Fabri-Perot resonances show up even without interactions, can cause misleading conclusions concerning the origin of signatures in the conductance. For a further in-depth analysis on the implication of the QPC's geometry on both transport and local properties we refer to our publication Heyder et al. (2014).

3.1.3 The distinctiveness of the sub-open regime

Upon narrowing the QPC (by decreasing the gate voltage) the influence of many-body processes on its physics increases; particles are now forced to come closer as they traverse the QPC, feeling their mutual presence more and more. In fact, explicit calculations show [Lunde et al. (2009)], that the effective strength of interactions scales as $1/l_y$ within a saddle-point potential[2]. Interactions manifest particularly strong in a QPC narrowed down to a width where only one mode contributes to the conductance. Here, in the lowest subband, they cause the *0.7 anomaly*. But even in an almost pinched-off QPC, we find that most of the measured conductance curve, at $B = V_{sd} = 0$ and sufficiently small T, seems to be in agreement with noninteracting theory and that interactions modify the shape of g primarily at the onset of the first step. To illustrate this point we compare the measured conductance of the $n = 1$ (where the QPC is narrow and interactions are "strong") and the $n = 3$ subband (where the QPC is wide and interactions are "weak") in the inset of Fig. 3.1(a). For best comparison we shifted the two curves in gate voltage to conincide near $g = 0.5$. The $n = 1$ conductance features a weak *0.7 anomaly* due to electron-electron interactions, which is clearly absent in the conductance of the wider QPC . Yet, the overall shape of both conductance steps is remarkably similar and the many-body feature in the first subband is somewhat limited to the sub-open regime ($0.5 \lesssim g \lesssim 0.9$), where it can be interpreted as an interaction-induced reduction of the noninteracting conductance curve, caused by the strong confinement of the QPC's geometry. Of course, phenomena caused by interactions can survive until deep in the pinch-off regime ($g \ll 0.5$, see Sec. 2.4), but the modulation of conductance even at negligible excitation energies highlights the sub-open regime as the home of the *0.7 anomaly*.

In order to understand why the sub-open regime of the first conductance step plays a distinctive role in the transport through a QPC, we continue by applying the following strategy: We investigate the physics of a parabolic barrier in absence of interactions first (Sec. 3.2) and add interactions on a later stage (Sec. 3.3). Such a procedure allows to distinguish many-body effects from the more "trivial" single-particle physics and helps to classify the role of interactions in detail.

3.2 Non-interacting physics of a parabolic barrier

Predictions of noninteracting theory are important benchmarks for experiments in a QPC; in order to identify a measured effect as interaction-induced it is essential to first eliminate the possibility that an explanation within noninteracting theory exists. Otherwise one might draw incorrect conclusions about the origin of a feature. Hence, we devote this section to the single-particle physics of a parabolic barrier, with the goal to provide both understanding and intuition for the underlying mechanisms.

We present analytic derivations for noninteracting transport (Sec. 3.2.1) and local properties (Sec. 3.2.2), highlighting the transmission through the barrier (Eq. (3.10)) and the local density of states (LDOS) of the barrier (Eqs. 3.14-3.15). The transmission is a smooth function of energy, as also discussed in Sec. 2.3.2 and Sec. 3.1.2. The LDOS exhibits a maximum in the sub-open regime at the chemical potential as function of barrier height V_c [Sloggett et al. (2008)]. We will see in Sec. 3.3 that this structure is responsible for the anomalous conductance reduction that occurs in the presence of interactions.

To determine analytic expressions for physical quantities we use the following strategy: We solve the Schrödinger equation of the parabolic barrier Hamiltonian. The corresponding eigenstates describe left-, and right-moving electrons, that are subject to scattering at the potential. We present an asymptotic decomposition of the states in terms of an incident, a reflected and a transmitted partial wave [Bohr and Mottelson (1998)]. This representation then allows for a calculation of all desired physical quantities.

---

[2] Their result is somewhat preliminary though as they did non include screening.

3.2.1 The non-interacting transmission and conductance of a parabolic barrier

Here, we calculate noninteracting transport through a quadratic barrier, which is parametrized as in Eq. (3.1). We determine the transmission through the barrier, which then allows for a calculation of the conductance $g(B, T, V_{sd})$ via Eqs. (2.9)-(2.11).

In a classical, deterministic world the transmission would be a simple step function,

$$\mathcal{T}_{cl}(\varepsilon) = \begin{cases} 1, & \text{if } \varepsilon > V_c \\ 0, & \text{else.} \end{cases} \tag{3.3}$$

In particular, $\mathcal{T}_{cl}(\varepsilon)$ is determined by the potential height only and does not depend on the detailed shape of the barrier. In a quantum world, however, the barrier shape causes distinctive features in the transmission: Here, incident waves are subject to energy-dependent scattering at the potential and the resulting interference effects drastically change the transmission w. r. t. the simple classical case. We will now specify this for a parabolic barrier.

The physics of the quadratic potential barrier is described by the 1D Hamiltonian

$$\mathcal{H}_0 = -\frac{\hbar^2}{2m}\partial_x^2 + V(x) = -\frac{\hbar^2}{2m}\partial_x^2 + V_c + \mu - \frac{m}{2\hbar^2}\Omega_x^2 x^2. \tag{3.4}$$

Its geometry is defined by two scales: The energy Ω_x (defining the potential's curvature) and the harmonic oscillator length $l_x = \hbar/\sqrt{2m\Omega_x}$. Hence, a particle with large effective mass m sees a "short" barrier and vice versa. In order to keep notation clear we introduce the dimensionless position, barrier height and energies

$$\begin{aligned} \tilde{x} &= x/l_x, \\ \tilde{V}_c &= V_c/\Omega_x, \\ \tilde{\varepsilon} &= (\varepsilon - V_c - \mu)/\Omega_x, \\ \tilde{\varepsilon}_\mu &= (\varepsilon - \mu)/\Omega_x, \end{aligned} \tag{3.5}$$

Note that we measure the energy $\tilde{\varepsilon}$ w. r. t. the barrier maximum and the energy $\tilde{\varepsilon}_\mu$ (similar to the barrier height $\tilde{V}_c$) w. r. t. the chemical potential. The former simplifies the notation within the following calculations, since the barrier height determines the energy-dependence of the eigenfunctions of the Hamiltonian, Eq. (3.4). The latter proves useful, as the linear conductance (Eqs. (2.8)-(2.10)) is governed by particles with energy at (for temperature $T = 0$) or close to (for $T \neq 0$) the chemical potential.

The eigenfunctions $\psi(\tilde{\varepsilon}, \tilde{x})$ of the normalized Hamiltonian $\tilde{\mathcal{H}}_0 = \mathcal{H}_0/\Omega_x$ are given as solutions of the time-independent Schrödinger equation

$$[\partial_{\tilde{x}}^2 + \frac{1}{4}\tilde{x}^2 + \tilde{\varepsilon}]\psi(\tilde{\varepsilon}, \tilde{x}) = 0. \tag{3.6}$$

The parabolic potential describes an open structure, which does not confine electronic states to a finite region. Hence, the eigenstates of $\tilde{\mathcal{H}}_0$ form a continuous energy spectrum and are scattering states which cannot be normalized in the usual sense (in contrast to bound states in a confining geometry). Yet, we show in Sec. 3.2.2, that one can impose a normalization by semi-classical arguments, which then allows for an exact calculation of the $LDOS$ of the system.

Eq. (3.6) is known as Weber differential equation. Its solutions are given by

$$\begin{aligned}\psi_R(\tilde{\varepsilon},\tilde{x}) &= c(\tilde{\varepsilon})D(-1/2-i\tilde{\varepsilon},e^{i\pi/4}\tilde{x}),\\ \psi_L(\tilde{\varepsilon},\tilde{x}) &= c(\tilde{\varepsilon})D(-1/2+i\tilde{\varepsilon},e^{i\pi 3/4}\tilde{x}),\end{aligned} \tag{3.7}$$

where $D(a,z)$ is the parabolic cylinder function[3] and $c(\tilde{\varepsilon})$ is an energy-dependent prefactor (once again, $c(\tilde{\varepsilon})$ must be fixed in order to calculate local properties of the system, see Sec. 3.2.2 below). The upper solution of Eq. (3.7) describes scattering states incident from the left (right movers ψ_R), and the lower solution scattering states incident from the right (left movers ψ_L). As a consequence of the symmetry of the potential barrier in real space, $V(\tilde{x})=V(-\tilde{x})$, the two solution are related to each other by $\psi_R(\tilde{\varepsilon},\tilde{x}) = \psi_L^*(\tilde{\varepsilon},-\tilde{x})$, where the superscript * denotes the complex conjugate. This symmetry allows us to discuss all properties of the potential barrier in terms of the right movers only and refrain from an additional discussion of the left movers.

Since the right-moving wave function in Eq. (3.7) is a scattering state it is possible to decompose it in an incident wave $\phi_R^{in}(\tilde{\varepsilon},\tilde{x})$, a reflected wave $\phi_R^{re}(\tilde{\varepsilon},\tilde{x})$ and a transmitted wave $\phi_R^{tr}(\tilde{\varepsilon},\tilde{x})$. In fact one can find an asymptotic representation [Bohr and Mottelson (1998)] of the parabolic cylinder function

$$\begin{aligned}\lim_{\tilde{x}\to-\infty}\psi_R(\tilde{\varepsilon},\tilde{x}) &= c(\tilde{\varepsilon})[\phi_R^{in}(\tilde{\varepsilon},\tilde{x})+\phi_R^{re}(\tilde{\varepsilon},\tilde{x})],\\ \lim_{\tilde{x}\to\infty}\psi_R(\tilde{\varepsilon},\tilde{x}) &= c(\tilde{\varepsilon})\phi_R^{tr}(\tilde{\varepsilon},\tilde{x}),\end{aligned} \tag{3.8}$$

with

$$\begin{aligned}\phi_R^{in}(\tilde{\varepsilon},\tilde{x}) &= -\frac{(2\pi)^{1/2}}{\Gamma(i\tilde{\varepsilon}+1/2)}|\tilde{x}|^{i\tilde{\varepsilon}-1/2}\exp\left(-\frac{\pi\tilde{\varepsilon}}{4}+\frac{7i\pi}{8}+\frac{i}{4}\tilde{x}^2\right),\\ \phi_R^{re}(\tilde{\varepsilon},\tilde{x}) &= |\tilde{x}|^{-i\tilde{\varepsilon}-1/2}\exp\left(-\frac{3\pi\tilde{\varepsilon}}{4}+\frac{3i\pi}{8}-\frac{i}{4}\tilde{x}^2\right),\\ \phi_R^{tr}(\tilde{\varepsilon},\tilde{x}) &= \tilde{x}^{-i\tilde{\varepsilon}-1/2}\exp\left(\frac{\pi\tilde{\varepsilon}}{4}-\frac{i\pi}{8}-\frac{i}{4}\tilde{x}^2\right).\end{aligned} \tag{3.9}$$

Here, $\Gamma(z)=(z-1)!$ is the Gamma function. These forms can be obtained by a Wenzel-Kramer-Brillouin (WKB) approximation, which becomes exact in the asymptotic limit $|\tilde{x}|\to\infty$. The physical interpretation for the representation in Eq. (3.9) is straightforward: A right-moving incident wave is scattered at the potential barrier, leading to a reflected and a transmitted partial wave. This situation is depicted in Fig. 3.2(a) for a scattering state with energy close to $\tilde{\varepsilon}=0$ (i.e. close to the barrier height). Although we have not yet fixed the prefactor in Eq. (3.7), we can now calculate the transmission probability, which is simply given by the fraction of the transmitted waves' and the ingoing waves' modulus squared,

$$\mathcal{T}(\tilde{\varepsilon}) = \frac{|\phi_R^{tr}(\tilde{\varepsilon},\tilde{x})|^2}{|\phi_R^{in}(\tilde{\varepsilon},\tilde{x})|^2} = \frac{|\Gamma(1/2+i\tilde{\varepsilon})|^2}{2\pi}\exp(\pi\tilde{\varepsilon}) = \frac{\exp(\pi\tilde{\varepsilon})}{2\cosh(\pi\tilde{\varepsilon})} = \frac{1}{1+\exp(-2\pi\tilde{\varepsilon})}. \tag{3.10}$$

Hence, the transmission through a parabolic barrier, plotted in Fig. 3.2(b), has the functional form of a Fermi distribution function with "temperature" $\Omega_x/(2\pi)$, defining the step width. In comparison to the classical case (Eq. (3.3), dashed line in Fig. 3.2(b)) the transmission is reduced for $\tilde{\varepsilon}>0$ ($\tilde{\varepsilon}_\mu>\tilde{V}_c$), due to "above the barrier" scattering, and enhanced for $\tilde{\varepsilon}<0$ ($\tilde{\varepsilon}_\mu<\tilde{V}_c$), where quantum mechanical tunneling is possible. The classical case is reproduced in the limit $\Omega_x\to 0$.

We use Eqs. (2.9)-(2.11) to calculate the conductance as function of the barrier height $\tilde{V}_c$, for external parameters magnetic field $\tilde{B}=B/\Omega_x$, temperature $\tilde{T}=T/\Omega_x$ and source-drain voltage $\tilde{V}_{sd}=V_{sd}/\Omega_x$.

---

[3] see e.g. http://mathworld.wolfram.com/ParabolicCylinderFunction.html

Note, that $\mathcal{T}(\mu) = \mathcal{T}(\tilde{\varepsilon} = -\tilde{V}_c)$, since that implies $\tilde{\varepsilon}_\mu = 0$. The results are shown in Fig. 3.2(c). For a detailed discussion we refer to Sec. 2.4, where these calculations serve as comparison to the data of various measurements.

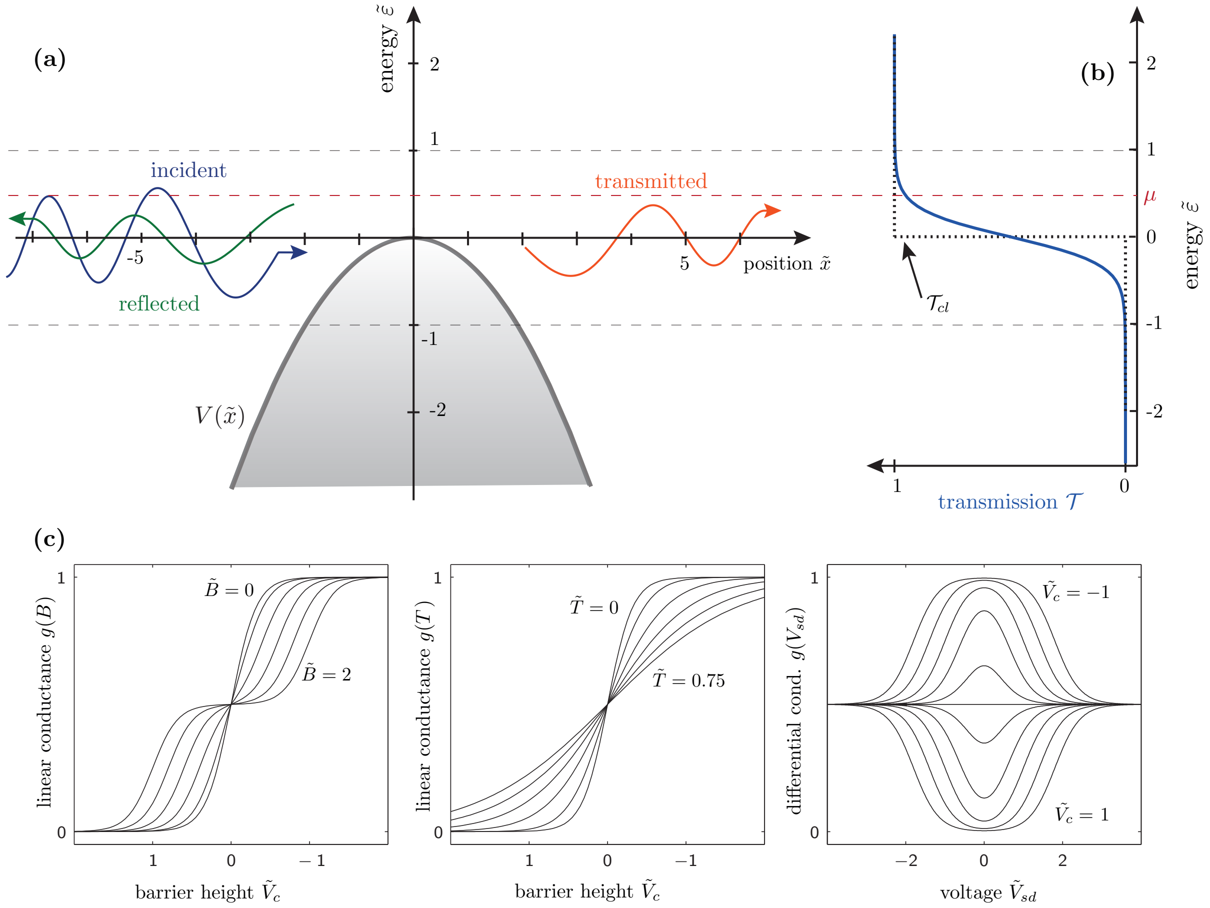

Figure 3.2: *Noninteracting transport through a quadratic barrier.* **(a)** Scheme of scattering at a quadratic potential barrier. The solution of the Schrödinger equation (Eq. (3.7)) can be decomposed into an incident, a reflected and a transmitted wave (Eq. (3.9)). **(b)** Energy-dependent transmission through the parabolic barrier (Eq. (3.10)). Quantum effects smear out the classical transmission function (dashed line) in symmetric fashion on a scale set by the potential curvature Ω_x. **(c)** The evolution of the noninteracting conductance of a parabolic barrier as function of gate voltage $\tilde{V}_c = V_c/\Omega_x$ with magnetic field $\tilde{B} = B/\Omega_x$, temperature $\tilde{T} = T/\Omega_x$ and source drain voltage $\tilde{V}_{sd} = V_{sd}/\Omega_x$, calculated via Eqs. (2.8)-(2.11). For a detailed discussion see Sec. 2.4.

3.2.2 The noninteracting LDOS of a parabolic barrier

Next, we turn the discussion to local properties of a parabolic barrier. We calculate and discuss the local density of states of the system, thereby placing special focus on energies close to the barrier top ($|\tilde{\varepsilon}| \lesssim \Omega_x$) and positions in the vicinity of the barrier center ($|\tilde{x}| \lesssim l_x$).

Again, let us briefly consider the situation in a classical world: Upon heading towards the barrier center a classical particle slows down as its kinetic energy converts gradually into potential energy. In the process, the velocity of the particle is purely determined by the local height of the potential, $v_{cl}(\varepsilon, x) = \sqrt{2(\varepsilon - V(x))/m}$. In particular, the particle stops at the barrier top, if its energy coincides with the barrier height.

We will now discuss how the situation changes in a quantum world. In order to calculate the LDOS of the system, we have to fix the energy-dependent prefactor of the scattering state in Eq. (3.7). Let us make some considerations first: The wave nature of a quantum state is especially of physical significance, if the wave is subject to interference; for instance, the physical properties of a plane wave in an infinite homogeneous system ($V(x) = 0$) can be described within classical theory by appropriate correspondence. This involves, that the local density of states of the homogeneous system is inverse proportional to the velocity of a classical particle, $\mathrm{LDOS}_{hom}(\varepsilon) = 2/(h\ v_{cl}(\varepsilon))$. This correspondence looses validity upon breaking translational invariance by adding an arbitrary potential $V(x) \neq 0$. The wave is now subject to scattering and subsequent superposition and interference modify the LDOS in such a way that a description in terms of the classical velocity is clearly insufficient. In fact it is this scattering which makes the task to find the proper prefactor somewhat non-trivial, since this situation clearly applies to the scattering state of the parabolic barrier. An elegant way to nevertheless use the correspondence between classical velocity and quantum mechanical LDOS is provided by Eq. (3.9). Here, the scattering state is represented by an asymptotic decomposition into an incident, a reflected and a transmitted wave. Each of these describes a single propagating wave with definite direction, which is therefore not subject to interference and superposition. In particular, the incident wave (unlike the full scattering state) can be associated with a classical velocity, which then corresponds to a quantum-mechanical local density of states

$$\mathrm{LDOS}_{in}(\varepsilon, x) = \frac{2}{h v_{cl}(\varepsilon, x)}. \tag{3.11}$$

Note that this is now true even in the presence of the finite potential barrier, since we "eliminated" interference by the decomposition. This consideration provides us with a direct way to calculate the full LDOS of the system: If we demand, that the modulus squared of the incoming wave is identical to $\mathrm{LDOS}_{in}(\varepsilon, x)$ (thereby fixing the prefactor), then the scattering states' modulus squared will evidently describe the LDOS of the full quantum mechanical system, including all modulations due to scattering at the barrier and consequential superposition. Since Eq. (3.9) provides an exact expression for the incident wave in the asymptotic limit, $\tilde{x} \to -\infty$, we have (for simplicity expressed in the natural units, see. Eq. (3.5))

$$\lim_{\tilde{x} \to -\infty} |c(\tilde{\varepsilon})|^2 |\phi_R^{in}(\tilde{\varepsilon}, \tilde{x})|^2 \overset{!}{=} \lim_{\tilde{x} \to -\infty} \mathrm{LDOS}_{in}(\tilde{\varepsilon}, \tilde{x}) = \lim_{\tilde{x} \to -\infty} \frac{1}{2\pi} \sqrt{\frac{1}{\tilde{\varepsilon} + 1/4\tilde{x}^2}} = \frac{1}{\pi \tilde{x}}. \tag{3.12}$$

Inserting the explicit form of the incident wave yields

$$|c(\tilde{\varepsilon})|^2 = \frac{e^{\pi \tilde{\varepsilon}/2}}{2\pi \cosh(\pi \tilde{\varepsilon})}. \tag{3.13}$$

We use Eq. (3.13) to write down the analytic expression for the LDOS of the full system (note that we have to include the left-movers as well to have the complete set of eigenstates):

$$\begin{aligned}\mathrm{LDOS}(\tilde{\varepsilon},\tilde{x}) &= \frac{1}{2}\left[|\psi_R(\tilde{\varepsilon},\tilde{x})|^2 + |\psi_L(\tilde{\varepsilon},\tilde{x})|^2\right] = \frac{1}{2}\left[|\psi_R(\tilde{\varepsilon},\tilde{x})|^2 + |\psi_R(\tilde{\varepsilon},-\tilde{x})^*|^2\right] \\ &= \frac{e^{\pi\tilde{\varepsilon}/2}}{4\pi\cosh(\pi\tilde{\varepsilon})}\left(\left|D(-1/2-i\tilde{\varepsilon},e^{i\pi/4}\tilde{x})\right|^2 + \left|D(-1/2+i\tilde{\varepsilon},e^{i\pi 3/4}\tilde{x})\right|^2\right). \qquad (3.14)\end{aligned}$$

Fig. 3.3(a) shows the noninteracting LDOS in the vicinity of the barrier center for energies close to the potential top. It features a ridge-like (black) structure just above the barrier. This "van Hove ridge" can be interpreted as remnant of the one-over-square-root divergency (van-Hove singularity) in a homogeneous system (or likewise as a scattering-induced modification of LDOS_{in}), which is smeared out by the inhomogeneity of the potential barrier (see Fig. 3.3(c) for an illustration for the case $\tilde{x} = 0$). Its maximum, $\tilde{\varepsilon}^{max}(\tilde{x})$, is shifted w. r. t. the potential on an energy scale set by the curvature Ω_x. For energies below the barrier top ($\tilde{\varepsilon} < 0$) the LDOS shows standing wave patterns, caused by the

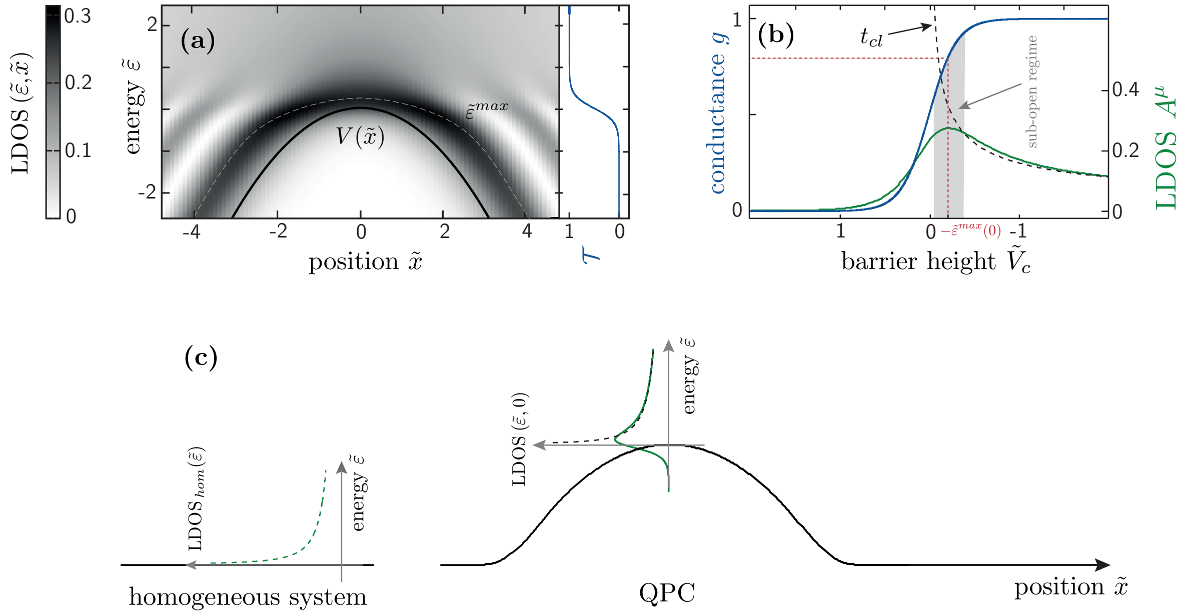

Figure 3.3: *Local properties of a parabolic barrier.* **(a)** The local density of states as function of position and energy. The distinct "van Hove ridge" (black) is located just above the potential barrier. **(b)** The LDOS, $A^{\mu}(\tilde{V}_c)$, as function of barrier height shows a maximum in the sub-open regime corresponding to $g \approx 0.8$. This structure causes the anomalous conductance features at finite interaction strength, known as 0.7 anomaly (see Sec. 3.3). The black dashed line shows for comparison the corresponding classical time an electron spends in the vicinity of the barrier center (in arbitrary units). **(c)** An illustration of the modification of the LDOS by the inhomogeneity. In the QPC's center the LDOS is shifted and smeared by the potential barrier.

interference of incoming and reflected wave. These features are absent for energies above the barrier ($\tilde{\varepsilon} > 0$). Here, single-particle scattering is exponentially supressed (see Eq. (3.10)) and the LDOS is approximately given by Eq. (3.11).

Let us make a connection of this structure to transport through the barrier. The linear conductance is determined by electrons within an energy intervall of width of the temperature, centered at the chemical potential (see Eqs. (2.8)-(2.10)). This is easy to understand, since applying an infinitesimal source-drain voltage will cause an imbalance between left and right-movers in said intervall. Additionally, the impact of the barrier on traversing electrons is strongest in the vicinity of its maximum. Hence, it is particularly instructive to investigate the LDOS in the center, $\tilde{x} = 0$, at the chemical potential, μ, for varying barrier height, $\tilde{V}_c$. Evaluating Eq. (3.14) at $\tilde{x} = 0$ provides the compact form

$$A^{\mu}(\tilde{V}_c) := \mathrm{LDOS}(-\tilde{V}_c, \tilde{x} = 0) = \frac{1}{4\sqrt{2}\pi^2} e^{-\pi \tilde{V}_c/2} \left| \Gamma\left(1/4 + 1/2 i \tilde{V}_c\right) \right|^2 , \tag{3.15}$$

where the superscript indicates that we evaluate Eq. (3.14) at the chemical potential. A^{μ} is plotted in Fig. 3.3(b) as function of gate voltage (green line). It features a maximum at $\tilde{V}_c \approx -0.2$, which, by comparison with the subsequent linear conductance g (blue line), is found to be positioned in the sub-open regime, corresponding to a noninteracting linear conductance $g \approx 0.8$ (see red dashed line). Again, this peculiar structure has its origin in the van-Hove singularity of a homogeneous system, but is smeared and shifted by scattering at the harmonic barrier.

3.2.3 Buildung a bridge to interactions

It is quite natural that the maximum of $A^{\mu}(\tilde{V}_c)$ in the sub-open regime has drastic influence on the conductance upon turning on interactions; the large number of available states (or likewise the large weight of those states) close to the chemical potential will increase the likelyhood of elastic and inelastic scattering. Let us introduce a semi-classical intuitive picture to illustrate this point: The LDOS, $A^{\mu}(\tilde{V}_c)$, can be interpreted as proportional to the time a traversing electron (with energy $\varepsilon_{\mu} = 0$) spends in the vicinity of the barrier center. This time determines how long (and therefore how strong) it is subject to the local interactions close to $\tilde{x} = 0$. Therefore, we expect a strong reaction on interactions for the barrier heights $\tilde{V}_c$ where $A^{\mu}(\tilde{V}_c)$ is large. Indeed, we show in Sec. 3.3, that the maximum of $A^{\mu}(V_c)$ in the sub-open regime is decisive for the strong interaction-induced reduction of linear conductance (enhanced backscattering), therefore lying at the heart of our interpretation for the 0.7 anomaly.

3.3 Physics of a parabolic barrier in the presence of interactions

The appearence of the 0.7 anomaly in the lowest conductance step of a QPC cannot be explained by non-interacting theory. The anomalous reduction of conductance in the sub-open regime as function of external parameters (B, T, V_{sd}) as well as the accompanying signatures in quantities such as shot noise and thermo power must be attributed to many-body effects. Hence, in order to make specific statements about the origin of the *0.7 anomaly* we have to add interactions to our 1-dimensional QPC model, Eq. (3.1).

3.3.1 Interacting Model

We describe the effect of interactions by an effective parameter $U(x, x')$, which represents the strength of mutual interactions felt by two electrons situated at positions x and x'. When traversing the QPC electrons are subjected to interactions particularly strong in the vicinity of the effective 1D barrier top.

Here, the electronic density is low. This naturally limits the systems possibilities to counteract the effect of interactions by a rearrangement of charge. In other word: Screening effects are rather weak around $\tilde{x}=0$. This situation changes in the flanks of the QPC potential and especially in the homogeneous 2DES. Here, the high electronic density enables rather effective screening. As a consequence electrons feel their mutual presence only close to the barrier top and a short-ranged interaction should be a sufficient choice for our model to capture the essential physics of the *0.7 anomaly*.

The influence of interactions on the conductance of a QPC must be calculated numerically; an analytic ansatz is hardly feasible, as the inhomogeneity of the potential must be treated with due accuracy. In particular, this makes calculation in real space inevitable. Since numerics cannot deal with the infinite Hilbert space of a continuous system, we discretize the x-axis using the method of finite differences [4] and a set of grid points $\{x_j\}$. The discretization is straightforward and details can be found in Heyder (2014), where we discuss different discretization schemes in great detail. In second quantization the discretized 1D model Hamiltonian is a tight binding chain

$$\mathcal{H}_0 = \sum_{j\sigma}[E_j^\sigma n_{j\sigma} - \tau_j(d_{j\sigma}^\dagger d_{j+1\sigma} + \text{h.c.})], \tag{3.16}$$

with onsite energy $E_j^\sigma = E_j - \sigma B/2 = V_j + \tau_{j-1} + \tau_j - \sigma B/2$, site-dependent hopping amplitude $\tau_j = \hbar^2/(2ma_j^2)$, spacing $a_j = x_{j+1} - x_j$ and potential $V_j = V(x_j)$. Furthermore, $d_{j\sigma}$ destroys an electron with spin σ at the grip point x_j and n_j counts the number of electrons at x_j. In order to make calculations within an infinite system feasible we devide the chain into three parts: The inhomogeneity ($V_j \neq 0$) is restricted to a finite region $|j| \leq N'$ ($N' \approx 100$), which we call the "central constriction region" (CCR). Here, the parabolic barrier of height $V_c + \mu \gg \Omega_x$ drops smoothly to zero upon approaching $|j| = N'$. The influence of the homogeneous outer regions $|j| > N'$ (the left and right lead) can be described by the lead contribution to the CCR self energy, which is determined by standard projection method on the CCR (see e.g. appendix A of Bauer et al. (2014)). This allows for an effective (and exact) description of the system within the Hilbert space of the CCR only.

In order to investigate the physics of a QPC in the presence of interactions we add the interaction term

$$\mathcal{H}_{int} = \sum_j U_j n_{j\uparrow} n_{j\downarrow}, \tag{3.17}$$

where U_j is non-zero only within the CCR. Note, that we choose an onsite interaction, which is the most extreme case of short-ranged interactions. This approach may well be justified by the above considerations about screening. A treatment incorporating the effect of screening, while going beyond the scope of this work, is nevertheless highly desirable and left for future studies. We find qualitative agreement with longer-ranged calculations (in preparation), where the range of interactions is of order $\mathcal{O}(l_x)$ which is usually about ten sites in our discretization scheme. Since interactions influence transport mainly close to the barrier top, the qualitative nature of the results depends on the strength of interactions in the vicinity of the barrier center rather than the overall functional form along the whole CCR. We choose $U_j = U$ to be constant apart from the outermost sites, where it drops smoothly to zero (similar to V_j).

3.3.2 Treatment of interactions

Since the effect of many-body physics in extended inhomogeneous systems, such as Eq. (3.16), cannot be calculated exactly, this necessitates using approximation schemes, which, importantly, provide qualitatively reliable results and allow for a physical interpretation of the data. We calculate the influence of interactions using two different perturbative approaches: (i) The functional renormalization group (fRG) for calculations at $T = V_{sd} = 0$ and (ii) second order perturbation theory (SOPT) for calculations at finite excitations $T \neq 0$ or $V_{sd} \neq 0$. The former approach is discussed in detail both in our nature publication Bauer et al. (2013) and the subsequent technical paper Bauer et al. (2014). The latter is covered in great detail in Heyder (2014) and the appendix of Bauer et al. (2013).

---

[4] see e.g. http://en.wikipedia.org/wiki/Finite_difference_method

The functional renormalization group (fRG)

This section is mainly adressed to experts in diagramatics and/or functional field theory. Since fRG is discussed in great detail both in our publications [Bauer et al. (2013), Bauer et al. (2014), Heyder et al. (2014), Goulko et al. (2014)] and the overall literature [see e.g. Meden et al. (2002),Karrasch (2006), Jakobs et al. (2010)], we restrict the discussion to a brief introduction to the main idea of fRG in the one-particle irreducible (1PI) version. This requires background knowledge in Green's and vertex function theory as well as in many-body diagramatics.

In order to calculate physical properties of a many-body Hamiltonian $\mathcal{H} = \mathcal{H}_0 + \mathcal{H}_{int}$ one has to determine the interacting one-particle Green's function, given by the Dyson equation

$$\mathcal{G} = [\mathcal{G}_0^{-1} - \Sigma]^{-1}. \tag{3.18}$$

The bare Greens function $\mathcal{G}_0$ depends on the noninteracting part $\mathcal{H}_0$ of the Hamiltonian only and can be calculated with arbitrary precision (assuming the Hilbert space of $\mathcal{H}_0$ is not too large). This reduces the problem to the calculation of the self-energy $\Sigma = -\gamma_1$, where γ_1 is the 1PI one-particle vertex function. Furthermore, some physical quantities require additional calculation of n-particle Greens functions ($n > 1$), which in turn require information about the higher order n-particle vertex functions γ_n as well. In most cases it is virtually impossible to calculate the γ_n's exactly. Rather, they are given as infinite series of 1PI diagrams. Exemplary, we show the lowest order (in the bare vertex) diagrams of the self-energy and two-particle vertex, which are given as the sum of all 1PI diagrams with 2 and 4 amputated external legs, respectively. Representing the bare interaction vertex by a black circle and the bare Green's function by a directed line, we have

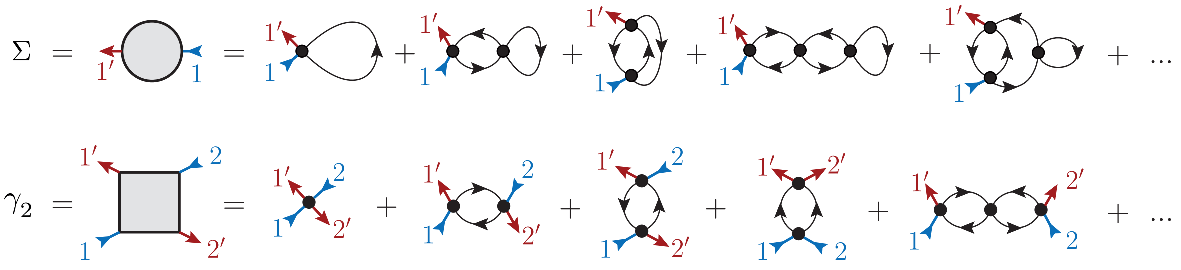

(3.19)

where the composite indices $1, 2$ $(1', 2')$ carry all the quantum numbers and the time/frequency argument of the corresponding annihilation (creation) operator. To evaluate a diagram the arguments of internal bare Greens functions are summed over. Generally, these series of diagrams cannot be calculated accurately. Hence, one often relies on schemes that truncate them, if possible in a somewhat controlled manner. As a simple example consider plain perturbation theory, where the truncation is done strictly after a given order in the bare vertex. Other versions involve the summation of certain infinite sub-series, such as self-consistent Hartree for the self-energy, or the random phase approximation (RPA) for the two-particle vertex.

fRG provides an alternative and very powerful approach: It introduces a parameter Λ into the bare propagator, $\mathcal{G}_0 \rightarrow \mathcal{G}_0^{\Lambda}$. Obviously, this introduces a Λ-dependence in the vertex functions as well,

$\gamma_n \to \gamma_n^\Lambda$. In principle, the choice of Λ is arbitrary; it can be a physical parameter (like temperature, magnetic field, voltage, etc.) or an arbitrary artificial quantity. In order to make use of this parameter, it is important, that all γ_n's are known at some initial value Λ_i, i.e. that all infinite vertex series can be evaluated exactly for this special case. Note, that this requires perfect knowledge of a fully interacting physical system, in case that Λ is a physical parameter.

In the next step the vertex functions are differenciated w. r. t. the parameter, $d\gamma_n^\Lambda/d\Lambda$. Importantly, the structure of the vertex and Greens functions is such, that now the r. h. s. of every vertex series derivative is a functional of up to one order higher vertex functions and single-particle propagators (note that this implies that the diagramatic series of the derivative factorizes into vertex and Greens functions):

$$\frac{d\gamma_n^\Lambda}{d\Lambda} = \mathcal{F}(\Lambda; \mathcal{G}_0^\Lambda, \gamma_1^\Lambda, \dots, \gamma_{n+1}^\Lambda). \tag{3.20}$$

In the language of functional field theory this is owed to the fact that the generating functional of vertex functions and the generating functional of connected Greens functions are related via a Legendre transformation. For an explicit illustration of Eq. (3.20) by diagrammatic evaluation of $d\Sigma^\Lambda/d\Lambda = -d\gamma_1^\Lambda/d\Lambda$ we refer to Appendix B of Heyder (2014), where the necessary steps are performed in some detail. Taking all n into account Eq. (3.20) is an infinite system of coupled differential equations for the n-particle vertex function, the so called fRG flow equations. Note that these describe the exact vertices, since no approximation has been carried out so far. In that sense, Eq. (3.20) can be regarded as a clever resummation of the initial vertex series Eq. (3.19). Provided one has a proper initial condition at Λ_i, the full theory is recovered at a final value Λ_f, where the physical parameter reaches the desired value or where the artificial parameter vanishes by construction.

Of course, solving the full system of fRG flow equations is equally impossible to calculating the infinite vertex series of the form Eq. (3.19). Hence, one has to choose a truncation scheme within fRG as well. This is usually done by setting $\gamma_{n>n'}^\Lambda = 0$, where n' defines the "order" of truncation. This closes the flow equations, yielding a system of coupled ODEs for the remaining non-trivial vertices $\gamma_1, \dots, \gamma_{n'}$ only, which can be solved numerically be means of standard Runge-Kutta routines. Since a vertex γ_n carries the quantum numbers of n creation and n annihilation operators, including $2n-1$ independent times or frequencies, its number of independent variables increases hugely with n. This usually demands a truncation beyond second order, $n' = 2$, in almost all practical cases, including the treatment of interactions in our QPC model, Eq. (3.16) and Eq. (3.17). The resulting two coupled differential equations for the self-energy and the two-particle vertex have the diagrammatic representation

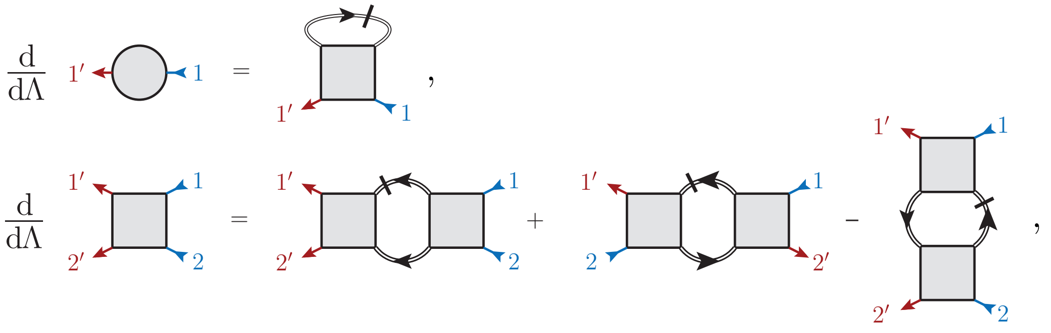

(3.21)

where double lines indicate fully interacting Greens functions. The crossed out directed double line represents the so called single-scale propagator, $S^\Lambda = \mathcal{G}^\Lambda \partial_\Lambda [\mathcal{G}_0^\Lambda]^{-1} \mathcal{G}^\Lambda$.

Due to the discretization of real space in our interacting model the number of independent variables of the two-particle vertex is $\mathcal{O}(N^4 N_f^3)$, where $N = 2N' + 1$ is the number of sites within the CCR and N_f is the number of discrete points per frequency used in the numerics. Since this is still far from feasible with present computer power we employ an additional approximation, to be called coupled ladder approximation (CLA) in frequency-, and real space. This scheme reduces the number of independent variables of γ_2 to $\mathcal{O}(N^2 N_f)$, thereby being exact to second order in the bare interaction vertex. The CLA is best described as a coupled RPA approach, where all vertex channels contribute on equal footing. Technical details are presented in our paper Bauer et al. (2014).

After truncation, fRG is still a perturbative method. This implies that interactions should not be too large (what that means in practice has to be determined from case to case individually) and that the validity of the results must be checked carefully for the system in question. We find, that the CLA yields reliable qualitative results at least up to interaction strengths of $U = 3.5/(\Omega_x l_x)$, where Ω_x is the curvature of the parabolic potential and l_x the corresponding harmonic oscillator length (see Sec. 3.2.1). In Sec. 3.4 as well as in Bauer et al. (2013), Bauer et al. (2014) and Heyder et al. (2014), we show that this value is sufficient to generate a 0.7 anomaly.

Up to date our fRG approach is Matsubara-based, which limits reliable conductance results to zero temperature and zero source-drain voltage, $T = V_{sd} = 0$. In order to calculate transport at finite excitations one has to implement a Keldysh version of the fRG flow, which provides a number of nontrivialities and is a subject of our recent studies.

Second order perturbation theory (SOPT)

Our fRG scheme is implemented for zero excitation energies only so far. Hence, all theoretical results at $T \neq 0$ and $V_{sd} \neq 0$ within this thesis are SOPT calculations. This amounts to a truncation of the self-energy and two-particle vertex series beyond second order in the bare vertex, which follows the idea of Oguri (2001). While this approach is rather elementary, SOPT is nevertheless numerically very demanding and, importantly, capable of capturing essential interacting physics of a QPC at finite excitation energies. This is particularly true, since SOPT includes the second order Fock-diagram (the third diagram in the Σ-series), which considers the effect of the LDOS via inelastic scattering events. We find that SOPT produces qualitative reliable transport results up to about $U = 2.5/(\Omega_x l_x)$.

3.3.3 The effective interaction strength - a simple Hartree argument

In Sec. 3.2.3 we argued that the impact of interactions on transport through the system is closely related to the LDOS at the chemical potential in the barrier center, $A^\mu(\tilde{V}_c)$. Here we want to further elaborate on this point by discussing the effect of many-body processes to first order in the interaction parameter U. In other words, we consider the first diagram in the self-energy series (Eq. (3.19)), which describes Hartree type physics only. This provides intuition as to why the effective strength of interactions, i.e. the measure how strongly the system is influenced by electron-electron processes, can be written as product of the interaction parameter and the local density of states:

$$U_{\text{eff}}(V_c) = U \ \times \ A^\mu(V_c). \tag{3.22}$$

Once again, we can interpret this result in a (somewhat loose but nevertheless instructive) semiclassical picture in terms of the electron's velocity: Slow electrons feel interactions particularly strong.

Let us make some considerations how interactions influence the propagation of a charge carrier in the QPC: An electron that enters the QPC region sees not only the effective 1D barrier $V(x)$ but in addition feels the presence of other electrons in the constriction. To first order in the interaction this amounts to an enhancement of the barrier by the Hartree self-energy $\Sigma^h(x) = n_0(x)U$ due to the repulsive force of the noninteracting electronic density $n_0(x)$ (note that in similar manner the electrostatic QPC potential is created by the electronic density in the metallic gates above the 2DES). The resulting potential

$$V^h(x) = V(x) + \Sigma^h(x) \tag{3.23}$$

is called the effective Hartree barrier (depicted in Fig. 3.4(a)). To first order transport is determined by $V^h(x)$ rather than by the bare potential $V(x)$. Let us calculate how the barrier height of the Hartree potential, $V_c^h = V^h(0)$, evolves with the barrier height of the bare potential, V_c. Since an increase in V_c decreases the noninteracting density in the barrier center (with growing barrier height more and more electrons are pushed into the leads), we know that V_c^h increases less than V_c:

$$\frac{dV_c^h}{dV_c} = \frac{d}{dV_c}\left[V_c + \Sigma^h(0)\right] = 1 + U\frac{dn_0(0)}{dV_c} < 1. \tag{3.24}$$

We evaluate the change in noninteracting density in the barrier center due to a potential shift, i.e. the derivative on the r.h.s. of Eq. (3.24). Since the density is given by the energy integral over the LDOS (see Eq. (3.14)) up to the chemical potential (for simplicity evaluated at temperature $T=0$),

$$n_0(0) = \int_{-\infty}^{-\tilde{V}_c} d\tilde{\varepsilon}\ \mathrm{LDOS}(\tilde{\varepsilon}, \tilde{x}=0), \tag{3.25}$$

its derivative w.r.t. V_c is just equal to the negative of the $LDOS$ at the chemical potential in the barrier

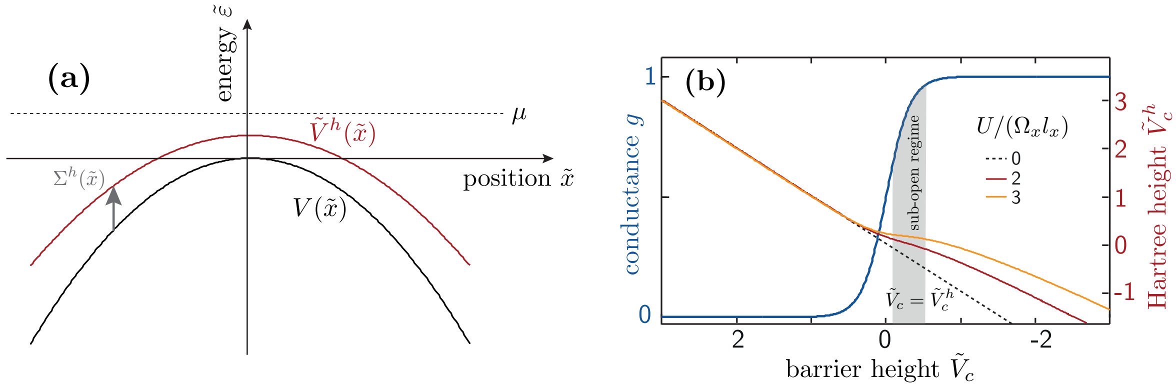

Figure 3.4: *The Hartree barrier:* **(a)** Illustration of the bare ($U=0$) potential $V(\tilde{x})$ and the Hartree potential $V^h(\tilde{x})$ in the vicinity of the barrier top. The combination of finite density $n_0(\tilde{x})$ and finite interaction strength U causes an enhancement w. r. t. the bare barrier given by the Hartree self-energy $\Sigma^h(\tilde{x})=n_0(\tilde{x})U$. **(b)** The barrier height V_c^h of the effective Hartree potential depends nonlinear on the original barrier height V_c: Beyond pinch-off ($\tilde{V}_c \gg 0$), where all density is pushed away from the QPCs center, both coincide independent from the value of U. Yet, in the sub-open regime the dependence of V_c^h on V_c descreases with increasing U. The plot shows exemplary calculations for several values of the interaction parameter U.

center. Hence, we find (from Eq. (3.24))

$$\frac{dV_c^h}{dV_c} = 1 - U \cdot A^{\mu}(V_c) = 1 - U_{\text{eff}}(V_c). \tag{3.26}$$

This is a logical, but nevertheless remarkable result which we illustrate in Fig. 3.4(b). A change in the actual barrier height of the interacting system (to first order given by V_c^h) with the bare barrier height is strongly dependent on V_c via the LDOS, $A^{\mu}(V_c)$. This implies that V_c^h changes least quickly with $\tilde{V}_c$ in the sub-open regime. Note that this indirectly supports the picture of a weaker dependence of conductance on V_c in the sub-open regime, in other words provides a possible mechanism for the formation of an interaction-induced plateau-like structure even at $B\!=\!T\!=\!V_{sd}\!=\!0$.

It is important to note though, that not only the height of the potential, but of course also its overall geometry is influenced by interactions. Surely this includes a change in the barrier curvature Ω_x, which subsequently changes transmission and conductance. From this perspective the above calculation is insufficient to draw definite conclusions about the shape of the conductance in the presence of interactions. Rather, we present it here to provide the reader with intuition, why the local density of states $A^{\mu}(\tilde{V}_c)$ determines the interacting physics of a QPC via $U_{\text{eff}}(\tilde{V}_c)$. Still, Hartree contributions are of great importance for the physics of the *0.7 anomaly*. In order to produce reliable results for the shape of the conductance step in the presence of interactions, it is necessary to include them to all orders: The density $n_0(x)$ within the QPC gives rise to an enhanced Hartree barrier, which in turn generates a modified density $n_1(x)$ etc. This provides an infinite feedback loop and a self-consistency condition for the Hartree density, $n_{i+1}(x)\!=\!n_i(x)$. The number of iterations needed to fulfill this condition with due accuracy depends sensitively on the value of $A^{\mu}(\tilde{V}_c)$ and thus sensitively on the barrier height. In addition, successive orders usually show oscillatory behavior, meaning an alternating overestimate and underestimate of interactions before convergence. Hence, truncation at low (or too low) orders leads to an inconsistent description of interactions along the conductance step. Since Hartree contribution are of particular interest for the physics at zero excitation-energy $T = V_{sd} = 0$, where inelastic scattering (covered by Fock contributions) is forbidden, we refrain from drawing conclusions about the detailed shaping of the zero temperature linear conductance curve from our SOPT results (in which Hartree contributions are restricted to second order). In contrast, fRG provides a generic way to sum up Hartree contributions to infinite order, hence allowing for an interpretation of the shaping of the $T = V_{sd} = 0$ conductance step.

After having presented a simple Hartree argument, which makes anomalous conductance bahavior in the sub-open regime plausible, we now present fRG calculation for the linear conductance, which show that our model is indeed capable of reproducing the features of the 0.7 anomaly.

3.4 Interacting conductance of a parabolic barrier - the 0.7 anomaly

Since all our results for the conductance and local properties of a parabolic barrier in the presence of finite electron-electron interactions are discussed in detail in our various publications, collected in subsequent chapters, we want to emphasize just one key features here: The U-dependence of the conductance, i.e. the evolution of the linear conductance step with increasing interaction strength at $B\!=\!T\!=\!0$, which highlights the importance of the LDOS, $A^{\mu}(\tilde{V}_c)$, for the occurance of the 0.7 anomaly. The results, calculated with fRG, are in beautiful agreement with the experimental data from the group of Stefan Ludwig. For a further in-depth discussion of the U-dependence we refer to Bauer et al. (2013).

Fig. 3.5(a) shows the linear conductance step for several values of the interaction parameter U at $B = T = 0$. In agreement with a Hartree picture (the presence of charge carriers in the barrier center enhances the barrier w. r. t. the bare case, thus reducing the linear conductance, see Sec. 3.3.3) the conductance curve is shifted towards smaller values of V_c. In addition, we find the step widening and its slope decreasing with increasing U. This happens in asymmetric fashion, featuring the formation of a weak, shoulder-like structure in the sub-open regime (at the onset of the plateau) at intermediate interaction strength - *the 0.7 anomaly*. The position of this structure coincides with the maximum of $A^{\mu}(\tilde{V}_c)$, the local density of states in the barrier center at the chemical potential, which is plotted in Fig. 3.5(b) for the same values of U. This corroborates the importance of the LDOS for the interaction-induced features in the conductance of a QPC: The high local density of states at the chemical potential in the barrier center indicates a high cross section for elastic and (at finite T or V_{sd}) inelastic scattering events. This leads to an enhanced probability of backscattering, causing a strong decrease in the transmission probability through the barrier and a subsequent strong supression of conductance in the sub-open regime as function of various external parameters. It is remarkable that the seed for this behavior is found in the noninteracting physics of a QPC, namely the noninteracting LDOS given by Eq. (3.15), which strongly amplifies the effect of interactions.

In Fig. 3.5(c)-(d) we compare noninteracting and interacting conductance curves from theory and experiment. In accordance with the discussion in Sec. 3.1.2 we assume, that the shape of the third step

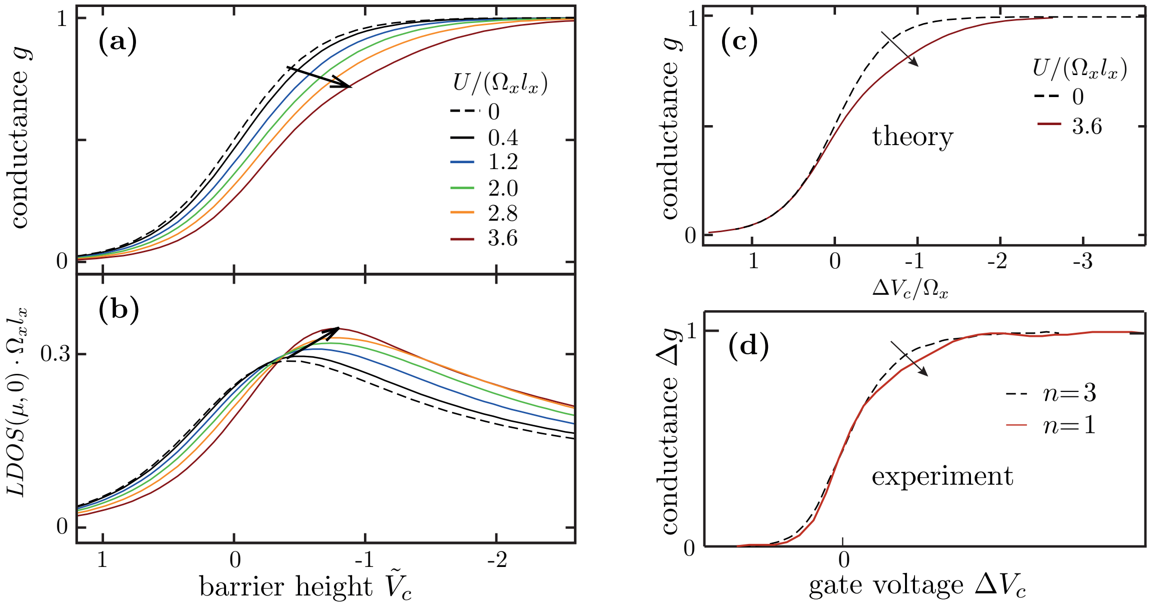

Figure 3.5: *Formation of the 0.7 anomaly with increasing interactions:* **(a)** The evolution of the linear conductance g as function of barrier height V_c for increasing interaction parameter U, calculated using fRG. The data features a weak 0.7 shoulder at intermediate interaction strength. **(b)** Its origin can be associated with a maximum in $A^{\mu}(\tilde{V}_c)$ in the sub-open regime, which indicates slow electrons in the barrier center at the chemical potential. These are subject to an enhanced backscattering probability as a consequence of strong local interactions at the barrier top. **(c),(d)** Comparison between "noninteracting" and "interacting" conductance. The data were shifted in V_c for clarity. Note the remarkable similarity between theory and experiment.

in experiment can be explained mainly by noninteracting transport through a parabolic barrier. There we used comparison to the shape of the first conductance step to show the distinctiveness of the sub-open regime. Our fRG data show a remarkably similar behavior: The strong reduction of conductance at $U = 3.6/(\Omega_x l_x)$ w. r. t. the noninteracting case (after shifting the curves to lie on top of each other in the pinch-off regime) is somewhat limited to the sub-open regime.

3.4.1 Conclusion

In this chapter we have presented a microscopic 1D model of the lowest transport mode of a QPC, featuring a parabolic barrier and short-ranged electron-electron interactions (EEI). Detailed noninteracting calculations were presented for both the transmission probability and the LDOS. The latter exhibits a maximum just above the potential barrier - the van-Hove ridge. Adding interactions, we find an interplay between EEI and the van-Hove ridge responsible for the anomalous conductance features, i.e. the *0.7 anomaly*. In order to sharpen intuition for the underlying physical mechanics, we use a semi-classical picture: For a sub-open QPC we associate the van-Hove ridge with slow electrons at the chemical potential in the barrier center. These are subject to a strongly enhanced probability of backscattering once EEI are present.

Chapter 4

Microscopic origin of the *0.7 anomaly* in quantum point contacts

This chapter presents the paper "*Microscopic origin of the 0.7 anomaly in quantum point contacts*", published in NATURE [Bauer et al. (2013)]. The scientific results of this work originate from a collaboration between theory (von Delft group) and experiment (Ludwig group). On the theory side, we propose a one-dimensional (1D) model with a parabolic potential barrier and short-ranged Coulomb interactions (see also Sec. 3.3.1) to describe the physics of the lowest subband of a quantum point contact (QPC). The model qualitatively reproduces the main features of the well-known *0.7 anomaly* in QPCs, including the anomalously strong reduction of the conductance in the sub-open regime, i.e. at the onset of the first plateau, as function of magnetic field B (calculated using the functional renormalization group (fRG), see Sec. 3.3.2 and Sec. 6), temperature T and source-drain voltage V_{sd} (calculated using second order perturbation theory (SOPT), see Sec. 3.3.2 and Sec. 8). Our theoretical setup allows for a thorough investigation of the microscopic origin of this peculiar conductance behavior: We find that the local density of states (LDOS) of the QPC exhibits a broad maximum at energies just above the 1D effective barrier. We argue that this "van Hove ridge" (see also Sec. 3.2.2 and Fig. 3.3 therein) gives rise to an enhanced probability of backscattering in the sub-open regime in the presence of interactions, which explains the anomalous conductance features; at finite magnetic field the strong reduction of conductance is mainly caused by an interaction-amplified depopulation of the disfavoured spin species' subband, originating from strong exchange interactions ("Stoner-type" physics). At finite temperature/finite bias voltage (i.e. finite excitation energies) the interplay between the van Hove ridge and finite interaction strength generates an increase in inelastic backscattering (similar arguments were used in Sloggett et al. (2008) and Lunde et al. (2009). On the experimental side the group of Stefan Ludwig uses a metallic gate structure of particularly high tunability, which enables a fine-tuning of the QPC's electrostatic potential ("geometry"). As a result they can, importantly, define a QPC that features a parabolic effective 1D barrier. Their measurement reveals an asymmetric shape of the first conductance step even at $B = T = V_{sd} = 0$, which is in beautiful agreement with our theoretical prediction from fRG calculations (see also Fig. 3.5). Their data show the typical dependencies of the *0.7 anomaly* on external parameters, all of which are qualitatively reproduced by our theoretical calculations and can be explained within the van Hove ridge scenario. They find that the energy-scales B_*, T_* and V_{sd*}, defined via the leading quadratic order of the conductance on the parameters B, T or V_{sd} respectively, show exponential dependence on gate voltage towards pinch-off. We argue that this functional form is a remnant of the noninteracting physics of a parabolic barrier.

The publication is divided into two major parts: The main text tells a consistent story of the van

Hove ridge scenario and shows and discusses the major results from both the theory and experimental side. The supplementary material provides comprehensive information about the experimental setup, specific details about data analysis, the theoretical 1D model and the numerical methods to treat interactions, as well as information about implications and predictions of our theory.

LETTER

doi:10.1038/nature12421

Microscopic origin of the ‘0.7-anomaly’ in quantum point contacts

Florian Bauer[1,2]*, Jan Heyder[1,2]*, Enrico Schubert[1], David Borowsky[1], Daniela Taubert[1], Benedikt Bruognolo[1,2], Dieter Schuh[3], Werner Wegscheider[4], Jan von Delft[1,2] & Stefan Ludwig[1]

Quantum point contacts are narrow, one-dimensional constrictions usually patterned in a two-dimensional electron system, for example by applying voltages to local gates. The linear conductance of a point contact, when measured as function of its channel width, is quantized[1–3] in units of $G_Q = 2e^2/h$, where e is the electron charge and h is Planck’s constant. However, the conductance also has an unexpected shoulder at $\sim 0.7G_Q$, known as the ‘0.7-anomaly’[4–12], whose origin is still subject to debate[11–21]. Proposed theoretical explanations have invoked spontaneous spin polarization[4,17], ferromagnetic spin coupling[19], the formation of a quasi-bound state leading to the Kondo effect[13,14], Wigner crystallization[16,20] and various treatments of inelastic scattering[18,21]. However, explicit calculations that fully reproduce the various experimental observations in the regime of the 0.7-anomaly, including the zero-bias peak that typically accompanies it[6,9–11], are still lacking. Here we offer a detailed microscopic explanation for both the 0.7-anomaly and the zero-bias peak: their common origin is a smeared van Hove singularity in the local density of states at the bottom of the lowest one-dimensional subband of the point contact, which causes an anomalous enhancement in the Hartree potential barrier, the magnetic spin susceptibility and the inelastic scattering rate. We find good qualitative agreement between theoretical calculations and experimental results on the dependence of the conductance on gate voltage, magnetic field, temperature, source–drain voltage (including the zero-bias peak) and interaction strength. We also clarify how the low-energy scale governing the 0.7-anomaly depends on gate voltage and interactions. For low energies, we predict and observe Fermi-liquid behaviour similar to that associated with the Kondo effect in quantum dots[22]. At high energies, however, the similarities between the 0.7-anomaly and the Kondo effect end.

In our measurements, we use the multigate layout on the surface of a GaAs/AlGaAs heterostructure shown in Fig. 1a. By suitably tuning the central- and side-gate voltages, V_c and V_s, at a fixed top-gate voltage, V_t, we can use the device to define a short, one-dimensional (1D) channel, containing a smooth, symmetric barrier, in the two-dimensional electron system (2DES) buried in the heterostructure. To describe such a quantum point contact (QPC), we adopt a 1D model with local interactions and a smooth potential barrier. We treat interactions perturbatively, using either second-order perturbation theory[23] (SOPT) or the functional renormalization group[24–26] (FRG) approach (Supplementary Information, sections 7 and 6, respectively). The lowest 1D subband of the device is modelled by

$$\hat{H} = \sum_{j\sigma}\left[E_{j\sigma}\hat{n}_{j\sigma} - \tau_j\left(d^{\dagger}_{j+1\,\sigma}d_{j\sigma} + \text{h.c.}\right)\right] + \sum_{j} U_j \hat{n}_{j\uparrow}\hat{n}_{j\downarrow} \qquad (1)$$

Here $\hat{n}_{j\sigma} = d^{\dagger}_{j\sigma}d_{j\sigma}$ counts the number of electrons with spin σ (spin up, $\sigma = \uparrow$ or $+$; spin down, $\sigma = \downarrow$ or $-$) at site j of an infinite, tight-binding chain with hopping amplitude τ_j, on-site interaction U_j and potential energy $E_{j\sigma} = E_j - \sigma\tilde{B}/2$ (Supplementary Fig. 8), and ‘h.c.’ denotes Hermitian conjugate. The Zeeman energy, $\tilde{B} = |g_{\mathrm{el}}|\mu_B B$, describes the effect of a uniform external parallel magnetic field B, where μ_B is the Bohr magneton and g_{el} is the effective g factor (<0 in GaAs). (When similar symbols are used for model parameters and experimental parameters, we add tildes to the former to distinguish them from the latter.) We neglect spin–orbit interactions and other orbital effects. The parameters E_j, U_j and τ_j vary smoothly with j and differ from their bulk values, $E_{\mathrm{bulk}} = U_{\mathrm{bulk}} = 0$ and $\tau_{\mathrm{bulk}} = \tau$ (taken as the unit of energy), only within a central constriction region (CCR) of N sites around $j = 0$, representing the QPC. Sites $j < -N/2$ and $j > N/2$ represent two non-interacting leads, each with bandwidth 4τ, chemical potential μ and bulk Fermi energy $\varepsilon_F = 2\tau + \mu$; we choose $\mu = 0$, implying half-filled leads (Fig. 1b). We set U_j to a fixed value, U, for all but the outermost sites of the CCR, where it drops smoothly to zero.

Within the CCR, we define the QPC barrier by specifying the shape of the ‘band bottom’ as $\omega_j^{\min} = E_j - (\tau_{j-1} + \tau_j) - \mu$ (Fig. 1b, solid black line). We choose $\omega_j^{\min}$ to define a smooth, symmetric barrier within the CCR, parabolic near the top[3], where we parameterize it as $\omega_j^{\min} \approx \tilde{V}_c - \Omega_x^2 j^2/4\tau_0$ (Supplementary Information, section 4D). Here $\tilde{V}_c$ sets the barrier height with respect to μ (Fig. 1b, dashed black line), and $\Omega_x \ll \tau$ characterizes its curvature. We first consider the theoretical case of zero temperature, $\tilde{T} = k_B T$ (k_B, Boltzmann’s constant), source–drain voltage, $\tilde{V}_{\mathrm{sd}} = |e|V_{\mathrm{sd}}$, and field, $\tilde{B}$: $\tilde{T} = \tilde{V}_{\mathrm{sd}} = \tilde{B} = 0$. As $\tilde{V}_c$ is decreased below 0, the conductance, $g = G/G_Q$, increases from 0 to 1, showing a step of width $\sim\Omega_x$ (about 1.5 meV in our experiment), whose shape depends on U (Fig. 1k). In the upper part of the step, say $0.5 \lesssim g \lesssim 0.9$, we say that the QPC is ‘sub-open’; the sub-open regime is of special interest because for measured $g(V_c)$ curves it contains the 0.7-anomaly.

The bare local density of states (LDOS), $A_j^0(\omega)$, for equation (1) has a strong maximum just above the band bottom[18], seen as a yellow–red ridge-like structure in Fig. 1b. In a semiclassical picture, $A_j^0(\omega) \propto 1/v_j(\omega)$, where $v_j(\omega)$ is the velocity at site j of an electron with energy ω with respect to μ. The ridge-like maximum of $A_j^0(\omega)$ above the barrier reflects the fact that electrons move slowest there. In the CCR’s outer flanks, this ridge develops smoothly into the van Hove singularity, $A_{\mathrm{bulk}}^0 \propto \left[\left(\omega - \omega_{\mathrm{bulk}}^{\min}\right)\tau\right]^{-1/2}$, in the bulk LDOS at the bulk band bottom in the leads, $\omega_{\mathrm{bulk}}^{\min} = -\varepsilon_F$. We therefore call this LDOS structure a ‘van Hove ridge’. Near the barrier’s centre, its curvature causes the singularity to be smeared out on a scale set by Ω_x. This limits the amplitude of the van Hove ridge to $\max\left[A_j^0(\omega)\right] \propto \mathcal{O}(\Omega_x\tau_0)^{-1/2}$ and shifts it upwards in frequency relative to the band by $\mathcal{O}(\Omega_x)$ (Fig. 1f–h).

The van Hove ridge has a strong, $\tilde{V}_c$-dependent effect on numerous QPC properties. Near those spatial locations where the ridge intersects the chemical potential ($\omega = 0$), the LDOS is enhanced, thus amplifying the effects of interactions by $\mathcal{O}(\Omega_x\tau_0)^{-1/2}$ (which grows with QPC

---

[1]Center for NanoScience and Fakultät für Physik, Ludwig-Maximilians-Universität München, Geschwister-Scholl-Platz 1, 80539 München, Germany. [2]Arnold Sommerfeld Center for Theoretical Physics, Ludwig-Maximilians-Universität München, Theresienstrasse 37, D-80333 München, Germany. [3]Institut für Angewandte Physik, Universität Regensburg, D-93040 Regensburg, Germany. [4]Laboratory for Solid State Physics, ETH Zürich, CH-8093 Zürich, Switzerland.

*These authors contributed equally to this work.

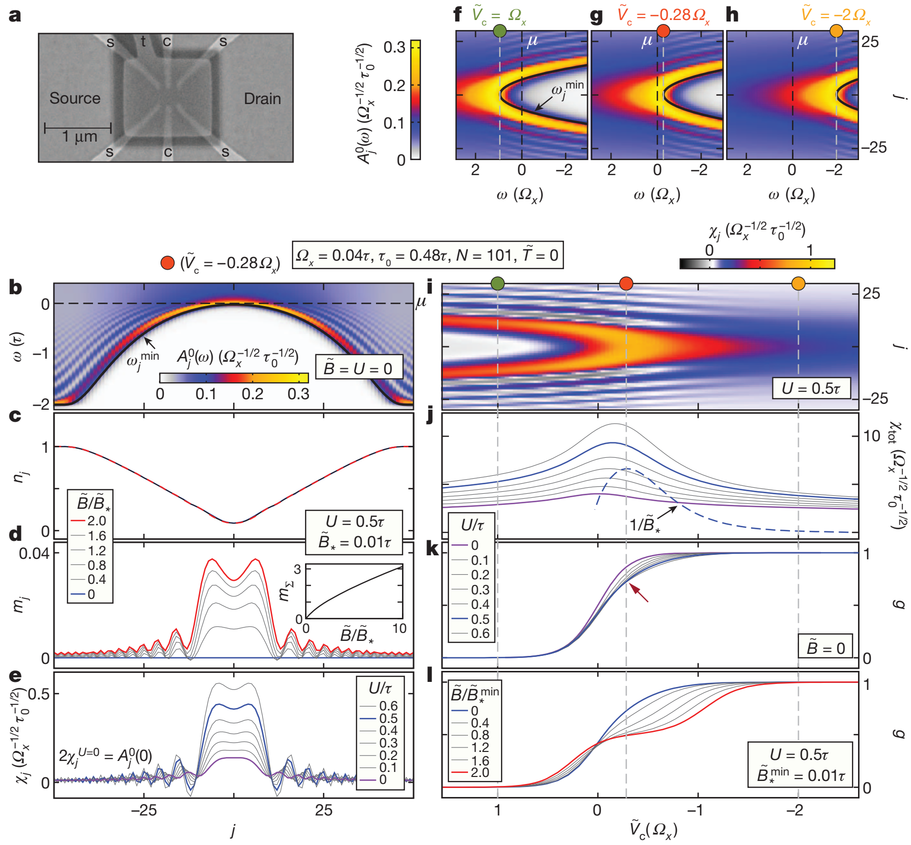

Figure 1 | Experimental set-up and model. **a**, Scanning electron microscope picture of the gate layout, featuring a top gate (t) at voltage V_t, two central gates (c) at voltage V_c and four side gates (s) at voltage V_s. Negative voltages V_c and V_s locally deplete the 2DES, which is 85 nm beneath the sample surface. Together with V_t, they induce a tunable electrostatic potential landscape in the 2DES. **b**, Barrier shape and LDOS. The bare ($U_j = 0$, $\tilde{B} = 0$) 1D LDOS per spin species, $A_j^0(\omega)$ (colour scale), as a function of energy, ω, and site index, j, for $\tilde{V}_c = -0.28\Omega_x$. The barrier shape is defined by the solid black line, showing the band bottom, $\omega_j^{\min}$. The LDOS vanishes exponentially rapidly below $\omega_j^{\min}$ (Supplementary Fig. 11), and has a van Hove ridge (yellow–red) just above it, followed by Friedel oscillations (white fringes) at higher energies (up to $\omega \lesssim \tilde{V}_c$). **c–e**, Local properties of a sub-open QPC: FRG results for the sub-open barrier shown in **b**. **c**, **d**, The local density, n_j (**c**), and the magnetization, m_j (**d**), for several values of magnetic field, $\tilde{B}$. Inset of **d**, $m_\Sigma = \sum_{|j| \le 10} m_j$ as a function of $\tilde{B}$. **e**, The local spin susceptibility, χ_j, for several values of interaction strength, U. The shapes of m_j and χ_j are modulated by Friedel oscillations inherited from the bare LDOS (**b**), with locally varying wavelength, $\lambda \approx 1/n_j$. **f–l**, Changing barrier height. **f–h**, The bare LDOS, $A_j^0(\omega)$, for three successively lower barrier heights, $\tilde{V}_c/\Omega_x = 1$ (**f**), -0.28 (**g**) and -2 (**h**). The LDOS pattern is fixed with respect to $\tilde{V}_c$ (grey dashed lines) but shifts with respect to μ (black dashed lines). **i–l**, FRG results for the $\tilde{V}_c$ dependence of the local spin susceptibility, χ_j (colour scale), at fixed $U = 0.5\tau$ (**i**); the total spin susceptibility, $\chi_{\rm tot} = \sum_j^{\rm CCR} \chi_j$, for several U values (solid lines), and the inverse low-energy scale, $1/\tilde{B}_*$, for $U = 0.5\tau$ (dashed line) (**j**); the zero-temperature linear-response ($V_{\rm sd} = 0$) conductance, $g = G/G_Q$, for several U values (at fixed $\tilde{B} = 0$) (**k**) and for several $\tilde{B}$ values (at fixed $U = 0.5\tau$) (**l**). For a large enough interaction, $U = 0.5\tau$, even for $\tilde{B} = \tilde{T} = \tilde{V}_{\rm sd} = 0$ (blue lines in **k** and **l**), $g(\tilde{V}_c)$ has a shoulder (red arrow) at $g \approx 0.7$, the 0.7-anomaly. Three vertical dashed lines in **i–l** mark the three $\tilde{V}_c$ values used in **f–h**, as indicated by dots of matching colours.

length). In semiclassical terms, slow electrons feel interactions particularly strongly. When lowering the barrier top, $\tilde{V}_c$, to open the QPC, the van Hove ridge sweeps downwards (Fig. 1f–h); its interaction-amplifying effects are strongest in the $\tilde{V}_c$ regime where its apex, which has most weight, crosses μ. This happens for $0 \gtrsim \tilde{V}_c \gtrsim -\mathcal{O}(\Omega_x)$ (Fig. 1g), which, very importantly, encompasses the sub-open regime containing the 0.7-anomaly. Below, we show that the 0.7-anomaly and the zero-bias peak (ZBP) stem precisely from the amplification of interaction effects where the van Hove ridge intersects μ. The relevant implications are enhancements in the effective Hartree barrier governing elastic transmission, the spin susceptibility and the inelastic scattering rate, all of which lead to an anomalous reduction of g in the sub-open regime, especially for $T, B, V_{\rm sd} > 0$.

Figure 1c–e illustrates several local properties, calculated at $\tilde{T} = 0$ using FRG, for the sub-open QPC barrier shown in Fig. 1b. We note four salient features, all intuitively expected. First, the local density, $n_j = \langle \hat{n}_{j\uparrow} + \hat{n}_{j\downarrow} \rangle$, is minimal at the barrier centre (Fig. 1c). Second, the local magnetization, $m_j = \langle \hat{n}_{j\uparrow} - \hat{n}_{j\downarrow} \rangle / 2$, vanishes at $\tilde{B} = 0$ (Fig. 1d, blue line); this reflects a physical assumption entailed in our calculations (Supplementary Information, section 6), namely that no spontaneous magnetization occurs, in contrast to the spontaneous spin splitting scenario advocated in refs 4, 8, 17. Third, m_j increases without saturation when $\tilde{B}$ becomes large (Fig. 1d, inset), indicating a smooth redistribution of spin, as expected for an open structure. Fourth, the local spin susceptibility, $\chi_j = (\partial m_j / \partial \tilde{B})_{\tilde{B}=0}$, is strongly enhanced with increasing U (Fig. 1e), because interactions amplify any field-induced spin imbalance.

The j dependence of χ_j is governed by that of $A_j^0(0)$ (in fact, $\chi_j^{U=0} = A_j^0(0)/2$), which is maximal near those sites where the van Hove ridge intersects μ. When $\tilde{V}_c$ is decreased through 0 (Figs 1f–h), these intersection points sweep out a parabolic arch in the $\tilde{V}_c$–j plane, along which $\chi_j(\tilde{V}_c)$ (Fig. 1i, colour scale) is peaked, with most weight near the arch's apex. This leads to a corresponding peak in the total spin susceptibility, $\chi_{\rm tot} = \sum_j^{\rm CCR} \chi_j$, as a function of $\tilde{V}_c$ (Fig. 1j). This peak is strongly enhanced by increasing U (in accordance with the fourth feature above) and is located near the $\tilde{V}_c$ value where g ≈ 0.7 (Fig. 1k). We will see further below that this peak strongly affects the $\tilde{B}$ dependence of the conductance (Fig. 1l).

Note that the spatial structure for $\chi_j(\tilde{V}_c)$ in Fig. 1i, namely two peaks merging into one as $\tilde{V}_c$ is lowered, is consistent with that, shown in fig. 2b of ref. 14, for the density of spin-up electrons calculated using spin-density-functional theory, initialized in a small applied field to break spin symmetry. In ref. 14, the local maximum in the spin-up density was interpreted as evidence for a 'quasi-bound state' that was argued to host a spin-1/2 local moment; in contrast, features one and, especially, three above imply that our model yields no local moment.

Next we discuss the effect of the van Hove ridge on the conductance, $g(\tilde{V}_c)$, starting with its U dependence at $\tilde{B}=\tilde{T}=0$ (Fig. 1k). Increasing U skews the shape of the step in $g(\tilde{V}_c)$, which eventually develops a shoulder near $g\approx 0.7$ (red arrow). This shoulder develops because the increase in local density with decreasing $\tilde{V}_c$ is slightly nonlinear when the apex of the van Hove ridge drops past μ, causing a corresponding nonlinear upward shift in the effective Hartree barrier. For a parabolic barrier top, this occurs for $g\approx 0.7$. If the shape of the barrier top is changed to be non-parabolic, both the shape of the bare conductance step and the energy distance between the van Hove ridge apex and μ will change, which can cause the interaction-induced shoulder in g to shift away from 0.7. This explains the experimentally observed spread[6,12] of shoulders (that is, plateau values of the 0.7-anomaly) for $0.5 \lesssim g \lesssim 1$.

On increasing $\tilde{B}$ for fixed U and $\tilde{T}=0$ (Figs 1l and 2a), the shoulder in $g(\tilde{V}_c)$ becomes more pronounced, eventually developing into a spin-split plateau. Comparison of Fig. 2a with Fig. 2e shows that this development qualitatively agrees with experiment; the agreement was optimized by using U as fit parameter. Inspecting how the corresponding spin-resolved conductances, $g_\uparrow$ and $g_\downarrow$, change with $\tilde{B}$ (Fig. 2b), we note a strong asymmetry: although the bare barrier heights for spins ↑ and ↓ are shifted symmetrically by $-\tilde{B}/2$ and $\tilde{B}/2$, respectively, $g_\downarrow$ is decreased much more strongly than $g_\uparrow$ is increased. This is due to exchange interactions: increasing the spin-up density near the CCR centre (Fig. 1d) strongly raises the Hartree barrier, and more so for spin-down electrons than spin-up, owing to Pauli's exclusion principle. The consequences are most pronounced in the sub-open regime, owing to the van-Hove-ridge-induced peak in χ_{tot} there (Fig. 1j). We note, however, that $g_\uparrow = g_\downarrow$ at $\tilde{B}=0$, reflecting our above-mentioned assumption that no spontaneous spin splitting occurs.

Our FRG approach is limited to the case of zero temperature and zero source–drain voltage, for which no inelastic scattering occurs. To access qualitatively the effects of the latter at fixed U, we have instead used SOPT (Supplementary Information, section 7). Figure 2c–h shows a comparison of our SOPT results for the linear conductance, $g(\tilde{V}_c)$, calculated for several values of magnetic field, $\tilde{B}$, and temperature, $\tilde{T}=k_B T$, and our experimental data for $g(V_c)$. The measured conductance step shows a shoulder (Fig. 2e, f, red arrows) that becomes increasingly more pronounced with both increasing field, B (Fig. 2e), and increasing temperature, T (Fig. 2f), which is the hallmark of the 0.7-anomaly. Our perturbative calculations qualitatively reproduce both trends remarkably well. The only caveat is that the experimental curves in Fig. 2e, f show more pronounced shoulders than do the respective SOPT curves in Fig. 2c, d. This failure of SOPT to

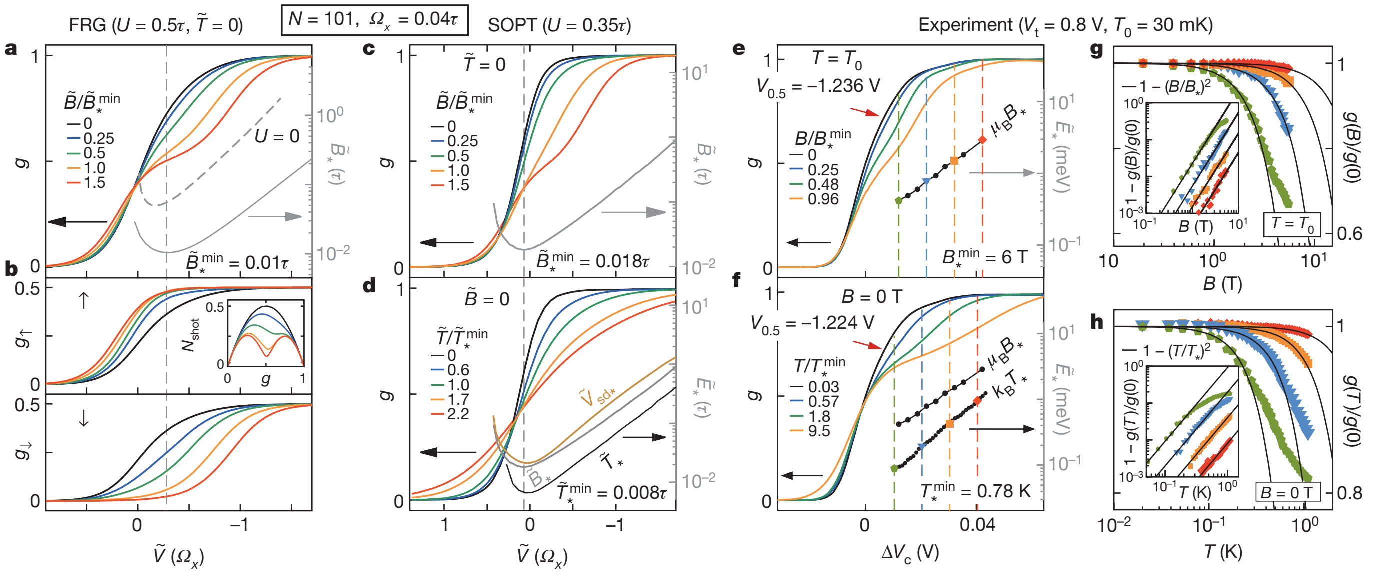

Figure 2 | Conductance: theory versus experiment. **a**, **b**, FRG results: the linear response conductance, $g(\tilde{V}_c, \tilde{B})$, of a QPC (**a**), and its spin-resolved components, $g_\uparrow$ and $g_\downarrow$ (**b**), plotted as functions of $\tilde{V}_c/\Omega_x$ for several values of $\tilde{B}$ at $\tilde{T}=0$ (but finite interaction U). The grey dashed and solid lines in **a** show the low-energy scale $\tilde{B}_*(\tilde{V}_c)$ for $U=0$ and $U=0.5$, respectively, plotted on the log-linear scale indicated on the right-hand axis (as also done in **c**–**f**). The small-field magnetoresponse in **a** is strongest when $\tilde{B}_*$ takes its smallest value, $\tilde{B}_*^{\min}$ (vertical dashed lines). Inset of **b**, the shot noise factor, $N_{\text{shot}} = \sum_\sigma g_\sigma(1-g_\sigma)/2$, plotted as function of g. Its asymmetric development with $\tilde{B}$, which reflects that of $g_\uparrow$ and $g_\downarrow$, agrees qualitatively with experiment (see fig. 4d of ref. 7). **c**, **d**, SOPT results: $g(\tilde{V}_c, \tilde{B})$ at $\tilde{T}=0$ for several values of $\tilde{B}$ (**c**) and $g(\tilde{V}_c, \tilde{T})$ at $\tilde{B}=0$ for several values of $\tilde{T}$ (**d**), both plotted as functions of $\tilde{V}_c/\Omega_x$. The low-energy scale $\tilde{B}_*(\tilde{V}_c)$ is shown as a thin grey line in **c** and repeated in **d**; $\tilde{T}_*(\tilde{V}_c)$ and $\tilde{V}_{\text{sd}*}(\tilde{V}_c)$ are respectively shown as thin black and brown lines in **d**. The vertical dashed line indicates where $\tilde{B}_*$ takes its minimal value, $\tilde{B}_*^{\min}$. For $\tilde{V}_c$ values below this dashed line, the lines for $\tilde{B}_*$, $\tilde{T}_*$ and $\tilde{V}_{\text{sd}*}$ in **d** are nearly straight on the log-linear scale, implying the behaviour summarized by equation (3), and are nearly parallel to each other, implying that the ratios $\tilde{B}_*/\tilde{T}_*$ and $\tilde{V}_{\text{sd}*}/\tilde{T}_*$ are essentially independent of $\tilde{V}_c$ there. **e**, **f**, Experiments—pinch-off curves. **e**, $g(V_c)$ measured at a low 2DES temperature, T_0, for various magnetic fields parallel to the 2DES, plotted as a function of $\Delta V_c = V_c - V_{0.5}$, where $V_{0.5}$ is the gate voltage for which the conductance at $B=0$ and $T=T_0$ is $g(V_{0.5})=0.5$. **f**, Analogous to **e**, but for $B=0$ and various temperatures T. Colours in **e** and **f** are chosen to provide comparability with theory curves in **a**, **c** and **d** (with the correspondence $|e|\Delta V_c \propto -\tilde{V}_c$). **g**, **h**, Experiments—Fermi-liquid behaviour: $g(B)/g(0)$ as function of B at temperature T_0 (**g**), and $g(T)/g(T_0)$ as function of T at $B=0$ (**h**), shown on log-linear scales (insets show their differences from unity on log-log scales) to emphasize small values of B and T. Coloured symbols distinguish data taken at different fixed V_c values, indicated by dashed lines of corresponding colour in **e** and **f**. The quadratic B and T dependences observed in **g** and **h** for each fixed V_c value confirm equation (2) and were used to determine the corresponding scales $B_*(V_c)$ and $T_*(V_c)$. (Black lines in **g** and **h** show $1-(B/B_*)^2$ and $1-(T/T_*)^2$, respectively.) The resulting energies, $E_* = \mu_B B_*(V_c)$ and $E_* = k_B T_*(V_c)$, are shown as functions of V_c in **e** (for B_*) and **f** (for both B_* and T_*) on a log-linear scale. The shape of these measured functions agrees qualitatively with the SOPT predictions in **c** and **d**, confirming the nearly exponential $\tilde{V}_c$ dependences and the nearly V_c-independent B_*/T_* ratio, discussed above. (For additional data, similar to that in **g** and **h**, see Supplementary Information, section 2B.)

produce real shoulders is present both in the low-field dependence at low temperature (compare Fig. 2e with Fig. 2c; the former, but not the latter, shows a weak shoulder even at zero field) and in the temperature dependence at zero field (compare Fig. 2f and Fig. 2d). In contrast, the more powerful FRG approach does reproduce the weak shoulder even for $\tilde{B}=\tilde{T}=0$, as discussed above; compare the black $g(\tilde{V}_{\rm c})$ curves in Fig. 2a (FRG) and Fig. 2c (SOPT). (That the latter curve, in contrast to the former, lies above its non-interacting version, $g^0(\tilde{V}_{\rm c})$, is an artefact of SOPT; see Supplementary Information, section 7D.)

We next focus on the limit of small energies $\tilde{B}$, $\tilde{T}$ and $\tilde{V}_{\rm sd}$. Here our SOPT calculations yield three predictions, enumerated below, that are all consistent with our measurements. First, for fixed $\tilde{V}_{\rm c}$, the leading dependence of the nonlinear conductance, $g_{\rm nl}=({\rm d}I/{\rm d}\tilde{V}_{\rm sd})/G_{\rm Q}$, on $\tilde{B}$, $\tilde{T}$ and $\tilde{V}_{\rm sd}$ is predicted to be quadratic, as confirmed by the measured data in Figs 2g, h and 3a. This implies an expansion of the form

$$\frac{g_{\rm nl}(\tilde{B},\,\tilde{T},\,\tilde{V}_{\rm sd})}{g_{\rm nl}(0,\,0,\,0)}\approx 1-\frac{\tilde{B}^2}{\tilde{B}_*^2}-\frac{\tilde{T}^2}{\tilde{T}_*^2}-\frac{\tilde{V}_{\rm sd}^2}{\tilde{V}_{\rm sd*}^2} \tag{2}$$

for $\tilde{B}/\tilde{B}_*$, $\tilde{T}/\tilde{T}_*$, $\tilde{V}_{\rm sd}/\tilde{V}_{\rm sd*}\ll 1$, where $\tilde{B}_*$, $\tilde{T}_*$ and $\tilde{V}_{\rm sd*}$ are $\tilde{V}_{\rm c}$-dependent crossover scales that govern the 'strength' of the 0.7-anomaly for $U\neq 0$: the smaller these scales, the stronger the dependence on $\tilde{B}$, $\tilde{T}$ and $\tilde{V}_{\rm sd}$ for a given $\tilde{V}_{\rm c}$. Our SOPT results for these crossover scales are shown as thin lines on log-linear scales in Fig. 2c and Fig. 2d, respectively. Second, in that part of the sub-open regime where $g_{\rm nl}(0,\,0,\,0)\approx 1$, they all depend exponentially on $\tilde{V}_{\rm c}$:

$$\tilde{B}_*,\ \tilde{T}_*,\ \tilde{V}_{\rm sd*}\propto \exp\left(-\pi\tilde{V}_{\rm c}/\Omega_x\right) \tag{3}$$

Third, and again for $g_{\rm nl}(0,\,0,\,0)\approx 1$, the ratios $\tilde{B}_*/\tilde{T}_*$ and $\tilde{V}_{\rm sd*}/\tilde{T}_*$ are essentially independent of $\tilde{V}_{\rm c}$ (Supplementary Fig. 4). Remarkably, both the second and third predictions are confirmed by our experimental results (Fig. 2e for B_*, Fig. 2f for T_* and Supplementary Fig. 3 for $V_{\rm sd*}$). The behaviour predicted by equation (3) for $\tilde{T}_*$ is also in accord with previous experiments[6] and with a perturbative treatment of interactions using Wentzel–Kramers–Brillouin wavefunctions[21]. Remarkably, the exponential $\tilde{V}_{\rm c}$ dependence of the crossover scales stated in equation (3) can be understood from a non-interacting ($U=0$) theory, by using the bare transmission probability[3]

$$T_\sigma^0(\omega)=\left[{\rm e}^{-2\pi\left(\omega-\tilde{V}_{\rm c}+\sigma\tilde{B}/2\right)/\Omega_x}+1\right]^{-1} \tag{4}$$

in the Landauer–Büttiker formula. A detailed analysis (Supplementary Information, section 5) shows that the crossover scales experience a further exponential reduction with increasing effective interaction strength, $U/\sqrt{\Omega_x\tau_0}$.

When plotted as a function of $\tilde{V}_{\rm c}$, $1/\tilde{B}_*$ has a peak in the sub-open regime just before the onset of the exponential dependence of equation (3) (Fig. 1j). This peak is roughly similar in shape and position to that in $\chi_{\rm tot}(\tilde{V}_{\rm c})$ (compare dashed and solid blue lines in Fig. 1j), except that the latter has a finite offset, reflecting the non-zero spin susceptibility of an open QPC. Thus, we predict, fourth, that $1/\tilde{B}_*$, which characterizes the strength of the low-field magnetoconductance, is roughly proportional to the spin susceptibility, $\chi_{\rm tot}$, of the CCR.

Next we address the remarkable experimental fact[6] that many low-energy properties of the 0.7-anomaly (including our first and third predictions) are similar to those seen in transport through a Kondo quantum dot (KQD). This led to the proposal[13,14] that a QPC harbours

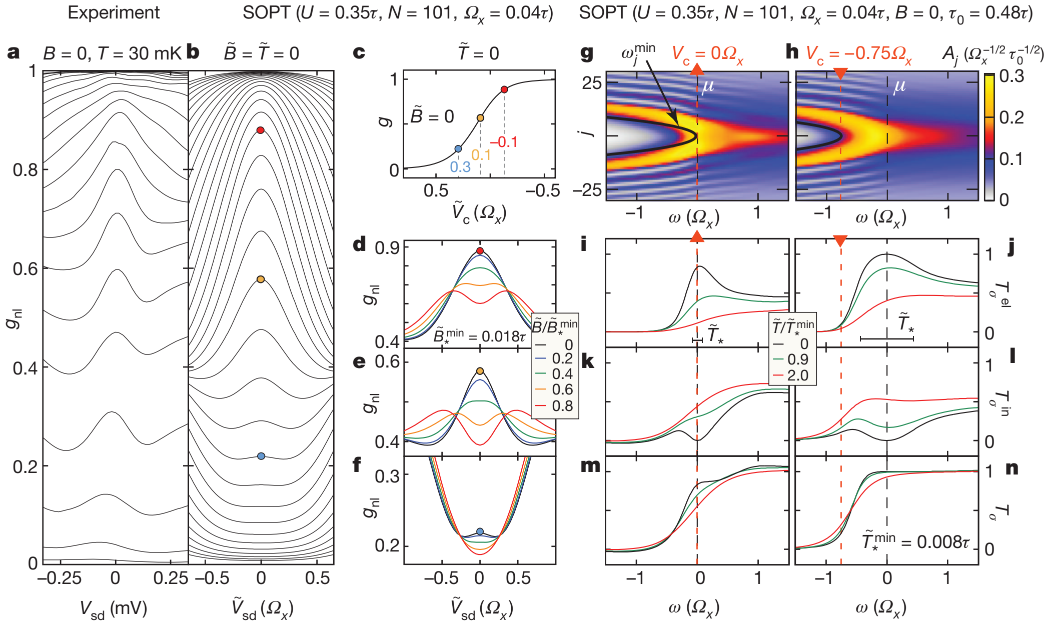

Figure 3 | Finite excitation energies. a–f, Zero-bias peak. **a**, Experimental data for the nonlinear conductance, $g_{\rm nl}$, as a function of source–drain voltage, measured for several $V_{\rm c}$ values at a fixed low temperature and zero field. **b**, Keldysh SOPT results for $g_{\rm nl}(\tilde{V}_{\rm sd})$ for several $\tilde{V}_{\rm c}$ values at $\tilde{T}=\tilde{B}=0$, showing qualitative agreement with **a**. **c**, The linear-response conductance, $g=g_{\rm nl}(\tilde{V}_{\rm sd}=0)$, as a function of $\tilde{V}_{\rm c}$. **d–f**, $g_{\rm nl}(\tilde{V}_{\rm sd})$ as in **b**, but for three different $\tilde{V}_{\rm c}$ values (compare colour-matched dots in **c** and **b**) and five different magnetic field values in each panel. Increasing $\tilde{B}$ causes the ZBP to split into two subpeaks once $\tilde{B}\gtrsim\tilde{B}_*$; the splitting is therefore most pronounced in **e**, for which $\tilde{B}_*$ is smallest. A detailed discussion of the ZBP, including its T dependence, will be published elsewhere. Here we would like to point out the qualitative agreement of **d–f** with published data; see, for example, fig. 2d of ref. 6. **g**, **h**, Interacting LDOS: $A_j(\omega)$, calculated using SOPT, shown for two fixed gate voltage values, $\tilde{V}_{\rm c}/\Omega_x=0$ (**g**) and -0.75 (**h**) (red dashed lines). **i–n**, Equilibrium transmission probabilities: the corresponding elastic, inelastic and total transmission probabilities, $T_\sigma^{\rm el}$ (**i**, **j**), $T_\sigma^{\rm in}$ (**k**, **l**) and T_σ (**m**, **n**), calculated using SOPT and shown as functions of energy, ω, for three different temperatures. At $\tilde{T}=0$ (black curves) $T_\sigma^{\rm in}(\omega)$ vanishes at $\omega=0$, where there is no phase space for inelastic scattering. However, it increases as ω changes from zero, causing a corresponding reduction in the elastic transmission for $\omega\neq 0$, such that $T_\sigma^{\rm el}(\omega)$ has a narrow 'low-energy peak' around $\omega=0$. On increasing the temperature, the probability of inelastic scattering increases, causing the minimum in $T_\sigma^{\rm in}(\omega)$ and the peak in $T_\sigma^{\rm el}(\omega)$ to be smeared out. This leads to a net $\tilde{T}$-induced reduction in the total transmission, $T_\sigma(\omega)$ near $\omega=0$, causing a corresponding reduction in the conductance (Fig. 2d, f). This reduction is stronger for $\tilde{V}_{\rm c}/\Omega_x=0$ (**m**) than for $\tilde{V}_{\rm c}/\Omega_x=-0.75$ (**n**), because the probability of electron–hole pair creation during inelastic scattering is largest when apex of the van Hove ridge lies closest to μ (compare **g** and **h**).

a quasi-bound state, whose local moment gives rise to the Kondo effect. In contrast, our van-Hove-ridge scenario fully explains the 0.7-anomaly without invoking the Kondo effect. In particular, we find no indications that a smooth parabolic barrier hosts a discrete, localized spin (compare with the third feature above), and no Kondo effect/0.7-anomaly similarities (experimentally or theoretically) at high energies ($\gtrsim \tilde{B}_*$), where the Kondo effect is governed by an unscreened local moment. Nevertheless, the two phenomena do have similar low-energy behaviour. This is because both involve a spin-singlet ground state featuring spatially confined spin fluctuations. For a KQD they result from screening of the localized spin, whereas for a QPC they result from the extended structure of the van Hove ridge (Fig. 1i); but this distinction, which is important on short length scales (high energies), does not matter on long ones (low energies). These spin fluctuations are characterized by exponentially small energy scales, the Kondo temperature for a KQD, and $\tilde{T}_*$ for a QPC, both scaling inversely with the local spin susceptibility (for a QPC, this follows from prediction four). For a KQD, the local spin fluctuations can be described by Nozières–Fermi-liquid theory[27,28] in terms of scattering phase shifts, which determine its low-energy properties. Because a QPC, like a KQD, harbours spatially confined spin fluctuations, a similar Nozières–Fermi-liquid framework applies, explaining why its low-energy transport properties are similar to those of a KQD.

We next study finite excitation energies ($\tilde{T}$, $\tilde{V}_{\mathrm{sd}} > 0$), where inelastic scattering becomes important (Fig. 3). We begin by considering the nonlinear differential conductance, g_{nl}, as a function of source–drain voltage, V_{sd}. Experimentally, g_{nl} shows a narrow peak at $V_{\mathrm{sd}} = 0$ (Fig. 3a; see also refs 6, 9, 10). This ZBP appears strongest in the sub-open regime, but remains visible even very close to pinch off[10] ($g \to 0$). It splits with increasing field once B exceeds a V_{c}-dependent crossover value that is smallest when $g \approx 0.7$ (see fig. 2d of ref. 6). Remarkably, our model, treated using Keldysh SOPT (Supplementary Information, section 7B), yields a ZBP (Fig. 3b, d–f) that qualitatively reproduces this behaviour. In the sub-open regime ($0.5 \lesssim g \lesssim 0.9$), a ZBP arises even without interaction (this follows from equation (4)), but interactions modify it in two ways (Supplementary Information, section 7C): a finite V_{sd} causes a net charge enhancement at the barrier, resulting in a reduction of transmission due to Coulomb repulsion; and opens up a finite phase space for inelastic backscattering. Both effects strongly depend on the LDOS near μ (Fig. 3g, h), and are thus strongest when the apex of the van Hove ridge lies near μ (as in Figs 3g and 1g). However, the van Hove ridge intersects μ also for $g < 0.5$ (as in Fig. 1f), which explains why a ZBP is experimentally observed even close to pinch off[10].

The two modification mechanisms just discussed also apply to the case of increasing temperature. To highlight the role of inelastic scattering, we now discuss (for $\tilde{B} = \tilde{V}_{\mathrm{sd}} = 0$) the transmission probability $T_\sigma(\omega) = T_\sigma^{\mathrm{el}}(\omega) + T_\sigma^{\mathrm{in}}(\omega)$, written as the sum of elastic and inelastic contributions corresponding respectively to transmission without or with the creation of electron–hole pairs (see Supplementary Information, section 7A, for their precise definition). Figure 3i–n shows examples of these quantities. With increasing temperature, the probability for inelastic scattering increases, causing $T_\sigma^{\mathrm{in}}(\omega)$ to increase (Fig. 3k, l) and $T_\sigma^{\mathrm{el}}(\omega)$ to decrease (Fig. 3i, j). This leads to a net temperature-induced reduction in the total transmission, $T_\sigma(\omega)$ (Fig. 3m, n), near $\omega = 0$, causing a corresponding reduction in the conductance (Fig. 2d, f). Importantly, this reduction is V_{c} dependent: it is strongest when the apex of the van Hove ridge lies near μ (as in Fig. 3m) and decreases away from this point (as in Fig. 3n), because the probability for electron–hole pair creation during inelastic scattering increases with the LDOS near μ. The fact that $T_\sigma(\omega)$ acquires a non-trivial, interaction-induced dependence on $\tilde{T}$ in the sub-open regime is consistent with the fact that near $g \approx 0.7$ the measured thermopower violates the Mott relation[5], which is based on the assumption of non-interacting electrons.

Finally, we note that we have studied the magnetic field dependence of the transconductance, $\mathrm{d}G/\mathrm{d}V_{\mathrm{c}}$, both experimentally and by using FRG. We obtain excellent qualitative agreement between experiment and theory, showing that such measurements can be understood without invoking spontaneous spin polarization, as is often advocated to explain them[4,8,17]. A detailed analysis (Supplementary Information, section 2C, and Supplementary Fig. 5) establishes that the g factor is enhanced significantly by interactions, and that interaction strength can be tuned experimentally using a top gate.

We have presented detailed microscopic calculations that qualitatively reproduce the full phenomenology of the 0.7-anomaly. We argued that a van Hove ridge in the LDOS, combined with interactions, provides a natural explanation for the anomalous behaviour of the conductance of a sub-open ($g \gtrsim 0.5$) QPC. The experimentally observed[6] similarities between the 0.7-anomaly and the Kondo effect at low energies arise because both phenomena involve spatially localized spin fluctuations; at high energies, the similarities cease. We verified our Fermi-liquid predictions for the QPC conductance by systematic measurement of the conductance as a function of V_{c}, B and T. Strikingly, we demonstrated that the zero-bias peak in a QPC arises from the interplay of interactions and geometry. By implication, anomalous zero-bias behaviour might also arise in other systems involving interacting electrons traversing 1D low-density regions with slowly varying spatial inhomogeneities, such as the gated nanowires being studied in the search for Majorana fermions[29].

METHODS SUMMARY

The nanostructure is laterally defined in a 2DES located 85 nm beneath the surface of a GaAs/AlGaAs heterostructure. The low-temperature carrier density and mobility are $1.9 \times 10^{11}\,\mathrm{cm}^{-2}$ and $1.2 \times 10^{6}\,\mathrm{cm}^{2}\,\mathrm{V}^{-1}\,\mathrm{s}^{-1}$, respectively. Electron-beam lithography was used to create the Ti/Au gates. The top gate is electrically insulated from the others by cross-linked poly(methyl methacrylate). Perfect alignment of magnetic fields parallel to the 2DES and the 1D channel defining the QPC was ensured by using a two-axis magnet and was controlled by magnetotransport measurements. We used a dilution refrigerator and reached electron temperatures as low as $T_{\mathrm{2DES}} \approx 30\,\mathrm{mK}$.

Our most accurate theoretical results were obtained by using FRG[24–26] to calculate $T = 0$ properties. FRG amounts to doing renormalization-group-enhanced perturbation theory in the interaction U. In setting up our FRG flow equations, we made two approximations, both exact to second order in U: we truncated the infinite hierarchy of flow equations by neglecting the flow of the three-particle vertex; and we set to zero all components of the two-particle vertex that are not already generated to second order in the interaction (coupled-ladder approximation).

To access the effects of inelastic scattering for $\tilde{T} > 0$ or $\tilde{V}_{\mathrm{sd}} > 0$ at fixed U, we used SOPT: we dressed bare Green's functions by evaluating the self-energy perturbatively to second order in the interaction. For $\tilde{V}_{\mathrm{sd}} = 0$, we calculated the linear conductance following the strategy in ref. 23, generalized to $\tilde{B} \neq 0$ and broken electron–hole symmetry. For $\tilde{V}_{\mathrm{sd}} > 0$, we calculated the nonlinear conductance, $g_{\mathrm{nl}} = (\mathrm{d}I/\mathrm{d}\tilde{V}_{\mathrm{sd}})/G_{\mathrm{Q}}$, using the Meir–Wingreen formula for the current (equation (6) of ref. 30).

Received 16 November 2012; accepted 26 June 2013.

Published online 28 August 2013.

1. van Wees, B. J. *et al.* Quantized conductance of point contacts in a two-dimensional electron gas. *Phys. Rev. Lett.* **60,** 848–850 (1988).
2. Wharam, D. A. *et al.* One-dimensional transport and the quantisation of the ballistic resistance. *J. Phys. C* **21,** L209–L214 (1988).
3. Büttiker, M. Quantized transmission of a saddle-point constriction. *Phys. Rev. B* **41,** 7906(R) (1990).
4. Thomas, K. J. *et al.* Possible spin polarization in a one-dimensional electron gas. *Phys. Rev. Lett.* **77,** 135–138 (1996).
5. Appleyard, N. J. *et al.* Direction-resolved transport and possible many-body effects in one-dimensional thermopower. *Phys. Rev. B* **62,** R16275–R16278 (2000).
6. Cronenwett, S. M. *et al.* Low-temperature fate of the 0.7 structure in a point contact: a Kondo-like correlated state in an open system. *Phys. Rev. Lett.* **88,** 226805 (2002).
7. DiCarlo, L. *et al.* Shot-noise signatures of 0.7 structure and spin in a quantum point contact. *Phys. Rev. Lett.* **97,** 036810 (2006).
8. Koop, E. J. *et al.* The influence of device geometry on many-body effects in quantum point contacts: signatures of the 0.7-anomaly, exchange and Kondo. *J. Supercond. Nov. Magn.* **20,** 433–441 (2007).
9. Sarkozy, S. *et al.* Zero-bias anomaly in quantum wires. *Phys. Rev. B* **79,** 161307R (2009).
10. Ren, Y. *et al.* Zero-bias anomaly of quantum point contacts in the low-conductance limit. *Phys. Rev. B* **82,** 045313 (2010).

11. Micolich, A. P. What lurks below the last plateau: experimental studies of the $0.7 \times 2e^2/h$ conductance anomaly in one-dimensional systems. *J. Phys. Condens. Matter* **23,** 443201 (2011).
12. Burke, A. *et al.* Extreme sensitivity of the spin-splitting and 0.7 anomaly to confining potential in one-dimensional nanoelectronic devices. *Nano Lett.* **12,** 4495–4502 (2012).
13. Meir, Y., Hirose, K. & Wingreen, N. S. Kondo model for the 0.7 anomaly in transport through a quantum point contact. *Phys. Rev. Lett.* **89,** 196802 (2002).
14. Rejec, T. & Meir, Y. Magnetic impurity formation in quantum point contacts. *Nature* **442,** 900–903 (2006).
15. Ihnatsenka, S. & Zozoulenko, I. V. Conductance of a quantum point contact based on spin density-functional theory. *Phys. Rev. B* **76,** 045338 (2007).
16. Matveev, K. A. Conductance of a quantum wire at low electron density. *Phys. Rev. B* **70,** 245319 (2004).
17. Reilly, D. J. Phenomenological model for the 0.7 conductance feature in quantum wires. *Phys. Rev. B* **72,** 033309 (2005).
18. Sloggett, C. Milstein, A. I. & Sushkov, O. P. Correlated electron current and temperature dependence of the conductance of a quantum point contact. *Eur. Phys. J. B* **61,** 427–432 (2008).
19. Aryanpour, K. & Han, J. E. Ferromagnetic spin coupling as the origin of 0.7 anomaly in quantum point contacts. *Phys. Rev. Lett.* **102,** 056805 (2009).
20. Güçlü, A. D. *et al.* Localization in an inhomogeneous quantum wire. *Phys. Rev. B* **80,** 201302(R) (2009).
21. Lunde, A. M. *et al.* Electron-electron interaction effects in quantum point contacts. *New J. Phys.* **11,** 023031 (2009).
22. Goldhaber-Gordon, D. *et al.* Kondo effect in a single-electron transistor. *Nature* **391,** 156–159 (1998).
23. Oguri, A. Transmission probability for interacting electrons connected to reservoirs. *J. Phys. Soc. Jpn* **70,** 2666–2681 (2001).
24. Andergassen, S. *et al.* Renormalization-group analysis of the one-dimensional extended Hubbard model with a single impurity. *Phys. Rev. B* **73,** 045125 (2006).
25. Karrasch, C., Enss, T. & Meden, V. Functional renormalization group approach to transport through correlated quantum dots. *Phys. Rev. B* **73,** 235337 (2006).
26. Metzner, W. *et al.* Functional renormalization group approach to correlated fermion systems. *Rev. Mod. Phys.* **84,** 299–352 (2012).
27. Nozières, P. A ''fermi-liquid'' description of the Kondo problem at low temperatures. *J. Low Temp. Phys.* **17,** 31–42 (1974).
28. Glazman, L&. Pustilnik, M. in *Nanophysics: Coherence and Transport* (eds Bouchiat, H. *et al.*) 427–478 (Elsevier, 2005).
29. Mourik, V. *et al.* Signatures of Majorana fermions in hybrid superconductor-semiconductor nanowire devices. *Science* **336,** 1003–1007 (2012).
30. Meir, Y. & Wingreen, N. S. Landauer formula for the current through an interacting electron region. *Phys. Rev. Lett.* **68,** 2512–2515 (1992).

Supplementary Information is available in the online version of the paper.

Acknowledgements We thank B. Altshuler, P. Brouwer, R. Egger, J. Folk, L. Glazman, V. Golovach, A. Hamilton, A. Högele, Y. Imry, M. Kiselev, J. Kotthaus, D. Logan, D. Loss, C. Marcus, Y. Meir, H. Monien, M. Pepper, M. Pustilnik, A. Rosch, K. Schönhammer, B. Spivak and A. Yacoby for discussions, and, in particular, S. Andergassen, C. Honerkamp, S. Jakobs, C. Karrasch, V. Meden, M. Pletyukhov and H. Schoeller for FRG-related help and advice. We acknowledge support from the DFG through SFB-631, SFB-TR12, De730/3-2, De730/4-1, De730/4-2, De730/4-3, HO 4687/1-3, LU819/4-1 and the Cluster of Excellence Nanosystems Initiative Munich; from the Center for NanoScience; and from the US National Science Foundation under grant no. NSF PHY05-51164. S.L. acknowledges support through a Heisenberg fellowship of the DFG.

Author Contributions J.v.D. and S.L. coordinated the project: J.v.D. initiated and supervised the theoretical work, and S.L. planned and supervised the experiments and their analysis. F.B. and J.H. carried out the calculations using FRG, and J.H., F.B. and B.B. carried out the calculations using perturbation theory. D.S. and W.W. provided the wafer material, and D.B. fabricated the nanostructure. E.S., D.B., D.T. and S.L. carried out the measurements, and E.S., D.B., F.B. and J.H. carried out the experimental data analysis. J.H. and F.B. prepared the figures, and J.v.D., S.L., F.B., J.H. and E.S. wrote the paper.

Author Information Reprints and permissions information is available at www.nature.com/reprints. The authors declare no competing financial interests. Readers are welcome to comment on the online version of the paper. Correspondence and requests for materials should be addressed to J.v.D. (vondelft@lmu.de) or S.L. (ludwig@lmu.de).

doi:10.1038/nature12421

Contents

S-1. Overview 1

PART I: EXPERIMENT VS. THEORY 2

S-2. Our experimental data vs. theory 2
  A. Experimental setup 2
  B. Fermi liquid properties 2
  C. Top-gate tuning of effective g_{ss}-factor 3

S-3. Other experimental data vs. fRG 7
  A. Spin-resolved conductance, shot noise 7
  B. Compressibility and charge susceptibility 8

PART II: THEORETICAL DETAILS 10

S-4. Models used for barrier shape 10
  A. Hamiltonian, chemical potential, U_j 10
  B. Model I 12
  C. Bare local density of states (LDOS) 12
  D. Model II 14
  E. Comparison: bare LDOS of QPC and QD 15

S-5. The low-energy scale $\widetilde{B}_*$ 16
  A. Exponential $\widetilde{V}_{\mathrm{c}}$-dependence of $\widetilde{B}_*$ 16
  B. Effects of interactions on $\widetilde{B}_*$ and $\widetilde{T}_*$ 18
  C. Geometry-dependence of interaction U 20

S-6. Functional renormalization group 20
  A. Observables 21
  B. fRG strategy and approximations 21
  C. fRG Flow equations 21
  D. fRG for non-uniform systems 22
  E. Zero-temperature limit 23
  F. Static fRG 24

S-7. Second-order perturbation theory 25
  A. Equilibrium SOPT 25
  B. Nonequilibrium SOPT 25
  C. $\widetilde{B}$-, $\widetilde{T}$- , and $\widetilde{V}_{\mathrm{sd}}$-dependence of $g(\widetilde{V}_{\mathrm{c}})$ 26
  D. SOPT artefact arising for increasing U 27

References 28

S-1. OVERVIEW

The following supplementary material provides additional information related to various aspects of the main article. Its sections can be read independently and in arbitrary order. They are grouped into two parts: Part I (Secs. S-2 and S-3) is devoted to experiments and their comparison with theory; Part II (Secs. S-4 to S-7 C) provides further theoretical details.

Section S-2 gives supplementary information about our measurements discussed in the main article. Section S-2 A describes the experimental setup. In Sec. S-2 B we present the raw data on which the experimental tests of Fermi liquid predictions in the main article are based, together with corresponding results obtained by the functional renormalization group (fRG) (Fig. S2). We also present additional data (Fig. S3) illustrating the gate-voltage dependence of the crossover scales in magnetic field, temperature and source-drain-voltage, B_*, T_* and $V_{\mathrm{sd}*}$, together with corresponding calculations using second-order perturbation theory (SOPT). Sec. S-2 C explains in detail how the effective g-factor g_{ss} is extracted from the transconductance for large fields (Fig. S5), and offers some comments on the much-discussed scenario that the 0.7-anomaly is due to spontaneous spin polarization in the QPC region.

Sec. S-3 presents further $T = 0$ fRG results (Figs. S6 and S7) that demonstrate qualitative agreement with shot noise and compressibility measurements by other groups. These fRG results, and those in Sec. S-5, were calculated using "static" fRG, which differs from the "dynamic" fRG approach used in the main text by neglecting the frequency dependence of the self-energy and all vertices (see Sec. S-6 F). Static fRG yields results that are very similar to those of dynamic fRG (see Fig. S15), while being numerically cheaper by a factor $\sim 10^3$.

Section S-4 describes our theoretical model in detail. We have used two slightly different parametrizations of the QPC barrier shape, called "model I" and "model II", which both describe parabolic barrier tops and hence give essentially equivalent results for QPC properties. They are defined in Secs. S-4 B and S-4 D, respectively (the main article uses only model II). Sections S-4 C and S-4 E explain how the effects of geometry are encoded in the bare local density of states (LDOS), focussing in particular on the van Hove ridge of a QPC, which is key to understanding the 0.7-anomaly.

Section S-5 focuses on the low-energy scale $\widetilde{B}_*(\widetilde{V}_{\mathrm{c}})$ for a QPC: it shows that its exponential $\widetilde{V}_{\mathrm{c}}$-dependence has a purely geometric origin, and that the strength of its U-dependence likewise depends on the shape of the barrier.

Sections S-6 and S-7 discuss details of the two theoretical methods used here to incorporate the effect of interaction: the functional Renormalization Group (fRG) and second order perturbation theory (SOPT), respectively. Section S-7 C is devoted to a detailed description of our

SOPT results for finite temperature or finite source-drain voltage, offering a summary of the features of the 0.7-anomaly which SOPT does or does not capture qualitatively. Finally, Sec. S-7 D discusses an SOPT artefact that arises with increasing U.

Equation and figure and section numbers from the main article or the supplementary material are prefaced below by A (for "article") vs. S (for "supplementary"), respectively, e. g. Eq. (A1), Fig. A1**f**, Sec. A-2 vs. Eq. (S1), Fig. S2**b**, Sec. S-4. As in the main article, we use tildes to distinguish theory parameters from those used in experiment, writing, e. g. $\widetilde{T} = k_{\rm B}T$, $\widetilde{B} = |g_{\rm el}|\mu_{\rm B}B$, and $\widetilde{V}_{\rm c,s} \propto -|e|V_{\rm c,s}$.

PART I: EXPERIMENT VS. THEORY

S-2. OUR EXPERIMENTAL DATA VS. THEORY

A. Experimental setup

The gate layout of our sample, shown in Fig. A1**a** for a dummy sample whose layout is identical to that of the actual sample, provides a particularly high tunability of the central constriction region (CCR). The gates can be used to laterally define either a quantum point contact (QPC) or a quantum dot (QD) in the two-dimensional electron system (2DES) 85 nm beneath the surface of a GaAs/AlGaAs heterostructure. In this work, we focus exclusively on the QPC geometry; a study of the crossover from QD to QPC will be published elsewhere.[1] More information about the experimental conditions is provided in the methods summary section of the main article.

In our two-terminal transport measurements the current $I_{\rm sd}$ flows through the nanostructure between ohmic contacts marked by "source" and "drain" in Fig. A1**a**, and we measure the differential conductance $g = ({\rm d}I_{\rm sd}/{\rm d}V_{\rm sd})/G_{\rm Q}$ (henceforth simply called conductance) using lockin methods. In all measurements discussed in this paper we apply a negative voltage $V_{\rm c}$ to both center gates and a negative voltage $V_{\rm s}$ to all four side gates. This depletes the 2DES in the vicinity of the gates, so that propagation between source and drain through the CCR is confined to a narrow channel, leading to the quantization of transverse modes. (Further variations of individual gate voltages allow additional control of the lateral symmetry properties of the CCR, but such studies are not included in this work.) Moreover, our sample also contains a global top gate (see Fig. A1**a**).

In this work, we focus on gate voltages such that transport is carried solely by the first subband, corresponding to the lowest transverse mode. Its behavior can be described by a one-dimensional effective model for motion in the longitudinal (say x-) direction. The shape of the effective potential $V_{\rm eff}(x)$ in the CCR can be changed by tuning $V_{\rm c}$, $V_{\rm s}$ and $V_{\rm t}$. Increasing the top gate voltage $V_{\rm t}$ increases the carrier density of the 2DES in the contacts of the CCR and hence the chemical potential, thereby deepening (w. r. t. μ) the trenches between the regions of high potential energy caused by the central and side gates[4]. This changes not only the shape of $V_{\rm eff}(x)$, but also causes the transverse wave functions to be more localized and hence increases the effective one-dimensional on-site interaction strength U within the CCR. For future reference, we summarize this trend as follows:

$$\text{The effective interaction strength } U \text{ can be increased experimentally by increasing } V_{\rm t}. \qquad \text{(S1)}$$

For a QPC geometry, increasing $V_{\rm t}$ has an additional effect: due to the deepened trenches in the potential landscape, the energy spacing of the transverse eigenmodes increases, resulting in an increased subband spacing[5]. This trend is demonstrated in Fig. S1 based on measured pinch-off curves of our QPC for varying top-gate voltages. It can be used, in principle, to quantify the $V_{\rm t}$-induced increase in U in terms of the $V_{\rm t}$-induced increase in subband spacing[6], as will be elaborated in Sec. S-5 C below.

B. Fermi liquid properties

Figs. S2**b** and S2**c** show the raw experimental data for the measured linear response conductance of our QPC (a constant lead resistance has already been subtracted for all data). They show how the pinch-off curves depend on magnetic field and temperature, respectively. For comparison, Fig. S2**a** shows corresponding fRG data calculated for zero temperature as a function of the magnetic field $\widetilde{B}$. Both calculated and measured data exhibit the expected transition from a weak kink at $g \simeq 0.7$ at small T and B to a pronounced 0.7-anomaly if either magnetic field (measured and calculated data) or temperature (measured data) is substantially increased.

The raw data from Figs. S2**b** and S2**c** underly the experimental results presented in Figs. A2**e-h** of the main article. Figs. S3**a-d** shows additional data sets, plotted in the same way as in Figs. A2**g** and A2**h**, but displaying data not shown there for lack of space. Together, these data confirm the Fermi-liquid behavior expected theoretically for sufficiently low fields and temperatures: Figures A2**g** and S3**a**,**b** show that at sufficiently low temperatures, $T_0 \ll T_*$ (in our measurements $T_0 = T_{\rm 2DES} \simeq 30\,{\rm mK}$), the leading magnetic field-dependence of the linear conductance is quadratic,

$$g(B)/g(0) = 1 - (B/B_*)^2\,, \qquad B \ll B_*\,, \qquad \text{(S2a)}$$

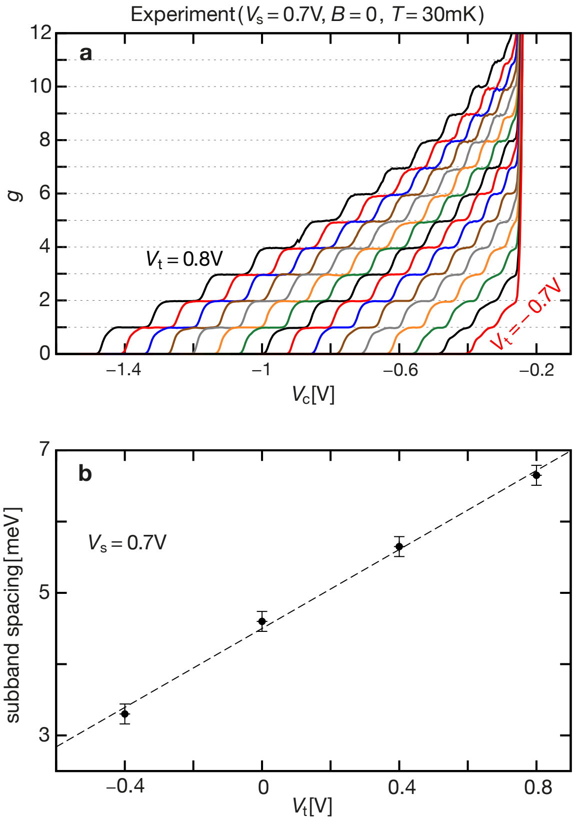

Figure S1: **V_t-dependence of subband spacing.** **a**, Measured pinch-off curves $g(V_c)$ of our QPC for a series of top-gate voltages in the range $-0.7\,\mathrm{V} \leq V_t \leq 0.8\,\mathrm{V}$. As V_t is decreased the carrier density also becomes smaller which, in turn, results in a larger pinch-off voltage V_c and, clearly, in more narrow plateaus at integer g. The steep increase of $g(V_c)$ independent of V_t at $V_c \simeq -0.25\,\mathrm{V}$ indicates the transition from 1D to 2D transport as the 2DES directly below the center gates is no longer depleted. **b**, Energy spacing between the lowest two 1D subbands as a function of V_t. The data points were evaluated from finite-V_{sd} measurements (raw data[2] not shown), using a procedure described in Refs. [2,3], whose uncertainty is indicated by the error bars. The resulting subband spacing is approximately proportional to the width of the first conductance plateau in **a**. As expected from a simple capacitive model, it is also proportional to V_t (the dashed straight line is a guide for the eye).

as expected from Eq. (A2). Similarly, Figs. A2**h** and S3**c**,**d** show that at zero field ($B = 0$), the leading temperature dependence is likewise quadratic,

$$g(T)/g(T_0) = 1 - (T/T_*)^2 \,, \qquad T \ll T_* \,. \qquad \text{(S2b)}$$

Fitting Eqs. (S2a) and (S2b) to the data in Figs. S2**b** and S2**c**, respectively, yields the low-energy scales $B_*(V_c)$ and $T_*(V_c)$ used in Figs. A2**g** and A2**h** and depicted by colored symbols in Figs. A2**e** and A2**f**, respectively (and similarly for Figs. S3**a-d**). The scaled conductance curves displayed in Figs. S3**a-d** are plotted only in the restricted ranges $g(B)/g(0) \gtrsim 0.8$ and $g(T)/g(T_0) \gtrsim 0.8$, respectively. For smaller conductances, where the conditions $B \ll B_*$ or $T \ll T_*$ no longer hold, the measured B- and T-dependences of the conductance deviate from quadratic behavior by bending upward, tending toward saturation (as shown in Figs. A2**g**,**h**).

The fit parameters B_* and T_* are compared in the half-logarithmic presentation in Fig. A2**f** as functions of the center gate voltage ΔV_c. For convenience, this data is shown again in Fig. S3**f**, together with the low-energy source-drain voltage scale $V_{\mathrm{sd}*}$. The latter was obtained by determining the curvature of the nonlinear conductance curves $g_{\mathrm{nl}}(V_{\mathrm{sd}})$ (shown in Fig. A3**i**) at $V_{\mathrm{sd}} = 0$:

$$g_{\mathrm{nl}}(V_{\mathrm{sd}})/g_{\mathrm{nl}}(0) = 1 - (V_{\mathrm{sd}}/V_{\mathrm{sd}*})^2, \quad V_{\mathrm{sd}} \ll V_{\mathrm{sd}*} \,. \quad \text{(S2c)}$$

Compared to our determinations of B_* and T_* from linear-response data, those for $V_{\mathrm{sd}*}$ have rather larger error margins, since for technical reasons the non-linear conductance data was measured with a smaller signal-to-noise ratio.

As mentioned in the main article, SOPT makes two predictions for the $\widetilde{V}_c$-dependence of the crossover scales $\widetilde{B}_*$, $\widetilde{T}_*$ and $\widetilde{V}_{\mathrm{sd}*}$ in the V_c-range where $g \to 1$: first, all three scales depend exponentially on V_c (Fig. S3**e**); and second, the ratios $\widetilde{B}_*/\widetilde{T}_*$ and $\widetilde{V}_{\mathrm{sd}*}/\widetilde{T}_*$ are, to within a few %, independent of $\widetilde{V}_c$ (as illustrated in Fig. S4 for a range of U-values). The experimental results for B_*, T_* and $V_{\mathrm{sd}*}$ shown in Fig. S3**f** confirm both predictions. This demonstrates that at low energies a QPC shows Fermi-liquid behavior, as argued in detail in the main article.

C. Top-gate tuning of effective g_{ss}-factor

In a QPC geometry, interactions are known to enhance the effective electronic g-factor[7–9]. For large fields ($B \gg B_*$), an effective g-factor, say g_{ss}, can be extracted from the transconductance dg/dV_c, by exploiting the fact that the measured field-induced subband splitting of the first conductance step, say ΔE, increases linearly with field, $\Delta E = g_{\mathrm{ss}} B$. In previous experiments with in-plane fields (B in the 2DES plane), $|g_{\mathrm{ss}}|$-values have been observed exceeding the bulk value ($g_{\mathrm{GaAs}} \simeq -0.45$) by up to a factor of 6[9,10], an increase that was attributed by Koop *et al.* to interaction effects[9].

In Fig. S5 we present the results of fRG calculations and measurements of the transconductance and the top-gate dependence of g_{ss} that confirm this interpretation. We numerically deduce the transconductance $\mathrm{d}G/\mathrm{d}V_c$ ($\mathrm{d}G/\mathrm{d}\widetilde{V}_c$) from both the measured and calculated conductance data. Typical experimental results are plotted in Fig. S5**a** for the range $0 < g < 1$ as a function of V_c. They show two peaks whose splitting ΔE increases linearly for large fields, as $\Delta E \simeq g_{\mathrm{ss}} B + \Delta_{\mathrm{hfo}}$ (Fig. S5**b**), where both the slope g_{ss} and the "high-field offset" Δ_{hfo} are found to increase with top-gate voltage V_t (Fig. S5**c**).

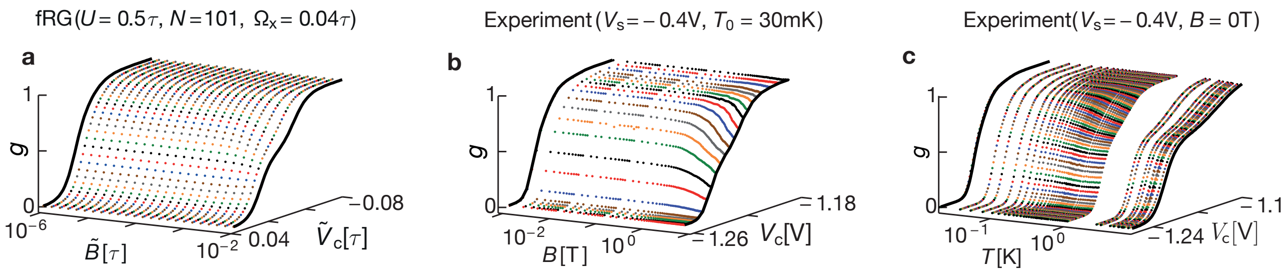

Figure S2: QPC theory versus experiment, raw data: **a**, fRG data (model II) for the normalized conductance $g = G/G_\mathrm{Q}$, calculated at $T = 0$ and fixed side gate voltage $\widetilde{V}_\mathrm{s} = 1.75\tau$ as function of center gate voltage $\widetilde{V}_\mathrm{c}$ and magnetic field $\widetilde{B}$. **b**, **c** Experimental data for the normalized linear response conductance $g = (\mathrm{d}I/\mathrm{d}V_\mathrm{sd})/G_\mathrm{Q}$ (lead resistance subtracted), measured at fixed side and top gate voltages, $V_\mathrm{s} = -0.4\,\mathrm{V}$ and $V_\mathrm{t} = 0.8\,\mathrm{V}$. **b** g at $T_\mathrm{2DES} = T_0 = 30\,\mathrm{mK}$, measured as function of center gate voltage V_c and inplane magnetic field B aligned along the narrow constriction. **c**, g at $B = 0$, measured as function of V_c and temperature T. The data presented here are the raw data used for Figs. 2e-h in the main article and in Figs. S3**a-d** below. For better visibility, the pinch-off curves at minimal and maximal magnetic field / temperature have been highlighted by thick black lines, serving as guides for the eyes. The best signal-to-noise ratio was achieved by slowly sweeping B at constant V_c in **b**, and by sweeping V_c at constant T in **c**.

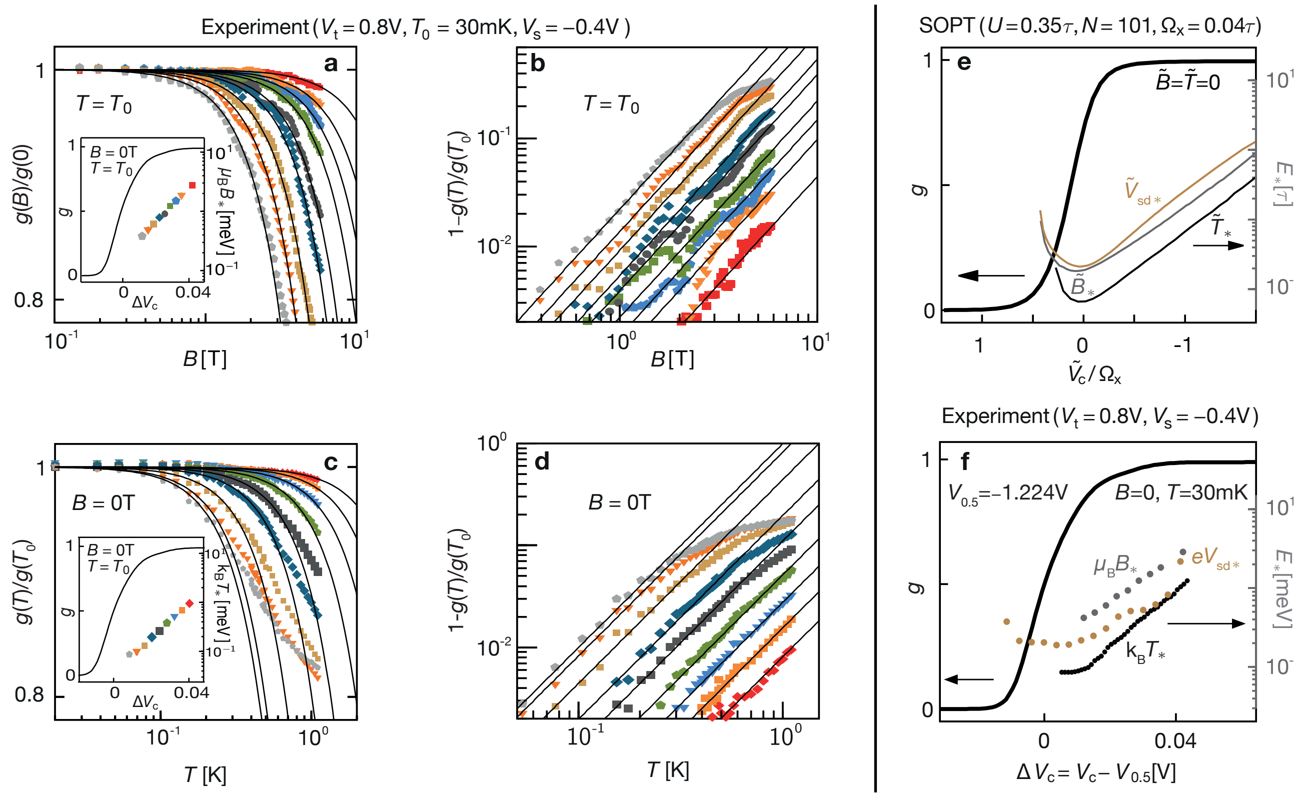

Figure S3: **a-d, Experiments; Fermi-liquid behavior.** **a**, $g(B)/g(0)$ on a lin-log-scale and **b**, $1 - g(B)/g(0)$ on a log-log-scale. **c** and **d**, as in **a** and **b** but for temperature instead of magnetic field dependence. These data supplement similar data shown in Figs. A2**g** and A2**h**, not repeated here. Black lines are fits of the form $g(X)/g(0) = 1 - X^2/X_*^2$ and express the leading quadratic decrease in both temperature and magnetic field. Insets demonstrate the exponential dependence of the scaling energies $\mu_\mathrm{B} B_*$ and $k_\mathrm{B} T_*$ (extracted from the fits) on V_c, respectively. Colored symbols in the main plots and corresponding insets have the same V_c-values. **e, f, Comparison of low-energy scales from theory and experiment: e** SOPT results for model II, for the conductance g (thick black line) and the low-energy scales $\widetilde{B}_*$, $\widetilde{T}_*$ and $\widetilde{V}_{\mathrm{sd}*}$ (thin grey, black and brown lines, respectively), as functions of $\widetilde{V}_\mathrm{c}$. **f** Corresponding experimental results for g, $\mu_\mathrm{B} B_*$ and $k_\mathrm{B} T_*$ (data repeated from insets of **a** and **c**) and $eV_{\mathrm{sd}*}$ as functions of $\Delta V_\mathrm{c} = V_\mathrm{c} - V_{0.5}$, where $V_{0.5}$ is the gate voltage for which the conductance at $B = 0$ and $T = T_0$ is $g(V_{0.5}) = 0.5$. $V_{\mathrm{sd}*}$ has been extracted from the leading quadratic dependence of the ZBP (as in **a-d** for $X = V_\mathrm{sd}$). Note the strikingly good qualitative agreement between the SOPT results in **e** and the experimental results in **f**, for the gate-voltage dependence of all three low-energy scales.

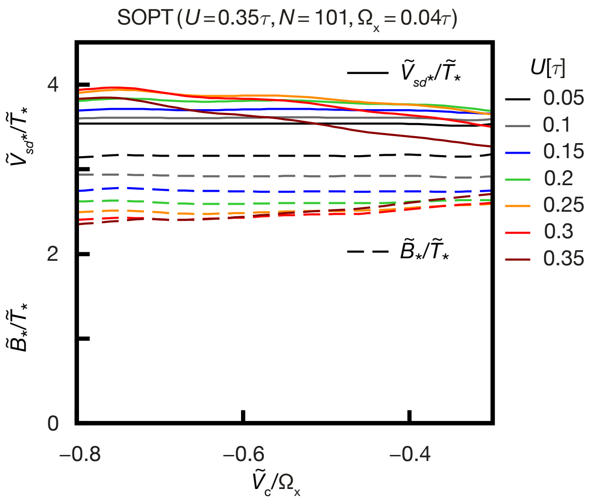

Figure S4: The ratios $\widetilde{V}_{\mathrm{sd}*}/\widetilde{T}_*$ (solid lines) and $\widetilde{B}_*/\widetilde{T}_*$ (dashed lines) as functions of $\widetilde{V}_{\mathrm{c}}/\Omega_x$ for several different U-values, calculated by SOPT for model II, using the same QPC barrier shape as used for Figs. A2**c**, **d**.

The effect of increasing V_{t} can be mimicked in our model by increasing U (for reasons explained in Supplementary Sec. S-2 A). Indeed, the results of our fRG calculations, shown in Fig. S5**d-f**, qualitatively match the trends shown by the experimental data in Fig. S5**a-c**. This establishes several important points. First, interactions are the reason why the g-factor extracted from $\Delta E(B)$ is anomalously large. Second, the effective interaction strength can be tuned experimentally via a top gate voltage. Third, the experimental observation of $\Delta_{\mathrm{hfo}} \neq 0$ can be understood *without* adopting the spontaneous spin polarization scenario that is often advocated[7,9,31] to explain it. Let us now elaborate these points in more detail.

We theoretically studied the U-dependence of g_{ss} by using fRG to calculate pinch-off curves for parabolic QPC barrier shapes such as that of Fig. A1**b**, for a range of fields $\widetilde{B}$ and interaction strengths U. Fig. S5**d** plots the transconductance, i. e. the derivative $-dg(\widetilde{V}_{\mathrm{c}})/d\widetilde{V}_{\mathrm{c}}$ as function of $\widetilde{V}_{\mathrm{c}}$ (varied over a range corresponding to $0 \leq g \leq 1$), for a large number of different $\widetilde{B}$-fields, at $U = 0.5\tau$. In such a plot the field-induced spin splitting of the conductance step manifests itself as a pair of local maxima[7–9,11]. The $\widetilde{V}_{\mathrm{c}}$-separation of their peaks, say ΔE, is proportional to the effective $\widetilde{B}$-induced subband splitting. Evidently ΔE increases with $\widetilde{B}$. Fig. S5**e** shows $\Delta E(\widetilde{B})$ vs. $\widetilde{B}$ for six values of U, including the data extracted from Fig. S5**d**. For large fields ($\widetilde{B} \gg \widetilde{B}_*$) we find a linear relation,

$$\Delta E(\widetilde{B}) \simeq (g_{\mathrm{ss}}/g_{\mathrm{el}})\widetilde{B} + \Delta_{\mathrm{hfo}} \, , \tag{S3}$$

where Δ_{hfo} represents the “high-field offset” as defined by Koop *et al.*[9], i. e. the linear extrapolation of the high-field behavior to $\widetilde{B} = 0$. Fig. S5**f** and its inset show that both the slope and the offset increase with U, implying that both g_{ss} and Δ_{hfo} serve as measures of the effective interaction strength.

Koop *et al.* have reported a strong enhancement of the g-factor as the spacing ω_{12} between the electronic subbands of the QPC is increased[9]. Our theory nicely explains this finding: an increase in ω_{12} corresponds to a smaller transverse channel width, implying an enhanced interaction strength (as argued at the end of section S-2 A) and hence an increase in g_{ss} (see Fig. S5**f**).

This interpretation is confirmed by the experimental data shown in Fig. S5**a-c**. This data was measured using a second sample (“sample 2”), of similar design than that used to study the Fermi-liquid properties of Figs. A2**e-h** discussed in the main text (“sample 1”). For sample 2, we measured $\Delta E(B) = a \cdot \Delta V_{\mathrm{c}}$ (for the values of the conversion factor a see table in Fig. S5**b**) as function of top gate voltage V_{t}, which corresponds to tuning the effective interaction strength. According to our theoretical considerations, increasing V_{t} causes increasing U [see Eq. (S1)] and hence increasing g_{ss} (by Fig. S5**f**). Fig. S5**a-c** present experimental results corresponding to the predictions in Fig. S5**d-f** (using V_{t} instead of U). They qualitatively confirm our numerical results, especially that both g_{ss} and Δ_{hfo} increase with V_{t} and, therefore, the interaction strength. (In contrast to us, Koop *et al.* did not observe a systematic correlation between g_{ss} and Δ_{hfo}. A possible reason is that their study varied the shape of the QPC potential by varying the width and length of the QPC, whereas we varied V_{t}. Our studies thus differ from theirs in the detailed shape of the 2D potential landscape. The effective interaction strength is very sensitive towards the latter, as discussed in more detail in Sec. S-5 C.)

We conclude our discussion on $\Delta E(B)$ with an important comment on the high-field offset Δ_{hfo}. In several experimental studies of the 0.7-anomaly[7–9], the observation of a nonzero value for Δ_{hfo} was interpreted as evidence “that there is a possible spin polarization of the 1D electron gas in zero magnetic field” (the quote is from Thomas *et al.*[7]). Our fRG results show that this interpretation is not compelling, since we obtain $\Delta_{\mathrm{hfo}} \neq 0$ without any spontaneous spin polarization. $\Delta_{\mathrm{hfo}} \neq 0$ simply implies that the $\widetilde{B} = 0$ conductance step $g(\widetilde{V}_{\mathrm{c}})$ is somewhat skewed (see Figs. A1**k**, A1**l**, A2**a**), so that the peak in the transconductance is not symmetric (as seen in Fig. S5**d**); as shown here, this can be achieved with a magnetization that is strictly zero. Indeed, our fRG approach assumes from the outset that the magnetization per site, $m_j = \frac{1}{2}(n_{j\uparrow} - n_{j\downarrow})$, is strictly zero at $\widetilde{B} = 0$ (see blue line in Fig. A1d, and introduction of Sec. S-6). This *a priori* assumption is justified *a posteriori* by the good qualitative agreement between fRG and experiment found throughout this work, and in Fig. S5 in particular. Moreover, this assumption is a prerequisite for understanding the low-energy Fermi-liquid properties of the 0.7-anomaly discussed in the main text, and the resulting analogies between the 0.7-anomaly and the Kondo effect: for the latter, there is zero spin polarization at

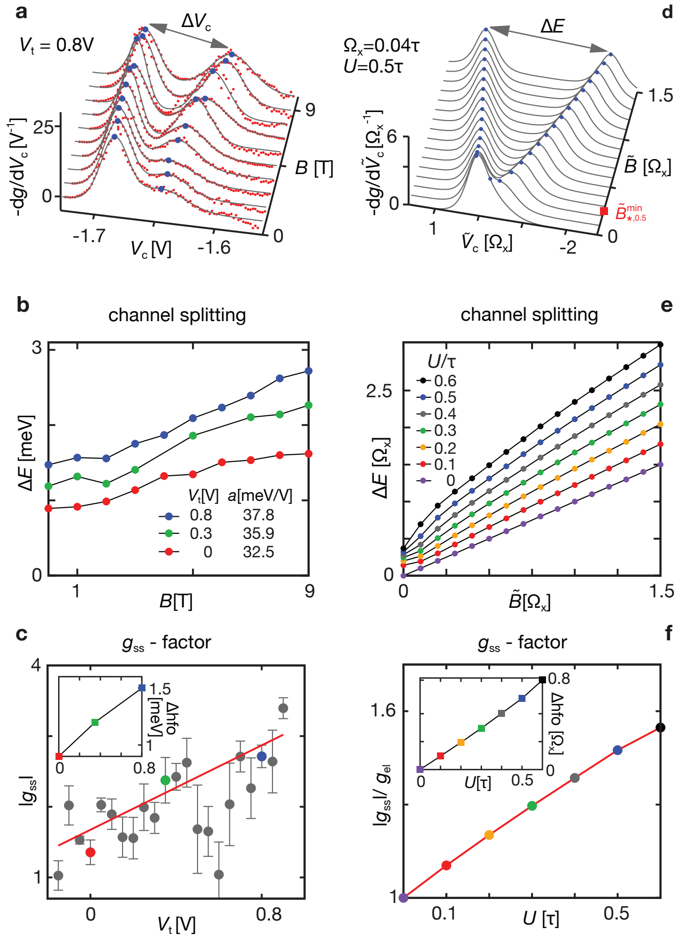

Figure S5: **Determination of the subband-splitting g-factor** g_{ss}. **a**-**c**. Results from experimental measurements on a sample ("sample 2") of similar design as that discussed in the main text ("sample 1"). **d**-**f**, Corresponding results from fRG calculations. **a**,**d**, The transconductance, i.e. the derivative of the conductance with respect to gate voltage (V_{c} in **a**, $\widetilde{V}_{\mathrm{c}}$ in **d**), plotted as a function of gate voltage, for several magnetic fields. An increasing magnetic field lifts the spin degeneracy, causing the conductance step to split into two spin-resolved sub-steps and giving rise to two local maxima in **a**,**d** (marked by blue dots). In **d**, $\widetilde{B}^{\mathrm{min}}_{*,0.5}$ (red square) stands for $\widetilde{B}^{\mathrm{min}}_{*}$ at $U = 0.5$. **b**,**e**. The peak distance ΔE, determined by fitting a pair of Gaussians (shown by gray lines in **a**) to the peak pairs in **a**,**d**, is plotted as function of magnetic field, in **b** for three different top gate voltages, and in **e** for seven different values of the on-site interaction U. Linear least-square fits to such curves in the range of large fields, using $\Delta E \simeq g_{\mathrm{ss}} B + \Delta_{\mathrm{hfo}}$, yield the effective g-factor g_{ss} and high-field offset Δ_{hfo}. Errors, s. e. m. ($n = 5$ - 7). (To convert ΔV_{c} in **a** to ΔE in **b**, we used the V_{t}-dependent conversion factors $a = \Delta E/\Delta V_{\mathrm{c}}$ listed in the legend of **b**, obtained approximately from nonlinear transport measurements[7,9].) **c**,**f**, $|g_{\mathrm{ss}}|$ (and in insets, Δ_{hfo}), plotted as a function of V_{t} (in **c**) or U (in **f**). The red straight line in **c** is a error-weighted least square fit. Both theory and experiment show the same trend, namely that g_{ss} and Δ_{hfo} increase with the effective interaction strength U (which increases with V_{t} in our sample geometry.

$\widetilde{B} = T = 0$, because lead electrons screen the local spin into a spin singlet.

It is noteworthy, though, that the linear increase in $\Delta E(\widetilde{B})$ in Fig. S5**e** sets in already at rather small fields, of order $\mathcal{O}(\widetilde{B}_*)$ and similarly for $\Delta E(B)$ in Fig. S5**b**. The reason is that at small fields the spin polarization *rapidly* grows with field, since the spin susceptibility is *large*. It is large because it is strongly enhanced by interactions (Fig. A1**j**), as recognized and emphasized by Thomas *et al.*[7], and because the effects of interactions are further enhanced by the van Hove ridge in the QPC, as discussed in the main article. According to our analysis, the large spin susceptibility goes hand in hand with a strong interaction-induced enhancement in the inverse scale $1/B_*(\propto \chi_{\mathrm{tot}})$ [Fig. A1**j**], as discussed in the main article, and also in Sec. S-5 B below.

The scale $\widetilde{B}_*$ governs the "strength" of the 0.7-anomaly, in that the conductance is significantly reduced once $\widetilde{B}$ or $\widetilde{T}$ increase past $\widetilde{B}_*$. In an alternative model proposed by Reilly *et al.*[12], one of the advocates of spontaneous spin polarization, the strength of the 0.7-anomaly is governed by the size of the spin gap. This model was used successfully, for example, to model the shot noise measurements of Ref. 13. The Reilly model assumes that the spin gap increases strongly with decreasing V_{c}, i. e. with increasing density in the QPC-region. Note that this $\widetilde{V}_{\mathrm{c}}$-dependence of the proposed spin gap shows the same tendency as that shown by the Hartree-enhancement of the barrier size in our work, which likewise increases linearly with increasing density as $\widetilde{V}_{\mathrm{c}}$ is made more negative. (The density near the CCR center also increases as temperature or source-drain voltage is increased, and becomes strongly spin-asymmetry as $\widetilde{B}$ increases.) In this sense, our work sheds light on why the Reilly model is phenomenologically successful at large energies: it makes qualitatively correct assumptions about the V_{c}-dependence of the effective barrier height that governs the strength of the conductance's B- or T-dependence. That having been said, we emphasize once more that our Hartree-shift in barrier height is not a spin gap, and that our scenario differs decidedly from that of the Reilly model for energies below B_*: there we assert the appearance of Fermi-liquid behavior that is not compatible with spontaneous spin polarization. In our theory, a spin splitting sets in only once spin symmetry is broken by finite $\widetilde{B}$ (though a spin-symmetric Hartree-shift in barrier height is present even at $\widetilde{B} = 0$). The spin gap predicted by our theory for $\widetilde{B} \neq 0$ does increase with the density in the QPC, as in the Reilly model, since it arises from Hartree contributions to the self-energy (see Eq. (S42) in our fRG scheme, or the first two diagrams in Eq. (S53) when doing perturbation theory).

S-3. OTHER EXPERIMENTAL DATA VS. FRG

This section presents additional fRG results on the zero-temperature behavior of the conductance, the shot noise, and the charge susceptibility. Their $\widetilde{V}_c$- and $\widetilde{B}$-dependence is found to be in qualitative agreement with that observed experimentally by other groups (DiCarlo *et al.* for the shot noise[13], Smith *et al.* for the compressibility[14].

The fRG results presented below were obtained using "static" fRG, a simplified version of the "dynamic" fRG scheme used in the main text. Static fRG neglects the frequency dependence of the self-energy and all vertices (see Sec. S-6 F). This simplification reduces computational costs by a factor of 10^3. Nevertheless, for the model studied here the results of static fRG turn out to be qualitatively very similar to those of dynamic fRG (see Fig. S15 below). Hence we have opted to use static fRG for the results presented in Secs. S-3 and S-5.

A. Spin-resolved conductance, shot noise

This subsection presents a detailed discussion of the spin-resolved conductance. It is based on calculations using model I (defined in Sec. S-4 B), but the results are fully analogous to those shown in Figs. A2**a**, **b** for model II (defined in Sec. S-4 D).

The role of interactions for the magnetoconductance of a QPC at zero temperature can be very clearly revealed by studying the spin-resolved conductance $g_\sigma = \mathcal{T}_\sigma$ and the shot noise factor[15]

$$\mathcal{N} = \frac{1}{2}\sum_\sigma g_\sigma(1-g_\sigma). \tag{S4}$$

Fig. S6 shows these quantities together with the full conductance $g = g_\uparrow + g_\downarrow$, all calculated at $T = 0$ as functions of $\widetilde{V}_c$, for various fields. To highlight the effect of interactions, we also show corresponding results for the bare ($U = 0$) model, which we discuss first.

We begin with some elementary observations: First, the bare transmission probability $\mathcal{T}^0_\sigma(\widetilde{V}_c, 0)$ at zero field, studied as function of $\widetilde{V}_c$, is antisymmetric w. r. t. the point $\mathcal{T}^0_\sigma(0,0) = 0.5$ [cf. Eq. (S30) below]:

$$\mathcal{T}^0_\sigma(\widetilde{V}_c, 0) = 1 - \mathcal{T}^0_\sigma(-\widetilde{V}_c, 0)\ . \tag{S5}$$

A finite field $\widetilde{B}$ shifts the bare potential in opposite directions for opposite spins, $\delta\widetilde{V}_j = -\frac{\sigma}{2}\widetilde{B}$ (with $\sigma = \pm 1$ for ↑, ↓). Thus the bare spin-resolved transmission probability $\mathcal{T}^0_\sigma$ at finite $\widetilde{B}$ is equal to that at $\widetilde{B} = 0$ but for a shifted value of $\widetilde{V}_c$:

$$\mathcal{T}^0_\sigma(\widetilde{V}_c, \widetilde{B}) = \mathcal{T}^0_\sigma(\widetilde{V}_c - \tfrac{\sigma}{2}\widetilde{B}, 0). \tag{S6}$$

This implies that $\widetilde{B}$ induces a shift (but not a change in shape) for the spin-resolved conductance step in g_σ by $\frac{\sigma}{2}\widetilde{B}$ (see Figs. S6**b**-**c**). Nevertheless, since Eqs. (S6) and (S5) together imply

$$\mathcal{T}^0_\sigma(\widetilde{V}_c, \widetilde{B}) = 1 - \mathcal{T}^0_{\bar\sigma}(-\widetilde{V}_c, \widetilde{B})\ , \tag{S7}$$

the full conductance remains antisymmetric w. r. t. the point $\mathcal{T}^0_\sigma(0, \widetilde{B}) = 0.5$ even for finite $\widetilde{B}$ (see Fig. S6**a**):

$$g^0(\widetilde{V}_c, \widetilde{B}) = 1 - g^0(-\widetilde{V}_c, \widetilde{B})\ . \tag{S8}$$

Eq. (S7) also implies that the bare shot noise, $\mathcal{N}^0$, is symmetric w. r. t. $\widetilde{V}_c = 0$, or $g = 0.5$ (see Fig. S6**j**).

The above antisymmetry of $g(\widetilde{V}_c)$ w. r. t. $\widetilde{V}_c = 0$ is broken in the presence of interactions, in a manner that becomes increasingly more pronounced with increasing field, see Figs. S6**d** and S6**g**, for $U/\tau = 0.2$ and 0.45, respectively. In the latter case the broken antisymmetry is visible already at zero field, in that the fRG conductance curve shows a slight 0.7-shoulder, in agreement with experiment (cf. Fig. A2**e**). This shoulder at $\widetilde{B} = \widetilde{T} = 0$ occurs because the interaction-induced increase of the effective potential barrier is enhanced by the van Hove ridge in the local density of states (LDOS) and hence is nonuniform in $\widetilde{V}_c$ (see the main article for a detailed explanation). The breaking of $\widetilde{V}_c$-antisymmetry increases with $\widetilde{B}$ because (exchange) interactions amplify the field-induced asymmetry in the population of spin-up and -down electrons in the CCR, in particular near the top of the barrier: a small $\widetilde{B}$-induced surplus of spin-up electrons leads to a significantly increased Hartree barrier, and more so for spin-down electrons than for spin-up electrons (due to the Pauli principle), causing a strong decrease of $g_\downarrow$ relative to $g_\uparrow$. This effect, whose strength increases with U (compare 2nd and 3rd columns of Fig. S6) results in the field-induced strengthening of the 0.7-shoulder that is characteristic of the 0.7-anomaly, and its evolution into a double step for large fields.

The increasing $\widetilde{V}_c$-asymmetry (i. e. departure from perfect antisymmetry) in $g_\sigma(\widetilde{V}_c)$ as $\widetilde{B}$ increases is also reflected in the shot noise factor $\mathcal{N}(g)$ [Eq. (S4)], see Figs. S6**k** and S6**l**, for $U/\tau = 0.2$ and 0.45, respectively. For zero applied field, $\mathcal{N}(g)$ is symmetric w. r. t. $g = 0.5$; this follows directly from the form of Eq. (S4) (which holds whenever a Fermi-liquid description applies), and our assumption that there is no spontaneous breaking of spin symmetry at $\widetilde{B} = 0$, implying $g_\uparrow = g_\downarrow$. With increasing field, $\mathcal{N}(g)$ develops an g-asymmetry w. r. t. $g = 0.5$, being somewhat suppressed in the range $g > 0.5$ relative to its values in the range $g < 0.5$. This field-induced g-asymmetry is in good qualitative agreement with the experimental measurements of the noise factor by DiCarlo *et al.*, cf. Fig. 4(d) of Ref. 13. Note, though, that the measured noise factor shows an g-asymmetry even at zero field, in contrast to our fRG predictions; we believe that this remnant g-asymmetry is a finite-temperature effect that will gradually disappear if the experimental temperature is lowered further. Reproducing this behavior explicitly by a finite-temperature calculation of the

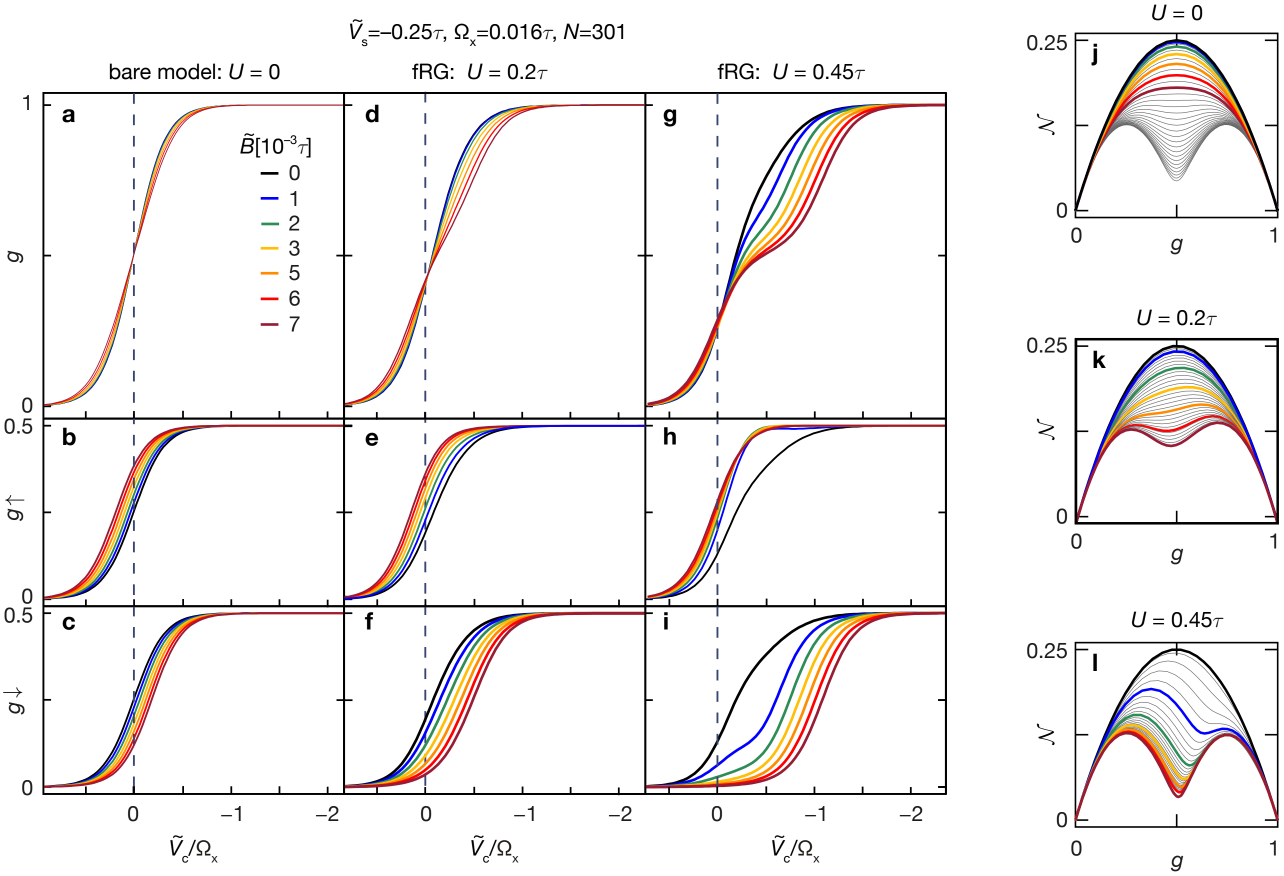

Figure S6: Comparison of results for model I, for its bare $U = 0$ version (first column), or treated using static fRG for $U/\tau = 0.2$ and 0.45 (second and third columns, respectively). The top, middle and bottom rows show, respectively, the full QPC conductance $g = g_\uparrow + g_\downarrow$ and its spin-resolved contributions $g_\uparrow$ and $g_\downarrow$, all plotted as functions of $\widetilde{V}_c/\Omega_x$ for several values of magnetic field $\widetilde{B}$. The fourth column shows a similar comparison for the shot noise factor $\mathcal{N}$ [Eq. (S4)], plotted as function of g.

noise factor for our model is left as a task for future study.

B. Compressibility and charge susceptibility

Recently, Smith *et al.*[14] have experimentally studied the compressibility of the electron gas of a QPC. In particular, they measured the V_c-dependence of the compressibility in the vicinity of the 0.7-anomaly and studied its evolution with increasing temperature and magnetic field. The compressibility is a measure of the density of states at the chemical potential. In a QPC geometry, its V_c-dependence is thus governed by that of the LDOS maxima at the bottom of the 1D band, i. e. by the van Hove ridge discussed in detail in the main article and in Sec. S-4 C below (see the yellow ridges in Fig. A1**b** and Fig. S10**d**); and its B-dependence is governed by the spin splitting of this van Hove ridge.

Within our model, the compressibility can be associated with the charge susceptibility of the CCR,

$$\chi_\mu = \frac{dn_{\mathrm{tot}}}{d\mu}, \qquad n_{\mathrm{tot}} = \sum_{j\sigma}^{\mathrm{CCR}} n_{j\sigma} , \tag{S9}$$

where n_{tot} is the total charge in the CCR and μ the chemical potential. Figs. S7**a** and S7**b** show zero-temperature fRG results for the conductance $g(\widetilde{V}_c)$ and the charge susceptibility $\chi_\mu(\widetilde{V}_c)$, respectively. The results exhibit a number of features, enumerated below, that are qualitatively consistent with features observed by Smith *et al.*[14].

Consider first the noninteracting case, $U = 0$ (black dashed lines for g^0 and χ^0_μ): When $\widetilde{V}_c$ is lowered past 0, the bare charge susceptibility $\chi^0_\mu(\widetilde{V}_c)$ in Fig. S7**b** traverses a single broad peak, aligned with the center of the corresponding conductance step in Fig. S7**a**. This peak arises because the bare charge susceptibility equals the bare total density of states at the chemical potential [cf.

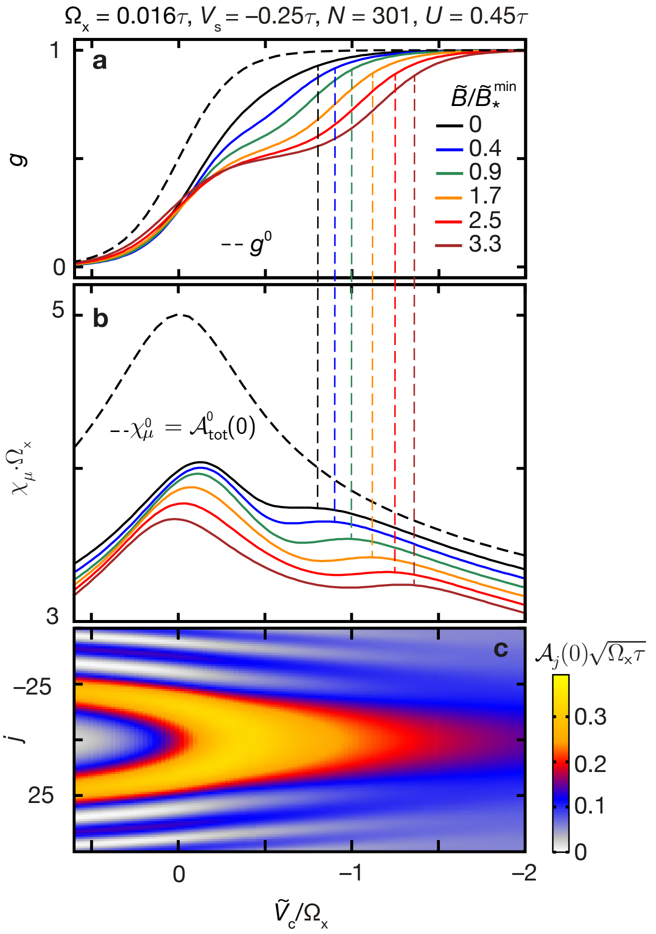

Figure S7: **Charge Susceptibility.** Static fRG results (model I) for (a) the conductance $g(\widetilde{V}_c)$ and (b) the charge susceptibility $\chi_\mu(\widetilde{V}_c)$ [Eq. S9] as function of $\widetilde{V}_c$, calculated for six values of $\widetilde{B}$ at a fixed $\widetilde{V}_s$ and $\widetilde{T} = 0$. Black dashed lines in **a** and **b** show the bare ($U = 0$, $\widetilde{B} = 0$) curves, g^0 and $\chi_\mu^0 = \mathcal{A}_{\mathrm{tot}}^0(0)$, respectively. Vertical dashed lines are a guide for the eyes and mark the weak shoulder or second maximum of $\chi_\mu(\widetilde{V}_c)$. **c**, The full ($U \neq 0$) LDOS at the chemical potential, $\mathcal{A}_j(0)$, as function of gate voltage $\widetilde{V}_c$ and site index j.

Eq. (S39)],

$$\chi_\mu^0 = \sum_{j\sigma}^{\mathrm{CCR}} \mathcal{A}_{j\sigma}^0(0) = \mathcal{A}_{\mathrm{tot}}^0(0), \tag{S10}$$

which traverses a peak when the spin-degenerate van Hove ridge is lowered past μ. For nonzero U but still $\widetilde{B} = 0$ (black solid lines), $\chi_\mu(\widetilde{V}_c)$ is reduced, since interactions tend to counteract the (infinitesimal) increase in charge induced by an (infinitesimal) increase in μ [Eq. (S9)]. This reduction occurs in such a way that (i) $\chi_\mu(\widetilde{V}_c)$ retains a dominant peak, with (ii) a weak shoulder developing on its right (even though $\widetilde{B} = 0$), roughly aligned with the roll-over of $g(\widetilde{V}_c)$ towards the first conductance plateau. This shoulder arises because when $\widetilde{V}_c$ decreases into the open-channel regime, the van Hove ridge apex drops so far below μ that $\mathcal{A}_j(0)$, the LDOS at μ, decreases rapidly (Fig. S7**c**). As a result, its interaction-enhancing effects, and hence also the Coulomb-blockade reduction in χ_μ, weaken rapidly, resulting in a shoulder in χ_μ.

The colored lines in Fig. S7 show the evolution of the conductance $g(\widetilde{B})$ and charge susceptibility $\chi_\mu(\widetilde{V}_c)$ with magnetic field for $U = 0.45\tau$. While the conductance step evolves into the familiar spin-split double step with increasing field (Fig. S7**a**), (iii) the dominant peak in $\chi_\mu(\widetilde{V}_c)$ (Fig. S7**b**) remains aligned with the center of the first conductance step, while (iv) the shoulder in $\chi_\mu(\widetilde{V}_c)$ develops into a weak peak that shifts towards the right, remaining roughly aligned with the roll-over to the second conductance plateau (as indicated by dashed colored lines between Figs. S7**a** and S7**b**). This reflects the field-induced spin-splitting of the van Hove ridge into two spin-resolved sub-ridges, which get lowered past μ at different $\widetilde{V}_c$-values. As a result, (v) $\chi_\mu(\widetilde{V}_c)$ develops a weak minimum between the two peaks.

Features (i)-(v) can also be found, on a qualitative level, in Figs. 2 and 3(a) of Smith *et al.*. Their measured signal, called $dV_{\mathrm{sg}}/dV_{\mathrm{mid}}$ there, has minima when the compressibility has maxima, and vice versa. In their Fig. 2(a), the red curve shows a strong dip at $V_{\mathrm{mid}} = 0.14$ V and a very weak minimum at 0.22 V. We associate these, respectively, with the dominant peak (i) and the weak shoulder (ii) in $\chi_\mu(\widetilde{V}_c)$ discussed above. In their Fig. 2(b), the two dips in the red curve at $V_{\mathrm{mid}} = 0.12$ V and 0.19 V, correspond, respectively, to the two maxima mentioned in (iii) and (iv) above. And in their Fig. 3(a), the peak marked by an arrow corresponds to the dip mentioned in (v). We thus conclude that the measured compressibility maxima accompanying the conductance steps are indeed due to maxima in the density of states at the band bottom, as suggested by Smith *et al.* themselves (and in Ref. 16). This supports our contention that van Hove ridges play a central role in the physics of the 0.7-anomaly. By implication it also confirms the presence of the “quasi-bound states” advocated by Meir and collaborators[17–19], provided that we identify their “quasi-bound states” with our van Hove ridges – as argued in Sec. S-4 E below, both names refer to the same peaked structures in the LDOS.

This identification was not clear at the time of writing of Ref. 14, however. Instead, Smith *et al.* argued that they see “no evidence of the formation of the quasi-bound state predicted by the Kondo model”. This statement was based on a comparison of their $B = 0$ data for $dV_{\mathrm{sg}}/dV_{\mathrm{mid}}$ to simulations[16] using density-functional theory (DFT) combined with the local spin density approximation (LSDA). These data and the simulation results are shown, respectively, as black and red curves in Fig. 4(b) of Ref. 14. The simulations yielded an additional strong dip [indicated by an arrow in Fig. 4(b)], aligned with the onset of the conductance plateau, that had no counterpart in the measured data. We suspect that this additional strong dip might be an artefact of the tendency of DFT+LSDA calculations, when initialized using a small nonzero magnetic field[19,20], to yield a nonzero spin polarization in regions where the spin susceptibility is large (as is the case in the QPC). We assert, however, that at $B = 0$ the spin polarization is strictly zero (in contrast to views expressed in Refs. 7,8,14), since this is a prerequisite for understanding the Fermi-liquid properties discussed in the main article. Our fRG calculations for $\widetilde{B} = 0$ thus assume zero spin polarization from the outset. Remarkably they yield, instead of the strong additional peak found by DFT+LSDA, only the weak shoulder (ii) mentioned above, which is consistent with the compressibility data of Smith *et al.* Further arguments in support of the absence of spontaneous spin polarization at zero field are offered at the end of Sec. S-2 C.

PART II: THEORETICAL DETAILS

S-4. MODELS USED FOR BARRIER SHAPE

In the course of our studies of the 0.7-anomaly, we have explored many different parametrizations of smooth, symmetric QPC barrier shapes. We found that as long as the barrier top is parabolic, characterized by a barrier height $\widetilde{V}_c$ (w. r. t. to the chemical potential) and a curvature parameter Ω_x, the details of the parametrization of the barrier do not matter.

In this section we present the details of two different parametrizations for parabolic barriers, to be called "model I" and "model II", whose results for QPC properties are fully equivalent when expressed as functions of $\widetilde{V}_c$ and Ω_x. Both models use the same Hamiltonian, choice of chemical potential and local interaction strength U_j, specified in Sec. S-4 A, but differ in their choices for the hopping amplitude τ_j (which is j-independent for Model I but not for Model II) and the on-site potential E_j.

Model I is presented in Sec. S-4 B: its hopping amplitude is j-independent, $\tau_j = \tau$, and the barrier shape is specified by parametrizing E_j in terms of a central gate voltage $\widetilde{V}_c$ and a side gate voltage $\widetilde{V}_s$. It is designed to allow a theoretic study of the crossover between a Kondo quantum dot (KQD) and a QPC by continuously deforming the 1D potential from a double-barrier to a single-barrier shape (see Figs. S9**c** and S9**d** below, respectively). (The results of a corresponding study will be published elsewhere[1].) Here we use model I to calculate numerous QPC properties presented in various parts of the supplementary material (Figs. S6, S7, S10, S11, S13 and S14). Moreover, model I allows instructive insights into the similarities and differences between the bare density of states of a QD and a QPC, which are key to understanding the similarities and differences between the Kondo effect and the 0.7-anomaly, as briefly discussed in Sec. S-4 C.

For model II, presented in Sec. S-4 D, τ_j depends nontrivially on j, and the barrier shape is specified solely in terms of a central gate voltage $\widetilde{V}_c$ and the barrier curvature Ω_x (adjusted via the length N of the CCR, but without reference to a side gate voltage). Compared to model I, model II has technical advantages when treated using SOPT (as explained below). For clarity, model II was used for all numerical results (both from fRG and SOPT) presented in the main article. It was also used for Figs. S2, S4, S12, S16 in the supplementary material. We emphasize that the results obtained using models I and II are qualitatively consistent.

To conclude our introductory comments on the models used here, we remark that the idea of studying the 0.7-anomaly using an effective 1D model with a smoothly varying QPC potential and local interactions has of course been pursued previously by numerous authors. For example, a model with local exchange interactions was studied in Refs. 21 and 22, a model with an unscreened Coulomb interaction in Ref. 6, and a model with a point like interaction restricted to the center of the QPC potential in Ref. 23. Our work is similar in spirit to these, but our use of fRG allows us to treat the effects of interactions more systematically than Refs. 21 and 6, and for longer chains than Ref. 22, which also did not have access to the limit $T \to 0$. Works based on 2D or 3D density-functional theory calculations[16–20] treat the potential landscape more realistically than we do, but at the expense of not treating correlation effects as accurately as fRG does. In particular, our fRG treatment allows accurate predictions for the conductance at zero temperature, which is beyond the scope of all previous treatments. Moreover, our SOPT calculations at finite source-drain voltages are first to give a detailed description of the origin of the ZBP.

A. Hamiltonian, chemical potential, U_j

The model Hamiltonian defined in the main article,

$$\hat{H} = \sum_{j\sigma}\Big[E_{j\sigma}\hat{n}_{j\sigma} - \tau_j(d^{\dagger}_{j+1\,\sigma}d_{j\sigma} + \text{h.c.})\Big] + \sum_{j}U_j\hat{n}_{j\uparrow}\hat{n}_{j\downarrow}, \tag{S11}$$

with $E_{j\sigma} = E_j - \frac{\sigma}{2}\widetilde{B}$, is depicted schematically in Fig. S8. It shows a tight-binding chain divided into two semi-infinite, non-interacting, uniform leads on the left and right, connected to the central constriction region (CCR),

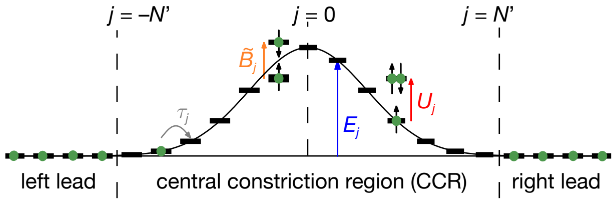

Figure S8: Schematic depiction of the one-dimensional model of Eq. (S11) (for a QPC barrier shape). It represents an infinite tight-binding chain with hopping matrix element τ_j (gray); the prescribed local potential E_j (blue) and on-site interaction U_j (red) are nonzero only within a central constriction region (CCR) of $N = 2N' + 1$ sites. The CCR is connected to two semi-infinite non-interacting leads on the left and right. A homogeneous Zeeman magnetic field $\widetilde{B}$ (orange) can be switched on along the whole chain.

consisting of an odd number $N = 2N'+1$ of sites centered on $j = 0$. The lattice does not represent actual atomic sites, but instead is merely used to obtain a discrete, coarse-grained description of transport in the lowest subband. The position-dependent parameters U_j and E_j, nonzero only within the CCR, are taken to vary slowly on the scale of the lattice spacing a. (We set $a = 1$ in our calculations.)

Choice of μ: Since the chemical potential is a property of the bulk, we begin by considering our model for $E_j = U_j = 0$ and $\tau_j = \tau$, representing a bulk tight-binding chain (infinite, homogeneous). The eigenergies ϵ_k corresponding to wave number k have dispersion

$$\epsilon_k = -2\tau\cos(ka) \;\in [-2\tau, 2\tau]\,, \tag{S12}$$

plotted in Fig. S9**a**. To describe the phenomena of present interest, the chemical potential μ should lie somewhere within this band, not too close to its edges; the precise value does not matter. All our numerical calculations (fRG and SOPT) used $\mu = 0$, implying half-filled leads; but for the sake of generality, we keep μ arbitrary below, particularly in Figs. S9**a**,**b** and S10**a**,**b**.) The energy difference between the chemical potential and the bulk band bottom defines the bulk Fermi energy,

$$\varepsilon_{\mathrm{F}} = 2\tau + \mu \quad (> 0)\,. \tag{S13}$$

Choice of U_j: In choosing a purely on-site interaction in Eq. (S11), we implicitly assume that screening is strong enough to render the interaction short-ranged. (A more realistic treatment of screening is beyond the scope of this work.) We set the on-site interaction U_j equal to U throughout the CCR, except near its edges, where it drops smoothly to zero to avoid spurious backscattering effects (Fig. S9**e**):

$$U_j = \begin{cases} 0\,, & \forall \quad N' \le |j|\,, \\ U \exp\left[-\dfrac{(\frac{j}{N'})^6}{1-(\frac{j}{N'})^2}\right] & \forall \quad |j| \le N'\,. \end{cases} \tag{S14}$$

U is to be regarded as an effective parameter, whose value is influenced by the transverse modes not treated explicitly in our model. In particular, the effect of increasing the top gate voltage V_{t} can be mimicked by increasing U [Eq. (S1)], as will be discussed in more detail in Sec. S-5 C. We typically take U to be somewhat smaller than the maximum value of the inverse bare LDOS, since if $U \cdot \max[\mathcal{A}^0_j(\omega)]$, is too large, the fRG calculations do not converge. We remark that we have also explored the option of taking U_j to be proportional to E_j, or of taking the range of sites where $U_j = U$ to be several times larger than that where $E_j \neq 0$. Such modifications change details of the results, such as the precise shape of the con-

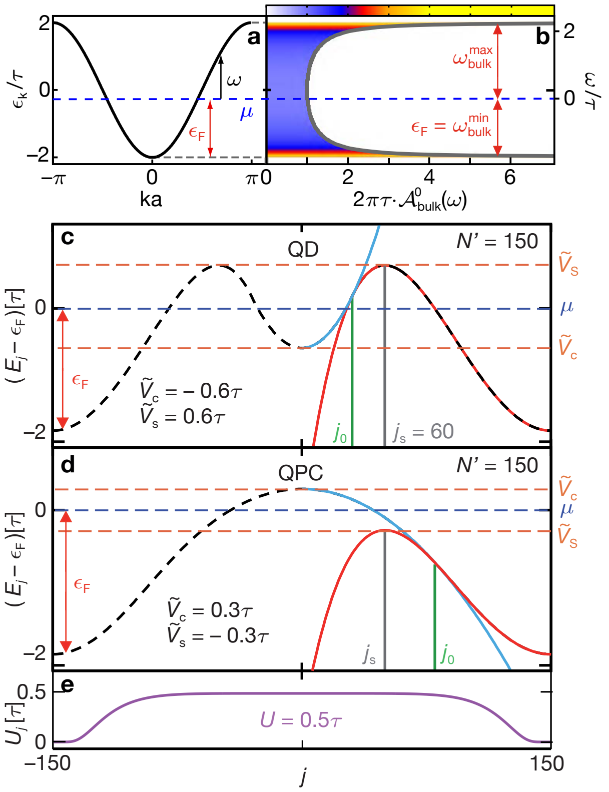

Figure S9: **a**, Dispersion relation ϵ_k vs. k [Eq. (S12)] for a bulk non-interacting tight-binding chain without magnetic field (infinite, homogeneous, $E_{j\sigma} = U_j = 0$). The filling factor in the leads is controlled by the global chemical potential μ (blue dashed line); it is here drawn at $\mu \neq 0$ for generality, although our fRG calculations use $\mu = 0$. **b**, The corresponding j-independent bulk LDOS [Eq. (S19)], shown both as $\mathcal{A}^0_{\mathrm{bulk}}(\omega)$ (on x-axis) versus $\omega = \epsilon_k - \mu$ (on y-axis), and using a color scale. The distance from the chemical potential to the bulk band bottom $\omega^{\mathrm{min}}_{\mathrm{bulk}}$ is $\varepsilon_{\mathrm{F}} = 2\tau + \mu = -\omega^{\mathrm{min}}_{\mathrm{bulk}}$ (> 0). **c** and **d**, Model I: The one-dimensional potential E_j of Eq. (S15) (thick dashed black line) for a QD potential ($\widetilde{V}_{\mathrm{s}} > \widetilde{V}_{\mathrm{c}}$) and a QPC potential ($\widetilde{V}_{\mathrm{c}} > \widetilde{V}_{\mathrm{s}}$), respectively. In the outer region of the CCR ($j_0 \le |j| \le N'$), E_j is described by quartic polynomial, in the inner region ($|j| < j_0$) by a quadratic one (thin red and blue lines, respectively, shown only for $j > 0$.) For given N', j_{s}, $\widetilde{V}_{\mathrm{s}}$ and $\widetilde{V}_{\mathrm{c}}$, the parameters j_0 and $\overline{\Omega}_x$ are adjusted such that the resulting potential E_j depends smoothly on j throughout the CCR. **e**, The on-site interaction U_j of Eq. (S14).

tails of the results, such as the precise shape of the conductance $g(\widetilde{V}_\mathrm{c}, \widetilde{V}_\mathrm{s})$ as function of $\widetilde{V}_\mathrm{c}$ or $\widetilde{V}_\mathrm{s}$, but not the qualitative trends discussed in the main article, as long as U_j drops smoothly to zero near the edges of the CCR.

B. Model I

For model I, we choose the the hopping amplitude to be j-independent, $\tau_j = \tau$, while the on-site potential E_j describes a reflection-symmetric barrier within the CCR. Its shape is tunable between a double barrier describing a QD (Fig. S9**c**) and a single barrier describing a QPC (Fig. S9**d**) (thick dashed black lines). We have parametrized it as follows:

$$E_j = \begin{cases} 0\,, & \forall\, |j| \geq N', \\ (\widetilde{V}_\mathrm{s} + \varepsilon_\mathrm{F}) \left[2 \left(\frac{|j| - N'}{j_\mathrm{s} - N'} \right)^2 - \left(\frac{|j| - N'}{j_\mathrm{s} - N'} \right)^4 \right], & \\ & \forall\, j_0 \leq |j| \leq N', \\ \widetilde{V}_\mathrm{c} + \varepsilon_\mathrm{F} + \frac{\overline{\Omega}_x^2 j^2}{4\tau} \operatorname{sgn}(\widetilde{V}_\mathrm{s} - \widetilde{V}_\mathrm{c}), & \forall\, 0 \leq |j| < j_0. \end{cases} \tag{S15}$$

The sites $\pm j_0$ divide the CCR into two "outer regions", where the potential is a quartic polynomial in j, and an "inner region", where it is quadratic in j. In the latter, the magnitude of the curvature is governed by the parameter $\overline{\Omega}_x$ (≥ 0), which has units of energy. (The quadratic term for the inner region was chosen to have the form $\frac{1}{2} m \omega_x^2 x^2$ used in Ref. 5, with $\omega_x = \overline{\Omega}_x / \hbar$, $x = aj$ and $m = \hbar^2 / (2\tau a^2)$ corresponding to the effective mass at the bottom of a tight-binding chain.) The shape of E_j is controlled by four independent parameters: (i) N', which sets the halfwidth of the CCR; (ii) j_s, which governs the width of the outer flanks of the potential; (iii) $\widetilde{V}_\mathrm{s}$ and (iv) $\widetilde{V}_\mathrm{c}$, which give the potential's height w. r. t. ε_F at the sites $j = \pm j_\mathrm{s}$ and 0, respectively:

$$E_{\pm j_\mathrm{s}} = \widetilde{V}_\mathrm{s} + \varepsilon_\mathrm{F}; \quad E_{j=0} = \widetilde{V}_\mathrm{c} + \varepsilon_\mathrm{F}\,. \tag{S16}$$

Once the four parameters N', j_s, $\widetilde{V}_\mathrm{s}$ and $\widetilde{V}_\mathrm{c}$ have been specified, the dependent parameters j_0 and $\overline{\Omega}_x$ are chosen such that E_j is a smooth function of j at the boundaries $\pm j_0$ between the inner and outer regions.

An electron incident at the chemical potential has energy ε_F w. r. t. to the bulk band bottom and hence sees a relative potential of height $E_j - \varepsilon_\mathrm{F}$ at site j. For $\widetilde{V}_\mathrm{s} > \widetilde{V}_\mathrm{c}$, the relative potential describes a QD potential with two maxima of height $\widetilde{V}_\mathrm{s}$ at $j = \pm j_\mathrm{s}$ and a local parabolic minimum of height $\widetilde{V}_\mathrm{c}$ at $j = 0$. For $\widetilde{V}_\mathrm{c} > \widetilde{V}_\mathrm{s}$ (the case of present interest), it describes a QPC potential with a single parabolic maximum at $j = 0$, of height $\widetilde{V}_\mathrm{c}$. The crossover point between QD and QPC lies at $\widetilde{V}_\mathrm{s} = \widetilde{V}_\mathrm{c}$ (for which $\overline{\Omega}_x = 0$). Evidently $\widetilde{V}_\mathrm{c}$ and $\widetilde{V}_\mathrm{s}$ respectively mimick the role of the voltages applied to the central gates (V_c) and side gates (V_s) in the experiment (with $\widetilde{V}_\mathrm{c,s} \propto -|e| V_\mathrm{c,s}$).

Figure	N'	$\widetilde{V}_\mathrm{c}[\tau]$	$\widetilde{V}_\mathrm{s}[\tau]$	Ω_x	j_s
Fig. S6	150	-0.035 to 0.015	-0.25	0.016	60
Fig. S7	150	-0.032 to 0.01	-0.25	0.016	60
Fig. S9**a-b**	150	-2	-2	0	-
Fig. S9**c**	150	-0.6	0.6	0.0416	60
Fig. S9**d**	150	0.3	-0.3	0.023	60
Fig. S10**a**	150	-0.5	0.5	0.037	60
Fig. S10**b**	150	0.5	-0.5	0.027	60
Fig. S10**c**	150	-0.025	0	0.005	60
Fig. S10**d**	150	0.008	-0.25	0.016	60
Fig. S11	150	0	-0.25	0.016	60
Fig. S13	150	-0.016 to 0.006	-0.25	0.016	60
Fig. S14	150	-0.02 to 0.02	-0.25	0.016-0.048	60

Table I: Parameters used for model I [defined in Eq. (S15)] for the fRG results shown in various figures of the supplementary information.

We emphasize that the QPC barriers studied in this work are all *parabolic* near the top. For quantitative studies of the 0.7-anomaly using model I, we fix N', j_s and V_s, and tune the QPC from closed to open by lowering $\widetilde{V}_\mathrm{c}$ past 0, at which the bare ($U = 0$) conductance g^0 equals 0.5. The width of the conductance step [see Fig. A1**k**, and Eq. (S30)] is governed by the curvature parameter at this point, $\Omega_x = \overline{\Omega}_x|_{\widetilde{V}_\mathrm{c}=0}$, which we will simply call "curvature" henceforth. ($\overline{\Omega}_x$ itself changes slightly during this crossover, but for the barrier shapes used in this work this change is typically less than 10% between $\widetilde{V}_\mathrm{c} = \pm\Omega_x$.) The curvature Ω_x also governs the exponential $\widetilde{V}_\mathrm{c}$-dependence of $\widetilde{B}_*$ [Eq. (S35a)]. Note that formulas such as Eqs. (S30) and (S35a) would change for non-parabolic QPC barriers, e. g. barriers with a flat top. Studying the 0.7-anomaly for such situations would be an interesting extension of the present work, which we leave for the future[24].

C. Bare local density of states (LDOS)

In the main article we have argued that geometry strongly influences the 0.7-anomaly, via its effect on the local density of states (LDOS) and the van Hove ridge of the latter. Here we elaborate this in detail, by discussing the geometry-dependence of the noninteracting LDOS (for model I). We do so not only for the QPC barrier shape of present interest, but also for a QD barrier shape. This lays the ground for a subsequent comparison, presented in Sec. S-4 E below, of the LDOS structures of a QPC and a QD, which sheds light on the similarities and differences between the 0.7-anomaly and the Kondo effect.

The LDOS per spin species σ at energy ω (measured

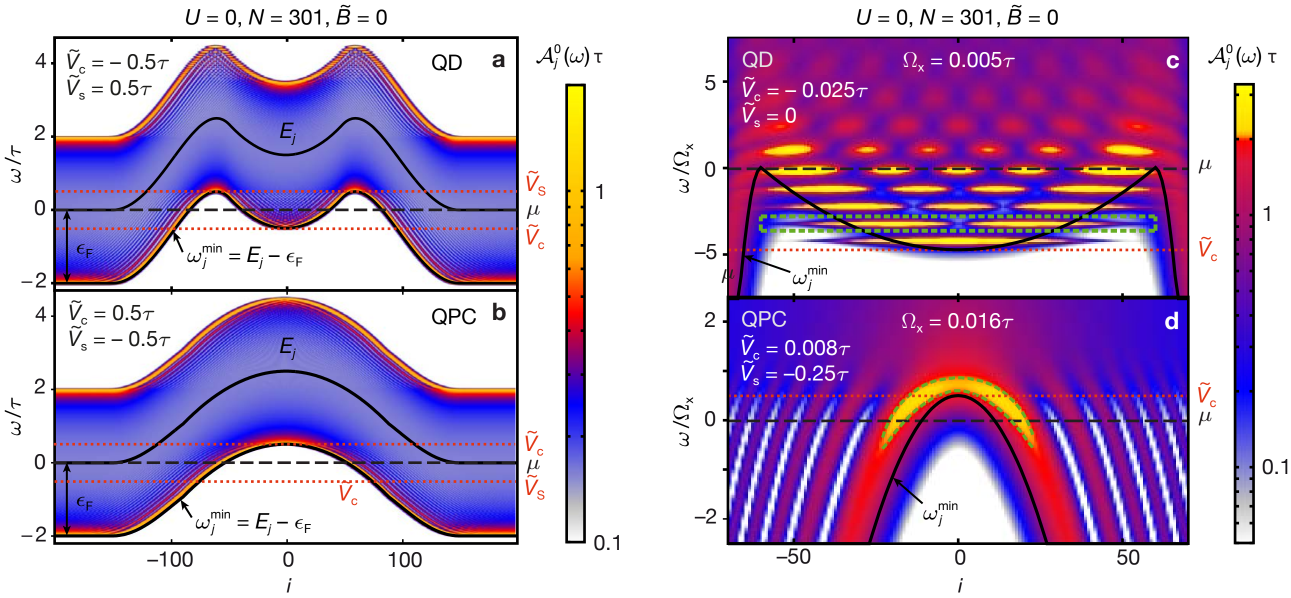

Figure S10: Model I: Noninteracting zero-field LDOS per spin species of **a**,**c**, a QD, and **b**,**d**, a QPC, for potential shapes shown by thin black lines (marked by black arrows) for $\omega_j^{\min} = E_j - \varepsilon_{\mathrm{F}}$. (The logarithmic color scale shows $\mathcal{A}_j^0(\omega)$ smeared by a Lorentzian of width $\delta = 0.001\tau$, in order to render very sharp structures visible.) Panels **c**,**d** focus on the central region of the CCR and energies close to μ (black dashed lines); the $\widetilde{V}_{\mathrm{c}}$- and $\widetilde{V}_{\mathrm{s}}$-choices differ from those used in **a**,**b**. Thin green dashed lines in **c**,**d** indicate the shape of the "LDOS ridges" discussed in the text. For the KQD, they enclose an area in the j-ω plane on which the corresponding LDOS ridge has weight 1; for the QPC, they trace a contour along which $\mathcal{A}_j^{0,\mathrm{QPC}}(\omega) = 0.7$.

relative to the chemical potential μ) is defined as

$$\mathcal{A}_j^\sigma(\omega) = -\frac{1}{\pi}\mathrm{Im}\mathcal{G}_{jj}^{\sigma R}(\omega) \ , \tag{S17}$$

where $\mathcal{G}_{ij}^{\sigma R}(\omega)$ is the Fourier transform of the retarded $T = 0$ propagator[25],

$$\mathcal{G}_{ij}^{\sigma R}(t) = -i\theta(t)\langle G|\{d_{i\sigma}(t), d_{j\sigma}^\dagger(0)\}|G\rangle \ , \tag{S18}$$

where $|G\rangle$ is the model's ground state. In this subsection we will discuss only the spin-degenerate case of zero field ($\widetilde{B} = 0$) and zero interaction ($U_j = 0$). We thus drop the spin index σ (as in the main article) and instead put a superscript 0 on $\mathcal{A}_j^0(\omega)$ to denote the bare LDOS.

For $E_j = 0$, representing an infinite, homogenous, bulk tight-binding chain, the LDOS of Eq. (S17) is j-independent and equal to the 1D bulk LDOS,

$$\mathcal{A}_{\mathrm{bulk}}^0(\omega) = \frac{a}{\pi}\left[\frac{\partial k}{\partial \epsilon_k}\right]_{\epsilon_k = \omega + \mu} . \tag{S19a}$$

This is nonzero only for $\omega_{\mathrm{bulk}}^{\min} < \omega < \omega_{\mathrm{bulk}}^{\max}$, where

$$\omega_{\mathrm{bulk}}^{\min} = -\varepsilon_{\mathrm{F}} \ , \quad \omega_{\mathrm{bulk}}^{\max} = -\varepsilon_{\mathrm{F}} + 4\tau \ , \tag{S19b}$$

denote the bottom and top of the band, measured w. r. t. μ, respectively. Within these limits, it has the form

$$\mathcal{A}_{\mathrm{bulk}}^0(\omega) = \frac{1}{\pi\sqrt{(\omega_{\mathrm{bulk}}^{\max} - \omega)(\omega - \omega_{\mathrm{bulk}}^{\min})}} \ , \tag{S19c}$$

shown in Fig. S9**b**, featuring square-root van Hove singularities near the band edges (yellow fringes in Fig. S9**b**). While the upper van Hove singularity (of unoccupied states) may be viewed as an artefact of describing the lowest subband using a tight-binding chain, the lower one is realistic for effective one-dimensional geometries; it would also arise, e. g., when using a free-electron model.

Now consider a nonzero potential E_j that is smooth on the scale of the lattice spacing, modelling a QD or QPC in the CCR, as shown by the thick black lines in Figs. S10**a-d**. The color scale in these figures indicates the corresponding j-dependent LDOS, $\mathcal{A}_j^0(\omega)$. The latter has an ω-dependence that, for fixed j, is reminiscent of the bulk case, but with several differences, caused by the spatial structure in E_j. First, the band edges now are j-dependent and follow the shape of the potential, with

$$\omega_j^{\min} = E_j - \varepsilon_{\mathrm{F}} \ , \quad \omega_j^{\max} = E_j - \varepsilon_{\mathrm{F}} + 4\tau \ . \tag{S20}$$

In particular, the band bottom at the CCR center, $j = 0$, is given by $\omega_0^{\min} = \widetilde{V}_{\mathrm{c}}$. Second, $\mathcal{A}_j^0(\omega)$ exhibits narrow fringes (visible clearly in Figs. S10**a-d**), due to the fact that the electronic wave functions form standing wave patterns. In the central part of the QD potential (Fig. S10**a**), and in the central part of the QPC potential for energies $\omega > \omega_{\mathrm{bulk}}^{\max}$ (Fig. S10**b**), these standing waves correspond to bound state wave functions. (For the case of the QPC these bound states are artefacts and they are avoided in model II.) In the outer regions of both QD and QPC potentials they correspond to Friedel oscilla-

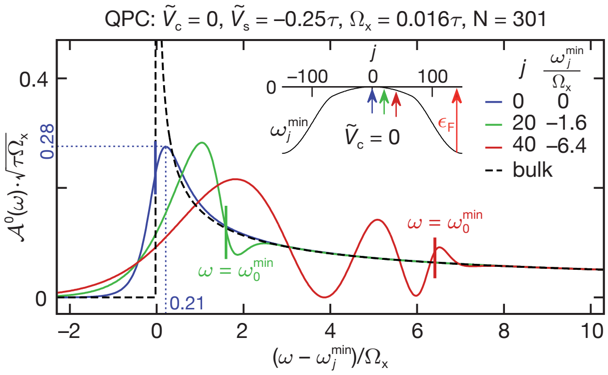

Figure S11: Inset: The band bottom ω_j^{min} (black line) as function of j, for a 301-site CCR with a parabolic QPC barrier (model I) with curvature Ω_x and height $\widetilde{V}_c = \omega_0^{\mathrm{min}} = 0$. Main plot: Energy dependence of the LDOS near the band bottom, showing $\mathcal{A}^0_{\mathrm{bulk}}(\omega)$ (dashed), and $\mathcal{A}_j^{0,\mathrm{QPC}}(\omega)$ (solid) for three j-values near the center, all plotted as functions of $(\omega-\omega_j^{\mathrm{min}})/\Omega_x$ (blue line corresponds to Fig. 1 in Ref. 23). Arrows of matching colors in the inset indicate the corresponding values of j (namely 0, 20 and 40). The short, heavy, colored vertical lines in the main panel indicate where the energy coincides with the barrier top, $\omega = \omega_0^{\mathrm{min}}$; the corresponding values of the x-coordinate $(\omega_0^{\mathrm{min}} - \omega_j^{\mathrm{min}})/\Omega_x$ (namely 0, 1.6 and 6.4) give the remaining barrier height as seen from site j. In the bulk, $\omega_j^{\mathrm{min}} = -\varepsilon_{\mathrm{F}}$. The peak of $\mathcal{A}_j^{0,\mathrm{QPC}}(\omega)$ lies at an energy $\omega_j^{\mathrm{H}} = \omega_j^{\mathrm{min}} + \mathcal{O}(\Omega_x)$. For $j = 0$ it lies at $\omega_0^{\mathrm{H}} = 0.21\Omega_x$ and has height $0.28/\sqrt{\tau\Omega_x}$ (dotted blue lines). Note that $\mathcal{A}_j^{0,\mathrm{QPC}}(\omega)$ matches $\mathcal{A}^0_{\mathrm{bulk}}(\omega)$ once the energy ω lies above ω_0^{min} by more than $\mathcal{O}(\Omega_x)$, corresponding to free propagation above the barrier.

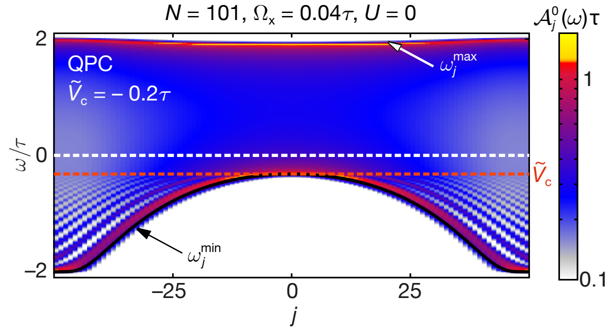

Figure S12: Noninteracting zero-field LDOS per spin species, $\mathcal{A}_j^0(\omega)$, shown on a logarithmic color scale, for the QPC model II defined by Eqs. (S22) and (S23). The thin black line (marked by black arrow) indicates the lower band edge, ω_j^{min} [Eq. (S24)]. The curvature of the lower and upper band edges is, respectively, negative and positive throughout the CCR, ensuring that no bound states occur.

tions. Third, the van Hove singularities are somewhat smeared out on the outer flanks of the QD, and throughout the entire QPC, in the latter case on a scale set by Ω_x (see Fig. S11).

For the rest of this subsection, we focus on the QPC barrier of Figs. S10**b**,**d**. (The QD barrier of Figs. S10**a**,**c** is revisited in Sec. S-4 E below, where we compare its LDOS to that of a QPC.) For a QPC, $\mathcal{A}_j^{0,\mathrm{QPC}}(\omega)$ depends *smoothly* on ω and j near the center of the CCR, its weight being concentrated along a curved, broad "van Hove ridge" (framed by the green dashed lines in Fig. S10**d**). This ridge originates from a van Hove singularity just above the band bottom that has been pushed upward by the QPC potential barrier. The van Hove ridge has limited spatial extent when traversed at constant ω, reflecting the limited spatial size of the QPC. At the outside flanks of the CCR barrier, the tails of the ridge split up into discrete fringes, representing Friedel oscillations associated with standing waves that build up near the barrier (as also seen in Figs. S10**a**,**b**). For given j, the ω-dependence of the van Hove ridge, shown in Fig. S11, is asymmetric w. r. t. to its maximum, with a steep, exponentially decaying flank below the maximum, and above it a long tail, whose envelope decays as $[\tau(\omega-\omega_j^{\mathrm{min}})]^{-1/2}$, reflecting the ω-asymmetry of the bulk van Hove singularity of Eq. (S19). The divergence of the latter is cut off here, due to the absence of translational invariance, on a scale set by the barrier curvature. Indeed, the maximum value taken by the van Hove peak in $\mathcal{A}_j^{0,\mathrm{QPC}}(\omega)$ occurs at an energy, say ω_j^{H}, that lies above the lower band edge by an amount of order Ω_x,

$$\omega_j^{\mathrm{H}} = \omega_j^{\mathrm{min}} + \mathcal{O}(\Omega_x)\ . \tag{S21}$$

For example, for a purely parabolic barrier top, the van Hove peak in $\mathcal{A}_{j=0}^{0,\mathrm{QPC}}(\omega)$, the LDOS at the center of the QPC, lies at $\omega_0^{\mathrm{H}} = \omega_0^{\mathrm{min}} + 0.21\Omega_x$. In that case, the van Hove peak lies precisely at the chemical potential, $\omega_0^{\mathrm{H}} = 0$, when $\widetilde{V}_c = -0.21\Omega_x$.

Eq. (S21) implies not only that the van Hove peak energy depends on Ω_x, but also that its height (i. e. the maximum value of the LDOS) scales as $1/\sqrt{\tau\Omega_x}$. As a consequence, all local quantities that depend on $\mathcal{A}_j^{0,\mathrm{QPC}}(\omega)$, such as the local magnetic susceptibility χ_j, depend on Ω_x, too. In this way they acquire an explicit dependence on the shape of the QPC barrier.

D. Model II

In this section we describe model II, used for all numerical results (fRG and SOPT) presented in the main article. For model II, designed to model exclusively a QPC, we have modified the choice of E_j and τ_j in two minor ways relative to model I of Sec. S-4 B, which turn out to facilitate SOPT calculations. The two changes, described below, are designed (i) to allow using a shorter CCR while maintaining a small curvature Ω_x at the barrier top, and (ii) to avoid the occurrence of artificial bound states in the bare density of states of the QPC (such as those seen in Fig. S10**b** near the upper band edge, for energies $\omega > \omega_{\mathrm{bulk}}^{\mathrm{max}}$).

(i) Modified potential shape: We define the onsite potential E_j by

$$E_j = \begin{cases} 0\,, & \forall \quad N' \leq |j|\,, \\ \dfrac{(\widetilde{V}_{\mathrm{c}} + \varepsilon_{\mathrm{F}})}{1+2b} \exp\left[- \dfrac{\left(\frac{j}{N'}\right)^2}{1 - \left(\frac{j}{N'}\right)^2} \right] & \forall \quad |j| \leq N'\,, \end{cases} \tag{S22}$$

where the parameter b is defined in *(ii)* below. This yields a smooth parabolic barrier near the CCR center and rapidly decaying flanks, allowing the CCR to be chosen shorter than for the potential of Eq. (S15). Using a short CCR is advantageous in particular for SOPT calculations: due to the matrix structure of the Greens function and the summation/integration over internal frequencies, the computation of the self-energy Σ and the vertex correction P needed for SOPT [see Eq. (S53) and Eq. (S52)] is rather time-consuming.

(ii) Modified hopping: For model I, the QPC potential barrier of Eq. (S15) (at $\widetilde{B} = 0$) yields a bare band whose upper edge has a maximum in energy at $j = 0$, causing a large number of bound states in the energy range $\omega \in [\omega^{\max}_{\mathrm{bulk}}, \omega^{\max}_{\mathrm{bulk}} + \widetilde{V}_{\mathrm{c}}]$ (visible as narrow fringes in Fig. S10). Though these artificial bound states are completely irrelevant for the physics of the 0.7-anomaly, the corresponding poles in the bare Green's functions nevertheless would have to be treated with due accuracy in the energy integrals involved in SOPT. To avoid the occurrence of such poles, model II takes the hopping matrix element τ_j in Eq. (S11) to be site-dependent within the CCR, $\tau_j = \tau - \delta\tau_j$, involving a smooth (adiabatic) reduction proportional to the local barrier height:

$$\delta\tau_j = \tfrac{1}{2}(E_j + E_{j+1})b \quad (>0)\,, \quad -N' \leq j < N', \tag{S23}$$

and $\delta\tau_j = 0$ otherwise. Then the lower and upper band edges are approximately given by

$$\left.\begin{matrix} \omega_j^{\min} \\ \omega_j^{\max} \end{matrix}\right\} = -\mu \mp 2\bar{\tau}_j + E_j\,, \quad \bar{\tau}_j = \tfrac{1}{2}(\tau_j + \tau_{j-1}). \tag{S24}$$

Here $\bar{\tau}_j$, the average hopping matrix element involving site j, is approximately equal to $\bar{\tau}_j \simeq \tau - bE_j$, since the potential varies smoothly with j. Eq. (S24) implies a j-dependent bandwidth, $4\bar{\tau}_j$. For the upper band edge $\omega_j^{\max}$, the upward shift contributed by E_j inside the CCR is counteracted by a downward shift, contributed by $2\bar{\tau}_j$, of $-2\delta\bar{\tau}_j \simeq -2bE_j$. The latter can be ensured to overcompensate the former by choosing the numerical factor b to be larger than $1/2$ (we choose $b = 0.55$). Then the upper band edge $\omega_j^{\max}$ throughout the CCR lies *below* the bulk band edge $\omega^{\max}_{\mathrm{bulk}}$, ensuring that no bound states occur near the upper band edge. This is illustrated in Fig. S12, which is to be contrasted to the bound states seen in Fig. S10**b** for model I, with j-independent hopping.

The prefactor $1/(1+2b)$ in Eq. (S22) ensures that $\widetilde{V}_{\mathrm{c}}$ corresponds to the effective barrier height w.r.t. the chemical potential, $\widetilde{V}_{\mathrm{c}} = \omega^{\min}_{j=0}$ [as is the case for Eq. (S15)]. Finally, the parameter Ω_x is defined as the curvature of the band bottom at $\widetilde{V}_{\mathrm{c}} = 0$, obtained by expanding Eq. (S24) to second order in j [in analogy to Eq. (S15)]: $\omega_j^{\min}|_{\widetilde{V}_{\mathrm{c}}=0} \simeq -\Omega_x^2 j^2/(4\bar{\tau}_0)$. For the choice $\mu = 0$ used here, $\bar{\tau}_0 \simeq \tau/(1+2b)$. We have checked that with this definition of Ω_x, the bare transmission probability for model II, calculated numerically, agrees well with the analytic prediction of Eq. (S30) below (and that of model I). For all calculations performed in this with with model II, we chose $N' = 50$ and $b = 0.55$, in which case $\Omega_x = 0.04\tau$.

We emphasize that transport and local properties are not modified in any essential way by the changes (i) and (ii) of model II w.r.t. model I. Their effect is solely to reduce the computation time.

E. Comparison: bare LDOS of QPC and QD

In this subsection, we offer a detailed comparison of the bare LDOS structures for a QPC and a QD. They are shown in Figs. S10**d** and S10**c**, respectively, which focus on the CCR-center and energies near $\omega = 0$. They evidently exhibit numerous differences, but also some similarities. These are key to understanding the differences and similarities between the 0.7-anomaly and the Kondo effect.

For a QPC, $\mathcal{A}_j^{0,\mathrm{QPC}}(\omega)$ exhibits a prominent, smooth van Hove ridge (Fig. S10**d**), as discussed in detail in Sec. S-4 C. In contrast, for a QD, $\mathcal{A}_j^{0,\mathrm{QD}}(\omega)$ has appreciable weight only along a set of "ridges" at *discrete* energies, one of which is marked by the green box in Fig. S10**c**. Each ridge is associated with a discrete eigenstate of the bare QD potential: it is characterized by a discrete eigenenergy, say ω_α, and its spatially confined, oscillatory j-dependence reflects that of $|\psi_\alpha(j)|^2$, where the wavefunction $\psi_\alpha(j)$ represents a confined standing wave. Its spatial extent is approximately set by the classical turning points (where $\omega_\alpha = \omega_j^{\min}$), though it tunnels a bit beyond these. Each ridge has a small but nonzero width in ω, due to tunneling into the leads outside the QD, and a quantized total weight of 1 when j-summed over the range of $\psi_\alpha(j)$ and ω-integrated over its width, as indicated by the green box in Fig. S10**c**.

(Parenthetic remark: When interactions are turned on, the detailed shape of the LDOS will change, since barrier heights and energy levels will be renormalized. Nevertheless, the full $\mathcal{A}_j(\omega)$ will retain the generic properties illustrated in Figs. S10**c**,**d**, namely discrete ridges for the QD and a single broad ridge for the QPC. Many-body correlations may lead to additional fine structures in the full LDOS, such as a narrow Kondo resonance at the Fermi energy for $\mathcal{A}_j^{\mathrm{KQD}}(\omega)$. However, such many-body effects do not concern us at the present qualitative level of argumentation, which merely seeks to identify the geometric prerequisites for their occurrence.)

The most important difference between the bare LDOS of a QD and a QPC lies in the following fact, evident from Figs. S10**a-d**: near the center of the CCR, $\mathcal{A}_j^{0,\mathrm{QD}}(\omega)$ consists of a series of discrete ridges of quantized weight, whereas $\mathcal{A}_j^{0,\mathrm{QPC}}(\omega)$ does not, being dominated by just a single ridge of nonquantized weight. The physical reason for this difference clearly is that a QD constitutes a closed structure that hosts discrete, localized states, whereas a QPC, being truly open, does not. This difference is responsible for the different behavior between a KQD and a QPC for large fields: for $\widetilde{B} \gg \widetilde{B}_*$, the magnetization of a KQD saturates, whereas that of a QPC does not (as seen in Fig. A1d and its inset). This behavior reflects the fact that for the KQD the spin of only the single odd electron in the topmost nonempty level is being polarized in a large field, whereas for the QPC, whose LDOS has no discrete structure, there is no intrinsic limit for the magnitude of the magnetization.

While the differences between the LDOS ridge structures of KQD and QPC matter at high energies, the low-energy behavior ($\widetilde{B}, \widetilde{T} \ll B_*$) is governed by a generic *common* feature shared by the LDOS of both geometries: the very existence of a $\widetilde{V}_\mathrm{c}$-tunable ridge with a strongly peaked dependence on both ω and j. (Details such as the number of such ridges or their internal spatial structure are irrelevant for the ensuing argument.) The existence of such a ridge guarantees a strong magnetic response in both the conductance and the magnetization when $\widetilde{V}_\mathrm{c}$ is tuned such that the (interaction-shifted version of the) ridge is located energetically somewhat below μ. For a KQD, this is the local moment regime; for the QPC, it is the regime where $g \simeq 0.7$. This situation is particularly inductive to a strong local magnetic response, for two reasons: First, when spin symmetry is broken by turning on a magnetic field (say $\widetilde{B} > 0$), the $\widetilde{B}$-induced surplus of spin-up over spin-down electrons is enhanced by the presence of an LDOS ridge below the chemical potential, because this ridge constitutes a large density of states in a confined region of space. Second, interactions will generally act to further increase this surplus by repelling spin-down electrons, and will be aided in this by the fact that the ridge, and hence the region in which the surplus is large, has a limited spatial extent.

This microscopic mechanism generates a strong, local magnetic response *irrespective* of whether the LDOS ridge has quantized weight or not. Thus, this mechanism applies equally to a KQD and a QPC, and in this respect the low-energy behavior of the Kondo effect and the 0.7-anomaly are indeed similar. This similarity was first pointed out in Ref. 26 and emphasized, in particular, by Meir and collaborators[17–19]: the "narrow transmission resonances above the barrier" or "quasi-bound state" evoked in their arguments correspond to the van Hove ridge in $\mathcal{A}_j^{0,\mathrm{QPC}}(\omega)$ described above. Indeed, the asymmetric bare LDOS peak at the QPC barrier center found by us [Fig. S11, blue line for $\mathcal{A}_{j=0}^{0,\mathrm{QPC}}(\omega)$] is qualitatively similar to that found in Ref. 17 [see Fig. 3a there, right inset, solid line for $\nu_\uparrow(\epsilon)$] by spin-density-functional theory (SDFT) in a small applied field. Moreover, the van Hove ridge in our Figs. S10**b**,**d** corresponds to the bright spot seen in the center of Fig. 3a of Ref. 19 by Rejec and Meir, which shows the full spin-up LDOS $\mathcal{A}_j(\omega)$ as function of position and energy, again calculated by SDFT in a small applied field. Though SDFT includes interactions and our bare LDOS does not, interactions affect the minority species much more strongly than the majority species. We therefore expect that the geometry-dependence of the majority LDOS obtained from SDFT should be similar to that of a noninteracting theory. Thus, we believe that Meir and Rejec's "quasi-bound states" are synonymous to our "van Hove ridges". (We somewhat prefer the latter nomenclature, since it indicates the origin of these LDOS structures.) It would be highly desirable to have a plot similar to Fig. S10**d** for the full $\mathcal{A}_j^{\mathrm{QPC}}(\omega)$ calculated using fRG, but its energy dependence is not accessible by static fRG. To obtain a first impression, we have calculated it using perturbation theory, see Fig. A3**g**,**h**; calculating it with Keldysh fRG would be an interesting goal for future studies.

We wish to emphasize that the details of the magnetic response of a KQD and a QPC will be similar *only as long as the conditions* $\widetilde{B}, \widetilde{T} \ll \widetilde{B}_*$ *hold*; once they are violated, the differences in the LDOS ridges, discrete for QD vs. continuous for QPC, begin to matter. This caveat, not discussed in Refs. 17–19, prevents the similarity between Kondo effect and 0.7-anomaly from extending to the regime of large energies.

A detailed comparative study of the similarities and differences in the behavior of a KQD and QPC, all originating from the similarities and differences between their LDOS ridges, will be published elsewhere[1].

S-5. THE LOW-ENERGY SCALE $\widetilde{B}_*$

This section covers the influence of geometry and interactions on the low-energy scale $\widetilde{B}_*$ for a QPC. In Sec. S-5 A we show that the exponential dependence of the low-energy scale $\widetilde{B}_*(\widetilde{V}_\mathrm{c})$ has a purely geometric origin, and contrast this to the more complicated case of the Kondo temperature for a KQD. Sec. S-5 B discusses the effects of interactions on $\widetilde{B}_*$ and $\widetilde{T}_*$ for a QPC. Finally, Sec. S-5 C discusses the extent to which the interaction parameter U itself depends on the 2D potential landscape.

A. Exponential $\widetilde{V}_\mathrm{c}$-dependence of $\widetilde{B}_*$

In the main article we reported that for a QPC the low-energy scale $B_*(V_\mathrm{c})$ depends exponentially on V_c (see Eq. (A3), Figs. A2**a**, **c**, **e**). The same is true for $T_*(V_\mathrm{c})$ (see Eq. (A3), Figs. A2**d**, **f**), as was first found in Ref. 26. In this subsection, we explain the origin of this exponential V_c-dependence. It is present already for the noninteracting ($U = 0$) version of our model, hence we begin by discussing the latter.

According to the Landauer-Büttiker formula, the non-interacting differential conductance $g^0_{\mathrm{nl}}(\widetilde{T}, \widetilde{B}, \widetilde{V}_{\mathrm{sd}})$ as a function of temperature $\widetilde{T} = k_{\mathrm{B}}T$, magnetic field $\widetilde{B} = |g_{\mathrm{el}}|\mu_{\mathrm{B}}B$ and source-drain voltage $\widetilde{V}_{\mathrm{sd}} = -|e|V_{\mathrm{sd}}$ is given by

$$g^0_{\mathrm{nl}}(\widetilde{T}, \widetilde{B}, \widetilde{V}_{\mathrm{sd}}) = \frac{d}{d\widetilde{V}_{\mathrm{sd}}} \frac{1}{2} \sum_{\sigma=\pm} \int_{-\infty}^{\infty} d\omega\, \mathcal{T}(\omega + \tfrac{1}{2}\sigma\widetilde{B}) \times \left[f(\omega - \tfrac{1}{2}\widetilde{V}_{\mathrm{sd}}) - f(\omega + \tfrac{1}{2}\widetilde{V}_{\mathrm{sd}}) \right] \quad \text{(S25)}$$

where $f(\omega) = [e^{\omega/\widetilde{T}} + 1]^{-1}$ is the Fermi function, and $\mathcal{T}(\omega)$ is the noninteracting transmission probability across the QPC barrier of a lead electron incident with energy ω w. r. t. μ, at $\widetilde{B} = 0$. Let us expand it in powers of energy:

$$\mathcal{T}(\omega) = \mathcal{T}^{(0)} + \mathcal{T}^{(1)}\omega + \frac{1}{2}\mathcal{T}^{(2)}\omega^2 + \ldots\,, \quad \text{(S26)}$$

where $\mathcal{T}^{(0)} = \mathcal{T}(0)$ is the transmission probability at the chemical potential. Inserting Eq. (S26) into (S25) leads to the following expression for the leading dependence of the bare conductance on $\widetilde{T}^2$, $\widetilde{B}^2$ and $\widetilde{V}^2_{\mathrm{sd}}$ (at fixed $\widetilde{V}_{\mathrm{c}}$ and $\widetilde{V}_{\mathrm{s}}$)

$$\frac{g^0_{\mathrm{nl}}(\widetilde{T}, \widetilde{B}, \widetilde{V}_{\mathrm{sd}})}{\mathcal{T}^{(0)}} = \left[1 - \left(\frac{\widetilde{T}}{\widetilde{T}^0_*}\right)^2 - \left(\frac{\widetilde{B}}{\widetilde{B}^0_*}\right)^2 - \left(\frac{\widetilde{V}_{\mathrm{sd}}}{\widetilde{V}^0_{\mathrm{sd}*}}\right)^2 \right], \quad \text{(S27)}$$

with low-energy scales $\widetilde{T}^0_*$, $\widetilde{B}^0_*$ and $\widetilde{V}^0_{\mathrm{sd}*}$ given by

$$-\frac{8\mathcal{T}^{(0)}}{\mathcal{T}^{(2)}} = \left(\widetilde{B}^0_*\right)^2 = \left(\widetilde{V}^0_{\mathrm{sd}*}\right)^2 = \frac{4\pi^2}{3}\left(\widetilde{T}^0_*\right)^2 . \quad \text{(S28)}$$

Their mutual ratios hence are independent of $\widetilde{V}_{\mathrm{c}}$:

$$\frac{\widetilde{B}^0_*}{\widetilde{T}^0_*} = \frac{2\pi}{\sqrt{3}}, \qquad \frac{\widetilde{V}^0_{\mathrm{sd}*}}{\widetilde{B}^0_*} = 1\,. \quad \text{(S29)}$$

(Remark: Depending on the height and shape of the potential barrier, $\mathcal{T}^{(2)}$ can be either negative or positive; in the latter case, the scales $\widetilde{B}^0_*$, $\widetilde{T}^0_*$ and $\widetilde{V}^0_{\mathrm{sd}*}$ as defined here would be imaginary. In the following, we are interested only in the former case.)

Now consider a purely parabolic QPC potential barrier with height $\widetilde{V}_{\mathrm{c}}$ and longitudinal curvature $\frac{1}{4\tau}\Omega_x^2$ [as in Eq. (S15)]. Then the bare transmission $\mathcal{T}(\omega)$ at $\widetilde{B} = 0$ is given by[5]

$$\mathcal{T}(\omega) \simeq \frac{1}{e^{-2\pi(\omega - \widetilde{V}_{\mathrm{c}})/\Omega_x} + 1}\,. \quad \text{(S30)}$$

Recall that $\widetilde{V}_{\mathrm{c}} = \omega^{\mathrm{min}}_{j=0}$ is the height of the band bottom's maximum at the central site w. r. t. the chemical potential. When $\widetilde{V}_{\mathrm{c}}$ is decreased to open up the QPC, the bare transmission of an electron incident at the chemical potential ($\omega = 0$) increases past $\mathcal{T}(0) = 0.5$ when $\widetilde{V}_{\mathrm{c}}$ decreases past 0. [We obtained Eq. (S30) from Eq. (4) of Ref. 5, which in turn was derived by a semiclassical treatment of transmission through a parabolic barrier[27,28], assuming a quadratic dispersion of the form $p^2/2m$. The latter assumption is applicable for our situation in the limit that our tight-binding band is much wider than the energy range over which the transmission changes rapidly, $\tau \gg \Omega_x$. This allows a quadratic approximation for the dispersion [Eq. (S12)] near the band bottom, $\epsilon_k \simeq -2\tau + \tau k^2 a^2$, implying an effective mass of $m = \hbar^2/(2\tau a^2)$.]

The bare dimensionless conductance at $\widetilde{B} = \widetilde{T} = \widetilde{V}_{\mathrm{sd}} = 0$, viewed as function of $\widetilde{V}_{\mathrm{c}}$, is then given by

$$g^0_{\mathrm{nl}} = g^0_{\mathrm{nl}}(0,0,0) = \mathcal{T}^{(0)} = \frac{1}{e^{-2\pi\widetilde{V}_{\mathrm{c}}/\Omega_x} + 1}\,. \quad \text{(S31)}$$

Let us now focus on the regime of negative $\widetilde{V}_{\mathrm{c}} = -|\widetilde{V}_{\mathrm{c}}|$, where for the quadratic potential top considered here the bare magnetoconductance is strictly negative. Evaluating Eq. (S28) for $\widetilde{B}^0_*$ using Eq. (S30), one finds:

$$\widetilde{B}^0_* = \frac{\Omega_x}{\pi}\sqrt{2\coth(\pi|\widetilde{V}_{\mathrm{c}}|/\Omega_x)}\, e^{\pi|\widetilde{V}_{\mathrm{c}}|/\Omega_x} \quad \text{(S32a)}$$

$$= \frac{\Omega_x}{\pi}\frac{1}{\sqrt{g^0 - 1/2}}\sqrt{\frac{g^0}{1 - g^0}}\,. \quad \text{(S32b)}$$

(The second line follows from the first by inverting Eq. (S31).) Expression (S32a) for the low-energy scale in the absence of interactions, $\widetilde{B}^0_*$, agrees to within a few percent with our numerical calculations for $U = 0$, shown by the black dashed line in Fig. S13**a**. It states that $\widetilde{B}^0_*$ diverges both when $|\widetilde{V}_{\mathrm{c}}| \to 0^+$ (i. e. $g^0 \to 1/2$ from above) and when $|\widetilde{V}_{\mathrm{c}}|/\Omega_x \gg 1$ (i. e. $g^0 \to 1$ from below). Between these two limiting cases $\widetilde{B}^0_*$ has a minimum, which turns out to occur at a bare conductance of $g^0_* = 1/\sqrt{2} \simeq 0.707$.

The message of the above analysis is that the experimentally observed exponential V_{c}-dependence of the low-energy scales B_* and T_* reported in the main article (and for T_* also in Ref. 26) has a *purely geometric origin, which can already be understood within a noninteracting model.* It arises simply because for a quadratic barrier the transmission amplitude above the barrier depends exponentially on its height (as can be made explicit in a semiclassical WKB treatment of the transmission problem[27,28]). Moreover, the scale for the $\widetilde{V}_{\mathrm{c}}$-dependence is set solely by Ω_x, the curvature at the top of the barrier [Eq. (S15)].

The fact that for a QPC the exponential $\widetilde{V}_{\mathrm{c}}$-dependence of $\widetilde{B}_*$ can be found without considering interactions at all stands in striking contrast to the case of a KQD: there $\widetilde{B}_*$ is proportional to the Kondo temperature, which likewise depends exponentially on $\widetilde{V}_{\mathrm{c}}$, but the exponent is quadratic in $\widetilde{V}_{\mathrm{c}}$, and the scale of its $\widetilde{V}_{\mathrm{c}}$-dependence is set by the interaction strength U and effective level width Γ. To be explicit, for the single-impurity

Anderson model, with level position $\varepsilon_d = \widetilde{V}_\mathrm{c}$, the Kondo temperature corresponding to $\widetilde{T}_*$ is given by[29]

$$\widetilde{T}_\mathrm{K} = \sqrt{U\Gamma/2} \exp\left[\frac{\pi \widetilde{V}_\mathrm{c}(\widetilde{V}_\mathrm{c}+U)}{2\Gamma U}\right] . \tag{S33}$$

It arises as the low-energy scale $\widetilde{T}_\mathrm{K} \propto e^{-1/j_\mathrm{eff}}$ characterizing the onset of a logarithmic infrared divergence that occurs when doing perturbation theory in the effective exchange interaction between the spins of a local moment and a conduction band. The form of the corresponding effective dimensionless exchange coupling j_eff, given by

$$j_\mathrm{eff} = \frac{2\Gamma}{\pi}\left[\frac{1}{\widetilde{V}_\mathrm{c}+U} - \frac{1}{\widetilde{V}_\mathrm{c}}\right] , \tag{S34}$$

is found by a Schrieffer-Wolff transformation. Evidently, such KQD results can not be obtained without considering the role of interactions from the outset. In contrast, for a QPC the origin of the exponential $\widetilde{V}_\mathrm{c}$-dependence of $\widetilde{B}_*$ is decidedly different and can be understood already for a noninteracting theory, as described above. In particular, at high energies a QPC does *not* display local-moment behavior, so that the corresponding logarithmic infrared divergence characteristic of the Kondo effect does not occur.

Having made this point, we hasten to add that $\widetilde{B}_*$ is of course affected by interactions for a QPC too, albeit less severely than for a KQD. The role of interactions is discussed in the next subsection.

B. Effects of interactions on $\widetilde{B}_*$ and $\widetilde{T}_*$

While the fact that the low-energy scales $\widetilde{B}_*$, $\widetilde{T}_*$ and $\widetilde{V}_{\mathrm{sd}*}$ for a QPC depend exponentially on gate voltage, as $e^{\pi|\widetilde{V}_\mathrm{c}|/\Omega_x}$, has an elementary geometric origin, the behavior of the pre-exponential factor is more subtle: quite generally this pre-exponential factor will depend on the interaction strength U and gate voltage $\widetilde{V}_\mathrm{c}$. A detailed theoretical analysis of this issue is beyond the scope of the present paper. Here we just want to make two points, the first regarding the ratio $\widetilde{B}_*/\widetilde{T}_*$, the second regarding the U-dependence of $\widetilde{B}_*$.

The ratio $\widetilde{B}_*/\widetilde{T}_*$*:* When interactions are turned on, the effects of finite $\widetilde{B}$ or finite $\widetilde{T}$ are, in general, not equivalent: Finite $\widetilde{B}$ shifts the effective barrier height seen by spin-up and spin-down electrons in opposite directions, in a way that is enhanced by interactions (which amplifies the imbalance between spin up and spin down), however without opening up the possibility of inelastic scattering. Finite $\widetilde{T}$ causes an effective increase in barrier height, too, due to an increase in density near the barrier center (because the LDOS is ω-asymmetric there), but it does not involve any imbalance between spin-up and -down. Moreover, finite $\widetilde{T}$ also leads to inelastic scattering. In lowest-order perturbation theory for the self-energy (Sec. S-7), shifts in barrier height (both $\widetilde{B}$-induced, spin-asymmetric and $\widetilde{T}$-induced, spin-symmetric shifts) are described by the Hartree contribution, and $\widetilde{T}$-induced inelastic scattering by the Fock contribution [see Eq. (S53)]. In general, the relative strength of these two effects will depend not only on U but also on gate voltage. Since the strength of the (negative) conductance response to increasing $\widetilde{B}$ or $\widetilde{T}$ is characterized by $1/\widetilde{B}_*$ or $1/\widetilde{T}_*$, respectively, the ratio $\widetilde{B}_*/\widetilde{T}_*$, too, will in general likewise depend not only on U, but also directly on $\widetilde{V}_\mathrm{c}$.

In the light of the above comments, it is all the more remarkable that the experimentally observed ratio $B_*/\widetilde{T}_*$ *does*, in fact, become essentially independent of V_c in the V_c-regime well below V_c0, where $g \to 1$ (compare thin grey and black lines in Fig. A2**f**). In the main article we have already pointed out that this V_c-independence of B_*/T_* for $g \simeq 1$ is characteristic of the Fermi-liquid behavior expected from Nozières' treatment of the Kondo problem in the limit $B, T \ll T_\mathrm{K}$.

Once the condition $g \simeq 1$ is relaxed, the experimentally determined B_*/T_* does acquire a dependence on V_c, in accord with the expectations stated above. Indeed, in Fig. A2**f** the measured ratio B_*/T_* *increases* with increasing $\widetilde{V}_\mathrm{c}$ as B_* and T_* approach their minimal values. Remarkably, our model qualitatively reproduces this behavior when we treat interactions using SOPT (compare the lines for $\widetilde{B}_*$ and $\widetilde{T}_*$ in Fig. A2**d**). An increase in $\widetilde{B}_*/\widetilde{T}_*$ means that the conductance reduction induced by increasing $\widetilde{T}$ grows relative to that induced by increasing $\widetilde{B}$, implying that inelastic scattering [Fock term, diagram **c** in Eq. (S53)] gains importance relative to the $\widetilde{B}$-induced enhancement of the barrier height [Hartree terms, diagrams **a** and **b** in Eq. (S53)]. Moreover, Fig. S4 above shows that $\widetilde{B}_*/\widetilde{T}_*$ decreases with increasing U, implying that in general interactions have a stronger effect on the low-$\widetilde{B}$ dependence of the conductance than on its low-$\widetilde{T}$ dependence.

U-dependence of $\widetilde{B}_*$*:* We have used fRG to explore in some more detail how interactions affect the $\widetilde{V}_\mathrm{c}$-dependence of $\widetilde{B}_*$ for a QPC. (Similar studies of $\widetilde{T}_*$ are not possible using static fRG, but would be worth pursuing by Keldysh fRG). As in Sec. S-5 A above, we focus on the regime $g \simeq 1$ (say $|\widetilde{V}_\mathrm{c}| \gtrsim 0.75\Omega_x$). Our results for this regime can be summarized by stating that for U small enough to be treatable by fRG, $\widetilde{B}_*$ shows the following behavior:

$$\widetilde{B}_*(\widetilde{V}_\mathrm{c}, U) \simeq \frac{\sqrt{2}\Omega_x}{\pi} e^{-F(U)} e^{\pi|\widetilde{V}_\mathrm{c}|/\Omega_x} , \tag{S35a}$$

$$F(U) \simeq (0.8 \pm 0.05) U/\sqrt{\tau\Omega_x} . \tag{S35b}$$

The behavior of Eq. (S35a) is illustrated in Fig. S13**a**, which shows $\ln(\widetilde{B}_*)$ as function of $|\widetilde{V}_\mathrm{c}|/\Omega_x$ for several values of U: for $|\widetilde{V}_\mathrm{c}|/\Omega_x \gtrsim 0.75$ the resulting lines all have roughly the same slope, but are shifted downward

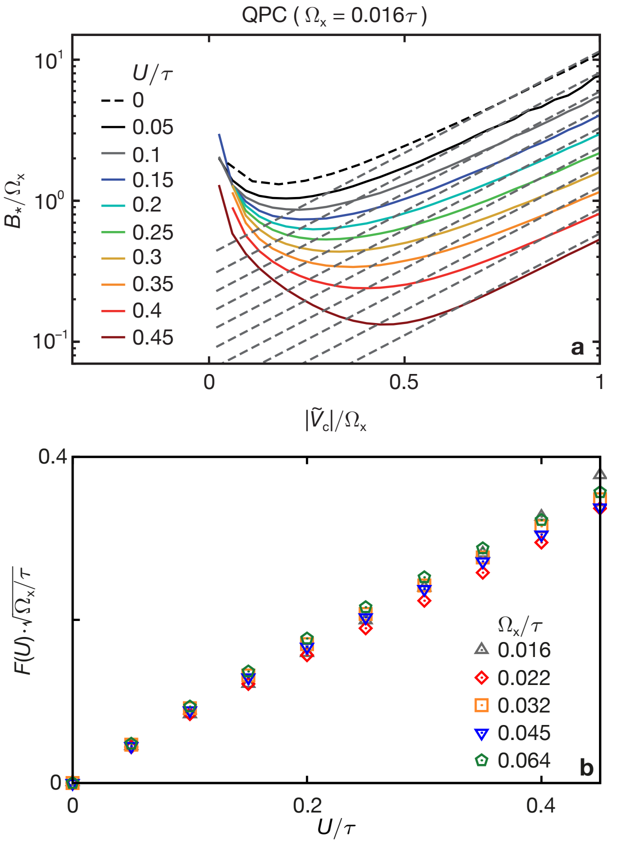

Figure S13: Effect of interaction strength U on the low-energy scale $\widetilde{B}_*$, in the regime of negative $\widetilde{V}_{\rm c} = -|\widetilde{V}_{\rm c}|$ (calculated for model I using static fRG). **a**, $\widetilde{B}_*/\Omega_x$ as function of $|\widetilde{V}_{\rm c}|/\Omega_x$. Grey dashed lines indicate linear fits of $\ln(\widetilde{B}_*)$ vs. $|\widetilde{V}_{\rm c}|/\Omega_x$ in the range $0.8 \leq |\widetilde{V}_{\rm c}|/\Omega_x < 1$, the offsets of which yield $F(U)$. **b**, The function $F(U)$ vs. U for several choices of Ω_x, plotted in scaled fashion to illustrate the behavior of Eq. (S35b).

in uniformly-spaced steps when U is increased in uniform steps. This implies that $\widetilde{B}_*$ is exponentially suppressed with increasing U (which also shifts the minimum in $\widetilde{B}_*$ towards more positive $|\widetilde{V}_{\rm c}|$-values). The function $F(U)$ that characterizes the exponential suppression can be obtained from the offsets of linear fits to $\ln(\widetilde{B}_*)$ vs. $\pi|\widetilde{V}_{\rm c}|/\Omega_x$, repeated for various U-value. The resulting function $F(U)$, shown in Fig. S13**b** for several values of the curvature Ω_x, exhibits the behavior described by Eq. (S35b) quite well: it increases linear with U, on a scale set by $\sqrt{\tau\Omega_x}$. This reflects the fact that in static fRG, the dimensionless quantity that governs the effective interaction strength is $U\mathcal{A}_j(0)$ (cf. Sec. S-6), and at the barrier top we have [cf. Eq. (S19c) and Fig. S11]

$$U\mathcal{A}_{j=0}(0) \propto U/\sqrt{\tau\Omega_x} \, . \tag{S36}$$

Paraphrasing Eq. (S35a), we can formulate the following conclusions for how the $\widetilde{V}_{\rm c}$-dependence of $\widetilde{B}_*$ in the regime $g \simeq 1$ is affected by turning on U: (i) The factor $e^{\pi|\widetilde{V}_{\rm c}|/\Omega_x}$ from Eq. (S32) persists, essentially without a change in the numerical prefactor π/Ω_x of $|\widetilde{V}_{\rm c}|$ in the exponent. (ii) The pre-exponential factor decreases exponentially with U, in a fashion that corresponds to shifting $\widetilde{V}_{\rm c} \to \widetilde{V}_{\rm c} + \Omega_x F(U)/\pi$. The physical interpretation is that local interactions increase the Hartree potential and hence the effective barrier height [causing (ii)], but do not significantly change its effective curvature [resulting in (i)]. Of course, the latter statements are true only approximately, in that Fig. S13 does exhibit slight deviations between the actual data and the behavior stated by Eqs. (S35).

Together, points (i) and (ii) suggest that for a QPC, the qualitative effect of interactions on $\widetilde{B}_*$ can already be found by *perturbatively* calculating the Hartree potential. We have done so, obtaining results (not shown here) in qualitative agreement with those just discussed. A simpler treatment of the same effects might be possible using semiclassical WKB wave functions, as done in Ref. 6 in a calculation of the Fock contribution to $\widetilde{T}_*$, but this is left as a topic for future study. (We remark that when the calculation of $\widetilde{T}_*$ in Ref. 6, extractable from their Eq. (33), is specialized to a point-like interaction with range zero, the result yields precisely the same $e^{\pi|\widetilde{V}_{\rm c}|/\Omega_x}$ dependence for $\widetilde{T}_*$ as found by us in Eq. (S32) above.)

Note from Eq. (S35) that decreasing the curvature Ω_x at the top of the QPC barrier or increasing the interaction strength U (e. g. using a top gate) have qualitatively similar effects, in that both tend to decrease $\widetilde{B}_*$ and hence to strengthen the low-$\widetilde{B}$ response of the conductance. Likewise, decreasing Ω_x or increasing U also cause similar changes in the conductance step at $\widetilde{B} = \widetilde{T} = 0$, in that both tend to make the 0.7-shoulder more prominent. This is illustrated in Fig. S14, whose panels **b** and **c** offer a succinct summary of how the 0.7-anomaly depends on geometry and interactions, respectively.

Since Ω_x sets both the width of the conductance step [Eq. (S31)] and the slope of $\ln(\widetilde{B}_*)$ vs. $|\widetilde{V}_{\rm c}|$ [Eq. (S35a)], an experimental consistency check is possible: We have determined the said step width and slope from Fig. A2**e** and extracted Ω_x-values from each, finding $\Omega_x^{\rm step} \simeq a \times 0.026$ V from the step width and $\Omega_x^{\rm slope} \simeq a \times 0.048$ V from the slope ($a \simeq 37$ meV/V is a geometric conversion factor between applied gate voltage (in V) and the resulting electrostatic potential energy (in meV), such that $\widetilde{V}_{\rm c} = -a\,V_{\rm c}$). The fact that $\Omega_x^{\rm step}$ and $\Omega_x^{\rm slope}$ agree within a factor of two is quite satisfactory, given the fact that we made no attempt to realistically model the shape of the QPC potential. Possible reasons for why the agreement is not perfect are that the experimental QPC potential was not perfectly parabolic, and that our use of a purely on-site (instead of longer-range) interaction is an over-simplification. (See also Sec. S-5 C below.)

To conclude this subsection, let us emphasize once more its most important qualitative conclusion: *inter-*

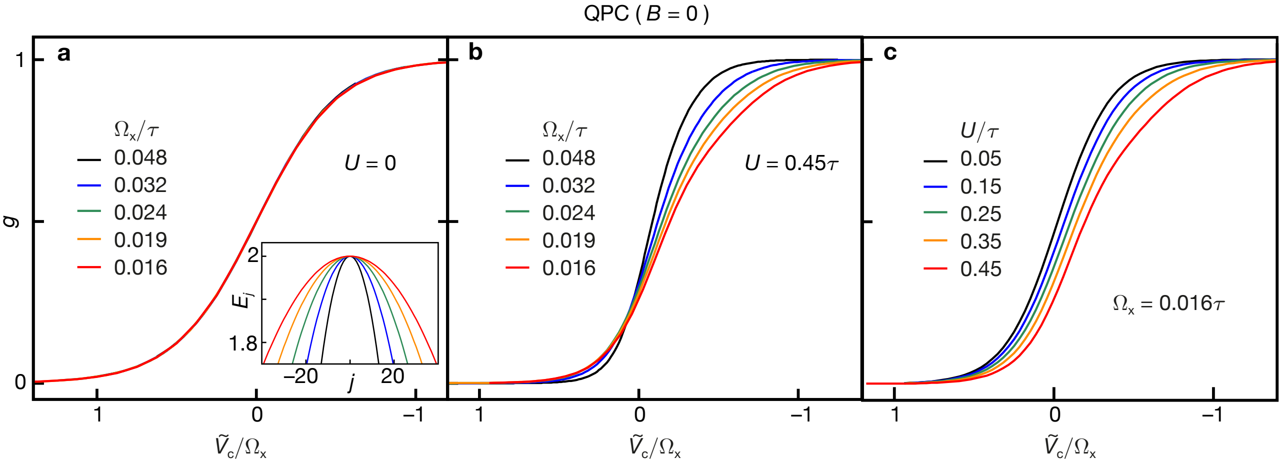

Figure S14: Effect of barrier curvature Ω_x (panels **a**,**b**) and interaction strength U (panel **c**) on the conductance through a QPC (model I), calculated by static fRG. The inset to **a** shows the top of a parabolic QPC barrier for several values of the curvature Ω_x. **a**, In the absence of interactions ($U = 0$) the conductance curves $g(\widetilde{V}_c)$, calculated for different Ω_x, all collapse onto a single curve when plotted as function of $\widetilde{V}_c/\Omega_x$, as expected from Eq. (S30). **b**, Similar plot as **a**, but for $U \neq 0$, which prevents a scaling collapse. **c**, Conductance curves $g(\widetilde{V}_c)$ calculated for fixed Ω_x but several different values of U, and scaled as in **a** and **b**. As explained in the main article, the combination of enhanced spectral weight at the Fermi energy $\mathcal{A}_{j=0}(0)$ and interaction U lowers the conductance in the vicinity of $\widetilde{V}_c \simeq 0$, resulting in an asymmetric and broadened conductance step. The strength of this effect is governed by the product $U\mathcal{A}_{j=0}(0) \propto U/\sqrt{\tau\Omega_x}$ [cf. Eq. (S36)]. This increases with decreasing Ω_x at fixed U (panel **b**) or likewise with increasing U at fixed Ω_x (panel **c**), causing an enhancement of the 0.7-shoulder in both cases.

actions cause an exponential reduction in $\widetilde{B}_*$, which can thus be significantly smaller than the QPC's natural energy scale Ω_x. (In Fig. A2**f**, the smallest values reported for $\mu_B B_*$ and $k_B T_*$ are 0.3 meV and 0.08 meV, respectively, significantly smaller than the above estimates of $\Omega_x^{\rm step} \simeq 1$ meV.) While the detailed form of the function $F(U)$ describing this suppression may be model-dependent, we believe the strong suppression of $\widetilde{B}_*$ with increasing U to be generic. This is a crucial ingredient for understanding the 0.7-anomaly, since it becomes more pronounced the smaller this crossover scale.

C. Geometry-dependence of interaction U

It would be interesting to experimentally study the interaction- and geometry dependence of B_* more systematically, by using the side- and top-gate voltages V_s and V_t to vary the effective barrier shape and interaction strength. Of course numerous studies of the 0.7-anomaly in varying geometries do exist[4,8–10,12,30,31], but to systematically check the predictions of Eq. (S35) for $\widetilde{B}_*(\widetilde{V}_c, \Omega_x, U)$, it would be necessary to simultaneously monitor the V_t- and V_s-dependence of $B_*(V_c)$, Ω_x *and* U. Indeed, whereas our model treats U as a fixed, given constant, in reality the effective interaction strength is geometry-dependent. We have already pointed out in Sec. S-2 A that it depends on the lateral confinement in the QPC region; more specifically, the effective interaction constant for a 1D model will depend on the spatial extent, say l_y, of the transverse wave-function, which, in turn, can depend quite delicately on the amount of screening, etc.

If no realistic modelling of the latter is available (we have not attempted any), the evolution of interaction strength with geometry is best gauged by tracking the evolution of experimentally accessible quantities such as $g_{\rm ss}$ and $\Delta_{\rm hfo}$. To be specific, the conductance $g(V_c, B, T)$ could be measured for various settings of V_t and V_s. A measure for the resulting changes in the effective interaction strength U could be obtained from the transconductance dG/dV_c at low T by monitoring the corresponding changes in $g_{\rm ss}$ or $\Delta_{\rm hfo}$ (as in Fig. S5**b**, **c**). Simultaneously, estimates for Ω_x and l_y could be extracted, respectively, from the widths of the first step and first plateau of the conductance curve at low T; and B_* and T_* from the low-energy B- and T-dependence of the conductance (as in Figs. A2**e**, **f**). This would yield enough information to check Eq. (S35) in detail. We leave such a study for future work.

S-6. FUNCTIONAL RENORMALIZATION GROUP

In this section and the next, we describe the details of the two theoretical approaches used here: The present section is devoted to the functional renormalization group (fRG) which we used to study the $\widetilde{B}$-dependent quantities at $\widetilde{T} = \widetilde{V}_{\rm sd} = 0$. Section S-7 outlines the second-order perturbation theory (SOPT) approach which we used to explore the properties of our model for fixed U at $\widetilde{T} \neq 0$ or $\widetilde{V}_{\rm sd} \neq 0$.

Both fRG and SOPT are set up as perturbation expansions with respect to a noninteracting ground state that has zero magnetization in the absence of a magnetic field, hence both yield perturbed ground states that also have this property. The possibility of spontaneous breaking of spin symmetry is thus ruled out *a priori* within both approaches. In choosing to set them up in this way, we therefore make the physical assumption that spontaneous symmetry breaking need not be invoked to explain the 0.7-anomaly. This assumption is justified *a posteriori* by the agreement between our fRG results and our experiments for the magnetic-field dependence of the 0.7-anomaly (as discussed in detail in Sec. S-2 C).

The present section summarizes the central ingredients of the fRG approach in the one-particle irreducible version[32] used here. The details of our approach, using the Matsubara formalism, are very similar to those of Refs. 33,34,40 and 41; technical aspects going beyond the latter works will be presented in detail elsewhere[36]. The main purpose here is to explicitly formulate the approximations that we have employed for the translationally nonuniform system with on-site interactions defined by Eq. (A1) of the main text [or Eq. (S11)]. (For completeness, we remark that the fRG approach described below is also capable of dealing with the Kondo effect in a 1D-model of a quantum dot, described by a double-barrier potential. Corresponding results will be presented elsewhere, in a comparative study of the Kondo effect and the 0.7-anomaly.[1])

A. Observables

Our goal is to calculate the conductance g through the CCR and the average number $n_{j\sigma}$ of spin-σ electrons at site j, at zero temperature. Following Ref. 33,34, we proceed in three steps. (i) We integrate out the two semi-infinite, noninteracting leads to the left and right of the CCR, using a standard projection technique; this results in a bare Matsubara Green's function for the CCR, $(\mathcal{G}_0)^\sigma_{ji}(i\omega)$, with a matrix structure in real space, $j, i \in [-N', N']$ being site indices. (ii) We incorporate interactions in the CCR by using fRG to calculate the full Matsubara Green's function of the CCR, $\mathcal{G}^\sigma_{ji}(i\omega)$; this step will be described in more detail in the next subsection. (iii) We calculate g and $n_{j\sigma}$ at $T = 0$ using

$$g = \frac{1}{2}\sum_\sigma \mathcal{T}_\sigma(0) \, , \tag{S37}$$

$$\mathcal{T}_\sigma(\omega) = \left|2\pi\tau^2\rho_0^\sigma(\omega)\mathcal{G}^\sigma_{-N',N'}(\omega+i0^+)\right|^2 \, , \tag{S38}$$

$$\begin{aligned} n_{j\sigma} &= \langle \hat{n}_{j\sigma}\rangle_T = \int_{-\infty}^{\infty} d\omega\, f(\omega)\mathcal{A}_{j\sigma}(\omega) \\ &= T\sum_n \mathcal{G}(i\omega_n) + \frac{1}{2} \, , \end{aligned} \tag{S39}$$

$$\mathcal{A}_{j\sigma}(\omega) = -\frac{1}{\pi}\,\mathrm{Im}\mathcal{G}^\sigma_{jj}(\omega+i0^+) \, . \tag{S40}$$

Here $\mathcal{T}_\sigma(\omega)$ is the spin-dependent transmission probability for a spin-σ electron incident with energy ω relative to the chemical potential μ, and $\rho_0^\sigma(\omega)$ is the local density of states at the first site of a semi-infinite noninteracting tight-binding chain, representing a lead. For our fRG calculations we have chosen $\mu = 0$, implying half-filled leads.

B. fRG strategy and approximations

fRG may be viewed as RG-enhanced perturbation theory in the interaction. It is based on solving a hierarchy of coupled ordinary differential equations, the *flow equations*, for the system's n-particle vertex functions, γ_n^Λ. The flow parameter Λ controls the RG flow from an initial cutoff Λ_i, at which all vertex functions are known and simple, to a final cutoff Λ_f, at which the full theory is recovered. Solving the full hierarchy of flow equations, however, is impossible in practice and simplifying approximations are needed to render them tractable. When setting up our flow equations, we make two technical approximations, which are both exact to second order in the interaction U. We briefly summarize them here, and provide more details in the subsequent technical discussions.

(i) We truncate the fRG hierarchy by setting $\gamma^\Lambda_{n\geq 3} = 0$. This standard approximation[32] offers a systematic way of summing up parquet-type diagrams (i. e. diagrams that result from coupled RPA-equations)[32] for the two-particle vertex. However, due to the neglect of higher order terms, it fails if the interaction becomes too large (on a scale set by the local density of states at the chemical potential).

(ii) We apply the coupled-ladder approximation[40,41] to treat the frequency dependence of the vertex, and extend this scheme to also treat the real space structure of the vertex. The coupled-ladder approximation sets to zero all components of the vertex except those that are generated already to second order in the bare (onsite) interaction, but retains the latter components throughout the flow.

C. fRG Flow equations

We introduce Λ as an infrared cut-off in the bare Matsubara propagator,

$$\mathcal{G}_0^\Lambda(i\omega) = \Theta_T(|\omega|-\Lambda)\mathcal{G}_0(i\omega) \, , \ \Lambda_i = \infty, \ \Lambda_f = 0 \, , \tag{S41}$$

where Θ_T is a step function that is broadened on the scale of the temperature T (we discuss the limit $T = 0$ in Sec. S-6 E below). The fRG approach in the one-particle irreducible version then leads to the following set of equations. (For a derivation, see e. g. Refs. 32,37; very detailed discussions are given e. g. in Refs. 33,38, for a diagrammatic derivation see Ref. 39.) The flow of the self-energy $\Sigma^\Lambda = -\gamma_1^\Lambda$ is given by

$$\frac{d}{d\Lambda}\gamma_1^\Lambda(q_1',q_1) = T\sum_{q_2',q_2}\mathcal{S}^\Lambda_{q_2,q_2'}\gamma_2^\Lambda(q_2',q_1';q_2,q_1)\ , \tag{S42a}$$

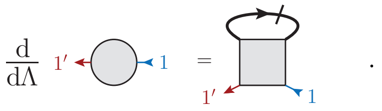

(S42b)

Here $\mathcal{S}^\Lambda$ is defined in terms of the scale-dependent full propagator $\mathcal{G}^\Lambda$,

$$\mathcal{S}^\Lambda = \mathcal{G}^\Lambda\partial_\Lambda\left[\mathcal{G}_0^\Lambda\right]^{-1}\mathcal{G}^\Lambda = \tag{S43a}$$

,

$$\mathcal{G}^\Lambda = \left[\left[\mathcal{G}_0^\Lambda\right]^{-1} - \Sigma^\Lambda\right]^{-1} = \tag{S43b}$$

,

and γ_2^Λ is the two-particle irreducible vertex.

The flow of the latter can be arranged into three contributions (or parquet channels),

$$\frac{d}{d\Lambda}\gamma_2^\Lambda = \frac{d}{d\Lambda}(\gamma_p^\Lambda + \gamma_x^\Lambda + \gamma_d^\Lambda)\ , \tag{S44}$$

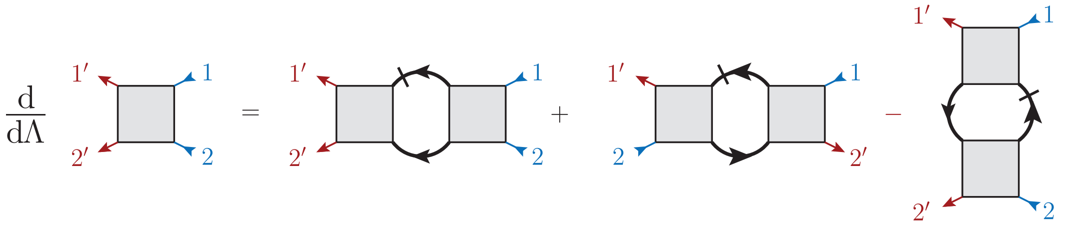

(S45)

called the particle-particle channel (P), and the exchange (X) and direct (D) contributions to the particle-hole channel, respectively, with the following explicit forms:

$$\frac{d}{d\Lambda}\gamma_p^\Lambda(q_1',q_2';q_1,q_2) = T\sum_{q_3',q_3,q_4',q_4}\gamma_2^\Lambda(q_1',q_2';q_3,q_4)\mathcal{S}^\Lambda_{q_3,q_3'}\mathcal{G}^\Lambda_{q_4,q_4'}\gamma_2^\Lambda(q_3',q_4';q_1,q_2), \tag{S46a}$$

$$\frac{d}{d\Lambda}\gamma_x^\Lambda(q_1',q_2';q_1,q_2) = T\sum_{q_3',q_3,q_4',q_4}\gamma_2^\Lambda(q_1',q_4';q_3,q_2)\left[\mathcal{S}^\Lambda_{q_3,q_3'}\mathcal{G}^\Lambda_{q_4,q_4'} + \mathcal{G}^\Lambda_{q_3,q_3'}\mathcal{S}^\Lambda_{q_4,q_4'}\right]\gamma_2^\Lambda(q_3',q_2';q_1,q_4)\ , \tag{S46b}$$

$$\frac{d}{d\Lambda}\gamma_d^\Lambda(q_1',q_2';q_1,q_2) = -T\sum_{q_3',q_3,q_4',q_4}\gamma_2^\Lambda(q_1',q_3';q_1,q_4)\left[\mathcal{S}^\Lambda_{q_4,q_4'}\mathcal{G}^\Lambda_{q_3,q_3'} + \mathcal{G}^\Lambda_{q_4,q_4'}\mathcal{S}^\Lambda_{q_3,q_3'}\right]\gamma_2^\Lambda(q_4',q_2';q_3,q_2)\ . \tag{S46c}$$

All higher order vertices $\gamma_{n\geq 3}$ have been set to zero. For the purpose of treating the inhomogeneous chain model of Eq. (S11), the quantum numbers q_i denote a composite index of site, spin and Matsubara-frequency, $q_1 = (j_1, \sigma_1, i\omega_n^1)$, etc.

D. fRG for non-uniform systems

A standard strategy for getting an initial impression of the system's behavior is to neglect the flow of the two-particle vertex completely. For the present model, the results so obtained[36] turn out to be similar to those obtained from SOPT – they capture the effects of interactions quite well qualitatively, but not quantitatively. To allow quantitative comparisons to experiment, we have therefore included the flow of the two-particle vertex for all fRG results shown in this work. We now describe how this was done.

Since the bare propagators are not site-diagonal, the number of independent variables needed to describe the vertex $\gamma_2^\Lambda(q_1',q_2';q_1,q_2)$ generated by Eq. (S46) is very large, $\mathcal{O}(N^4N_\mathrm{f}^3)$ (N_f is the number of Matsubara-frequencies used in the numerics). To deal with this complication we use the coupled-ladder approximation[40,41] for the frequency dependence of γ_2^Λ and treat its site-dependence in a similar manner. Given the structure of the flow equation (S46) for γ_2^Λ, it is natural to divide the flowing vertex into four parts[41]:

$$\gamma_2^\Lambda = v + \gamma_p^\Lambda + \gamma_x^\Lambda + \gamma_d^\Lambda\ , \qquad \gamma_p^{\Lambda_i} = \gamma_x^{\Lambda_i} = \gamma_d^{\Lambda_i} = 0\ . \tag{S47}$$

Here v is the bare vertex, and γ_2^p, γ_2^x and γ_2^d, whose flows by definition are given by Eqs. (S46a), (S46b) and (S46c), sum up the P-, X- and D-channels, respectively (see Sec.

S-6 C).

Now, since the bare vertex is site-diagonal, only $\mathcal{O}(N^2 N_\mathrm{f})$ of the $\mathcal{O}(N^4 N_\mathrm{f}^3)$ different components in each channel are generated already to order v^2 [i. e. if, at the beginning of the flow, γ_2^Λ is replaced by v on the r. h. s. of Eq. (S46)]. We exploit this fact by making the following simplifying approximation in the spatial structure of γ_2: in each channel *we set to zero all components except those that are generated already to order v^2, but retain the latter components throughout the flow.* The dropped components are all of order v^3 or higher, which justifies their neglect as long as U_j is not too large. Furthermore *we only keep the intrinsic frequency dependence of each channel* (i. e. the frequency-dependence generated to 2nd order). Each channel thus depends only on a single bosonic frequency, denoted by Π, X and Δ for the P-, X- and D-channels, respectively. The feed-back into the other channels is performed using only the static part of each channel, i. e. its value evaluated at zero frequency[41]. By exploiting various symmetry relations, the retained components of γ_2^Λ can be parametrized in terms of four frequency-dependent matrices, $P_{ij}^\Lambda(\Pi)$, $X_{ij}^\Lambda(\mathrm{X})$, $D_{ij}^{\uparrow\Lambda}(\Delta)$ and $D_{ij}^{\downarrow\Lambda}(\Delta)$, defined as follows (and shown together with the diagrams that generate them to lowest order):

$$P_{ji}^\Lambda(\Pi) := \gamma_p^\Lambda\left(j\sigma\,\Pi-\omega'_n, j\bar\sigma\,\omega'_n; i\sigma\,\Pi-\omega_n, i\bar\sigma\,\omega_n\right) = -\gamma_p^\Lambda\left(j\sigma\,\Pi-\omega'_n, j\bar\sigma\,\omega'_n; i\bar\sigma\,\Pi-\omega_n, i\sigma\,\omega_n\right), \tag{S48a}$$

$\overset{\mathcal{O}(v^2)}{\simeq}$

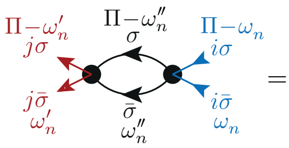
$\Pi-\omega'_n$
$j\sigma$
$\Pi-\omega''_n$
σ
$\Pi-\omega_n$
$i\sigma$
$j\bar\sigma$
ω'_n
$\bar\sigma$
ω''_n
$i\bar\sigma$
ω_n

$= -$

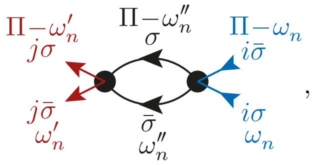
$\Pi-\omega'_n$
$j\sigma$
$\Pi-\omega''_n$
σ
$\Pi-\omega_n$
$i\bar\sigma$
$j\bar\sigma$
ω'_n
$\bar\sigma$
ω''_n
$i\sigma$
ω_n

,

$$X_{ji}^\Lambda(\mathrm{X}) := \gamma_x^\Lambda\left(j\sigma\,\mathrm{X}+\omega'_n, i\bar\sigma\,\omega_n; i\sigma\,\mathrm{X}+\omega_n, j\bar\sigma\,\omega'_n\right) = -\gamma_d^\Lambda\left(j\sigma\,\mathrm{X}+\omega'_n, i\bar\sigma\,\omega_n; j\bar\sigma\,\omega'_n, i\sigma\,\mathrm{X}+\omega_n\right), \tag{S48b}$$

$\overset{\mathcal{O}(v^2)}{\simeq}$

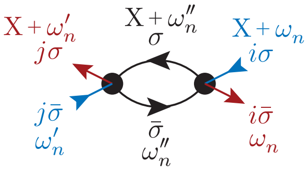
$\mathrm{X}+\omega'_n$
$j\sigma$
$\mathrm{X}+\omega''_n$
σ
$\mathrm{X}+\omega_n$
$i\sigma$
$j\bar\sigma$
ω'_n
$\bar\sigma$
ω''_n
$i\bar\sigma$
ω_n

$= -$

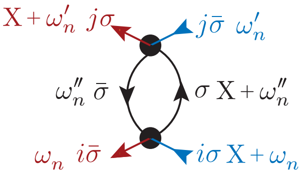
$\mathrm{X}+\omega'_n$ $j\sigma$
$j\bar\sigma$ ω'_n
ω''_n $\bar\sigma$
σ $\mathrm{X}+\omega''_n$
ω_n $i\bar\sigma$
$i\sigma\,\mathrm{X}+\omega_n$

,

$$D_{ji}^{\sigma\Lambda}(\Delta) := \gamma_d^\Lambda\left(j\sigma\,\Delta+\omega'_n, i\sigma\,\omega_n; j\sigma\,\omega'_n, i\sigma\,\Delta+\omega_n\right) = -\gamma_x^\Lambda\left(j\sigma\,\Delta+\omega'_n, i\sigma\,\omega_n; i\sigma\,\Delta+\omega_n, j\sigma\omega'_n\right), \tag{S48c}$$

$\overset{\mathcal{O}(v^2)}{\simeq}$

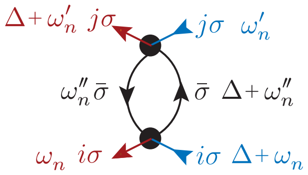
$\Delta+\omega'_n$ $j\sigma$
$j\sigma$ ω'_n
$\omega''_n\bar\sigma$
$\bar\sigma$ $\Delta+\omega''_n$
ω_n $i\sigma$
$i\sigma$ $\Delta+\omega_n$

$= -$

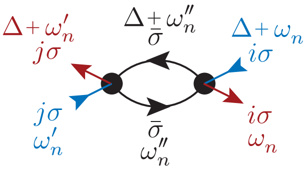
$\Delta+\omega'_n$
$j\sigma$
$\Delta+\omega''_n$
$\bar\sigma$
$\Delta+\omega_n$
$i\sigma$
$j\sigma$
ω'_n
$\bar\sigma$
ω''_n
$i\sigma$
ω_n

.

Note that these diagrams do not depend on ω_n and ω'_n; this is the reason why the coupled-ladder approximation allows each channel to be parametrized by just a single frequency. A detailed analysis of the flow of P_{ij}^Λ, X_{ij}^Λ and $D_{ij}^{\sigma\Lambda}$, to be published elsewhere[36], shows that the exchange channel X_{ij}^Λ, which grows significantly during the flow, is the dominant one. This lends *a posteriori* support to an assertion made in numerous works[4,7–9,12,14,20–22,30,31,42], namely that exchange interactions in the low-density inner region of the QPC play a dominant role for the 0.7-anomaly.

The parameter controlling the convergence of the fRG equations is $U \cdot \max_{\widetilde{V}_\mathrm{c},j}[\mathcal{A}_j(0)]$; if it is too large, these equations do not converge. For a QPC, the maximum value of the bare LDOS $\mathcal{A}_j^0(0)$ scales as $1/\sqrt{\tau\Omega_x}$ (see Sec. S-4 C).

E. Zero-temperature limit

The fRG flow equations discussed above apply to an arbitrary temperature T. However, the conductance at $T \neq 0$ depends on the retarded correlator $\mathcal{G}^R(\omega) = \mathcal{G}(i\omega_n \to \omega + i0^+)$ as well as the retarded parts of the vertex channels (e.g. $P(i\Pi_n \to \Pi + i0^+)$), which have to be obtained by analytic continuation from the imaginary to the real frequency axis. In numerical practice, this analytical continuation turned out to be unfeasible for the present problem. Therefore, we have here studied only the $T = 0$ limit, in which the Matsubara frequencies form a continuum and the conductance [Eq. (S37)] is expressed in terms of the zero-energy transmission $\mathcal{T}_\sigma(0)$. For numerical computations, we represented the continuum of Matsubara frequencies by a discrete set, and used its smallest positive member to evaluate the Matsubara Green's function $\mathcal{G}^\sigma_{-N',N'}(i0^+)$ needed for $\mathcal{T}_\sigma(0)$ [Eq. (S38)].

In the limit $T \to 0$, the cut-off function Θ_T in Eq. (S41) becomes a sharp step function, with $\Theta_0(0) = \frac{1}{2}$ and $\partial_\omega \Theta_0(\omega) = \delta(\omega)$. Since a combination of δ- and Θ-functions occurs in the fRG flow equations, the limit $T \to 0$ has to be taken with care, with the result[40]:

$$\mathcal{S}^\Lambda(i\omega) \overset{T\equiv 0}{=} \delta(|\omega| - \Lambda)\widetilde{\mathcal{G}}^\Lambda(i\omega), \tag{S49a}$$

$$\widetilde{\mathcal{G}}^\Lambda(i\omega) = \left[[\mathcal{G}_0(i\omega)]^{-1} - \Sigma^\Lambda(i\omega) \right]^{-1}, \tag{S49b}$$

$$\mathcal{S}^\Lambda_{i,j}(i\omega)\mathcal{G}^\Lambda_{k,l}(i\omega') \overset{T\equiv 0}{=} \delta(|\omega| - \Lambda)\widetilde{\mathcal{G}}^\Lambda_{i,j}(i\omega) \times\Theta(|\omega'| - \Lambda)\widetilde{\mathcal{G}}^\Lambda_{k,l}(i\omega'). \tag{S49c}$$

F. Static fRG

Most of our exploratory work on the zero-temperature properties of the 0.7-anomaly was done using "static" fRG (here denoted by fRG^0). It entails a further approximation relative to the "dynamic" fRG approach described above (here denoted by fRG$^\omega$), in that fRG^0 neglects the frequency dependence of the self-energy and all vertices. This is done by setting all three bosonic frequencies Π, X and Δ to zero. As a result the self-energy is frequency-independent, too. fRG^0 leads to reliable results only for the zero-frequency Green's function at zero temperature. If knowing the latter suffices (such as when studying the magnetic field-dependence at $\widetilde{T} = 0$), fRG^0 is a very flexible and efficient tool, computationally cheaper than our full coupled-ladder scheme fRG$^\omega$ by a factor of 10^3. Moreover, for the model studied here its results turn out to be qualitatively very similar to those of fRG$^\omega$. This is illustrated in Fig. S15, from which we note the following salient features.

The main difference in the conductance curves calculated by the two methods is an overall interaction-induced, U-dependent shift of the position of the fRG^0 conductance step w. r. t. to that of fRG$^\omega$, towards somewhat smaller values of $\widetilde{V}_c$ (compare Figs. S15**a**,**b**); however the *shapes* of the corresponding curves (modulo the shift) are essentially identical (Fig. S15**c**). The shift itself merely amounts to a small change in overall chemical potential and can be regarded as an insignificant detail, in particular in the context of the 0.7-anomaly, where both in theoretical and experimental studies, the focus is on the shape of the step, not its position.

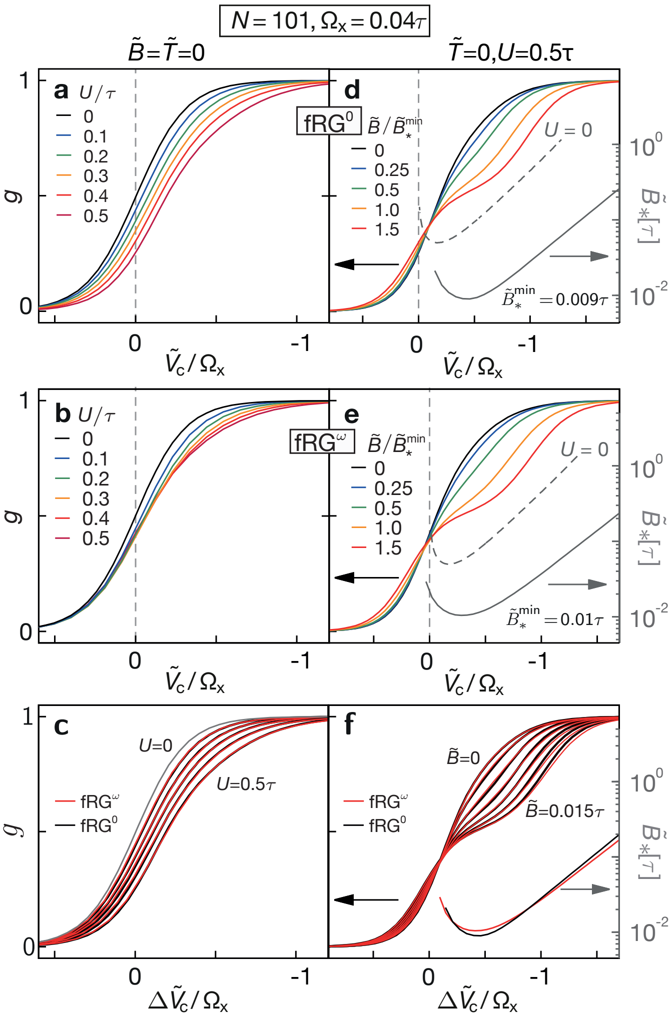

Figure S15: Comparison of results from static fRG (fRG^0, top panels) and dynamic fRG (fRG$^\omega$, middle panels, reproduced from Figs. A1k and A2a, respectively). The bottom panels show that after compensating for a U-dependent shift (here applied to the fRG$^\omega$ curves to get best overlap with the fRG^0 curves) both sets of curves have almost identical shapes. Left panels: The interaction dependence of the conductance $g(\widetilde{V}_c)$ at $\widetilde{B} = \widetilde{T} = 0$. Right panels: The magnetic-field dependence of the $\widetilde{T} = 0$ conductance $g(\widetilde{V}_c)$ at fixed $U = 0.5\tau$.

Closer inspection reveals that the magnetic field dependence (at fixed U) of the fRG^0 conductance curves is slightly stronger for small fields and slightly weaker for large fields, compared to that of fRG$^\omega$ (see Figs. S15**d**-**f**). This implies small quantitative differences in the low-energy scale $\widetilde{B}_*$ and the effective g-factor g_{ss}.

All in all, for the purposes of exploring the field-dependence of the 0.7-anomaly at fixed U, the differences in results between fRG$^\omega$ and fRG^0 are evidently very small. Hence we have opted to use the computationally much cheaper fRG^0 for the results presented in Secs. S-3 and S-5.

S-7. SECOND-ORDER PERTURBATION THEORY

The main limitation of our calculations using static fRG is their restriction to $\omega = 0$ and hence to zero temperature and zero source-drain voltage. As a first step toward exploring the properties of our model at $\widetilde{T} \neq 0$ and $\widetilde{V}_{\rm sd} \neq 0$, we have calculated the conductance of a QPC using second-order perturbation theory (SOPT), applied to model II (see Supplementary Sec. S-4 D). Sec. S-7 A presents the diagrams used for this purpose, and Sec. S-7 B discusses how we treat non-equilibrium transport using Keldysh-SOPT. Sec. S-7 C elaborates the main article's discussion of the SOPT results for the $\widetilde{B}$-, $\widetilde{T}$- and $\widetilde{V}_{\rm sd}$-dependence of the conductance, which are in fairly good qualitative agreement with experiment. Sec. S-7 D concludes with some comments regarding an SOPT artefact that arises with increasing U.

A. Equilibrium SOPT

We follow the strategy of Oguri[43], who has carried out a similar calculation for a particle-hole symmetric version of our model (with $N \leq 4$) at zero field. It is straightforward to generalize his equations to the case of present interest, with broken particle-hole symmetry and nonzero field. The conductance is calculated from

$$g = \frac{1}{2}\sum_{\sigma}\int_{-\infty}^{\infty} d\omega \left[-\frac{\partial f(\omega)}{\partial \omega}\right] \mathcal{T}_\sigma(\omega) \,. \tag{S50}$$

where $\mathcal{T}_\sigma(\omega)$ is calculated using Oguri's[43] equations (2.36-38) and (4.10). They can be graphically depicted as

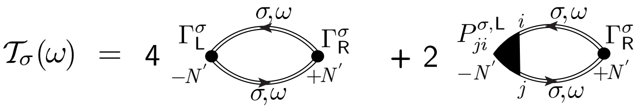

$\mathcal{T}_\sigma(\omega)$ = 4
$\Gamma^\sigma_{\mathsf{L}}$
σ,ω
$\Gamma^\sigma_{\mathsf{R}}$
$-N'$
$+N'$
σ,ω
+ 2
$P^{\sigma,\mathsf{L}}_{ji}$
i
σ,ω
$\Gamma^\sigma_{\mathsf{R}}$
$-N'$
$+N'$
j
σ,ω

(S51)

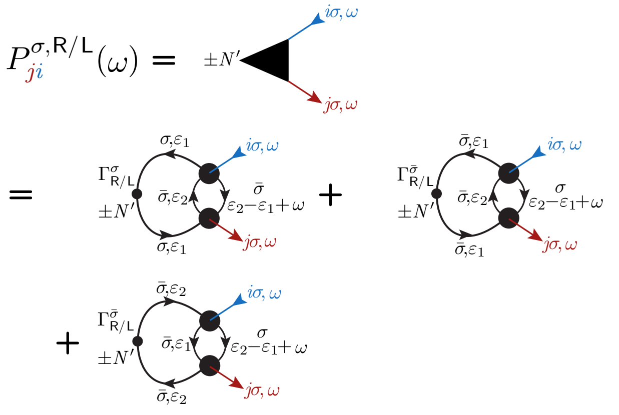

$P^{\sigma,\mathsf{R/L}}_{ji}(\omega)$ =
$\pm N'$
$i\sigma,\omega$
$j\sigma,\omega$
=
$\Gamma^{\sigma}_{\mathsf{R/L}}$
$\pm N'$
σ,ε_1
$\bar\sigma,\varepsilon_2$
σ,ε_1
$i\sigma,\omega$
$\bar\sigma$
$\varepsilon_2-\varepsilon_1+\omega$
$j\sigma,\omega$
+
$\Gamma^{\bar\sigma}_{\mathsf{R/L}}$
$\pm N'$
$\bar\sigma,\varepsilon_1$
$\bar\sigma,\varepsilon_2$
$\bar\sigma,\varepsilon_1$
$i\sigma,\omega$
σ
$\varepsilon_2-\varepsilon_1+\omega$
$j\sigma,\omega$
+
$\Gamma^{\bar\sigma}_{\mathsf{R/L}}$
$\pm N'$
$\bar\sigma,\varepsilon_2$
$\bar\sigma,\varepsilon_1$
$\bar\sigma,\varepsilon_2$
$i\sigma,\omega$
σ
$\varepsilon_2-\varepsilon_1+\omega$
$j\sigma,\omega$

(S52)

where large black dots depict the bare interaction vertex, small black dots the coupling $\Gamma^{\sigma}_{R/L}(\epsilon)$ to the reservoirs, and the double lines represent the retarded interacting Green's function $\mathcal{G}^R = [(\mathcal{G}^{0\,R})^{-1} - \Sigma^R]^{-1}$. Its self-energy Σ^R is calculated to second order using the following diagrams:

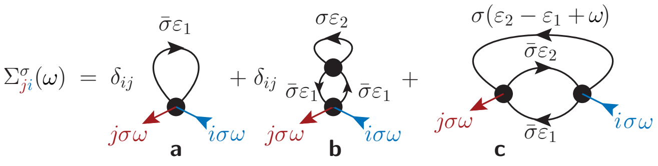

$\Sigma^{\sigma}_{ji}(\omega)$ = δ_{ij}
$\bar\sigma\varepsilon_1$
$j\sigma\omega$
$i\sigma\omega$
a
+ δ_{ij}
$\sigma\varepsilon_2$
$\bar\sigma\varepsilon_1$
$\bar\sigma\varepsilon_1$
$j\sigma\omega$
$i\sigma\omega$
b
+
$\sigma(\varepsilon_2-\varepsilon_1+\omega)$
$\bar\sigma\varepsilon_2$
$\bar\sigma\varepsilon_1$
$j\sigma\omega$
$i\sigma\omega$
c

(S53)

Diagram **c** corresponds to Oguri's[43] Fig. 6, which represent the Fock contribution. Our treatment differs from Oguri's only regarding the Hartree diagrams **a** and **b**. Whereas he incorporates their effects in an implicit manner by exploiting particle-hole symmetry, this symmetry is not present in our problem, hence we include the Hartree diagrams explicitly in the self-energy.

The diagrams in Eqs. (S52) and (S53) involve Matsubara frequencies; they have to be analytically continued to real frequencies before being used in Eq. (S51) for $\mathcal{T}_\sigma(\omega)$, as discussed in detail by Oguri. The resulting formulas, obtained by generalizing Oguri's[43] equations [his (4.2), (4.3) for the Fock diagram, and (4.10) for the current vertex] to the spin-dependent case of non-zero field, will be presented elsewhere[36].

In the main article, the transmission probability is written as

$$\mathcal{T}_\sigma(\omega) = \mathcal{T}^{\rm el}_\sigma(\omega) + \mathcal{T}^{\rm in}_\sigma(\omega), \tag{S54}$$

where $\mathcal{T}^{\rm el}_\sigma(\omega)$ and $\mathcal{T}^{\rm in}_\sigma(\omega)$, given by the first and second terms of Eq. (S51), describe the elastic and inelastic contributions to the transmission probability, respectively. They are related by a generalized Ward identity that is respected within the approximation scheme described above (Eq. (3.120) in Ref. 43):

$$-\,{\rm Im}\Sigma^{\sigma,R}_{ji}(\omega) = \sum_{\alpha=L/R} P^{\sigma,\alpha}_{ji}(\omega) \,. \tag{S55}$$

This relation links the current vertex to the inelastic decay rate, governed by the imaginary part of the self-energy. An increase in the contribution of the current vertex, therefore, goes hand in hand with an increase in inelastic scattering.

SOPT calculations turn out to be computationally significantly more costly than fRG calculations. Therefore, all our SOPT calculations were done using model II, which has some computational advantages over model I, as explained in Supplementary Sec. S-4 D.

B. Nonequilibrium SOPT

In order to calculate the differential conductance

$$g_{\rm nl} = \frac{dI}{d\widetilde{V}_{\rm sd}} \tag{S56}$$

at finite bias voltage ($\widetilde{V}_{\mathrm{sd}} \neq 0$) we use the Meir-Wingren formula for the current through a region of interacting electrons[44]:

$$I = \frac{ie}{2h}\int d\varepsilon \Big(\mathrm{Tr}\{[f_L\Gamma^L - f_R\Gamma^R](\mathcal{G}^R - \mathcal{G}^A)\} + \mathrm{Tr}\{[\Gamma^L - \Gamma^R]\mathcal{G}^<\}\Big), \tag{S57}$$

with $\mathcal{G}^< = \frac{1}{2}\left(\mathcal{G}^K - \mathcal{G}^R + \mathcal{G}^A\right)$. The finite bias $\widetilde{V}_{\mathrm{sd}}$ enters via the occupation functions of the left and right lead:

$$f_{R/L}(\omega) = f(\omega \mp \widetilde{V}_{\mathrm{sd}}/2). \tag{S58}$$

The retarded, advanced and Keldysh Green's functions $\mathcal{G}^{R/A/K}$ are given by Dyson equations:

$$\begin{aligned}\mathcal{G}^{R/A} &= \frac{1}{(G^{R/A})^{-1} - \Sigma^{R/A}}.\\ \mathcal{G}^K &= \mathcal{G}^R[(G^R)^{-1}G^K(G^A)^{-1} + \Sigma^K]\mathcal{G}^A,\end{aligned} \tag{S59}$$

The non-equilibrium retarded, advanced and Keldysh self-energies occurring herein, $\Sigma^{R/A/K}$, are calculated to second order in the interaction, using standard Keldysh techniques. The corresponding diagrams are again given by Eq. (S53), but now feature an additional Keldysh index.

C. $\widetilde{B}$-, $\widetilde{T}$- , and $\widetilde{V}_{\mathrm{sd}}$-dependence of $g(\widetilde{V}_{\mathrm{c}})$

In this section, we give a detailed discussion of the SOPT results presented in the main text for the $\widetilde{B}$-, $\widetilde{T}$- and $\widetilde{V}_{\mathrm{sd}}$-dependence of the conductance $g(\widetilde{V}_{\mathrm{c}})$. In particular, we analyse their similarities and differences w. r. t. our fRG results and experimental measurements.

Dependence on magnetic field at zero temperature: To gauge the reliability of SOPT, we begin by comparing its results for the magnetic field dependence of the conductance (Fig. A2**c**) to those obtained from fRG (Fig. A2**a**) and from experimental measurements (Fig. A2**e**). Though some details differ, the qualitative agreement is very good. It includes, in particular, the following two important features: (i) The conductance $g(\widetilde{V}_{\mathrm{c}})$ is strongly suppressed with increasing $\widetilde{B}$ for $\widetilde{V}_{\mathrm{c}} < 0$, leading to the evolution of a kink around 0.5 (thick red line in Fig. A2**c**). (ii) $\ln(\widetilde{B}_*)$ increases nearly linearly with decreasing $\widetilde{V}_{\mathrm{c}}$ in the regime where $g \to 1$ (thin grey line in Fig. A2**c**); in fact, even the slope of the linear increase is nearly the same as that found by fRG (grey line in Fig. A2**a**). This remarkable agreement between SOPT and fRG for the $\widetilde{V}_{\mathrm{c}}$-dependence of $\widetilde{B}_*$ implies that the latter is determined mainly by geometry (corroborating a similar conclusion from Sec. S-5), i. e. interactions, which are underestimated in SOPT, influence the $\widetilde{V}_{\mathrm{c}}$-dependence only weakly.

As an aside, we note that both of the above-mentioned features (i) and (ii) survive[45] (data not shown) even if SOPT is simplified by neglecting the Fock contribution to the self-energy [diagram **c** of Eq. (S53)], retaining only the first- and second-order Hartree terms [diagrams **a** and **b** of Eq. (S53)]. Thus, the $\widetilde{B}$-dependence is dominated by Hartree terms (describing shifts in the barrier heights for spin-up vs. spin-down electrons), rather than Fock terms (describing inelastic scattering, which is relevant only at finite temperatures and finite bias voltage). This conclusion is consistent with the fact that the approach of Lunde *et al.*, Ref. 6, which properly incorporated the (model) system's geometry-dependence by using WKB wave functions, is nevertheless unable to reproduce the energy scale $\widetilde{B}_*$ from the magnetic field dependence as long as only Fock-like diagrams are considered[46].

Next, we mention an important instance in which SOPT fails to agree with experimental and fRG results for the conductance (compare Fig. A2**c** to Fig. A2**e** and Fig. A2**a**): SOPT does not yield the 0.7-shoulder in the conductance at $\widetilde{T} = \widetilde{B} = 0$. (A shoulder does develop for larger U ($\gtrsim 0.5\tau$), for which, however, SOPT can no longer be trusted.)

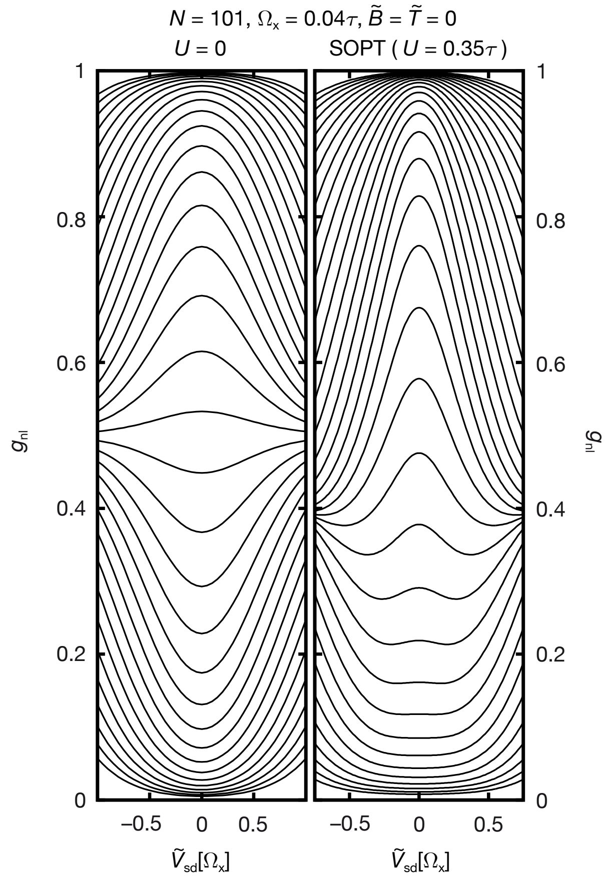

Figure S16: Differential conductance for model II at $\widetilde{B} = \widetilde{T} = 0$, plotted as a function of bias voltage for several $\widetilde{V}_{\mathrm{c}}$-values, calculated **a** without and **b** with interactions, the latter treated using second order perturbation theory (SOPT) (see Sec. S-7 B).

To summarize: SOPT correctly captures several important features of the field dependence of the conductance at zero temperature, but not all details. The same turns out to be true for the temperature dependence at zero field, as we discuss next:

Dependence on temperature at zero magnetic field: Fig. A2**d** presents SOPT results for the temperature-dependence of the conductance at zero field. Comparing these to the corresponding experimental results of Fig. A2**f**, we note that SOPT correctly reproduces the main effect of increasing temperature, namely to reduce the conductance. However, SOPT does not fully succeed in reproducing the detailed shape of the experimental pinch-off curves: the SOPT curves lack the tendency of the experimental curves to show a well-defined shoulder that is amplified by increasing temperature.

Dependence on bias voltage: Fig. S16**a** shows the bare ($U = 0$) differential conductance $g^0_{\rm nl}$ as a function of bias voltage $\widetilde{V}_{\rm sd}$ for several $\widetilde{V}_{\rm c}$-values ranging from the open channel ($g \simeq 1$) to the pinched-off regime ($g \simeq 0$). The bare conductance can easily be calculated from the Landauer-Büttiker formula (S25), using Büttiker's formula (S30) for the transmission. The resulting $g^0_{\rm nl}(\widetilde{V}_{\rm sd})$ exhibits a zero bias peak (ZBP) for linear conductance $g > 0.5$ ($\widetilde{V}_{\rm c} < 0$), and a zero bias minimum in the tunneling regime, where $\widetilde{V}_{\rm c} > 0$ and $g < 0.5$.

Turning on interaction (see Fig. A3**i**, as well as Fig. S16**b**) causes the following effects on $g_{\rm nl}$: First, a ZBP forms even when the linear conductance is $g < 0.5$, and second, the width of the ZBP is reduced across the whole $\widetilde{V}_{\rm c}$-range. These two interaction-induced characteristics can be understood in terms of two main mechanisms: (i) Applying finite bias generates a net charge flow into the barrier region (since there the LDOS is ω-asymmetric around $\omega = 0$), thereby enhancing the effective barrier height for electrons entering the CCR. For sufficiently large interaction this leads to a reduction of conductance (Hartree effect). (ii) Turning on $\widetilde{V}_{\rm sd}$ opens phase space for inelastic scattering. Consequently the combination of a large LDOS in the vicinity of the classical turning points (where $\omega^{\rm min}_j \simeq 0$), interactions, and $\widetilde{V}_{\rm sd} > 0$, leads to a high probability for backscattering, hence a reduction of conductance. We note that both mechanisms (i) and (ii) also apply when the temperature is increased; in this sense, the temperature- and bias-dependencies of the 0.7-anomaly are manifestations of the similar physical processes.

We take the SOPT results shown in Fig. A2**d** and Figs. A3**b**,**d-f** as encouraging indications that our model has the potential to properly describe properties of the 0.7-anomaly at finite temperature and bias. To summarize: the anomalous conductance decrease with increasing $\widetilde{T}$ or $\widetilde{V}_{\rm sd}$ in the sub-open regime originates from the enhancement, by the van Hove ridge apex near μ, of the $\widetilde{T}$- or $\widetilde{V}_{\rm sd}$-induced increase of (i) the net charge and (ii) the amount of inelastic scattering in the CCR.

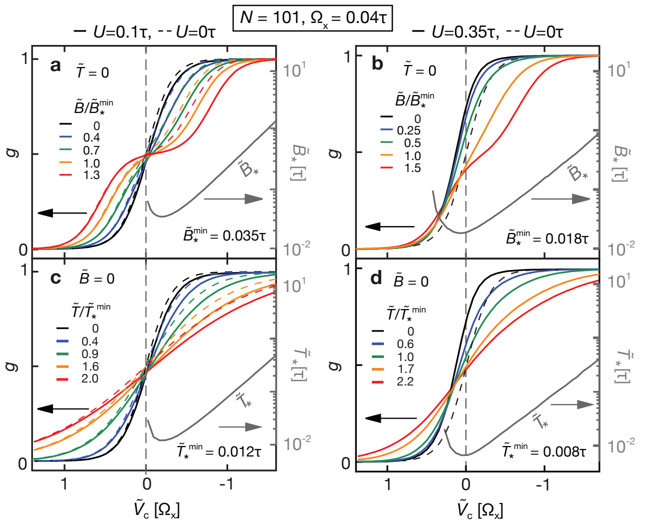

Figure S17: SOPT results (solid lines) for the conductance $g(\widetilde{V}_{\rm c})$ as function of $\widetilde{V}_{\rm c}$, illustrating the qualitative changes incurred when interactions are increased from being weak (left panels) to rather strong (right panels, reproduced from Figs. A2**c**, **d**). Panels (a,b) show the $\widetilde{B}$-dependence of the conductance at $\widetilde{T} = 0$, panels (c,d) show its $\widetilde{T}$-dependence at $\widetilde{B} = 0$. Dashed lines show corresponding curves for the bare $U = 0$ conductance, $g^0(\widetilde{V}_{\rm c})$.

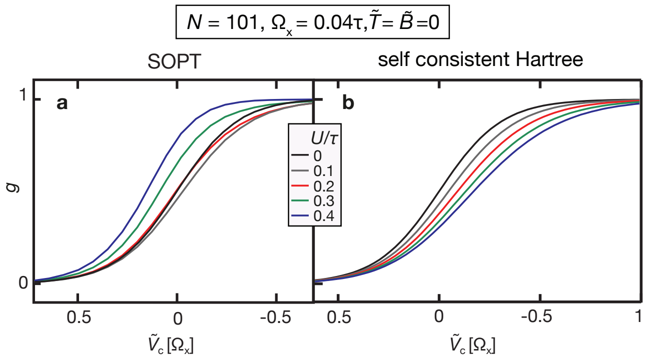

Figure S18: The zero-temperature linear conductance $g(\widetilde{V}_{\rm c})$ as function of $\widetilde{V}_{\rm c}$, for several values of U, calculated **a**, using pure SOPT, and **b**, using a self-consistent Hartree approach (without Fock contributions). The non-monotonic behavior of $g(\widetilde{V}_{\rm c})$ as function of increasing U seen in **a** is an SOPT artefact, caused by the neglect of terms beyond 2nd order; this artefact is avoided by the self-consistent Hartree approach, as seen in **b**.

D. SOPT artefact arising for increasing U

We conclude with some comments on the choice of interaction strength used for our SOPT calculations. Fig. S17 compares the SOPT results for the $\widetilde{B}$- and $\widetilde{T}$-dependence of $g(\widetilde{V}_{\rm c})$ calculated at $U = 0$ (left panels, dashed lines), $U = 0.1\tau$ (left panels, solid lines) and $U = 0.35\tau$ (right panels, solid lines). The left panels show that upon turning on a weak interaction (solid lines), the conductance g at fixed values of $\widetilde{V}_{\mathrm{c}}$, $\widetilde{B}$ and $\widetilde{T}$ is shifted slightly downward due to the increase of the Hartree barrier, leading to a slight skewing of the shape of the conductance step relative to the corresponding non-interacting value $g^0(\widetilde{V}_{\mathrm{c}})$ (dashed lines). However, significantly larger values of U are needed (right panels) to yield the strong type of skewing characteristic for measured conductance curves that exhibit the 0.7-anomaly.

Note that due to this large choice of U in the right panels, the SOPT conductance curve $g(\widetilde{V}_{\mathrm{c}})$ at $\widetilde{B} = \widetilde{T} = 0$ (solid black) has been shifted upwards to actually lie *above* its non-interacting value (dashed black). This non-monotonic behavior of $g(\widetilde{V}_{\mathrm{c}})$ for increasing U (the shift being initially downwards, then upwards, illustrated clearly in Fig. S18**a**) is an artefact of SOPT's neglect of terms beyond 2nd order: the signs ($+$ or $-$) of Hartree contributions are known to alternate with the order of expansion, hence truncating the latter beyond 2nd order generates non-monotonic behavior for the shift with increasing U once the 2nd-order term becomes larger than the 1st-order term. (fRG avoids this problem by summing up, in effect, a series of diagrams to all orders, resulting in a monotonic dependence of $g(\widetilde{V}_{\mathrm{c}})$ on U, see Fig. A1**k**.)

We emphasize that this SOPT artefact is problematic only if one is interested in following the evolution of physical properties with increasing U (examples of such evolution, calculated by fRG, are shown in Figs. A1**e**,**j**,**k**). However, for the purpose of studying physical properties *at fixed* U, SOPT does quite well: it succeeds in qualitatively illustrating the generic, experimentally observed trends of how interactions affect the $\widetilde{B}$-, $\widetilde{T}$-, and $\widetilde{V}_{\mathrm{sd}}$-dependence of the conductance even if the (fixed) value of U is rather large, because the physical origin of these trends is robust. A detailed discussion of this point will be published elsewhere.

Finally, we note that the above-mentioned artefact can be avoided by adopting an approach similar in spirit to SOPT, but using a self-consistently-determined Hartree potential (thus treating Hartree and Fock terms on unequal footing): For $\widetilde{T} = \widetilde{V}_{\mathrm{sd}} = 0$, calculate the self-energy from just the first-order Hartree diagram Eq. (S53)**a** to obtain a Hartree-shifted local potential $E_{j\sigma} + U_j n_{j\sigma}$, determine the local charge $n_{j\sigma}$ self-consistently, and calculate the QPC transmission using Hartree-dressed Green's functions (see Fig. S18**b**).

For nonzero $\widetilde{T}$ or $\widetilde{V}_{\mathrm{sd}}$, use Hartree-dressed (instead of bare) Green's functions for all thin lines in the SOPT Eqs. (S51) to Eq. (S53), but include only the Fock diagram in the latter, to avoid double-counting Hartree contributions. The Ward identity [Eq. (S55)] relating the current vertex to the self-energy would remain intact in this approach. Pursuing it in detail is left as a topic for future study.

---

[1] Heyder, J., Bauer, F., E. Schubert, D. Borowsky, D. Taubert, D. Schuh, W. Wegscheider, J. von Delft & S. Ludwig. Comparative study of the Kondo effect and the 0.7-anomaly. *To be published.*

[2] D. Borowski. Transportmessungen zur Untersuchung der 0.7-Struktur in Quantenpunktkontakten. *Diploma Thesis*, Ludwig-Maximilians-Universität München (2011).

[3] Patel, N. K., Nicholls, J. T., Martín-Moreno, L., Pepper, M., Frost, J. E. F., Ritchie, D. A. & Jones, G. A. C. Evolution of half plateaus as a function of electric field in a ballistic quasi-one-dimensional constriction. *Phys. Rev. B*, **44**, 13549-13555 (1991).

[4] Reilly, D. J., Facer, G. R., Dzurak, A. S., Kane, B. E., & Clark, R. G. Many-body spin-related phenomena in ultra low-disorder quantum wires. *Phys. Rev. B* **63**, 121311(R) (2001).

[5] Büttiker, M. Quantized transmission of a saddle-point constriction. *Phys. Rev. B* **41**, 7906(R) (1990).

[6] Lunde, A. M., De Martino, A., Schulz, A., Egger, R., and Flensberg, K., Electron-electron interaction effects in quantum point contacts. *New J. Phys.* **11**, 023031 (2009).

[7] Thomas, K. J., Nicholls, J. T., Simmons, M. Y., Pepper, M., Mace, D. R. Possible Spin Polarization in a One-Dimensional Electron Gas. *Phys. Rev. Lett.* **77**, 135-138 (1996).

[8] Thomas, K. J., Nicholls, J. T., Appleyard, N. J., Simmons, M. Y., Pepper, M., Mace, D. R., Tribe, W. R., & Ritchie, D. A. Interaction effects in a one-dimensional constriction. *Phys. Rev. B* **58**, 4846-4852 (1998).

[9] Koop, E., Lerescu, A., Liu, J., van Wees, B., Reuter, D., Wieck A.D. & van der Wal, C. The Influence of Device Geometry on Many-Body Effects in Quantum Point Contacts: Signatures of the 0.7 Anomaly, Exchange and Kondo *J. Supercond. Nov. Magn.* **20**, 433-441 (2007).

[10] Burke A. M., Klochan O., Farrer I., Ritchie D. A., Hamilton A. R. & Micolich A. P. Extreme Sensitivity of the Spin-Splitting and 0.7 Anomaly to Confining Potential in One-Dimensional Nanoelectronic Devices. *Nano Letters*, Article ASAP, DOI: 10.1021/nl301566d (2012).

[11] Patel, N. K., Nicholls, J. T., Martn-Moreno, L., Pepper, M., Frost, J. E. F., Ritchie, D. A. & Jones, G. A. C. Properties of a ballistic quasi-one-dimensional constriction in a parallel high magnetic field. *Phys. Rev. B* **44**, 10973-10975 (1991).

[12] Reilly, D. J., Buehler, T. M., O'Brien, J. L., Hamilton, A. R., Dzurak, A. S., Clark, R. G., Kane, B. E., Pfeiffer, L. N. & West, K. W. Density-Dependent Spin Polarization in Ultra-Low-Disorder Quantum Wires. *Phys. Rev. Lett.* **89**, 246801 (2002).

[13] DiCarlo, L., Zhang, Y., McClure, D. T., Reilly, D. J., Marcus, C. M., Pfeiffer, L. N. & West, K. W. Shot-Noise Signatures of 0.7 Structure and Spin in a Quantum Point Contact. *Phys. Rev. Lett.*, **97**, 036810 (2006).

[14] Smith, L. W., Hamilton, A. R., Thomas, K. J., Pepper, M., Farrer, I., Griffths, J. P., Jones, G. A. C. &Ritchie, D. A. Compressibility measurements of quasi-one-dimensional

quantum wires Phys. Rev. Lett. **107**, 126801 (2011).

[15] Blanter, Ya. M. & Büttiker. Shot noise in mesoscopic conductors. *Physics Reports,* **336** 1-166, (2000).

[16] Lüscher, S., Moore, L. S., Rejec, T., Meir, Y., Shtrikman, H. & Goldhaber-Gordon, D. Charge Rearrangement and Screening in a Quantum Point Contact. *Phys. Rev. Lett.* **98**, 196805 (2007).

[17] Meir, Y., Hirose, K. & Wingreen, N. S. Kondo Model for the 0.7 Anomaly in Transport through a Quantum Point Contact. *Phys. Rev. Lett.* **89**, 196802 (2002).

[18] Golub, A., Aono, T. & Meir, Y. Suppression of Shot Noise in Quantum Point Contacts in the "0.7 Regime". *Phys. Rev. Lett.* **97**, 186801 (2006).

[19] Rejec, T. & Meir, Y. Magnetic impurity formation in quantum point contacts. *Nature* **442**, 900-903 (2006).

[20] Wang, C.-K. & Berggren, K.-F. Local spin polarization in ballistic quantum point contacts. *Phys. Rev. B* **57**, 4552-4556 (1998).

[21] Tokura, Y. & Khaetski, A. Towards a microscopic theory of the 0.7 anomaly. *Physica E: Low-dimensional Systems and Nanostructures*, **12**, 711 (2002).

[22] Aryanpour, K. & Han, J. E. Ferromagnetic Spin Coupling as the Origin of 0.7 Anomaly in Quantum Point Contacts. *Phys. Rev. Lett.*, **102**, 056805 (2009).

[23] C. Sloggett, C., Milstein, A. I., & Sushkov, O. P. Correlated electron current and temperature dependence of the conductance of a quantum point contact. *Eur. Phys. J. B* **61**, 427432 (2008).

[24] Theoretical work on nonparabolic barriers is being pursued in the group of H. Baranger, private communication (2012).

[25] Mahan, D. Many-Particle Physics. Kluwer Academic, New York (2000).

[26] Cronenwett, S. M., Lynch, H. J., Goldhaber-Gordon, D., Kouwenhoven, L. P., Marcus, C. M. Low-Temperature Fate of the 0.7 Structure in a Point Contact: A Kondo-like Correlated State in an Open System. *Phys. Rev. Lett.* **88**, 226805 (2002).

[27] Connor, J. N. L. On the semiclassical approximation for double well potentials. *Mol. Phys.*, **15**, 37 (1968).

[28] Miller, W. H. Semiclassical Treatment of Multiple Turning-Point Problems – Phase Shifts and Eigenvalues. *J. Chem. Phys.*, *48*, 1651 (1968).

[29] Haldane, F. D. M. Scaling Theory of the Asymmetric Anderson Model. *Phys. Rev. Lett.* **40**, 416-419 (1978).

[30] Thomas, K. J., Nicholls, J. T., Pepper, M., Tribe, W. R., Simmons, M. Y. & Ritchie, D. A. Spin properties of low-density one-dimensional wires. *Phys. Rev. B* **61**, R13365-13368 (2000).

[31] Reilly, D. J. Phenomenological model for the 0.7 conductance feature in quantum wires. *Phys. Rev. B*, **72**, 033309 (2005).

[32] Metzner, W., Salmhofer, M., Honerkamp, C., Meden, V. & Schönhammer, K. Functional renormalization group approach to correlated fermion systems. *Rev. Mod. Phys.* **84**, 299 (2012).

[33] Karrasch, C. Transport through Correlated Quantum Dots - a Functional Renormalization Group Approach. *Diploma thesis*, Universität Götingen (2006).

[34] Karrasch, C., Enss, T. & Meden, V. Functional renormalization group approach to transport through correlated quantum dots. *Phys. Rev. B*, **73**, 235337 (2006).

[35] Karrasch, C., Hecht, T., Weichselbaum, A., Oreg, Y. & von Delft, J. Mesoscopic to Universal Crossover of the Transmission Phase of Multilevel Quantum Dots. *Phys. Rev. Lett.* **98**, 186802 (2007).

[36] Bauer, F., Heyder, J. & von Delft, J. Functional Renormalization Group Treatment of a Quantum Chain Model for the Kondo Effect and the 0.7-Anomaly. *to be published.*

[37] Andergassen, S., Enss, T., Meden, V., Metzner, W. & Schollwöck, U. Functional renormalization group for Luttinger liquids with impurities. *Phys. Rev. B* **70**, 075102 (2004).

[38] Bauer, F. 0.7 Anomaly of Quantum Point Contacts: Treatment of Interactions with Functional Renormalization Group. *Diploma thesis*, LMU Munich (2008).

[39] Jakobs, S. G., Meden, V. & Schoeller, H. Nonequilibrium Functional Renormalization Group for Interacting Quantum Systems. *Phys. Rev. Lett.* **99**, 150603 (2007).

[40] Karrasch, C., Hedden, R., Peters, R., Pruschke, T., Schönhammer, K. & Meden, V. A finite-frequency functional RG approach to the single impurity Anderson model. *J. Phys.: Condensed Matter*, 20, 345205 (2008).

[41] Jakobs, S. G., Pletyukhov, M. & Schoeller, H. Nonequilibrium functional RG with frequency dependent vertex function - a study of the single impurity Anderson model. *Phys. Rev. B*, **81**, 195109 (2010).

[42] Wang, C.-K. & Berggren, K.-F. Spin splitting of subbands in quasi-one-dimensional electron quantum channels. *Phys. Rev. B* **54**, R14257-14260 (1996).

[43] Oguri, A. Transmission Probability for Interacting Electrons Connected to Reservoirs. *J. Phys. Soc. Jap.* **70**, 2666 (2001).

[44] Y. Meir & N. S. Wingreen. Landauer formula for the current through an interacting electron region. *Phys. Rev. Lett.* **68**, 2512-2515 (1992).

[45] Bruognolo, B. Störungstheoretische Analyse der Magnetfeldabhängigkeit der 0.7 Anomalie in Quantenpunktkontakten. *Bachelor Thesis*, LMU Munich (2011).

[46] Gangkofner, D. WKB-Calculations on the 0.7-Conductance Anomaly of Quantum Point Contacts. *Bachelor Thesis*, LMU Munich (2010).

Chapter 5

On the relation between the *0.7 anomaly* and the Kondo effect

This section presents the publication *"On the relation between the 0.7-anomaly and the Kondo effect: Geometric Crossover between a Quantum Point Contact and a Kondo Quantum Dot"* [(Heyder et al., 2014)]. In this work we investigate the similarities and differences between the physics of a quantum point contact (QPC) in the sub-open regime, where its conductance famously exhibits the *0.7 anomaly*, and the physics of a quantum dot (QD) in the regime of the Kondo effect, both experimentally and theoretically. According to our van Hove scenario a sub-open QPC features a particularly high LDOS at the chemical potential, resulting in strong spin fluctuations in the vicinity of the QPC's center. A Kondo QD (KQD) exhibits strong spin fluctuations, too, associated with screening of the localized QD spin [Glazman and Raikh (1988)]. This correspondence explains the similar low-energy behavior of the conductance of both geometries as function of magnetic field, temperature and source-drain voltage. We show theoretically that in both cases a strong reduction of conductance goes hand in hand with a strongly enhanced spin susceptibility. The finding of an enhanced spin susceptibility in the sub-open regime of a QPC is the key motivation for an experiment presented in Schubert et al. (2014) (Sec. 9), which aims at measuring the magnetization of a QPC in a small magnetic field with the help of Faraday rotation. These similarities were the basis for our suggestion, in Bauer et al. (2013), that a sub-open QPC in the low-energy regime can be described in terms of a Nozières Fermi liquid [Nozieres (1974)]. At high energies the two geometries, QPC with *0.7 anomaly* and KQD, exhibit different physics, as the unscreened local moment of the KQD does not have a counterpart in the open structure of the QPC.

The Ludwig group uses the highly tunable experimental setup introduced in Sec. 3.1.1 to investigate the continuous geometric crossover from a single barrier QPC to a double barrier QD. This crossover is accomplished by a continuous decrease in the side gate voltage V_s: For $V_c \ll V_s$, the influence of the central gate voltage V_c on the 2DES outweights the influence of V_s. Hence, the 1D effective barrier of the system has a single central maximum defining a QPC. For $V_c \gg V_s$ the situation is reversed. Now the effective potential features a double barrier defining a QD. In the QPC regime, the measurement reveals Fabri-Perot oscillations in the first conductance plateau in both short and long QPC geometries. This hints at a non-parabolic 1D effective barrier top. The intermediate regime, in contrast, shows a flat first plateau, which indicates a parabolic barrier. The crossover data displays a regime of coexistence between QPC and QD, where the conductance step of the QPC geometry is modulated by strong oscillations, indicating the emergence of quasi-localized states in the vicinity of the barrier. Finally, the QD regime is dominated by Coulomb blockade oscillations.

Theoretically, we investigate the crossover using the 1D model introduced in Sec. 3.3.1, extended by an additional parameter V_s, which simulates the influence of the side gate voltage. We calculate physical properties of our model using the functional renormalization group (fRG) in two different versions: Our standard CLA approach (Sec. 6) failes in shallow QD geometries, where interactions cannot be regarded as "intermediate" anymore. Here, we use a more elementary version of fRG, which neglects the flow of the two-particle vertex. Our theoretical results reproduce all the main features of the measured crossover.

On the relation between the 0.7-anomaly and the Kondo effect: Geometric Crossover between a Quantum Point Contact and a Kondo Quantum Dot

Jan Heyder,[1,2] Florian Bauer,[1,2] Enrico Schubert,[1] David Borowsky,[1]
Dieter Schuh,[3] Werner Wegscheider,[4] Jan von Delft,[1,2] and Stefan Ludwig[1]
[1]*Center for NanoScience and Fakultät für Physik, Ludwig-Maximilians-Universität München, Geschwister-Scholl-Platz 1, 80539 München, Germany*
[2]*Arnold Sommerfeld Center for Theoretical Physics, Ludwig-Maximilians-Universität München, Theresienstrasse 37, D-80333 München, Germany*
[3]*Institut für Angewandte Physik, Universität Regensburg, D-93040 Regensburg, Germany*
[4]*Laboratory for Solid State Physics, ETH Zürich, CH-8093 Zürich, Switzerland*

(Dated: September 12, 2014)

arXiv:1409.3415v1 [cond-mat.str-el] 11 Sep 2014

Quantum point contacts (QPCs) and quantum dots (QDs), two elementary building blocks of semiconducting nanodevices, both exhibit famously anomalous conductance features: the 0.7-anomaly in the former case, the Kondo effect in the latter. For both the 0.7-anomaly and the Kondo effect, the conductance shows a remarkably similar low-energy dependence on temperature T, source-drain voltage V_{sd} and magnetic field B. In a recent publication [F. Bauer *et al.*, Nature, **501**, 73 (2013)], we argued that the reason for these similarities is that both a QPC and a KQD feature *spin fluctuations* that are induced by the sample geometry, confined in a small spatial regime, and enhanced by interactions. Here we further explore this notion experimentally and theoretically by studying the geometric crossover between a QD and a QPC, focussing on the B-field dependence of the conductance. We introduce a one-dimensional model that reproduces the essential features of the experiments, including a smooth transition between a Kondo QD and a QPC with 0.7-anomaly. We find that in both cases the anomalously strong negative magnetoconductance goes hand in hand with strongly enhanced local spin fluctuations. Our experimental observations include, in addition to the Kondo effect in a QD and the 0.7-anomaly in a QPC, Fano interference effects in a regime of coexistence between QD and QPC physics, and Fabry-Perot-type resonances on the conductance plateaus of a clean QPC. We argue that Fabry-Perot-type resonances occur generically if the electrostatic potential of the QPC generates a flatter-than-parabolic barrier top.

I. INTRODUCTION

A QPC is a narrow one-dimensional (1D) constriction and a QD a small isolated puddle of charges, patterned in a two-dimensional electron system (2DES), e. g. by applying voltages to local gates. Being key ingredients of semiconductor-based quantum circuits, much effort has been devoted to understand their behavior at a fundamental level. Here, we investigate the geometric crossover between a QPC and a QD. The motivation for this study is to shed light on similarities and differences between the 0.7-anomaly exhibited by the conductance of a QPC, and the Kondo effect found in a Kondo quantum dot (KQD) that hosts an odd number of electrons and hence contains a localized spin.

The linear conductance $G(V_{\mathrm{c}})$ of a QPC is famously quantized in units of $G_{\mathrm{Q}} = 2e^2/h$, when measured as function of the gate voltage V_{c} defining the channel width[1–3]. The 0.7-anomaly is observed as an additional shoulder when the dimensionless conductance, $g = G/G_{\mathrm{Q}}$, reaches the value $g \simeq 0.7$ in the first conductance step[4–14]. It shows strikingly anomalous behavior as function of temperature (T), magnetic field (B) and source-drain voltage (V_{sd}), which can not be explaqined within a non-interacting model. The *low-energy* T-, B- and V_{sd}-dependencies of the 0.7-anomaly are similar to those of a KQD[15–22] at excitation energies well below its Kondo temperature, T_{K}: for both QPC and KQD, the linear conductance strongly decreases with increasing B and T, while the non-linear conductance shows a zero-bias peak as function of V_{sd}, that splits into two subpeaks with increasing B. We will call this similar behavior the "0.7-Kondo-similarity" (.7KS). To explain it, Meir and collaborators[23–25] have argued that a "quasi-bound state" in the QPC, predicted via spin-density-functional theory, harbors a localized spin that causes Kondo-like conductance anomalies.

We have recently proposed a scenario that explains the microscopic origin of the 0.7-anomaly and of the .7KS without invoking a localized spin[14]. In a nutshell, we argue that the 0.7-anomaly is a direct consequence of a "van Hove ridge", i. e. a smeared van Hove peak in the local density of states (LDOS) at the bottom of the lowest 1D sub-band of the QPC, whose shape follows that of the QPC potential barrier. Invoking a semi-classical picture, the LDOS is inversely proportional to the velocity of an electron with given energy at a given position; the van Hove ridge, which corresponds to a locally enhanced LDOS, thus reflects the fact that electrons are being slowed down while they cross the 1D barrier constituting the QPC. The slow electrons experience strongly enhanced mutual interactions. When the QPC barrier is tuned to lie just below the chemical potential, transport properties are significantly affected by these strongly enhanced electron interactions. In Ref. 14 we have shown that this amplification of interaction effects is sufficient to fully explain the 0.7-anomaly.

The above-mentioned two scenarios for explaining the 0.7-anomaly, evoking a quasi-localized state or a van Hove ridge, respectively, have an important common feature, namely that in both cases, the physics is governed by slow electrons above the barrier top. In this regard, it is not surprising that both scenarios are compatible in their predictions for the low-energy behavior of the 0.7-anomaly, which, as mentioned above, is similar to that of the Kondo effect. In Ref. 14, we attributed this .7KS to the fact that both a KQD and a QPC involve a spin-singlet ground state featuring *spatially confined spin fluctuations*. While for a KQD they are associated with the screening of a truly localized spin, for a QPC they result from the extended but curved structure of the van Hove ridge and include a large number of spins. In both cases, these spin fluctuations are characterized by an exponentially small energy scale, called B_* in Ref. 14, which goes hand in hand with an enhanced local spin susceptibility. For a KQD this low-energy scale corresponds to the Kondo temperature, T_{K}. The .7KS pertains to energies well below B_*; we have argued in Ref. 14 that it results from the fact that for such low energies, both a KQD and a QPC show Fermi-liquid behavior of the type associated with quasi-particles experiencing spatially localized interactions. For the Kondo effect, a corresponding Fermi-liquid theory has been worked out by Nozières[26]; doing the same for a QPC would be an interesting challenge for the future.

Though slow electrons form the common ground for both the van Hove ridge scenario and quasi-localized state scenario, the two scenarios differ substantially in their microscopic description of the slow electrons' dynamics. The van Hove ridge scenario describes them via the LDOS, thus incorporating the geometric shape of the barrier. In contrast, the quasi-localized state scenario describes them more simplistically in terms of a magnetic moment, i.e. a truly localized state, thus arriving at a seemingly simpler model, akin to the single-impurity Anderson model. This apparent simplification, however, comes at a price: the physics of the Anderson model involves a free local moment high energies, and Fermi-liquid behavior emerges only at low energies, when the local moment is screened. For a QPC such a "detour" (first evoke a local moment, then argue that it is screened) is in our opinion not needed: in our van Hove ridge scenario, Fermi-liquid behavior is present *a priori*. Moreover, in Ref. 14 we have found no indications that a smooth parabolic barrier hosts a discrete, truly localized spin, and no similarities (in our experimental results or theoretical predictions) between the Kondo effect and the 0.7-anomaly at high energies ($\gtrsim B_*$), where the Kondo effect is governed by an unscreened local moment. This shows that when the "slow electrons" in a QPC are probed at energies $\gtrsim B_*$, they do behave differently from the magnetic moment in a KQD. (In Sec. VI we offer additional evidence for this conclusion by comparing the behavior of the magnetization of a KQD and a QPC at large magnetic fields.)

The differences between a KQD and a QPC come to the fore very explicitly in the functional dependence of the low-energy scale B_* on system parameters such as the gate voltage and the interaction strength (discussed in detail in Sec. IV C below). For a KQD, the scale B_*^{KQD} can not meaningfully be defined in the absence of interactions (since then no local moment forms), and $\ln B_*^{\mathrm{KQD}}$ depends quadratically on gate voltage[19,22,27]. For a QPC, in contrast, B_*^{QPC} can be meaningfully defined even in the absence of interactions, and $\ln B_*^{\mathrm{QPC}}$ depends linearly on gate voltage. When interactions are turned on, B_*^{QPC} is reduced strongly, but its functional dependence on gate voltage hardly changes (see Ref. 14, Sec. S-5).

The present paper aims to elaborate the relation between local spin fluctuations and the .7KS in more detail, and, more generally, to analyse the similarities and differences between the Kondo effect and the 0.7-anomaly, focussing on their dependence on magnetic field at low temperature, in equilibrium. We experimentally and theoretically study the smooth *geometric crossover* between a KQD and a QPC, and hence between the Kondo effect and the 0.7-anomaly. Experimentally, we measure the conductance throughout the QD-QPC crossover using a highly tunable nanostructure tailor-made for this purpose. In our theoretical work, we consider a 1D model with local interactions and a smooth potential barrier, similar to that used in Ref. 14, but now tune the shape of the potential barrier in such a way that it smoothly crosses over between a single barrier, representing a QPC, and a double barrier, representing a KQD. We use the functional renormalization group (fRG)[28–31] to calculate how transport and thermodynamic properties at $T = 0$ change during this crossover. This allows us to track the extent to which features characteristic for Kondo correlations do or do not survive in the QPC regime. A central finding is that the strongly enhanced local spin susceptibility in the center of the system that is found for both a QPC and a KQD goes hand in hand with an anomalously strong magnetic field dependence of the conductance. This is actually not surprising, since a large spin susceptibility indicates a strong depletion of that spin species that is energetically disfavoured in the presence of a small magnetic field. Our analysis pinpoints the enhanced local spin susceptibility as the common feature of both systems that underlies the .7KS regarding its dependence on magnetic field.

The paper is organized as follows: Sec. II describes our experimental setup and our measurements for the QD-QPC crossover. Sec. III presents the model by which we describe this crossover, discusses how the geometry of the QPC or QD barrier influences the noninteracting LDOS and noninteracting transmission probability, and summarizes the key elements of our fRG approach for treating interactions. Sec. IV compares fRG results and experimental data for this crossover, showing that our model captures its main features in a qualitatively correct manner. Sec. V presents the results of fRG calculations for local properties, such as the local density, magnetization and spin susceptibility for both a QPC and a KQD, and for the spin susceptibility during the QPC-QD crossover, which very clearly reveals the origin of the .7KS. Sec. VI presents fRG results on the evolution of the magnetization with $\widetilde{B}$, highlighting the difference between a KQD and QPC when probed at energies beyond B_*. Sec. VII offers a summary and outlook. An appendix presents and discusses a movie with fRG results that show how the conductance evolves with magnetic field during the QD-QPC crossover.

II. EXPERIMENTAL SETUP

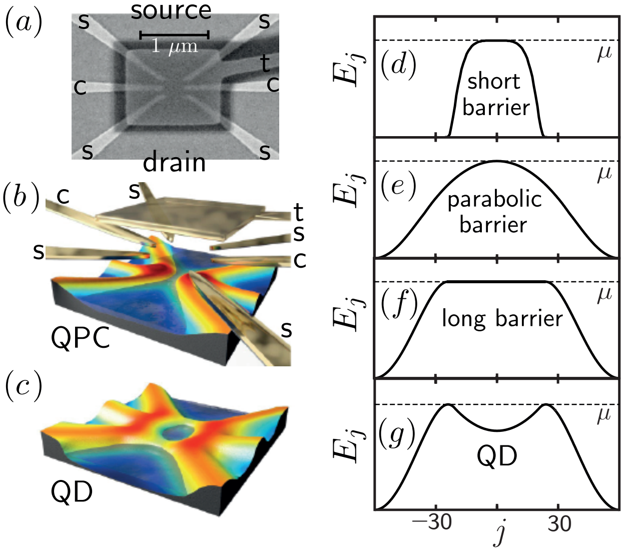

Figure 1. Geometric crossover between QPC and QD – sample and shape of effective potential. (a) Scanning electron microscope picture of the gate layout, which features a top gate at voltage V_t, two central gates at voltage V_c, and four side gates at voltage V_s. Negative voltages V_c and V_s deplete the 2DES 85 nm beneath the sample surface, inducing a tunable effective electrostatical potential landscape there. (b,c) Artist's depiction of this landscape for a QPC and QD, respectively [red/yellow: high electrostatic potential; blue: low potential, Fermi sea darkened; golden structures at top of (b): gates]. (d-g) The effective potential E_j of the Hamiltonian given in Eq. (1), shown for four different choices of the barrier shape (black lines), tuned by adjusting the central barrier height $\widetilde{V}_c = E_{j=0} - \varepsilon_F$, the side barrier height $\widetilde{V}_s$ (with $\widetilde{V}_{c,s} \propto -|e|V_{c,s}$), and the barrier width. These choices correspond to (d) a short QPC with a flat potential top ($\widetilde{V}_c = \widetilde{V}_s$); (e) a QPC described by a parabolic potential top ($\widetilde{V}_c > \widetilde{V}_s$); (f) a long QPC with a flat potential top ($\widetilde{V}_c = \widetilde{V}_s$); and (f) a QD ($\widetilde{V}_c < \widetilde{V}_s$).

We use the multigate layout shown in Fig. 1(a) to laterally define a nanostructure in the two-dimensional electron system (2DES) located 85 nm beneath the surface of our GaAs/AlGaAs heterostructure. The low temperature charge carrier density is $1.9 \times 10^{11}\,\mathrm{cm}^{-2}$ and the mobility $1.2 \times 10^6\,\mathrm{cm}^2/\mathrm{Vs}$. Magnetic fields are aligned parallel to the 2DES and to the 1D channel defining the QPC (current direction). The field's alignment is optimized by use of a two-axis magnet and controlled by magnetotransport measurements. The electron temperature in all measurements presented here is $T_0 \simeq 30\,\mathrm{mK}$ according to our estimations from separate temperature dependent measurements (not shown, see also Ref. 14).

Seven gates provide a particularly high tunability of the central constriction region (CCR) of our device, located at the center of Fig. 1(a) between the tips of six gates. We apply one voltage, say V_c, to both central gates, and another, say V_s, to all four side gates. Our sample also contains a global top gate [see Fig. 1(a),(b)], electrically insulated from other gates by a layer of cross-linked PMMA (plexiglass). The top gate can be used to adjust the carrier density of the 2DES in the contacts of the CCR and thereby control the effective interaction strength between electrons[14]. In this article we keep V_t fixed at 0.8 V. By suitably tuning V_c and V_s, we are able to smoothly reshape the potential landscape in the 2DES in such a way that it crosses over from a saddle point potential defining a QPC [Fig. 1(b)] to a symmetric local minimum defining a QD [Fig. 1(c)]. The corresponding effective 1D potential barrier shape crosses over from a single barrier [Figs. 1(d-f)], whose top is parabolic only in a relative narrow range of gate voltages, to a symmetric double barrier [Fig. 1(g)].

Experimentally we have studied this smooth transition from a QD to a QPC by measuring the two-terminal differential conductance g via the linear response of the current to small modulations of the applied source-drain voltage. Fig. 2 shows raw data (albeit already corrected for the lead resistances) measured at $B = 0$ as a function of V_c and V_s. For our most negative V_s-values and near pinch-off, i. e. also negative V_c, the conductance traces show pronounced Coulomb blockade oscillations as function of V_c (at the bottom center part of the figure). This indicates that the CCR constitutes a single, well-defined QD with a substantial Coulomb charging energy. When V_s is made less negative the Coulomb blockade oscillations disappear altogether. The reason is that the local electrostatic potential near the side gates decreases and eventually becomes smaller than the electrostatic potential between the center gates, corresponding to a transition from a double barrier potential as in Fig. 1(g) to a single barrier top as in Figs. 1(d-f). In the process the QD disappears, and with it the localized states, and a clean QPC remains. Its barrier top may or may not be parabolic, depending on the value of V_s. At $V_s \simeq -0.4\,\mathrm{V}$, $g(V_c)$ clearly shows several smooth conductance steps as function of V_c, as expected for the pinch-off curves of a clean parabolic QPC.

The broad transition regime between QPC and QD

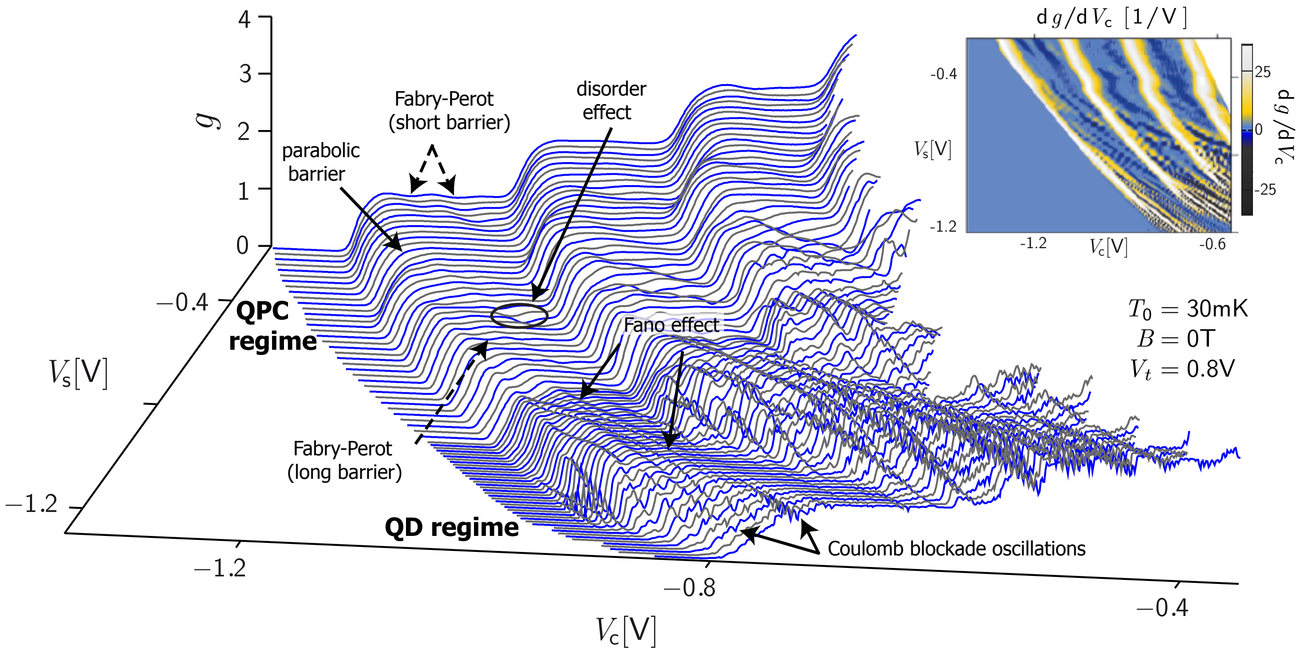

Figure 2. The linear-response differential conductance g (main panel) and transconductance dg/dV_c (inset) as a function of V_c and V_s, showing the geometric crossover between a QD and a QPC. Detailed measurements of the 0.7-anomaly at fixed side gate voltage, reported in Ref. 14 and shown in part in Fig. 6(d) below, were performed at $V_s = -0.4\,\text{V}$, where the first plateau is absolutely flat, implying a parabolic barrier top. Features marked by arrows are explained in the main text.

displays a combination of both 1D conductance steps and Coulomb blockade oscillations. The latter are most pronounced at the steps between conductance plateaus ($0 < g < 1$, $1 < g < 2$, ...) and occur in clusters with a rather similar structure, as can be best seen in the inset of Fig. 2, which shows $\mathrm{d}g/\mathrm{d}V_c$ using a color scale. This repeating pattern of Coulomb blockade oscillations indicates a coexistence of a QD in the not yet (fully) occupied one-dimensional subband of the CCR with already fully occupied lower one-dimensional subbands contributing to QPC-behavior. This causes the charge configurations of the QD to repeat at adjacent QPC conductance steps when the number of occupied one-dimensional subbands changes by one. Note that as V_s becomes more negative, the spacing between Coulomb blockade peaks within each cluster tends to increase (causing the cluster to "fan out", see Fig. 2, inset, bottom right corner). This reflects an increase in the QD charging energy, brought about by the steepening of the confinement potential when its side barriers become higher.

Whenever a Coulomb blockade oscillation enters a conductance plateau at $g = 1, 2, \ldots$ the corresponding conductance maxima of the QD turn into narrow conductance dips, some of which are marked by solid arrows in Fig. 2. We interpret these dips as Fano resonances between the 1D channel of the QPC and localized states of the QD.

We also observe broader and very shallow conductance oscillations on the conductance plateaus deeper in the QPC regime (at larger V_s), marked by dashed arrows in Fig. 2. They are absent only in a narrow region around $V_s \simeq -0.4\,\text{V}$ (on the first plateau), and the oscillation period observed for $V_s < -0.4\,\text{V}$ is shorter than that observed for $V_s > -0.4\,\text{V}$. We interpret these as Fabry-Perot-like resonances that arise whenever the barrier shape is not parabolic: as V_s is increased within the regime of a clean QPC, starting from around $V_s \simeq -0.8\,\text{V}$, we observe a transition from a long flat barrier via a parabolic barrier near $V_s \simeq -0.4\,\text{V}$ to a short flat barrier for $V_s > -0.4\,\text{V}$, where also $V_s \gg V_c$, (as sketched in Figs. 1(d-f) and indicated in Fig. 2). We will discuss the origin and behavior of these Fabry-Perot resonances in more detail in sections III B and III C below.

At a particular side gate voltage, near $V_s \simeq -0.6\,\text{V}$, two conductance traces show a marked dip (indicated by an ellipse) near the end of the first plateau. We interpret this distinct reduction of the conduction as reflection of electrons caused by disorder in the form of a distinct defect.

The multi-gate tunability of our device has the important advantage that it allows these type of effects (Fabry-Perot and/or disorder) to be avoided, if desired. Indeed, at side gate voltages near $V_s \simeq -0.4\,\text{V}$, no such effects are seen around the first conductance plateau is completely flat. We have therefore used $V_s = -0.4\,\text{V}$ for the detailed measurements of the 0.7-anomaly reported in Ref. 14, some of which are also shown in Fig. 6(d) below. An additional option would be to apply various different voltages to the individual four side gates or the two central gates to overcome possible disorder effects. However, the high quality of our sample rendered such options unnecessary, allowing us to maintain a high degree of symmetry of the electrostatic potential defining the CCR.

Fig. 2 displays two additional remarkable trends: (i) the quantized plateaus in $g(V_\mathrm{c})$ become wider as V_s is increased. (ii) This goes along with an increase of the step width between plateaus as is best seen in the inset of Fig. 2 (consider the width of the white-yellow bands in the upper half of the plot, the QPC regime). Trend (i) indicates that the lateral confinement becomes stronger with more positive V_s, leading to a larger characteristic energy spacing between the 1D subbands. This also implies a larger on-site exchange energy, U, between the electrons. Trend (ii) confirms our statement, above, that the width of the barrier, seen by electrons, decreases as V_s is increased, because a narrower barrier causes the step width to become wider (see the discussion in Sec. III B and Figs. 3(a-c) below). Both trends together (which further depend on the topgate voltage, see Supplementary Material in Ref. 14) provide us with an experimental toolkit to precisely measure the geometry dependence of the 0.7-anomaly. This could be used for a detailed test of the predictions of our model in Ref. 14. A study of this kind is beyond the scope of this work and left for the future.

III. THEORETICAL MODEL

In this section we present the one-dimensional model used for our theoretical description of the QD-QPC crossover, featuring a smooth barrier and short-ranged interactions [Sec. III A]. We first illustrate its geometrical properties in the absence of interactions, by showing results for the noninteracting LDOS and noninteracting transmission [Sec. III B]. Within this noninteracting framework we explain why Fabry-Perot-type resonances occur whenever the barrier top is not parabolic [Sec. III C]. Finally, we summarize the key ingredients of the fRG approach used here to treat interaction effects [Sec. III D].

A. Hamiltonian

To describe the QD-QPC crossover we restrict ourself to the lowest 1D subband of the CCR and adopt the model introduced in Ref. 14 (see its Supplementary Information, Section S-4.B, “model I”), whose notational conventions we adopt here, too. The Hamiltonian has the form

$$H = \sum_{j\sigma} \Big[E_{j\sigma} \hat{n}_{j\sigma} - \tau (d^\dagger_{j+1\,\sigma} d_{j\sigma} + \text{h.c.}) \Big] + \sum_j U_j n_{j\uparrow} n_{j\downarrow}, \tag{1}$$

where $\hat{n}_{j\sigma} = d^\dagger_{j\sigma} d_{j\sigma}$ counts the number of electrons with spin σ $(= \pm$ for $\uparrow,\downarrow)$ at site j. It describes an infinite tight-binding chain with constant lattice spacing $a = 1$ (taken as length unit), constant hopping amplitude $\tau = 1$ (taken as energy unit), on-site interaction U_j and on-site potential energy $E_{j\sigma} = E_j - \frac{\sigma}{2}\widetilde{B}$. Here $E_j = \widetilde{E}(ja)$ models the smooth electrostatic potential $\widetilde{E}(x)$ defined by gates, and the Zeeman energy $\widetilde{B}$ accounts for a uniform external parallel magnetic field. (We use tildes to distinguish model parameters from experimental ones, with $\widetilde{B} = |g_\mathrm{el}|\mu_\mathrm{B} B$ for the magnetic field, where $g_\mathrm{el} < 0$ for GaAs, $\widetilde{T} = k_\mathrm{B} T$ for temperature, and $\widetilde{V}_\mathrm{c,s} \propto -|e|V_\mathrm{c,s}$ for the central and side gate voltages.) We neglect spin-orbit interactions and other orbital effects. We take U_j and E_j to be nonzero only within a central constriction region (CCR) of $N = 2N' + 1$ sites around $j = 0$, representing the QD or QPC. The rest of the chain represents two noninteracting leads with effective mass $m = \hbar^2/(2\tau a^2)$ (defined as the curvature of the dispersion at the band bottom in the bulk), chemical potential μ and bulk Fermi energy $\varepsilon_\mathrm{F} = 2\tau + \mu$; we choose $\mu = 0$, implying half-filled leads. U_j is set to a constant value U within the CCR for all but the outermost sites of the CCR, where it drops smoothly to zero. (For an explicit formula for U_j, see Eq. (S14) of the Supplementary Information of Ref. 14.) The shape of E_j is governed by two parameters, $\widetilde{V}_\mathrm{c}$ and $\widetilde{V}_\mathrm{s}$, that respectively mimic the effects of the central and side gates in experiment. $\widetilde{V}_\mathrm{c} < \widetilde{V}_\mathrm{s}$ defines a QD with side barrier height $\widetilde{V}_\mathrm{s}$ w. r. t. μ [Fig. 1(f)]. $\widetilde{V}_\mathrm{c} > \widetilde{V}_\mathrm{s}$ yields a QPC with a single central barrier [Fig. 1(d)]. Its shape near the top is chosen to be parabolic[3], unless stated otherwise [Fig. 4 features non-parabolic barrier tops]. We parametrize parabolic barrier tops by

$$\widetilde{E}(x) \simeq \widetilde{V}_\mathrm{c} + \varepsilon_\mathrm{F} - \frac{m\Omega_x^2 x^2}{2\hbar^2} \, . \tag{2}$$

Here $\widetilde{V}_\mathrm{c}$ is the barrier height measured w. r. t. the chemical potential, and the barrier curvature is characterized by an energy scale Ω_x. We emphasize that by “parabolic” barrier, we mean that the quadratic x-dependence of Eq. (2) holds over an energy range of at least Ω_x from the barrier top (i.e. up to x-values large enough that $E(0) - E(x) \gtrsim \Omega_x$). Then the width of the conductance step is given by Ω_x.

Typical choices of the potentials described by E_j are shown in Figs. 1(d-g), Figs. 3(a-f) and to some extent Fig. 4 (inset). For situations where the shape of E_j is not shown explicitly [Figs. 5(a-c), Fig. 6, Figs. 7(i-l)], it is chosen according to a formula given by Eq. (S15) of the Supplementary Information of Ref. 14, with $j_s = 60$ and $N' = 150$ there.

B. Noninteracting LDOS and transmission

To convey some intuition for the geometrical properties of this model in the absence of interactions, Fig. 3 shows

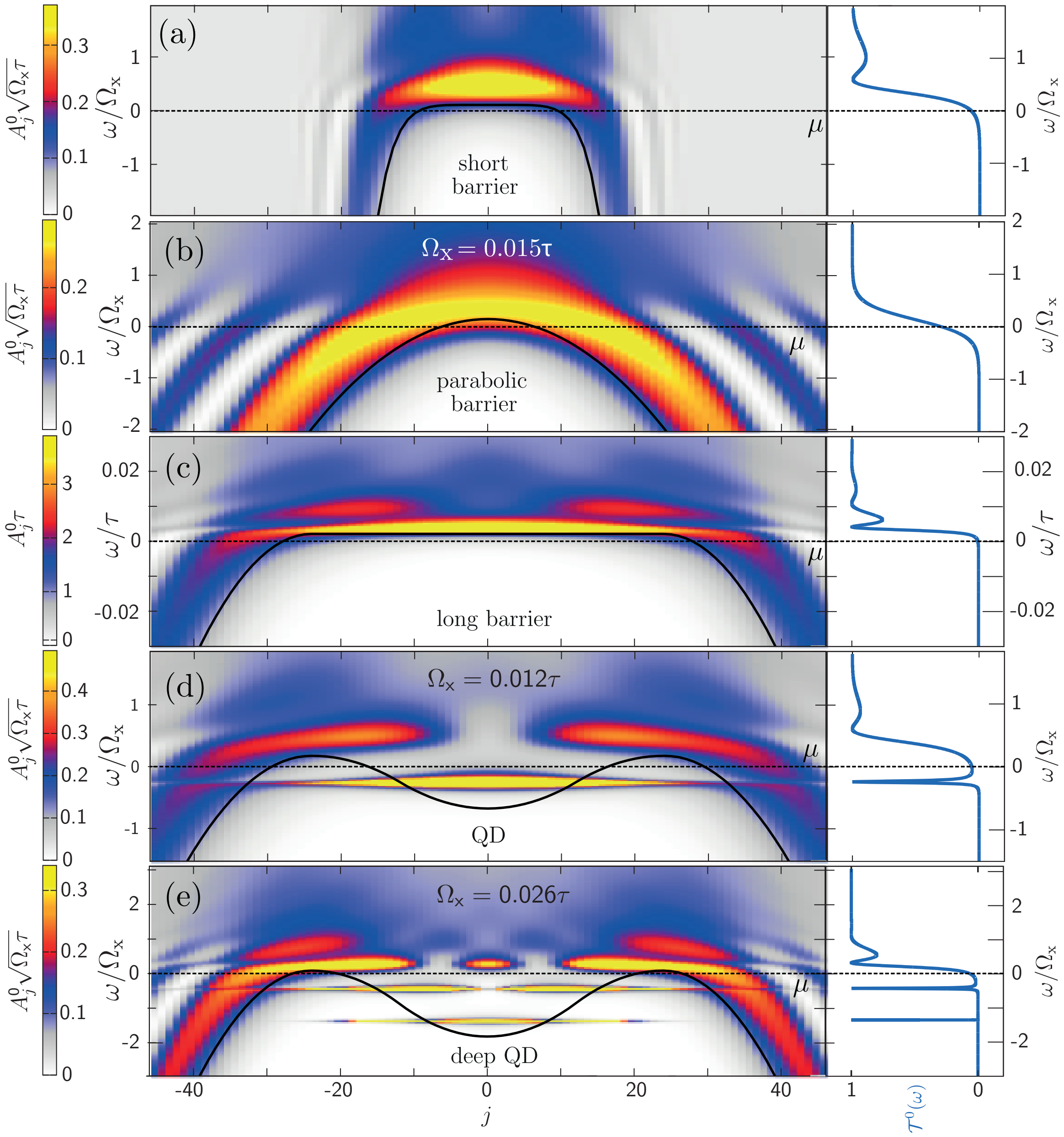

Figure 3. Noninteracting local density of states per spin species, $\mathcal{A}^0_j(\omega)$, and the noninteracting transmission per spin species, $\mathcal{T}^0(\omega)$, for $\widetilde{B} = 0$. The energy ω is measured w. r. t. the chemical potential. The five panels show five potential barrier shapes occuring during the QPC-QD crossover, namely (a) a QPC with a short flat barrier, (b) a QPC with a parabolic barrier, (c) a QPC with a long flat barrier, (d) a shallow QD with just one discrete orbital state, and (e) a deeper QD with two discrete orbital states.

the noninteracting LDOS, $\mathcal{A}^0_j(\omega)$, and the noninteracting transmission probability, $\mathcal{T}^0(\omega)$ (with ω measured w. r. t. the chemical potential), for five different choices of the barrier shape, chosen to represent various states of the geometric crossover between a QPC and a QD. For a parabolic QPC [Fig. 3(b)], the LDOS exhibits a broad ridge (yellow-red) just above the band bottom, $\omega^{\mathrm{min}}_j = E_j - \varepsilon_{\mathrm{F}}$ (solid black line), which follows the shape of the barrier. This is the van Hove ridge mentioned in the introduction; it originates from the 1D van Hove singularity at the band bottom, which in the CCR is smeared out on a scale set by the barrier curvature Ω_x. When ω is increased from below to above the barrier top, set by $\widetilde{V}_{\mathrm{c}}$, the transmission $\mathcal{T}^0(\omega)$ changes from 0 to 1 in the form of a smooth monotonic step of width Ω_x, centered at $\omega = \widetilde{V}_{\mathrm{c}}$.

Upon raising the side gate parameter $\widetilde{V}_s$ at fixed $\widetilde{V}_c$, the effective barrier top eventually turns flat [Fig. 3(c)] and the ridge in the LDOS narrows (while the maximal value of the LDOS above the barrier increases accordingly). This flatter-than-parabolic barrier shape causes the noninteracting transmission $\mathcal{T}^0(\omega)$ to show wiggles at the onset of the $\mathcal{T}^0(\omega) = 1$ plateau, which we interpret as Fabry-Perot-like resonances. They are discussed in more detail in the next subsection. Experimentally, we also observe the case of a short flat barrier for quite large V_s, which we simulate in Fig. 3(a) by using a short barrier with a quartic top (described by Eq. (3) below, with $n = 4$). In agreement with the measured $g(V_c)$ in Fig. 2 we observe Fabry-Perot-like resonances in $\mathcal{T}^0(\omega)$ for both cases, short versus long flat barriers in panels (a) and (c), and the period of the wiggles is longer for the shorter barrier, as expected.

When the central gate parameter $\widetilde{V}_c$ is lowered below $\widetilde{V}_s$, we enter the QD regime [Figs. 3(d) and 3(e)]. The LDOS now develops bound states, very narrow in energy, that are spatially localized inside the QD and define its single-particle spectrum. They are accompanied by resonances in the noninteracting transmission. Note, though, that the energy beyond which the $\mathcal{T}^0(\omega) = 1$ plateau associated with full transmission sets in, is still determined by the broader LDOS ridges above the tops of the left and right barriers, which are remnants of the van Hove ridge found for the parabolic and flat barrier shapes in (b) and (a,c), respectively. This is clearly seen in the transmission curves in panels (c) and (e), which exhibit very similar Fabry-Perot-like resonances near $\mathcal{T}^0(\omega) = 1$. In addition, $\mathcal{T}^0(\omega)$ in panels (d,e) shows sharp resonances at $\omega < 0$, reflecting the bound states in the LDOS. The occurrence of a conductance step together with sharp resonances is a clear signature of the coexistence of a QD and a QPC; our experimental data show corresponding features in the QD regime of Fig. 2.

In the outer flanks of the potential barrier, the LDOS has interference fringes with a period that scales as $1/v$, and the LDOS value averaged over several such fringes likewise scales as $1/v$, where $v_j(\omega)$ is the semiclassical velocity of an electron with kinetic energy $\omega - \omega_j^{\min}$ at site j. This explains the strikingly different behavior of the LDOS at the flanks of the potential maxima in Figs. 3(a) and 3(b): For the short, flat barrier with steep flanks in Fig. 3(a), the velocity $v_j(\omega)$ of electrons with $\omega \simeq \mu$ increases rapidly with $|j|$. As a consequence the LDOS at μ decreases rapidly and forms interference fringes with an correspondingly rapidly decreasing period. For the parabolic barrier of Fig. 3(b) the flanks decrease much more slowly with increasing $|j|$, thus the corresponding increase in Fermi velocity, the decrease in the average LDOS and the decrease in the interference period all occur more slowly, too.

C. Fabry-Perot resonances

In this section, we discuss the Fabry-Pero-like resonances (wiggles) that are seen in both the measured conductance in Fig. 2 (marked by dashed arrows) as well as in the calculated $\mathcal{T}^0(\omega)$, e. g. in Figs. 3(a,c), in more detail.

For our 1D model, studied in the absence of interactions, we find, in particular, that $\mathcal{T}^0(\omega)$ shows Fabry-Pero-like resonances whenever the QPC barrier top is flatter than parabolic. This is illustrated in Fig. 4, which shows the noninteracting conductance $g^0(\widetilde{V}_c)$ for a se-

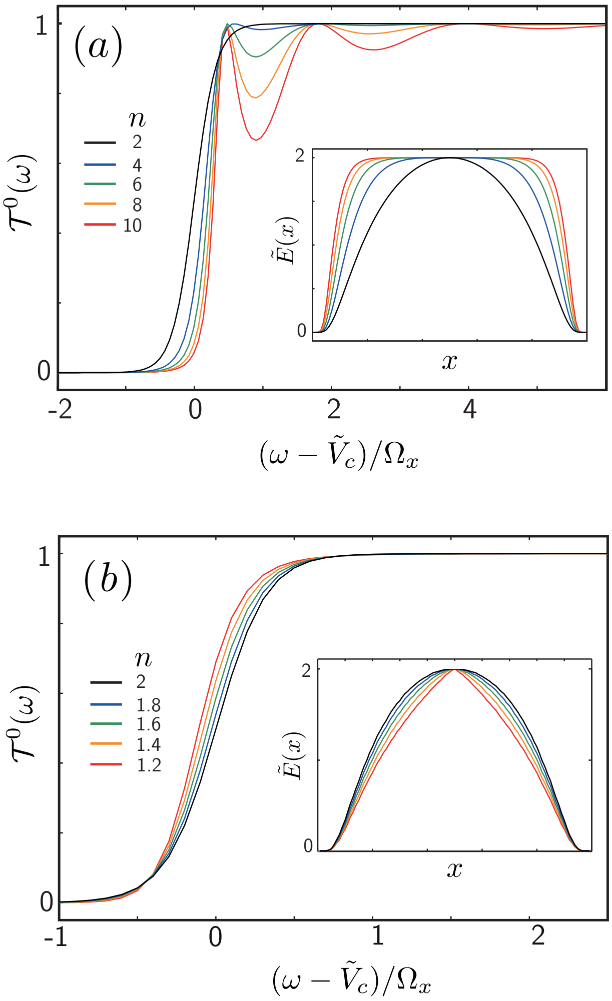

Figure 4. Noninteracting transmission $\mathcal{T}^0(\omega)$ as function of central gate voltage for several different barrier shapes, depicted in the insets, with barrier tops governed by $|x|^n$ according to Eq. (3). (a) Flatter-than parabolic barriers with $n \geq 2$, which arise during the QPC-KQD crossover; (b) sharper-than parabolic barriers with $n \leq 2$, shown for completeness.

quence of barrier shapes with barrier tops given by

$$\widetilde{E}(x) = \widetilde{V}_{\mathrm{c}} + \varepsilon_{\mathrm{F}} - \Omega_x \left(\frac{|x|}{l_x}\right)^n , \quad l_x = \sqrt{\frac{2\hbar^2}{m\Omega_x}} , \tag{3}$$

where l_x is a characteristic length. The noninteracting transmission of a purely parabolic barrier top (n=2, black line) is a smooth function of energy, given by[3]

$$\mathcal{T}^0(\omega) = [e^{2\pi(\widetilde{V}_{\mathrm{c}}-\omega)/\Omega_x} + 1]^{-1} . \tag{4}$$

In contrast, making the barrier top flatter than parabolic by increasing n introduces additional wiggles or resonances in $\mathcal{T}^0(\omega)$, see Fig. 4(a). Note that such structures occur naturally in the conductance of longer QPCs and we suspect that some previously published QPC measurements have likely been performed in this regime of flatter-than-parabolic barriers[32,33]. Our own experimental results, displayed in Fig. 2, demonstrate that the transition from a gate defined QD to a QPC likely covers the regime of a long QPC with a flatter-than-parabolic barrier top and, moreover, a short QPC with steep flanks can also result in a flatter-than-parabolic barrier and Fabry-Perot-like resonances.

For completeness, Fig. 4(b) shows examples of $n \leq 2$. Here, the transmission increases purely monotonically, without any Fabry-Perot-like resonances. With decreasing n, the potential flanks tend to "flatten", causing the conductance step to develop an increasingly skewed shape: the step's onset becomes noticeably steeper, while the onset of the plateau is affected only weakly.

We note that it is not straightforward to distinguish Fabry-Perot-type resonances, that occur even without interactions, from many-body effects, that arise in the presence of interactions. In the light of recent experimental work on shape-dependent barriers, including Refs. 32 and 33 and this work, a systematic theoretical study of how Fabry-Perot-type resonances are affected by turning on interactions would be very interesting, but is beyond the scope of this work.

D. fRG approach

To theoretically study the effect of interactions on the properties of the CCR at zero temperature, we used fRG[28–31], a renormalization-group-enhanced perturbative expansion in the interaction. We used it to calculate the linear conductance g of the CCR, and three local quantities, the occupation n_j, magnetization m_j and spin susceptibility χ_j of site j, defined, respectively, as

$$n_j = \langle \hat{n}_{j\uparrow} + \hat{n}_{j\downarrow} \rangle , \tag{5a}$$

$$m_j = \langle \hat{n}_{j\uparrow} - \hat{n}_{j\downarrow} \rangle / 2 , \tag{5b}$$

$$\chi_j = \partial_{\widetilde{B}} m_j |_{\widetilde{B}=0} . \tag{5c}$$

The results are presented in Secs. IV and V, below.

The details of our fRG approach are explained concisely in the supplement of Ref. 14, and in more detail in Ref. 31. Here we just summarize some key aspects. We restrict ourselves to zero-temperature calculations in the Matsubara formalism. Our fRG flow equations are based on two criteria. First, we assume that $m_j = 0$ for $\widetilde{B} = 0$, thus spontaneous symmetry breaking is ruled out *a priori*. This assumption is justified *a posteriori* by the agreement of our fRG results with experiment, both in Ref. 14 and in the present paper. Second, we neglect all contributions to the flow of the interaction vertex that are not already generated to second order in the bare (onsite) interaction, but feed back all other terms. This so-called coupled latter approximation[31] amounts to including all RPA-like channels on equal footing, while feeding back all Hartree-like terms into the Fock-like equations and vice versa. As a computational simplification, we here use a "static" version of the coupled-ladder approximation, which neglects all frequency dependencies in self-energies and vertices. For the model of present interest, the results for the zero-temperature conductance obtained via this static simplification are qualitatively essentially the same as those obtained by a "dynamic" calculation in which the frequency dependence is retained, as shown explicitly in Refs. 14 and 31 for a parabolic QPC potential.

The effective expansion parameter for static fRG is $U_j \mathcal{A}_j^0(0)$. As a result, we find that the fRG equations describing vertex flow do not converge for geometries that cause $\mathcal{A}_j^0(\omega)$ to be sufficiently sharply peaked near the chemical potential, i. e. near $\omega = 0$. This problem occurs in the QD regime, where the shallow few-electron QD has wide barriers near μ. We have therefore neglected vertex flow for plots that involve this regime, i. e. in Figs. 5(a-c), and for the movie discussed in App. A. Vertex flow was included, however, for all other fRG results shown in this paper, and is essential for obtaining the 0.7-shoulder in the QPC conductance even at $\widetilde{B} = \widetilde{T} = 0$, as discussed in Sec. IV B below.

In Ref. 14, we showed that our model and fRG treatment of interactions are able to capture key elements of the 0.7-anomaly in a QPC in a qualitatively correct manner, including its magnetoconductance. In the next section, we show that this is true also for the Kondo effect in a KQD, and in fact for the entire QD-QPC crossover.

IV. MAGNETOCONDUCTANCE

In this section, we compare zero-temperature fRG results and low-temperature experimental data for the conductance during geometrical QD-QPC crossover, for three different magnetic fields [Sec. IV A]. We also discuss the magnetoconductance in the KQD and QPC regimes in more detail, showing that fRG reproduces the characteristic magnetic-field dependence associated with the Kondo effect and the 0.7-anomaly, respectively [Sec. IV B]. Moreover, we discuss the $\widetilde{V}_{\mathrm{c}}$-dependence of the characteristic low-energy scale, $\widetilde{B}_*$, that characterizes the strength of the magnetoconductance at low fields, and its relation to the static spin susceptibility of the CCR [Sec. IV C].

A. QPC-QD crossover at finite magnetic field

Fig. 5 compares fRG results and experimental data for the QD-QPC crossover at three magnetic fields, including the $B = 0$ data already shown in Fig. 2. Figs. 5(a-c) present model calculations of the zero-temperature linear conductance $g(\widetilde{V}_{\mathrm{c}}, \widetilde{V}_{\mathrm{s}})$ (using fRG without vertex flow) for three magnetic field values, and Figs. 5(d-f) corresponding experimental data. The pinch-off value of V_{c} around which the measured conductance drops to zero as V_{c} is decreased, say $V_{\mathrm{c}}^{\mathrm{pinch}}$, is indicated using red lines in the raw data for $B = 0$ in Figs. 5(h,i), which are miniature versions of Fig. 2 and its inset. Note that $V_{\mathrm{c}}^{\mathrm{pinch}}$ shifts as a function of V_{s}, reflecting the capacitive influence of V_{s} on the local potential between the center gates. This effect is absent in the calculated data, since our model does not include such a cross-coupling. For better comparison between theory and experiment, this cross-coupling is corrected for in the measured data in Figs. 5(d-f), by plotting them as function of $\Delta V_{\mathrm{c}} = V_{\mathrm{c}} - V_{\mathrm{c}}^{\mathrm{pinch}}$.

The measured transition from a QD to a QPC in Figs. 5(d-f) is smooth regardless of B. Our calculations qualitatively reproduce the main features of the measured QPC-QD crossover: Just as for the $B = 0$ data in Fig. 2, both the calculated and measured conductance traces in Figs. 5(a-f) show the transition between a single QD with Coulomb blockade oscillations and a QPC with a smooth conductance step. A movie showing how this crossover evolves continuously with magnetic field is presented and discussed in App. A.

Moreover, both the calculated (at $T = 0$) and measured (at $T_0 \simeq 30\,\mathrm{mK}$) data exhibit the Kondo effect in the QD regime: it manifests itself as an enhanced conductance in the Coulomb blockade regime if an odd number of electrons charges the QD. In such Kondo valleys, highlighted in Figs. 5(a-f) by red lines, the Kondo-enhanced conductance is strongly suppressed with increasing field. Fig. 5(g) illustrates this for the measured data by showing in a single panel the three colored pinch-off curves from Figs. 5(d-f), taken for three comparable values of side gate voltage V_{s}. (These three values, $V_{\mathrm{s}} = -1.18$, -1.14 and -1.18, are not all the same, because a random charge fluctuation had occurred in the sample between the respective measurement runs, shifting the potential landscape by a small but noticable amount.) The solid red arrows in Fig. 5(g) mark the two Kondo valleys corresponding to the red lines in Figs. 5(d-f). The dashed red arrow in Fig. 5(g) marks a third Kondo valley at a smaller V_{c}-value, where, however, the Kondo effect is already very weak, since the coupling to the leads is so small that $T_{\mathrm{K}} < T$.

In the regime of a QPC defined by a parabolic barrier (small $\widetilde{V}_{\mathrm{s}}$, large V_{s}), both measurements and calculations display the typical magnetic field dependence of the 0.7-anomaly [marked by orange lines in Figs. 5(a-f)], namely the development from a weak shoulder at $g \simeq 0.7$ for $B = 0$ to a pronounced plateau at a reduced conductance for finite magnetic fields.

B. Magnetoconductance of QPC and KQD

In this subsection we compare theory and experiment in more detail, for the magnetoconductance at two fixed values of side gate voltage, for which the system forms a KQD or a QPC, respectively. For the QPC, we have tuned the experimental system to have a smooth plateau at $g = 1$ without any Fabry-Perot resonances on the first conductance plateau ($V_{\mathrm{s}} = -0.4\,\mathrm{V}$, compare Fig. 2), while we use a parabolic barrier top for the theoretical calculations.

Figs. 6(a,b) show measured conductance of a KQD and a QPC, respectively, at several magnetic fields, $0 \le B \le 5.8\,\mathrm{T}$, and Figs. 6(c,d) show corresponding fRG results (calculated with flowing vertex). The fRG calculations qualitatively reproduce the gate voltage and field dependencies observed by us and numerous other experimental groups: The conductance of the KQD [Fig. 6(c)] shows a Kondo plateau for $\widetilde{B} = 0$, which is suppressed into a dip with increasing field, as expected theoretically[29,34] and observed experimentally in Ref. 20 and for our own data [Fig. 5(g), Fig. 6(a)]. The conductance step of the QPC [Fig. 6(d)] exhibits a 0.7-shoulder at $\widetilde{B} = 0$, which, as $\widetilde{B}$ is increased, is suppressed into a double step whose width is proportional to the magnetic field, as also seen in numerous experiments[4,7,9], including our own (Fig. 6(b), see also Ref. 14).

Note that the shoulder at $g \simeq 0.7$ is visible in Fig. 6(d) even for $B = 0$, much more so than in Fig. 5(a) above; the reason is that the fRG scheme without vertex flow used for Figs. 5(a-c) underestimates the effects of interactions compared to the fRG scheme that includes vertex flow, used for Figs. 6(c,d). For a detailed discussion of this point, see Ref. 14.

C. Low-energy scale and excess spin susceptibility

For both KQD and QPC, the low-field expansion of g,

$$g(\widetilde{B}) \simeq g(0)\big[1 - (\widetilde{B}/\widetilde{B}_*)^2\big] \quad (\widetilde{B} \ll \widetilde{B}_*) , \qquad (6)$$

can be used to characterize the strength of the $\widetilde{B}$-dependence in terms of a $\widetilde{V}_{\mathrm{c}}$-dependent energy scale, $\widetilde{B}_*$: the smaller $\widetilde{B}_*$, the larger the magnetoconductance. For KQDs, the scale $\widetilde{B}_*$ in Eq. (6) corresponds to the Kondo temperature, $\widetilde{B}_*^{\mathrm{KQD}} = k_{\mathrm{B}} T_{\mathrm{K}}$, according to Nozières' Fermi-liquid[26,35] description of the low-energy limit of the Kondo model. The $\widetilde{B}^2$-dependence (6) has recently been observed experimentally for a KQD[22] and previously for a few electron double quantum dot[36]; for a

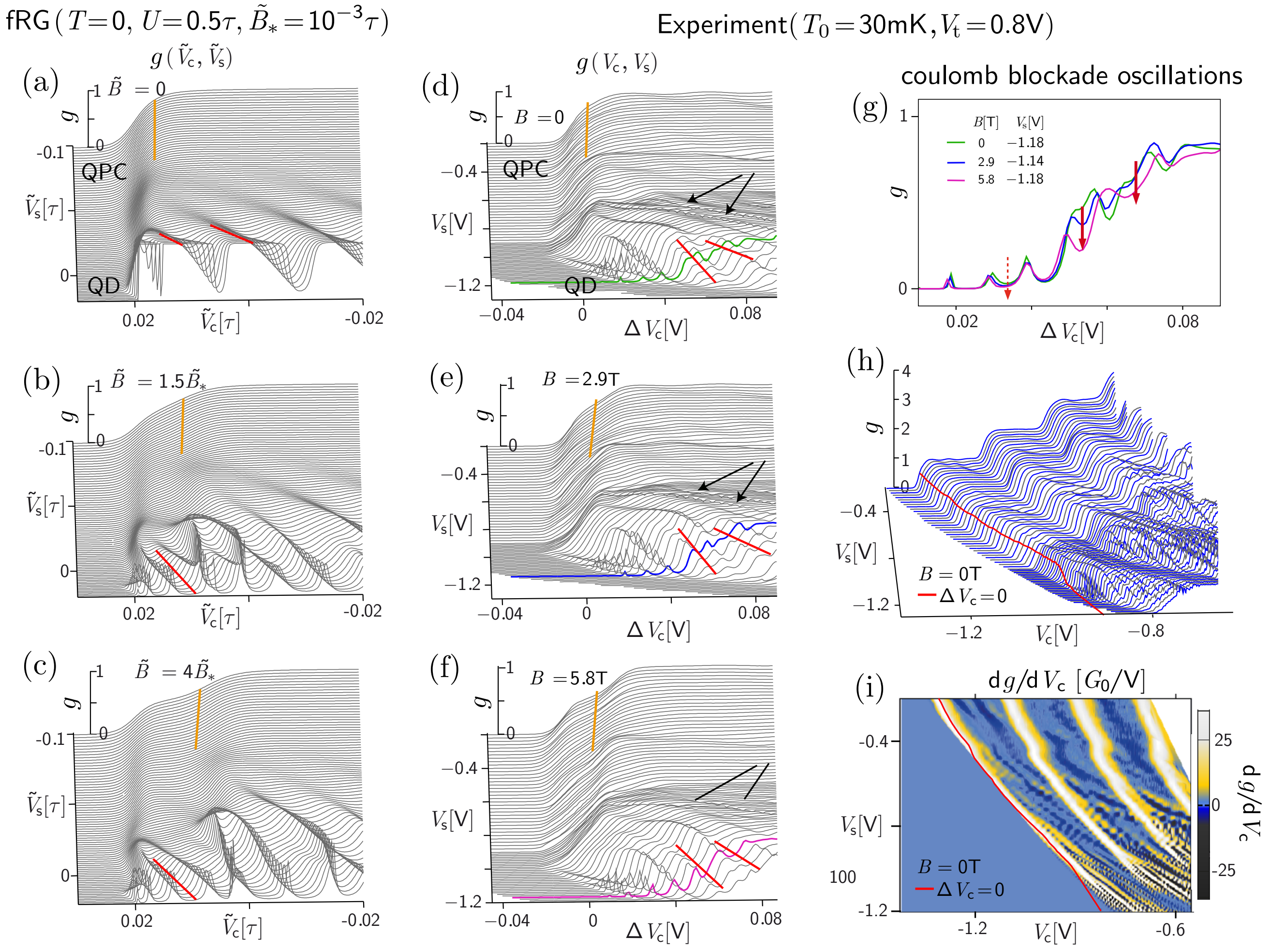

Figure 5. Transition from a QD to a QPC. (a-c) fRG1 results for the conductance $g(\widetilde{V}_c, \widetilde{V}_s)$, calculated at $T = 0$ and three different fields, and plotted as function of the central gate voltage $\widetilde{V}_c$ for a large number of different side gate voltages $\widetilde{V}_s$. (d-f) Analogous to (a-c), but showing experimental data for the conductance $g(V_c, V_s)$ in the range $0 \leq g \leq 1$, measured at a fixed low temperature, $T_0 = 30$ mK. For each side gate voltage V_s, the conductance trace is plotted as function of the shift $\Delta V_c = V_c - V_c^{\text{pinch}}$ in central gate voltage V_c relative to a V_s-dependent reference value $V_c^{\text{pinch}}(V_s)$, which is indicated by red lines in panels (h) and (i). [We chose V_c^{pinch} to statisfy $g(V_c^{\text{pinch}}) = 0.5$ in the QPC regime ($V_s > -1\widetilde{\text{V}}$), and to shift linearly with V_s in QD regime, with a slope chosen such that the red line does not cross any resonances.] Orange lines in (a-f) mark the 0.7-anomaly, red lines mark Kondo valleys; black arrows in (d-f) mark Fano resonances. (g) The three colored pinch-off curves from (d-f), all measured at $V_s = -1.18$ V, are plotted together to show how in Kondo valleys (marked by red arrows) the Kondo-enhanced conductance is suppressed by increasing field. (h) The raw experimental data for $g(V_c, V_s)$ at $B = 0$ [corresponding to (d)] is plotted over a larger range of (unshifted) gate voltages to show several conductance steps. (i) The derivative dg/dV_c of the data from panel (h). [(h) and (i) show identical data as Fig. 2 and its inset.] The red lines in (h) and (i) show $V_c^{\text{pinch}}(V_s)$, as used in (d-f).

QPC, it has been confirmed in Ref. 14 Fig. 2**g** there). Extracting $\widetilde{B}_*(V_c)$ from our fRG results (Figs. 6(e,f), red lines) we find that for both KQD and QPC it exhibits a distinct minimum, $\widetilde{B}_*^{\min}$, at (say) $\widetilde{V}_{c0}$, near which it behaves as

$$\widetilde{B}_*^{\text{KQD}} \propto \exp\left[c_1(\widetilde{V}_{c0} - \widetilde{V}_c)^2\right], \tag{7a}$$

$$\widetilde{B}_*^{\text{QPC}} \propto \exp\left[c_2(\widetilde{V}_{c0} - \widetilde{V}_c)/\Omega_x\right], \quad (\widetilde{V}_c < \widetilde{V}_{c0}), \tag{7b}$$

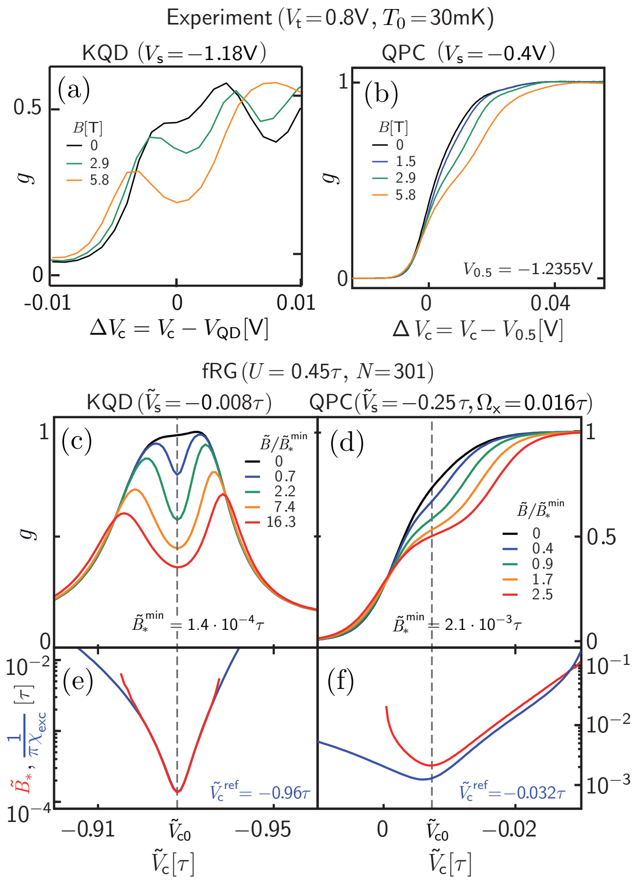

Figure 6. Magnetoconductance: experiment vs. theory. (a,b) Experimental conductance curves for a KQD and a QPC, at two different, fixed V_s-values and various magnetic fields measured at a low temperature $T_0 = 30\,\text{mK}$. Here, ΔV_c is the offset of the central gate voltage V_c relative to V_{QD} or $V_{0.5}$, denoting the middle of the Kondo valley or the middle of the first conductance step, respectively. The data in (a) are a subsection of those shown in Fig. 5(g); the data in (b) correspond to those shown in Ref. 14, Fig. 2**e**. (c,d) fRG results, plotted in a way analogous to (a,b), for the conductance $g(\widetilde{V}_c, \widetilde{B})$ at fixed $\widetilde{V}_s$ of a (deep) KQD containing $n^{\text{KQD}} = 49$ electrons, or for the lowest subband of a QPC, respectively. (e,f) The corresponding KQD and QPC low-energy scales $\widetilde{B}_*(\widetilde{V}_c)$ [red lines, from Eq. (6)] and inverse excess spin susceptibilities $1/[\pi\chi_{\text{exc}}(\widetilde{V}_c)]$ [blue lines, from Eq. (9)], plotted on a log-linear scale. Note that near the gate voltage $\widetilde{V}_{c0}$ [dashed line] where $\widetilde{B}_*$ reaches its minimum, $\widetilde{B}_*^{\min}$, the small-field magnetoresponse in (c,d) is strongest.

for the KQD and QPC geometries, respectively. (c_1 and c_2 are $\widetilde{V}_c$-independent constants.) Eq. (7a) reproduces for $\widetilde{B}_*$ the behavior theoretically predicted[27] and experimentally observed[19,22] for the Kondo temperature of a KQD. The linear exponential behavior described by Eq. (7b) for a QPC is valid even in the absence of interactions. There it follows directly from the non-interacting transmission formula for parabolic barriers, Eq. (4) (see Sec. S-5 of Ref. 14). Experimentally, Eq. (7b) has been confirmed in Ref. 14 (Fig. 2**e** there). Thus, our 1D model and fRG treatement of interactions correctly capture the full B- and V_c- dependence of the conductance of both KQD and QPC, including the exponential dependence of B_* on $\widetilde{V}_c^2$ or $\widetilde{V}_c$, respectively.

For the Kondo effect, the scale $\widetilde{B}_*$ defined by Eq. (6) is inversely proportional to the excess contribution of the KQD to the static spin susceptibility at zero temperature,

$$1/\widetilde{B}_*^{\text{KQD}} = \pi\chi_{\text{exc}}. \tag{8}$$

This relation, which links the strength of the magnetoconductance to that of local spin fluctuations, is a hallmark of Nozières's Fermi-liquid theory.[26] For our model, we define the excess spin susceptibility of the CCR by

$$\chi_{\text{exc}}(\widetilde{V}_c) = \sum_{j\in\text{CCR}} \left[\chi_j(\widetilde{V}_c) - \chi_j(\widetilde{V}_c^{\text{ref}})\right] , \tag{9}$$

where χ_j [Eq. (5c)] is the local zero-field spin susceptibility of site j, and $\widetilde{V}_c^{\text{ref}}$ a reference potential at which the magnetoconductance is very small. As reference for a KQD, we take $\widetilde{V}_c^{\text{ref}}$ to define an even QD (EQD) charged by an even number of electrons in an adjacent Coulomb-blockade valley; for a QPC, we take $\widetilde{V}_c^{\text{ref}}$ small enough to define a truly open 1D channel ($g > 0.999$). We find that the characteristic Fermi-liquid relation

$$1/\widetilde{B}_* \propto \chi_{\text{exc}} \tag{10}$$

is satisfied very well for the KQD for $\widetilde{V}_c$ near $\widetilde{V}_{c0}$ [Fig. 6(e)], as expected. Remarkably, we find that for a QPC, too, a small $\widetilde{B}_*$ goes hand in hand with a large χ_{exc}. In fact, by using $\widetilde{V}_c^{\text{ref}}$ as fit parameter, the inverse proportionality Eq. (10) can be achieved for a QPC over a rather large range of gate voltages $\widetilde{V}_c \lesssim \widetilde{V}_{c0}$, as shown in Fig. 6(f). That the inverse relation between $\widetilde{B}_*$ and χ_{exc} also holds roughly for a QPC (though not as well as for a KQD, and requiring a fit parameter in the definition of χ_{exc}) is truly remarkable and constitutes one of the main theoretical results of this paper: the link between the *magnetoconductance* and *local spin fluctuations* that characterizes the Fermi-liquid regime of the Kondo effect, namely Eq. (10), applies for the 0.7-anomaly as well. This substantiates the argumentation, presented by us in Ref. 14, that the .7KS is a manifestation of the fact that a KQD and a parabolic QPC show similar Fermi-liquid behavior at low energies.

Below, we further explore this link by theoretically studying the relation between the magnetoconductance and local properties in more detail, and for several different QD-QPC crossover trajectories.

V. LOCAL PROPERTIES

In this section we study the local properties of the CCR at zero temperature, calculated by fRG. We here focus on the local density n_j, magnetization m_j and spin susceptibility χ_j [defined in Eq. (5) above]. We find that a strong negative magnetoconductance goes hand in hand with an enhanced local spin susceptibility in the CCR, and argue that this connection is the microscopic origin of the .7KS.

Figs. 7(c-f) compare the $\widetilde{B}$-dependence of n_j and m_j of a KQD and a parabolic QPC near pinchoff, whose barrier shapes are shown by solid lines in Figs. 7(a,b), respectively. Towards the edges of the CCR (large $|j|$, $E_j \to 0$), the density n_j, plotted in Figs. 7(c,d), rises toward the filling of the non-interacting leads. For the KQD the charge near the center of the CCR is well-localized and discrete [n_j^{KQD} sums to $n^{\mathrm{KQD}} = 9$ between the two distinct minima in (c)]. For the parabolic QPC, in contrast, n_j^{QPC} is minimal at the center, showing no signs of localized charge. For $\widetilde{B} \neq 0$, both m_j^{KQD} and m_j^{QPC}, plotted in Figs. 7(e,f), show strongly-enhanced standing-wave oscillations in the CCR (with locally varying wavelength $\lambda \sim 1/n_j$), but significant differences arise when $\widetilde{B}$ increases far beyond $\widetilde{B}_*$: For a KQD, m_j^{KQD} saturates in magnitude, its maxima stay fixed in position, and n_j^{KQD} remains $\widetilde{B}$-independent, all indicating that a discrete spin is being polarized. In contrast, for a QPC, m_j^{QPC} *does not saturate* for $\widetilde{B} \gg \widetilde{B}_*$, its maxima shift outward, and n_j^{QPC} increases near the barrier center, all indicating that a smooth redistribution of charge and spin occurs during the polarization of the CCR, which ultimately causes the spin-split double conductance step at $\widetilde{B} \gg \widetilde{B}_*$. We conclude that whereas the KQD harbors a discrete, localized spin-$\frac{1}{2}$ local moment, a parabolic QPC does not, since the spins in its CCR are neither discrete nor localized. A detailed study of the behavior of the magnetization in large fields $B > B_*$ follows in the next section below.

Despite these differences, the KQD and QPC do show two striking similarities in the regime of small fields, $\widetilde{B} \ll \widetilde{B}_*$, relevant for the .7KS. First, m_j vanishes at $\widetilde{B} = 0$ (Figs. 7(e,f), blue lines), reflecting our fRG assumption that no spontaneous magnetization occurs, in contrast to the spontaneous spin splitting scenario advocated in Refs. 4–6, and 13 (see Ref. 14, Supplementary Information, p. 5 and 6, for a detailed discussion). Second, the local static spin susceptibility χ_j, shown in Figs. 7(g,h), exhibits a *strong enhancement* (modulated by standing-wave oscillations) in the CCR for *both KQD and QPC*. This enhancement arises through an interplay of geometry and interactions. In the absence of interactions, the bare local spin susceptibility in a QPC is directly proportional to the LDOS at the chemical potential, $\chi_j^0 = \mathcal{A}_j^0(0)/2$, and hence inherits the spatial dependence of the latter, reflecting the geometry of the system. Interactions enhance the spin susceptibility via a Stoner-type mechanism: upon turning on a small Zeeman field that favors spin up over spin down, interactions enhance the spin imbalance by further depleting the spin-down population. The same line of arguments applies for a KQD in the low-energy regime described by an effective Fermi-liquid Hamiltonian, involving quasi-particles that experience a local interaction whose strength is proportional to $1/T_{\mathrm{K}}$[26].

In contrast to a KQD, an EQD shows no χ_j-enhancement. This is illustrated by Figs. 7(i-l), which display $\chi_j(\widetilde{V}_{\mathrm{c}})$ and $g(\widetilde{V}_{\mathrm{c}})$ for four trajectories in the $(\widetilde{V}_{\mathrm{c}}, \widetilde{V}_{\mathrm{s}})$ plane, corresponding to four types of geometric crossovers. Fig. 7(i) shows a QD at fixed $\widetilde{V}_{\mathrm{s}}$, whose electron number (blue integers) is increased by lowering $\widetilde{V}_{\mathrm{c}}$. It exhibits odd-even effects for both $\chi_j(\widetilde{V}_{\mathrm{c}})$ and $g(\widetilde{V}_{\mathrm{c}})$: the Kondo-plateaus in $g(\widetilde{V}_{\mathrm{c}})$ for odd electron numbers (KQDs) are accompanied by distinct peaks in $\chi_j(\widetilde{V}_{\mathrm{c}})$ (white lines) whereas the Coulomb valleys for even electron numbers (EQDs) are not. Fig. 7(j) shows a QPC at fixed $\widetilde{V}_{\mathrm{s}}$, which is tuned from pinchoff into an open channel with $g = 1$ by lowering $\widetilde{V}_{\mathrm{c}}$. The 0.7-anomaly in $g(\widetilde{V}_{\mathrm{c}})$ occurs for $\widetilde{V}_{\mathrm{c}}$ values near $\widetilde{V}_{\mathrm{c}0}$ (red dashed line) where $\widetilde{B}_*$ is minimal. There the two maxima in χ_j merge into a single one (reminiscent of Figs. 2bA-C in Ref.[25]), indicating that the barrier top has dropped below 0 (compare panel Fig. 7(b), green circle), so that the chemical potential cuts through the apex of the Hove ridge. Fig. 7(k) shows a QPC-KQD crossover ending in an 11-electron KQD: χ_j exhibits strong maxima in the QPC, which weaken in the open-channel regime during the crossover to the KQD, where they become large again. Fig. 7(l) shows a QPC-EQD crossover ending in a 10-electron EQD, where χ_j remains very small, in contrast to the case of the 11-electron KQD in Fig. 7(k). Note that in the QPC parts of Figs. 7(j-l), χ_j exhibits a ridge-like, parabola-shaped main maximum as function of $\widetilde{V}_{\mathrm{c}}$ and j that mimicks (and indeed stems from) the Hove ridge in the LDOS as function of ω and j [Fig. 3(a)].

The main message of Figs. 7(i-l) is that the *negative magnetoconductance* seen for both KQDs and QPCs, but not for EQDs, goes hand in hand with a *strongly enhanced spin susceptibility*, whereas the latter vanishes or is weak for EQDs and open 1D channels. This is direct microsocopic evidence that the strong negative magnetoresistance observed in both a KQD and a QPC as one of the key features of the .7KS, originates from the fact that *a QPC harbors strong local spin fluctuations* similar to those of a KQD. In this regard, our scenario is fully consistent with the quasi-bound state Kondo scenario proposed by Meir and collaborators[23–25]. In fact, the spatial structure of χ_j^{QPC} seen in Figs. 7(j-l), namely two peaks that merge into one as $\widetilde{V}_{\mathrm{c}}$ is lowered, is consistent with that of the spin density of the "quasi-bound states" found for a QPC by SDFT calculations[25,37] (Figs. 2bA-C in Ref. 25). This is not surprising, since the SDFT calculations were initialized using a small magnetic field to break spin symmetry, which naturally gives rise to spin density maxima in regions of large spin susceptibility.

We emphasize, though, that the .7KS applies only for low energy scales, $\widetilde{B} \ll \widetilde{B}_*$, because while a KQD har-

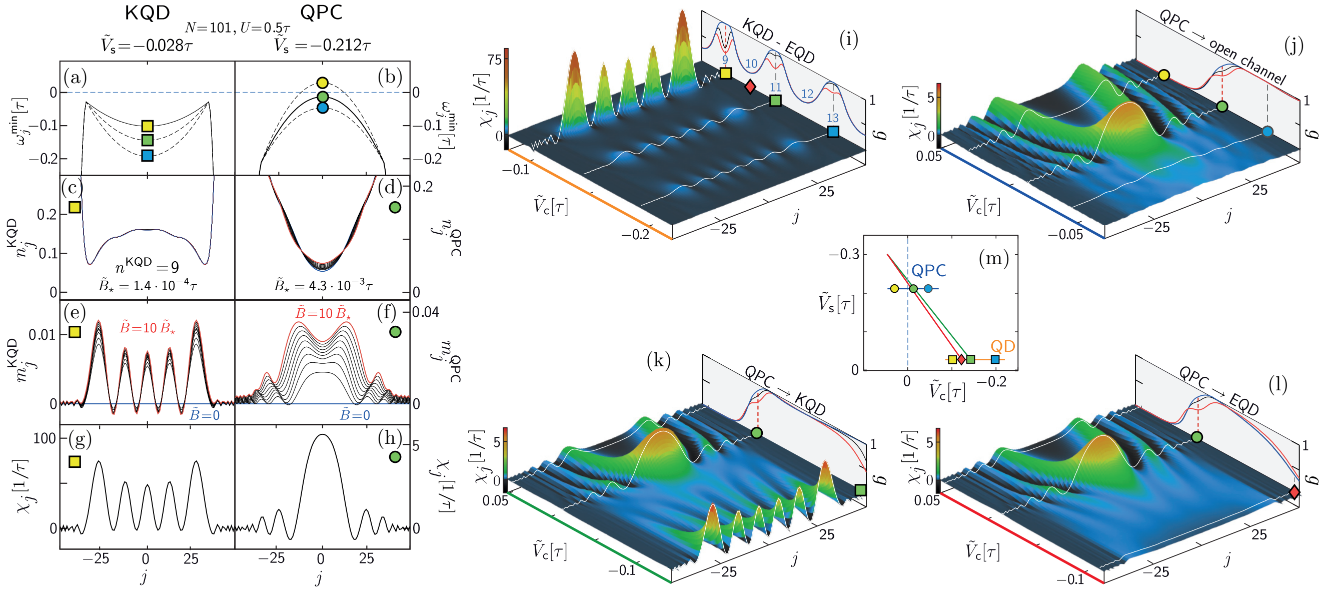

Figure 7. Local properties of KQD [charged with $n^{\mathrm{KQD}} = 9$ electrons for (c,e,g)] vs. QPC, calculated using fRG including vertex flow. (a-f) *Fixed geometries of KQD (left) and QPC (right)*: (a,b) The barrier tops for a (shallow) KQD and a QPC near pinchoff, respectively; for each, we show three barrier shapes $\omega_j^{\min} = E_j - \varepsilon_{\mathrm{F}}$, used to calculate the curves in (c-l) marked by matching colored symbols. (c,d) Local density n_j, and (e,f) local magnetization m_j, for 11 equidistant fields from $\widetilde{B} = 0$ (blue) to $\widetilde{B} = 10\widetilde{B}_*$ (red), for the KQD and QPC potentials shown by solid lines in (a,b), respectively. (g,h) The local spin susceptibility χ_j for the KQD and QPC potentials shown by solid lines in (a),(b), respectively; the spatial structure of χ_j reflects that of m_j for small fields, likewise showing strongly-enhanced standing-wave oscillations in the CCR. (i-l) *Geometric crossovers:* χ_j is shown as a function of site j and $\widetilde{V}_{\mathrm{c}} = \widetilde{V}_{j=0}$ for four trajectories in the $(\widetilde{V}_{\mathrm{c}}, \widetilde{V}_{\mathrm{s}})$ plane, drawn color-coded in panel (m) [where colored symbols mark $\widetilde{V}_{\mathrm{c}}$- and $\widetilde{V}_{\mathrm{s}}$-values used in (a-l)]. Each panel (i-l) also shows $g(\widetilde{V}_{\mathrm{c}})$ for three fields ($\widetilde{B}/\widetilde{B}_*^{\min} = 0$, ~ 1, and $\gg 1$), to indicate the $\widetilde{V}_{\mathrm{c}}$-dependence of the magnetoconductance; red dashed lines mark the gate voltage, $\widetilde{V}_{\mathrm{c}0}$, where $\widetilde{B}_*$ takes its minimal value, $\widetilde{B}_*^{\min}$. (i) A QD being charged starting from 9 electrons (up left) to 13 electrons (down right), showing Coulomb blockade oscillations, (j) a QPC tuned from pinchoff to an open channel, (k) a crossover from a QPC to a KQD with 11 electrons, and (l) a crossover from a QPC to an even QD (EQD) charged by 10 electrons.

bors a discrete, localized spin-$\frac{1}{2}$ local moment, a QPC does not, as argued above, and further elaborated in the next section. From the perspective of the quasi-bound state scenario of Meir and collaborators, this could be phrased by saying that the conditions for the formation of a quasi-bound state cease to exist at large fields. The differences between the 0.7-anomaly and the Kondo effect are therefore evident in deviations of the QPC conductance from the Kondo predictions as T or B approaches or exceeds T_* or B_*, as already detailed in Ref. 14.

VI. MAGNETIZATION

In the previous section we have argued that the local magnetization m_j of a KQD and QPC evolve in strikingly different ways when $\widetilde{B}$ increases far beyond $\widetilde{B}_*$ [Figures 7(e) and 7(f)]: For a KQD, m_j^{KQD} saturates in magnitude, indicating that a discrete spin is being polarized. In contrast, for a QPC, m_j^{QPC} shows no signs of saturation, indicating that a smooth redistribution of charge and spin occurs during the polarization of the CCR. (Microscopically, this originates from differences in the ω-dependence of the LDOS of a QD and QPC, illustrated in Fig. 3 and discussed in detail in Sec. S-4.E of Ref. 14.) To substantiate our conclusion that a QPC does not harbor a discrete, localized spin-$\frac{1}{2}$ local moment, in contrast to a KQD, we present in this section additional fRG results on the evolution with $\widetilde{B}$ of the magnetization, conductance and charge of a KQD and QPC. For comparison, we also include fRG results for the single-impurity Anderson model (SIAM), the paradigmatic model for local moment formation in metals.[38] It describes a local level with energy $\varepsilon_d = \widetilde{V}_{\mathrm{c}}$ and Coulomb repulsion U for double occupancy, that aquires a level width Γ via hybridization with a conduction band of width D (with $D \gg U \gg \Gamma$).

For this purpose, we define the total charge and magnetization in the "inner" region of the CCR by

$$n_{\mathrm{inner}} = \sum_{|j| \le j_{\mathrm{inner}}} n_j \;, \quad m_{\mathrm{inner}} = \sum_{|j| \le j_{\mathrm{inner}}} m_j \;. \qquad (11)$$

For the KQD geometry, we choose the inner region to lie

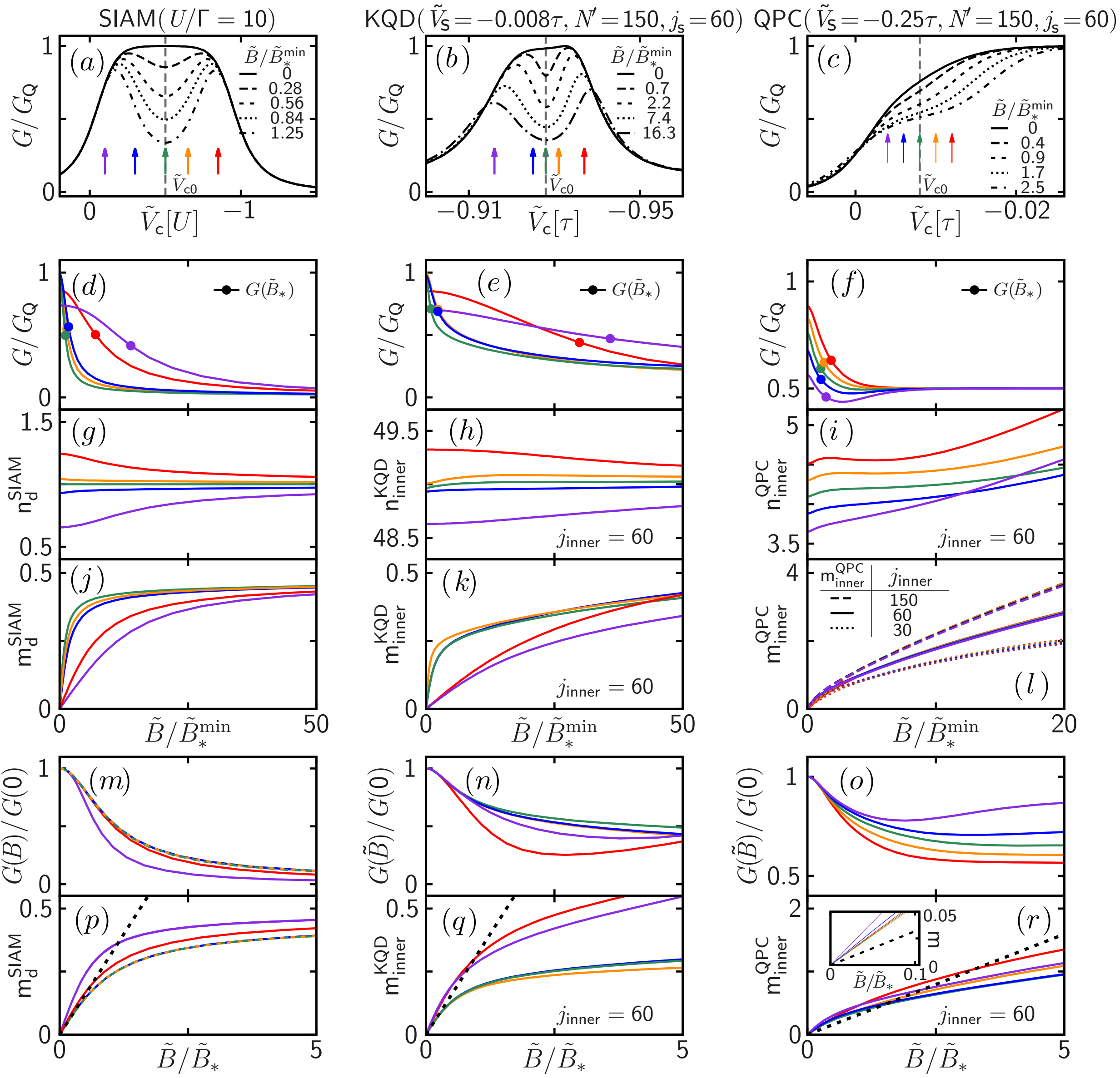

Figure 8. fRG results (with vertex flow included) for the large-field behavior of the single-impurity Anderson model (SIAM, left column), a KQD (middle column, same parameters as Fig. 6(c), and a QPC (right column, same parameters as Fig. 6(d)). (a-c) The conductance G, plotted as function of $\widetilde{V}_c$, for five values of magnetic field; vertical dashed lines indicate the $\widetilde{V}_c$-value where $\widetilde{B}_*$ is minimal, $\widetilde{B}_*(\widetilde{V}_{c0}) = \widetilde{B}_*^{\min}$. (d-f) The conductance, (g-i) the total charge n_{inner}, and (j-k) the total magnetization m_{inner} in the CCR's inner region, comprising sites $|j| \le j_{\text{inner}}$ [Eq. (11)]. These are plotted as functions of field $\widetilde{B}/\widetilde{B}_*^{\min}$, for five different values of gate voltage $\widetilde{V}_c$, indicated by arrows of corresponding color in (a-c). (For the SIAM, the CCR consists of just a single central site, which constitutes the local d-level of that model, thus $n_{\text{inner}}^{\text{SIAM}} = n_d^{\text{SIAM}}$ and $m_{\text{inner}}^{\text{SIAM}} = m_d^{\text{SIAM}}$.) (m-o) and (p-r) Same conductance and magnetization data as in (d-f) and (j-l), respectively, but plotted vs. $\widetilde{B}/\widetilde{B}_*$; black dotted lines in (p-r) have slope $1/\pi$, indicating the small-field limiting behavior $m_{\text{inner}} = \widetilde{B}/(\pi\widetilde{B}_*)$ expected in the Kondo limit [cf. Eq. (8)]. The inset of (r) shows a zoom of the limiting behavior for $\widetilde{B}/\widetilde{B}_* \to 0$.

between the two maxima of the KQD potential, say at $\pm j_{\text{inner}}^{\text{KQD}}$. The remaining CCR sites with $j_{\text{inner}}^{\text{KQD}} < |j| \le N'$ are excluded, since they lie outside the dot, in the CCR barrier's outer flanks. Although the contribution of each such site to the CCR's total charge or magnetization is small, their total contribution is proportional to the length of the outer flanks, i.e. extensive, and hence should be excluded when discussing intensive dot properties. For the QPC geometry, in contrast, there is no natural separation between an inner region and the barrier's outer flanks. We will show results for inner regions of three different sizes below: for fixed $N' = 150$, we choose $j^{\rm QPC}_{\rm inner} = 150$, 60 and 30 (they all yield qualitatively similar results).

Fig. 8 compares the large-field behavior of the conductance, charge and magnetization of a KQD (middle column) and a QPC (right column). The left column shows corresponding quantities for the SIAM, which corresponds to a CCR with just a single site. We denote its local charge and magnetization by $n_{\rm d}^{\rm SIAM}$ and $m_{\rm d}^{\rm SIAM}$, respectively.

Panels (a-c) of Fig. 8 show the conductance as function of $\widetilde{V}_{\rm c}$ for SIAM, KQD and QPC, respectively, for five magnetic fields, specified in units of the $\widetilde{V}_{\rm c}$-independent reference field $\widetilde{B}_*^{\rm min} = \min[\widetilde{B}_*(\widetilde{V}_{\rm c})]$ [cf. Figs. 6(c,d)]. Colored arrows indicate five fixed $\widetilde{V}_{\rm c}$-values used to calculate the corresponding curves in all other panels. These show the conductance (panels d-f), charge (panels g-i) and magnetization (panels j-l) as functions of $\widetilde{B}/\widetilde{B}_*^{\rm min}$, as well as the scaled conductance $G(\widetilde{B})/G(0)$ (panels m-o) and magnetization (panels p-r) as functions of $\widetilde{B}/\widetilde{B}_*$. For SIAM and KQD, the blue, green and orange curves correspond to the local-moment regime [$G/G_{\rm Q} \simeq 1$ in (a,b), local charge close to 1 in (g,h)], while the red and purple curves correspond to the mixed-valence regime.

Upon comparing the three columns, we note the following salient features: (i) For all five $\widetilde{V}_{\rm c}$-values, the charges $n_{\rm d}^{\rm SIAM}$, $n_{\rm inner}^{\rm KQD}$ and $n_{\rm inner}^{\rm QPC}$ all depend only weakly on $\widetilde{B}$ (g-i). In the small-field limit, the conductance and magnetization shows Fermi-liquid behavior in all cases: (ii) the conductance decreases quadratically with field (d-f), and (iii) the magnetization increases linearly with field (g-i). (iv) At intermediate fields both conductance (d-f) and magnetization (g-i) go through a crossover, during which their slopes decrease markedly in magnitude. (v) In the large-field regime beyond this crossover, the behavior of the SIAM and KQD differs strikingly from that of the QPC: SIAM and KQD exhibit behavior characteristic of a spin-$\frac{1}{2}$ local moment, whereas the QPC becomes spin-polarized with a magnetization much larger than $\frac{1}{2}$.

To be specific, the evidence for this interpretation of the large-field regime is as follows: (vi) For the SIAM, the plateau in $m_{\rm d}^{\rm SIAM}$ saturates towards 0.5 (j); this saturation is the hallmark of a polarized spin-$\frac{1}{2}$ local moment. (vii) At the same time, the conductance G continues to decrease with field, albeit very slowly (d). (For the SIAM this decrease is known to be logarithmic, $\sim 1/\ln(\widetilde{B}/\widetilde{B}_*)$, but fRG is not sufficiently accurate to reproduce purely logarithmic behavior.) The KQD exhibits qualitatively similar features, though with some quantitative differences: (viii) The plateau in $m_{\rm inner}^{\rm KQD}$ is fairly flat, too (k), although it does not truly saturate but instead slowly increases past 0.5 for sufficiently large fields. This reflects the fact that the KQD in Fig. 8 harbors not only one spin-$\frac{1}{2}$ local moment but many additional occupied levels ($n_{\rm inner} \simeq 50$); some of these begin to contribute to the magnetization when $\widetilde{B}$ becomes a sufficiently large fraction of the dot level spacing. (ix) The KQD conductance continues to decrease with field (e), but less slowly so than for the SIAM (d), due to contributions from the additional levels.

The above large-field features of the SIAM and a KQD stand in stark constrast to those of a QPC: (x) its magnetization continues to increase with field without any saturation (l) [the slope depends on the width of the inner region: the larger $j_{\rm inner}$, the larger the slope]; and (xi) the conductance fully saturates at $G = 0.5 G_{\rm Q}$ (f), corresponding to a spin-split conductance plateau. The absence of any saturation in the magnetization reflects the fact that the QPC barrier lacks the isolated "inner region" of a KQD. Instead, the CCR barrier is made up entirely of outer flanks, along which electrons of both spin species can freely move. As the magnetic field is increased, the magnetization of the QPC is thus free to increase without any intrinsic limit (in contrast to the case of a KQD). The spin-split conductance plateau sets in once the LDOS at the chemical potential is fully spin-polarized.

These differences between SIAM and KQD on the one hand and QPC on the other of course imply different behaviors when the conductance and magnetization are plotted versus $\widetilde{B}/\widetilde{B}_*$: (xii) For the local-moment curves (blue, green, orange) of the SIAM, the scaled conductance $G(\widetilde{B})/G(0)$ (m) and the magnetization (p) both collapse onto a single scaling curve when plotted versus $\widetilde{B}/\widetilde{B}_*$. (xiii) The same is true approximately for the KQD's conductance (n) and magnetization (q), though the collapse is not as perfect. Thus, for the SIAM and KQD, the $\widetilde{V}_{\rm c}$-*dependent* scale $\widetilde{B}_*$ governs both the small- *and* large-field behavior of the magnetization and conductance. (xiv) This is not the case for the QPC, whose conductance (o) and magnetization (r) do *not* show a collapse onto a single curve when plotted versus $\widetilde{B}/\widetilde{B}_*$. (xv) Instead, the large-field behavior of the magnetization is governed by a $\widetilde{V}_{\rm c}$-*in*dependent scale: when the $m_{\rm inner}^{\rm QPC}$-curves are plotted vs. $\widetilde{B}/\widetilde{B}_*^{\rm min}$, they all overlap (l), except in the limit $\widetilde{B} \ll \widetilde{B}_*^{\rm min}$ [not resolved in (l)]. Also, (xvi) the field scale at which the conductance saturates at $G = 0.5 G_{\rm Q}$ does not depend on $\widetilde{B}_*$ at all, but instead grows linearly with decreasing $\widetilde{V}_{\rm c}$ (f).

To summarize: when the SIAM and the KQD are tuned into their local moment regime, their conductance and magnetization exhibit the expected crossover, governed only by a single energy scale $\widetilde{B}_*(\widetilde{V}_{\rm c})$, between a Fermi-liquid and a local-moment fixed point that is characteristic of the Kondo effect, (xii,xiii). The QPC conductance and magnetization, however, do not, (xiv-xvi). This is an example, therefore, where the analogy between Kondo effect and 0.7-anomaly breaks down – at large fields, they are distinct physical effects.

The lack of local-moment behavior for the QPC magnetization at large fields is not surprising, given the open nature of the QPC geometry. Nevertheless – and this *is* surprising and remarkable – (xvii) the small-field limit ($\widetilde{B} \ll \widetilde{B}_*$) of the magnetization is governed by $\widetilde{B}_*$ not only for the SIAM and KQD in the local moment regime, but also for the QPC when $\widetilde{V}_c < \widetilde{V}_{c0}$: For all these, the *linear* response of the magnetization to field is proportional to $1/\widetilde{B}_*$, meaning that curves of m_{inner} vs. $\widetilde{B}/\widetilde{B}_*$ for different $\widetilde{V}_c$-values all have the same slope as $\widetilde{B}/\widetilde{B}_* \to 0$. [This is illustrated by the blue, green, orange lines in panels (p) and (q), which all have slope $1/\pi$ (dashed black line), in accord with Eq. (8); and by the green, orange and red curves in the inset of panel (r), which have mutually similar slopes, though these do not equal $1/\pi$ (dashed black line).] The fact that the small-field limit of the QPC magnetization is governed by $\widetilde{B}_*$, (xvii) has far-reaching consequences, in that it underlies the low-energy Fermi-liquid behavior of the QPC conductance mentioned in Sec. IV C above.

We end this subsection with a parenthetic remark: As an alternative to Eq. (11), outer flank contributions to the magnetization can also be eliminated by considering

$$m_{\text{exc}}(\widetilde{V}_c) = \sum_{j \in \text{CCR}} m_j(\widetilde{V}_c) - \sum_{j \in \text{CCR}} m_j(\widetilde{V}_c^{\text{ref}}) \, , \tag{12}$$

the excess magnetization of the CCR at central gate voltage $\widetilde{V}_c$ relative to its magnetization at a suitably chosen reference voltage $\widetilde{V}_c^{\text{ref}}$ [chosen to define an even QD (EQD) in an Coulomb blockade value adjacent to the odd KQD, or an open QPC, as discussed in conjunction with Eq. (9)]. Indeed, for small fields ($\widetilde{B}/\widetilde{B}_* \ll 1$) one finds $m_{\text{exc}}(\widetilde{B}) \simeq m_{\text{inner}}(\widetilde{B})$ when choosing $j_{\text{inner}} = j_s$, and the excess susceptibility defined in Eq. (9) corresponds to $\chi_{\text{exc}} = (\partial m_{\text{exc}}/\partial \widetilde{B})_{\widetilde{B}=0}$. However, for the large-field regime of interest in the present subsection, the subtraction scheme of Eq. (12) is not convenient, because at sufficiently large fields the second term becomes comparable in size to the first, causing m_{exc} to decrease.

VII. SUMMARY AND OUTLOOK

In Ref. 14, we have argued that the .7KS, i. e. the observed similarities in the low-energy behavior of the conductance for 0.7-anomaly and the Kondo effect, originate from geometry-induced, interaction-enhanced local spin fluctuations, that are present both in a QPC and a KQD. The goal of the present work has been to offer additional evidence for this conclusion, by studying the geometric crossover between a QD and a QPC, both experimentally and theoretically, focusing on the magnetic field dependence at low temperatures. Our experimental and numerical results were found to be in good qualitative agreement. This shows that the 1D-model with short-range interactions introduced here, together with the fRG approach used to treat interactions, succeeds in capturing the essential physics of the Kondo effect, the 0.7-anomaly and the geometric crossover between them.

Our initial motivation for studying the geometric crossover was the expectation that this would allow us to observe an adiabatic transition from Kondo correlations present in a KQD to the correlations present in a QPC showing the 0.7-anomaly. Indeed, this idea turned out to be fruitful: our fRG results show that an anomalously strong negative magnetoconductance, one of the key features of the .7KS, always goes hand in hand with strongly enhanced local spin fluctuations.

The spatial structure of the local spin fluctuations is inherited from that of the non-interacting local density of states at the chemical potential, and enhanced by interactions in Stoner-type fashion. Roughly speaking, local spin fluctuations are strong in those regions of space where the electrons near the chemical potential are "slow". For a parabolic QPC, slow electrons are found in the CCR when the barrier top is just below the chemical potential, whereas for a KQD the odd electron is slow simply because it is really trapped inside the dot. The difference between these two situations does not matter much for low energies ($\ll |\widetilde{B}_*|$), thus both show behavior characteristic of a Nozières-Fermi liquid with local interactions. (These local interactions are the reason why the .7KS also comprises similar temperature and source-drain voltage dependences for a KQD and a QPC, see Ref. 14 for a more detailed discussion of this point.) The difference does matter, though, for high energies, where we find no indications that a parabolic QPC harbors a localized state, and where indeed no .7KS is observed.

One of the lessons learnt from Figs. 7(i-l) is that the presence or absence of the two crucial properties discussed above, namely a strong negative magnetoconductance and strong local spin fluctuations, depends very much on the trajectory followed in the $(\widetilde{V}_c, \widetilde{V}_s)$ plane during the QD-QPC crossover. For example, for the trajectory studied in Fig. 7(k), *both* these features disappear in the intermediate regime between the KQD and the QPC, because there the barrier top is so far below the chemical potential that the system is essentially an open channel, with $g \simeq 1$.

It is, of course, possible to also implement QD-QPC crossover trajectories during which the barrier top always remains close to the chemical potential. Suppose that such a trajectory includes a wide, flat barrier top, such as that shown in Fig. 3(b). When this barrier top is just below the chemical potential, the electron density will be low throughout the wide barrier region, implying that interaction effects will become very strong there. This regime is conducive to the formation of a Wigner crystal, so that the conductance can be expected to show behavior different from that of a "standard" 0.7-anomaly. Indeed two recent experimental papers have studied this regime[32,33] and reported interesting differences from standard 0.7-phenomenology (such as a zero-bias peak that splits into two or even three subpeaks as the barrier width is varied).

In our own detailed studies of QPCs, both in Ref. 14 and here, we have so far purposefully chosen to avoid the regime of wide, flat barrier tops. Instead, we have focussed on parabolic barrier tops and demonstrated that these were sufficient to explain numerous features of the standard 0.7-anomaly. Nevertheless, it would be very interesting to systematically study the crossover from parabolic to wide, flat barrier tops. The latter lead to Fabry-Perot resonances even in the absence of interactions (as argued in Sec. III C), and the way in which Fabry-Perot structures in the density of states are modified or enhanced by interactions has not been explored systematically yet.

In the limit of a very wide and flat barrier, the CCR would represent a long 1D wire of low density, behaving as a spin-incoherent Luttinger liquid[39]. Since interaction effects become ever more important as the density decreases, fRG will at some point become unsuitable for a flat barrier top when either its width is made sufficiently wide or its top approaches the chemical potential sufficiently closely from below. However, more powerful numerical methods, such as the density matrix renormalization group, could be used to study such situations.

ACKNOWLEDGEMENTS

We thank B. Altshuler, P. Brouwer, R. Egger, J. Folk, L. Glazman, V. Golovach, A. Högele, Y. Imry, M. Kiselev, D. Logan, D. Loss, C. Marcus, Y. Meir, M. Pustilnik, A. Rosch, H. Sellier, K. Schönhammer, B. Spivak and A. Yacoby for stimulating discussions, and in particular S. Andergassen, C. Honerkamp, S. Jakobs, C. Karrasch, V. Meden, M. Pletyukhov and H. Schoeller for fRG-related help and advice. We also thank Christoph Hohmann for producing Figs. 1(b),(c). We acknowledge support from the DFG via SFB-631, SFB-TR12, De730/3-2, De730/4-1, De730/4-2, De730/4-3, HO 4687/1-3, LU819/4-1, and the Cluster of Excellence *Nanosystems Initiative Munich*, and the National Science Foundation under Grant No. NSF PHY05-51164. S.L. acknowledges support via a Heisenberg fellowship of the DFG.

Appendix A: Evolution of $g(\widetilde{V}_\mathrm{c}, \widetilde{V}_\mathrm{s})$ with $\widetilde{B}$ (movie)

In Sec. IV A, we showed fRG results (without vertex flow) for the QD-to-QPC crossover of the conductance $g(\widetilde{V}_\mathrm{c}, \widetilde{V}_\mathrm{s})$ as function of central and side gate voltage, for three values of magnetic field [Figs. 5(a-c)]. Its continuous evolution with $\widetilde{B}$, again calculated by fRG without vertex flow, can be viewed as a QuickTimas a separate figuras a separate figure Movie, see the file "fRG.mov" in the Supplementary Material. The movie shows simultaneously the evolution with $\widetilde{B}$ of three data sets: The central panel gives the conductance $g(\widetilde{V}_\mathrm{c}, \widetilde{V}_\mathrm{s})$ in a three-dimensional plot formatted in the same way as Figs. 5(a-c). The top left panel gives the frontmost curve of the central panel, $g(\widetilde{V}_\mathrm{c}, \widetilde{V}_\mathrm{s} = 0.018\tau)$, representing the pure QD regime; and the top right panel gives its backmost curve $g(\widetilde{V}_\mathrm{c}, \widetilde{V}_\mathrm{s} = 1.9\tau)$, representing the pure QPC regime. A moving horizontal line in the scale bar on the right hand side indicates the evolution of $\widetilde{B}$, and whenever it passes one of a selected set of $\widetilde{B}$ values, that value is indicated by a frozen horizontal line, while two curves of matching color freeze in the top left and top right panels.

The initial evolution for small fields ($\widetilde{B} \lesssim 2 \times 10^{-4}\tau$) shows how the Kondo plateaus of the first few Kondo valleys, whose typical Kondo temperatures increase with dot occupancy n, successively get suppressed as $\widetilde{B}$ increases [see top left panel]. For larger fields ($\widetilde{B} \gtrsim 2 \times 10^{-4}$), the conductance in the QPC regime also begins to develop a shoulder [see top right panel], which evolves (beyond $\widetilde{B} \gtrsim 3 \times 10^{-3}$) into an ever more pronounced double step. Note that the scale bar changes from logarithmic to linear at $\widetilde{B} \simeq \times 10^{-4}$, since the $\widetilde{B}$-dependence of the conductance at large fields is logarithmic for the Kondo effect, but linear for the 0.7-anomaly. (This is another indication that the latter does not involve local-moment physics at large fields.)

For large magnetic fields (beyond about $\widetilde{B} \gtrsim 10^{-4}$) the movie shows several sharp conductance resonances or peaks of height $g \simeq 1$, which move in the direction of decreasing $\widetilde{V}_\mathrm{c}$ (toward the right) with increasing magnetic field. An example of such a resonance, occuring for $\widetilde{B} = 1.4 \cdot 10^{-3}\tau$ and $\widetilde{V}_\mathrm{s} = 0.018\tau$ at $\widetilde{V}_\mathrm{c} = 0.01303\tau$, is shown in Fig. 9. We will call these "spin-flip resonances", since their origin lies in spin-flip transitions on the QD; in fact, they can be viewed as generalized versions of the singlet-triplet Kondo effect discussed in the literature (see Ref. 40, and references therein). Although the spin-flip resonances have no relevance for the 0.7-anomaly, they are interesting in their own right, hence we now explain their origin in some more detail.

With increasing magnetic field, the total spin of a Coulomb-blockaded QD will increase in discrete steps. This has been discussed in the past in terms of the Fock-Darwin spectrum of a QD, see e. g. Fig. 5 in Ref. 41. Such a step involves adding a spin-up electron to the lowest-lying empty dot level while removing a spin-down electron from the highest-lying doubly-occupied one, which occurs whenever the gain in Zeeman energy outweights the cost in kinetic energy. The latter depends on the QD's level spacing, and hence on $\widetilde{V}_\mathrm{c}$ and $\widetilde{V}_\mathrm{s}$. For given $\widetilde{B}$ and $\widetilde{V}_\mathrm{s}$, such a transition can thus also be induced changing $\widetilde{V}_\mathrm{c}$. To be specific, decreasing $\widetilde{V}_\mathrm{c}$ (as in Fig. 9) increases the level spacing and causes a spin-decreasing spin-flip transition, say from the dot configuration $(n_\uparrow^\mathrm{QD}, n_\downarrow^\mathrm{QD})$ to $(n_\uparrow^\mathrm{QD} - 1, n_\downarrow^\mathrm{QD} + 1)$. Precisely *at* the spin-flip transition, say for $\widetilde{V}_\mathrm{c} = \widetilde{V}_\mathrm{c}^\mathrm{flip}$, these two configurations are energetically degenerate, so that Kondo-like correlations between the QD and the leads can develop, which cause the conductance g to reach its maximum possible value, namely 1.

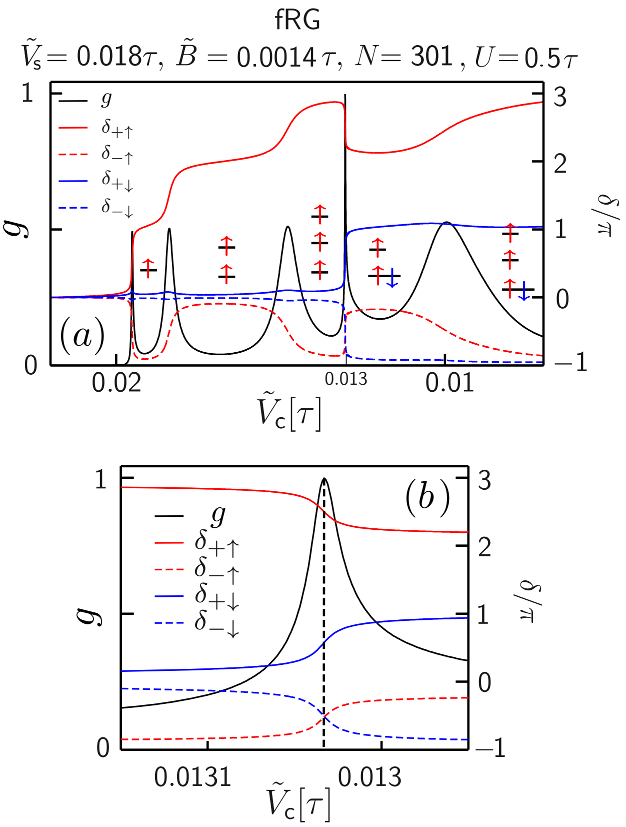

Figure 9. Example of a spin-flip resonance in the conductance of a QD. (a) Conductance (solid black line) and phases $\delta_{\sigma,+}/\pi = n_\sigma^{\mathrm{QD}}$ (solid lines) and $\delta_{\sigma,-}/\pi$ (dashed lines), for $\sigma = \uparrow$ (red lines) and $\sigma = \downarrow$ (blue lines), all calculated using fRG. The phases are all set to 0 at a reference voltage $\widetilde{V}_c^{\mathrm{r}} = 0.022$ so large that the CCR no longer represents a QD, but a pinched-off QPC, with $g = 0$ and $n_\sigma^{\mathrm{QD}} = 0$. As $\widetilde{V}_c$ decreases below 0.02τ where the dot is still empty, $n_\uparrow^{\mathrm{QD}}$ (red solid line) initially increases in roughly integer steps as the dot is being charged, while $n_\downarrow^{\mathrm{QD}}$ (blue solid line) stays essentially zero, because the fixed field $\widetilde{B}$ is large. However at $\widetilde{V}_c^{\mathrm{flip}} = 0.01303\tau$ (vertical dashed line) a spin-flip transition occurs, where $(n_\uparrow^{\mathrm{QD}}, n_\downarrow^{\mathrm{QD}})$ changes from $\simeq (3,0)$ to $\simeq (2,1)$, and the conductance shows a spin-flip resonance of height 1. (b) Zoom-in of the same data to the vicinity of the spin-flip transition at $\widetilde{V}_c^{\mathrm{flip}}$.

In the movie the heights of these spin-flip resonances typically do not reach unity, but rather fluctuate as a function of magnetic field. This is a numerical artefact caused by the insufficient resolution of $\widetilde{V}_c$ used when making the movie. The numerical effort that would have been needed to resolve these type of resonances in the movie would have been very high, since they are typically very narrow. (We note also that at finite temperature, the minimum width of these resonances would be set by temperature.)

The fact that $g = 1$ at a spin-flip resonance can be understood, following Ref. 40, using elementary concepts from the Fermi-liquid description of zero-temperature transport through a multi-level quantum dot. (For present purposes, we call the entire CCR a "QD"). Such a description is formulated in terms of the eigenphases, say $\delta_{\sigma,1}$ and $\delta_{\sigma,2}$, of the scattering matrix of the QD. (A detailed discussion of how these eigenphases can be calculated using fRG is given in our follow-up paper[42].) These eigenphases are defined w. r. t. a reference gate voltage $\widetilde{V}_c^{\mathrm{r}}$, at which we set $\delta_{\sigma,1} = \delta_{\sigma,2} = 0$. The even and odd linear combinations of these eigenphases,

$$\delta_{\sigma,\pm} = \delta_{\sigma,1} \pm \delta_{\sigma,2} \ , \tag{A1}$$

determine, respectively, the quantum dot's charge n^{QD} and conductance g. The charge n^{QD}, measured w. r. t. the reference point, is given by Friedel's sum rule:

$$n^{\mathrm{QD}} = n_\uparrow^{\mathrm{QD}} + n_\downarrow^{\mathrm{QD}} = \frac{1}{\pi}\left(\delta_{\uparrow,+} + \delta_{\downarrow,+}\right) . \tag{A2}$$

The conductance is given by the relation

$$g = \frac{1}{2}\sum_\sigma \sin^2 \delta_{\sigma,-} \ , \tag{A3}$$

valid for left-right symmetric couplings between QD and leads, as in our model. We choose $\widetilde{V}_c^{\mathrm{r}}$ to lie near the spin-flip transition, but sufficiently different from $\widetilde{V}_c^{\mathrm{flip}}$ that the conductance and the phases determining it are small at $\widetilde{V}_c^{\mathrm{r}}$, i. e. $g \ll 1$ and $|\delta_{\sigma,-}| \ll \pi/2$.

Now, when $\widetilde{V}_c$ is tuned through the spin-flip transition, the $\widetilde{V}_c$-induced changes in $\delta_{\sigma,-}$ and n_σ^{QD} (w. r. t. to their values, namely 0, at the reference voltage $\widetilde{V}_c^{\mathrm{r}}$) are related by

$$\Delta\delta_{\sigma,-} \simeq \pi\Delta n_\sigma^{\mathrm{QD}} \ . \tag{A4}$$

This equation follows from two facts: first, one of the spin-dependent eigenphases of the scattering matrix, either $\delta_{\sigma,1}$ or $\delta_{\sigma,2}$, turns out to be essentially independent of $\widetilde{V}_c$ throughout a Coulomb-blockade valley, so that $|\Delta\delta_{\sigma,-}| = |\Delta\delta_{\sigma,+}|$ [by Eq. (A1)]; second, the Friedel sum rule implies that $\Delta\delta_{\sigma,+} = \pi\Delta n_\sigma^{\mathrm{QD}}$. Now, since the total dot charge $n^{\mathrm{QD}} = n_\uparrow^{\mathrm{QD}} + n_\downarrow^{\mathrm{QD}}$ is fixed within the Coulomb blockade valley, the spin-dependent dot occupancies change in equal but opposite manner as $\widetilde{V}_c$ is tuned through the spin-flip transition: $\Delta n_\uparrow^{\mathrm{QD}} \simeq -\Delta n_\downarrow^{\mathrm{QD}}$. By Eq. (A4), this implies that both $|\Delta\delta_{\uparrow,-}|$ and $|\Delta\delta_{\downarrow,-}|$ will pass through $\pi/2$ at essentially the same value of $\widetilde{V}_c$, causing the conductance g [Eq. (A3)] to show a resonance of height $\simeq 1$ there. The case shown Fig. 9 is an example of a so-called "triplet-singlet" transition[40], where the spin of the QD changes from 3/2 to 1/2 as $\widetilde{V}_c$ decreases past $\widetilde{V}_c^{\mathrm{r}}$.

[1] B. J. van Wees, H. van Houten, C. W. J. Beenakker, J. G. Williamson, L. P. Kouwenhoven, D. van der Marel, and C. T. Foxon, Phys. Rev. Lett. **60**, 848 (1988).

[2] D. A. Wharam, T. J. Thornton, R. Newbury, M. Pepper, H. Ahmed, J. E. F. Frost, D. G. Hasko, D. C. Peacock, D. A. Ritchie, and G. A. C. Jones, Journal of Physics C: Solid State Physics **21**, L209 (1988).

[3] M. Büttiker, Phys. Rev. B **41**, 7906 (1990).

[4] K. J. Thomas, J. T. Nicholls, M. Y. Simmons, M. Pepper, D. R. Mace, and D. A. Ritchie, Phys. Rev. Lett. **77**, 135 (1996).

[5] K. J. Thomas, J. T. Nicholls, N. J. Appleyard, M. Y. Simmons, M. Pepper, D. R. Mace, W. R. Tribe, and D. A. Ritchie, Phys. Rev. B **58**, 4846 (1998).

[6] D. J. Reilly, G. R. Facer, A. S. Dzurak, B. E. Kane, R. G. Clark, P. J. Stiles, R. G. Clark, A. R. Hamilton, J. L. O'Brien, N. E. Lumpkin, L. N. Pfeiffer, and K. W. West, Phys. Rev. B **63**, 121311(R) (2001).

[7] S. M. Cronenwett, H. J. Lynch, D. Goldhaber-Gordon, L. P. Kouwenhoven, C. M. Marcus, K. Hirose, N. S. Wingreen, and V. Umansky, Phys. Rev. Lett. **88**, 226805 (2002).

[8] Y. Chung, S. Jo, D.-I. Chang, H.-J. Lee, M. Zaffalon, V. Umansky, and M. Heiblum, Phys. Rev. B **76**, 035316 (2007).

[9] E. Koop, A. Lerescu, J. Liu, B. van Wees, D. Reuter, A.D.Wieck, and C. van der Wal, J. Supercond. Nov. Magn. **20**, 433 (2007).

[10] M. Pepper and J. Bird, J. Phys. Cond. Mat. **20**, 160301 (2008).

[11] S. Nakamura, M. Hashisaka, Y. Yamauchi, S. Kasai, T. Ono, and K. Kobayashi, Phys. Rev. B **79**, 201308 (2009).

[12] Y. Komijani, M. Csontos, I. Shorubalko, T. Ihn, K. Ensslin, Y. Meir, D. Reuter, and A. D. Wieck, Eur. Phys. Lett. **91**, 67010 (2010).

[13] L. W. Smith, A. R. Hamilton, K. J. Thomas, M. Pepper, I. Farrer, J. P. Griffiths, G. A. C. Jones, and D. A. Ritchie, Phys. Rev. Lett. **107**, 126801 (2011).

[14] F. Bauer, J. Heyder, E. Schubert, D. Borowsky, D. Taubert, B. Bruognolo, D. Schuh, W. Wegscheider, J. von Delft, and S. Ludwig, Nature **501**, 73 (2013).

[15] L. Glazman and M. Raikh, JETP Lett. **47**, 452 (1988).

[16] T. K. Ng and P. A. Lee, Phys. Rev. Lett. **61**, 1768 (1988).

[17] D. Goldhaber-Gordon, H. Shtrikman, D. Mahalu, D. Abusch-Magder, U. Meirav, and M. A. Kastner, Nature **391**, 156 (1998).

[18] S. M. Cronenwett, T. H. Oosterkamp, and L. P. Kouwenhoven, Science **281**, 540 (1998), http://www.sciencemag.org/cgi/reprint/281/5376/540.pdf.

[19] W. G. van der Wiel, S. D. Franceschi, T. Fujisawa, J. M. Elzerman, S. Tarucha, and L. P. Kouwenhoven, Science **289**, 2105 (2000), http://www.sciencemag.org/cgi/reprint/289/5487/2105.pdf.

[20] J. Nygard, D. H. Cobden, and P. E. Lindelof, Nature **408**, 342 (2000).

[21] P. Jarillo-Herrero, J. Kong, H. S. van der Zant, C. Dekker, L. P. Kouwenhoven, and S. De Franceschi, Nature **434**, 484 (2005).

[22] A. V. Kretinin, H. Shtrikman, D. Goldhaber-Gordon, M. Hanl, A. Weichselbaum, J. von Delft, T. A. Costi, and D. Mahalu, Phys. Rev. B **84**, 245316 (2011).

[23] Y. Meir, K. Hirose, and N. S. Wingreen, Phys. Rev. Lett. **89**, 196802 (2002).

[24] A. Golub, T. Aono, and Y. Meir, Phys. Rev. Lett. **97**, 186801 (2006).

[25] T. Rejec and Y. Meir, Nature **442**, 900 (2006).

[26] P. Nozières, J. Low Temp. Phys. **17**, 31 (1974).

[27] F. D. M. Haldane, Phys. Rev. Lett. **40**, 416 (1978).

[28] S. Andergassen, T. Enss, V. Meden, W. Metzner, U. Schollwöck, and K. Schönhammer, Phys. Rev. B **73**, 045125 (2006).

[29] C. Karrasch, T. Enss, and V. Meden, Phys. Rev. B **73**, 235337 (2006).

[30] W. Metzner, M. Salmhofer, C. Honerkamp, V. Meden, and K. Schönhammer, Rev. Mod. Phys. **84**, 299 (2012).

[31] F. Bauer, J. Heyder, and J. von Delft, Phys. Rev. B **89**, 045128 (2014).

[32] M. J. Iqbal, R. Levy, E. J. Koop, J. B. Dekker, J. P. de Jong, J. H. M. van der Velde, D. Reuter, A. D. Wieck, R. Aguado, Y. Meir, and C. H. van der Wal, Nature **501**, 79 (2013).

[33] B. Brun, F. Martins, S. Faniel, B. Hackens, G. Bachelier, A. Cavanna, C. Ulysse, A. Ouerghi, U. Gennser, D. Mailly, S. Huant, V. Bayot, M. Sanquer, and H. Sellier, Nature Comm. **5**, 4290 (2014).

[34] T. A. Costi, Phys. Rev. B **64**, 241310 (2001).

[35] L. Glazman and M. Pustilnik, in *Nanophysics: Coherence and Transport*, edited by H. Bouchiat and *et al.* (Elsevier, Amsterdam, 2005) pp. 427–478, cond-mat/0501007.

[36] D. M. Schröer, A. K. Hüttel, K. Eberl, S. Ludwig, M. N. Kiselev, and B. L. Altshuler, Phys. Rev. B **74**, 233301 (2006).

[37] S. Ihnatsenka and I. V. Zozoulenko, Phys. Rev. B **76**, 045338 (2007).

[38] P. W. Anderson, Phys. Rev. **124**, 41 (1961).

[39] K. A. Matveev, Phys. Rev. B **70**, 245319 (2004).

[40] M. Pustilnik, L. I. Glazman, and W. Hofstetter, Phys. Rev. B **68**, 161303 (2003).

[41] L. P. Kouwenhoven, D. G. Austing, and S. Tarucha, Reports on Progress in Physics **64**, 701 (2001).

[42] J. von Delft, F. Bauer, and J. Heyder, to be published (2014).

Chapter 6

fRG Approach for Inhomogeneous Interacting Fermi Systems

This chapter presents the paper "*Functional Renormalization Group Approach for Inhomogeneous Interacting Fermi Systems*", published in *Physical Review B* [Bauer et al. (2014)]. The work provides a detailed description of the coupled-ladder approximation (CLA) in position and frequency basis, an approximation scheme within the context of the functional renormalization group (fRG), which we have derived specifically to calculate physical properties of inhomogeneous interacting Fermi systems. Most importantly we used the CLA to calculate the dependence of both linear transport and local properties of our one-dimensional quantum point contact model (see Eq. (3.16) and Eq. (3.17)) on interaction strength and magnetic field [Bauer et al. (2013)] at zero temperature. The CLA allows for an accurate description of interactions up to "intermediate" strength, while featuring a reasonable and (by current standards) feasible numerical calculation time. The CLA presented in Bauer et al. (2014) extends the work by Karrasch et al. (2008), where the CLA is formulated in frequency space only.

As discussed in Sec. 3.3.2, the full two-particle vertex function γ_2 of our QPC model has $\mathcal{O}(N^4 \cdot N_f^3)$ independent variables, where N is the number of sites of the interacting region (CCR) and N_f is the number of discrete frequencies used in the numerics. In order to resolve the inhomogeneity of the potential with due accuracy one usually needs $N \sim 100$ sites. It turns out that a similar number is necessary to keep track of the frequency dependence, $N_f \sim 100$. These numbers are large enough to make it unfeasible (with modern computer power) to solve the full fRG flow-equation of the two-particle vertex, Eq. (3.21) (this is a problem of both memory and speed). Thus, one must choose an approximation scheme that reduces the number of independent variables of the two-particle vertex to a manageable amount, while still capturing the essentials of the underlying physics. The CLA meets this requirement by retaining the dominant second-order space and frequency structure of the three individual vertex channels (single diagrams of the r.h.s. of Eq. (3.21)) but discarding all additional minor dependencies: In a first step the channels are decoupled, resulting in three independent flow-equations for the individual vertex components, all depending on a single frequency and two space quantum numbers only ($\mathcal{O}(N^2 \cdot N_f)$). A subsequent static and space-diagonal inter-channel feedback allows for a coupling of these contributions without generating additional variables. The consequence is a drastic reduction in calculation time. Importantly, the CLA is exact to second order, which includes the leading frequency-dependence of the two-particle vertex. It sums up Hartree contributions to infinite order and treats all random phase approximation (RPA) contributions of the two-particle vertex on equal footing.

We test the reliability of the CLA for our 1D model of a QPC using results for the linear conductance. We find that the CLA yields reliable results up to interaction strength of $U \sim 3.6/(\Omega_x l_x)$ (compare

Eq. (3.5)), even if we apply a static version of the CLA, which fully neglects the frequency dependence of the vertex functions.

Finally, we show how the fRG flow equation of the self energy provides a simple and efficient way to calculate response quantities in the presence of interactions, exemplarily presenting calculations for the spin susceptibility. A similar approach is used in Heyder (2014) (chapter 8), where we calculate the linear conductance formula of Oguri (2001) by treating the source-drain voltage as fRG flow-parameter.

Currently, we are working on setting up the CLA for longer-ranged interactions as well. This increases the number of independent variables within the CLA to $\mathcal{O}(N^2 L^2 N_f)$, where L defines the range of interactions.

Functional renormalization group approach for inhomogeneous interacting Fermi systems

Florian Bauer, Jan Heyder, and Jan von Delft
Arnold Sommerfeld Center for Theoretical Physics and Center for NanoScience, Ludwig-Maximilians-Universität München,
Theresienstrasse 37, D-80333 München, Germany

(Received 15 November 2013; revised manuscript received 17 December 2013; published 21 January 2014)

The functional renormalization group (fRG) approach has the property that, in general, the flow equation for the two-particle vertex generates $\mathcal{O}(N^4)$ independent variables, where N is the number of interacting states (e.g., sites of a real-space discretization). In order to include the flow equation for the two-particle vertex, one needs to make further approximations if N becomes too large. We present such an approximation scheme, called the coupled-ladder approximation, for the special case of an onsite interaction. Like the generic third-order-truncated fRG, the coupled-ladder approximation is exact to second order and is closely related to a simultaneous treatment of the random phase approximation in all channels, i.e., summing up parquet-type diagrams. The scheme is applied to a one-dimensional model describing a quantum point contact.

DOI: 10.1103/PhysRevB.89.045128 PACS number(s): 71.10.−w, 05.10.Cc, 05.60.Gg, 12.38.Bx

I. INTRODUCTION

The calculation of properties of an inhomogeneous interacting quantum system requires adequate care regarding a proper description of its spatial structure: for a lattice model, the resolution of a potential landscape, without generating additional finite-size effects, typically requires an extension of $\sim 10^2$ sites per spatial dimension. If, in addition, the strength of interactions can not be regarded as "weak," a reasonable approximation scheme must involve detailed information about higher-order correlations. This usually demands a huge effort for modern computers, both in memory and speed. Thus, for a system with nontrivial spatial structure, any approximation scheme necessarily involves a tradeoff between computational feasibility and accuracy.

In Ref. [1], we introduced such a scheme, both reasonably fast and accurate up to intermediate interaction strength, within the framework of the one-particle-irreducible version of the functional renormalization group (fRG) [2–10]. The goal of this paper is to supply a detailed description of this approximation scheme, called the coupled-ladder approximation (CLA), which is implemented within the context of generic, third-order-truncated fRG. In the latter, the flow of the three-particle vertex is set to zero, while the flow equation of the two-particle vertex (which we will call "vertex flow" in the following) is fully incorporated. This vertex flow has to be incorporated if interactions can not be considered small. In general, this constitutes a computational challenge since the vertex generated by this flow involves a large number $\mathcal{O}(N^4)$ of independent functions, each depending on three frequencies, where N is the number of sites of the interacting region. As a result, the flow equations involve $\mathcal{O}(N^4 N_\mathrm{f}^3)$ independent variables, where N_f is the number of discrete points per frequency used in the numerics. Previous schemes that included the vertex flow for models with large N made use of an additional symmetry, e.g., Refs. [5,6] described systems with a weak spatial inhomogeneity (either changing adiabatically with position, or confined to a small region), which could be treated as a perturbation, so that its feedback to the vertex could be neglected. The resulting equations for the vertex were solved in the momentum basis, exploiting the fact that the single-particle eigenstates could approximately be represented by plane waves. However, this is not possible for models with strong inhomogeneities. Our CLA scheme was developed to include the vertex flow for such models. It extends the idea of Refs. [7,11], where the CLA was introduced to parametrize the frequency dependence of the vertex for the single-impurity Anderson model, i.e., $N = 1$, which reduces the number of independent variables for that model to $\mathcal{O}(N_\mathrm{f})$. We show that the CLA can be applied to parametrize the spatial dependence of the vertex for models with a purely local interaction. The number of independent variables that represent the spatial dependence of the vertex then reduces to $\mathcal{O}(N^2)$, and the total number of independent variables representing the vertex to $\mathcal{O}(N^2 N_\mathrm{f})$. The CLA scheme is exact to second order [12,13] and effectively sums up diagrams of the random phase approximation (RPA) of all three interaction channels.

To illustrate the capabilities of our CLA scheme, we apply it, as in Ref. [1], to a one-dimensional chain modeling the lowest submode of a quantum point contact (QPC), a short constriction that allows transport only in one dimension. Its conductance is famously quantized [14–16] in units of $G_Q = 2e^2/h$. In addition to this quantization, measured conductance curves show a shoulder at around $0.7G_Q$. In this regime, quantities such as electrical and thermal conductance, noise, and thermopower have anomalous behavior [17–19]. These phenomena are collectively known as the "0.7 anomaly" in QPCs.

In Ref. [1], we showed that the 0.7 anomaly is reproduced by a one-dimensional model with a parabolic potential barrier and a short-ranged Coulomb interaction. We presented a detailed microscopic picture that explained the physical mechanism which causes the anomalous behavior. Its origin is a smeared van Hove singularity in the density of states (DOS) just above the band bottom which enhances effects of interaction causing an enhanced backscattering. We presented detailed results for the conductance at zero temperature, obtained using fRG in the CLA. These numerical data were in good qualitative agreement with our experimental measurements and showed that the model reproduces the phenomenology of the 0.7 anomaly. In this paper, we set forth and examine the approximation scheme in detail. We present additional numerical data to verify the reliability of the method for the case where it is applied to the model of a QPC. For this, we present and compare data obtained by different approximation schemes within the fRG, showing that the phenomenology is very robust, and can even be obtained by neglecting the vertex flow. However, including the vertex flow using the CLA reduces artifacts and gives an insightful view on the spin susceptibility. For the latter, we finally present a detailed quantitative error analysis.

II. MICROSCOPIC MODEL

The approximation scheme presented in this paper can be applied to any model Hamiltonian that can be written in the following form:

$$H = \sum_{ij,\sigma} h^{\sigma}_{ij} d^{\dagger}_{i\sigma} d_{j\sigma} + \sum_{j} U_j n_{j\uparrow} n_{j\downarrow}, \qquad (1)$$

where h^{σ} is a real, symmetric matrix, $d^{\dagger}_{j\sigma}$ ($d_{j\sigma}$) creates (annihilates) an electron at site j with spin σ ($= \uparrow, \downarrow$ or $+, -$, with $\bar{\sigma} = -\sigma$), and $n_{j\sigma} = d^{\dagger}_{j\sigma} d_{j\sigma}$ counts them (in general j can represent any quantum number, however, for simplicity we refer to it as a site index throughout the paper). In order to apply the CLA, the necessary property of this Hamiltonian is a short-ranged interaction. In principle, the approximation scheme can be set up for an interaction with finite range (over several sites), however, since the structure then becomes very complicated we will only discuss the case of a purely local, i.e., onsite interaction in this paper as given by Eq. (1). Whereas the system can extend to infinity, it is crucial that the number of sites N where U_j is nonzero is finite and not too large, as discussed in Sec. III H. If the system is extended to infinity, the effect of the noninteracting region can be calculated analytically using the projection method (see the Appendix and Refs. [8,20]). An extension to a Hamiltonian that is complex Hermitian and nondiagonal in spin space, needed, e.g., to include spin-orbit effects, is straightforward. In contrast, applying the scheme to spinless models, for which the interaction term has to be nonlocal to respect Pauli's exclusion principle, is more complicated.

III. fRG FLOW EQUATIONS

In this section, we describe the functional renormalization group (fRG) approach that we have employed to treat a translationally nonuniform Fermi system with onsite interactions, such as described by Eq. (1). We use the one-particle-irreducible (1PI) version of the fRG [2,21]. Its key idea is to approximately sum up a perturbative expansion, in our case in the interaction, by setting up and numerically solving a set of coupled ordinary differential equations (ODEs), the *flow equations*, for the system's 1PI n-particle vertex functions γ_n. This is typically done in such a way that the effects of higher-energy modes, lying above a flowing infrared cutoff parameter Λ, are incorporated before those of lower-energy modes lying below Λ. This yields a systematic way of summing up parquet-type diagrams for the two-particle vertex and for calculating the self-energy. Λ serves as *flow parameter* that controls the RG flow of the Λ-dependent vertex functions γ_n^{Λ} from an initial cutoff Λ_i, at which all vertex functions are known and simple, to a final cutoff Λ_f, at which the full theory is recovered.

This idea is implemented by replacing, in the generating functional for the vertex functions γ_n, the bare propagator $\mathcal{G}_0$ by a modified propagator $\mathcal{G}_0^{\Lambda}$,

$$\mathcal{G}_0 \to \mathcal{G}_0^{\Lambda}, \quad \text{with} \quad \mathcal{G}_0^{\Lambda_i} = 0, \quad \mathcal{G}_0^{\Lambda_f} = \mathcal{G}_0, \qquad (2)$$

constructed such that $\mathcal{G}_0^{\Lambda}$ is strongly suppressed for frequencies below Λ. The Λ dependence of the resulting vertex functions γ_n^{Λ} is governed by an infinite hierarchy of coupled ODEs, the *RG flow equations*, of the form

$$\frac{d}{d\Lambda}\gamma_n^{\Lambda} = \mathcal{F}\big(\Lambda, \mathcal{G}_0^{\Lambda}, \gamma_1^{\Lambda}, \ldots, \gamma_{n+1}^{\Lambda}\big), \qquad (3)$$

where $\gamma_1 = -\Sigma$ is the self-energy and γ_2 the two-particle vertex. At the beginning of the RG flow, the vertex functions are initialized to their bare values

$$\gamma_2^{\Lambda_i} = v, \quad \gamma_n^{\Lambda_i} = 0 \quad (n \neq 2), \qquad (4)$$

while their fully dressed values, corresponding to the full theory, are recovered upon integrating Eqs. (3) from Λ_i to Λ_f.

The infinite hierarchy of ODEs (3) is exact, but in most cases not solvable. In the generic, third-order-truncated fRG, all n-particle vertex functions with $n \geqslant 3$ are neglected

$$\frac{d}{d\Lambda}\gamma_n = 0 \quad (n \geqslant 3), \qquad (5)$$

and the resulting flow equations for γ_1^{Λ} and γ_2^{Λ} are integrated numerically. Due to this truncation, fRG is in essence an "RG-enhanced" perturbation expansion in the interaction, which will break down if U becomes too large. In fact, the flow equations can be derived by a purely diagrammatic procedure, without resorting to a generating functional, as explained in Ref. [22]. The diagrammatic structure is such that the flow of the self-energy and three different parquet channels (i.e., three coupled RPA-like series of diagrams) are treated simultaneously, feeding into each other during the flow (as discussed in more detail below). This moderates competing instabilities in an unbiased way. We also mention that this approach has been found to be particularly useful to treat models where infrared divergences play a role [3] (although the latter do not arise for the present model).

The following statements in this section hold for most, however, not for every flow parameter. For that reason, we explicitly define the Λ dependence at this point. If a different fRG scheme is used, one should carefully check all relations. The general idea should be applicable for all fRG schemes. We use fRG in the Matsubara formalism. In the following frequencies with subscripts n, n', n_1, etc., are defined to be purely imaginary:

$$\omega_n = iT\pi(2n+1). \qquad (6)$$

We introduce Λ as an infrared cutoff in the bare Matsubara propagator

$$\mathcal{G}_0^{\Lambda}(\omega_n) = \Theta_T(|\omega_n| - \Lambda)\mathcal{G}_0(\omega_n), \quad \Lambda_i = \infty, \quad \Lambda_f = 0, \qquad (7)$$

where Θ_T is a step function that is broadened on the scale of the temperature T.

For a derivation of the fRG flow equations, see, e.g., Refs. [3,5]; very detailed discussions are given, e.g., in

Refs. [8,23], for a diagrammatic derivation see Ref. [22]. The flow equation for the self-energy reads as

$$\frac{d}{d\Lambda}\gamma_1^\Lambda(q_1',q_1) = T\sum_{q_2',q_2}\mathcal{S}^\Lambda_{q_2,q_2'}\gamma_2^\Lambda(q_2',q_1';q_2,q_1), \tag{8}$$

where q_1, q_2, etc., label the quantum number and the fermionic Matsubara frequency. Here, $\mathcal{S}^\Lambda$ is defined in terms of the scale-dependent full propagator $\mathcal{G}^\Lambda$:

$$\mathcal{S}^\Lambda = \mathcal{G}^\Lambda\partial_\Lambda\left[\mathcal{G}_0^\Lambda\right]^{-1}\mathcal{G}^\Lambda, \tag{9a}$$

$$\mathcal{G}^\Lambda = \left[\left[\mathcal{G}_0^\Lambda\right]^{-1} - \Sigma^\Lambda\right]^{-1}. \tag{9b}$$

For later convenience, we divide the two-particle vertex γ_2 in four parts:

$$\gamma_2^\Lambda = v + \gamma_p^\Lambda + \gamma_x^\Lambda + \gamma_d^\Lambda, \tag{10}$$

where v is the bare vertex and γ_p^Λ, γ_x^Λ, and γ_d^Λ are called the particle-particle channel (P), and the exchange (X) and direct (D) contributions to the particle-hole channel, respectively. They are defined via their flow-equations with $\gamma_y^{\Lambda_i} = 0$:

$$\frac{d}{d\Lambda}\gamma_2^\Lambda = \frac{d}{d\Lambda}\left(\gamma_p^\Lambda + \gamma_x^\Lambda + \gamma_d^\Lambda\right). \tag{11}$$

Explicitly, these flow equations have the following forms:

$$\frac{d}{\Lambda}\gamma_p^\Lambda(q_1',q_2';q_1,q_2) = T\sum_{q_3',q_3,q_4',q_4}\gamma_2^\Lambda(q_1',q_2';q_3,q_4)\mathcal{S}^\Lambda_{q_3,q_3'}\mathcal{G}^\Lambda_{q_4,q_4'}\gamma_2^\Lambda(q_3',q_4';q_1,q_2), \tag{12a}$$

$$\frac{d}{d\Lambda}\gamma_x^\Lambda(q_1',q_2';q_1,q_2) = T\sum_{q_3',q_3,q_4',q_4}\gamma_2^\Lambda(q_1',q_4';q_3,q_2)\left[\mathcal{S}^\Lambda_{q_3,q_3'}\mathcal{G}^\Lambda_{q_4,q_4'} + \mathcal{G}^\Lambda_{q_3,q_3'}\mathcal{S}^\Lambda_{q_4,q_4'}\right]\gamma_2^\Lambda(q_3',q_2';q_1,q_4), \tag{12b}$$

$$\frac{d}{d\Lambda}\gamma_d^\Lambda(q_1',q_2';q_1,q_2) = -T\sum_{q_3',q_3,q_4',q_4}\gamma_2^\Lambda(q_1',q_3';q_1,q_4)\left[\mathcal{S}^\Lambda_{q_4,q_4'}\mathcal{G}^\Lambda_{q_3,q_3'} + \mathcal{G}^\Lambda_{q_4,q_4'}\mathcal{S}^\Lambda_{q_3,q_3'}\right]\gamma_2^\Lambda(q_4',q_2';q_3,q_2). \tag{12c}$$

Here, the higher-order vertices $\gamma_{n\geqslant 3}$ have already been set to zero.

A. Frequency parametrization

Due to energy conservation, the frequencies in Eqs. (8) and (12) are not independent:

$$\begin{gathered}\gamma_1(q_1',q_1) \propto \delta\left(\omega_{n_1'} - \omega_{n_1}\right),\\ \gamma_2(q_1',q_2';q_1,q_2) \propto \delta\left(\omega_{n_1'} + \omega_{n_2'} - \omega_{n_1} - \omega_{n_2}\right).\end{gathered} \tag{13}$$

In the case of the two-particle vertex, this gives a certain freedom to parametrize its frequency dependence. The natural choice, as will become apparent later on, is to parametrize it in terms of three bosonic frequencies:

$$\Pi = \omega_{n_1'} + \omega_{n_2'} = \omega_{n_1} + \omega_{n_2}, \tag{14a}$$

$$\mathrm{X} = \omega_{n_2'} - \omega_{n_1} = \omega_{n_2} - \omega_{n_1'}, \tag{14b}$$

$$\Delta = \omega_{n_1'} - \omega_{n_1} = \omega_{n_2} - \omega_{n_2'}. \tag{14c}$$

Note that due to their definition in terms of purely imaginary frequencies, the bosonic frequencies are imaginary too. Conversely, the fermionic frequencies can be expressed in terms of the bosonic ones:

$$\omega_{n_1'} = \tfrac{1}{2}(\Pi - \mathrm{X} + \Delta), \quad \omega_{n_2'} = \tfrac{1}{2}(\Pi + \mathrm{X} - \Delta), \tag{15a}$$

$$\omega_{n_1} = \tfrac{1}{2}(\Pi - \mathrm{X} - \Delta), \quad \omega_{n_2} = \tfrac{1}{2}(\Pi + \mathrm{X} + \Delta). \tag{15b}$$

B. Neglecting the vertex flow

For the purpose of treating the inhomogeneous model of Eq. (1), we take the quantum number that labels Green's functions and vertices to denote a composite index of site, spin, and Matsubara frequency $q_1 = (j_1,\sigma_1,\omega_1)$, etc. Since the bare propagators are nondiagonal in the site index, the number of independent variables $\gamma_2^\Lambda(q_1',q_2';q_1,q_2)$ generated by Eq. (12) is very large $\mathcal{O}(N^4N_\mathrm{f}^3)$, where N_f is the number of Matsubara frequencies per frequency argument kept track of in the numerics.

The simplest way to avoid this complication is to neglect the flow of the two-particle vertex:

$$\frac{d}{d\Lambda}\gamma_2 = 0. \tag{16}$$

This scheme, to be called fRG1, yields a frequency-independent self-energy, which, for the case of local interaction, is site diagonal. It is exact to first order in the interaction.

C. Coupled-ladder approximation

For models where the interaction can not be considered small, we introduced a novel scheme in Ref. [1], to be called dynamic fRG in CLA, to incorporate the effects of vertex flow. In the following, whenever the vertex flow is included, we treat it using the CLA, thus calling this approximation dfRG2, to distinguish it from fRG1, and from a static fRG scheme including the vertex flow sfRG2 to be introduced later. The dfRG2 scheme exploits the fact that the bare vertex

$$\begin{aligned}&v(j_1\sigma_1,j_2\sigma_2;j_3\sigma_3,j_4\sigma_4)\\ &\quad= U_{j_1}\delta_{j_1j_2}\delta_{j_3j_4}\delta_{j_1j_4}\delta_{\sigma_1\bar{\sigma}_2}\delta_{\bar{\sigma}_3\sigma_4}\left(\delta_{\sigma_1\sigma_3} - \delta_{\sigma_1\sigma_4}\right)\end{aligned} \tag{17}$$

is purely site diagonal, and parametrizes the vertex in terms of $\mathcal{O}(N^2N_\mathrm{f})$ independent variables.

To this end, we consider a simplified version of the vertex flow equation (12), where the feedback of the vertex flow is neglected: on the right-hand side we replace $\gamma_2^\Lambda \to v$. If the feedback of the self-energy were also neglected, this would be equivalent to calculating the vertex in second-order perturbation theory. As a consequence, all generated vertex contributions depend on two site indices and a single bosonic frequency. They have one of the following structures:

$$P^{\sigma\bar\sigma}_{ji}(\Pi) := \gamma^\Lambda_p\,(j\sigma\Pi-\omega_{n'},j\bar\sigma\omega_{n'};i\sigma\Pi-\omega_n,i\bar\sigma\omega_n)$$

$\overset{\mathcal{O}(v^2)}{\simeq}$

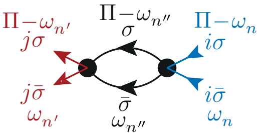
$\Pi-\omega_{n'}$
$j\sigma$
$\Pi-\omega_{n''}$
σ
$\Pi-\omega_n$
$i\sigma$
$j\bar\sigma$
$\omega_{n'}$
$\bar\sigma$
$\omega_{n''}$
$i\bar\sigma$
ω_n

, (18a)

$$\bar P^{\sigma\bar\sigma}_{ji}(\Pi) := \gamma^\Lambda_p\,(j\sigma\Pi-\omega_{n'},j\bar\sigma\omega_{n'};i\bar\sigma\Pi-\omega_n,i\sigma\omega_n)$$

$\overset{\mathcal{O}(v^2)}{\simeq}$

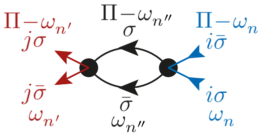
$\Pi-\omega_{n'}$
$j\sigma$
$\Pi-\omega_{n''}$
σ
$\Pi-\omega_n$
$i\bar\sigma$
$j\bar\sigma$
$\omega_{n'}$
$\bar\sigma$
$\omega_{n''}$
$i\sigma$
ω_n

, (18b)

$$X^{\sigma\bar\sigma}_{ji}(\mathrm{X}) := \gamma^\Lambda_x\,(j\sigma\mathrm{X}+\omega_{n'},i\bar\sigma\omega_n;i\sigma\mathrm{X}+\omega_n,j\bar\sigma\omega_{n'})$$

$\overset{\mathcal{O}(v^2)}{\simeq}$

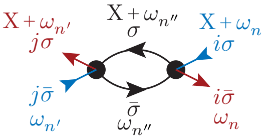
$\mathrm{X}+\omega_{n'}$
$j\sigma$
$\mathrm{X}+\omega_{n''}$
σ
$\mathrm{X}+\omega_n$
$i\sigma$
$j\bar\sigma$
$\omega_{n'}$
$\bar\sigma$
$\omega_{n''}$
$i\bar\sigma$
ω_n

, (18c)

$$X^{\sigma\sigma}_{ji}(\mathrm{X}) := \gamma^\Lambda_x\,(j\sigma\mathrm{X}+\omega_{n'},i\sigma\omega_n;i\sigma\mathrm{X}+\omega_n,j\sigma\omega_{n'})$$

$\overset{\mathcal{O}(v^2)}{\simeq}$

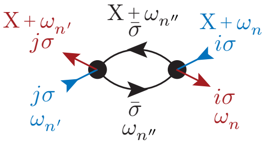
$\mathrm{X}+\omega_{n'}$
$j\sigma$
$\mathrm{X}+\omega_{n''}$
$\bar\sigma$
$\mathrm{X}+\omega_n$
$i\sigma$
$j\sigma$
$\omega_{n'}$
$\bar\sigma$
$\omega_{n''}$
$i\sigma$
ω_n

, (18d)

$$D^{\sigma\sigma}_{ji}(\Delta) := \gamma^\Lambda_d\,(j\sigma\Delta+\omega_{n'},i\sigma\omega_n;j\sigma\omega_{n'},i\sigma\Delta+\omega_n)$$

$\overset{\mathcal{O}(v^2)}{\simeq}$

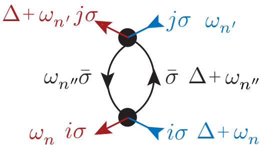
$\Delta+\omega_{n'}$ $j\sigma$
$j\sigma$ $\omega_{n'}$
$\omega_{n''}\bar\sigma$
$\bar\sigma$ $\Delta+\omega_{n''}$
ω_n $i\sigma$
$i\sigma$ $\Delta+\omega_n$

(18e)

$$D^{\sigma\bar\sigma}_{ji}(\Delta) := \gamma^\Lambda_d\,(j\bar\sigma\Delta+\omega_{n'},i\sigma\omega_n;j\sigma\omega_{n'},i\bar\sigma\Delta+\omega_n)$$

$\overset{\mathcal{O}(v^2)}{\simeq}$

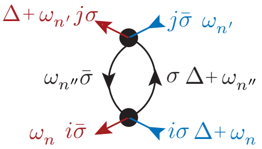
$\Delta+\omega_{n'}$ $j\sigma$
$j\bar\sigma$ $\omega_{n'}$
$\omega_{n''}\bar\sigma$
σ $\Delta+\omega_{n''}$
ω_n $i\bar\sigma$
$i\sigma$ $\Delta+\omega_n$

. (18f)

These second-order terms do not depend on the frequencies ω_n and $\omega_{n'}$. Now note that no additional terms are generated if we allow for a vertex feedback within the individual channels in Eqs. (12a), (12b), and (12c), i.e., if we take the flow equation of $\gamma_a(A)$ ($a = p,x,d$ and correspondingly $A = \Pi,\mathrm{X},\Delta$) and replace the feedback of the vertex on the right-hand side by

$$\gamma_2(\Pi,\mathrm{X},\Delta) \to v + \gamma_a(A). \tag{19}$$

This scheme is equivalent to solving RPA equations for the three individual channels P, X, and D (see Sec. III I), with an additional feedback of the self-energy via Eq. (9).

Note that if $i=j$ in Eq. (18), the terms a and c, b and f as well as d and e have the same structure w.r.t. their external site and spin indices. As a result, it is possible to account for an interchannel feedback in the vertex flow without generating additional terms if the feedback is restricted to purely site diagonal terms. As in Ref. [11], we avoid frequency mixing by limiting the interchannel feedback to the static part of the vertex, i.e., the vertex contributions are evaluated at zero frequency when fed into other channels. Putting everything together, the approximation scheme is defined by replacing the vertex on the right-hand side of the flow equation $\dot\gamma^\Lambda_a$ by (12):

$$\gamma_2 \to v + \gamma_a(A) + [\gamma_b(0) + \gamma_c(0)]\delta_{j_1 j_2}\delta_{j'_1 j'_2}\delta_{j_1 j'_1}, \tag{20}$$

where a,b,c are cyclic permutations of p,x,d, and A,B,C are the corresponding cyclic permutations of the frequencies Π,X,Δ. Since this equation is the central definition of this paper, we explicitly write it for each of the three channels:

$$\begin{aligned}\dot\gamma_p(\Pi) &: \gamma_2(j'_1,j'_2;j_1,j_2;\Pi,\mathrm{X},\Delta)\\ &\to v + \gamma_p(\Pi) + [\gamma_x(0) + \gamma_d(0)]\delta_{j_1 j_2}\delta_{j'_1 j'_2}\delta_{j_1 j'_1},\end{aligned} \tag{21a}$$

$$\begin{aligned}\dot\gamma_x(\mathrm{X}) &: \gamma_2(j'_1,j'_2;j_1,j_2;\Pi,\mathrm{X},\Delta)\\ &\to v + \gamma_x(\mathrm{X}) + [\gamma_p(0) + \gamma_d(0)]\delta_{j_1 j_2}\delta_{j'_1 j'_2}\delta_{j_1 j'_1},\end{aligned} \tag{21b}$$

$$\begin{aligned}\dot\gamma_d(\Delta) &: \gamma_2(j'_1,j'_2;j_1,j_2;\Pi,\mathrm{X},\Delta)\\ &\to v + \gamma_d(\Delta) + [\gamma_p(0) + \gamma_x(0)]\delta_{j_1 j_2}\delta_{j'_1 j'_2}\delta_{j_1 j'_1}.\end{aligned} \tag{21c}$$

This scheme generates a self-energy and a vertex which are both exact to second order in the interaction. To see this we note that first, the fRG flow equations without any truncation are exact, and second, in the fRG truncation (5) and in the CLA (20) the neglected terms are all of third or higher order in the interaction.

D. Symmetries

As can readily be checked, these flow equations respect the following symmetry relations:

$$\mathcal{G}^{\sigma\Lambda}_{ij}(\omega_n) = \mathcal{G}^{\sigma\Lambda}_{ji}(\omega_n) = \left[\mathcal{G}^{\sigma\Lambda}_{ij}(-\omega_n)\right]^*, \tag{22a}$$

$$\Sigma^{\sigma\Lambda}_{ij}(\omega_n) = \Sigma^{\sigma\Lambda}_{ji}(\omega_n) = \left[\Sigma^{\sigma\Lambda}_{ij}(-\omega_n)\right]^*, \tag{22b}$$

$$\begin{aligned}P^{\sigma\bar\sigma}_{ji} &= P^{\bar\sigma\sigma}_{ji} = P^{\sigma\bar\sigma}_{ij}, \quad \bar P^{\sigma\bar\sigma}_{ji} = \bar P^{\bar\sigma\sigma}_{ji} = \bar P^{\sigma\bar\sigma}_{ij},\\ P^{\sigma\bar\sigma}_{ji} &= -\bar P^{\sigma\bar\sigma}_{ji},\end{aligned} \tag{23a}$$

$$\begin{aligned}X^{\sigma\sigma'}_{ji} &= X^{\sigma\sigma'}_{ij} = \left[X^{\sigma'\sigma}_{ji}\right]^*, \quad D^{\sigma\sigma'}_{ji} = D^{\sigma\sigma'}_{ij} = \left[D^{\sigma'\sigma}_{ji}\right]^*,\\ X &= -D,\end{aligned} \tag{23b}$$

$$\begin{aligned}&P^{\sigma\bar\sigma}_{ji}(\Pi) = \left[P^{\sigma\bar\sigma}_{ji}(-\Pi)\right]^*, \quad X^{\sigma\sigma'}_{ji}(\mathrm{X}) = \left[X^{\sigma\sigma'}_{ji}(-\mathrm{X})\right]^*,\\ &D^{\sigma\sigma'}_{ji}(\Delta) = \left[D^{\sigma\sigma'}_{ji}(-\Delta)\right]^*,\end{aligned} \tag{23c}$$

$$X^{\sigma\sigma}, D^{\sigma\sigma} \in \mathbb{R}. \tag{23d}$$

As a result, only four independent symmetric frequency-dependent matrices are left, which we define as follows:

$$\begin{aligned}&P^{\Lambda}_{ji}(\Pi) = P^{\sigma\bar\sigma}_{ji}(\Pi), \quad X^{\Lambda}_{ji}(\mathrm{X}) = X^{\sigma\bar\sigma}_{ji}(\mathrm{X}),\\ &D^{\sigma\Lambda}_{ji}(\Delta) = D^{\sigma\sigma}_{ji}(\Delta),\end{aligned} \tag{24}$$

where the superscript Λ signifies a dependence on the flow parameter. At zero magnetic field, the number of independent matrices reduces to three since in this case $D^{\uparrow} = D^{\downarrow}$.

The flow equations for these matrices can be derived starting from Eqs. (12). The replacement (20) restricts the internal quantum numbers on the right-hand side of the flow equation q_3, q_4, q_3', and q_4' according to the definitions (18):

$$\begin{aligned}
\dot{P}^{\Lambda}_{ji}(\Pi) =& \dot{\gamma}^{\Lambda}_{p}\left(j\sigma\Pi{-}\omega_{n'}, j\bar{\sigma}\omega_{n'}; i\sigma\Pi{-}\omega_{n}, i\bar{\sigma}\omega_{n}\right)\\
=& T\sum_{kl,n''}\Big[\gamma^{\Lambda}_{2}\left(j\sigma\Pi{-}\omega_{n'}, j\bar{\sigma}\omega_{n'}; k\sigma\omega_{n''}, k\bar{\sigma}\Pi{-}\omega_{n''}\right)\mathcal{S}^{\sigma\Lambda}_{kl}(\omega_{n''})\mathcal{G}^{\bar{\sigma}\Lambda}_{kl}(\Pi{-}\omega_{n''})\gamma^{\Lambda}_{2}\left(l\sigma\omega_{n''}, l\bar{\sigma}\Pi{-}\omega_{n''}; i\sigma\Pi{-}\omega_{n}, i\bar{\sigma}\omega_{n}\right)\\
&+\gamma^{\Lambda}_{2}\left(j\sigma\Pi{-}\omega_{n'}, j\bar{\sigma}\omega_{n'}; k\bar{\sigma}\omega_{n''}, k\sigma\Pi{-}\omega_{n''}\right)\mathcal{S}^{\bar{\sigma}\Lambda}_{kl}(\omega_{n''})\mathcal{G}^{\sigma\Lambda}_{kl}(\Pi{-}\omega_{n''})\gamma^{\Lambda}_{2}\left(l\bar{\sigma}\omega_{n''}, l\sigma\Pi{-}\omega_{n''}; i\sigma\Pi{-}\omega_{n}, i\bar{\sigma}\omega_{n}\right)\Big],
\end{aligned} \tag{25a}$$

$$\begin{aligned}
\dot{X}^{\Lambda}_{ji}(\mathrm{X}) =& \dot{\gamma}^{\Lambda}_{x}\left(j\sigma\mathrm{X}{+}\omega_{n'}, i\bar{\sigma}\omega_{n}; i\sigma\mathrm{X}{+}\omega_{n}, j\bar{\sigma}\omega_{n'}\right)\\
=& T\sum_{kl,n''}\Big[\gamma^{\Lambda}_{2}\left(j\sigma\mathrm{X}{+}\omega_{n'}, k\bar{\sigma}\omega_{n''}; k\sigma\mathrm{X}{+}\omega_{n''}, j\bar{\sigma}\omega_{n'}\right)\mathcal{S}^{\bar{\sigma}\Lambda}_{kl}(\omega_{n''})\mathcal{G}^{\sigma\Lambda}_{lk}\left(\mathrm{X}{+}\omega_{n''}\right)\gamma^{\Lambda}_{2}\left(l\sigma\mathrm{X}{+}\omega_{n''}, i\bar{\sigma}\omega_{n}; i\sigma\mathrm{X}{+}\omega_{n}, l\bar{\sigma}\omega_{n''}\right)\\
&+\gamma^{\Lambda}_{2}\left(j\sigma\mathrm{X}{+}\omega_{n'}, k\bar{\sigma}\omega_{n''}; k\sigma\mathrm{X}{+}\omega_{n''}, j\bar{\sigma}\omega_{n'}\right)\mathcal{G}^{\bar{\sigma}\Lambda}_{kl}(\omega_{n''})\mathcal{S}^{\sigma\Lambda}_{lk}\left(\mathrm{X}{+}\omega_{n''}\right)\gamma^{\Lambda}_{2}\left(l\sigma\mathrm{X}{+}\omega_{n''}, i\bar{\sigma}\omega_{n}; i\sigma\mathrm{X}{+}\omega_{n}, l\bar{\sigma}\omega_{n''}\right)\Big],
\end{aligned} \tag{25b}$$

$$\begin{aligned}
\dot{D}^{\sigma\Lambda}_{ji}(\Delta) =& \dot{\gamma}^{\Lambda}_{d}\left(j\sigma\Delta{+}\omega_{n'}, i\sigma\omega_{n}; j\sigma\omega_{n'}, i\sigma\Delta{+}\omega_{n}\right)\\
=& -T\sum_{kl,n''}\Big[\gamma^{\Lambda}_{2}\left(j\sigma\Delta{+}\omega_{n'}, k\sigma\omega_{n''}; j\sigma\omega_{n'}, k\sigma\Delta{+}\omega_{n}\right)\mathcal{S}^{\sigma\Lambda}_{kl}(\omega_{n''})\mathcal{G}^{\sigma\Lambda}_{kl}(\Delta{+}\omega_{n''})\gamma^{\Lambda}_{2}\left(l\sigma\Delta{+}\omega_{n''}, i\sigma\omega_{n}; l\sigma\omega_{n''}, i\sigma\Delta{+}\omega_{n}\right)\\
&+\gamma^{\Lambda}_{2}\left(j\sigma\Delta{+}\omega_{n'}, k\sigma\omega_{n''}; j\sigma\omega_{n'}, k\sigma\Delta{+}\omega_{n}\right)\mathcal{G}^{\sigma\Lambda}_{kl}(\omega_{n''})\mathcal{S}^{\sigma\Lambda}_{kl}(\Delta{+}\omega_{n''})\gamma^{\Lambda}_{2}\left(l\sigma\Delta{+}\omega_{n''}, i\sigma\omega_{n}; l\sigma\omega_{n''}, i\sigma\Delta{+}\omega_{n}\right)\\
&+\gamma^{\Lambda}_{2}\left(j\sigma\Delta{+}\omega_{n'}, j\bar{\sigma}\omega_{n''}; j\sigma\omega_{n'}, j\bar{\sigma}\Delta{+}\omega_{n}\right)\mathcal{S}^{\bar{\sigma}\Lambda}_{ji}(\omega_{n''})\mathcal{G}^{\bar{\sigma}\Lambda}_{ij}(\Delta{+}\omega_{n''})\gamma^{\Lambda}_{2}\left(i\bar{\sigma}\Delta{+}\omega_{n''}, i\sigma\omega_{n}; i\bar{\sigma}\omega_{n''}, i\sigma\Delta{+}\omega_{n}\right)\\
&+\gamma^{\Lambda}_{2}\left(j\sigma\Delta{+}\omega_{n'}, j\bar{\sigma}\omega_{n''}; j\sigma\omega_{n'}, j\bar{\sigma}\Delta{+}\omega_{n}\right)\mathcal{G}^{\bar{\sigma}\Lambda}_{ji}(\omega_{n''})\mathcal{S}^{\bar{\sigma}\Lambda}_{ij}(\Delta{+}\omega_{n''})\gamma^{\Lambda}_{2}\left(i\bar{\sigma}\Delta{+}\omega_{n''}, i\sigma\omega_{n}; i\bar{\sigma}\omega_{n''}, i\sigma\Delta{+}\omega_{n}\right)\Big].
\end{aligned} \tag{25c}$$

As is the case for the diagrams (18), these equations do not depend on ω_n and $\omega_{n'}$, if the same holds for γ_2 on the right-hand side. The latter is of course not the case without the replacement (20). The initial conditions are

$$P^{\Lambda_i} = X^{\Lambda_i} = D^{\sigma\Lambda_i} = 0. \tag{26}$$

Performing the replacement (20), these equations can be compactly written in matrix form

$$\frac{d}{d\Lambda}P^{\Lambda}(\Pi) = \tilde{P}^{\Lambda}(\Pi)W^{p\Lambda}(\Pi)\tilde{P}^{\Lambda}(\Pi), \tag{27a}$$

$$\frac{d}{d\Lambda}X^{\Lambda}(\mathrm{X}) = \tilde{X}^{\Lambda}(\mathrm{X})W^{x\Lambda}(\mathrm{X})\tilde{X}^{\Lambda}(\mathrm{X}), \tag{27b}$$

$$\begin{aligned}\frac{d}{d\Lambda}D^{\sigma\Lambda}(\Delta) =& -\tilde{D}^{\sigma\Lambda}(\Delta)W^{\sigma d\Lambda}(\Delta)\tilde{D}^{\sigma\Lambda}(\Delta)\\ &- I^{\Lambda}W^{\bar{\sigma}d\Lambda}(\Delta)I^{\Lambda},\end{aligned} \tag{27c}$$

where we have introduced the definitions

$$\tilde{P}^{\Lambda}_{ji}(\Pi) = P^{\Lambda}_{ji}(\Pi) + \delta_{ji}\left(X^{\Lambda}_{jj}(0) + U_j\right), \tag{28a}$$

$$\tilde{X}^{\Lambda}_{ji}(\mathrm{X}) = X^{\Lambda}_{ji}(\mathrm{X}) + \delta_{ji}\left(P^{\Lambda}_{jj}(0) + U_j\right), \tag{28b}$$

$$\begin{aligned}\tilde{D}^{\sigma\Lambda}_{ji}(\Delta) &= D^{\sigma\Lambda}_{ji}(\Delta) + \delta_{ji}X^{\sigma\Lambda}_{jj}(0)\\ &= D^{\sigma\Lambda}_{ji}(\Delta) - \delta_{ji}D^{\sigma\Lambda}_{jj}(0),\end{aligned} \tag{28c}$$

$$I^{\Lambda}_{ji} = \delta_{ji}\left[P^{\Lambda}_{jj}(0) + X^{\Lambda}_{jj}(0) + U_j\right], \tag{28d}$$

which account for the interchannel feedback contained in Eq. (20). W^p, W^x, and $W^{\sigma d}$ each represent a specific bubble, i.e., a product of two propagators summed over an internal frequency:

$$W^{p\Lambda}_{ji}(\Pi) = T\sum_{\sigma n}\mathcal{S}^{\sigma\Lambda}_{ji}(\omega_n)\mathcal{G}^{\bar{\sigma}\Lambda}_{ji}(\Pi - \omega_n), \tag{29a}$$

$$\begin{aligned}W^{x\Lambda}_{ji}(\mathrm{X}) = T\sum_{n}\big[&\mathcal{S}^{\uparrow\Lambda}_{ji}(\omega_n)\mathcal{G}^{\downarrow\Lambda}_{ij}(\mathrm{X} + \omega_n)\\ &+ \mathcal{S}^{\downarrow\Lambda}_{ij}(\omega_n)\mathcal{G}^{\uparrow\Lambda}_{ji}(\omega_n - \mathrm{X})\big],\end{aligned} \tag{29b}$$

$$\begin{aligned}W^{\sigma d\Lambda}_{ji}(\Delta) = T\sum_{n}\big[&\mathcal{S}^{\sigma\Lambda}_{ji}(\omega_n)\mathcal{G}^{\sigma\Lambda}_{ij}(\Delta + \omega_n)\\ &+ \mathcal{S}^{\sigma\Lambda}_{ij}(\omega_n)\mathcal{G}^{\sigma\Lambda}_{ji}(\omega_n - \Delta)\big].\end{aligned} \tag{29c}$$

Using the above definitions, the flow equation of the self-energy (8) can be written explicitly as

$$\begin{aligned}\frac{d}{d\Lambda}\Sigma^{\sigma\Lambda}_{ji}(\omega_n) = -T\sum_{n'}\Bigg[&(\delta_{ji}U_j + P_{ji}(\omega_n + \omega_{n'})\\ &+ X_{ji}(\sigma(\omega_n - \omega_{n'})))\mathcal{S}^{\bar{\sigma}}_{ji}(\omega_{n'})\\ &- D^{\sigma}_{ji}(\omega_n - \omega_{n'})\mathcal{S}^{\sigma}_{ji}(\omega_{n'})\\ &+ \delta_{ji}\sum_{k}D^{\sigma}_{jk}(0)\mathcal{S}^{\sigma}_{kk}(\omega_{n'})\Bigg].\end{aligned} \tag{30}$$

To summarize, dfRG2 is defined by the flow equations (27) and (30), together with the definitions (9), (18), (24), (28), and (29).

E. Magnetic susceptibility

In this section, we demonstrate how the fRG approach can be used to derive expressions for linear response theory. We start by defining the magnetic susceptibility χ_i at a given site i as the linear response of the local magnetization m_i to a magnetic field B:

$$\chi_i = \partial_B m_i|_{B=0} = \tfrac{1}{2}\partial_B(n_i^{\uparrow} - n_i^{\downarrow})|_{B=0}, \tag{31}$$

where n_i^{σ} is the local occupation of site i with spin σ. Using the Matsubara sum representation of the local density $n_i^{\sigma} = T\sum_n \mathcal{G}_{ii}^{\sigma}(\omega_n)$, we explicitly calculate the derivative w.r.t. the magnetic field:

$$\begin{aligned}\chi_i &= \frac{T}{2}\sum_{n\sigma} \sigma\,\partial_B \mathcal{G}_{ii}^{\sigma}(\omega_n)|_{B=0} \\ &= \frac{T}{2}\sum_{n\sigma} -\sigma\mathcal{G}^{\sigma}(\omega_n)\partial_B[\sigma B/2 - \Sigma^{\sigma}(\omega_n)]\mathcal{G}^{\sigma}(\omega_n)|_{B=0} \\ &= -\frac{T}{2}\sum_{nj}\mathcal{G}_{ij}(\omega_n)\mathcal{G}_{ji}(\omega_n) \\ &\quad +\frac{T}{2}\sum_{nkl\sigma}\sigma\mathcal{G}_{ik}(\omega_n)\partial_B\Sigma_{kl}^{\sigma}(\omega_n)|_{B=0}\mathcal{G}_{li}(\omega_n).\end{aligned} \tag{32}$$

Note that the derivative of the self-energy w.r.t. the magnetic field B has the structure of the fRG flow equation of the self-energy (8). So, we perform the derivative by setting $\Lambda = B$ instead of the Λ dependence defined in Eq. (7). The single-scale propagator (9) with $\Lambda = B$ set to zero then is

$$\mathcal{S}^{\sigma,B=0} = \mathcal{G}\partial_B\left[\mathcal{G}_0^{\sigma}\right]_{B=0}^{-1}\mathcal{G} = \frac{\sigma}{2}\mathcal{G}^2. \tag{33}$$

Using this in combination with the flow equation of the self-energy (8),

$$\begin{aligned}\partial_B\Sigma_{kl}^{\sigma}(\omega_n) = \frac{T}{2}\sum_{n' j_1 j_2 j_3 \sigma'} & \sigma'\mathcal{G}_{j_1 j_2}^{\sigma'}(\omega_{n'})\mathcal{G}_{j_2 j_3}^{\sigma'}(\omega_{n'}) \\ & \times \gamma_2(j_3\sigma'\omega_{n'},k\sigma\omega_n;j_1\sigma'\omega_{n'},l\sigma\omega_n),\end{aligned} \tag{34}$$

one directly arrives at the well-known Kubo formula for the magnetic susceptibility, which is exact if the self-energy and the vertex are known exactly. For the coupled-ladder approximation, we directly use the explicit flow equation for the self-energy (30), which yields

$$\begin{aligned}\chi_i = &-\frac{T}{2}\sum_{n,j}\mathcal{G}_{ij}(\omega_n)\mathcal{G}_{ji}(\omega_n) \\ &+\frac{T^2}{4}\sum_{nn'klj}(\mathcal{G}_{ik}(\omega_n)\mathcal{G}_{li}(\omega_n)\mathcal{G}_{lj}(\omega_{n'})\mathcal{G}_{jk}(\omega_{n'}) \\ &\times[P_{kl}(\omega_n+\omega_{n'}) + X_{kl}(\omega_n-\omega_{n'}) + D_{kl}(\omega_n-\omega_{n'})] \\ &- \mathcal{G}_{ik}(\omega_n)\mathcal{G}_{ki}(\omega_n)D_{kl}(0)\mathcal{G}_{lj}(\omega_n)\mathcal{G}_{jl}(\omega_n)).\end{aligned} \tag{35}$$

F. Zero-temperature limit

For the numerical data presented in Sec. IV, we focused exclusively on the case of zero temperature. For the fRG scheme defined by Eq. (7), the limit $T \to 0$ has to be performed carefully [7]: $\omega_n \to i\omega$ ($\omega \in \mathbb{R}$) becomes a continuous variable and Θ_T a sharp step function, with $\Theta(0) = \frac{1}{2}$ and $\partial_\omega\Theta(\omega) = \delta(\omega)$. For this combination of δ and Θ functions, Morris' lemma [21] can be applied, which yields

$$\mathcal{S}^{\Lambda}(i\omega) \overset{T=0}{=} \delta(|\omega| - \Lambda)\widetilde{\mathcal{G}}^{\Lambda}(i\omega), \tag{36a}$$

$$\widetilde{\mathcal{G}}^{\Lambda}(i\omega) = [[\mathcal{G}_0(i\omega)]^{-1} - \Sigma^{\Lambda}(i\omega)]^{-1}, \tag{36b}$$

$$\begin{aligned}\mathcal{S}_{i,j}^{\Lambda}(i\omega_1)\mathcal{G}_{k,l}^{\Lambda}(i\omega_2) \overset{T=0}{=} &\ \delta(|\omega_1| - \Lambda)\Theta(|\omega_2| - \Lambda) \\ &\times \widetilde{\mathcal{G}}_{i,j}^{\Lambda}(i\omega_1)\widetilde{\mathcal{G}}_{k,l}^{\Lambda}(i\omega_2).\end{aligned} \tag{36c}$$

G. Static fRG

A further possible approximation is to completely neglect the frequency dependence of the vertex. This is done by setting all three bosonic frequencies Π, X, and Δ to zero throughout. As a result, the self-energy is frequency independent, too. This approach, called static fRG2 (sfRG2), loses the property of being exact to second order. It leads to reliable results only for the zero-frequency Green's function at zero temperature. If knowing the latter suffices (such as when studying the magnetic field dependence at $T = 0$), sfRG2 is a very flexible and efficient tool, computationally cheaper than our full coupled-ladder scheme.

H. Numerical implementation

Due to the slow decay of $\mathcal{S}^{\Lambda}$ for $\Lambda \to \infty$, integrating the flow equation (8) of the one-particle vertex γ_1 from $\Lambda = \infty$ to a large but finite value $\Lambda = \Lambda_0$ yields a finite contribution. For numerical implementations, the initial condition thus has to be changed to [5]

$$\gamma_1^{\Lambda_0}(q_1',q_1) = -\frac{1}{2}\sum_q v(q,q_1';q,q_1). \tag{37}$$

All numerically costly steps can be expressed as matrix operations, for which the optimized toolboxes BLAS and LAPACK can be used. The calculation time scales as $\mathcal{O}(N^3)$, due to the occurrence of matrix inversions (9) and matrix products (27). In the case of sfRG2 there are six matrix functions, each depending only on Λ. As a result, the integration is straightforward, and can be done, e.g., by a standard fourth-order Runge-Kutta with adaptive step-size control. We used the more efficient Dormand-Prince method [24], and mapped the infinite domain of $\Lambda \in [0,\infty)$ onto a finite domain using the substitution $\Lambda = \frac{x}{1-x}$ with $x \in [0,1)$. The upper bound for N, the maximal number of sites where $U_j \neq 0$, is mainly set by accessible memory. In the case of several gigabytes, N should not exceed 10^4 to 10^5. {We note in passing that for the one-dimensional Hubbard model [which is a special case of the model studied below, see Eq. (40)], N values of that magnitude would not yet be large enough to reach the Luttiger-liquid regime for the case of small interactions U. The reason is that for the Hubbard model the spectral weight and the conductance have a nonmonotonic dependence on energy:

as the energy is decreased, there is an intermediate regime in which they first increase, before the power-law decrease characteristic of Luttinger-liquid behavior finally sets in at very low energy scales, i.e. very large system sizes [6,25]. For small interactions $U \lesssim 0.5\tau$, the latter crossover only becomes accessible for system sizes well beyond 10^5 sites (see, e.g., Fig. 6 in Ref. [6]). To be able to see the low-energy decrease of spectral weight for system sizes of order 10^5, interactions would have to be chosen to be as large as $U \simeq 4\tau$, for which, however, the CLA can no longer be trusted.}

For dfRG2, all matrices depend additionally on the Matsubara frequency, which is, in the case of zero temperature, a continuous variable. This variable has to be discretized in the numerical implementation. A good and safe choice is a logarithmic discretization since analytic functions have most structure close to their branch cuts, i.e., small Matsubara frequencies. Another possible choice, used in Ref. [7], is a geometric mesh. Since an appropriate discretization consists of at least 100 frequencies, the upper bound for N is reduced to 10^3, for which the run time already becomes quite large.

For frequency values in-between the discrete frequencies on the mesh, the functions have to be interpolated. Intuitively, one might expect that a nonlinear interpolation, e.g., a cubic spline, would lead to better results. However, in our implementations this led to a self-enhanced oscillatory behavior of the self-energy as a function of frequency, even for a very dense discretization mesh. To avoid such numerical artifacts, the safest choice is a linear interpolation, where the density of the discretization is increased until the desired accuracy is reached.

I. Relation between fRG2 and RPA

In this section, we show that in the ladder approximation proposed here, fRG retains the quality of being closely related to parquet-type equations. This can be seen by considering a simplified version thereof, in which the coupling between the three channels is neglected, i.e., using replacement (19) instead of (20), and so is the feedback of the self-energy by replacing $\tilde{\mathcal{G}}^\Lambda$ by $\mathcal{G}_0$ in Eq. (29). In this case, each of the three differential equations (27) reduces to the generic form

$$\frac{d}{d\Lambda}\Gamma^\Lambda(\nu) = \Gamma^\Lambda(\nu) W^\Lambda(\nu) \Gamma^\Lambda(\nu), \tag{38}$$

with initial condition $\Gamma^{\Lambda_i} = \mathcal{U} = \delta_{ij} U_j$ (with $U_j \geqslant 0$, for present purposes). If Eq. (38) converges, its solution is given by

$$\Gamma(\nu) = \mathcal{U}\left[\mathbb{I} + W(\nu)\mathcal{U}\right]^{-1}, \tag{39a}$$

with

$$W(\nu) = \int_0^\infty d\Lambda\, W^\Lambda(\nu). \tag{39b}$$

Now note that Eq. (39) is also obtained if each channel is separately treated in the random phase approximation (RPA). Consequently, the full fRG2 scheme (either dynamic or static), described by Eqs. (27), amounts to a simultaneous treatment of all RPA channels with interchannel coupling via (28), and a feedback of Hartree-type diagrams via (9).

IV. fRG RESULTS

In this section, we will discuss some properties of the results obtained with the fRG equations stated in Sec. III, for the case of a QPC geometry. We will compare the results for the linear response conductance for the three approximation schemes and discuss the spin susceptibility within dfRG2.

A. Model for a QPC

We note that Eq. (1) applies to systems of arbitrary spatial dimensions. However, in this work we only present and discuss results for QPCs, thus restricting the model to one dimension. The lowest one-dimensional subband of the QPC is modeled by an inhomogeneous tight-binding chain, with onsite interactions:

$$H = \sum_{j\sigma}\left[E_j^\sigma n_{j\sigma} - \tau(d^\dagger_{j\sigma} d_{j+1\sigma} + \text{H.c.})\right] + \sum_j U_j n_{j\uparrow} n_{j\downarrow}, \tag{40}$$

with $E_j^\sigma = V_j + 2\tau - \frac{\sigma B}{2}$ where B is a Zeeman field. For low kinetic energies, this tight-binding model is a good approximation for a continuum model with mass $\frac{m}{\hbar^2} = \frac{1}{2\tau a^2}$ (where $\hbar$ is Plank's constant) and potential $V_j = V(x = ja)$ [26], provided that the lattice spacing a is much smaller than the length scales on which the potential changes. In order to keep computational time small, the model should always be chosen in such a way that the number of sites N where V_j or U_j are nonzero is as small as possible. In other words: The inhomogeneity should be incorporated within as few sites as possible, without loss of adiabaticity.

We model the QPC as a smooth one-dimensional potential barrier which is purely parabolic around its maximum at $x = 0$:

$$V(x) = V_g + \mu - \frac{m}{2\hbar^2}\Omega_x^2 x^2, \tag{41}$$

or in discrete version

$$V_j = V_g + \mu - \frac{\Omega_x^2}{4\tau} j^2 \quad (|j| < j_c). \tag{42}$$

Here, j_c defines the range of pure parabolicity, μ is the chemical potential, and Ω_x is the relevant energy scale for the QPC [16], which we define such that it has the dimension of an energy (not frequency). The condition that a has to be much smaller then the length scales on which the potential changes implies the condition $\Omega_x \ll \tau$. V_g is the gate voltage, which controls the height of the potential. For $|j| > j_c$, the potential is smoothly connected to homogenous semi-infinite noninteracting leads. The potential can be considered as purely parabolic regarding its low-energy transport properties if $j_c \gg \sqrt{\tau/\Omega_x}$. In the following, we use $\mu = 0.5\tau$, $\Omega_x = 0.04\tau$, $j_c = \sqrt{2\tau\mu}/\Omega_x$, and $N = 81$. These values optimize the conditions on Ω_x, j_c, and the smoothness of the potential on the one hand and the smallness of the number of sites N on the other hand. Typical experimental values for GaAs QPCs are $\Omega_x = 1$ meV and $m = 0.067 m_e$, where m_e is the electron mass. The latter fixes the hopping to $\tau = 25$ meV and thus the length unit to $a = \sqrt{\hbar^2/2\tau m} \simeq 5$ nm. These values should give a rough estimate for comparison with experiment, however, in the following we will use the system of measurement defined by τ and a, without referring to SI units.

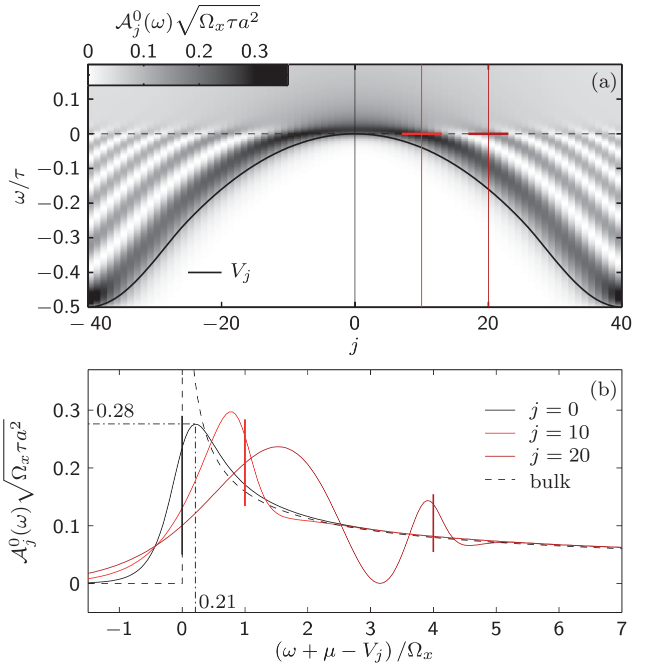

FIG. 1. (Color online) (a) Local density of states $\mathcal{A}_j(\omega)$ (color scale) for the noninteracting $U_j=0$, Hamiltonian Eq. (40) with potential (42) at $V_g=0$ (thick black line). (b) Local density of states $\mathcal{A}_j(\omega)$ as a function of $(\omega-V_j)/\Omega_x$ for a homogeneous tight-binding chain ($V_j=0$, gray line) and for the potential (42) at fixed site $j=0$ (blue), $j=10$ (green), and $j=20$ (red), indicated in (a) by vertical lines with corresponding colors.

B. Model properties

Having defined the model we first discuss its noninteracting ($U=0$) properties. Figure 1 shows the local density of states (LDOS)

$$\mathcal{A}_j(\omega)=-\frac{1}{a\pi}\mathrm{Im}\mathcal{G}_{jj}(\omega+i0^+) \qquad (43)$$

both in a grayscale plot as a function of site index and frequency [Fig. 1(a)] and at several fixed sites as a function of frequency [Fig. 1(b)]. Note that just above the potential [black line in Fig. 1(a)] the LDOS is enhanced [dark region in Fig. 1(a)]. This property originates from the fact that the density of states (DOS) of a one-dimensional system shows a divergence at zero velocity: indeed the DOS for the homogenous version [$V_j=0$, i.e., $V_g=\mu=\Omega_x=0$ in Eq. (42)] of our model [black dashed line in Fig. 1(b)] reads as

$$\mathcal{A}(\omega)=\frac{1}{\pi a\sqrt{\omega(4\tau-\omega)}}\overset{\omega\ll\tau}{\approx}\frac{1}{2\pi a\sqrt{\tau\omega}}\propto\frac{1}{v^{\mathrm{clas}}}, \qquad (44)$$

where v^{clas} is the classical velocity of the electron. Quantum mechanically, this divergence is smeared out by the inhomogeneity ($V_j\neq 0$) of a potential. Following Ref. [1], we call this smeared van Hove singularity in the LDOS that follows the potential a "van Hove ridge." In the case of a parabolic barrier with curvature given by Ω_x [Eq. (42)], the maximum of the LDOS is at an energy of $\mathcal{O}(\Omega_x)$ bigger than V_j and has a height of $\mathcal{O}(\sqrt{\tau\Omega_x})$ [see dashed-dotted line in Fig. 1(b)]. For energies below the potential maximum, electrons get reflected. This leads to standing waves, altering the LDOS by oscillations around its bulk value [white striped area in Fig. 1(a) and oscillations in dark red line Fig. 1(b)].

C. Conductance of a QPC

Having discussed the properties of the noninteracting model, we continue with the fRG results at finite interaction. For this we first define the spatial dependence of the interaction U_j, which, for the one-dimensional model is an effective one-dimensional interaction resulting from integrating out two space dimensions. Its strength depends on the geometry, and is larger if the spatial confinement perpendicular to the one-dimensional system is smaller. We assume that this confinement is independent of the position in the transport direction in the center of the QPC, with $U_{j=0}=U$. This is a fair assumption for a saddle-point approximation of the two-dimensional QPC potential. For $|j|\to N'=\frac{N-1}{2}$, U_j drops smoothly to zero, describing the adiabatic coupling to the two-dimensional electron system, represented by the semi-infinite tight-binding chain.

In Ref. [1], we showed that the 0.7 anomaly is caused by the van Hove ridge in the LDOS discussed above. Its apex crosses the chemical potential when the QPC is tuned into the subopen regime, i.e., the regime where the conductance takes values $0.5G_Q<G<0.9G_Q$. This high LDOS at the chemical potential enhances effect of interactions by two main mechanisms: first, the effective Hartree barrier depends nonlinearly on gate voltage and magnetic field, causing an enhanced elastic backscattering; and second, due to the high LDOS inelastic backscattering is enhanced once a phase space is opened up by a finite temperature or source-drain voltage. Both effects reduce the conductance in the subopen regime, causing the 0.7 anomaly. Since interactions are enhanced by the LDOS, the relevant dimensionless interaction strength is $U_j\mathcal{A}_j(\mu)a$, which scales like $U/\sqrt{\Omega_x\tau}$ in the subopen regime.

In this paper, we will concentrate on examining how the reliability of the method depends on the interaction, without explaining the physical mechanism underlying the 0.7 anomaly in detail (for the latter, we refer to Ref. [1]). For the model (40), no reliable results are available from other methods to which we could have compared our own. Instead, we here compare the results of the different fRG schemes fRG1, sfRG2, and dfRG2. These schemes differ in the prefactor of the perturbative expansion of terms in order U^2 and higher. If these terms are important, the three approximation schemes will deviate from each other. Hence, the qualitative and quantitative reliability can be deduced from the qualitative and quantitative deviations between these schemes.

The first observable we discuss is the linear response conductance at zero teperature [27]:

$$G=\frac{e^2}{h}\sum_\sigma\left|2\pi\rho^\sigma(i0^+)\mathcal{G}^\sigma_{-N'N'}(i0^+)\right|^2, \qquad (45)$$

where $\rho(\omega)$ is the density of states at the boundary of a semi-infinite tight-binding chain, representing the two-dimensional leads (for a derivation of the boundary Green's function, see the Appendix).

Particularly interesting in studying the 0.7 anomaly in QPCs is the shape of the conductance trace as a function

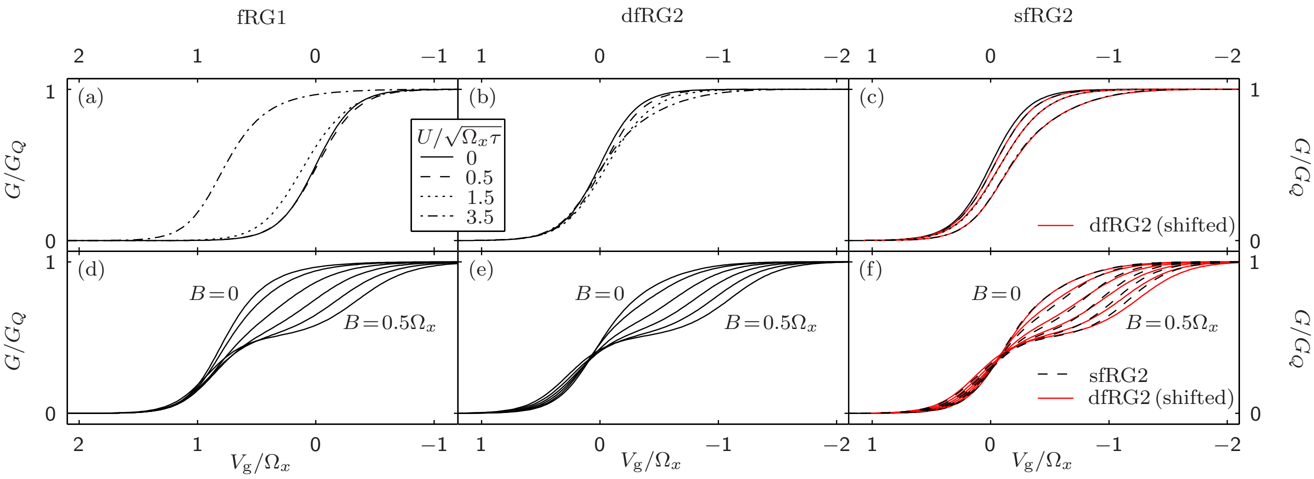

FIG. 2. (Color online) (a)–(c) Conductance G, as a function of gate voltage V_g, at zero magnetic field $B = 0$ for different values of interaction U. (d)–(f) Conductance G at fixed interaction strength $U = 3.5\sqrt{\Omega_x}$, for six equidistant magnetic fields B, between 0 and $0.5\Omega_x$. Conductance is calculated using fRG1 [(a), (d)], dfRG2 [(b), (c)], or sfRG2 [black lines in (c) and (f)]. Red lines in (c) and (f) show dfRG2 data repeated from (b) and (e) with a U-dependent shift ΔV_g in V_g direction ($\Delta V_g = 0, 0.001, 0.02$ and $0.15\Omega_x$ for $U = 0, 0.5, 1, 5$, and $3.5\sqrt{\Omega_x\tau}$, respectively).

of applied gate voltage in the region where its value (in units of G_Q) changes from zero to one, and how this shape changes with external parameters, such as applied magnetic field. First of all, we emphasize the good qualitative agreement of all three approximation schemes with each other as well as with experimental results [compare Figs. 2(d), 2(e), and 2(f) with Refs. [17,19] (a direct comparison of dfRG2 with experiment is given in Ref. [1])]. This confirms that the method qualitatively captures the physical mechanism with respect to the conductance at zero temperature very well.

For a more quantitative analysis, we first consider the position of the conductance step, say V_{po}; even though the actual position of the step is of minor interest experimentally, it gives information about how accurate Hartree-type correlations are treated. Figures 2(a), 2(b), and 2(c) show the conductance at $B = 0$ for increasing values of interaction U for fRG1, dfRG2, and sfRG2, respectively. While for dfRG2 and for sfRG2, V_{po} decreases with interaction, its behavior for fRG1 is nonmonotonic: V_{po} decreases slightly at small values of interaction, and increases strongly at larger values of interaction. Hence, the conductance at large interaction is higher than the bare $U = 0$ value. This behavior is unphysical: whenever the density is nonzero, an increase in U should cause an increase in the effective barrier height due to Coulomb repulsion, and hence a decrease in the conductance. This artifact is significantly reduced by the vertex flow of both dfRG2 and sfRG2. For the latter, interactions suppress the conductance more strongly than for the former. Due to these deviations between the three schemes, we can not make a quantitative statement about the exact position of the conductance step V_{po}.

The deviations just discussed make quantitative comparisons between these methods (or with others, such as RPA) difficult if interactions are large. The reason for the difficulty is that the V_g position of the conductance step depends sensitively on the precise way in which Hartree-type correlations are treated and hence differ for each of the above schemes. Hence, it would not be meaningful to compare their predictions for physical quantities calculated *at a given value* of V_g; instead, it is only meaningful to compare the shape of their evolution with V_g. Actually, the same is true for physical quantities that are dominated by Fock-type correlations since internal propagators have to be dressed by Hartree diagrams. Doing this is crucial for inhomogeneous systems such as ours since an inhomogeneous density causes these Hartree contributions to have a significant dependence on position and gate voltage. In the fRG approach, the feedback of the self-energy (9) always guarantees that internal lines are dressed in a self-consistent way.

Let us now compare the shapes of the V_g-dependent conductance curves for dfRG2 and sfRG2. To this end, we replotted the dfRG2 data from Fig. 2(b) in Fig. 2(c) with a U-dependent shift ΔV_g in the V_g direction (red lines). It can be seen from comparison with sfRG2 data that the shapes of the conductance curves are almost identical.

Next, we analyze the shape of the conductance step at finite interaction, and how it develops with magnetic field. The effect of an increasing magnetic field is qualitatively similar for the three approximation schemes [see Figs. 2(d), 2(e), and 2(f)]: the conductance step develops into a spin-resolved double step, in an asymmetric way: while the curves hardly change for V_g values where $G < 0.5G_Q$, they are strongly suppressed in the subopen regime, where the LDOS is large. For fRG1, the V_g range, where the lowest magnetic field $B = 0.1\Omega_x$ significantly reduces the conductance w.r.t. the conductance at $B = 0$, is larger than for dfRG2 and sfRG2. This is related to the fact that the magnetoconductance, the change of conductance with magnetic field, within fRG1 is negative even for V_g values where conductance is close to zero [this effect is too small to be visible in Fig. 2(d)]. Since this is not the case for dfRG2 and sfRG2 it is not possible to make a reliable statement about the sign of the magnetoconductance in the tunnel regime. Again, we reproduced the dfRG2 data from Fig. 2(e) in Fig. 2(f) with a shift ΔV_g in V_g (red line) in order to compare their shape with the sfRG2 data (black dashed line). The effect of the magnetic field on the conductance within sfRG is slightly larger for small fields and slightly smaller for large fields than for the dfRG2 results. Based on the facts that, first, the deviations between dfRG2 and sfRG2 are small and, second, sfRG2 is computationally much cheaper than dfRG2, we conclude that for preliminary studies, or when scanning a large parameter space, one should favor sfRG2 whenever it is sufficient to know the static part of vertex functions.

D. Susceptiblity

As explained in Ref. [1], the 0.7 anomaly is related to an enhanced spin susceptibility in the subopen regime of the QPC. For this quantity, an estimate of the error is available within the dfRG2 approximation scheme. We note that the spin susceptibility defined in Eq. (31) can be calculated in two ways: by numerical differentiation of the magnetization for a small magnetic field χ^{num}, or via Eq. (35), χ^{Kubo}. Like the conductance, the value of χ is not known exactly. Thus, we argue here as in the previous section. χ^{num} and χ^{Kubo} are both exact to second order in the interaction, as can easily be checked, but they differ in terms that are of order U^3 and higher. If the difference of χ^{num} and χ^{Kubo} is significant, the higher-order terms are non-negligible, and the results can not be trusted.

In Ref. [1] we showed that χ_j^{num} is enhanced due to the inhomogeneity of the QPC potential and in addition amplified by interactions. It has a strong V_g dependence, and is maximal when the QPC is tuned into the subopen regime. In this regime, at $V_g = -\Omega_x/4$, we compare χ^{num} (Fig. 3 black lines) with χ^{Kubo} (Fig. 3 red lines) for different values of interaction. For intermediate values of interaction $U = 1.5\sqrt{\Omega_x \tau}$, both results are essentially identical, while for a larger value of interaction $U = 3.5\sqrt{\Omega_x \tau}$ deviations are clearly visible, however still not too large. The qualitative features that the susceptibility strongly increases with interaction, and that it is enhanced in the center of the QPC, emphasized in Ref. [1], are confirmed by both results. Furthermore, they coincide in their spatial structure, i.e., two maxima in the center and a decaying oscillating behavior. This spatial structure is mainly given by the LDOS at the chemical potential (see Sec. IV B) and enhanced by interactions.

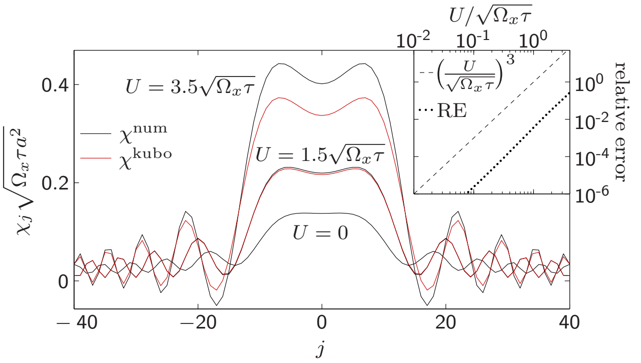

FIG. 3. (Color online) Local spin susceptibility χ_j [Eq. (31)] as a function of site index, for the QPC potential [Eq. (42)] at $V_g = -\Omega_x/4$, calculated using dfRG2 via the the numerical derivative of the local magnetization χ^{num} (black lines), as well as via the Kubo formula (35), χ^{kubo} (red lines), for three different values of interaction. Inset: relative error RE [Eq. (46)] (dots), as a function of interaction U, on a log-log scale. The error scales as U^3 (compare dashed line) since dfRG2 is exact to second order in the interaction U.

For a better quantification, we define the relative error

$$\text{RE} = 2\frac{\sum_j \left|\chi_j^{\text{Kubo}} - \chi_j^{\text{num}}\right|}{\sum_j \left|\chi_j^{\text{Kubo}} + \chi_j^{\text{num}}\right|}. \tag{46}$$

This error is shown on a log-log scale in the inset of Fig. 3 (dots). The relative error scales like U^3 since dfRG2, and thus χ^{num} and χ^{Kubo}, are exact to second order in U. For the larger value of interaction $U = 3.5\sqrt{\tau\Omega_x}$, the relative error of about 18% is quite significant and thus the value of χ is quantitatively not reliable. The reason for this is that the dimensionless interaction strength $U_j \mathcal{A}_j(\mu) a \approx 3.5 \times 0.3 \approx 1$ is already close to one. Nevertheless, the error is still dominated by the third-order term, implying that it is controlled.

Finally, we note that the spin susceptibility in the RPA approximation

$$\chi_i^{\text{RPA}} = \sum_j [W^d(0)[1 + \mathcal{U} W^d(0)]^{-1}]_{ij} \tag{47}$$

diverges at an interaction strength for which fRG is still well behaved. For example, if bare internal propagators are used to calculate W^d, $\chi_i^{\text{RPA}}(V_g)$ turns out to diverge at $U \simeq 3.3\sqrt{\Omega_x \tau}$. Moreover, the value of χ^{RPA} and thus also the U value for which it diverges depends on how one chooses to treat interactions for internal propagators of W^d. However, RPA itself gives no recipe how to do this. In contrast, the fRG approach gives a systematic framework for computing the two-particle vertex, the self-energy, and their feedback into each other, in a way that moderates competing instabilities in an unbiased way (as mentioned in Sec. III).

V. CONCLUSION AND OUTLOOK

We have derived a fRG based approximation scheme, called the coupled-ladder approximation (CLA), for spinful fermionic tight-binding models with a local interaction and an arbitrary potential. The main applications are systems with a significant spatial dependence, in particular, models where the electron density significantly changes with the position in real space.

The CLA is formulated within the context of third-order-truncated fRG schemes, in which the three-particle vertex is set to zero, while the flow of the two-particle vertex is fully incorporated. The CLA retains two of the main properties of third-order-truncated fRG: it is exact to second order, and sums up diagrams of the RPA in all channels. Since the CLA is based on a perturbative argument, it is reliable only if interactions are not too large.

We analyzed in detail the reliability of this approach for a one-dimensional tight-binding model with a parabolic potential barrier representing a QPC. For this, we compared results for the conductance and the spin susceptibility calculated using different approaches within the fRG for different interactions up to $U = 3.5\sqrt{\Omega_x \tau}$. We identified the magnetic field dependence of the conductance and the enhanced susceptibility related to the 0.7 anomaly [1], as robust properties of the model.

Finally, let us comment briefly on the prospects of using the CLA approach presented here to obtain finite-temperature results. While the formulas for the local density n and the local susceptibility χ [Eq. (35)] are valid for arbitrary temperature T, the conductance formula (45) holds only for the case of zero temperature. The generalization of this formula to finite temperature[28] involves an analytic continuation to the real axis for both self-energy and vertex w.r.t. their frequency arguments. However, performing such an analytic continuation for numerical data is a mathematically ill-defined problem and turns out to be especially difficult for matrix-valued functions.

One possibility to avoid this complication is to formulate our CLA scheme on the Keldysh contour, in which case there are several different possibilities for introducing the fRG flow parameter [29]. (For a fRG treatment of the single-impurity Anderson model, see Ref. [11].) When using Keldysh fRG to treat equilibrium properties, the number of independent correlators can be reduced by exploiting the Kubo-Martin-Schwinger conditions [30]. Moreover, Keldysh fRG in principle also allows nonequilibrium properties to be calculated. The actual implementation of Keldysh fRG for our model will be nontrivial, though, in particular since numerical integrations along the real axis, where Green's functions can have poles, can be challenging. Another problem at finite temperature is the violation of particle conservation due to the fRG truncation (5) [31]. The extent of this violation might be reduced by implementing the modified vertex flow suggested by Katanin [32]. We believe that it would be worth pursuing work in these directions.

ACKNOWLEDGMENTS

We thank S. Andergassen, S. Jakobs, V. Meden, and H. Schöller for very helpful discussions. We acknowledge support from the DFG via SFB-631, SFB-TR12, De730/4-3, and the Cluster of Excellence *Nanosystems Initiative Munich*.

APPENDIX: PROJECTION METHOD

The propagator in the fRG flow [Eqs. (8) and (12)], in general, lives on an infinite-dimensional chain. However, since the interacting region has finite extent, we only need to evaluate it on an N-dimensional subspace. Furthermore, for the evaluation of Eq. (35) we need to calculate the sum over all site indices j, including the infinite number of sites in the leads. To this end, we perform a standard projection procedure [8,20]. With this method, the influence of the leads on the propagator and their contribution to the sum can be calculated analytically if the diagonalization of the leads is known analytically. Therefore, we define projection operators C and L, with $C^2 = C$, $L^2 = L$, and $L + C = \mathbb{1}$ which divide the Hilbert space into the part that describes the leads L and the finite-dimensional part that describes the central region where interaction is nonzero C. Furthermore, we define for a given quadratic Hamiltonian H (for an interacting system H is replaced by $H_0 + \Sigma$), $H_c = CHC$, $H_c = CHC$, $H_{cl} = CHL$, $H_{lc} = LHC$, $\omega_l = \omega L$, and $\omega_c = \omega C$ and write the Hamiltonian in the basis defined by the projections

$$H = \begin{pmatrix} H_c & H_{cl} \\ H_{lc} & H_l \end{pmatrix}. \tag{A1}$$

Consequently, the Green's function in the same basis reads as

$$\mathcal{G} = \begin{pmatrix} \omega_c - H_c & -H_{cl} \\ -H_{lc} & \omega_l - H_l \end{pmatrix}^{-1} = \begin{pmatrix} \mathcal{G}_c & \mathcal{G}_{cl} \\ \mathcal{G}_{lc} & \mathcal{G}_l \end{pmatrix}. \tag{A2}$$

with

$$\mathcal{G}_c = \frac{1}{\omega_c - H_c - H_{cl} g_l H_{lc}}, \quad g_l = \frac{1}{\omega_l - H_l}, \tag{A3a}$$

$$\mathcal{G}_l = \frac{1}{\omega_l - H_l - H_{lc} g_c H_{cl}}, \quad g_c = \frac{1}{\omega_c - H_c}, \tag{A3b}$$

$$\mathcal{G}_{cl} = \mathcal{G}_c H_{cl} g_l = g_c H_{cl} \mathcal{G}_l, \tag{A3c}$$

$$\mathcal{G}_{lc} = g_l H_{lc} \mathcal{G}_c = \mathcal{G}_l H_{lc} g_c. \tag{A3d}$$

In the following, we will only use $\mathcal{G}_l$ and g_c as well as G_{cl} and G_{lc} expressed in terms $\mathcal{G}_l$ and g_c, so we use the shorthand notations $\mathcal{G} = \mathcal{G}_l$ and $g = g_l$ (whether $\mathcal{G}$ lives on the infinite-dimensional Hilbert space, or on the subspace of the central contact, will be clear from its site indices).

For the case of the infinite tight-binding chain defined by Eq. (40), the central region extends from site $-N'$ to site N', with $N' = \frac{N-1}{2}$, and the coupling to the leads can be expressed as

$$H_{cl} = -\tau(d^\dagger_{-N'} d_{-N'-1} + d^\dagger_{N'} d_{N'+1}), \tag{A4a}$$

$$H_{lc} = H^\dagger_{cl}. \tag{A4b}$$

Consequently,

$$\begin{aligned} H_{cl} g H_{lc} &= \tau^2 (d^\dagger_{-N'} d_{-N'-1} + d^\dagger_{N'} d_{N'+1}) \\ &\quad \times g(d^\dagger_{-N'-1} d_{-N'} + d^\dagger_{N'+1} d_{N'}) \\ &= \tau^2 b(n_{-N'} + n_{N'}), \end{aligned} \tag{A5}$$

where $b = g_{N'+1,N'+1}$ is the boundary Green's function of a half-infinite tight-binding chain. Transforming into k space and using the boundary condition $\langle d^\dagger_{N'} d_k \rangle = 0$ we get $\langle d^\dagger_{N'+1} d_k \rangle \propto \sin^2(k)$. Together with the dispersion $\varepsilon_k = -\mu - 2\tau\cos(k)$ and the proper normalization, this yields for $\mathrm{Im}(\omega_n) > 0$

$$\begin{aligned} b(\omega_n) &= \frac{1}{\pi} \int_{-\pi}^{\pi} dk \frac{\sin^2(k)}{\omega_n + \mu + 2\tau\cos(k)} \\ &= \frac{1}{2\tau^2}[\omega_n + \mu - i\sqrt{4\tau^2 - (\omega_n + \mu)^2}]. \end{aligned} \tag{A6}$$

The square root is defined to have a positive real part, and $b(-\omega_n) = b^*(\omega_n)$. (For the spin-dependent boundary Green's function at finite magnetic field, μ has to be replaced by $\mu + \sigma B/2$.)

Next, we calculate the infinite sum in Eq. (35). We split the sum into three parts and take k and l to be site indices in the central region

$$\begin{aligned} \sum_{j=-\infty}^{\infty} \mathcal{G}_{kj}\mathcal{G}_{jl} &= \left(\sum_{j=-\infty}^{-N'-1} + \sum_{j=-N'}^{N'} + \sum_{j=N'+1}^{\infty} \right) \mathcal{G}_{jk}\mathcal{G}_{jl} \\ &= \sum_{j=-N'}^{N'} \mathcal{G}_{jk}\mathcal{G}_{jl} + \tau^2 \mathcal{G}_{k,-N'} h^L \mathcal{G}_{-N',l} \\ &\quad + \tau^2 \mathcal{G}_{k,N'} h^R \mathcal{G}_{N',l}, \end{aligned} \tag{A7}$$

with

$$h^L = \sum_{j=-\infty}^{-N'-1} g_{-N'-1,j}\, g_{j,-N'-1}, \tag{A8a}$$

$$h^R = \sum_{j=N'+1}^{\infty} g_{N'+1,j}\, g_{j,N'+1}, \tag{A8b}$$

where we made use of Eqs. (A3c), (A3d), and (A4).

Finally, we note that the last two terms are identical and given by

$$\begin{aligned} h(\omega_n) &= h^L(\omega_n) = h^R(\omega_n) = [g^2(i\omega_n)]_{N'+1,N'+1} \\ &= \frac{1}{\pi}\int_{-\pi}^{\pi} dk \frac{\sin(k)^2}{[\omega_n + \mu + 2\tau\cos(k)]^2} \\ &= \frac{1}{2\tau^2}\left(\frac{\omega_n+\mu}{\omega_n+\mu-2\tau}\sqrt{\frac{\omega_n+\mu-2\tau}{\omega_n+\mu+2\tau}} - 1\right). \end{aligned} \tag{A9}$$

---

[1] F. Bauer, J. Heyder, E. Schubert, D. Borowsky, D. Taubert, B. Bruognolo, D. Schuh, W. Wegscheider, J. von Delft, and S. Ludwig, Nature (London) **501**, 73 (2013).
[2] C. Wetterich, Phys. Lett. B **301**, 90 (1993).
[3] W. Metzner, M. Salmhofer, C. Honerkamp, V. Meden, and K. Schönhammer, Rev. Mod. Phys. **84**, 299 (2012).
[4] V. Meden, W. Metzner, U. Schollwöck, and K. Schönhammer, Phys. Rev. B **65**, 045318 (2002).
[5] S. Andergassen, T. Enss, V. Meden, W. Metzner, U. Schollwöck, and K. Schönhammer, Phys. Rev. B **70**, 075102 (2004).
[6] S. Andergassen, T. Enss, V. Meden, W. Metzner, U. Schollwöck, and K. Schönhammer, Phys. Rev. B **73**, 045125 (2006).
[7] C. Karrasch, R. Hedden, R. Peters, T. Pruschke, K. Schnhammer, and V. Meden, J. Phys.: Condens. Matter **20**, 345205 (2008).
[8] C. Karrasch, Master's thesis, Georg-August Universität Göttingen, 2006, arXiv:cond-mat/0612329.
[9] C. Husemann, K.-U. Giering, and M. Salmhofer, Phys. Rev. B **85**, 075121 (2012).
[10] K.-U. Giering and M. Salmhofer, Phys. Rev. B **86**, 245122 (2012).
[11] S. G. Jakobs, M. Pletyukhov, and H. Schoeller, Phys. Rev. B **81**, 195109 (2010).
[12] C. Honerkamp, Eur. Phys. J. B **21**, 81 (2001).
[13] C. Honerkamp and M. Salmhofer, Phys. Rev. B **67**, 174504 (2003).
[14] B. J. van Wees, H. van Houten, C. W. J. Beenakker, J. G. Williamson, L. P. Kouwenhoven, D. van der Marel, and C. T. Foxon, Phys. Rev. Lett. **60**, 848 (1988).
[15] D. A. Wharam, T. J. Thornton, R. Newbury, M. Pepper, H. Ahmed, J. E. F. Frost, D. G. Hasko, D. C. Peacock, D. A. Ritchie, and G. A. C. Jones, J. Phys. C: Solid State Phys. **21**, L209 (1988).
[16] M. Büttiker, Phys. Rev. B **41**, 7906 (1990).
[17] K. J. Thomas, J. T. Nicholls, M. Y. Simmons, M. Pepper, D. R. Mace, and D. A. Ritchie, Phys. Rev. Lett. **77**, 135 (1996).
[18] N. J. Appleyard, J. T. Nicholls, M. Pepper, W. R. Tribe, M. Y. Simmons, and D. A. Ritchie, Phys. Rev. B **62**, R16275 (2000).
[19] S. M. Cronenwett, H. J. Lynch, D. Goldhaber-Gordon, L. P. Kouwenhoven, C. M. Marcus, K. Hirose, N. S. Wingreen, and V. Umansky, Phys. Rev. Lett. **88**, 226805 (2002).
[20] J. Taylor, *Scattering Theory: The Quantum Theory on Nonrelativistic Collisions* (Wiley, New York, 1972).
[21] T. R. Morris, Int. J. Mod. Phys. A **09**, 2411 (1994).
[22] S. G. Jakobs, V. Meden, and H. Schoeller, Phys. Rev. Lett. **99**, 150603 (2007).
[23] F. Bauer, Master's thesis, LMU-München, 2008.
[24] J. Dormand and P. Prince, J. Comput. Appl. Math. **6**, 19 (1980).
[25] D. Schuricht, S. Andergassen, and V. Meden, J. Phys.: Condens. Matter **25**, 014003 (2013).
[26] G. Forsythe and W. Wasow, *Finite-Difference Methods for Partial Differential Equations*, Applied Mathematics Series (Wiley, New York, 1960).
[27] S. Datta, *Electronic Transport in Mesoscopic Systems*, Cambridge Studies in Semiconductor Physics and Microelectronic Engineering (Cambridge University Press, Cambridge, UK, 1997).
[28] A. Oguri, J. Phys. Soc. Jpn. **70**, 2666 (2001).
[29] S. G. Jakobs, Ph.D. thesis, RWTH Aachen, 2009.
[30] S. G. Jakobs, M. Pletyukhov, and H. Schoeller, J. Phys. A: Math. Theor. **43**, 103001 (2010).
[31] T. Enss, Ph.D. thesis, Universität Stuttgart, 2005, arXiv:cond-mat/0504703.
[32] A. A. Katanin, Phys. Rev. B **70**, 115109 (2004).

Chapter 7

The effect of spin-orbit interactions on the *0.7 anomaly* in quantum point contacts

This chapter includes the paper "*The effect of spin-orbit interactions on the 0.7-anomaly in quantum point contacts*", submitted to *Physical Review Letters* [Goulko et al. (2014)]. In this work we theoretically investigate the influence of spin-orbit interactions (SOI) on the shape of the first linear conductance step of a QPC, placing special focus on their impact on the *0.7 anomaly*. SOI are relativistic corrections to the system's Hamiltonian, obtained by expanding the Dirac equation in powers of the electron's momentum [Birkholz (2008)]. In a 2DES they originate from the strong gradient of the confining electrostatic potential (Rashba SOI) and/or from an anisotropy of the underlying ionic crystal structure of the semiconducting material (Dresselhaus SOI). Their influence is best described by an effective magnetic field $\vec{B}_{SOI}$ that is proportional to the electron's wave vector $\hbar k$. In the presence of a magnetic field $\vec{B}$, SOI provoke an avoided crossing (for $\phi \neq 0$, where ϕ is the angle between $\vec{B}$ and $\vec{B}_{SOI}$) in the dispersion relation of the electrons and a subsequent spin-mixing within both dispersion branches. For a QPC geometry this results in distinct features in the linear conductance.

In order to calculate the effect of SOI on the physics of a QPC we add an additional (Rashba) SOI term to the Hamiltonian of our QPC model (Sec. 3.3.1). This provides the framework for a systematic study of transport in inhomogeneous 1D systems where both SOI and electron-electron interactions (EEI) are relevant. Importantly, we define an energy scale R that describes the strength of SOI in a parabolic QPC geometry (see Eq. (3.1)) in terms of the potential curvature Ω_x, the effective mass m and a parameter α describing the strength of SOI in the bulk. We argue that experimentally accessible values of R are sufficient to cause detectable modulations of the linear conductance in both electron ($R \lesssim 0.4$) and hole systems ($R \gtrsim 1$). We investigate the evolution of the first step's shape with increasing magnetic field $\vec{B}$ at finite $\vec{B}_{SOI}$ for different ϕ, both in the presence and absence of EEI. The former provides crucial intuition about the general effect of SOI in inhomogeneous 1D system, the latter reveals distinctive conductance features, resulting from the interplay between SOI and EEI, which predicts the outcome of future QPC experiments; most notably, this includes a double step in the linear conductance for $\phi = \pi/2$ at finite EEI, which hardly shows any dependence on magnetic field (unlike the usual linear Zeeman splitting).

Effect of Spin-Orbit Interactions on the 0.7 Anomaly in Quantum Point Contacts

Olga Goulko,[1,2] Florian Bauer,[1] Jan Heyder,[1] and Jan von Delft[1]
[1]*Physics Department, Arnold Sommerfeld Center for Theoretical Physics, and Center for NanoScience,*
Ludwig-Maximilians-Universität, Theresienstraße 37, 80333 Munich, Germany
[2]*Department of Physics, University of Massachusetts, Amherst, Massachusetts 01003, USA*
(Received 6 August 2014; published 24 December 2014)

We study how the conductance of a quantum point contact is affected by spin-orbit interactions, for systems at zero temperature both with and without electron-electron interactions. In the presence of spin-orbit coupling, tuning the strength and direction of an external magnetic field can change the dispersion relation and hence the local density of states in the point contact region. This modifies the effect of electron-electron interactions, implying striking changes in the shape of the 0.7-anomaly and introducing additional distinctive features in the first conductance step.

DOI: 10.1103/PhysRevLett.113.266402 PACS numbers: 71.70.Ej, 73.40.-c

Spin-orbit interactions (SOI) play an important role in a variety of fields within mesoscopic physics, such as spintronics and topological quantum systems. In this Letter we study the effects of SOI on the conductance of a quantum point contact (QPC), a one-dimensional constriction between two reservoirs [1,2]. The linear conductance G of a QPC is quantized in multiples of $G_Q = 2e^2/h$, showing the famous staircase as a function of gate voltage. In addition, at the onset of the first plateau, measured curves show a shoulderlike structure near $0.7G_Q$ [3]. In this regime QPCs exhibit anomalous behavior in the electrical and thermal conductance, noise, and thermopower [3–11]. The microscopic origin of this 0.7-anomaly has been the subject of a long debate [12–18]. It has recently been attributed to a strong enhancement of the effects of electron-electron interactions (EEI) by a smeared van Hove singularity in the local density of states (LDOS) at the bottom of the lowest QPC subband [15,18]. While this explains the 0.7-anomaly without evoking SOI, the presence of SOI can change the dispersion relation and hence the LDOS, thus strongly affecting the shape of the 0.7-anomaly. Previous studies of SOI in QPCs exist [19–23], but not with the present emphasis on their interplay with the QPC barrier shape and EEI, which are crucial for understanding the effect of SOI on the 0.7-anomaly.

Setup.—We consider a heterostructure forming a two-dimensional electron system (2DES) in the xy plane. Gate voltages are used to define a smooth, symmetric potential which splits the 2DES into two leads, connected by a short, one-dimensional channel along the x axis: the QPC [1,2]. The transition between the leads and the QPC is adiabatic. We also assume the confining potential in the transverse direction to be so steep that the subband spacing is much larger than all other energy scales relevant for transport, in particular those related to the magnetic field and SOI, and consider only transport in the first subband, corresponding to the lowest transverse mode. This can be described by a one-dimensional model with a smooth potential barrier and local EEI [18]. The magnetic field $\boldsymbol{B}$ is assumed to be in the xy plane, acting as a pure Zeeman field, without orbital effects.

A moving electron in an electric field can experience an effective magnetic field $\boldsymbol{B}_{\mathrm{SOI}}$ proportional to its momentum $\hbar k$. Depending on the origin of the electric field one distinguishes between Rashba and Dresselhaus terms, the former resulting from the gradient of the external potential, and the latter from the asymmetry of the ionic lattice [24]. To be able to rotate $\boldsymbol{B}$ through any angle φ w.r.t. $\boldsymbol{B}_{\mathrm{SOI}}$ we require that $\boldsymbol{B}_{\mathrm{SOI}}$ also lies in the xy plane. Without loss of generality (see the Supplemental Material [25]), we choose the y axis to be parallel to $\boldsymbol{B}_{\mathrm{SOI}}$, such that the SOI contribution to the Hamiltonian is $-\alpha\sigma_y k$, where α characterizes the strength of the (Rashba) SOI and σ_y is a Pauli matrix [26]. We only consider the leading SOI contribution proportional to k and choose the spin quantization direction along $\boldsymbol{B}$.

Without SOI, the dispersion relation $\hbar^2k^2/2m$ of a homogeneous one-dimensional model with effective mass m splits in the presence of a Zeeman field into two identical branches offset in energy by $\pm B/2$. On the other hand, without a Zeeman field, the momentum-dependent SOI splits the dispersion in k direction and also yields a negative spin-independent energy offset of magnitude $\Delta E_{\mathrm{SOI}} = \alpha^2 m/2\hbar^2$. In the following, we shift the energy origin by $-\Delta E_{\mathrm{SOI}}$ and quote all energies w.r.t. the new origin. If both $\boldsymbol{B}$ and $\boldsymbol{B}_{\mathrm{SOI}}$ are nonzero, their interplay depends on φ, as illustrated in Fig. 1(a1)–(a3). In (a1), where the fields are parallel ($\varphi = 0$), the energy offsets simply add, while for nonparallel fields a spin mixing occurs, resulting in an avoided crossing [27]. For orthogonal fields ($\varphi = \pi/2$), the lower dispersion branch exhibits either one broader minimum at $k = 0$ if $B \geq 4E_{\mathrm{SOI}}$, or two minima at finite k and a maximum at $k = 0$ otherwise. The latter case is shown in Fig. 1(a2)–(a3).

Model.—For the lowest subband we model the QPC by a symmetric potential barrier which is quadratic around its maximum,

© 2014 American Physical Society

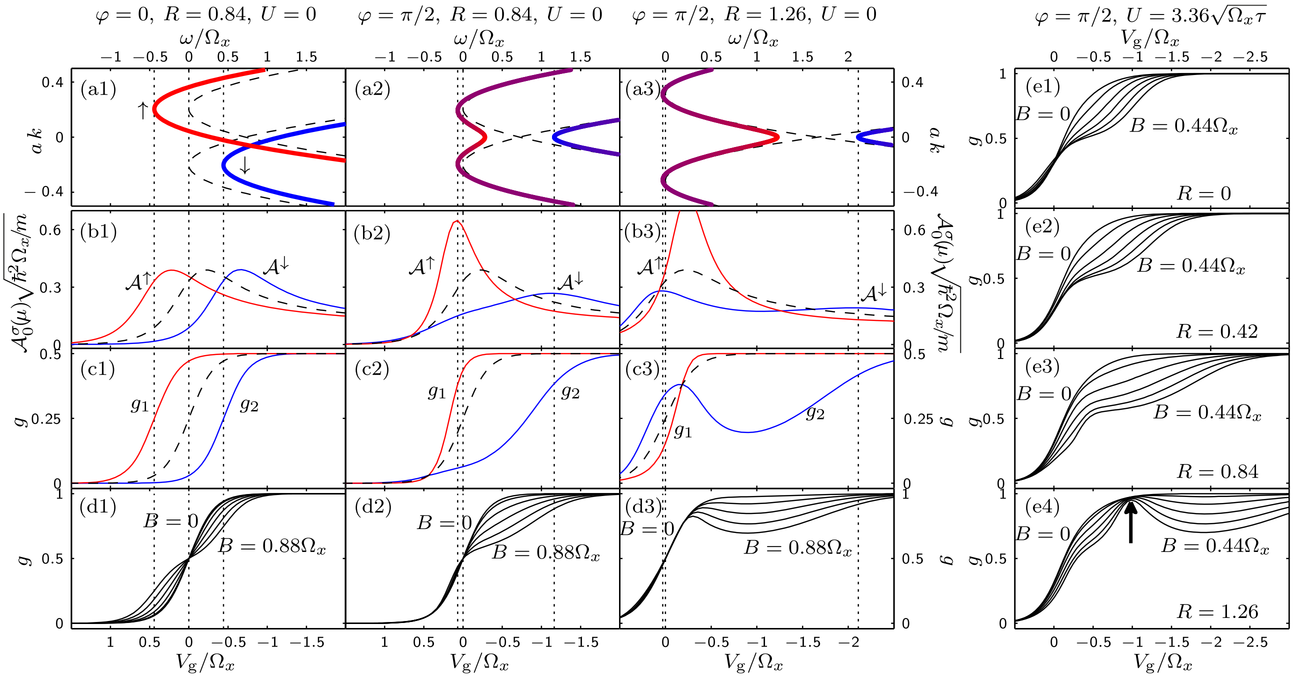

FIG. 1 (color online). Effect of SOI on the model without EEI, left columns (a1)–(d3), and with EEI, right column (e1)–(e4). The left columns (a1)–(d1), (a2)–(d2), and (a3)–(d3) represent different combinations of SOI strength R and angle φ between $\boldsymbol{B}$ and $\boldsymbol{B}_{\mathrm{SOI}}$. They highlight the correspondence between the dispersion relation $\omega(k)$ in a homogeneous system (a1)–(a3), the LDOS for fixed $\omega = \mu$ as function of V_g on the central site of a QPC with potential barrier (b1)–(b3), the conductances of the two QPC transmission channels (c1)–(c3), and the total conductance of the QPC for several equally spaced magnetic field values between $B = 0$ and $B = 0.88\Omega_x$ (d1)–(d3). In (a1)–(c3), the magnetic field is fixed at $B = 0.88\Omega_x$, with dashed lines showing the case $B = 0$ for comparison. The line colors in (a1)–(a3) quantify the contribution of each spin state (red = ↑, blue = ↓) in the dispersion branches, to illustrate the spin mixing at $\varphi \neq 0$. The right column (e1)–(e4) shows the total conductance for $U > 0$, with $\varphi = \pi/2$ and several combinations of R and B [the latter were chosen smaller than in (d1)–(d3), since EEI enhance the g-factor [18]].

$$V(x) \simeq V_g + \mu - C_b x^2/2, \tag{1}$$

and vanishes smoothly at the boundary of the QPC. The barrier height V_g, measured w.r.t. the chemical potential μ, mimics the role of the gate voltage. If V_g is swept downwards through zero, the conductance $g = G/G_Q$ increases from 0 to 1. For $B = 0$ this occurs in a single step whose width is given by the energy scale $\Omega_x = \sqrt{C_b C_d}$, which is set by the fixed curvature of the barrier C_b and the curvature of the bulk dispersion at its minimum C_d [28]. For $\varphi = 0$, $C_d = \hbar^2/m$.

For numerical purposes, we discretize real space and obtain an infinite tight-binding chain with spacing a, taking $\boldsymbol{B}$ and α constant throughout the chain. The noninteracting Hamiltonian is

$$H_0 = \sum_{j,\sigma,\sigma'} d^\dagger_{j\sigma}\left[(V_j + 2\tau)\delta_{\sigma\sigma'} - \frac{1}{2}(\boldsymbol{\sigma}\cdot\boldsymbol{B})_{\sigma\sigma'}\right] d_{j\sigma'} + \sum_{j,\sigma,\sigma'}\left[d^\dagger_{j+1\sigma}\left(-\tau_0\delta_{\sigma\sigma'} + \frac{i\alpha}{2}(\sigma_y)_{\sigma\sigma'}\right)d_{j\sigma'} + \mathrm{H.c.}\right], \tag{2}$$

where $d_{j\sigma}$ annihilates an electron with spin $\sigma \in \{\uparrow, \downarrow\} \equiv \{+, -\}$ at site j. The effective mass of the charge carrier is $m = \hbar^2/2\tau a^2$ with $\tau = \sqrt{\tau_0^2 + \alpha^2}$ [29]. We keep τ fixed when varying α. The QPC barrier potential $V_j = V(ja)$ (and later EEI) are nonzero only in a region of length $L = 2Na$ centered around $j = 0$, representing the QPC. All results shown are for $N = 50$. We use the smooth function $V(x) = (V_g + \mu)\exp\{-(2x/L)^2/(1 - [2x/L]^2)\}$ for the potential, with $\mu = 2\tau$. Sites $j < -N$ and $j > N$ represent two leads with bandwidth 4τ. The strength of SOI in a QPC is determined by the dimensionless parameter

$$R = \sqrt{\frac{\Delta E_{\mathrm{SOI}}}{\Omega_x}} = \frac{\alpha}{\hbar}\sqrt{\frac{m}{2\Omega_x}}. \tag{3}$$

SOI strengths of up to $\alpha \simeq 10^{-11}$ eVm have been reported in the literature [19,27,30,31]. Typical values of $\Omega_x \simeq 1$ meV and $m \simeq 0.05 m_e$ for InGaAs yield $R \simeq 0.2$. A stronger spin-orbit effect due to an enhancement of the anisotropic Lande g-factor is reported in Ref. [32]. Hole quantum wires have been used to observe the spin-orbit gap [27] and the anisotropic Zeeman splitting [33]. For hole QPCs, the larger effective hole mass and the resulting smaller Ω_x imply larger values of R. Here we consider both small and large R, where $R \lesssim 0.4$ is a realistic scale for electron systems and $R \gtrsim 1$ is accessible using hole systems [34], for QPCs with small barrier curvature C_b and hence small Ω_x.

System without EEI.—Many insights on the interplay between SOI and geometry can already be gained from the model without EEI, as shown in the left part (a1)–(d3) of Fig. 1.

We discuss exact results for two physical quantities, which we also relate to the bulk dispersion relation: the linear conductance g and the LDOS $\mathcal{A}_j^\sigma(\omega) = -\mathrm{Im}\mathcal{G}_{jj}^{\sigma\sigma}(\omega)/\pi a$, where $\mathcal{G}_{jj'}^{\sigma\sigma'}$ is the retarded propagator from site j' with spin σ' to site j with spin σ. Due to SOI, spin is not conserved for $\varphi \neq 0$ and hence $\mathcal{G}_{jj}^{\sigma\sigma'}$ is not spin-diagonal. However at $j = 0$ its off-diagonal elements turn out to be negligible compared to the diagonal ones. Thus it is meaningful to analyze the LDOS at $j = 0$ for given σ. The linear conductance at zero temperature can be calculated via $g = g_1 + g_2 \propto \mathrm{Tr}(t^\dagger t)$ [35], where $t^{\sigma\sigma'} = \mathcal{G}_{-N,N}^{\sigma\sigma'}(\mu)$ is the transmission matrix of the QPC and $\mathrm{Tr}(t^\dagger t)$ equals the sum of the eigenvalues of $t^\dagger t$. The spin structure of t depends on N, but the eigenvalues of $t^\dagger t$, which yield the conductances g_1 and g_2 of the two transmission channels, do not.

For $\varphi = 0$ (Fig. 1, left column) spin is conserved and SOI have no influence on the LDOS and the conductance. This case is analogous to the one discussed in Ref. [18]. The bulk [i.e., $V(x) = 0$] LDOS,

$$\mathcal{A}_{\mathrm{bulk}}^\sigma(\omega) \propto \left.\frac{\partial k}{\partial \omega}\right|_\sigma = \sqrt{\frac{m}{2\hbar^2(\omega + \sigma B/2)}}, \qquad (4)$$

has a van Hove singularity, diverging at the minimum $\omega = -\sigma B/2$ of the corresponding dispersion branch, where the electron velocity vanishes. In the QPC, the x-dependent LDOS is shifted in energy by the barrier potential $V(x)$. Since the barrier breaks translational invariance, the van Hove singularity is smeared out on a scale set by Ω_x [15], forming a ridgelike structure, called van Hove ridge in [18]. The LDOS height becomes finite, of order $\mathcal{O}(\sqrt{m/(\hbar^2\Omega_x)})$, determined by Ω_x and the curvature $\hbar^2/m$ of the bulk dispersion. At a given position x, the LDOS maximum occurs at an energy which is $\mathcal{O}(\Omega_x)$ larger than the corresponding potential energy $V(x) - \sigma B/2$. Here and henceforth we quote the LDOS as a function of V_g at fixed $\omega = \mu$. Figure 1(b1) shows it at the central site $j = 0$; the spatially resolved LDOS is shown in Fig. 1 of the Supplemental Material [25]. The LDOS has the same shape for both spins. Its structure is clearly inherited from that of the dispersion in (a1), with peak energies aligned with the dispersion minima up to the shift of $\mathcal{O}(\Omega_x)$. Similarly, the conductances $g_1(V_g)$ and $g_2(V_g)$ of the two channels in (c1) show steps of the same shape with widths $\propto \Omega_x$ [28], split by B and aligned with the dispersion minima. This causes the total conductance $g(V_g)$ in (d1) to split symmetrically into a double step with increasing field, just as for a QPC without SOI.

Next consider the case $\varphi = \pi/2$ shown in Fig. 1(a2)–(d3). Spin mixing leads to an avoided crossing with spin gap $\propto B$, which splits the dispersion into an upper branch with a narrow minimum and a lower branch with two minima and one maximum (for $B < 4E_{\mathrm{SOI}}$). Note that bulk LDOS structures separated in energy by less than Ω_x are not resolved within the QPC. In the following, we give an intuitive explanation of how the dispersion minima relate to the properties of the LDOS peaks and the conductance steps. The curvatures of the lower and upper dispersion branches are, respectively, smaller or larger than in (a1), $C_{d1} < C_d < C_{d2}$ (loosely speaking, C_{d1} is the effective curvature obtained by smearing the double dispersion minimum by Ω_x, yielding a single minimum). Because the barrier curvature C_b is fixed, this results in two modified energy scales $\Omega_{xi} = \sqrt{C_b C_{di}}$, with $\Omega_{x1} < \Omega_x < \Omega_{x2}$, which determine the LDOS peak heights and widths, as well as the conductance step widths. Consequently, in (b2) the LDOS peak for $\mathcal{A}_0^\downarrow$ is lower and wider than for $\mathcal{A}_0^\uparrow$. Likewise, in (c2) the conductance step for $g_2(V_g)$ is wider than for $g_1(V_g)$, causing $g(V_g)$ in (d2) to show a striking asymmetry for its B-induced evolution from a single to a double step. This asymmetry is reminiscent of but unrelated to that known for the 0.7-anomaly—the latter is driven by EEI, as discussed below—but should be observable in higher conductance steps, where EEI are weaker.

For $R \gtrsim 1$ more structures emerge, see Fig. 1(a3)–(b3). Spin-mixing produces an additional "emergent" peak in $\mathcal{A}_0^\downarrow$ (b3) and an additional step in $g_2(V_g)$ (c3) near $V_g \simeq 0$. Between the two steps, the transmission $g_2(V_g)$ has a minimum, corresponding to the spin gap, and the total conductance $g(V_g)$ in (d3) likewise develops a spin gap minimum with increasing B. These features can be understood by looking at the spin composition of the two bulk dispersion branches, depicted quantitatively through the colors in Fig. 1(a1)–(a3). At $k = 0$ the SOI field is zero and we have pure spin-states w.r.t. the chosen quantization. At larger $|k|$ the SOI field increases, leading to spin-mixing. In fact in the limit $k \to \infty$ we find a fully mixed state with equal up and down contributions. Since the upper branch minimum at $k = 0$ is in a pure spin-down state, it corresponds to a peak only in $\mathcal{A}^\downarrow$. But the minima of the lower branch are shifted away from $k = 0$ and have a spin-down share besides the dominant spin-up contribution. This causes the emergent peak in $\mathcal{A}^\downarrow$ at low frequencies, whose height increases with R, due to the stronger spin-mixing.

Interacting system.—We now include EEI via $H_{\mathrm{int}} = \sum_j U_j d_{j\uparrow}^\dagger d_{j\uparrow} d_{j\downarrow}^\dagger d_{j\downarrow}$. The on-site interaction $U_j = U(ja)$ is switched on smoothly over the QPC according to $U(x) = U \exp\{-(2x/L)^6/[1 - (2x/L)^2]\}$. We set $U_j = 0$ for $|j| > N$, because outside the QPC region transverse confinement is weak or absent, and screening strong [18,36]. We calculate the conductance at zero temperature with the functional renormalization group technique in the one-particle irreducible version [29,37–40] using the coupled ladder approximation, which was presented in Ref. [36] for a model without SOI. Generalizations necessary in the presence of SOI are described in the Supplemental Material [25].

The B dependence of the conductance for $\varphi = \pi/2$ and different R in the presence of EEI is shown in the right column (e1)–(e4) of Fig. 1 and the corresponding transconductance dg/dV_g in Fig. 2(b)–(f). The case $R = 0$ [see Figs. 1(e1) and 2(a)–(c)], which is equivalent to $\varphi = 0$, has been discussed in Refs. [18,36]: once a finite magnetic field breaks the spin degeneracy a surplus of spin-up electrons develops in the QPC, so that spin-down electrons experience both a Zeeman and a Coulomb energy cost. This Stoner-type effect depends on the LDOS at μ and hence is strongest when the apex of the van Hove ridge touches the chemical potential, i.e., when V_g is within $\simeq 0.5\Omega_x$ below 0 [18]. This causes an asymmetry w.r.t. $V_g = 0$ in the B-induced evolution of $g(V_g)$ from a single to a double step in Fig. 1(e1), in contrast to the case without EEI in Fig. 1(d1). This asymmetry is characteristic of the 0.7-anomaly. The corresponding transconductance in Fig. 2(b)–(c) shows a double peak whose spacing increases roughly linearly with B (with an EEI-enhanced g-factor), as seen in numerous experiments [3,10,18].

The Stoner-type Coulomb enhancement of a field-induced population imbalance is amplified when $R \neq 0$, as shown in Figs. 1(e2)–(e4) and 2(d)–(f), because of the height imbalance for the spin-up and spin-down LDOS peaks caused by SOI. Correspondingly, with increasing R the double-step structure in the conductance becomes more pronounced, the second substep becoming much broader than the first [see Figs. 1(e2)–(e3)] and the transconductance in Fig. 2(d)–(e) shows a weakening of the lower-V_g peak with increasing R. This reflects the increasing curvature C_{d2} of the upper dispersion branch (and hence larger step width Ω_{x2}). For $R \gtrsim 1$, additional features, inherited from the noninteracting case, emerge for $g(V_g)$ in Fig. 1(e4): a local maximum (marked by an arrow), followed by a spin gap minimum at lower V_g. For the transconductance, Fig. 2(f), these features show up as a strong secondary peak around $V_g/\Omega_x \simeq -1$ (marked by an arrow), followed by a region of negative transconductance (black). EEI also induce a secondary 0.7-type double-step feature in $g(V_g)$ for V_g/Ω_x between 0 and -1, Fig. 1(e4), which is similar to, but narrower than that for $R = 0$. It originates from the main LDOS peak in $\mathcal{A}_0^{\uparrow}$ and the *emergent* peak in $\mathcal{A}_0^{\downarrow}$. Unlike the regular $\mathcal{A}_0^{\downarrow}$ peak aligned with the upper dispersion branch, whose V_g position is governed by the magnetic field, the emergent $\mathcal{A}_0^{\downarrow}$ peak occurs, due to strong spin-mixing, at nearly B-independent energy close to the $\mathcal{A}_0^{\uparrow}$ peak. As a result, the two transconductance maxima in Fig. 2(f) remain parallel with increasing B, in strong contrast to the situation for $R < 1$ in Fig. 2(c)–(e).

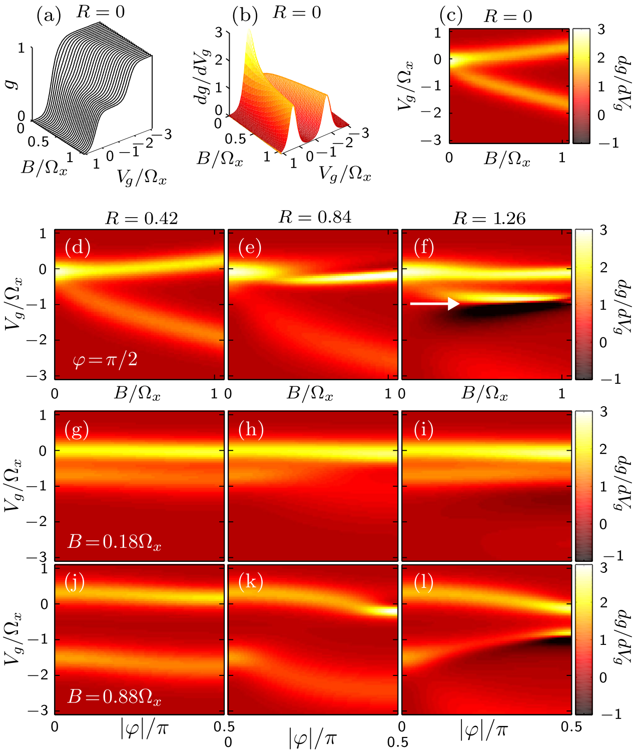

FIG. 2 (color online). Functional renormalization group results for the conductance g and transconductance dg/dV_g, for $U = 3.36\sqrt{\Omega_x \tau}$ at zero temperature. Top row: 3d or color-scale plots of the conductance (a) and the transconductance (b) and (c) as functions of V_g and B, for $R = 0$. Three bottom rows (d)–(l): Color-scale plots of the transconductance for three choices of R (three columns), plotted as a function of V_g and either B for fixed $\varphi = \pi/2$ (second row) or of φ for fixed $B = 0.18\Omega_x$ (third row) and $B = 0.88\Omega_x$ (fourth row).

Figures 2(g)–(l) show, for two fixed values of B, how the transconductance evolves as $|\varphi|$ is increased from 0 to $\pi/2$, thus switching on the effects of SOI. The decrease in peak spacing with increasing $|\varphi|$ in Fig. 2(l) strikingly reflects the increasing importance of spin mixing. The strong angle dependence predicted here is a promising candidate for an experimental test of our theory [41].

At small nonzero temperature, inelastic scattering causes a Fermi-liquid-type reduction of the conductance, $g(T, V_g)/g(0, V_g) = 1 - (T/T_*)^2$ for $T \ll T_*$, with a V_g-dependent low-energy scale $T_*(V_g)$. We expect its magnitude to be similar to the case without SOI, typically 18] $\simeq 1$ K]. Thus, for $T \lesssim 0.1$ K, the T-dependence should be very weak and the $T = 0$ predictions applicable.

In summary, we have shown that in the presence of SOI, the changes in the dispersion induced by the interplay of $\boldsymbol{B}$ and $\boldsymbol{B}_{\mathrm{SOI}}$ can strongly affect the shape of the 0.7-anomaly. In the absence of EEI, SOI cause an anisotropic response of the spin splitting to the applied in-plane magnetic field. With EEI, the 0.7-anomaly also develops an anisotropic response to magnetic field, and if SOI are strong, the conductance develops additional features due to the interplay of EEI and SOI: for $\varphi = \pi/2$ these include a field-induced double step in the conductance that does *not* split linearly with B, followed by a spin gap minimum. The dependence of the conductance on the angle between $\boldsymbol{B}$ and $\boldsymbol{B}_{\mathrm{SOI}}$ is already apparent for $R \simeq 0.4$, which is accessible in experiments with electron QPCs. Hole QPCs with $R \gtrsim 1$ would allow access to regimes with strong SOI.

An experimental verification of our predictions would highlight the influence of LDOS features on the conductance and thus lend further support to the van Hove scenario of Ref. [18] as microscopic explanation for the 0.7-anomaly. More generally, our work lays out a conceptual framework for analyzing the interplay of SOI, EEI, and barrier shape in quasi-1D geometries: examine how SOI and barrier shape modify the (bare) LDOS near μ—whenever the LDOS is large, EEI effects are strong. We expect this to be relevant for the more complicated hybrid superconductor-semiconductor junctions currently studied by seekers of Majorana fermions [42–44]. A proper analysis of such systems would require a generalization of our approach to include superconducting effects.

We thank S. Fischer, A. Hamilton, K. Hudson, S. Ludwig, C. Marcus, A. Micolich and A. Srinivasan for interesting and useful discussions and acknowledge support from the DFG via SFB-631, SFB-TR12, De730/4-3, and the Cluster of Excellence *Nanosystems Initiative Munich*. O. G. acknowledges support from the NSF under the Grant No. PHY-1314735.

[1] D. A. Wharam, T. J. Thornton, R. Newbury, M. Pepper, H. Ahmed, J. E. F. Frost, D. G. Hasko, D. C. Peacock, D. A. Ritchie, and G. A. C. Jones, J. Phys. C **21**, L209 (1988).

[2] B. J. van Wees, H. van Houten, C. W. J. Beenakker, J. G. Williamson, L. P. Kouwenhoven, D. van der Marel, and C. T. Foxon, Phys. Rev. Lett. **60**, 848 (1988).

[3] K. J. Thomas, J. T. Nicholls, M. Y. Simmons, M. Pepper, D. R. Mace, and D. A. Ritchie, Phys. Rev. Lett. **77**, 135 (1996).

[4] N. J. Appleyard, J. T. Nicholls, M. Pepper, W. R. Tribe, M. Y. Simmons, and D. A. Ritchie, Phys. Rev. B **62**, R16275 (2000).

[5] A. Kristensen, H. Bruus, A. E. Hansen, J. B. Jensen, P. E. Lindelof, C. J. Marckmann, J. Nygård, C. B. Sørensen, F. Beuscher, A. Forchel, and M. Michel, Phys. Rev. B **62**, 10950 (2000).

[6] S. M. Cronenwett, H. J. Lynch, D. Goldhaber-Gordon, L. P. Kouwenhoven, C. M. Marcus, K. Hirose, N. S. Wingreen, and V. Umansky, Phys. Rev. Lett. **88**, 226805 (2002).

[7] L. DiCarlo, Y. Zhang, D. T. McClure, D. J. Reilly, C. M. Marcus, L. N. Pfeiffer, and K. W. West, Phys. Rev. Lett. **97**, 036810 (2006).

[8] O. Chiatti, J. T. Nicholls, Y. Y. Proskuryakov, N. Lumpkin, I. Farrer, and D. A. Ritchie, Phys. Rev. Lett. **97**, 056601 (2006).

[9] L. W. Smith, A. R. Hamilton, K. J. Thomas, M. Pepper, I. Farrer, J. P. Griffiths, G. A. C. Jones, and D. A. Ritchie, Phys. Rev. Lett. **107**, 126801 (2011).

[10] A. P. Micolich, J. Phys. Condens. Matter **23**, 443201 (2011).

[11] R. Danneau, O. Klochan, W. R. Clarke, L. H. Ho, A. P. Micolich, M. Y. Simmons, A. R. Hamilton, M. Pepper, and D. A. Ritchie, Phys. Rev. Lett. **100**, 016403 (2008).

[12] D. J. Reilly, T. M. Buehler, J. L. O'Brien, A. R. Hamilton, A. S. Dzurak, R. G. Clark, B. E. Kane, L. N. Pfeiffer, and K. W. West, Phys. Rev. Lett. **89**, 246801 (2002).

[13] K. F. Berggren and I. I. Yakimenko, Phys. Rev. B **66**, 085323 (2002).

[14] Y. Meir, K. Hirose, and N. S. Wingreen, Phys. Rev. Lett. **89**, 196802 (2002).

[15] C. Sloggett, A. I. Milstein, and O. P. Sushkov, Eur. Phys. J. B **61**, 427 (2008).

[16] A. M. Lunde, A. D. Martino, A. Schulz, R. Egger, and K. Flensberg, New J. Phys. **11**, 023031 (2009).

[17] K. Aryanpour and J. E. Han, Phys. Rev. Lett. **102**, 056805 (2009).

[18] F. Bauer, J. Heyder, E. Schubert, D. Borowsky, D. Taubert, B. Bruognolo, D. Schuh, W. Wegscheider, J. von Delft, and S. Ludwig, Nature (London) **501**, 73 (2013).

[19] M. Kohda, S. Nakamura, Y. Nishihara, K. Kobayashi, T. Ono, J.-i. Ohe, Y. Tokura, T. Mineno, and J. Nitta, Nat. Commun. **3**, 1082 (2012).

[20] J.-H. Hsiao and T.-M. Hong, Phys. Rev. B **82**, 115309 (2010).

[21] M. P. Nowak, K. Kolasiński, and B. Szafran, Phys. Rev. B **90**, 035301 (2014)..

[22] R. Danneau, W. R. Clarke, O. Klochan, A. P. Micolich, A. R. Hamilton, M. Y. Simmons, M. Pepper, and D. A. Ritchie, Appl. Phys. Lett. **88**, 012107 (2006).

[23] F. Nichele, S. Chesi, S. Hennel, A. Wittmann, C. Gerl, W. Wegscheider, D. Loss, T. Ihn, and K. Ensslin, Phys. Rev. Lett. **113**, 046801 (2014).

[24] R. Winkler, *Spin-Orbit Coupling Effects in Two-Dimensional Electron and Hole Systems* (Springer, Berlin, 2003).

[25] See Supplemental Material at http://link.aps.org/supplemental/10.1103/PhysRevLett.113.266402 for geometric details of the model, plots of the spatially resolved LDOS, and details on the functional renormalization group formalism with SOI.

[26] L. Meier, G. Salis, I. Shorubalko, E. Gini, S. Schön, and K. Ensslin, Nat. Phys. **3**, 650 (2007).

[27] C. H. L. Quay, T. L. Hughes, J. A. Sulpizio, L. N. Pfeiffer, K. W. Baldwin, K. W. West, D. Goldhaber-Gordon, and R. de Picciotto, Nat. Phys. **6**, 336 (2010).

[28] M. Büttiker, Phys. Rev. B **41**, 7906(R) (1990).

[29] J. E. Birkholz, Ph.D. thesis, Georg-August-Universität zu Göttingen, 2008.

[30] J. Nitta, T. Akazaki, H. Takayanagi, and T. Enoki, Phys. Rev. Lett. **78**, 1335 (1997).

[31] T. Kita, T. Kakegawa, M. Akabori, and S. Yamada, Solid State Commun. **136**, 479 (2005).

[32] T. P. Martin, A. Szorkovszky, A. P. Micolich, A. R. Hamilton, C. A. Marlow, R. P. Taylor, H. Linke, and H. Q. Xu, Phys. Rev. B **81**, 041303 (2010).

[33] J. C. H. Chen, O. Klochan, A. P. Micolich, A. R. Hamilton, T. P. Martin, L. H. Ho, U. Zülicke, D. Reuter, and A. D. Wieck, New J. Phys. **12**, 033043 (2010).

[34] A. R. Hamilton, T. Li, O. P. Sushkov, and R. Winkler, private communication. For weakly 1D-confined holes, it can be argued that the dominant SOI term has the same $k\sigma_y$ form as used here.

[35] S. Datta, *Electronic Transport in Mesoscopic Systems* (Cambridge University Press, Cambridge, England, 1995).

[36] F. Bauer, J. Heyder, and J. von Delft, Phys. Rev. B **89**, 045128 (2014).

[37] C. Wetterich, Phys. Lett. B **301**, 90 (1993).

[38] J. E. Birkholz and V. Meden, Phys. Rev. B **79**, 085420 (2009).

[39] F. Bauer, Master's thesis, LMU-München, 2008.

[40] W. Metzner, M. Salmhofer, C. Honerkamp, V. Meden, and K. Schönhammer, Rev. Mod. Phys. **84**, 299 (2012).

[41] A. R. Hamilton, K. Hudson, A. P. Micolich, and A. Srinivasan, private communication.

[42] R. M. Lutchyn, J. D. Sau, and S. Das Sarma, Phys. Rev. Lett. **105**, 077001 (2010).

[43] Y. Oreg, G. Refael, and F. von Oppen, Phys. Rev. Lett. **105**, 177002 (2010).

[44] V. Mourik, K. Zuo, S. M. Frolov, S. R. Plissard, E. P. A. M. Bakkers, and L. P. Kouwenhoven, Science **336**, 1003 (2012).

Supplemental Material to "The effect of spin-orbit interactions on the 0.7-anomaly in quantum point contacts"

I. GEOMETRIC DETAILS OF THE MODEL

In our model the 2DES is in the xy-plane and the QPC is directed along the x-axis (this is the direction of motion of the charge carrier). For the directions of the $\boldsymbol{B}$ and $\boldsymbol{B}_{\mathrm{SOI}}$ fields we impose the following restrictions. To avoid orbital effects we require the magnetic field $\boldsymbol{B}$ to be in the xy-plane of the 2DES. We also want to be able to rotate $\boldsymbol{B}$ through any angle φ w.r.t. $\boldsymbol{B}_{\mathrm{SOI}}$, which implies that $\boldsymbol{B}_{\mathrm{SOI}}$ also must lie in the xy-plane. With the latter condition, the $\boldsymbol{B}_{\mathrm{SOI}}$ field can be either parallel to the direction of motion of the electrons (pure Dresselhaus contribution), or orthogonal to it (pure Rashba contribution), or a combination of the two. But for our mathematical model, the end results depend only on the relative angle φ between $\boldsymbol{B}$ and $\boldsymbol{B}_{\mathrm{SOI}}$. This means that we can choose the direction of $\boldsymbol{B}_{\mathrm{SOI}}$ without loss of generality. We choose $\boldsymbol{B}_{\mathrm{SOI}}$ to be parallel to the y-axis, c.f. Eq. (2) of the main text.

II. THE SPATIALLY RESOLVED LDOS

In Fig. 1(b1-b3) of the main text we show the LDOS at fixed μ as a function of V_{g} on the central site of the QPC. The behavior at the center captures all relevant features. For completeness we include here in Fig. 1 the spatially resolved plots of the LDOS $\mathcal{A}_j^\sigma$ for both spin states and the same parameter values as in Fig. 1 of the main text.

III. SECOND ORDER FRG

The functional Renormalization Group (fRG) method is an improved perturbation technique [1–5]. Rather than expanding the Green's function in orders of the coupling and truncating the expansion, fRG introduces a flow parameter Λ into the free Green's function $\mathcal{G}_0$. At zero temperature we define

$$\mathcal{G}_0(i\omega) \to \theta(|\omega| - \Lambda)\mathcal{G}_0(i\omega) \equiv \mathcal{G}_0^\Lambda(i\omega), \tag{1}$$

where $\theta(\omega)$ is the Heaviside step function. At the beginning of the flow, setting $\Lambda = \infty$ yields $\mathcal{G}_0^\Lambda = 0$, which means that the only contribution to the full Green's function comes from the bare vertex. At the end of the flow, $\Lambda = 0$ recovers the full model. The technical details of the one-particle irreducible version of the fRG employed in this work are presented in depth in [6]. We use the static approximation at zero temperature, which will be described below in Sec. III B. Since [6] does not deal with spin-orbit interactions, no spin-mixing is possible, which introduces additional symmetries into the system. In our case these symmetries are no longer present. In this Supplement we focus on the generalizations necessary to account for such spin-mixing terms.

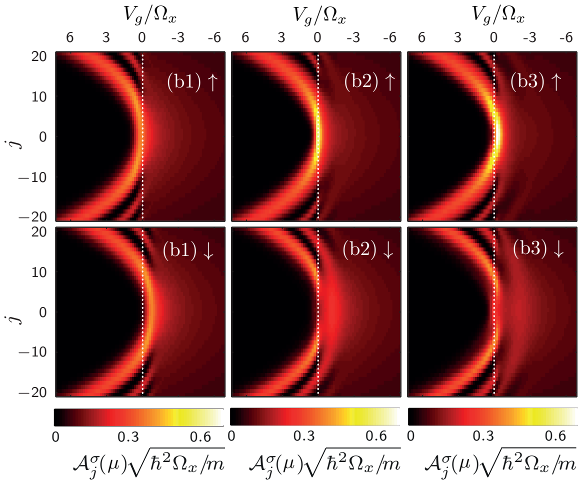

FIG. 1. Spatially resolved plots of the noninteracting LDOS $\mathcal{A}_j^\sigma$ at fixed $\omega = \mu$, plotted as a function of gate voltage V_{g} and site index j, for $B = 0.88\Omega_x$ and for spin $\sigma =\uparrow$ (top row) and $\sigma =\downarrow$ (bottom row). Left column: $R = 0.84$, $\varphi = 0$. Middle column: $R = 0.84$, $\varphi = \pi/2$. Right column: $R = 1.26$, $\varphi = \pi/2$. All results shown are for $N = 50$.

The second-order fRG flow equations in the one-particle irreducible version and in the static approximation are given by

$$\frac{\mathrm{d}}{\mathrm{d}\Lambda}\gamma_1^\Lambda(q_1',q_1) = \frac{1}{2\pi}\sum_{\omega=\pm\Lambda}\sum_{q_2',q_2}\widetilde{\mathcal{G}}^\Lambda_{q_2,q_2'}(i\omega)\gamma_2^\Lambda(q_2',q_1';q_2,q_1), \tag{2}$$

$$\frac{\mathrm{d}}{\mathrm{d}\Lambda}\gamma_2^\Lambda = \frac{\mathrm{d}}{\mathrm{d}\Lambda}(\gamma_p^\Lambda+\gamma_x^\Lambda+\gamma_d^\Lambda), \quad \text{where} \tag{3}$$

$$\frac{\mathrm{d}}{\mathrm{d}\Lambda}\gamma_p^\Lambda(q_1',q_2';q_1,q_2) = \frac{1}{2\pi}\sum_{\omega=\pm\Lambda}\sum_{q_3',q_3,q_4',q_4}\frac{1}{2}\gamma_2^\Lambda(q_1',q_2';q_3,q_4)\widetilde{\mathcal{G}}^\Lambda_{q_3,q_3'}(i\omega)\widetilde{\mathcal{G}}^\Lambda_{q_4,q_4'}(-i\omega)\gamma_2^\Lambda(q_3',q_4';q_1,q_2), \tag{4}$$

$$\frac{\mathrm{d}}{\mathrm{d}\Lambda}\gamma_x^\Lambda(q_1',q_2';q_1,q_2) = \frac{1}{2\pi}\sum_{\omega=\pm\Lambda}\sum_{q_3',q_3,q_4',q_4}\gamma_2^\Lambda(q_1',q_4';q_3,q_2)\widetilde{\mathcal{G}}^\Lambda_{q_3,q_3'}(i\omega)\widetilde{\mathcal{G}}^\Lambda_{q_4,q_4'}(i\omega)\gamma_2^\Lambda(q_3',q_2';q_1,q_4), \tag{5}$$

$$\frac{\mathrm{d}}{\mathrm{d}\Lambda}\gamma_d^\Lambda(q_1',q_2';q_1,q_2) = -\frac{1}{2\pi}\sum_{\omega=\pm\Lambda}\sum_{q_3',q_3,q_4',q_4}\gamma_2^\Lambda(q_1',q_3';q_1,q_4)\widetilde{\mathcal{G}}^\Lambda_{q_4,q_4'}(i\omega)\widetilde{\mathcal{G}}^\Lambda_{q_3,q_3'}(i\omega)\gamma_2^\Lambda(q_4',q_2';q_3,q_2), \tag{6}$$

where $-\gamma_1^\Lambda$ is the self-energy and γ_2^Λ is the two-particle irreducible vertex. All higher order vertices $\gamma_{n\geq 3}$ have been set to zero. Here $\widetilde{\mathcal{G}}^\Lambda$ is defined as

$$\widetilde{\mathcal{G}}^\Lambda = \left[\mathcal{G}_0^{-1}+\gamma_1^\Lambda\right]^{-1} = \frac{1}{i\omega - H_0 + \gamma_1^\Lambda}, \tag{7}$$

where H_0 is the (known) Hamiltonian of the non-interacting system. The quantum numbers q_i encode the spin and spatial degrees of freedom $q \equiv (\sigma, j)$. The flow of γ_2^Λ was split into three contributions called the particle-particle channel (P), and the exchange (X) and direct (D) contributions to the particle-hole channel, respectively. This will allow us to simplify the flow equations later.

For a derivation of Eqs. (2-6) see for instance [4, 6, 7].

A. Initial condition

For the numerical treatment we cannot set the initial value of the flow parameter Λ_{init} to infinity, but it is sufficient that it is much larger than all relevant energy scales. We have the following initial condition at Λ_{init} [4, 6, 7],

$$\gamma_2^{\Lambda_{\text{init}}}(q_1,q_2,q_3,q_4) = v_{q_1,q_2,q_3,q_4}, \tag{8}$$

$$\gamma_1^{\Lambda_{\text{init}}}(q_1,q_2) = -\frac{1}{2}\sum_q v_{q_1,q,q_2,q}, \tag{9}$$

where the vertex v_{q_1,q_2,q_3,q_4} is site diagonal and at site $j \equiv j_1 = j_2 = j_3 = j_4$ is given by

$$v_{q_1,q_2,q_3,q_4} = U_j\delta_{\sigma_1\bar{\sigma}_2}\left(\delta_{\sigma_1\sigma_3}\delta_{\sigma_2\sigma_4} - \delta_{\sigma_1\sigma_4}\delta_{\sigma_2\sigma_3}\right). \tag{10}$$

This means that the spins q_1 and q_2, as well as the spins q_3 and q_4 must be opposite. This leaves two possibilities: $\sigma_1 = \sigma_3 = \bar{\sigma}_2 = \bar{\sigma}_4$ that has positive sign, and $\sigma_1 = \sigma_4 = \bar{\sigma}_2 = \bar{\sigma}_3$ that has negative sign. Inserting this into the initial condition for γ_1^Λ yields

$$\gamma_1^{\Lambda_{\text{init}}}(q',q) = -(U_j/2)\delta_{\sigma'\sigma}. \tag{11}$$

B. Approximations

We use the following approximations, see [7] and references thereof. Firstly, we neglect the frequency dependence of γ_2^Λ. This is called the static approximation and is known to give good results at $T = 0$ [6]. Given the structure of the flow equation for γ_2^Λ above, it is natural to divide the flowing vertex into four parts as follows:

$$\gamma_2^\Lambda = v + \gamma_p^\Lambda + \gamma_x^\Lambda + \gamma_d^\Lambda. \tag{12}$$

Here v is shorthand for the bare vertex, and the flows of γ_p^Λ, γ_x^Λ and γ_d^Λ were given above. The initial value for γ_2^Λ is simply the bare vertex. If we insert the bare vertex into the flow equations for the components of γ_2^Λ we observe that some of its symmetries remain preserved in the derivative on the left hand side. For instance, for γ_p^Λ we see that the first two and the second two site indices must be identical and also that the first and the second pair of spin indices must be opposite, respectively. Similarly, for γ_x^Λ we see that the first and fourth site index, as well as the the second and third site index must be equal. For γ_d^Λ the first and the third, as well as the second and the fourth site indices are equal. There is no restriction on the any of the spin indices for either γ_x^Λ or γ_d^Λ.

The next iteration would break the remaining symmetries, since all three channels contribute to the derivative of γ_2^Λ and then back-feed into the differential equations for each channel. If instead we choose to only back-feed each channel into its own differential equation, we can preserve the symmetries described above. This immensely simplifies the treatment of the equations. By doing so, we only neglect contributions of order v^3 and higher, which justifies their neglect as long as U_j is not too large. Altogether we obtain the following contributions:

$$P_{ji}^{\sigma\bar{\sigma}} := \gamma_p^\Lambda\left(j\sigma, j\bar{\sigma}; i\sigma, i\bar{\sigma}\right) \tag{13}$$

$$\bar{P}_{ji}^{\sigma\bar{\sigma}} := \gamma_p^\Lambda\left(j\sigma, j\bar{\sigma}; i\bar{\sigma}, i\sigma\right) \tag{14}$$

$$X_{ji}^{\sigma_1\sigma_2\sigma_3\sigma_4} := \gamma_x^\Lambda\left(j\sigma_1, i\sigma_2; i\sigma_3, j\sigma_4\right) \tag{15}$$

$$D_{ji}^{\sigma_1\sigma_2\sigma_3\sigma_4} := \gamma_d^\Lambda\left(j\sigma_1, i\sigma_2; j\sigma_3, i\sigma_4\right) \tag{16}$$

Note that some elements of a channel can also satisfy the symmetries of another channel. So for instance the diagonal element $P_{jj}^{\sigma\bar{\sigma}}$ has the same symmetries as the diagonal elements $X_{jj}^{\sigma\bar{\sigma}\sigma\bar{\sigma}}$ and $D_{jj}^{\sigma\bar{\sigma}\sigma\bar{\sigma}}$. If we back-feed such elements too we preserve the symmetries in each channel, but obtain a more accurate approximation. Therefore, in each of the three flow equations for the channels of γ_2^Λ we replace γ_2^Λ on the right hand side by the appropriate channels plus the site diagonal contributions of the other channels that obey the same symmetries. The initial conditions for the three channels follow immediately from (12): $\gamma_p^{\Lambda_{\text{init}}} = \gamma_x^{\Lambda_{\text{init}}} = \gamma_d^{\Lambda_{\text{init}}} = 0$. Of course, for the differential equation for γ_1^Λ we need the full γ_2^Λ which is the sum of all three channels and the bare vertex.

C. Symmetries

Due to the hermiticity of the Hamiltonian the following relation holds for the Green's function

$$\mathcal{G}(i\omega) = \mathcal{G}^\dagger(-i\omega) \Leftrightarrow \mathcal{G}_{ij}(i\omega) = \mathcal{G}_{ji}^*(-i\omega). \tag{17}$$

We assume that this relation also holds for $\tilde{\mathcal{G}}^\Lambda$. If γ_1^Λ is hermitian then the assumption is obviously justified. Numerical results indeed confirm that γ_1^Λ is hermitian. We also have the following symmetries of γ_2:

$$\begin{aligned} \gamma_2(q_1, q_2, q_3, q_4) &= -\gamma_2(q_2, q_1, q_3, q_4) && (18)\\ &= -\gamma_2(q_1, q_2, q_4, q_3) && (19)\\ &= \gamma_2(q_2, q_1, q_4, q_3) && (20) \end{aligned}$$

This follows directly from the equation defining the two-particle vertex, see e.g. [4]. Again we assume that these relations hold also for γ_2^Λ and moreover for each of the separate channels. Their consistency with the numerical results will be demonstrated below. Altogether this yields the following symmetry relations for the different channels:

$$\begin{aligned} P_{ji}^{\sigma\bar{\sigma}} &= P_{ji}^{\bar{\sigma}\sigma} = -\bar{P}_{ji}^{\sigma\bar{\sigma}} && (21)\\ D_{ji}^{\sigma_1\sigma_2\sigma_3\sigma_4} &= D_{ij}^{\sigma_2\sigma_1\sigma_4\sigma_3} = -X_{ji}^{\sigma_1\sigma_2\sigma_4\sigma_3} && (22)\\ X_{ji}^{\sigma_1\sigma_2\sigma_3\sigma_4} &= X_{ij}^{\sigma_2\sigma_1\sigma_4\sigma_3} = -D_{ji}^{\sigma_1\sigma_2\sigma_4\sigma_3} && (23) \end{aligned}$$

We observe that $P^{\uparrow\downarrow} = P^{\downarrow\uparrow}$ and hence the spin indices for P will be dropped from now on, leaving only the site index. The alternative configuration $\bar{P}$ follows completely from P and does not need to be kept track of separately. Same applies to X and D which completely define each other. We choose to work with D. There are various symmetries of D but there is no restriction on the spin index. This means that there are $2^4 = 16$ different submatrices corresponding to 16 different spin configurations of D. We choose to arrange them as follows

$$D^{\sigma_1\sigma_2\sigma_3\sigma_4} = \left(\begin{array}{c|c|c|c} \uparrow\uparrow\uparrow\uparrow & \uparrow\uparrow\uparrow\downarrow & \uparrow\downarrow\uparrow\uparrow & \uparrow\downarrow\uparrow\downarrow \\ \hline \uparrow\uparrow\downarrow\uparrow & \uparrow\uparrow\downarrow\downarrow & \uparrow\downarrow\downarrow\uparrow & \uparrow\downarrow\downarrow\downarrow \\ \hline \downarrow\uparrow\uparrow\uparrow & \downarrow\uparrow\uparrow\downarrow & \downarrow\downarrow\uparrow\uparrow & \downarrow\downarrow\uparrow\downarrow \\ \hline \downarrow\uparrow\downarrow\uparrow & \downarrow\uparrow\downarrow\downarrow & \downarrow\downarrow\downarrow\uparrow & \downarrow\downarrow\downarrow\downarrow \end{array}\right) \tag{24}$$

Note that the first and third spin index are fixed along a row and correspondingly the second and fourth index are fixed along one column. This form of the matrix will prove convenient later. From the symmetries of D it follows that this matrix is symmetric. Numerically we also confirm the following relations between the different blocks, schematically

A_s	B	B^*	C
B^T	D_s	E_h	F
$(B^*)^T$	E_h^T	D_s^*	F^*
C^T	F^T	$(F^*)^T$	G_s

where identical symbols denote equal blocks and symmetric (hermitian) submatrices are labeled by the subscript s (h). There are only seven different blocks in total. Numerically we also show that the corner submatrices A_s, G_s, C and C^T are real. The other submatrices are complex in general. For a hermitian γ_1^Λ, the first flow equation implies that $\gamma_2^\Lambda(q_2', q_1'; q_2, q_1) = \gamma_2^{\Lambda *}(q_2, q_1; q_2', q_1')$. Translated to the separate channels this confirms that P must indeed be hermitian, since $P_{ij} = P_{ji}^*$, as well as all the remaining relations between the different submatrices of D.

D. Flow equation for the P-channel

Restricting γ_p^Λ according to the symmetries of the P-channel we obtain the following simplified equation for the derivative of P:

$$\frac{\mathrm{d}}{\mathrm{d}\Lambda}P_{ji} = \frac{\mathrm{d}}{\mathrm{d}\Lambda}\gamma_p^\Lambda\left(j\sigma, j\bar{\sigma}; i\sigma, i\bar{\sigma}\right) \tag{25}$$

$$\begin{aligned} &= \frac{1}{2\pi}\sum_{\omega=\pm\Lambda}\sum_{k,l}\frac{1}{2}\cdot\Big[\gamma_2^\Lambda(j\sigma, j\bar{\sigma}; k\sigma, k\bar{\sigma})\widetilde{\mathcal{G}}_{kl}^{\Lambda\sigma\sigma}(i\omega)\widetilde{\mathcal{G}}_{kl}^{\Lambda\bar{\sigma}\bar{\sigma}}(-i\omega)\gamma_2^\Lambda(l\sigma, l\bar{\sigma}; i\sigma, i\bar{\sigma}) \\ &\qquad + \gamma_2^\Lambda(j\sigma, j\bar{\sigma}; k\bar{\sigma}, k\sigma)\widetilde{\mathcal{G}}_{kl}^{\Lambda\bar{\sigma}\bar{\sigma}}(i\omega)\widetilde{\mathcal{G}}_{kl}^{\Lambda\sigma\sigma}(-i\omega)\gamma_2^\Lambda(l\bar{\sigma}, l\sigma; i\sigma, i\bar{\sigma}) \\ &\qquad + \gamma_2^\Lambda(j\sigma, j\bar{\sigma}; k\sigma, k\bar{\sigma})\widetilde{\mathcal{G}}_{kl}^{\Lambda\sigma\bar{\sigma}}(i\omega)\widetilde{\mathcal{G}}_{kl}^{\Lambda\bar{\sigma}\sigma}(-i\omega)\gamma_2^\Lambda(l\bar{\sigma}, l\sigma; i\sigma, i\bar{\sigma}) \\ &\qquad + \gamma_2^\Lambda(j\sigma, j\bar{\sigma}; k\bar{\sigma}, k\sigma)\widetilde{\mathcal{G}}_{kl}^{\Lambda\bar{\sigma}\sigma}(i\omega)\widetilde{\mathcal{G}}_{kl}^{\Lambda\sigma\bar{\sigma}}(-i\omega)\gamma_2^\Lambda(l\sigma, l\bar{\sigma}; i\sigma, i\bar{\sigma})\Big] \end{aligned} \tag{26}$$

Note that the first two terms and the last two terms in the sum are equivalent after summation over ω, due to the symmetry relations (19) and (20). We can thus keep one of the terms respectively and cancel the factor of $1/2$. With the definitions

$$\Pi_{kl}^{p\Lambda(1)} = \frac{1}{2\pi}\sum_{\omega=\pm\Lambda}\widetilde{\mathcal{G}}_{kl}^{\Lambda\bar{\sigma}\bar{\sigma}}(i\omega)\widetilde{\mathcal{G}}_{kl}^{\Lambda\sigma\sigma}(-i\omega) \tag{27}$$

$$\Pi_{kl}^{p\Lambda(2)} = \frac{1}{2\pi}\sum_{\omega=\pm\Lambda}\widetilde{\mathcal{G}}_{kl}^{\Lambda\bar{\sigma}\sigma}(i\omega)\widetilde{\mathcal{G}}_{kl}^{\Lambda\sigma\bar{\sigma}}(-i\omega) \tag{28}$$

the flow equation can be written more succinctly as

$$\frac{\mathrm{d}}{\mathrm{d}\Lambda}P_{ji} = \sum_{kl}\Big[\gamma_2^\Lambda(j\sigma, j\bar{\sigma}; k\sigma, k\bar{\sigma})\Pi_{kl}^{p\Lambda(1)}\gamma_2^\Lambda(l\sigma, l\bar{\sigma}; i\sigma, i\bar{\sigma}) + \gamma_2^\Lambda(j\sigma, j\bar{\sigma}; k\sigma, k\bar{\sigma})\Pi_{kl}^{p\Lambda(2)}\gamma_2^\Lambda(l\bar{\sigma}, l\sigma; i\sigma, i\bar{\sigma})\Big] \tag{29}$$

$$= \sum_{kl}\gamma_2^\Lambda(j\sigma, j\bar{\sigma}; k\sigma, k\bar{\sigma})\left[\Pi_{kl}^{p\Lambda(1)} - \Pi_{kl}^{p\Lambda(2)}\right]\gamma_2^\Lambda(l\sigma, l\bar{\sigma}; i\sigma, i\bar{\sigma}), \tag{30}$$

where in the last step we used symmetry relation (19). If we now define

$$\Pi_{kl}^{p\Lambda} \equiv \Pi_{kl}^{p\Lambda(1)} - \Pi_{kl}^{p\Lambda(2)} = \frac{1}{2\pi}\sum_{\omega=\pm\Lambda}\left[\widetilde{\mathcal{G}}_{kl}^{\Lambda\bar{\sigma}\bar{\sigma}}(i\omega)\widetilde{\mathcal{G}}_{kl}^{\Lambda\sigma\sigma}(-i\omega) - \widetilde{\mathcal{G}}_{kl}^{\Lambda\bar{\sigma}\sigma}(i\omega)\widetilde{\mathcal{G}}_{kl}^{\Lambda\sigma\bar{\sigma}}(-i\omega)\right] \tag{31}$$

we arrive at

$$\frac{\mathrm{d}}{\mathrm{d}\Lambda}P_{ji} = \tilde{P}_{jk}\Pi_{kl}^{p\Lambda}\tilde{P}_{li}, \tag{32}$$

where $\tilde{P}$ equals P plus the diagonal contributions from the other channels which have the same symmetries as P. Explicitly we get

$$\tilde{P}_{jk} = P_{jk} + \delta_{jk}\left(X_{jj}^{\sigma\bar{\sigma}\sigma\bar{\sigma}} + D_{jj}^{\sigma\bar{\sigma}\sigma\bar{\sigma}} + U_j\right) = P_{jk} + \delta_{jk}\left(-D_{jj}^{\sigma\bar{\sigma}\bar{\sigma}\sigma} + D_{jj}^{\sigma\bar{\sigma}\sigma\bar{\sigma}} + U_j\right) \tag{33}$$

Note also that the matrix $\Pi_{kl}^{p\Lambda}$ is hermitian, due to the symmetry (17) of the Green's function.

E. Flow equation for the D-channel

Restricting γ_d^Λ according to the symmetries of the D-channel we obtain the following simplified equation for the derivative of D:

$$\frac{\mathrm{d}}{\mathrm{d}\Lambda}D_{ji}^{\sigma_1\sigma_2\sigma_3\sigma_4} = \frac{\mathrm{d}}{\mathrm{d}\Lambda}\gamma_d^\Lambda\left(j\sigma_1, i\sigma_2; j\sigma_3, i\sigma_4\right) \tag{34}$$

$$= -\frac{1}{2\pi}\sum_{\omega=\pm\Lambda}\sum_{kl}\sum_{\sigma,\sigma',\sigma'',\sigma'''}\gamma_2^\Lambda(j\sigma_1, k\sigma; j\sigma_3, k\sigma')\widetilde{\mathcal{G}}_{kl}^{\Lambda\sigma'\sigma''}(i\omega)\widetilde{\mathcal{G}}_{lk}^{\Lambda\sigma'''\sigma}(i\omega)\gamma_2^\Lambda(l\sigma'', i\sigma_2; l\sigma''', i\sigma_4) \tag{35}$$

Observe that the summation goes over the second and fourth index of the first γ_2^Λ matrix and over the first and third index of the second γ_2^Λ matrix, while the other indices remain fixed. If we want to recast this expression as a matrix multiplication this indeed implies that the first and third spin index should be fixed along a row and the second and fourth index along one column. This justifies the matrix scheme (24). If we arrange the spin configurations according to this scheme we obtain the matrix equation

$$\frac{\mathrm{d}}{\mathrm{d}\Lambda} D_{ji}^{\sigma_1\sigma_2\sigma_3\sigma_4} = \sum_{kl} \sum_{\sigma,\sigma',\sigma'',\sigma'''} \gamma_2^\Lambda(j\sigma_1, k\sigma; j\sigma_3, k\sigma') \Pi_{kl}^{d\Lambda\sigma\sigma''\sigma'\sigma'''} \gamma_2^\Lambda(l\sigma'', i\sigma_2; l\sigma''', i\sigma_4) \tag{36}$$

where

$$\Pi_{kl}^{d\Lambda\sigma\sigma''\sigma'\sigma'''} \equiv -\frac{1}{2\pi} \sum_{\omega=\pm\Lambda} \widetilde{\mathcal{G}}_{kl}^{\Lambda\sigma'\sigma''}(i\omega) \widetilde{\mathcal{G}}_{lk}^{\Lambda\sigma'''\sigma}(i\omega). \tag{37}$$

Note that the order of the spin indices on Π is not the same as on the Green's functions. The symmetries from (24) remain valid. With our approximation we get

$$\frac{\mathrm{d}}{\mathrm{d}\Lambda} D_{ji}^{\sigma_1\sigma_2\sigma_3\sigma_4} = \tilde{D}_{jk}^{\sigma_1\sigma\sigma_3\sigma'} \Pi_{kl}^{d\sigma\sigma''\sigma'\sigma'''} \tilde{D}_{li}^{\sigma''\sigma_2\sigma'''\sigma_4} \tag{38}$$

where $\tilde{D}$ equals D plus the diagonal contributions from the other channels which have the same symmetries as D. Explicitly we get

$$\begin{aligned} \tilde{D}_{jk}^{\sigma_1\sigma_2\sigma_3\sigma_4} &= D_{jk}^{\sigma_1\sigma_2\sigma_3\sigma_4} + \delta_{jk}\left(X_{jj}^{\sigma_1\sigma_2\sigma_3\sigma_4} + (P_{jj}+U_j)\delta_{\sigma_1\bar{\sigma}_2}(\delta_{\sigma_1\sigma_3}\delta_{\sigma_2\sigma_4} - \delta_{\sigma_1\sigma_4}\delta_{\sigma_2\sigma_3})\right) \qquad (39) \\ &= D_{jk}^{\sigma_1\sigma_2\sigma_3\sigma_4} + \delta_{jk}\left(-D_{jj}^{\sigma_1\sigma_2\sigma_4\sigma_3} + (P_{jj}+U_j)\delta_{\sigma_1\bar{\sigma}_2}(\delta_{\sigma_1\sigma_3}\delta_{\sigma_2\sigma_4} - \delta_{\sigma_1\sigma_4}\delta_{\sigma_2\sigma_3})\right) \qquad (40) \end{aligned}$$

Just like D itself, the matrix $\Pi_{kl}^{d\Lambda\sigma\sigma''\sigma'\sigma'''}$ is symmetric, however in general not real. The structure of $\Pi_{kl}^{d\Lambda\sigma\sigma''\sigma'\sigma'''}$ in terms of its submatrices is the same as for D.

F. Flow equation for γ_1

For the self-energy equation

$$\frac{\mathrm{d}}{\mathrm{d}\Lambda} \gamma_1^\Lambda(k'\sigma', k\sigma) = \frac{1}{2\pi} \sum_{\omega=\pm\Lambda} \sum_{k_1,k_2,\sigma_1,\sigma_2} \widetilde{\mathcal{G}}_{k_2k_1}^{\Lambda\sigma_2\sigma_1}(i\omega) \gamma_2^\Lambda(k_1\sigma_1, k'\sigma'; k_2\sigma_2, k\sigma) \tag{41}$$

we need the full $\gamma_2^\Lambda = v + \gamma_p^\Lambda + \gamma_x^\Lambda + \gamma_d^\Lambda$. We abbreviate

$$\mathcal{S}_{k_2k_1}^{\sigma_2\sigma_1} = \frac{1}{2\pi} \sum_{\omega=\pm\Lambda} \widetilde{\mathcal{G}}_{k_2k_1}^{\Lambda\sigma_2\sigma_1}(i\omega). \tag{42}$$

Taking into account the symmetry of each channel we obtain

$$\begin{aligned} \frac{\mathrm{d}}{\mathrm{d}\Lambda} \gamma_1^\Lambda(k'\sigma', k\sigma) = {} & \delta_{\sigma\sigma'} \mathcal{S}_{kk'}^{\bar{\sigma}\bar{\sigma}}(P_{k'k} + \delta_{kk'}U_k) - \delta_{\sigma\bar{\sigma}'} \mathcal{S}_{kk'}^{\bar{\sigma}\sigma}(P_{k'k} + \delta_{kk'}U_k) \\ & - \sum_{\sigma_1\sigma_2} \mathcal{S}_{k'k}^{\sigma_2\sigma_1} D_{kk'}^{\sigma_1\sigma'\sigma\sigma_2} + \delta_{kk'} \sum_{l,\sigma_1,\sigma_2} \mathcal{S}_{ll}^{\sigma_2\sigma_1} D_{lk}^{\sigma_1\sigma'\sigma_2\sigma}. \end{aligned} \tag{43}$$

The first line accounts for the bare vertex and the $P/\bar{P}$-channel, while the second line contains the contribution from the X-channel and then the D-channel. Note that the D-channel only influences the diagonal elements of γ_1^Λ, due to its symmetry.

[1] C. Wetterich, Physics Letters B **301**, 90 (1993).

[2] J. E. Birkholz and V. Meden, Phys. Rev. B **79**, 085420 (2009).

[3] J. E. Birkholz, *Spin-orbit interaction in quantum dots and quantum wires of correlated electrons – A way to spintronics?*, Ph.D. thesis, Georg-August-Universität zu Göttingen (2008).

[4] F. Bauer, *0.7 Anomaly of Quantum Point Contacts: Treatment of Interactions with Functional Renormalization Group.*, Master's thesis, LMU-München (2008).

[5] W. Metzner, M. Salmhofer, C. Honerkamp, V. Meden, and K. Schönhammer, Rev. Mod. Phys. **84**, 299 (2012).

[6] F. Bauer, J. Heyder, and J. von Delft, Phys. Rev. B **89**, 045128 (2014).

[7] F. Bauer, J. Heyder, E. Schubert, D. Borowsky, D. Taubert, B. Bruognolo, D. Schuh, W. Wegscheider, J. von Delft, and S. Ludwig, Nature **501**, 73 (2013).

Chapter 8

Conductance Formula for Interacting Fermi Systems in Keldysh Formalism

This section includes the paper "*Conductance Formula for Interacting Fermi Systems in Keldysh Formalism*", [Heyder et al. (2014)]. This work provides a detailed theoretical Keldysh description of the second order perturbation theory (SOPT) strategy we applied in Bauer et al. (2013) in order to calculate the conductance of our one-dimensional (1D) quantum point contact (QPC) model (Sec. 3.3.1) at finite excitation energies (finite temperature/source-drain voltage). Additionally, it presents a Keldysh-based analytical derivation of the linear conductance formula for interacting Fermi systems formerly calculated in Matsubara formalism by Oguri (2001) (see Eq. (2.34)-(2.38) therein): We use the fRG flow equation of the self energy (e.g. Eq. (3.21)) to express the derivative of the self energy w.r.t. the bias voltage in terms of the two-particle vertex. In order to recover the result by Oguri we use a ward identity (corresponding to particle conservation of the system Hamiltonian), which connects a vertex correction term and the imaginary part of the self energy.

We apply this formula to calculate the linear conductance of our 1D model within second order perturbation theory (SOPT, see also Sec. 3.3.2): Following the strategy of Oguri we truncate the vertex functions (self energy and two-particle vertex) beyond second order in the bare interaction and plug those into the linear conductance formula. This approach provides qualitative reliable results up to interaction strength of $U \sim 2.5/(\Omega_x l_x)$ (compare Eq. (3.5)).

The calculation of the vertex functions in Keldysh formalism involves carrying out integrals along the real frequency axis, where the integrand is given as product of bare Green's functions. The structure of those along the real axis depends on the choice of position space discretization of the continuous 1D model (see Eq. (3.16)). In Heyder et al. (2014) we discuss consequences of different discretization schemes in detail: In case of a constant discretization (involving a site independent width of the model's energy band) the inhomogeneity of the CCR causes spatially confined bound states far above the potential barrier. These must be treated with adequate care when carrying out the frequency integrals, implying numerical evaluation of principal value integrals and convolutions of discrete and continuous functions. In order to avoid the resulting high numerical effort we introduce a non-constant discretization scheme, which narrows the energy band of the model in the vicinity of the CCR, restricting its energy range there to values within its energy range in the leads.

Conductance Formula for Interacting Fermi Systems in Keldysh Formalism

Jan Heyder, Florian Bauer, and Jan von Delft
Arnold Sommerfeld Center for Theoretical Physics and Center for NanoScience,
Ludwig-Maximilians-Universität München, Theresienstrasse 37, D-80333 München, Germany
(Dated: January 27, 2015)

We discuss various options for calculating the conductance through a central, interacting region coupled to non-interacting fermionic leads in the Keldysh formalisms. Our starting point is the well-known Meir-Wingreen formula for the current, whose derivative w.t.r. to the source-drain voltage yields the conductance. We explore various ways of performing this derivative analytically. They all exploit an exact flow equation from the function renormalization group (fRG), which expresses the flow w.r.t. voltage of the one-particle vertex, i.e. the self-energy, in terms of the two-particle vertex. One of these ways can be used to obtain a Keldysh-based derivation of a formula for the linear conductance that has previously been obtained by Oguri in the Matsubara formalism. We apply this formula to calculate the conductance for a model that has previously been shown to capture the essential physics of a quantum point contact (QPC) in the regime of the 0.7 anomaly. The model involves a tight-binding chain with a one-dimensional potential barrier and onsite interactions, which we treat using second order perturbation theory (SOPT). We show that numerical costs can be reduced significantly by using a non-uniform lattice spacing, chosen such that the occurence of artificial bound states close to the upper band edge is avoided.

I. INTRODUCTION

Two cornerstones of the theoretical description of transport through a mesoscopic system are the Landauer-Büttiker[1] and Meir-Wingreen[2] formulas for the conductance. The Landauer-Büttiker formula describes the conductance between two reservoirs connected by a central region in the absence of interactions. The Meir-Wingreen formula applies to the more general case that the central region contains electron-electron interactions: it expresses the current, in beautifully compact fashion, in terms of the Fermi functions of the reservoirs, and the retarded, advanced and Keldysh components of the Green's function for the central region.

To actually apply the Meir-Wingreen formula, these Green's functions have to be calculated explicitly, which in general is a challenging task. Depending on the intended application, a wide range of different theoretical tools have been employed for this purpose. Much attention has been lavished on the case of non-equilibrium transport through a quantum dot described by a Kondo or Anderson model, where the central interacting region consists of just a single localized spin or a single electronic level, see Refs. 3 and 4 for reviews. Here we are interested in the less well-studied case of systems, where the physics of the interacting region cannot be described by just a single site, but rather requires an extended modelling, consisting of many sites.

We have recently used a model of this type in a paper that offers an explanation for the microscopic origin of the 0.7-anomaly in the conductance through a QPC[5]. The model involves a tight-binding chain with a one-dimensional potential barrier and onsite interactions. In Ref. 5 we used two approaches to treat interactions: second-order perturbation theory (SOPT) and the functional renormalization group (fRG). Our calculations of the linear conductance were based on an exact formula derived by Oguri[6]. He started from the Kubo formula in the Matsubara formalism and performed the required analytical continuation of the two-particle vertex function occurring therein using Eliashberg theory[7].

Since Oguri's formula for the linear conductance is exact, it can also be used by employing methods more powerful and reliable than SOPT, for example fRG, to calculate the self-energy and two-particle vertex. If this is done in the Matsubara formalism, however (as in Ref. 5), one is limited, in practice, to the case of zero temperature, because finite-temperature calculations would require an analytic continuation of numerical data from the imaginary to the real frequency axis, which is a mathematically ill-defined problem. This problem can be avoided by calculating the self-energy and vertex directly on the real axis using the Keldysh formalism[8,9]. However, to then calculate the linear conductance, the ingredients occurring in Oguri's formula would have to be transcribed into Keldysh language, and such a transcription is currently not available in the literature in easily accesible form.

In the present paper, we find a Keldysh version of Oguri's formula by deriving it entirely within the Keldysh formalism. Our starting point is the Meir-Wingreen formula for the current, $J(V)$, with the conductance defined by $\mathrm{g} = \partial_V J$. Rather than performing this derivative numerically, we here perform it *analytically*, based on the following central observation: The voltage derivative of the Green's functions that occur in the Meir-Wingreen formula, $\partial_V \mathcal{G}$, all involve the voltage derivative of the self-energy, $\partial_V \Sigma$. The latter can be expressed in terms of the two-particle vertex by using an exact flow equation from the function renormalization group (fRG). We show that it is possible to use this observation to derive Oguri's formula for the linear conductance, expressed in Keldysh notation, provided that the Hamiltonian is symmetric and conserves particle number. Our argument evokes a Ward identity[10], following from $U(1)$-symmetry, which provides a relation between components of the self-energy and components of the vertex.

As an application of our Keldysh version of Oguri's conductance formula, we use Keldysh-SOPT to calculate the conductance through a QPC using the model of Ref. 5. We show that it is possible to greatly reduce the numerical costs by using a non-monotonic lattice spacing when formulating the discretized model. We present results for the conductance as function of barrier height for different choices of interaction strength U, magnetic field B and temperature T and discuss both the successes and limitations of the SOPT scheme.

The paper is organized as follows: After introducing the general interacting model Hamiltonian in Sec. II, we present the Keldysh derivation of Oguri's conductance formula in Sec. III. We set the stage for explicit conductance calculations by expressing the self-energy and the two-particle vertex within Keldysh SOPT in Sec. IV and introduce our the 1D-model of a QPC and show and discuss conductance results in Sec. V. A detailed collection of definitions and properties of both Green's and vertex functions in Keldysh formalism can be found in Appendix A and in Ref. 11 (in fact our paper closely follows the notation used therein). A diagrammatic derivation of the fRG flow-equation for the self-energy is given in Appendix B and the Ward identity resulting from particle conservation is presented in Appendix C. In Appendix D we perform an explicit calculation to show the fluctuation-dissipation theorem for the vertex-functions within SOPT. Finally, we apply the method of finite differences in Appendix E, to discretize the continuous Hamiltonian using a non-constant discretization scheme.

II. MICROSCOPIC MODEL

Within this work we consider a system composed of a finite central interacting region coupled to two non-interacting semi-infinite fermionic leads, a left lead, with chemical potential μ^l, temperature T^l and Fermi-distribution function f^l, and a right lead, with chemical potential μ^r, temperature T^r and Fermi-distribution function f^r. The two leads are not directly connected to each other, but only via the central region. A similar setup was considered in Ref. 2 and Ref. 6.

The general form of the model Hamiltonian reads

$$\mathcal{H} = \mathcal{H}_{\mathbf{0}} + \mathcal{H}_{\text{int}} = \sum_{ij} h_{ij} d_i^\dagger d_j + \sum_{ij} U_{ij} n_i n_j \ , \tag{1}$$

where h_{ij} is a hermitian matrix, and U_{ij} is a real, symmetric matrix, non-zero only for states i,j within the central region. $d_i^\dagger/d_i$ creates/destroys an electron in state i and $n_i = d_i^\dagger d_i$ counts the number of electrons in state i. While in general the index i can represent any set of quantum numbers we will regard it as a composite index, referring, e.g. to the site and spin of an electron for a spinful lattice model. Note, that the Hamiltonian conserves particle number, which is crucial in order to formulate a continuity equation for the charge current in the system.

Defining operators $L/C/R$, which project onto the subspace of the central region/left lead/right lead respectively, we can represent the quadratic part of the Hamiltonian as

$$\mathcal{H}_0 = \begin{pmatrix} L\mathcal{H}_{\mathbf{0}}L & L\mathcal{H}_{\mathbf{0}}C & 0 \\ C\mathcal{H}_{\mathbf{0}}L & C\mathcal{H}_{\mathbf{0}}C & C\mathcal{H}_{\mathbf{0}}R \\ 0 & R\mathcal{H}_{\mathbf{0}}C & R\mathcal{H}_{\mathbf{0}}R \end{pmatrix} = \begin{pmatrix} \mathcal{H}_l & \mathcal{H}_{lc} & 0 \\ \mathcal{H}_{cl} & \mathcal{H}_{\mathbf{0},c} & \mathcal{H}_{cr} \\ 0 & \mathcal{H}_{rc} & \mathcal{H}_r \end{pmatrix} . \tag{2}$$

We note that all matrices on the r.h.s. have the dimension of the full bare Hilbert space, but are non-zero only in the corresponding sub-space, e.g. an entry $\mathcal{H}_{lc,ij}$ of the coupling matrix can differ from zero only if i is a quantum state of the left lead and j is a quantum state of the central region.

III. TRANSPORT FORMULAS

We henceforth work in the Keldysh formalism. Our notation for Keldysh indices, which mostly follows that of Ref. 11, is set forth in detail in Appendix A, to allow the main text to focus only on the essential steps of the argument.

A. Current formula

We begin by retracing the derivation of the Meir-Wingreen formula. In steady state the number of particles in the central region is constant. Hence, the particle current from the left lead into the central region is equal to the particle current from the central region into the right lead, $J := J_{l\to c} = J_{c\to r}$[We remark that this continuity equation can also be obtained by imposing the invariance of the partition sum under a gauged $U(1)$ transformation, following from particle conservation of the Hamiltonian, see Appendix C]. This allows us to focus on the current through the interface between left lead and central region. Expressing the current in terms of the time-derivative of the total particle number operator of the left lead, $n_l = \sum_{i\in L} n_i$, we obtain the Heisenberg equation of motion $J = -e\langle \dot{n}_l\rangle = -ie/\hbar\langle[\mathcal{H}, n_l]\rangle$, where e is the electronic charge and $\hbar$ is Planck's constant. Thus, considering the above definition of the Hamiltonian, Eq.(1), the current reads

$$\begin{aligned} J &= -\frac{ie}{\hbar}\sum_{\substack{i\in L\\ j\in C}} \Big[h_{ij}\langle d^-_j(t)[d^+_i]^\dagger(t)\rangle - h_{ji}\langle d^-_i(t)[d^+_j]^\dagger(t)\rangle\Big] \\ &= \frac{e}{\hbar}\Big[\mathrm{Tr}\{(\mathcal{H}_{lc} - \mathcal{H}_{cl})G^{-|+}\}\Big] , \end{aligned} \tag{3}$$

with the interacting equal-time lesser Green's function $G^{-|+}_{i|j} = G^{-|+}_{i|j}(t|t) = -i\langle d^-_i(t)[d^+_j]^\dagger(t)\rangle$ (here we used time-translational invariance of the steady-state). Fourier transformation of Eq.(3) yields

$$J = \frac{e}{h}\int d\varepsilon\, \mathrm{Tr}\big\{(\mathcal{H}_{lc} - \mathcal{H}_{cl})\mathcal{G}^{-|+}(\varepsilon)\big\}, \tag{4}$$

with $h = 2\pi\hbar$. We introduced the symbol $\mathcal{G}$ for a Green's function that depends on a single frequency only (as opposed to the Fourier transform of the time-dependent

Green's function G, which, in general, depends on two frequencies, see Appendix A, Eq.(A.7), for details).

Following the strategy of Ref. 2, we use Dyson's equation, Eq.(A.26), to express the current in terms of the central region Green's function $\mathcal{G}_c$ and rotate from the contour basis into the Keldysh basis (the explicit Keldysh rotation is given by Eq.(A.10) and Eq.(A.14c)). This yields

$$J=\frac{ie}{2h}\int d\varepsilon\ \mathrm{Tr}\{\Gamma^l[\mathcal{G}_c^{2|2}-(1-2f^l)(\mathcal{G}_c^{2|1}-\mathcal{G}_c^{1|2})]\}, \quad (5)$$

with retarded, $\mathcal{G}_c^{2|1}(\varepsilon)$, advanced, $\mathcal{G}_c^{1|2}(\varepsilon)$, and Keldysh central region Green's function, $\mathcal{G}_c^{2|2}(\varepsilon)$, and the hybridization function $\Gamma^l(\varepsilon)=i\ H_{cl}(g_l^{2|1}(\varepsilon)-g_l^{1|2}(\varepsilon))H_{lc}$, where $g_l(\varepsilon)$ is the Green's function of the isolated left lead. Here and below we omit the frequency argument for all quantities that depend on the integration variable only. Eq.(5) is the celebrated Meir-Wingreen formula for the current [c.f. Eq.(6) in Ref. 2 for a symmetrized version].

We now present a version of the Meir-Wingreen formula in terms of the interacting one-particle irreducible self-energy Σ (with retarded, $\Sigma^{1|2}$, advanced, $\Sigma^{2|1}$ and Keldysh component $\Sigma^{1|1}$ [Eq.(A.3), Eq.(A.7), Eq.(A.13)]). It can be derived by means of Dyson's equation, Eq.(A.25), which enables a reformulation of the Green's functions in Eq.(5) in terms of the hybridization functions Γ, the lead distribution functions f and the self-energy Σ:

$$\begin{aligned}\mathcal{G}_c^{2|1}-\mathcal{G}_c^{1|2}&=\mathcal{G}_c^{2|1}\big(\big[\mathcal{G}_c^{1|2}\big]^{-1}-\big[\mathcal{G}_c^{2|1}\big]^{-1}\big)\mathcal{G}_c^{1|2}\\&=\mathcal{G}_c^{2|1}\big(-i(\Gamma^l+\Gamma^r)+\Sigma^{1|2}-\Sigma^{2|1}\big)\mathcal{G}_c^{1|2},\\\mathcal{G}_c^{2|2}&=\mathcal{G}_c^{2|1}\big(-i\sum_{k=l,r}(1-2f^k)\Gamma^k+\Sigma^{1|1}\big)\mathcal{G}_c^{1|2}.\end{aligned}\quad (6)$$

Hence, the current formula can be written as the sum of two terms,

$$\begin{aligned}J=&\frac{e}{h}\int d\varepsilon(f^l-f^r)\mathrm{Tr}\{\Gamma^l\mathcal{G}_c^{2|1}\Gamma^r\mathcal{G}_c^{1|2}\}+\\&+\frac{ie}{2h}\int d\varepsilon\mathrm{Tr}\{\Gamma^l\mathcal{G}_c^{2|1}\Big(\Sigma^{1|1}-(1-2f^l)(\Sigma^{1|2}-\Sigma^{2|1})\Big)\mathcal{G}_c^{1|2}\}.\end{aligned}\quad (7)$$

In equilibrium, i.e. $f:=f^l=f^r$, the current must fulfill $J=0$. With the first term of Eq.(7) vanishing trivially, this imposes the fluctuation-dissipation theorem (FDT) for the self-energy at zero bias voltage, $\Sigma^{1|1}=(1-2f)(\Sigma^{1|2}-\Sigma^{2|1})$. Note that a similar FDT can be formulated for the Green's function in Eq.(5).

B. Differential conductance formula

Differentiating Eq.(5) w.r.t. the source-drain voltage $V=(\mu_l-\mu_r)/e$, i.e. the voltage drop from the left to the right lead, provides the differential conductance $\mathrm{g}_V=\partial_V J$. We denote derivatives w.r.t. frequency by a prime, e.g. $f^{l\prime}:=\partial_\varepsilon f^l$, and derivatives w.r.t. the source-drain voltage by a dot, $\dot{\mathcal{G}}_c:=\partial_V\mathcal{G}_c$. Using Dyson's equation [Eq.(A.25)], we can express the derivative of the Green's function in terms of derivatives of the self-energy:

$$\begin{aligned}\dot{\mathcal{G}}_c^{\alpha|\alpha'}&=\sum_{\beta,\beta'}\mathcal{G}_c^{\alpha|\beta'}\dot{\Sigma}^{\beta'|\beta}\mathcal{G}_c^{\beta|\alpha'}+S^{\alpha|\alpha'},\\S^{1|1}&=S^{1|2}=S^{2|1}=0\ ,\ S^{2|2}=\mathcal{G}_c^{2|1}\dot{\Sigma}_{\mathrm{lead}}^{1|1}\mathcal{G}_c^{1|2}.\end{aligned}\quad (8)$$

Here we introduced the so called single scale propagator S and the lead self-energy $\Sigma_{\mathrm{lead}}^{1|1}=-i\sum_{k=l,r}(1-2f^k)\Gamma^k$ [Eq.(A.21)]. Hence, we can write the differential conductance in the form

$$\begin{aligned}\mathrm{g}_V=\frac{ie}{2h}\int d\varepsilon\mathrm{Tr}\{\Gamma^l[&\sum_{\beta,\beta'}\mathcal{G}_c^{\alpha|\beta'}\dot{\Sigma}^{\beta'|\beta}\mathcal{G}_c^{\beta|\alpha'}+S^{2|2}\\&-(1-2f^l)(\mathcal{G}_c^{2|1}\dot{\Sigma}^{1|2}\mathcal{G}_c^{2|1}-\mathcal{G}_c^{1|2}\dot{\Sigma}^{2|1}\mathcal{G}_c^{1|2})\\&+2\dot{f}^l(\mathcal{G}_c^{2|1}-\mathcal{G}_c^{1|2})]\}.\end{aligned}\quad (9)$$

We specify the voltage via the chemical potentials in the leads, $\mu^l=\mu+\alpha eV$ and $\mu^r=\mu+(\alpha-1)eV$, with $\alpha\in[0,1]$. This provides

$$S^{2|2}=-2ie\ \mathcal{G}_c^{2|1}\Big[\alpha f^{l\prime}\Gamma^l+(\alpha-1)f^{r\prime}\Gamma^r\Big]\mathcal{G}_c^{1|2}. \quad (10)$$

Note that in the special case $\alpha=0$, i.e. if the voltage is applied to the right lead only, the last term in Eq.(9) vanishes and the differential conductance takes a particularly simple form. This is a consequence of our initial choice to express the current via the time derivative of the left lead's occupation.

The above derived formula for the differential conductance of an interacting Fermi system involves derivatives of all self-energy components, $\dot{\Sigma}$. Below, we show how these can be expressed in terms of the irreducible two-particle vertex $\mathcal{L}$ and the single scale propagator S using the fRG flow equation for the self-energy. While we apply this scheme only to derive a Keldysh Kubo-type linear conductance formula, which for a symmetric Hamiltonian yields a Keldysh version of Oguri's formula, we want to stress that an extension to finite bias is trivial and that Eq.(9) can likewise be written in terms of the two-particle vertex, following the recipe below.

In Ref. 5 we used Eq.(9) (with $\alpha=1/2$) to calculate the differential conductance of a 1D parabolic potential barrier in the presence of an onsite electron-electron interaction (see Sec.V for details of the model). There we used second order perturbation theory (SOPT, details are presented in Sec.IV) to evaluate both the self-energy and its derivative with respect to voltage. We showed that the model, which is designed to mimick the lowest transport mode of a quantum point contact (QPC), qualitatively reproduces the main feature of the 0.7 conductance anomaly, including both its typical magnetic field and temperature dependence as well as the zero-bias peak, which usually accompanies the anomaly.

C. Linear conductance formula

In linear response, i.e. $V \to 0$, the linear conductance g_0 does not depend on the specific choice of α. For the sake of simplicity we use $\alpha = 1$, which corresponds to a voltage setup $\mu^l = \mu + eV$ and $\mu^r = \mu$. Henceforth, a dot implies the derivative *at zero bias*, e.g. $\dot{f}^l = \partial_V f^l\big|_{V=0}$, and we have $\dot{f}^l = -ef'$ and $\dot{f}^r = 0$. Differentiating Eq.(7) w.r.t. the voltage, followed by setting $V = 0$, yields the *linear* conductance formula

$$\begin{aligned} \mathrm{g}_0 &= \partial_V J\big|_{V=0} \\ &= -\frac{e^2}{h}\int d\varepsilon f' \mathrm{Tr}\{\Gamma^l \mathcal{G}_c^{2|1}(\Gamma^r + i(\Sigma^{1|2} - \Sigma^{2|1}))\mathcal{G}_c^{1|2}\} \\ &\quad + \frac{e^2}{h}\int d\varepsilon \mathrm{Tr}\{\Gamma^l \mathcal{G}_c^{2|1} \Phi^l \mathcal{G}_c^{1|2}\}. \end{aligned} \tag{11}$$

All quantities in the integrand are evaluated in equilibrium. The voltage derivatives of the self-energy are combined in the expression

$$\Phi^l = \frac{i}{2e}\left[\dot{\Sigma}^{1|1} - (1-2f)\left(\dot{\Sigma}^{1|2} - \dot{\Sigma}^{2|1}\right)\right]. \tag{12}$$

Provided that all components of the self-energy and its derivative in Eq.(12) are known at zero bias, Eq.(11) is sufficient to calculate the linear conductance. But, as is shown below, it is possible to express the voltage derivatives of Σ directly in terms of the two-particle vertex $\mathcal{L}$, i.e. the rank-four tensor defined as the sum of all one-particle irreducible diagrams with four external amputated legs (see Appendix A). This not only reduces the numbers of objects to be calculated, but more importantly, it completely eliminates the voltage from the linear conductance formula: whereas the derivative $\dot{\Sigma}$ needs information of the self-energy at finite bias, the two-particle vertex does not. Finally, it allows for a very compact representation of the linear conductance formula with a clear interpretation of the individual terms.

To this end we use the fact that an exact expression for the derivative of the self-energy w.r.t. some parameter Λ is provided by the so called flow equation of the functional renormalization group (fRG) (for a diagrammatic derivation of this equation see Appendix B and Ref. 12. A rigorous functional derivation of the full set of coupled fRG equations for all 1PI vertex functions is given in e.g. Ref. 13). Usually, Λ is taken to be some high-energy cutoff, but it can equally well be a physical parameter of the system, such as magnetic field, temperature or, as in the case in question, voltage: $\Lambda = V$. The general flow equation reads

$$\partial_\Lambda \Sigma_{i|j}^{\alpha'|\alpha}(\varepsilon) = \frac{1}{2\pi i}\int d\varepsilon' \sum_{\substack{\beta\beta' \\ kl\in C}} S_{\Lambda,k|l}^{\beta|\beta'}(\varepsilon')\mathcal{L}_{\Lambda,ik|jl}^{\alpha'\beta'|\alpha\beta}(\varepsilon',\varepsilon;0), \tag{13}$$

where $\mathcal{L}(\varepsilon',\varepsilon;0)$ is the irreducible two-particle vertex, defined via Eq.(A.4) and Eq.(A.7). The specific form of this equation for a given flow-parameter Λ is encoded in the single-scale propagator S, which is given by

$$S_\Lambda = -\mathcal{G}_c \partial_\Lambda \left[\mathcal{G}_{\mathbf{0},c}\right]^{-1} \mathcal{G}_c = \mathcal{G}_c \mathcal{G}_{\mathbf{0},c}^{-1}\left[\partial_\Lambda \mathcal{G}_{\mathbf{0},c}\right]\mathcal{G}_{\mathbf{0},c}^{-1}\mathcal{G}_c, \tag{14}$$

with bare central region Green's function $\mathcal{G}_{0,c}(\varepsilon)$. According to Eq.(A.22) only its Keldysh component, $\mathcal{G}_{\mathbf{0},c}^{2|2}$, depends explicitly on the voltage. Additionally, we use $\left[\mathcal{G}_{\mathbf{0},c}^{-1}\right]^{2|2} = 0$, following from causality, Eq.(A.12), which yields:

$$\begin{aligned} S_{V=0}^{2|2} &= \mathcal{G}_c^{2|1}\left[\mathcal{G}_{\mathbf{0},c}^{-1}\right]^{1|2} \partial_{V=0}\mathcal{G}_{\mathbf{0},c}^{2|2}\left[\mathcal{G}_{\mathbf{0},c}^{-1}\right]^{2|1}\mathcal{G}_c^{1|2} \\ &= \; -2ief'\mathcal{G}_c^{2|1}\Gamma^l\mathcal{G}_c^{1|2}, \\ S_{V=0}^{1|1} &= S_{V=0}^{1|2} = S_{V=0}^{2|1} = 0. \end{aligned} \tag{15}$$

It is instructive to realize that this is indeed the single-scale propagator already introduced in the derivation of the differential conductance via Eq.(10). The trivial Keldysh structure of S now implies, that the $\alpha'|\alpha$-dependence of the self-energy derivatives only enters via that of the two-particle vertex:

$$\dot{\Sigma}_{i|j}^{\alpha'|\alpha}(\varepsilon) = \frac{1}{2\pi i}\int d\varepsilon' \sum_{kl\in C} S_{V=0,k|l}^{2|2}(\varepsilon')\mathcal{L}_{il|jk}^{\alpha'2|\alpha 2}(\varepsilon',\varepsilon;0). \tag{16}$$

This allows us to write Eq.(12) in the form

$$\Phi_{i|j}^l(\varepsilon) = \frac{1}{2\pi i}\int d\varepsilon' f'(\varepsilon') \sum_{kl\in C}\left[\mathcal{G}_c^{2|1}(\varepsilon')\Gamma^l(\varepsilon')\mathcal{G}_c^{1|2}(\varepsilon')\right]_{k|l} K_{il|jk}(\varepsilon',\varepsilon;0), \tag{17}$$

with vertex response part

$$K_{il|jk}(\varepsilon',\varepsilon;0) = \mathcal{L}_{il|jk}^{12|12}(\varepsilon',\varepsilon;0) - (1-2f(\varepsilon))(\mathcal{L}_{il|jk}^{12|22}(\varepsilon',\varepsilon;0) - \mathcal{L}_{il|jk}^{22|12}(\varepsilon',\varepsilon;0)). \tag{18}$$

We use the invariance of the trace under a cyclic permutation, $\mathrm{Tr}\{\Gamma^l\mathcal{G}_c^{2|1}\Phi^l\mathcal{G}_c^{1|2}\} = \mathrm{Tr}\{\Phi^l\mathcal{G}_c^{1|2}\Gamma^l\mathcal{G}_c^{2|1}\}$, and interchange the frequency labels, $\varepsilon \leftrightarrow \varepsilon'$, to obtain the linear conductance formula

$$\mathrm{g}_0 = -\frac{e^2}{h}\int d\varepsilon f' \mathrm{Tr}\{\Gamma^l \mathcal{G}_c^{2|1}\left(\Gamma^r + i(\Sigma^{1|2} - \Sigma^{2|1})\right)\mathcal{G}_c^{1|2}\} + \frac{e^2}{h}\int d\varepsilon f' \mathrm{Tr}\{\Gamma^l \mathcal{G}_c^{1|2}\tilde{\Phi}^l \mathcal{G}_c^{2|1}\}, \tag{19}$$

with the resorted vertex correction term

$$\tilde{\Phi}^l_{l|k}(\varepsilon) = \frac{1}{2\pi i}\int d\varepsilon' \sum_{ij\in C}\left[\mathcal{G}_c^{1|2}(\varepsilon')\Gamma^l(\varepsilon')\mathcal{G}_c^{2|1}(\varepsilon')\right]_{j|i} K_{il|jk}(\varepsilon,\varepsilon';0). \tag{20}$$

In appendix C we show that particle conservation requires, that the imaginary part of the self-energy is connected to the vertex correction part via a Ward identity

$$i[\Sigma^{1|2}(\varepsilon) - \Sigma^{2|1}(\varepsilon)] = \tilde{\Phi}^l + \tilde{\Phi}^r. \tag{21}$$

This result is obtained by demanding the invariance of the physics under a gauged, local $U(1)$ transformation, which must hold for any Hamiltonian that conserves the particle number in the system. This symmetry implies an infinite hierarchy of relations connecting different Green's functions. The first equation in this hierarchy reproduces the continuity equation used in the beginning of the above derivation. The second equation in the hierarchy is Eq.(21), which connects parts of one-particle and two-particle Green's function. Inserting the ward identity in Eq.(19) yields

$$\mathrm{g}_0 = -\frac{e^2}{h}\int d\varepsilon f'(\varepsilon)\mathrm{Tr}\{\Gamma^l(\varepsilon)\mathcal{G}_c^{2|1}(\varepsilon)\left[\Gamma^r(\varepsilon) + \tilde{\Phi}^l(\varepsilon) + \tilde{\Phi}^r(\varepsilon)\right]\mathcal{G}_c^{1|2}(\varepsilon)\} + \frac{e^2}{h}\int d\varepsilon f'(\varepsilon)\mathrm{Tr}\{\Gamma^l(\varepsilon)\mathcal{G}_c^{1|2}(\varepsilon)\tilde{\Phi}^l(\varepsilon)\mathcal{G}_c^{2|1}(\varepsilon)\}. \tag{22}$$

This formula is the central result of this chapter. It expresses the linear conductance in terms of the two-particle vertex $\mathcal{L}$, which enters via the vertex part $\tilde{\Phi}$ [Eq.(20)] and the response vertex K [Eq.(18)]. Note that the two terms in Eq.(22) differ in their Keldysh structure via the Keldysh indexing of the full Green's functions, which prevents further compactification of Eq.(22) for a non-symmetric Hamiltonian (e.g. in the presence of finite spin-orbit interactions, see. e.g. Ref. 14). If, in contrast, the Hamiltonian of Eq.(1) is symmetric (i.e. $h_{ij} = h_{ji}$), Eq.(22) can be compactified significantly using the following argument: A symmetric Hamiltonian implies that the Green's function $\mathcal{G}$, the self-energy Σ and the hybridization Γ are symmetric, too. This in turn gives a symmetric $\tilde{\Phi}$ via Eq.(21). Hence, the trace in the first term of Eq.(22) is taken over the product of four symmetric matrices, and transposing yields $\mathrm{Tr}\{\Gamma^l\mathcal{G}_c^{2|1}\left[\Gamma^r + \tilde{\Phi}^l + \tilde{\Phi}^r\right]\mathcal{G}_c^{1|2}\} = \mathrm{Tr}\{\Gamma^l\mathcal{G}_c^{1|2}\left[\Gamma^r + \tilde{\Phi}^l + \tilde{\Phi}^r\right]\mathcal{G}_c^{2|1}\}$. Hence, all contributions involving $\tilde{\Phi}^l$ cancel in Eq.(22) and the linear conductance now simply reads

$$\mathrm{g}_0 = -\frac{e^2}{h}\int_{-\infty}^{\infty} d\varepsilon f'(\varepsilon)\mathrm{Tr}\{\Gamma^l(\varepsilon)\mathcal{G}_c^{1|2}(\varepsilon)[\Gamma^r(\varepsilon) + \tilde{\Phi}^r(\varepsilon)]\mathcal{G}_c^{2|1}(\varepsilon)\}. \tag{23}$$

A Matsubara version of this linear conductance formula for a symmetric Hamiltonian has been derived before in Ref. 6 using Eliashberg theory in order to perform the analytic continuation of the vertex from Matsubara space to the real axis. Comparison of the two formulas allows for a connection between the three Keldysh vertex components in Eq.(18) and the ones used in Oguri's derivation.

D. Thermal conductance formula

We end this chapter with some considerations regarding thermal conductance, i.e. the conductance induced by a temperature difference between the leads. In the following we assume zero bias voltage, $V = 0$. The left lead is in thermal equilibrium with $T^l = T + \tilde{T}$ and the right lead in thermal equilibrium with temperature $T^r = T$. Thus, the temperature gradient between the leads will provide a charge current through the central region. Similar to above, we are now interested in the linear response thermal conductance formula, $\mathrm{g}_{0,T} = \partial_{\tilde{T}=0} J$, which we could calculate in similar fashion as the linear conductance g_0. Much easier is the following though: all terms in Eq.(22) were obtained by once time taking the derivative of the Fermi distribution f^l w.r.t. the voltage, partly explicitly in Eq.(7) and partly from evaluating the single-scale propagator in Eq.(15). Now note, that $\partial_{\tilde{T}=0} f^l = \frac{\varepsilon-\mu}{T} f' = -\frac{(\varepsilon-\mu)}{eT}\partial_{V=0} f^l$. For a symmetric Hamiltonian this directly implies, that the linear thermal conductance is given by

$$\mathrm{g}_{0,T} = \frac{e}{hT}\int_{-\infty}^{\infty} d\varepsilon(\varepsilon-\mu) f'(\varepsilon)\mathrm{Tr}\{\Gamma^l(\varepsilon)\mathcal{G}_c^{1|2}(\varepsilon)[\Gamma^r(\varepsilon) + \tilde{\Phi}^r(\varepsilon)]\mathcal{G}_c^{2|1}(\varepsilon)\}. \tag{24}$$

IV. VERTEX FUNCTIONS IN SOPT

In order to apply the above defined conductance formulas we calculate the self-energy Σ and the two-particle vertex $\mathcal{L}$ in second order perturbation theory (SOPT). Both are defined in Eq. (A.7) and occur in the conductance formula (22). The SOPT-strategy is to approximate them by a diagrammatic series truncated beyond second order in the bare interaction vertex ν, defined below.

Within this section the compact composite index notation used above is dropped in favor of a more explicit one. We henceforth use blue *roman* subscripts ($i_1, i_2, ...$) for site indices only and explicitly denote spin dependencies using $\sigma \in \{\uparrow, \downarrow\} = \{+, -\}$. A green number subscript denotes an object's order in the interaction, e.g. $\Sigma_{\mathbf{2}}$ is the desired self-energy to second order in the bare vertex ν.

Below, the quadratic part of the model Hamiltonian, Eq.(1), is is represented by a real matrix that is symmetric in position basis and diagonal in spin space

$$h^{\sigma}_{ij} = h^{\sigma}_{ji} \in \mathbb{R} \quad , \quad h = h^{\uparrow} + h^{\downarrow}. \tag{25}$$

In consequence, the bare Green's function, too, is diagonal in spin space and symmetric in position space:

$$\mathcal{G}_{\mathbf{0},i\sigma|j\sigma'} = \delta_{\sigma\sigma'}\mathcal{G}^{\sigma}_{\mathbf{0},i|j} \quad , \quad \mathcal{G}^{\sigma}_{\mathbf{0},i|j} = \mathcal{G}^{\sigma}_{\mathbf{0},j|i}. \tag{26}$$

We distinguish between composite quantum numbers including contour indices $k_n = (a_n, i_n, \sigma_n)$ and composite quantum numbers including Keldysh indices $\kappa_n = (\alpha_n, i_n, \sigma_n)$. The noninteracting Green's function is represented by a directed line

$$\mathcal{G}_{\mathbf{0},k_1|k_1'}(\varepsilon) = \quad . \tag{27}$$

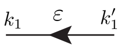

We choose an onsite interaction, which reduces the quartic term in Eq.(1) to a single sum

$$\mathcal{H}_{int} = \sum_{i \in C} U_i n_{i\uparrow} n_{i\downarrow}, \tag{28}$$

i.e. we evaluate the vertex functions for the case of an onsite electron-electron interaction. Since the two-particle interaction is instantaneous in time, we construct the anti-symmetrized bare interaction vertex as

$$\begin{aligned}\nu_{k_1',k_2'|k_1,k_2}(t_1',t_2'|t_1,t_2) &= U_{i_1}\delta_{i_1 i_2}\delta_{i_1 i_1'}\delta_{i_1 i_2'}(-a_1)\delta_{a_1 a_2}\delta_{a_1 a_1'}\delta_{a_1 a_2'} \\ &\quad \times \delta(t_1 - t_2)\delta(t_1 - t_1')\delta(t_1 - t_2') \\ &\quad \times \delta_{\sigma_1\bar{\sigma}_2}\delta_{\sigma_1'\bar{\sigma}_2'}(\delta_{\sigma_1'\sigma_1} - \delta_{\sigma_1'\sigma_2}),\end{aligned} \tag{29}$$

with $\bar{\sigma} = -\sigma$. Note that its spin-dependence is determined by Pauli's exclusion principle and the Slater-determinant character of the fermionic state. After Fourier transformation [Eq.(A.6), Eq.(A.7)] and Keldysh rotation [Eq.(A.10), Eq.(A.11)] we find

$$\nu_{\kappa_1',\kappa_2'|\kappa_1\kappa_2}(\varepsilon_1',\varepsilon_2'|\varepsilon_1,\varepsilon_2) = 2\pi\delta(\varepsilon_1+\varepsilon_2-\varepsilon_1'-\varepsilon_2')\bar{u}_{\kappa_1',\kappa_2'|\kappa_1\kappa_2}, \tag{30}$$

where we introduced the bare vertex

$$\begin{aligned}\bar{u}_{\kappa_1',\kappa_2'|\kappa_1\kappa_2} &= u_{i_1}\delta_{i_1 i_2}\delta_{i_1 i_1'}\delta_{i_1 i_2'}\xi^{\alpha_1'\alpha_2'|\alpha_1\alpha_2} \\ &\quad \times \delta_{\sigma_1\bar{\sigma}_2}\delta_{\sigma_1'\bar{\sigma}_2'}(\delta_{\sigma_1'\sigma_1} - \delta_{\sigma_1'\sigma_2}) \\ &= \quad ,\end{aligned} \tag{31}$$

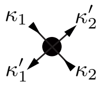

with $u_i = U_i/2$ and the modulo operation

$$\xi^{\alpha_1'\alpha_2'|\alpha_1\alpha_2} = \begin{cases} 1, & \text{if } \alpha_1' + \alpha_2' + \alpha_1 + \alpha_2 = \text{odd} \\ 0, & \text{else.} \end{cases}$$

A. The two-particle vertex in SOPT

Our goal is to approximate the vertex part, Eq.(18), to second order in the interaction. The fully interacting two-particle vertex, $\mathcal{L}(\varepsilon, \varepsilon'; 0)$, has the following diagrammatic representation:

$$\mathcal{L}_{\kappa_1'\kappa_2'|\kappa_1\kappa_2}(\varepsilon', \varepsilon; 0) \quad = \tag{32}$$

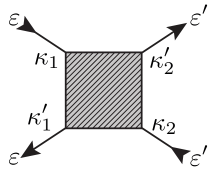

In SOPT, the vertex $\mathcal{L}_{\mathbf{2}}$ is given by the sum of all 1PI diagrams with four external amputated legs and not more than two bare vertices. Defining the frequencies

$$p = \varepsilon + \varepsilon' \quad , \quad x = \varepsilon - \varepsilon', \tag{33}$$

the vertex reads

$$\mathcal{L}_{\mathbf{2}}(\varepsilon', \varepsilon; 0) = \bar{u} + \mathcal{L}^{p}_{\mathbf{2}}(p) + \mathcal{L}^{x}_{\mathbf{2}}(x) + \mathcal{L}^{d}_{\mathbf{2}}(0), \tag{34}$$

with particle-particle channel $\mathcal{L}^{p}_{\mathbf{2}}$, particle-hole channel $\mathcal{L}^{x}_{\mathbf{2}}$ and direct channel $\mathcal{L}^{d}_{\mathbf{2}}$ defined as

$$\mathcal{L}^{p}_{\mathbf{2},\kappa_1'\kappa_2'|\kappa_1\kappa_2}(p) =$$

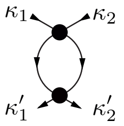

$$= \frac{i}{2\pi}\int_{-\infty}^{\infty} d\varepsilon'' \sum_{q_1 q_2 q_1' q_2'} \bar{u}_{\kappa_1'\kappa_2'|q_1 q_2}\mathcal{G}_{\mathbf{0},q_1|q_1'}(p-\varepsilon'')\mathcal{G}_{\mathbf{0},q_2|q_2'}(\varepsilon'')\bar{u}_{q_1'q_2'|\kappa_1\kappa_2}, \tag{35a}$$

$$\mathcal{L}^{x}_{\mathbf{2},\kappa_1'\kappa_2'|\kappa_1\kappa_2}(x) =$$

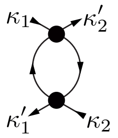

$$= \frac{i}{2\pi}\int_{-\infty}^{\infty} d\varepsilon'' \sum_{q_1 q_2 q_1' q_2'} \bar{u}_{\kappa_1'q_2'|q_1\kappa_2}\mathcal{G}_{\mathbf{0},q_1|q_1'}(\varepsilon'')\mathcal{G}_{\mathbf{0},q_2|q_2'}(\varepsilon''+x)\bar{u}_{q_1'\kappa_2'|\kappa_1 q_2}, \tag{35b}$$

$$\mathcal{L}^{d}_{\mathbf{2},\kappa_1'\kappa_2'|\kappa_1\kappa_2}(0) =$$

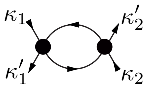

$$= \frac{-i}{2\pi}\int_{-\infty}^{\infty} d\varepsilon'' \sum_{q_1 q_2 q_1' q_2'} \bar{u}_{\kappa_1'q_2'|\kappa_1 q_1}\mathcal{G}_{\mathbf{0},q_1|q_1'}(\varepsilon'')\mathcal{G}_{\mathbf{0},q_2|q_2'}(\varepsilon'')\bar{u}_{q_1'\kappa_2'|q_2\kappa_2}. \tag{35c}$$

These expressions can be derived by a straightforward perturbation theory.

Using Eq.(26) and Eq.(31), we can identify the only non-vanishing components in spin- and real space,

$$\Pi^{\sigma\bar{\sigma}}_{ij}(p) = \mathcal{L}^{p}_{\mathbf{2},i\sigma i\bar{\sigma}|j\sigma j\bar{\sigma}}(p), \tag{36a}$$

$$X^{\sigma\sigma'}_{ij}(x) = \mathcal{L}^{x}_{\mathbf{2},i\sigma j\sigma'|j\sigma i\sigma'}(x), \tag{36b}$$

$$\Delta^{\sigma\sigma'}_{ij}(0) = \mathcal{L}^{d}_{\mathbf{2},i\sigma j\sigma'|i\sigma' j\sigma}(0). \tag{36c}$$

Eq.(25) and the channel definitions, Eq.(35), imply the symmetries

$$\Pi_{ij} = \Pi_{ji}\ ,\ X_{ij} = X_{ji}\ ,\ \Delta_{ij} = \Delta_{ji}, \tag{37a}$$

$$\Pi(p) = \Pi^{\sigma\bar{\sigma}}(p) = \Pi^{\bar{\sigma}\sigma}(p), \tag{37b}$$

$$X^{\sigma\sigma'}(x) = X^{\sigma'\sigma}(-x), \tag{37c}$$

$$\Delta^{\sigma\sigma'}(0) = \Delta^{\sigma'\sigma}(0). \tag{37d}$$

Moreover, and directly following from the Keldysh structure of the bare vertex in Eq.(31), we are left with only four non-zero components per channel in Keldysh space. This is best seen from realizing, that the internal Keldysh structure of the diagrams in Eq.(35) only depends on whether the sum of external indices belonging to the same bare vertex is even/odd. Furthermore, from the Keldysh structure of the bare vertex, combined with $\mathcal{G}^{1|1} = 0$ and the analytic properties of $\mathcal{G}$, it follows that $\mathcal{L}^{22|22} = 0$. Hence, SOPT preserves the theorem of causality, Eq.(A.12), as it should. (this has also been shown for a wide range of approximation schemes in Ref. 15). Thus, the Keldysh structure of the channels $Y = \Pi, X, \Delta$ is given by the matrix representation

$$Y = \begin{pmatrix} Y^{K} & Y^{R} \\ Y^{A} & 0 \end{pmatrix} = \begin{pmatrix} Y^{1|1} & Y^{1|2} \\ Y^{2|1} & Y^{2|2} \end{pmatrix}. \tag{38}$$

We define the individual components according to the Keldysh structure of the full vertex,

$$\begin{aligned}\mathcal{L}^{\alpha_1'\alpha_2'|\alpha_1\alpha_2}_{\mathbf{2}} = {} & \Pi^{\psi(\alpha_1',\alpha_2')|\psi(\alpha_1,\alpha_2)} \\ & +X^{\psi(\alpha_1',\alpha_2)|\psi(\alpha_1,\alpha_2')} \\ & +\Delta^{\psi(\alpha_1',\alpha_1)|\psi(\alpha_2,\alpha_2')},\end{aligned} \tag{39}$$

where we introduced the modified modulo operation

$$\psi(\alpha_1, \alpha_2, ..., \alpha_n) = \begin{cases} 1, & \text{if } \sum_{\mathrm{i}=1,\dots,\mathrm{n}} \alpha_{\mathrm{i}} = \text{odd} \\ 2, & \text{else.} \end{cases}$$

That leaves us with the following explicit formulas

$$\begin{aligned}\Pi^{1|2}_{ij}(p) = -\frac{u_i u_j}{2\pi i}\int d\varepsilon\Big[& \mathcal{G}^{\sigma,2|1}_{\mathbf{0},i|j}(p-\varepsilon)\mathcal{G}^{\bar{\sigma},2|2}_{\mathbf{0},i|j}(\varepsilon) \\ & +\mathcal{G}^{\sigma,2|2}_{\mathbf{0},i|j}(p-\varepsilon)\mathcal{G}^{\bar{\sigma},2|1}_{\mathbf{0},i|j}(\varepsilon)\Big],\end{aligned} \tag{40a}$$

$$\Pi^{2|1} = \Big[\Pi^{1|2}\Big]^{*}, \tag{40b}$$

$$\begin{aligned}\Pi^{1|1}_{ij}(p) = -\frac{u_i u_j}{2\pi i}\int d\varepsilon\Big[& \mathcal{G}^{\sigma,2|2}_{\mathbf{0},i|j}(p-\varepsilon)\mathcal{G}^{\bar{\sigma},2|2}_{\mathbf{0},i|j}(\varepsilon) \\ & +\mathcal{G}^{\sigma,2|1}_{\mathbf{0},i|j}(p-\varepsilon)\mathcal{G}^{\bar{\sigma},2|1}_{\mathbf{0},i|j}(\varepsilon) \\ & +\mathcal{G}^{\sigma,1|2}_{\mathbf{0},i|j}(p-\varepsilon)\mathcal{G}^{\bar{\sigma},1|2}_{\mathbf{0},i|j}(\varepsilon)\Big],\end{aligned} \tag{40c}$$

$$\Pi^{1|1}(p)\Big|_{V=0} = [1+2b(p-\mu)]\Big[\Pi^{1|2}(p) - \Pi^{2|1}(p)\Big]_{V=0}, \tag{40d}$$

$$X^{\sigma\sigma',1|2}_{ij}(x) = -\frac{u_i u_j}{2\pi i}\int d\varepsilon \Big[\mathcal{G}^{\bar\sigma,1|2}_{\mathbf{0},i|j}(\varepsilon)\mathcal{G}^{\bar\sigma',2|2}_{\mathbf{0},i|j}(\varepsilon+x) + \mathcal{G}^{\bar\sigma,2|2}_{\mathbf{0},i|j}(\varepsilon)\mathcal{G}^{\bar\sigma',2|1}_{\mathbf{0},i|j}(\varepsilon+x)\Big], \tag{41a}$$

$$X^{2|1} = \Big[X^{1|2}\Big]^*, \tag{41b}$$

$$X^{\sigma\sigma',1|1}_{ij}(x) = -\frac{u_i u_j}{2\pi i}\int d\varepsilon \Big[\mathcal{G}^{\bar\sigma,2|2}_{\mathbf{0},i|j}(\varepsilon)\mathcal{G}^{\bar\sigma',2|2}_{\mathbf{0},i|j}(\varepsilon+x) + \mathcal{G}^{\bar\sigma,2|1}_{\mathbf{0},i|j}(\varepsilon)\mathcal{G}^{\bar\sigma',1|2}_{\mathbf{0},i|j}(\varepsilon+x)\Big] + \mathcal{G}^{\bar\sigma,1|2}_{\mathbf{0},i|j}(\varepsilon)\mathcal{G}^{\bar\sigma',2|1}_{\mathbf{0},i|j}(\varepsilon+x)\Big], \tag{41c}$$

$$X^{1|1}(x)\Big|_{V=0} = [1+2b(x+\mu)]\big[X^{1|2}(x) - X^{2|1}(x)\big]_{V=0}, \tag{41d}$$

$$\Delta^{\sigma\sigma',1|2}_{ij}(0) = \frac{u_i u_j}{2\pi i}\int d\varepsilon \Big[\mathcal{G}^{\bar\sigma,1|2}_{\mathbf{0},i|j}(\varepsilon)\mathcal{G}^{\bar\sigma',2|2}_{\mathbf{0},i|j}(\varepsilon) + \mathcal{G}^{\bar\sigma,2|2}_{\mathbf{0},i|j}(\varepsilon)\mathcal{G}^{\bar\sigma',2|1}_{\mathbf{0},i|j}(\varepsilon)\Big], \tag{42a}$$

$$\Delta = \Delta^{2|1} = \Delta^{1|2}, \tag{42b}$$

$$\Delta^{1|1} = 0. \tag{42c}$$

Here, we introduced the Bose distribution function, $b(z) = 1/(e^{(z-\mu)/T} - 1)$, with chemical potential μ and temperature T. $[\,]^*$ denotes the complex conjugate. Note that the components of every individual channel fulfill a fluctuation dissipation theorem (FDT) in equilibrium [Eqs.(40d,41d,42c)], warranting the choice of notation introduced in Eq.(38). We derive this FDT in detail in Appendix D.

Finally we write down the three components of the SOPT two-particle vertex that occur in the vertex-correction part, Eq.(18):

$$\mathcal{L}^{12|22}_{\mathbf{2},i\sigma,l\sigma'|j\sigma,k\sigma'}(\varepsilon',\varepsilon;0) = \delta_{\sigma\bar\sigma'}\delta_{ij}\delta_{ik}\delta_{il}u_i + \delta_{\sigma\bar\sigma'}\delta_{il}\delta_{jk}\Pi^{1|2}_{ij}(p) + \delta_{ik}\delta_{jl}X^{\sigma\sigma',1|2}_{ij}(x) + \delta_{\sigma\sigma'}\delta_{ij}\delta_{kl}\Delta^{\sigma\sigma'}_{ik}(0), \tag{43a}$$

$$\mathcal{L}^{22|12}_{\mathbf{2}} = \bar u + \Pi^{2|1} + X^{2|1} + \Delta, \tag{43b}$$

$$\mathcal{L}^{12|12}_{\mathbf{2}} = \Pi^{1|1} + X^{1|1}. \tag{43c}$$

Utilizing the equilibrium's FDT for the Π-, and X-channel [Eq.(40d), Eq.(41d)], we find

$$K_{i\sigma,l\sigma'|j\sigma,k\sigma'}(\varepsilon',\varepsilon;0) = \delta_{\sigma\bar\sigma'}\delta_{il}\delta_{jk}\,[2f(\varepsilon)+2b(p-\mu)]\,(\Pi^{1|2}_{ij}(p) - \Pi^{2|1}_{ij}(p)) + \delta_{ik}\delta_{jl}\,[2f(\varepsilon)+2b(x+\mu)]\,(X^{\sigma\sigma',1|2}_{ij}(x) - X^{\sigma\sigma',2|1}_{ij}(x)). \tag{44}$$

We note, that this result (for $\mu=0$) has been obtained before by Oguri (see Eq.(4.7) of Ref. 6) using Matsubara formalism and an analysis of the two-particle vertex following Eliashberg[7].

B. The self-energy in SOPT

Our goal is to approximate the self-energy to second order in the interaction. The fully interacting self-energy, $\Sigma(\varepsilon)$, has the following diagrammatic representation:

$$\Sigma_{\kappa_1'|\kappa_1}(\varepsilon) \quad = \tag{45}$$

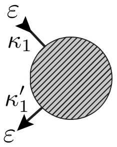

In SOPT, the self-energy $\Sigma_{\mathbf{2}}$ is given by the sum of all 1PI diagrams with two external amputated legs and not more than two bare vertices. This amounts to three topologically different diagrams (the static first and second order Hartree diagrams and the frequency-dependent second order Fock diagram):

$$\Sigma_{\mathbf{2},\kappa_1'|\kappa_1}(\varepsilon) \quad = $$

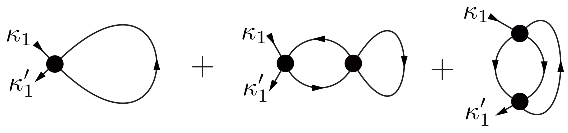

$$= \frac{-i}{2\pi}\int_{-\infty}^{\infty} d\varepsilon' \sum_{q_1 q_1'} \big[\bar u_{k_1' q_1'|k_1 q_1} + \gamma^d_{\mathbf{2},k_1'q_1'|k_1q_1}(0) + \gamma^p_{\mathbf{2},k_1'q_1'|k_1q_1}(\varepsilon+\varepsilon')\big]\mathcal{G}_{\mathbf{0},q_1|q_1'}(\varepsilon'). \tag{46}$$

We note that, equivalently, the Fock diagram can also be expressed via either spin configuration, $X^{\sigma\sigma}$ or $X^{\sigma\bar\sigma}$, [Eq.(41a), Eq.(48a)] of the particle-hole vertex channel $\gamma^x_{\mathbf{2}}$ instead of the particle-particle channel $\gamma^p_{\mathbf{2}}$.

As a consequence of the spin-dependence of both the noninteracting Green's function and the bare vertex, Eq.(26) and Eq.(31), as well as the real space symmetry of the Hamiltonian, Eq.(25), the self-energy, too, is spin-diagonal and symmetric in real space:

$$\Sigma_{i\sigma|j\sigma'} = \delta_{\sigma\sigma'}\Sigma^{\sigma}_{i|j} \quad , \quad \Sigma^{\sigma}_{i|j} = \Sigma^{\sigma}_{j|i}. \tag{47}$$

The Keldysh structure of the self-energy is given by matrix structure [Eq.(A.13)] with $\Sigma^R = \Sigma^{1|2}$. The theorem of causality demands $\Sigma^{2|2} = 0$ [Eq.(A.12)]. Finally, explicit evaluation of the diagrams in Eq.(46) yields

$$\Sigma^{\sigma,1|2}_{\mathbf{2},i|j}(\varepsilon) = \frac{-i}{2\pi}\int d\varepsilon' \Big[\delta_{ij}u_i\mathcal{G}^{\bar\sigma,2|2}_{\mathbf{0},i|i}(\varepsilon') + \delta_{ij}\sum_k \mathcal{G}^{\sigma,2|2}_{\mathbf{0},k|k}(\varepsilon')\Delta^{\sigma\sigma}_{ik}(0) + \mathcal{G}^{\sigma,2|2}_{\mathbf{0},i|j}(\varepsilon')X^{\sigma\sigma,1|2}_{ij}(\varepsilon-\varepsilon') + \mathcal{G}^{\sigma,2|1}_{\mathbf{0},i|j}(\varepsilon')X^{\sigma\sigma,1|1}_{ij}(\varepsilon-\varepsilon')\Big], \tag{48a}$$

$$\Sigma^{21}_{\mathbf{2}} = \left[\Sigma^{12}\right]^*, \tag{48b}$$

$$\Sigma^{\sigma,1|1}_{\mathbf{2},i|j}(\varepsilon) = \frac{-i}{2\pi}\int d\varepsilon' \left[\mathcal{G}^{\sigma,2|2}_{\mathbf{0},i|j}(\varepsilon')X^{\sigma\sigma,1|1}_{ij}(\varepsilon-\varepsilon') + \mathcal{G}^{\sigma,2|1}_{\mathbf{0},i|j}(\varepsilon')X^{\sigma\sigma,1|2}_{ij}(\varepsilon-\varepsilon') + \mathcal{G}^{\sigma,1|2}_{\mathbf{0},i|j}(\varepsilon')X^{\sigma\sigma,21}_{ij}(\varepsilon-\varepsilon')\right], \tag{48c}$$

$$\Sigma^{\sigma,1|1}_{\mathbf{2},i|j}(\varepsilon)|_{V=0} = (1-2f(\varepsilon))\left[\Sigma^{\sigma,1|2}_{\mathbf{2},i|j}(\varepsilon) - \Sigma^{\sigma,2|1}_{\mathbf{2},i|j}(\varepsilon)\right]_{V=0}. \tag{48d}$$

We derive the FDT, Eq.(48d), in Appendix D.

C. Voltage derivative of the self-energy in SOPT

In order to calculate the differential conductance via Eq.(9) we now provide explicit formulas for the voltage derivative of the self-energy components. In principle we could use the natural approach and differentiate the r.h.s. of the self-energy expressions, Eq.(48), with the corresponding vertex components given by Eqs.(40)-(42). To illustrate the power of the fRG flow equation we choose an alternative, more direct route, by expanding Eq.(16) up to second order in the bare interaction and allow for arbitrary values of the voltage V.

To first order in the interaction the single-scale propagator, Eq.(14), reads

$$S^{2|2}_{\mathbf{1},V} = \dot{\mathcal{G}}^{2|2}_{\mathbf{0}} + \mathcal{G}^{2|1}_{\mathbf{0}}\Sigma^{1|2}_{\mathbf{1}}\dot{\mathcal{G}}^{2|2}_{\mathbf{0}} + \dot{\mathcal{G}}^{2|2}_{\mathbf{0}}\Sigma^{2|1}_{\mathbf{1}}\mathcal{G}^{1|2}_{\mathbf{0}}. \tag{49}$$

Inserting both Eq.(49) and the SOPT vertex, Eq.(43c), in Eq.(16) directly yields

$$\begin{aligned}\dot\Sigma^{\sigma,1|2}_{\mathbf{2},i|j}(\varepsilon) &= \frac{-i}{2\pi}\int d\varepsilon' \Big[\delta_{ij}u_i\dot{\mathcal{G}}^{\bar\sigma,2|2}_{0,i|i} + \delta_{ij}\sum_k\Big[u_i\Big(\mathcal{G}^{\bar\sigma 2|1}_{0,i|k}\Sigma^{\bar\sigma 1|2}_{\mathbf{1},k|k}\dot{\mathcal{G}}^{\bar\sigma 2|2}_{0,k|i} + \dot{\mathcal{G}}^{\bar\sigma,2|2}_{0,i|k}\Sigma^{\bar\sigma,2|1}_{\mathbf{1},k|k}\mathcal{G}^{\bar\sigma,1|2}_{0,k|i}\Big) + \dot{\mathcal{G}}^{\sigma,2|2}_{\mathbf{0},k|k}\Delta^{\sigma\sigma}_{ik}(0)\Big] \\ &\qquad + \dot{\mathcal{G}}^{\sigma,2|2}_{\mathbf{0},i|j}X^{\sigma\sigma,1|2}_{ij}(x) + \dot{\mathcal{G}}^{\bar\sigma,2|2}_{\mathbf{0},i|j}\big(X^{\sigma\bar\sigma,1|2}_{ij}(x) + \Pi^{1|2}_{ij}(p)\big)\Big], \\ \dot\Sigma^{\sigma,2|1}_{i|j}(\varepsilon) &= \left[\dot\Sigma^{\sigma,1|2}_{i|j}(\varepsilon)\right]^*, \\ \dot\Sigma^{\sigma,1|1}_{i|j}(\varepsilon) &= \frac{-i}{2\pi}\int d\varepsilon' \left[\dot{\mathcal{G}}^{\sigma,2|2}_{\mathbf{0},i|j}X^{\sigma\sigma,1|1}_{ij}(x) + \dot{\mathcal{G}}^{\bar\sigma,2|2}_{\mathbf{0},i|j}\left(X^{\sigma\bar\sigma,1|1}_{ij}(x) + \Pi^{1|1}_{ij}(p)\right)\right],\end{aligned} \tag{50}$$

where the derivative of the Keldysh bare Green's function is given by [e.g. Eq.(A.22)]

$$\dot{\mathcal{G}}^{2|2}_{\mathbf{0}} = \mathcal{G}^{2|1}_{\mathbf{0}}\dot\Sigma^{1|1}_{\text{lead}}\mathcal{G}^{1|2}_{\mathbf{0}} = 2i\mathcal{G}^{2|1}_{\mathbf{0}}\Big(\sum_{k\in l,r}\dot f^k\Gamma^k\Big)\mathcal{G}^{1|2}_{\mathbf{0}}. \tag{51}$$

For compactness, we dropped all arguments that match the integration frequency in Eq.(50).

It is important to note that the energy integral $\int d\varepsilon'$ in Eq.(50) can be performed trivially for the special case of zero temperature, $T=0$: Then the derivative of the Fermi functions in $\dot{\mathcal{G}}^{2|2}_{\mathbf{0}}$ are Dirac delta functions [for the definition of the voltage see Sec.(III B)]:

$$\begin{aligned}\dot f^l(\varepsilon') &\overset{T=0}{\equiv} e\alpha\cdot\delta(\varepsilon'-\mu-e\alpha V) \\ \dot f^r(\varepsilon') &\overset{T=0}{\equiv} e(\alpha-1)\cdot\delta(\varepsilon'-\mu-e(\alpha-1)V).\end{aligned} \tag{52}$$

This reduces the integration in Eq.(50) to evaluating the integrand at the chemical potentials of the left and right lead, respectively. Naturally, this simplification proves extremely beneficial: We can express the self-energy at arbitrary voltage as

$$\Sigma(V) = \Sigma(0) + \int_0^V dV' \, \dot{\Sigma}(V'). \tag{53}$$

Numerically calculating this voltage integration provides both the self-energy $\Sigma(V')$ and its derivative $\dot{\Sigma}(V')$ within the whole intervall $0 \le V' \le V$. Hence, this procedure can save orders of magnitude of calculation time compared to the direct evaluation of the self-energy and its voltage derivative via Eq.(48) and Eq.(50), respectively.

V. 1D MODEL OF A QPC

As an application of the above formalism, we now study the influence of electron-electron interactions on the linear conductance of a one-dimensional symmetric potential barrier of height V_c (measured w.r.t. the chemical potential μ) and parabolic near the top,

$$V(x) = V_c + \mu - \frac{m\Omega_x^2}{2\hbar^2} x^2, \tag{54}$$

where m is the electron's mass. The geometry of the barrier is determined by the energy scale Ω_x and the length scale $l_x = \hbar/\sqrt{2m\Omega_x}$. While the system extends to infinity, the potential is non-zero only within the central region C, defined by $-\ell/2 < x < \ell/2$, and drops smoothly to zero as $|x|$ approaches $|\ell|/2$. We call the outer homogeneous regions the left lead L ($x < -\ell/2$) and the right lead R ($x > \ell/2$).

Numerics cannot deal with the infinite Hilbert space of this continuous system. Hence, we discretize real space using the method of finite differences (see Appendix E for details), which maps the system onto a discrete set of space points $\{x_j\}$. This results in the tight-binding representation

$$H = \sum_{j\sigma} [E_j^\sigma n_{j\sigma} - \tau_j (d_{j\sigma}^\dagger d_{j+1\sigma} + \text{h.c.})] + \sum_{j \in C} U_j n_{j\uparrow} n_{j\downarrow}, \tag{55}$$

with spin-dependent onsite energy $E_j^\sigma = E_j - \sigma B/2 = V_j + \tau_{j-1} + \tau_j - \sigma B/2$, site-dependent hopping amplitude $\tau_j = \hbar^2/(2ma_j^2)$, spacing $a_j = x_{j+1} - x_j$ and potential energy $V_j = V(x_j)$. Note that we included a homogeneous Zeeman-field B to investigate magnetic field dependencies, as well as an onsite-interaction, whose strength is tuned by the site-dependent parameter U_j.

In Ref.5 we have used this model to investigate the physics of a quantum point contact (QPC), a short one-dimensional constriction We showed that the model suffices to reproduce the main features of the 0.7 anomaly, including the strong reduction of conductance as function of magnetic field, temperature and source-drain voltage in a sub-open QPC (see below). We argued, that the appearance of the 0.7 anomaly is due to an interplay of a maximum in the local density of states (LDOS) just above the potential barrier (the "van-Hove ridge") and electron-electron interactions.

Here, we show that a proper choice of real space discretization scheme can minimize numerical costs. We discuss both the noninteracting physics of the model as well as the magnetic field and temperature dependence of the linear conductance in the presence of interactions using SOPT.

A. The choice of discretization

For a proper description of the continuous case it is essential to choose the spacing much smaller than the length scale on which the potential changes (condition of adiabatic discretization). We model the central region by $N = 2N' + 1$ sites, located at the space points $\{x_{-N'}, x_{-N'+1}, \ldots, x_{N'-1}, x_{N'}\}$, where $N \gtrsim 100$ proves sufficient for a potential of the form Eq. (54). Due to the parity symmetry of the barrier we always choose $x_0 = 0$ and $x_j = -x_{-j}$.

The discretization of real space introduces an upper bound, $E^{\max} = \max(V_j + 2\tau_{j-1} + 2\tau_j)$, for the eigenenergies of the bare Hamiltonian. In addition, it causes the formation of a site-dependent energy band, defined as the energy intervall where the local density of states (LDOS) is non-negligible, i.e. where eigenstates have non-negligible weight. In case of an adiabatic discretization this energy band follows the shape of the potential. At a site j it is defined within the upper and lower band edge

$$\varepsilon_j^{\min} = V_j, \qquad \varepsilon_j^{\max} = V_j + w_j, \tag{56}$$

where the band width depends on the local spacing, i.e. on the choice of discretization (see Appendix E for additional information):

$$w_j = 2\tau_{j-1} + 2\tau_j = \frac{\hbar^2}{m} \left(\frac{1}{a_{j-1}^2} + \frac{1}{a_j^2} \right). \tag{57}$$

Note that a larger distance between successive sites leads to a narrowing of the energy band and vice versa; while the lower band edge is, for any adiabatic discretization, directly given by the potential, the upper band edge depends sensitively on the applied discretization scheme.

In the following we discuss and compare two different discretization procedures: The standard approach of equidistant discretization (constant hopping τ) causes a local maximum $\varepsilon_0^{\max} = V_0 + 2\tau$ of the upper band edge in the vicinity of the barrier center. This approach leads to artificial bound states far above the potential barrier, which complicate numerical implementation and calculation. Hence, we recommend and apply an alternative adaptive scheme where the spacing increases (the band width decreases) with increasing potential, i.e. towards $j = 0$. Note that this still implies a constant hopping $\tau_{|j|>N'} = \tau$ in the leads.

1. *Constant discretization*

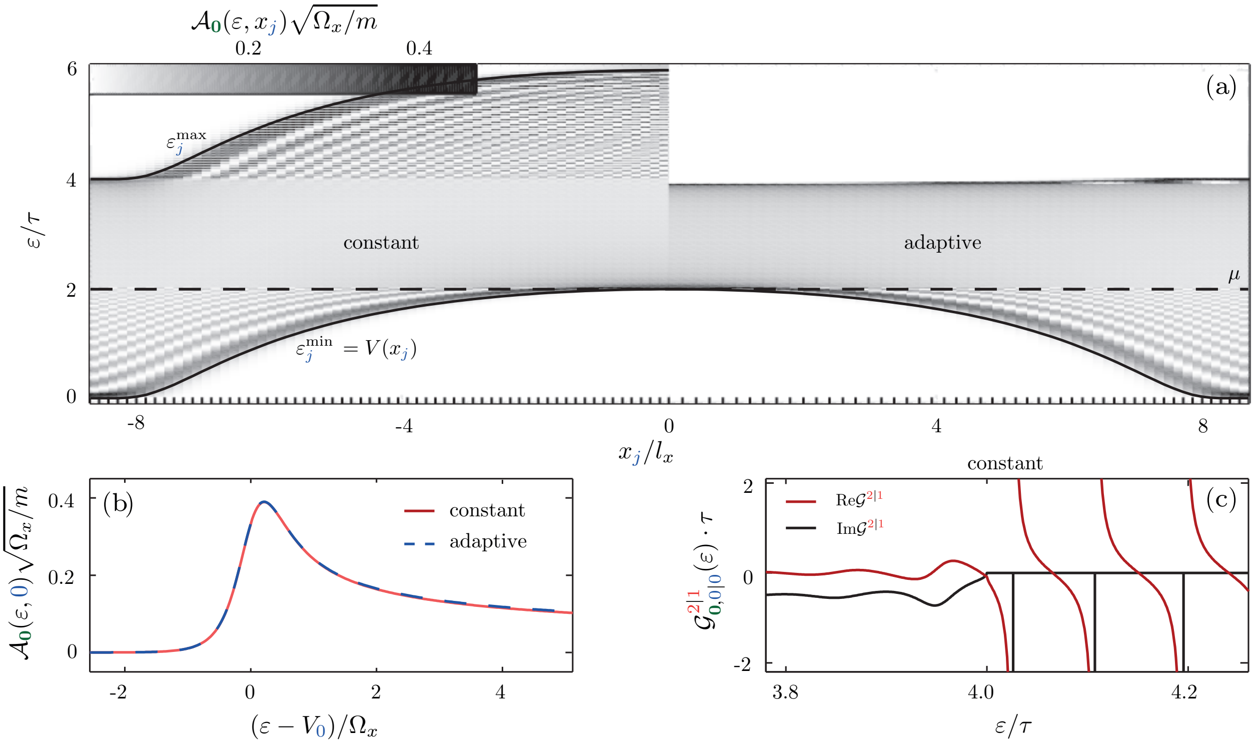

Figure 1. (a), left half: The non-interacting LDOS of the central region, $\mathcal{A}_{\mathbf{0}}(\varepsilon,x_j)$, resulting from a constant real-space discretization. The position of the discrete points x_j is indicated by the x-axis ticks. Both the lower and upper band edge follow the shape of the potential: $\varepsilon_j^{\min}=V(x_j)$ and $\varepsilon_j^{\max}=V(x_j)+4\tau$. The local maximum of $\varepsilon_j^{\max}$ at $j=0$ causes the formation of bound states for energies $\varepsilon>4\tau$. (c), their discrete spectrum shows up as poles in the non-interacting Green's function $\mathcal{G}_{\mathbf{0},0|0}(\varepsilon)$. (a), right half: The non-interacting LDOS of the central region resulting from an adaptive real-space discretization with $c=0.55$ [Eq.(60)], i.e. the spacing a_j increases towards the barrier center (see x-axis ticks). Hence, the band width decreases with increasing barrier height, resulting in a local minimum of $\varepsilon_j^{\max}$ at $j=0$. (b), the LDOS at the central site, $\mathcal{A}_{\mathbf{0}}(\varepsilon,0)$, for both schemes.

We discuss the case of constant spacing $a=a_j$, implying grid points $x_j=aj$ and a constant hopping $\tau=\hbar^2/(2ma^2)$. In a homogeneous system, $V(x_j)=0$, the energy eigenstates are Bloch waves $\psi_k(x_j)=e^{ikaj}$, which form an energy band $\varepsilon_k=2\tau[1-\cos(ka)]$ of width $w=4\tau$. Adding the parabolic potential,

$$V(x_j)=V_c+\mu-\frac{\Omega_x^2}{4\tau}j^2, \tag{58}$$

these states are now subject to scattering at the barrier which causes the formation of standing wave patterns for energies $\varepsilon<V_0=V(0)=V_c+\mu$ below the barrier top. The left half ($x_j<0$) of Fig. 1(a) shows the noninteracting central region's local density of states (LDOS), $\mathcal{A}^{\sigma}_{\mathbf{0}}(x_j,\varepsilon)=-1/(\pi a)\cdot\mathrm{Im}\mathcal{G}^{\sigma,2|1}_{\mathbf{0},j|j}(\varepsilon)$ at $B=0$, as a function of position x_j and energy ε. Due to the condition of adiabaticity the energy band smoothly follows the shape of the potential, implying a site-dependent upper band edge, $\varepsilon^{\max}(x_j)=V_j+4\tau$.

The local maximum of $\varepsilon^{\max}(x_j)$ in the central region's center generates artificial bound states, owed to the discretization scheme, in the energy interval $\varepsilon\in[4\tau,4\tau+V_0]$. This is illustrated in Figure 1(c), where the real and imaginary parts of the bare Green's function of the central site, $\mathcal{G}^{2|1}_{\mathbf{0},0|0}(\varepsilon)$, are plotted. These bound states result from the shape of the upper band edge: Since the band in the homogeneous leads is restricted to energies below 4τ (unlike in the continuous case), all states with higher energy are spacially confined to within the central region, have an infinite lifetime and form a discrete spectrum, determined by the shape of the applied potential $V(x_j)$.

The calculation of self-energy and two particle vertex, Eq.(48) and Eq.(42), is performed by ad-infinitum frequency integrations over products of Green's functions. Thus, the energy region of the upper band edge and the local bound states must be included in their calculation with adequate care. This involves determining the exact position and weigth of the bound states, which requires high numerical effort, as well as dealing with the numerical evaluation of principal value integrals and convolutions, where one function has poles and the other one is continuous. While all this is doable with sufficient dedication, we can avoid such complications entirely by adapting the discretization scheme, discussed next.

2. Adaptive discretization

According to Eq. (56) and Eq. (57) we can modify the band width locally by choosing non-equidistant discretization points. In the following we discuss a non-constant discretization scheme that reduces the band width within the central region enough so that the upper band edge exhibits a local minimum at x_0 rather than a local maximum (as in the case of constant spacing). In consequence the Green's functions are continuous within the whole energy band, which facilitates a numerical treatment of interactions.

For a non-constant real space discretization it proves useful to first define the onsite energy E_j and the hopping τ_j of the discrete tight-binding Hamiltonian Eq. (55) and then use these expressions to calculate the geometry of the corresponding physical barrier, i.e. its height V_c and curvature Ω_x.

We specify the onsite energy to be quadratic near the top with

$$E_j = \tilde{E}_j + 2\tau \simeq \tilde{E}_0 \left[1 - \frac{j^2}{N'^2}\right] + 2\tau, \tag{59}$$

where $\tilde{E}_0$ is positive. We use the shape of $\tilde{E}_j$ within C (which, apart from its height and the quadratic shape around the top does not influence transport properties, as long as $\tilde{E}_j$ goes adiabatically to zero upon approaching $j = |N'|$) to define a site-dependent hopping (amounting to a site-dependent spacing)

$$\tau_j = \tau \left[1 - \frac{c}{2\tau}\left(\tilde{E}_j + \tilde{E}_{j+1}\right)\right], \tag{60}$$

where we have introduced a dimensionless positive parameter $c < \tau/\tilde{E}_0$ that determines how strongly the band width is to be reduced. Note that Eq. (60) describes a hopping, that is constant ($= \tau$) in the leads, where $\tilde{E}_j = V_j = 0$, and decreases with increasing $\tilde{E}_j$ in the central region. This corresponds to a site-dependent lattice spacing $a_j = a\sqrt{\tau/\tau_j}$, which increases towards the center of the central region. The real space position x_j that corresponds to a site j is given by

$$x_j = \operatorname{sgn}(j) \sum_{j'=1}^{|j|} a_{j'} = a\sqrt{\tau}\, \operatorname{sgn}(j) \sum_{j'=1}^{|j|} \frac{1}{\sqrt{\tau_j}}, \tag{61}$$

where $\operatorname{sgn}(x)$ is the sign function. Following Eq. (56), the construction introduced in Eq.(59) and Eq.(60) leads to an upper band edge given by

$$\varepsilon_j^{\max} \simeq E_j + \tau_{j-1} + \tau_j \simeq 4\tau + (1 - 2c)\tilde{E}_j, \tag{62}$$

which for the choice $c > 0.5$ indeed exhibits a smooth local minimum at $j = 0$, thus avoiding the bound states discussed above for the constant discretization, $c = 0$.

Despite the drastic manipulation of $\varepsilon_j^{\max}$, the lower band edge still serves as a proper potential barrier,

$$\varepsilon_j^{\min} = V_j \simeq (1 + 2c)\tilde{E}_j, \tag{63}$$

with a quadratic potential barrier top whose height now depends on the compensation factor c:

$$V_j \simeq (1 + 2c)\tilde{E}_j \left[1 - \frac{j^2}{N'^2}\right]. \tag{64}$$

Finally, we write the potential barrier in the form given in Eq.(58), i.e. express the curvature Ω_x in units of the constant lead-hopping τ. By comparison we find

$$V_c = V_0 - \mu, \qquad \Omega_x = \frac{2}{N'}\sqrt{V_0 \tau_0}. \tag{65}$$

The right half ($x_j > 0$) of Fig. 1(a) shows the LDOS of the central region for an adaptive discretization with $c = 0.55$. All additional parameters are chosen such that the resulting potential barrier matches the case of constant discretization (plotted for $x_j < 0$). Most importantly, the minimum of $\varepsilon_j^{\max}$ at $j = 0$ prevents the occurance of bound states above the barrier, which allows for a faster numerical evaluation of the vertex functions. Importantly, both discretization schemes approximate the same physical system; their differences are non-neglegible only for energies far above the barrier, i.e. far away from the energies relevant for transport. This can be seen from the matching grey scale at the interface $j = 0$ for energies $\varepsilon < V_0 + \mathcal{O}(\Omega_x)$, as well as from comparison of the central site's LDOS in Fig. 1(c).

B. The choice of system parameters

To ensure that the discrete model reflects the transport properties of the continuous barrier, Eq. (54), the chemical potential of the system (or of both leads in non-equilibrium) must be chosen far enough below the global minimum of $\varepsilon^{\max}(x_j)$. Only in this case the unphysical upper band edge does not contribute to the results. The onsite-energy is chosen as

$$\tilde{E}_j = \theta(N' - |j|)\tilde{E}_0 \exp\left(-\frac{\left(\frac{j}{N'}\right)^2}{1 - \left(\frac{j}{N'}\right)^2}\right), \tag{66}$$

where $\theta(x)$ is the Heavyside step function. Note, that this definition is consistent with Eq.(59). In order to calculate the site-dependent coupling we use $c = 0.55$ in Eq. (60). Hence, for a barrier height $V_0 = \mu$ (corresponding to a noninteracting transmission $\mathcal{T}_0 = 0.5$, see Eq.(68) below), we get a potential curvature $\Omega_x = 0.039\tau$. Finally, the shape of the onsite interaction is chosen as

$$U_j = \theta(N' - |j|)U_0 \exp\left(-\frac{\left(\frac{j}{N'}\right)^6}{1 - \left(\frac{j}{N'}\right)^2}\right). \tag{67}$$

C. Non-interacting properties of the model

In Ref. 5 we argued that the model of Eq.(55), combined with a potential with parabolic barrier top,

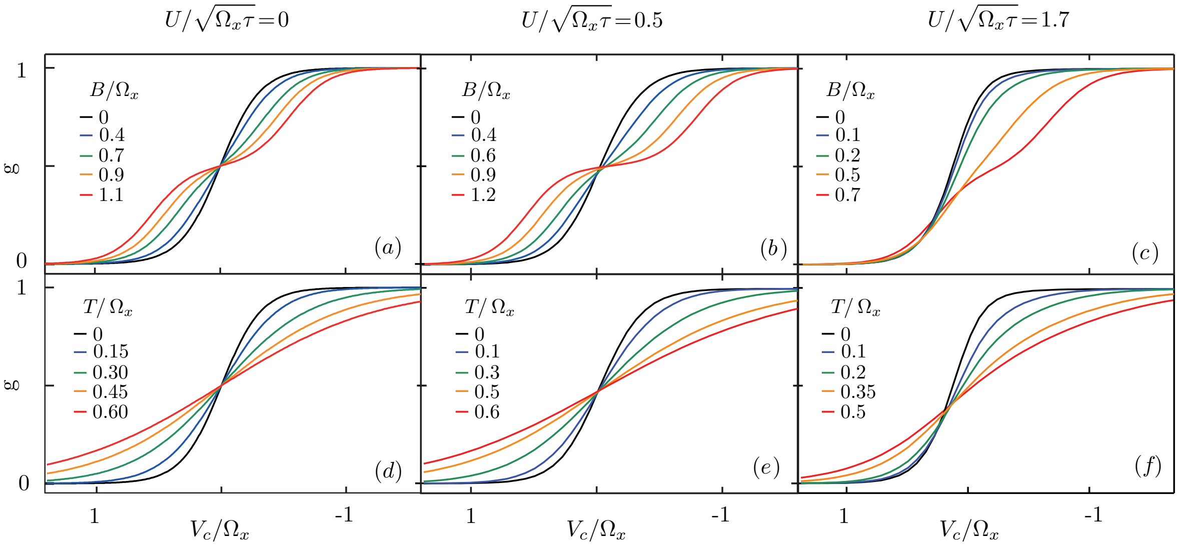

Figure 2. : (a)-(c), Linear conductance as a function of barrier height V_c for some values of magnetic field B with interaction strength U increasing from left to right. (d)-(f), Linear conductance as a function of barrier height V_c for some values of temperature T with interaction strength U increasing from left to right. Interactions cause an asymmetric evolution of conductance with magnetic field and temperature due to the interaction-enhanced reduction of conductance in the sub-open regime – the 0.7 anomaly.

Eq.(54), is sufficient to describe the physics of the lowest subband of a QPC: Making a saddle-point ansatz for the electrostatic potential caused by voltages applied to a typical QPC gate structure provides an effective 1D-potential of the form Eq.(54). Information about the transverse geometry of the QPCs potential can be incorporated into the site-dependent effective interaction strength U_j, see Eq.(67).

The non-interacting, spin-dependent transmission through a quadratic barrier of height $V_0 = V_c + \mu$ and curvature Ω_x, Eq. (54), in the presence of a magnetic field B can be derived analytically[16] and is given by

$$\mathcal{T}_0^\sigma(\varepsilon) = \frac{1}{e^{-2\pi(\varepsilon - V_0 + \sigma B/2)/\Omega_x} + 1}. \qquad (68)$$

Hence, according to the Landauer-Büttiker formula, the non-interacting (bare) linear conductance,

$$g_0 = -\frac{e^2}{h}\sum_\sigma \int_{-\infty}^{\infty} f'(\varepsilon)\mathcal{T}_0^\sigma(\varepsilon), \qquad (69)$$

is a step function of width Ω_x at $B = T = 0$, changing from 0 to 1, when the barrier top is shifted through μ from above. This step gets broadened with temperature [see Figure 2(d)] and develops a double-step structure with magnetic field [see Figure 2(a)]. For all B and T the bare conductance obeys the symmetry $g_0(V_c) = 1 - g_0(-V_c)$.

Furthermore, an analytic expression for the non-interacting LDOS at the chemical potential in the barrier center as function of barrier height V_c can be calculated [see e.g. Ref. 17],

$$\mathcal{A}_0(\varepsilon = \mu, 0) = \frac{\left|\Gamma\left(1/4 + iV_c/(2\Omega_x)\right)\right|^2}{4\sqrt{2}\pi^2 e^{\pi V_c/(2\Omega_x)}}, \qquad (70)$$

where $\Gamma(z)$ is the complex gamma-function. This is a smeared and shifted version of the 1D van Hove singularity [see Ref. 5 for further details], peaked at $V_c = -\mathcal{O}(\Omega_x)$, i.e. if the barrier top lies sightly below the chemical potential. Here, the value of the noninteracting conductance is given by $g_0 \approx 0.8$. Hence, we call this parameter regime *sub-open*.

D. Interacting results

As was discussed in Ref. 5, the shape of the LDOS in the barrier center lies at the heart of the mechanism causing the 0.7 conductance anomaly: Semiclassically, the LDOS can be interpreted as being inversely proportional to the velocity v of the charge carriers, $\mathcal{A}_0(\varepsilon, x_j) \propto 1/v_j(\varepsilon)$. Hence, the average time that a non-interacting electron with energy $\varepsilon = \mu$ spends in the vicinity of the barrier center is maximal in the sub-open regime (where $\mathcal{A}_0(\mu, 0)$ is maximal), resulting in an enhanced scattering probability and thus a strong reduction of conductance at finite interaction strength in this parameter regime.

Figure 2 compares the bare conductance, calculated via the Landauer-Büttiker formula [Eq.(69)], with the conductance obtained by taking into account interactions using SOPT, calculated via the Keldysh version of Oguri's formula [Eq.(23)], as a function of barrier height

V_c for several values of magnetic field (panels (a)-(c)) and temperature (panels (d)-(f)), for three interaction strengths increasing from left to right. For small but finite interactions, $U\sqrt{\Omega_x\tau} = 0.5$, the shape of the LDOS causes a slight asymmetry in the conductance curves at (b) finite magnetic field or (e) finite temperature: A finite magnetic field induces an imbalance of spin-species in the vicinity of the barrier center. This imbalance is enhanced by exchange interactions via Stoner-type physics, where the disfavoured spin species (say spin down) is pushed out of the center region by the coulomb blockade of the the favoured spin-species (say spin up). Hence, transport is dominated by the spin-up channel, resulting in a strong reduction of total conductance in the sub-open regime even for a small magnetic field. A finite temperature, on the other hand, opens phase-space for inelastic scattering, which, again, is strongest for large LDOS, again resulting in the reduction of conductance in the sub-open regime. This interaction-induced trend continues with increasing interactions, and gives rise to a weak 0.7 anomaly at $B \neq 0$, Figure 2(c), or $T \neq 0$, Figure 2(f), for intermediate interaction strength, $U\sqrt{\Omega_x\tau} = 1.7$. Upon a further increase of interactions, SOPT breaks down (see below), and more elaborate methods are needed to obtain qualitatively correct results. This was done in Ref. 5 and Ref. 18, where we used fRG to reach interaction strength of up to $U\sqrt{\Omega_x\tau} = 3.5$; they yielded a pronounced 0.7 anomaly even at $B = T = 0$ and its typical magnetic field development into the spin-resolved conductance steps at high field.

The main limitations of SOPT when treating the inhomogeneous system, introduced in Eq.(54), can be explained as follows: Upon increasing interactions, the LDOS is shifted towards higher energy, as Hartree contributions cause an effective higher potential barrier compared to the non-interaction case. As a consequence, a proper description of interactions requires information about this shift to be incorporated into the calculation of the vertex functions via feed-back of the self-energy into all propagators. However, SOPT calculates the self-energy and the two-particle vertex [Section IV] using only bare propagators, which only carry information of the bare LDOS. Together with the drastic truncation of the perturbation series beyond second order, this limits the quantitative validity of SOPT to weak interaction strength and the qualitative validity of SOPT to intermediate interaction strength. Nevertheless, SOPT suffices to illustrate the essential physics involved in the appearance of the 0.7 conductance anomaly.

VI. CONCLUSION AND OUTLOOK

In this paper we discuss electronic transport through an interacting region of arbitrary shape using the Keldysh formalism. Starting from the well-established Meir-Wingreen formula for the system's current we derive formulas for both the differential and linear conductance. In the latter case we use the fRG flow-equation for the self-energy as well as a Ward identity, following from the Hamiltonian's particle conservation, to obtain a Keldysh version of Oguri's linear conductance formula. As an application we calculate the conductance of the lowest subband of a QPC, which we model by a one-dimensional parabolic potential barrier and onsite interactions - a setup we have recently used to explore the microscopic origin of the 0.7 conductance anomaly[5]. We present detailed discussion of the model's properties and argue that an adaptive, non-constant real space discretization scheme greatly facilitates numerical effort. We treat the influence of interactions using SOPT, presenting all details that are necessary to employ the derived conductance formulas. Our SOPT-results for the linear conductance as function of magnetic field and temperature illustrate that the anomalous reduction of conductance in the sub-open regime of a QPC is due to an interplay of the van-Hove ridge and electron-electron interactions.

In order to improve on the interacting results we are currently setting up Keldysh fRG. Since approximation schemes within the fRG violate particle conservation at finite excitation energies, future studies must prioritize to quantify how severe this violation influences the validity of transport results. A possible alternative are self-consistent approximation schemes, where the $U(1)$-symmetry of the Hamiltonian is preserved by construction.

Appendix A: Properties of Green's and vertex functions in Keldysh formalism

To investigate transport properties of the system in and out of equilibrium, we apply the well-established Keldysh formalism[8,9]. Here we collect some of its standard ingredients. In large parts, we follow the definitions and conventions given in Ref.[11].

All operators carry Keldysh time-contour indices, $a_1, a_1', a_2, ... = \{+, -\}$, marking the position of the time argument t of an operator as lying on the forward $(-)$ or backward $(+)$ branch of the Keldysh contour. We use Keldysh indices with or without a prime, a or a', to label the time arguments of annihilation or creation operators, respectively. Since the model Hamiltonian, Eq.(1), is time-independent, the only non-zero matrix elements of the Hamiltonian in contour space have equal contour indices:

$$\begin{aligned} \mathcal{H}_{\mathbf{0}}^{a_1 a_1'} &= -a_1 \cdot \delta_{a_1 a_1'} H_{\mathbf{0}}, \\ \mathcal{H}_{int}^{a_1 a_2 | a_1' a_2'} &= -a_1 \cdot \delta_{a_1 a_2} \delta_{a_1 a_1'} \delta_{a_1 a_2'} H_{int}, \end{aligned} \tag{A.1}$$

with $\{a\}$ labeling the time arguments of annihilation operators and $\{a'\}$ labeling the time arguments of creation operators. Note that a calligraphic $\mathcal{H}$ carries contour indices, while a capital H does not.

We define time-dependent, n-particle Keldysh Green's functions as the expectation values

$$\begin{aligned} &G^{n,\boldsymbol{a}|\boldsymbol{a}'}_{\boldsymbol{i}|\boldsymbol{i}'}(\boldsymbol{t}|\boldsymbol{t}') = G^{a_1,...,a_n|a_1',...a_n'}_{i_1,...,i_n|i_1',...i_n'}(t_1,...,t_n|t_n',...,t_1') = \\ &(-i)^n \langle \mathcal{T}_c d^{a_1}_{i_1}(t_1)...d^{a_n}_{i_n}(t_n)[d^{a_n'}_{i_n'}]^\dagger(t_n')...[d^{a_1'}_{i_1'}]^\dagger(t_1')\rangle, \end{aligned} \tag{A.2}$$

where we use boldface notation for multi-indices $\boldsymbol{x} = (x_1, ..., x_n)$. The operator $d_i^a(t)/\,[d_i^a]^\dagger(t)$ destroys/creates an electron at time t on contour branch a in quantum state i, and the time-ordering operator $\mathcal{T}_c$ moves later contour times to the left. In case of equal time arguments, annihilation operators are always arranged to the right of creation operators. The bare, non-interacting Green's function, whose time-dependence is governed by the quadratic part of the Hamiltonian, $\mathcal{H}_\mathbf{0}$, carries an additional subscript, $G_\mathbf{0}$.

We define anti-symmetrized, irreducible, n-particle vertex functions, $\gamma^{n,\boldsymbol{a}'|\boldsymbol{a}}_{\boldsymbol{i}'|\boldsymbol{i}}(\boldsymbol{t}'|\boldsymbol{t})$, as the sum of all 1-particle irreducible (1PI) diagrams with n amputated ingoing and n amputated outgoing legs. For an explicit series representation of the one- and two-particle vertex, see Eq.(B.1). A formula for the prefactor of every single diagram is given by Eq.(20) of Ref.[11].

The Dyson equation provides a direct relation between the one-particle Green's and vertex function:

$$G(t_1|t_1')=G_\mathbf{0}(t_1|t_1')-\int d\tau_1 d\tau_1' G_\mathbf{0}(t_1|\tau_1')\gamma(\tau_1'|\tau_1)G(\tau_1|t_1'). \tag{A.3}$$

Here and below, whenever quantum state indices i and contour indices a/Keldysh indices α are implicit, they are understood to be summed over in products.

Decomposing the two-particle Green's yields a connection to the two-particle vertex function via

$$\begin{aligned} G(t_1,t_2|t_1',t_2') &= G(t_1|t_1')G(t_2|t_2') - G(t_1|t_2')G(t_2|t_1') \\ &-i\int d\boldsymbol{\tau} G(t_1|\tau_1')G(t_2|\tau_2')\gamma(\tau_1',\tau_2'|\tau_1,\tau_2)G(\tau_1|t_1')G(\tau_2|t_2'). \end{aligned} \tag{A.4}$$

Since the Hamiltonian, Eq.(1), is time-independent, the Green's/vertex functions are translationally invariant in time, implying that n-particle functions depend on $2n-1$ time arguments only:

$$\begin{aligned} G(t_1,...,t_n|t_1',...t_n') &= G(0,...,t_n-t_1|t_1'-t_1,...,t_n'-t_1), \\ \gamma(t_1',...,t_n'|t_1,...t_n) &= \gamma(0,...,t_n'-t_1'|t_1-t_1',...,t_n-t_1'). \end{aligned} \tag{A.5}$$

As a consequence, the Fourier-transform,

$$\begin{aligned} G(\boldsymbol{\varepsilon}|\boldsymbol{\varepsilon}') &= \int d\mathbf{t}d\mathbf{t}'\ e^{i\boldsymbol{\varepsilon}\mathbf{t}}e^{-i\boldsymbol{\varepsilon}'\mathbf{t}'}G(\mathbf{t}|\mathbf{t}'), \\ \gamma(\boldsymbol{\varepsilon}'|\boldsymbol{\varepsilon}) &= \int d\mathbf{t}d\mathbf{t}'\ e^{i\boldsymbol{\varepsilon}'\mathbf{t}'}e^{-i\boldsymbol{\varepsilon}\mathbf{t}}\gamma(\mathbf{t}'|\mathbf{t}), \end{aligned} \tag{A.6}$$

fulfills energy conservation. In particular, this allows for the following representation for the one- and two-particle functions, where calligraphic letters $\mathcal{G}$ and $\mathcal{L}$ are used when a δ-function has been split off:

$$\begin{aligned} &G(\varepsilon_1|\varepsilon_1') = 2\pi\delta(\varepsilon_1-\varepsilon_1')\mathcal{G}(\varepsilon_1), \\ &G(\varepsilon_1,\varepsilon_2|\varepsilon_1',\varepsilon_2') = 2\pi\delta(\varepsilon_1+\varepsilon_2-\varepsilon_1'-\varepsilon_2')\mathcal{G}(\varepsilon_2,\varepsilon_1';\varepsilon_1-\varepsilon_1'), \\ &\gamma(\varepsilon_1'|\varepsilon_1) = -2\pi\delta(\varepsilon_1'-\varepsilon_1)\Sigma(\varepsilon_1'), \\ &\gamma(\varepsilon_1',\varepsilon_2'|\varepsilon_1,\varepsilon_2) = 2\pi\delta(\varepsilon_1'+\varepsilon_2'-\varepsilon_1-\varepsilon_2)\mathcal{L}(\varepsilon_2',\varepsilon_1;\varepsilon_1'-\varepsilon_1). \end{aligned} \tag{A.7}$$

The one-particle vertex-function Σ, introduced above, is called the interacting irreducible self-energy. We Fourier-transform Dyson's equation, Eq.(A.3), which provides

$$\mathcal{G}(\varepsilon)=\mathcal{G}_\mathbf{0}(\varepsilon)+\mathcal{G}_\mathbf{0}(\varepsilon)\Sigma(\varepsilon)\mathcal{G}(\varepsilon)=\left[[\mathcal{G}_\mathbf{0}(\varepsilon)]^{-1}-\Sigma(\varepsilon)\right]^{-1}. \tag{A.8}$$

Note that this is a matrix equation in both Keldysh and position space.

The four single-particle Green's functions and self-energies in contour space are called chronological ($\mathcal{G}^{-|-}$, $\Sigma^{-|-}$), lesser ($\mathcal{G}^{-|+}$, $\Sigma^{-|+}$), greater ($\mathcal{G}^{+|-}$, $\Sigma^{+|-}$) and anti-chronological ($\mathcal{G}^{+|+}$, $\Sigma^{+|+}$). As a consequence of the definition, Eq.(A.2), the single-particle Green's functions fulfill the contour-relation

$$\mathcal{G}^{+|+} + \mathcal{G}^{-|-} = \mathcal{G}^{-|+} + \mathcal{G}^{+|-}. \tag{A.9}$$

We define the transformation from contour space ($a = \{-,+\}$) into Keldysh space ($\alpha = \{1,2\}$) by the rotation

$$R = \begin{pmatrix} R^{-|1} & R^{-|2} \\ R^{+|1} & R^{+|2} \end{pmatrix} = \frac{1}{\sqrt{2}}\begin{pmatrix} 1 & 1 \\ -1 & 1 \end{pmatrix}. \tag{A.10}$$

Hence, any n-th rank tensor $A^{n,\boldsymbol{\alpha}'|\boldsymbol{\alpha}}$ in Keldysh space is represented in contour space by

$$A^{n,\boldsymbol{\alpha}|\boldsymbol{\alpha}'} = \sum_{\boldsymbol{a},\boldsymbol{a}'}\left[R^{-1}\right]^{\boldsymbol{\alpha}|\boldsymbol{a}} A^{n,\boldsymbol{a}|\boldsymbol{a}'} R^{\boldsymbol{a}'|\boldsymbol{\alpha}'}. \tag{A.11}$$

As can be shown explicitly (see Chapter 3.3 of Ref.11) the Green's and vertex functions fulfill a theorem of causality:

$$\begin{aligned} \mathcal{G}^{1...1|1...1} &= 0, \\ \mathcal{L}^{2...2|2...2} &= 0. \end{aligned} \tag{A.12}$$

The remaining three non-zero Keldysh components of the single-particle functions are called retarded ($\mathcal{G}^{2|1}$, $\Sigma^{1|2}$), advanced ($\mathcal{G}^{1|2}$, $\Sigma^{2|1}$) and Keldysh ($\mathcal{G}^{2|2}$, $\Sigma^{1|1}$):

$$\begin{aligned} \mathcal{G} &= \begin{pmatrix} 0 & \mathcal{G}^A \\ \mathcal{G}^R & \mathcal{G}^K \end{pmatrix} = \begin{pmatrix} 0 & \mathcal{G}^{1|2} \\ \mathcal{G}^{2|1} & \mathcal{G}^{2|2} \end{pmatrix}, \\ \Sigma &= \begin{pmatrix} \Sigma^K & \Sigma^R \\ \Sigma^A & 0 \end{pmatrix} = \begin{pmatrix} \Sigma^{1|1} & \Sigma^{1|2} \\ \Sigma^{2|1} & 0 \end{pmatrix}. \end{aligned} \tag{A.13}$$

The transformation, Eq.(A.11), provides the identities

$$\mathcal{G}^{-|+} = \frac{1}{2}\left[\mathcal{G}^{2|2} - \left(\mathcal{G}^{2|1} - \mathcal{G}^{1|2}\right)\right], \tag{A.14a}$$

$$\mathcal{G}^{+|-} - \mathcal{G}^{-|+} = \mathcal{G}^{2|1} - \mathcal{G}^{1|2}, \tag{A.14b}$$

$$\mathcal{H}_\mathbf{0}^{1|2} = \mathcal{H}_\mathbf{0}^{2|1} = H_\mathbf{0}\ ,\ \mathcal{H}_\mathbf{0}^{1|1} = \mathcal{H}_\mathbf{0}^{2|2} = 0, \tag{A.14c}$$

all of which are used in the derivation of the conductance formula in Sec.I. Note that a calligraphic $\mathcal{H}$ carries Keldysh indices, while a capital H does not. The retarded/advanced components are analytic in the upper/lower half plane of the complex frequency plane. Hence, the following notation is always implied,

$$\mathcal{G}^{2|1}(\varepsilon) = \mathcal{G}^{2|1}(\varepsilon+i\delta)\ ,\ \Sigma^{1|2}(\varepsilon) = \Sigma^{1|2}(\varepsilon+i\delta), \tag{A.15}$$

$$\mathcal{G}^{1|2}(\varepsilon) = \mathcal{G}^{1|2}(\varepsilon-i\delta)\ ,\ \Sigma^{2|1}(\varepsilon) = \Sigma^{2|1}(\varepsilon-i\delta), \tag{A.16}$$

with real, infinitesimal, positive δ. In contrast, the Keldysh component is a response function, restricted to the real frequency axis. In equilibrium, the single-particle functions fulfill a fluctuation dissipation theorem (FDT):

$$\Sigma^{1|1}(\varepsilon) = (1-2f(\varepsilon))\left[\Sigma^{1|2}(\varepsilon)-\Sigma^{2|1}(\varepsilon)\right], \tag{A.17a}$$

$$\mathcal{G}^{2|2}(\varepsilon) = (1-2f(\varepsilon))\left[\mathcal{G}^{2|1}(\varepsilon)-\mathcal{G}^{1|2}(\varepsilon)\right], \tag{A.17b}$$

where $f(\varepsilon) = 1/(1+\exp[(\varepsilon-\mu)/T])$ is the Fermi distribution function.

Within this work we consider a system composed of a finite central interacting region coupled to two non-interacting fermionic leads: The left lead L, with chemical potential μ_L and temperature T_L, and the right lead R, with chemical potential μ_R and temperature T_R. Defining operators $C/L/R$, which project onto the subspace of the central region/left lead/right lead respectively, we can represent the quadratic part of the Hamiltonian as

$$\mathcal{H}_{\mathbf{0}} = \begin{pmatrix} L\mathcal{H}_{\mathbf{0}}L & L\mathcal{H}_{\mathbf{0}}C & 0 \\ C\mathcal{H}_{\mathbf{0}}L & C\mathcal{H}_{\mathbf{0}}C & C\mathcal{H}_{\mathbf{0}}R \\ 0 & R\mathcal{H}_{\mathbf{0}}C & R\mathcal{H}_{\mathbf{0}}R \end{pmatrix} = \begin{pmatrix} \mathcal{H}_l & \mathcal{H}_{lc} & 0 \\ \mathcal{H}_{cl} & \mathcal{H}_{\mathbf{0},c} & \mathcal{H}_{cr} \\ 0 & \mathcal{H}_{rc} & \mathcal{H}_r \end{pmatrix}. \tag{A.18}$$

where the matrices $\mathcal{H}_l$ and $\mathcal{H}_r$ fully define the properties of the isolated leads, and the matrix $\mathcal{H}_{\mathbf{0},c}$ describes the non-interacting physics of the isolated central region. Finally, $\mathcal{H}_{cl}$ and $\mathcal{H}_{cr}$ specify the coupling of the central region to the corresponding lead. Similarly, we write the system's Green's function, $\mathcal{G}(\varepsilon)$ [Eq.(A.8)], in the same basis (for the bare, non-interacting Green's function $\mathcal{G}_{\mathbf{0}}$ we set $\Sigma = 0$):

$$\mathcal{G} = \begin{pmatrix} L\mathcal{G}L & L\mathcal{G}C & 0 \\ C\mathcal{G}L & C\mathcal{G}C & C\mathcal{G}R \\ 0 & R\mathcal{G}C & R\mathcal{G}R \end{pmatrix} = \begin{pmatrix} \mathcal{G}_l & \mathcal{G}_{lc} & 0 \\ \mathcal{G}_{cl} & \mathcal{G}_c & \mathcal{G}_{cr} \\ 0 & \mathcal{G}_{rc} & \mathcal{G}_r \end{pmatrix}. \tag{A.19}$$

We use the *small letter* g to denote the Green's function of an isolated subsystem, e.g. $g_l(\varepsilon)$ is the Green's function of the isolated left lead L. The non-interacting Green's function of the central region is given by Dyson's equation

$$\mathcal{G}_{\mathbf{0},c} = g_{\mathbf{0},c} + g_{\mathbf{0},c}\Sigma_{\text{lead}}\mathcal{G}_{\mathbf{0},c} = \left[[g_{\mathbf{0},c}]^{-1} - \Sigma_{\text{lead}}\right]^{-1}. \tag{A.20}$$

Again note that this is a matrix equation in Keldysh and position space. We incorporated environment contributions into the lead self-energy

$$\Sigma_{\text{lead}} = \sum_{k=l,r} \mathcal{H}_{ck} g_k \mathcal{H}_{kc}. \tag{A.21}$$

The individual Keldysh components of the non-interacting Green's function are given by

$$\mathcal{G}^{1|2}_{\mathbf{0},c}(\varepsilon) = \left(\varepsilon - H_{\mathbf{0},c} - \Sigma^{2|1}_{\text{lead}}(\varepsilon)\right)^{-1}, \tag{A.22a}$$

$$\mathcal{G}^{2|1}_{\mathbf{0},c}(\varepsilon) = \left(\varepsilon - H_{\mathbf{0},c} - \Sigma^{1|2}_{\text{lead}}(\varepsilon)\right)^{-1}, \tag{A.22b}$$

$$\begin{aligned} \mathcal{G}^{2|2}_{\mathbf{0},c}(\varepsilon) &= \mathcal{G}^{2|1}_{\mathbf{0},c}(\varepsilon)\Sigma^{1|1}_{\text{lead}}(\varepsilon)\mathcal{G}^{1|2}_{\mathbf{0},c}(\varepsilon) \\ &= -i\sum_{k=l,r}[1-2f^k(\varepsilon)]\mathcal{G}^{2|1}_{\mathbf{0},c}(\varepsilon)\Gamma^k(\varepsilon)\mathcal{G}^{2|1}_{\mathbf{0},c}(\varepsilon), \end{aligned} \tag{A.22c}$$

where we introduced the hybridization function, $\Gamma^k(\varepsilon) = iH_{ck}(g^{2|1}_k(\varepsilon) - g^{1|2}_k(\varepsilon))H_{kc}$.

With the interaction being restricted to the central region we use the notation $\Sigma = \Sigma_c = C\Sigma C$ for the interacting self-energy. Dyson's equation, Eq.(A.8), and the real space structure, Eq.(A.19), yields

$$\mathcal{G}_c(\varepsilon) = \left[[\mathcal{G}_{\mathbf{0},c}(\varepsilon)]^{-1} - \Sigma(\varepsilon)\right]^{-1}. \tag{A.23}$$

The matrix representation of its Keldysh structure is given by

$$\begin{pmatrix} 0 & \mathcal{G}^{1|2}_c \\ \mathcal{G}^{2|1}_c & \mathcal{G}^{2|2}_c \end{pmatrix} = \left[\begin{pmatrix} 0 & \mathcal{G}^{1|2}_{\mathbf{0},c} \\ \mathcal{G}^{2|1}_{\mathbf{0},c} & \mathcal{G}^{2|2}_{\mathbf{0},c} \end{pmatrix}^{-1} - \begin{pmatrix} \Sigma^{1|1} & \Sigma^{1|2} \\ \Sigma^{2|1} & 0 \end{pmatrix}\right]^{-1}. \tag{A.24}$$

Block matrix inversion then provides the components

$$\mathcal{G}^{1|2}_c(\varepsilon) = \left(\varepsilon - H_{\mathbf{0},c} - \Sigma^{2|1}_{\text{lead}}(\varepsilon) - \Sigma^{2|1}(\varepsilon)\right)^{-1}, \tag{A.25a}$$

$$\mathcal{G}^{2|1}_c(\varepsilon) = \left(\varepsilon - H_{\mathbf{0},c} - \Sigma^{1|2}_{\text{lead}}(\varepsilon) - \Sigma^{1|2}(\varepsilon)\right)^{-1}, \tag{A.25b}$$

$$\mathcal{G}^{2|2}_c(\varepsilon) = \mathcal{G}^{2|1}_c(\varepsilon)\left[\Sigma^{1|1}_{\text{lead}} + \Sigma^{1|1}\right]\mathcal{G}^{1|2}_c(\varepsilon). \tag{A.25c}$$

From Eq.(A.8), we can show, that the off-diagonal components of the full Green's function, are given by

$$\mathcal{G}_{kc} = g_k\mathcal{H}_{kc}\mathcal{G}_c\ ,\ \mathcal{G}_{ck} = \mathcal{G}_c\mathcal{H}_{ck}g_k. \tag{A.26}$$

For a symmetric, real Hamiltonian, the following symmetries hold

$$\mathcal{G}^{1|2}_{\mathbf{0},i|j} = \left[\mathcal{G}^{2|1}_{\mathbf{0},i|j}\right]^*, \mathcal{G}^{1|2}_{i|j} = \left[\mathcal{G}^{2|1}_{i|j}\right]^*, \Sigma^{1|2}_{i|j} = \left[\Sigma^{2|1}_{i|j}\right]^*, \tag{A.27a}$$

$$\mathcal{G}^{1|2}_{\mathbf{0},i|j} = \mathcal{G}^{1|2}_{\mathbf{0},j|i}\ ,\ \mathcal{G}^{1|2}_{i|j} = \mathcal{G}^{1|2}_{j|i}\ ,\ \Sigma^{1|2}_{i|j} = \Sigma^{1|2}_{j|i}, \tag{A.27b}$$

$$\mathcal{G}^{2|1}_{\mathbf{0},i|j} = \mathcal{G}^{2|1}_{\mathbf{0},j|i}\ ,\ \mathcal{G}^{2|1}_{i|j} = \mathcal{G}^{2|1}_{j|i}\ ,\ \Sigma^{2|1}_{i|j} = \Sigma^{2|1}_{j|i}, \tag{A.27c}$$

$$\mathcal{G}^{2|2}_{\mathbf{0},i|j} = -\left[\mathcal{G}^{2|2}_{\mathbf{0},j|i}\right]^*, \mathcal{G}^{2|2}_{i|j} = -\left[\mathcal{G}^{2|2}_{j|i}\right]^*, \Sigma^{1|1}_{i|j} = -\left[\Sigma^{1|1}_{j|i}\right]^*. \tag{A.27d}$$

Appendix B: Diagrammatic derivation of the fRG flow-equation of the self-energy

Here, we provide a diagrammatic derivation of the fRG flow-equation for the self-energy, Eq.(13). We use the observation, that every diagram in the diagrammatic series of the self-energy contains a sub-diagram which appears in the diagrammatic series of the two-particle vertex. As a consequence, taking the derivative of the self-energy, $\partial_\Lambda \Sigma$, w.r.t. some parameter Λ allows for a resummation of diagrams, such that the full two-particle vertex series can be factorized. Hence, we get an equation which can formally be written as $\partial_\Lambda \Sigma_\Lambda = \int S_\Lambda \mathcal{L}_\Lambda$, with the so called single-scale propagator S and the two-particle vertex $\mathcal{L}$, both depending on the parameter Λ.

The self-energy Σ and two-particle vertex $\mathcal{L}$ are diagrammatically defined as the sum of all one-particle irreducible diagrams with two and four amputated external legs, respectively. Using the graphical representation of the bare Green's function, Eq.(27), and the bare vertex, Eq.(31), the first terms of their perturbation series are (we omit the arrows for the sake of simplicity)

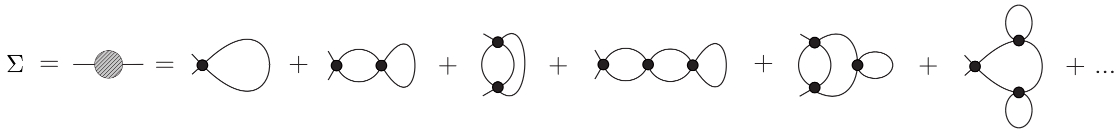

(B.1a)

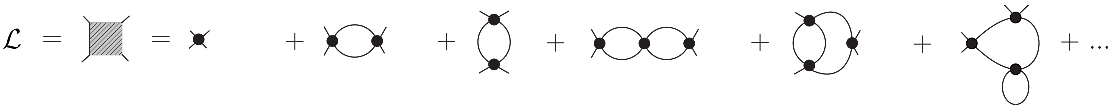

(B.1b)

We introduce a parameter Λ into the bare propagator, $\mathcal{G}_\mathbf{0} \to \mathcal{G}_\mathbf{0}^\Lambda$, and represent its derivative w.r.t. Λ by a crossed-out line, $\partial_\Lambda \mathcal{G}_\mathbf{0}^\Lambda =$ 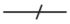. Hence, the derivative of the self-energy is given by

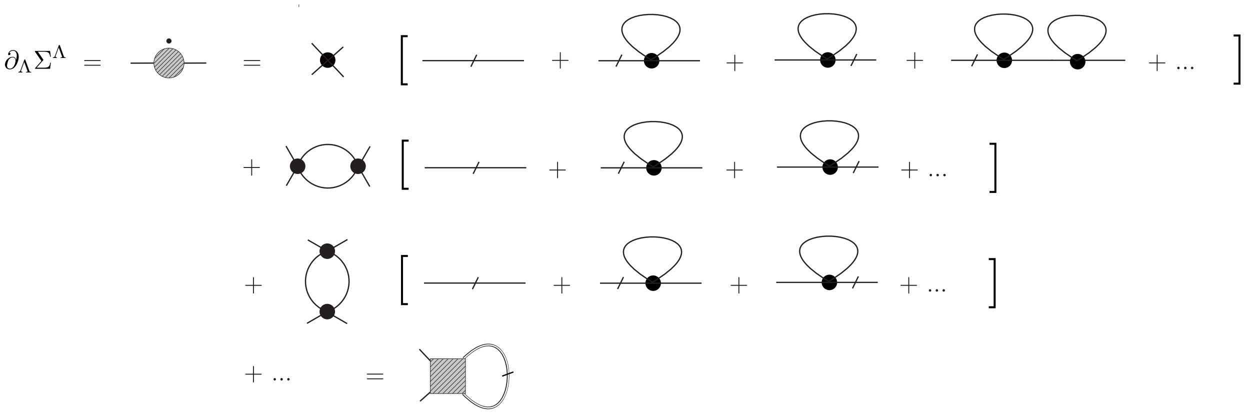

(B.2)

where we introduced the so called single scale propagator

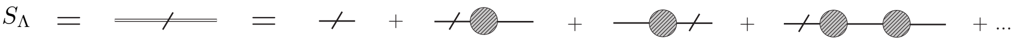

$$\begin{aligned} &= [1+\mathcal{G}_\mathbf{0}\Sigma + \mathcal{G}_\mathbf{0}\Sigma\mathcal{G}_\mathbf{0}\Sigma + ...]\,\partial_\Lambda\mathcal{G}_\mathbf{0}^\Lambda\,[1+\Sigma\mathcal{G}_\mathbf{0}+\Sigma\mathcal{G}_\mathbf{0}\Sigma\mathcal{G}_\mathbf{0}+...] \\ &= \mathcal{G}\,[\mathcal{G}_\mathbf{0}]^{-1}\,\partial_\Lambda\mathcal{G}_\mathbf{0}^\Lambda\,[\mathcal{G}_\mathbf{0}]^{-1}\,\mathcal{G} \end{aligned} \tag{B.3}$$

Finally, we fix the prefactor of the diagram on the r.h.s. in Eq.(B.2) by the following argument: The first order self-energy, $\Sigma_\mathbf{1}$, is of Hartree-type and hence purely determined by the local density n_j and the local interaction strength U_j. We use the bare local density of states, $\mathcal{A}_{\mathbf{0},j}(\varepsilon) = -1/\pi \cdot \mathrm{Im}\mathcal{G}^{2|1}_{\mathbf{0},j|j}(\varepsilon)$, and calculate the first order self-energy in equilibrium

$$\Sigma_{\mathbf{1},j}|_{V=0} = n_j U_j = 2\bar{u}_j \int d\varepsilon f(\varepsilon)\mathcal{A}_{\mathbf{0},j}(\varepsilon) = \pi i \bar{u}_j \int d\varepsilon f(\varepsilon)(\mathcal{G}^{2|1}_{\mathbf{0},j|j} - \mathcal{G}^{1|2}_{\mathbf{0},j|j}) = \frac{1}{2\pi i}\bar{u}_j \int d\varepsilon\, \mathcal{G}^{2|2}_{\mathbf{0},j|j}(\varepsilon). \tag{B.4}$$

Hence, we end up with Eq.(13) for the derivative of the self-energy:

$$\partial_\Lambda \Sigma^{\alpha'|\alpha}_{i|j}(\varepsilon) = \frac{1}{2\pi i}\int d\varepsilon' \sum_{\substack{\beta\beta' \\ kl\in C}} S^{\beta|\beta'}_{\Lambda,k|l}(\varepsilon')\mathcal{L}^{\alpha'\beta'|\alpha\beta}_{ik|jl}(\varepsilon',\varepsilon;0). \tag{B.5}$$

Appendix C: Charge conservation - Ward identity

Here we derive the Ward identity, Eq.(21), from variational principles; since the action corresponding to the Hamiltonian, Eq.(1), is invariant under a global $U(1)$ symmetry, it satisfies a conservation law. Starting from the path integral representation of expectation values using Grassmann variables, the requirement of vanishing variation under the gauged $U(1)$ transformation yields both a continuity equation for particle current and the desired connection between the interacting self-energy Σ, introduced in Eq.(A.7), and the vertex part Φ, defined in Eq.(20).

Within this Appendix we combine the left and right lead to $\mathbb{L} = L \bigotimes R$, thus representing the Hamiltonian and the Green's function by

$$\mathcal{H}_{\mathbf{0}} = \begin{pmatrix} C\mathcal{H}_{\mathbf{0}}C & C\mathcal{H}_{\mathbf{0}}\mathbb{L} \\ \mathbb{L}\mathcal{H}_{\mathbf{0}}C & \mathbb{L}\mathcal{H}_{\mathbf{0}}\mathbb{L} \end{pmatrix} = \begin{pmatrix} \mathcal{H}_{\mathbf{0},c} & \mathcal{H}_{c\ell} \\ \mathcal{H}_{\ell c} & \mathcal{H}_{\ell} \end{pmatrix}, \; \mathcal{G} = \begin{pmatrix} C\mathcal{G}C & C\mathcal{G}\mathbb{L} \\ \mathbb{L}\mathcal{G}C & \mathbb{L}\mathcal{G}\mathbb{L} \end{pmatrix} = \begin{pmatrix} \mathcal{G}_c & \mathcal{G}_{c\ell} \\ \mathcal{G}_{\ell c} & \mathcal{G}_{\ell} \end{pmatrix}. \tag{C.1}$$

Let $\{\psi\}, \{\bar{\psi}\}$ be sets of Grassmann variables, i.e. fermionic fields. We write n-particle expectation values in terms of the functional path integral,

$$G^{n,\boldsymbol{a}|\boldsymbol{a'}}_{\boldsymbol{i}|\boldsymbol{i'}}(\boldsymbol{t}|\boldsymbol{t'}) = (-i)^n\langle\psi^{a_1}_{i_1}(t_1)...\psi^{a_n}_{i_n}(t_n)\bar{\psi}^{a'_n}_{i'_n}(t'_n)...\bar{\psi}^{a'_1}_{i'_1}(t'_1)\rangle = (-i)^n\int\mathcal{D}(\bar{\boldsymbol{\psi}}\boldsymbol{\psi})\psi^{a_1}_{i_1}(t_1)...\psi^{a_n}_{i_n}(t_n)\bar{\psi}^{a'_n}_{i'_n}(t'_n)...\bar{\psi}^{a'_1}_{i'_1}(t'_1)e^{iS[\bar{\boldsymbol{\psi}},\boldsymbol{\psi}]}, \tag{C.2}$$

where the Keldysh action is given by the Keldysh contour time integral

$$\begin{aligned} S[\bar{\boldsymbol{\psi}},\boldsymbol{\psi}] &= \int_{\mathcal{C}} dt \sum_{ii'} \bar{\psi}_{i'}(t)\overbrace{(i\delta_{i'i}\partial_t - \mathcal{H}_{\mathbf{0},i'i})}^{[G_{\mathbf{0}}(t)^{-1}]_{i'i}}\psi_i(t) + S_{\text{int}}[\bar{\boldsymbol{\psi}},\boldsymbol{\psi}] = \int_{-\infty}^{\infty} dt \sum_{a,ii'}(-a)\bar{\psi}^a_{i'}(t)\,(i\delta_{i'i}\partial_t - H_{\mathbf{0},i'i})\,\psi^a_i(t) + S_{\text{int}}[\bar{\boldsymbol{\psi}},\boldsymbol{\psi}] \\ &= \int_{-\infty}^{\infty} dt \sum_a (-a)\bar{\boldsymbol{\psi}}^a(t)(i\boldsymbol{\partial}_t - H_{\mathbf{0}})\,\boldsymbol{\psi}^a(t) + S_{\text{int}}[\bar{\boldsymbol{\psi}},\boldsymbol{\psi}]. \end{aligned} \tag{C.3}$$

In the last line we introduced the vector notation $\boldsymbol{\psi} = \begin{pmatrix}\psi_1 \\ \psi_2 \\ \vdots\end{pmatrix}$ and $\bar{\boldsymbol{\psi}} = (\psi_1, \psi_2, \ldots)$. Note that $\boldsymbol{\partial}_t$ is a diagonal matrix.

1. Gauge transformation

The action, Eq.(C.3), is invariant under the global $U(1)$ transformation $\boldsymbol{\psi} \to \boldsymbol{\psi}e^{i\alpha}$ and $\bar{\boldsymbol{\psi}} \to \bar{\boldsymbol{\psi}}e^{-i\alpha}$, where α is a real constant. Gauging this transformation, i.e. making α space-, and time-dependent, yields to linear order in α

$$\delta\psi^a_i(t) = i\alpha^a_i(t)\psi^a_i(t)\;,\;\delta\bar{\psi}^a_{i'}(t') = -i\alpha^a_{i'}(t')\bar{\psi}^a_{i'}(t'). \tag{C.4}$$

Since we are interested in the current through the system, from one lead to another, it is convenient to pick α non-vanishing only in the central region:

$$\alpha^a_i(t) = \begin{cases} \alpha^a(t), & \text{if} \quad i \in C \\ 0, & \text{if} \quad i \in \mathbb{L}. \end{cases} \tag{C.5}$$

This is equivalent to first deriving the Ward identity using an arbitrary α and then summing over the central region. The requirement of vanishing variation under the gauged $U(1)$ transformation now reads:

$$\delta G^{n,\boldsymbol{a}|\boldsymbol{a'}}_{\boldsymbol{i}|\boldsymbol{i'}}(\boldsymbol{t}|\boldsymbol{t'}) = 0. \tag{C.6}$$

2. The continuity equation (zeroth order Ward identity)

For $n=0$, Eq.(C.6) sets a condition on the variation of the partition sum. Since the measure of the path integral is invariant under the transformation in Eq.(C.4) (implying that the $U(1)$-symmetry is not anomalous), this in turn sets a condition on the variation of the action:

$$0 = \delta\left[\int \mathcal{D}(\bar{\boldsymbol{\psi}}\boldsymbol{\psi}) e^{iS[\bar{\boldsymbol{\psi}},\boldsymbol{\psi}]}\right] = i\int \mathcal{D}(\bar{\boldsymbol{\psi}}\boldsymbol{\psi})\delta S[\bar{\boldsymbol{\psi}},\boldsymbol{\psi}] e^{iS[\bar{\boldsymbol{\psi}},\boldsymbol{\psi}]}. \tag{C.7}$$

The quartic term, S_{int}, describes a density-density interaction. Hence, its variation vanishes trivially and the variation of the total action reduces to the variation of the quadratic term:

$$\begin{aligned}\delta S[\bar{\boldsymbol{\psi}},\boldsymbol{\psi}] &= \int_{-\infty}^{\infty} dt \sum_{a,i}(-a)\Big[\alpha_i^a(t)\bar{\psi}_i^a(t)\partial_t\psi_i^a(t) - \bar{\psi}_i^a(t)\partial_t(\alpha_i^a(t)\psi_i^a(t)) + \sum_{i'}\left[i\alpha_{i'}^a(t) - i\alpha_i^a(t)\right]\bar{\psi}_{i'}^a(t)H_{\mathbf{0},i'i}\psi_i^a(t)\Big] \\ &= \int_{-\infty}^{\infty} dt \sum_{a}(-a)\alpha^a(t)\Big[\partial_t\big(\bar{\boldsymbol{\psi}}_c^a(t)\boldsymbol{\psi}_c^a(t)\big) - i\bar{\boldsymbol{\psi}}_c^a(t)H_{cl}\boldsymbol{\psi}_l^a(t) + i\bar{\boldsymbol{\psi}}_l^a(t)H_{lc}\boldsymbol{\psi}_c^a(t)\Big] \\ &= \int_{-\infty}^{\infty} dt \sum_{a}(-a)\alpha^a(t)\Big[-\partial_t\big(\boldsymbol{\psi}_c^a(t)\bar{\boldsymbol{\psi}}_c^a(t)\big) + i\mathrm{Tr}\big\{H_{cl}\boldsymbol{\psi}_l^a(t)\bar{\boldsymbol{\psi}}_c^a(t)\big\} - i\mathrm{Tr}\big\{H_{lc}\boldsymbol{\psi}_c^a(t)\bar{\boldsymbol{\psi}}_l^a(t)\big\}\Big],\end{aligned} \tag{C.8}$$

where we used integration by parts in the first term Since Eq.(C.7) must hold for arbitrary $\alpha(t)$ this provides the continuity equation

$$-\partial_t\langle\boldsymbol{\psi}_c^a(t)\bar{\boldsymbol{\psi}}_c^a(t)\rangle = i\mathrm{Tr}\big\{H_{lc}\langle\boldsymbol{\psi}_c^a(t)\bar{\boldsymbol{\psi}}_l^a(t)\rangle\big\} - i\mathrm{Tr}\big\{H_{cl}\langle\boldsymbol{\psi}_l^a(t)\bar{\boldsymbol{\psi}}_c^a(t)\rangle\big\}\,. \tag{C.9}$$

In steady-state, the time derivative of the density term on the l.h.s. vanishes and Eq.(C.9) reduces to current conservation, i.e. the current into the central region equals the current out of the central region:

$$\mathrm{Tr}\big\{H_{lc}G_{cl}^{-|+}(0)\big\} = \mathrm{Tr}\big\{H_{cl}G_{lc}^{-|+}(0)\big\}. \tag{C.10}$$

Here we made use of the time-translational invariance of the Green's function, Eq.(A.5), and the equivalence of the contour Green's function components for equal-time arguments $G^{-|+}(t,t) = G^{-|-}(t,t) = G^{+|+}(t,t)$.

3. Relation between self-energy and two-particle vertex (first order Ward identity)

For $n=1$, Eq.(C.6) reads

$$0 = \delta\langle\psi_i^a(t)\bar{\psi}_{i'}^{a'}(t')\rangle = \int\mathcal{D}(\bar{\boldsymbol{\psi}}\boldsymbol{\psi})\left[(\delta\psi_i^a(t))\,\bar{\psi}_{i'}^{a'}(t') + \psi_i^a(t)(\delta\bar{\psi}_{i'}^{a'}(t')) + i\psi_i^a(t)\bar{\psi}_{i'}^{a'}(t')(\delta S[\bar{\boldsymbol{\psi}},\boldsymbol{\psi}])\right] e^{iS[\bar{\boldsymbol{\psi}},\boldsymbol{\psi}]}. \tag{C.11}$$

Since the r.h.s. contains both terms quadratic and quartic in ψ, this equation will eventually lead to a relation between the self-energy and the two-particle vertex. For states $i, i' \in C$ Eq.(C.11) can be written as

$$\begin{aligned}0 = \int_{\infty}^{\infty} dt'' \sum_{a''}(-a'')i\alpha^{a''}(t'')\Bigg\{\int\mathcal{D}(\bar{\boldsymbol{\psi}}\boldsymbol{\psi})\psi_i^a(t)\bar{\psi}_{i'}^{a'}(t')\Bigg[&(-a)\delta(t''-t)\delta_{aa''} + a'\delta(t''-t')\delta_{a'a''} \\ &+ \sum_{j\in C}\partial_{t''}\left(\bar{\psi}_j^{a''}(t'')\psi_j^{a''}(t'')\right) \\ &+ i\sum_{j_1,j_2}\left(\bar{\psi}_{j_1}^{a''}(t'')H_{\ell c,j_1|j_2}\psi_{j_2}^{a''}(t'') - \bar{\psi}_{j_2}^{a''}(t'')H_{c\ell,j_2|j_1}\psi_{j_1}^{a''}(t'')\right)\Bigg]e^{iS[\bar{\boldsymbol{\psi}},\boldsymbol{\psi}]}\Bigg\}.\end{aligned} \tag{C.12}$$

Again, this must be true for arbitrary $\alpha(t)$, providing

$$\begin{aligned}&[(-a)\delta(t''-t)\delta_{aa''} + a'\delta(t''-t')\delta_{a'a''}]\,G_{i|i'}^{a|a'}(t|t') \\ &= \sum_{j_1,j_2}\left[H_{\ell c,j_1|j_2}G_{j_2 i|j_1 i'}^{a''a|a''a'}(t''t|t''t') - H_{c\ell,j_2|j_1}G_{j_1 i|j_2 i'}^{a''a|a''a'}(t''t|t''t')\right] - i\partial_{t''}\sum_{j\in C}G_{ji|ji'}^{a''a|a''a'}(t''t|t''t').\end{aligned} \tag{C.13}$$

We proceed by decomposing the 2-particle Green's function in the first term of the r.h.s. according to Eq.(A.4). Since the first disconnected term, $G(t''|t'')G(t|t')$, vanishes due to the current conservation, Eq.(C.9), we get

$$\begin{aligned}
&[(-a)\delta(t''-t)\delta_{aa''}+a'\delta(t''-t')\delta_{a'a''}]\,G^{a|a'}_{i|i'}(t|t')\\
&=-\sum_{j_1,j_2}\Big[G^{a|a''}_{i|j_1}(t|t'')H_{\ell c,j_1|j_2}G^{a''|a'}_{j_2|i'}(t''|t')-G^{a|a''}_{i|j_2}(t|t'')H_{c\ell,j_2|j_1}G^{a''|a'}_{j_1|i'}(t''|t')\Big]-i\partial_{t''}\sum_{j\in C}G^{a''a|a''a'}_{ji|ji'}(t''t|t''t')\\
&-i\sum_{j_1,j_2}\sum_{\boldsymbol{k},\boldsymbol{b}}\int d\boldsymbol{\tau}\;G^{a|b_2'}_{i|k_2'}(t|\tau_2')\Big[G^{b_1|a''}_{k_1|j_1}(\tau_1|t'')H_{\ell c,j_1|j_2}G^{a''|b_1'}_{j_2|k_1'}(t''|\tau_1')-(j_1\leftrightarrow j_2,H_{\ell c}\leftrightarrow H_{c\ell})\Big]\,\gamma^{b_1'b_2'|b_1b_2}_{k_1'k_2'|k_1k_2}(\tau_1',\tau_2'|\tau_1,\tau_2)G^{b_2|a'}_{k_2|i'}(\tau_2|t').
\end{aligned}\tag{C.14}$$

We find the corresponding relation in frequency domain after Fourier transformation w.r.t. all time arguments t,t',t'',

$$\begin{aligned}
&(-a)\delta_{aa''}\mathcal{G}^{a|a'}_{i|i'}(\varepsilon+\omega)+a'\delta_{a'a''}\mathcal{G}^{a|a'}_{i|i'}(\varepsilon)\\
&=-\sum_{j_1,j_2}\Big[\mathcal{G}^{a|a''}_{i|j_1}(\varepsilon+\omega)H_{\ell c,j_1|j_2}\mathcal{G}^{a''|a'}_{j_2|i'}(\varepsilon)-(j_1\leftrightarrow j_2,H_{\ell c}\leftrightarrow H_{c\ell})\Big]-\frac{\omega}{2\pi}\int d\varepsilon'\sum_{j\in C}\mathcal{G}^{a''a|a''a'}_{ji|ji'}(\varepsilon,\varepsilon';\omega).\\
&-\frac{i}{2\pi}\sum_{\substack{\boldsymbol{k},\boldsymbol{b}\\ j_1,j_2}}\mathcal{G}^{a|b_2'}_{i|k_2'}(\varepsilon)\Big\{\int d\varepsilon'\Big[\mathcal{G}^{b_1|a''}_{k_1|j_1}(\varepsilon')H_{\ell c,j_1|j_2}\mathcal{G}^{a''|b_1'}_{j_2|k_1'}(\varepsilon'+\omega)-(j_1\leftrightarrow j_2,H_{\ell c}\leftrightarrow H_{c\ell})\Big]\mathcal{L}^{b_1'b_2'|b_1b_2}_{k_1'k_2'|k_1k_2}(\varepsilon,\varepsilon';\omega)\Big\}\mathcal{G}^{b_2|a'}_{k_2|i'}(\varepsilon+\omega).
\end{aligned}\tag{C.15}$$

We set $\omega=0$ and sum over a'' on both sides to get the matrix equation

$$\sum_{a''}[(-a)\delta_{aa''}+a'\delta_{a'a''}]\,\mathcal{G}^{a|a'}_{c}(\varepsilon)=Y^{a|a'}(\varepsilon),\tag{C.16}$$

where we defined the response object

$$\begin{aligned}
Y^{a|a'}_{i|i'}(\varepsilon)=&-\sum_{a''}\sum_{j_1,j_2}\Big[\mathcal{G}^{a|a''}_{i|j_1}(\varepsilon)H_{\ell c,j_1|j_2}\mathcal{G}^{a''|a'}_{j_2|i'}(\varepsilon)-(j_1\leftrightarrow j_2,H_{\ell c}\leftrightarrow H_{c\ell})\Big]\\
&-\frac{i}{2\pi}\sum_{a''}\sum_{\substack{\boldsymbol{k},\boldsymbol{b}\\ j_1,j_2}}\mathcal{G}^{a|b_2'}_{i|k_2'}(\varepsilon)\Big\{\int d\varepsilon'\Big[\mathcal{G}^{b_1|a''}_{k_1|j_1}(\varepsilon')H_{\ell c,j_1|j_2}\mathcal{G}^{a''|b_1'}_{j_2|k_1'}(\varepsilon')-(j_1\leftrightarrow j_2,H_{\ell c}\leftrightarrow H_{c\ell})\Big]\mathcal{L}^{b_1'b_2'|b_1b_2}_{k_1'k_2'|k_1k_2}(\varepsilon,\varepsilon';0)\Big\}\mathcal{G}^{b_2|a'}_{k_2|i'}(\varepsilon).
\end{aligned}\tag{C.17}$$

With two independent contour arguments, a and a', Eq.(C.16) results in four independent contour space relations

$$0=Y^{+|+}=Y^{-|-}\ ,\ -2\mathcal{G}^{+|-}_c=Y^{+|-}\ ,\ 2\mathcal{G}^{-|+}_c=Y^{-|+}.\tag{C.18}$$

Adding up all equations and transforming into Keldysh space [Eq.(A.10)] yields

$$\begin{aligned}
&2(\mathcal{G}^{+|-}_c-\mathcal{G}^{-|+}_c)=Y^{+|+}+Y^{-|-}-Y^{+|-}-Y^{-|+}\\
&\overset{\text{Eq.(A.10)}}{\Leftrightarrow}\quad \mathcal{G}^{2|1}_c-\mathcal{G}^{1|2}_c=Y^{1|1}.
\end{aligned}\tag{C.19}$$

As a consequence of the theorem of causality [Eq.(A.12)] we have $\mathcal{G}^{1|1}=0$. Hence, only the summand with $a''=2$ in $Y^{1|1}$ is non-zero:

$$Y^{1|1}(\varepsilon)=b^{1|1}(\varepsilon)-i\mathcal{G}^{1|2}_c(\varepsilon)\tilde{\Phi}(\varepsilon)\mathcal{G}^{2|1}_c(\varepsilon),\tag{C.20}$$

where we defined the coupling term

$$\begin{aligned}
b^{\alpha|\alpha'}&=\mathcal{G}^{\alpha|2}_cH_{c\ell}\mathcal{G}^{2|\alpha'}_{\ell c}-\mathcal{G}^{\alpha|2}_{c\ell}H_{\ell c}\mathcal{G}^{2|\alpha'}_c\\
&\overset{\text{Eq.(A.26)}}{=}\mathcal{G}^{\alpha|2}_cH_{c\ell}\sum_{\beta,\gamma}g^{2|\beta}_\ell\mathcal{H}^{\beta|\gamma}_{\ell c}\mathcal{G}^{\gamma|\alpha'}_c-\sum_{\beta,\gamma}\mathcal{G}^{\alpha|\beta}_c\mathcal{H}^{\beta|\gamma}_{c\ell}g^{\gamma|2}_\ell H_{\ell c}\mathcal{G}^{2|\alpha'}_c,
\end{aligned}\tag{C.21}$$

and the response function

$$\tilde{\Phi}_{k_2'|k_2}(\varepsilon)=\frac{1}{2\pi}\int d\varepsilon'\sum_{\substack{b_1,b_1'\\ k_1,k_1'}}b^{b_1|b_1'}_{k_1|k_1'}(\varepsilon')\mathcal{L}^{b_1'2|b_12}_{k_1'k_2'|k_1k_2}(\varepsilon,\varepsilon';0).\tag{C.22}$$

Using the hybridization, $\Gamma = iH_{c\ell}(g_\ell^{2|1} - g_\ell^{1|2})H_{\ell c}$, we find

$$b^{1|1} = -i\mathcal{G}_c^{1|2}\Gamma\mathcal{G}_c^{2|1} \ , \ b^{1|2} = -b^{2|1} = (1-2f)b^{1|1}. \tag{C.23}$$

Hence, the response function reads (since $\gamma^{22|22}=0$)

$$\begin{aligned}\tilde{\Phi}_{k_2'|k_2}(\varepsilon) = \frac{1}{2\pi i}\int d\varepsilon' \sum_{\substack{j_1,j_1' \\ k_1,k_1'}} \mathcal{G}^{1|2}_{k_1|j_1'}(\varepsilon')\Gamma_{j_1'|j_1}(\varepsilon')\mathcal{G}^{2|1}_{j_1|k_1'}(\varepsilon') \\ \times \left[\mathcal{L}^{12|12}_{k_1'k_2'|k_1k_2}(\varepsilon,\varepsilon';0) - (1-2f(\varepsilon'))\left(\mathcal{L}^{12|22}_{k_1'k_2'|k_1k_2}(\varepsilon,\varepsilon';0) - \mathcal{L}^{22|12}_{k_1'k_2'|k_1k_2}(\varepsilon,\varepsilon';0)\right)\right],\end{aligned} \tag{C.24}$$

in accord with Eq.(20). Finally, we multiply $\left[\mathcal{G}^{1|2}\right]^{-1}$ from the left and $\left[\mathcal{G}^{2|1}\right]^{-1}$ from the right in Eq.(C.19), which provides

$$\left[\mathcal{G}^{1|2}(\varepsilon)\right]^{-1} - \left[\mathcal{G}^{2|1}(\varepsilon)\right]^{-1} = -i\left[\Gamma(\varepsilon) + \tilde{\Phi}(\varepsilon)\right]. \tag{C.25}$$

Inserting Eq.(A.25) and using $\Sigma^{1|2}_{\text{lead}}(\varepsilon) - \Sigma^{2|1}_{\text{lead}}(\varepsilon) = -i\Gamma(\varepsilon)$ [see Eq.(A.21)] the hybridization terms cancel and we recover Eq.(21) (note that we combined the left and right lead, which implies $\tilde{\Phi} = \tilde{\Phi}^l + \tilde{\Phi}^r$):

$$i\left[\Sigma^{1|2}(\varepsilon) - \Sigma^{2|1}(\varepsilon)\right] = \tilde{\Phi}(\varepsilon). \tag{C.26}$$

This equation is a necessary condition that any method for describing the influence of interactions has to satisfy in order to produce quantitative reliable results for transport properties of the system. If Eq.(C.26), and therefore particle conservation, is violated by a chosen approach (such as e.g. truncated fRG schemes) one should exercise great caution in interpreting the results.

Appendix D: Derivation of the fluctuation-dissipation theorem for the vertex channels and the self-energy

Below, we derive the fluctuation-dissipation theorem in SOPT for both the frequency-dependent vertex channels, Eq.(40d) and Eq.(41d), and the self-energy, Eq.(48d).

1. FDT for the Π-channel

We use the FDT for the bare Green's function, Eq.(A.17), to write the Keldysh Green's function in terms of the difference between the retarded and advanced Green's function. With that we can write the Keldysh component of the Π-channel as

$$\begin{aligned}\Pi^{1|1}_{ij}(p) &= -\frac{u_i u_j}{2\pi i}\int d\varepsilon \Big[\mathcal{G}^{\sigma,2|2}_{\mathbf{0},i|j}(p-\varepsilon)\mathcal{G}^{\bar{\sigma},2|2}_{\mathbf{0},i|j}(\varepsilon) + \mathcal{G}^{\sigma,2|1}_{\mathbf{0},i|j}(p-\varepsilon)\mathcal{G}^{\bar{\sigma},2|1}_{\mathbf{0},i|j}(\varepsilon) + \mathcal{G}^{\sigma,1|2}_{\mathbf{0},i|j}(p-\varepsilon)\mathcal{G}^{\bar{\sigma},1|2}_{\mathbf{0},i|j}(\varepsilon)\Big] \\ &= -\frac{u_i u_j}{\pi i}\int d\varepsilon \Big[1 - f(\varepsilon) - f(p-\varepsilon) + 2f(\varepsilon)f(p-\varepsilon)\Big]\left(\mathcal{G}^{\sigma,2|1}_{\mathbf{0},i|j}(\varepsilon) - \mathcal{G}^{\sigma,1|2}_{\mathbf{0},i|j}(\varepsilon)\right)\left(\mathcal{G}^{\bar{\sigma},2|1}_{\mathbf{0},i|j}(p-\varepsilon) - \mathcal{G}^{\bar{\sigma},1|2}_{\mathbf{0},i|j}(p-\varepsilon)\right),\end{aligned} \tag{D.1}$$

where we added zeros $\int d\varepsilon\ \mathcal{G}^{2|1}_{\mathbf{0}}(\varepsilon)\mathcal{G}^{1|2}_{\mathbf{0}}(p-\varepsilon) = \int d\varepsilon\ \mathcal{G}^{1|2}_{\mathbf{0}}(\varepsilon)\mathcal{G}^{2|1}_{\mathbf{0}}(p-\varepsilon) = 0$. We then use the relation

$$2f(\varepsilon)f(p-\varepsilon) = 2b(p-\mu)[1 - f(p-\varepsilon) - f(\varepsilon)], \tag{D.2}$$

which yields

$$\begin{aligned}\Pi^{1|1}_{ij}(p) &= -\frac{u_i u_j}{\pi i}\Big[1 + 2b(p-\mu)\Big]\int d\varepsilon \Big[1 - f(\varepsilon) - f(p-\varepsilon)\Big]\left(\mathcal{G}^{\sigma,2|1}_{\mathbf{0},i|j}(\varepsilon) - \mathcal{G}^{\sigma,1|2}_{\mathbf{0},i|j}(\varepsilon)\right)\left(\mathcal{G}^{\bar{\sigma},2|1}_{\mathbf{0},i|j}(p-\varepsilon) - \mathcal{G}^{\bar{\sigma},1|2}_{\mathbf{0},i|j}(p-\varepsilon)\right) \\ &= \Big[1 + 2b(p-\mu)\Big]\Big[\Pi^{1|2}_{ij}(p) - \Pi^{2|1}_{ij}(p)\Big].\end{aligned} \tag{D.3}$$

This proves Eq.(40d).

2. FDT for the X-channel

A similar calculation as above shows the FDT for the x-channel:

$$\begin{aligned}
X_{ij}^{\sigma\sigma',1|1}(x) &= -\frac{u_i u_j}{2\pi i}\int d\varepsilon\Big[\mathcal{G}_{\mathbf{0},i|j}^{\bar\sigma,2|2}(\varepsilon)\mathcal{G}_{\mathbf{0},i|j}^{\bar\sigma',2|2}(\varepsilon+x)+\mathcal{G}_{\mathbf{0},i|j}^{\bar\sigma,2|1}(\varepsilon)\mathcal{G}_{\mathbf{0},i|j}^{\bar\sigma',1|2}(\varepsilon+x)+\mathcal{G}_{\mathbf{0},i|j}^{\bar\sigma,1|2}(\varepsilon)\mathcal{G}_{\mathbf{0},i|j}^{\bar\sigma',2|1}(\varepsilon+x)\Big]\\
&= -\frac{u_i u_j}{\pi i}\int d\varepsilon\Big[f(\varepsilon)-f(\varepsilon+x)-2f(\varepsilon)f(-\varepsilon-x+2\mu)\Big]\Big(\mathcal{G}_{\mathbf{0},i|j}^{\bar\sigma,2|1}(\varepsilon)-\mathcal{G}_{\mathbf{0},i|j}^{\bar\sigma,1|2}(\varepsilon)\Big)\Big(\mathcal{G}_{\mathbf{0},i|j}^{\bar\sigma',2|1}(\varepsilon+x)-\mathcal{G}_{\mathbf{0},i|j}^{\bar\sigma',1|2}(\varepsilon+x)\Big)\\
&= -\frac{u_i u_j}{\pi i}\Big[1+2b(x+\mu)\Big]\int d\varepsilon\Big[f(\varepsilon+x)-f(\varepsilon)\Big]\Big(\mathcal{G}_{\mathbf{0},i|j}^{\bar\sigma,2|1}(\varepsilon)-\mathcal{G}_{\mathbf{0},i|j}^{\bar\sigma,1|2}(\varepsilon)\Big)\Big(\mathcal{G}_{\mathbf{0},i|j}^{\bar\sigma',2|1}(\varepsilon+x)-\mathcal{G}_{\mathbf{0},i|j}^{\bar\sigma',1|2}(\varepsilon+x)\Big)\\
&= \Big[1+2b(x+\mu)\Big]\Big[X_{ij}^{\sigma\sigma',1|2}(x)-X_{ij}^{\sigma\sigma',2|1}(x)\Big]. \qquad \text{(D.4)}
\end{aligned}$$

3. FDT for the self-energy

Finally we show the FDT for the self-energy: Using the FDT for both the X-channel of the vertex as well as of the bare Green's function, we can rewrite the Keldysh component of the self-energy:

$$\begin{aligned}
\Sigma_{\mathbf{2},i|j}^{\sigma,1|1}(\varepsilon) &= -\frac{1}{2\pi i}\int d\varepsilon'\left[\mathcal{G}_{\mathbf{0},i|j}^{\sigma,2|2}(\varepsilon')X_{ij}^{\sigma\sigma,1|1}(\varepsilon-\varepsilon')+\mathcal{G}_{\mathbf{0},i|j}^{\sigma,2|1}(\varepsilon')X_{ij}^{\sigma\sigma,1|2}(\varepsilon-\varepsilon')+\mathcal{G}_{\mathbf{0},i|j}^{\sigma,1|2}(\varepsilon')X_{ij}^{\sigma\sigma,2|1}(\varepsilon-\varepsilon')\right]\\
&= -\frac{1}{2\pi i}\int d\varepsilon'\left([1-2f(\varepsilon')]\left[1+2b(\varepsilon-\varepsilon'+\mu)\right]+1\right)\Big(\mathcal{G}_{\mathbf{0},i|j}^{\sigma,21}(\varepsilon')-\mathcal{G}_{\mathbf{0},i|j}^{\sigma,12}(\varepsilon')\Big)\Big(X_{ij}^{\sigma\sigma,1|2}(\varepsilon-\varepsilon')-X_{ij}^{\sigma\sigma,2|1}(\varepsilon-\varepsilon')\Big)\\
&= -\frac{1}{2\pi i}[1-2f(\varepsilon)]\int d\varepsilon'\left[2-2f(\varepsilon')+2b(\varepsilon-\varepsilon'+\mu)\right]\Big(\mathcal{G}_{\mathbf{0},i|j}^{\sigma,21}(\varepsilon')-\mathcal{G}_{\mathbf{0},i|j}^{\sigma,12}(\varepsilon')\Big)\Big(X_{ij}^{\sigma\sigma,1|2}(\varepsilon-\varepsilon')-X_{ij}^{\sigma\sigma,2|1}(\varepsilon-\varepsilon')\Big)\\
&. = [1-2f(\varepsilon)]\left[\Sigma_{\mathbf{2},i|j}^{\sigma,1|2}(\varepsilon)-\Sigma_{\mathbf{2},i|j}^{\sigma,2|1}(\varepsilon)\right]. \qquad \text{(D.5)}
\end{aligned}$$

Here we added zeros, $\int d\varepsilon'\mathcal{G}_{\mathbf{0}}^{2|1}(\varepsilon')X^{2|1}(\varepsilon-\varepsilon')=\int d\varepsilon'\mathcal{G}_{\mathbf{0}}^{1|2}(\varepsilon')X^{1|2}(\varepsilon-\varepsilon')=0$, to get to the second line. Furthermore we used the relation

$$b(\varepsilon-\varepsilon'+\mu)\left[f(\varepsilon)-f(\varepsilon')\right]=-f(\varepsilon)f(-\varepsilon'+2\mu)=-f(\varepsilon)+f(\varepsilon)f(\varepsilon'). \qquad \text{(D.6)}$$

Appendix E: Method of finite differences for non-uniform grid

Our goal in this appendix is to derive a discrete description of a continuous system having the Hamiltonian $\mathcal{H}(x)=\hbar^2/(2m)\partial_x^2+V(x)$. *While the standard precedure usually involves discretization via a grid with constant spacing, we focus on the more general case, where the spacing is non-constant. This bypasses, for a proper choice of non-monotonic discretization, the occurence of artificial bound states close to the upper band edge, which are a consequence of the inhomogeneity* $V(x)$.

We discretize real space using a set of grid points $\{x_j\}$ (see Fig.(3)). The distance between two successive points is given by $a_j=x_{j+1}-x_j$. Now, a function $\psi(x)$ and its first and second derivatives $\psi'(x)$ and $\psi''(x)$ are discretized as

$$\psi_j=\psi(x_j),$$

$$\psi'_{j+1/2}=\frac{\psi(x_{j+1})-\psi(x_j)}{a_j},$$

$$\begin{aligned}
\psi''_j &= \frac{\psi'_{j+1/2}-\psi'_{j-1/2}}{\frac{a_j+a_{j-1}}{2}} = 2\frac{\frac{\psi_{j+1}-\psi_j}{a_j}-\frac{\psi_j-\psi_{j-1}}{a_{j-1}}}{a_j+a_{j-1}}\\
&\simeq \frac{1}{a_{j-1}^2}\psi_{j-1}-\left(\frac{1}{a_{j-1}^2}+\frac{1}{a_j^2}\right)\psi_j+\frac{1}{a_j^2}\psi_{j+1}, \qquad \text{(E.1)}
\end{aligned}$$

where we demanded that the spacing changes smoothly

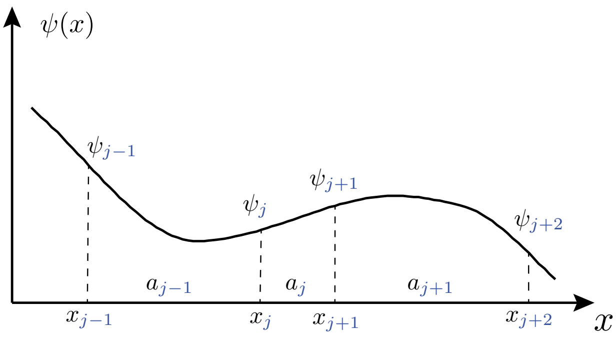

Figure 3. Illustration of the choice of notation used to discretize real space.

as a function of j, implying $(a_j + a_{j-1})a_j \simeq 2a_j^2$ and $(a_j + a_{j-1})a_{j-1} \simeq 2a_{j-1}^2$. Note that the first derivative is defined 'in between' grid points.

Hence, the discretized version of the Hamiltonian $H(x) = -\frac{\hbar^2}{2m}\partial_x^2 + V(x)$ at a point x_j is given by

$$H\psi_j = -\tau_{j-1}\psi_{j-1} - \tau_j\psi_{j+1} + E_j\psi_j, \tag{E.2}$$

with site-dependent hopping $\tau_j = 1/(2ma_j^2)$ (here and below we set $\hbar = 1$) and the onsite-energy $E_j = \tau_{j-1} + \tau_j + V_j$.

---

[1] R. Landauer. Spatial Variation of Currents and Fields Due to Localized Scatterers in Metallic Conduction. *IBM Journal of Research and Development* **1**, 223-231

[2] Y. Meir & N. S. Wingreen. Landauer formula for the current through an interacting electron region. *Phys. Rev. Lett.* **68**, 2512-2515 (1992).

[3] J. Eckel, F. Heidrich-Meisner, S. G. Jakobs, M. Thorwart, M. Pletyukhov, and R. Egger, *New J. Phys.* **12**, 043042 (2010).

[4] S. Andergassen, V. Meden, H. Schoeller, J. Splettstoesser, and M. R. Wegewijs, *Nanotechnology* **21**, 272001 (2010).

[5] F. Bauer, J. Heyder, E. Schubert, D. Borowsky, D. Taubert, B. Bruognolo, D. Schuh, W. Wegscheider, J. von Delft, and S. Ludwig, *Nature* **501**, 73 (2013).

[6] A. Oguri, Transmission Probability for Interacting Electrons Connected to Reservoirs. *J. Phys. Soc. Jap.* **70**, 2666 (2001).

[7] G.M.Eliashberg, Transport equation for a degenerate system of fermi particles, *JETP*41,1241-1251 (1962)

[8] L.V.Keldysh. *Zh. Eksp. Teor. Fiz.* **47**, 1515 (1964).

[9] A.Kamenev, A. Levchenko. *arXiv*: 0901.3586

[10] J.C. Ward, *Phys. Rev.* **78**,182 (1950)

[11] S. G. Jakobs et al. Properties of multi-particle Green's and vertex functions within Keldysh formalism *J. Phys. A: Math. Theor.* **43**,103001 (2010)

[12] S. G. Jakobs, M. Pletyukhov, H.Schoeller, Nonequilibrium functional renormalization group with frequency-dependent vertex function: A study of the single-impurity Anderson model *Phys. Rev. B* **81**,195109 (2010)

[13] Walter Metzner, Manfred Salmhofer, Carsten Honerkamp, Volker Meden, and Kurt Schnhammer. Functional renormalization group approach to correlated fermion systems. *Rev. Mod. Phys.*, **84**,299-352

[14] O.Goulko, F.Bauer, J.Heyder, J. von Delft, Effect of Spin-Orbit Interactions on the 0.7 Anomaly in Quantum Point Contacts, *Phys. Rev. Lett.*, **113**, 266402 (2014)

[15] S.Jakobs, Functional renormalization group studies of quantum transport through mesoscopic systems, *Dissertation*

[16] M. Buettiker, *Phys. Rev. B*41, 7906 (1990).

[17] C. Sloggett, A. I. Milstein, & O. P. Sushkov, Correlated electron current and temperature dependence of the conductance of a quantum point contact. *Eur. Phys. J. B* **61**, 427432 (2008).

[18] F.Bauer, J.Heyder, J.von Delft, Functional Renormalization Group Approach for Inhomogeneous Interacting Fermi-Systems *arXiv*:1311.3210

Chapter 9

Towards combined transport and optical studies of the *0.7 anomaly* in a QPC

This chapter includes the paper *"Towards combined transport and optical studies of the 0.7 anomaly in a QPC"*, published in *physica status solidi* B [Schubert et al. (2014)]. In Bauer et al. (2013) we present functional renormalization group (fRG) calculations for the spin suspectibility of our one-dimensional (1D) quantum point contact (QPC) model (Sec. 3.3.1). We find an interaction-induced enhancement of the QPC's local spin susceptibility in the sub-open regime, originating from an interplay between the van Hove ridge in the local density of states (LDOS) and strong exchange interactions in the vicinity of the barrier center. In Schubert et al. (2014) Enrico Schubert and Alexander Högele present an experiment which aims at confirmation of this prediction by measuring the local magnetization of a QPC in a small magnetic field with the help of Faraday rotation technique. Additionally, they intend to measure spin-selective transport by injecting spin-polarized electrons near the QPC. This experiment provides the opportunity to confirm important predictions of the van Hove scenario, thus shedding additional light on the microscopic origin of the *0.7 anomaly*.

Phys. Status Solidi B **251**, No. 9, 1931–1937 (2014) / **DOI** 10.1002/pssb.201350218

Part of Special Issue on
Semiconductor Spintronics

physica status solidi b
www.pss-b.com
basic solid state physics

Toward combined transport and optical studies of the 0.7-anomaly in a quantum point contact

Enrico Schubert[*,1], **Jan Heyder**[1,2], **Florian Bauer**[1,2], **Bernd Waschneck**[1], **Wolfgang Stumpf**[3],
Werner Wegscheider[3], **Jan von Delft**[1,2], **Stefan Ludwig**[1], **and Alexander Högele**[1]

[1] Center for NanoScience and Department of Physics, Ludwig-Maximilians-Universität München, Geschwister-Scholl-Platz 1, 80539 München, Germany
[2] Arnold Sommerfeld Center for Theoretical Physics, Ludwig-Maximilians-Universität München, Theresienstrasse 37, 80333 München, Germany
[3] Laboratory for Solid State Physics, ETH Zurich, 8093 Zurich, Switzerland

Received 18 September 2013, revised 14 February 2014, accepted 5 March 2014
Published online 12 April 2014

Keywords 0.7-anomaly, optical spectroscopy, quantum point contacts, two-dimensional electron systems

---

[*] Corresponding author: e-mail enrico.schubert@physik.uni-muenchen.de, Phone: +49 89 2180 3349, Fax: +49 89 2180 3182

OPEN This is an open access article under the terms of the Creative Commons Attribution License, which permits use, distribution and reproduction in any medium, provided the original work is properly cited.

A quantum point contact (QPC) causes a one-dimensional constriction on the spatial potential landscape of a two-dimensional electron system. By tuning the voltage applied on the QPC gates which form the constriction at low temperatures the resulting regular step-like electron conductance quantization can show an additional kink near pinch-off around $0.7(2e^2/h)$, called 0.7-anomaly. In a recent publication, we presented a combination of theoretical calculations and transport measurements that lead to a detailed understanding of the microscopic origin of the 0.7-anomaly. Functional renormalization group-based calculations were performed exhibiting the 0.7-anomaly even when no symmetry-breaking external magnetic fields are involved. According to the calculations the electron spin susceptibility is enhanced within a QPC that is tuned in the region of the 0.7-anomaly. Moderate externally applied magnetic fields impose a corresponding enhancement in the spin magnetization. In principle, it should be possible to map out this spin distribution optically by means of the Faraday rotation technique. Here we report the initial steps of an experimental project aimed at realizing such measurements. Simulations were performed for a heterostructure designed to combine transport and optical studies. Based on the simulation results a sample was built and its basic transport and optical properties were investigated.

1 Introduction

A quantum point contact (QPC) is a short, one-dimensional constriction usually realized within a two-dimensional electron system (2DES), by applying voltage to metallic gates, thereby depleting the electrons beneath and only leaving a narrow transport channel whose width can be tuned by the applied gate voltage. When a QPC is opened up by changing the applied gate voltage, its conductance rises in integer steps of the conductance quantum, $G_Q = 2e^2/h$ [1–3], but also shows a shoulder-like intermediate step at the onset of the first plateau around $\simeq 0.7G_Q$. This phenomenon, known as the 0.7-anomaly, has a very intriguing dependence on temperature (T), magnetic field (B), and source–drain voltage (V_{SD}) [4–7]. A summary of the status of various previous theoretical treatments thereof may be found in [8].

In a recent publication [9], we presented a combination of theoretical calculations and transport measurements that lead to a detailed understanding of the microscopic origin of the 0.7-anomaly. The anomaly is caused by a smeared van Hove peak in the local density of states (LDOS), whose weight, shape, and position depends on sample geometry (width, length, and shape of the QPC confinement potential). The van Hove peak enhances the effect of interaction by two main mechanisms: first, it enhances the effective Hartree barrier, and thus the elastic back-scattering due to Coulomb repulsion; second, it opens up a phase space for inelastic scattering

© 2014 The Authors. *Phys. Status Solidi B* is published by WILEY-VCH Verlag GmbH & Co. KGaA, Weinheim

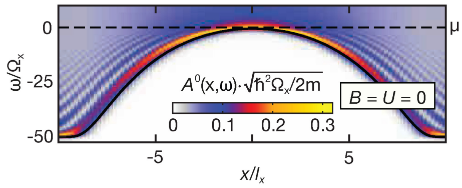

Figure 1 The bare local density of states, $A^0(x, \omega)$, in the central region of the QPC as a function of position x and energy ω. The maximum of A^0_j follows the shape of the band, i.e., the shape of the applied potential, resulting in a distinct ridge-like structure (yellow), the van Hove ridge.

which is enhanced further by increasing the temperature or the source–drain bias voltage.

The present paper serves two purposes. First, in Section 2 we summarize some of the main results from [9], highlighting, in particular, one of its central predictions: the local spin susceptibility is predicted to be anomalously enhanced in the vicinity of the QPC. Second, in Section 3 we describe the initial stages of an experimental project that ultimately aims at detecting the predicted anomalous behavior of the spin susceptibility in a QPC by optical methods.

2 Microscopic origin of the 0.7-anomaly

In experiments, QPCs are commonly defined using the field effect to create an electrostatic saddle point potential (see, e.g., Ref. [9], Fig. 1). To model this effective 1D constriction we use a strict 1D-barrier along the electronic transport direction x. We choose the potential, $V(x)$, to be symmetric around $x = 0$ and parabolic near the top,

$$V(x) = \tilde{V}_\mathrm{c} + \mu - \frac{m}{2\hbar^2}\Omega_x^2 x^2, \qquad (1)$$

where $\hbar$ is Planck's constant and m the effective electron mass. The barrier height is governed by $\tilde{V}_\mathrm{c}$, which mimics the role of gate voltage in experiment; it is chosen such that for $\tilde{V}_\mathrm{c} = 0$, the barrier top lies at the chemical potential μ. The barrier curvature Ω_x defines the effective length of the QPC, which is proportional to $l_x = \sqrt{\hbar^2/(2m\Omega_x)}$ (see [10] and supplementary information of [9] for more details). Figure. 1 shows the bare LDOS, $A^0(x, \omega)$, of the QPC as a function of position x and energy ω (measured relative to μ). The LDOS has a maximum right above the potential $V(x)$ (black thick line), visible as a yellow-red structure. This structure, which lies at the heart of the explanation for the 0.7-anomaly, will be called a "van Hove ridge." Near the barrier center the ridge maximum lies slightly higher in energy than the potential $V(x)$, by an amount that scales like the barrier curvature Ω_x.

To theoretically investigate the influence of magnetic field and interactions, we study a one-dimensional tight-binding chain with lattice spacing a, an onsite energy given by a discretized version of the potential (1), a local Zeeman energy $-\sigma B/2$ (thus B denotes g-factor times magnetic field), and a purely local (onsite) interaction U. The effective strength of interaction effects scales as U/U_c, where $U_\mathrm{c} = \sqrt{\hbar^2\Omega_x/(2ma^2)}$ is inversely proportional to A^0_max, the height of the van Hove ridge at the barrier center (for details see [10]). For this model we calculated the linear conductance and the local density and magnetization per site at zero temperature, incorporating interaction effects using the functional Renormalization Group (fRG) [9–14].

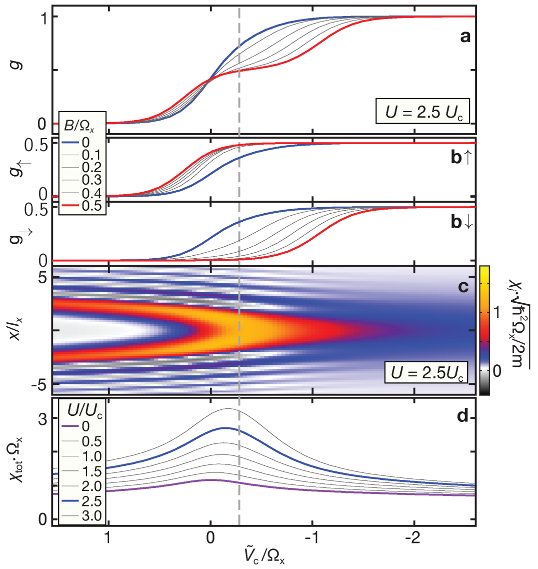

Figure 2 (a) Calculated linear conductance $g(V_\mathrm{c})$ as a function of barrier height for several values of magnetic field, at zero temperature. Interactions cause a weak shoulder even at zero field, which strengthens for intermediate fields and eventually develops into a spin-resolved conductance step at high field. (b↑/b↓) Calculated spin-resolved conductance curves for the same magnetic fields as in (a). The conductance curves for spin-up and spin-down react in an asymmetric fashion on an applied field: a combination of Pauli exclusion principle and Coulomb blockade (Hartree effect) leads to a strong reduction of ↓-conductance, resulting in the phenomenon of the 0.7-anomaly. (c) Local spin susceptibility, $\chi(x, \tilde{V}_\mathrm{c})$, as a function of position x and barrier height $\tilde{V}_\mathrm{c}$ for a fixed value of interaction strength, $U = 2.5\,U_\mathrm{c}$. The strongest response of the system to a small applied magnetic field happens in the center of the barrier and coincides with the barrier height for which the 0.7-anomaly occurs (see (a)), highlighted with the gray dashed vertical line around $\tilde{V}_\mathrm{c} = -0.25\Omega_x$. (d) The total spin-susceptibility of the QPC, χ_tot, for several values of interaction strength.

Figure 2a shows the calculated $\tilde{V}_\mathrm{c}$-dependence of the linear conductance $g = G/G_\mathrm{Q}$ of the lowest mode of a QPC for several values of magnetic field and a finite interaction strength. We find very good qualitative agreement with measured curves (see, e.g. [9]) not only for zero field, where the asymmetry of the step becomes manifest in a weak shoulder (marked by gray dashed vertical line), but also at finite field, where the single step develops via a 0.7-anomaly into a double step of width $g_\mathrm{eff}\mu_\mathrm{B}B$. Figure 2b↑ and Fig. 2b↓ show the calculated spin-resolved conductance for the same fields and interaction used in Fig. 2a. As expected, the conductance

© 2014 The Authors. *Phys. Status Solidi B* is published by WILEY-VCH Verlag GmbH & Co. KGaA, Weinheim

increases/decreases for the favored/disfavored (spin-up/spin-down) electrons. But unlike in the non-interacting case (not shown) the spin-down step is shifted much more strongly toward negative values of $\tilde{V}_c$ than the spin-up shift is shifted toward positive values of $\tilde{V}_c$. This can be explained as follows: Once a finite field breaks spin-symmetry, interactions push away spin-down electron out of the QPC's center, thereby depleting their density around the barriers top and consequently strongly reducing their probability of transmission. The 0.7-anomaly at finite magnetic field is a natural consequence of this interaction-induced asymmetry.

As explained in detail in Ref. [9], the origin of the 0.7-anomaly is caused by the presence of the van Hove ridge in the LDOS. Its apex crosses the chemical potential, when the QPC is tuned into the sub-open regime, that is, when the conductance takes values $0.5 \lesssim g \lesssim 1$. As a consequence, the local spin-susceptibility, $\chi(x) = \frac{1}{2}\left(\partial_h m(x)\right)_{h=0}$, shows not only a strong spatial dependence due to the inhomogeneity of the QPC, but also a strong $\tilde{V}_c$-dependence, when the potential is shifted through μ (see Fig. 2c). This also manifests itself in the total spin-susceptibility of the QPC, $\chi_{\mathrm{tot}} = \int_{x \in \mathrm{QPC}} \mathrm{d}x\, \chi(x)$, which is plotted in Fig. 2d for several values of interaction strength. Three direct consequences of interactions stand out: First, interactions strongly enhance the effect of an applied magnetic field. Second, the maximum in the QPC's susceptibility is shifted to somewhat lower values of $\tilde{V}_c$ and, third, this maximum occurs when the QPC is sub-open (gray dashed vertical line in Fig. 2, compare with conductance curves in Fig. 2a). These anomalous spatial structures in the spin susceptibility serve as the main incentive for the experimental work described further below, whose ultimate goal is to detect these structures by opto-transport hybrid measurements.

3 Motivation for the experiment

Next, we describe ongoing experimental work, whose ultimate goal is to test the following prediction emerging from the theoretical work described above: For a QPC tuned in the regime of the 0.7-anomaly at zero external magnetic field, theory predicts an enhancement in the local electron spin susceptibility [9]. At finite magnetic fields the enhanced spin susceptibility should give rise to electron-spin polarization with a spatial distribution characteristic of a QPC operated at the point of the 0.7-anomaly (see Fig. 2a). Moreover, this polarization would also result in spin-sensitive conductance. In principle, both signatures could be probed by optical means: while spatially-resolved Kerr or Faraday rotation could be used to map out the local spin-polarization in the vicinity of the QPC, polarization-selective optical spin-injection could be exploited to create an electron-spin imbalance across the QPC to drive spin-polarized currents. Our first step en-route to combined transport and optical spectroscopy of a QPC in the 0.7-anomaly regime was to design a heterostructure that would allow to implement both spin-sensitive Faraday rotation and spin-selective charge carrier injection.

The following experimental part is divided into three sections. In Section 3.1 we discuss the optimization process of the heterostructure design and the results of the simulations performed with *nextnano3* [15]. In Section 3.2 we present initial transport and optical characterization measurements of the heterostructure. Section 3.3 describes the present stage of our experiments and provides perspectives for the combined transport and optical spectroscopy of the 0.7-anomaly in a QPC.

3.1 Semiconductor heterostructure design and simulations

The design of the heterostructure for combined transport and optical experiments was guided by two main objectives. On one hand, we intended to realize a high quality two-dimensional electron system (2DES) suited for the observation of the 0.7-anomaly in a QPC. On the other hand, the sample structure should be designed to allow for spin-selective optical excitations of charge carriers from the valence band into the conduction band states of the 2DES just above the Fermi level, and at the same time avoid excitations of charge carriers in any other heterostructure layer. To make all sample regions but the 2DES transparent to light at optical frequencies that meet the resonance condition for interband excitation of electrons into the Fermi sea we chose to embed an $\mathrm{In}_x\mathrm{Ga}_{(1-x)}\mathrm{As}$ quantum well (QW) hosting the 2DES in higher bandgap materials such as GaAs and AlGaAs. Accordingly, optical excitations from the valence band states into the conduction band states within the $\mathrm{In}_x\mathrm{Ga}_{(1-x)}\mathrm{As}$ QW exhibit the smallest energy for interband transitions, provided that the concentration x of indium is finite. At the same time quantum confinement associated with the QW removes the degeneracy of heavy- and light-hole subbands at the Γ-point of bulk zinc blende semiconductors, which in turn ensures "clean" dipolar selection rules for spin-selective optical excitations from the heavy hole subband at E_{hh} into the states at E_{F} of the 2DES.

Figure 3 illustrates the basic layout of our heterostructure. The corresponding layer sequence along the sample growth direction is shown in the left panel of Fig. 3. The $\mathrm{In}_x\mathrm{Ga}_{(1-x)}\mathrm{As}$ QW of variable thickness z_{QW} and an indium fraction x in the range of $0 < x < 0.1$ is sandwiched between GaAs and $\mathrm{Al}_{0.235}\mathrm{Ga}_{0.765}\mathrm{As}$ that contains a δ-doping region located at a distance z_δ above the QW. The AlGaAs layer acts as a tunnelling barrier between the 2DES and the semitransparent Schottky gate deposited on top of the heterostructure. The overall thickness of the AlGaAs barrier was set to half of the wavelength of the expected QW interband transition to minimize optical interference effects. The silicon δ-doping provides excess electrons to form a 2DES inside the QW and the final GaAs top cap layer prevents oxidization of the AlGaAs barrier. In the right panel of Fig. 3 the corresponding band structure profile calculated with *nextnano3* is shown for zero external gate voltage, $V_t = 0$, and $x = 0.07$, $z_{\mathrm{QW}} = 10$ and $z_\delta = 50$ nm. The band profile bending is due to the built-in Schottky potential, accounting for the lowest QW electron level E_e to lie below the Fermi energy, in accord with our intention to create a modulation-doped 2DES within the InGaAs QW.

We recall the main properties of the intended heterostructure. First the QW containing the 2DES should exhibit the

© 2014 The Authors. *Phys. Status Solidi B* is published by WILEY-VCH Verlag GmbH & Co. KGaA, Weinheim

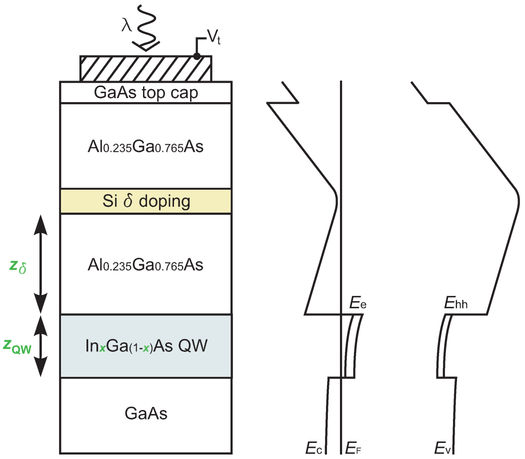

Figure 3 Left: Schematic design of the heterostructure. It consists of a GaAs substrate on which an InGaAs quantum well (blue), AlGaAs spacer with a Si δ-doping layer (yellow), and a GaAs cap are grown. The 2DES formed in the InGaAs quantum well is populated by electron transfer from the δ-doping layer. A GaAs top cap layer terminates the heterostructure. A semitransparent metal gate on top of the heterostructure gives rise to a built-in Schottky potential and allows to further bend the band structure via a voltage V_t. The quantum well thickness z_{QW}, the indium concentration x and the distance z_δ from the quantum well and the δ-doping region were used as optimization parameters in simulations with *nextnano3*. Right: Band structure profile along the heterostructure growth direction obtained from simulations for $V_t = 0$. E_c and E_v denote the conduction and valance band edges, E_e and E_{hh} the lowest electron and heavy-hole levels confined in the quantum well, and E_F is the Fermi energy, respectively.

smallest interband transition energy with well defined dipolar selection rules for spin-selective excitations. Second the semiconductor matrix above and below the QW should be transparent at the intended optical frequencies. Both criteria can be satisfied by the heterostructure layout of Fig. 3. Finally, the density of the 2DES should be at least 2×10^{11} cm^{-2} to ensure the required transport characteristics.

To this end we used *nextnano3* to monitor the 2DES density as a function of the optimization parameters x, z_{QW} and z_δ. The objective was to achieve a maximum electron density inside the QW of about 3×10^{11} cm^{-2}. Simultaneously the interband transition wavelength of the QW region, which follows from the energy difference between the lowest QW hole level and the Fermi energy, was intended to lie above 830 nm in order to not overlap with optical transitions of carbon impurities [16] inherent to the molecular beam epitaxy (MBE) growth process of the heterostructure. In Fig. 3 these adjustable parameters for the simulations are highlighted in green. Raising the QW thickness z_{QW} as well as the QW indium content x mainly increases the QW interband transition wavelength. Reducing the distance z_δ between the QW and the δ-doping layer tends to increase the 2DES density. However, at small QW thickness, proximity of the QW 2DES and the doping layer, and a high indium concentration typically reduce the mobility of the QW electrons and should be avoided.

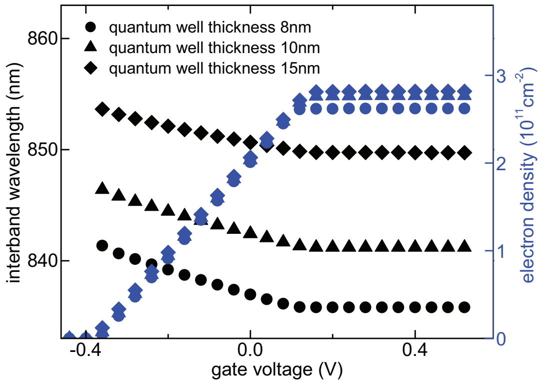

Figure 4 Simulation results for the QW electron density (blue) and the interband transition wavelength (black) as a function of gate voltage. Results are shown for three different QW thicknesses of $z_{QW} = 8$ nm (circles), 10 nm (triangles), and 15 nm (squares) for a fixed indium content of $x = 0.07$ and a fixed spacer distance between the doping region and the QW of $z_\delta = 50$ nm.

Figure 4 shows the simulation results for three different heterostructures with an indium concentration of $x = 0.07$ and $z_{QW} = 50$ nm. The QW thickness was taken as 8, 10, and 15 nm to obtain a variation in the QW electron density (blue) and the interband transition wavelength (black) as a function of the voltage applied to the semitransparent top gate. Decreasing the gate voltage increases the energy of the QW electron levels with respect to the Fermi energy which gradually depletes the 2DES density inside the QW. This depletion becomes increasingly pronounced below gate voltages of 0.15 V until the pinch-off is reached at about −0.4 V for all three heterostructures. The interband wavelength remains constant for $V_t > 0.25$ V. At more negative gate voltages the simulations predict a redshift of the resonance condition that is associated with a decrease of the Fermi energy. In Fig. 4 the maximum 2DES density as well as the optical transition wavelength are close to our intended values.

3.2 Basic transport and optical characteristics

Based on these simulation results a heterostructure was grown by MBE with an indium concentration of $x = 0.07$, the separation between the QW and the δ-doping layer of $z_{QW} = 50$ nm, and a QW thickness of 10 nm (compare Fig. 3). Subsequently the sample material was characterized with respect to basic transport and optical properties. To determine the electron density and mobility of the 2DES a standard Hall bar geometry was used. The Hall bar mesa was fabricated by conventional wet etching techniques and AuGe/Ni/AuGe Ohmic contacts were defined as Ohmic contacts to the 2DES. To allow control of the electron density a semitransparent titanium gate with a thickness of 5 nm

© 2014 The Authors. *Phys. Status Solidi B* is published by WILEY-VCH Verlag GmbH & Co. KGaA, Weinheim

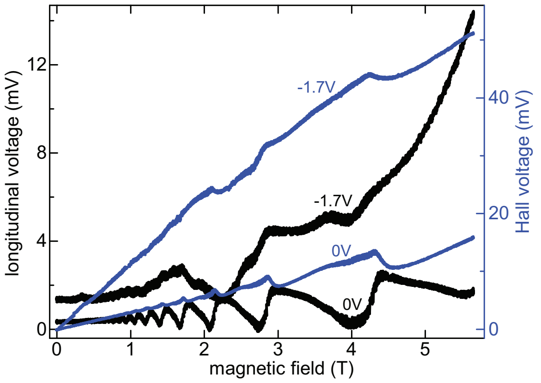

Figure 5 Measured longitudinal (black) and Hall voltages (blue) as a function of the perpendicularly applied magnetic field at top gate voltages of 0 V and -1.7 V ($T = 4.2$ K). Distortions of the Hall voltage between plateaus are due to an asymmetry of the used Hall bar geometry which gives rise to an Ohmic resistance contribution to the Hall voltage.

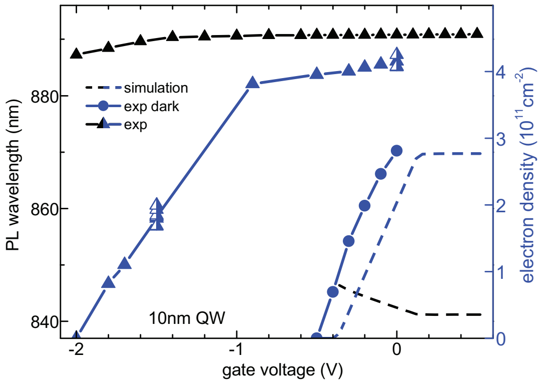

Figure 6 Transport and optical characterization of the heterostructure. Data (symbols; lines are guides to the eye) and corresponding simulations as in Fig. 4 (dashed lines) for a heterostructure with a QW of thickness $z_{\mathrm{QW}} = 10$ nm, 7% of indium concentration, and $z_\delta = 50$ nm. The wavelength of the photoluminescence peak maximum and the electron density of the QW 2DES are shown as a function of gate voltage in black and blue, respectively. Circles and triangles indicate the measurement results before and after light illumination of the Hall bar, respectively. Half-filled triangles correspond to electron densities measured after repeated illumination of the sample. The photoluminescence was obtained from the central region of the Hall bar using a confocal setup with excitation powers of 7 μW in the range of $+0.6$ to -1.0 V and 0.3 μW below -1.0 V at an excitation wavelength of 830 nm. The 2DES density was derived from standard Hall measurements. All measurements were carried out at 4.2 K.

was deposited on top of the central region of the Hall bar structure.

The electron density and mobility were extracted from four-terminal dc Hall voltage measurements before the sample was subjected to light. Magnetic fields of up to 5.7 T were applied perpendicularly to the QW plane. By fitting the Hall voltage U_{xy} versus the applied magnetic field B in the linear regime at low B (Fig. 5) the carrier density of the 2DES is extracted by

$$n_{\mathrm{2DES}} = \frac{I}{e \cdot \mathrm{d}U_{\mathrm{xy}}/\mathrm{d}B}. \tag{2}$$

e is the elementary charge and I is the current through the Hall bar. The mobility μ_{2DES} of the electron system inside the QW was obtained from the longitudinal voltage at zero magnetic field $U_{\mathrm{xx}}(B = 0)$ (Fig. 5) using the relation

$$\mu_{\mathrm{2DES}} = \frac{0.75}{e \cdot n_{\mathrm{2DES}} \cdot U_{\mathrm{xx}}(B = 0)} \tag{3}$$

and the electron density n_{2DES} obtained according to Eq. (2). The number in the numerator is a scaling factor imposed by the particular geometry of the employed Hall bar structure. The same procedure was also carried out after broad-band illumination of the sample.

In a second step we studied basic optical properties of the sample by investigating the photoluminescence (PL) from the Hall bar. A cryogenic confocal microscope with an optical spot size of 1 μm was used to record the local PL response, which was then spectrally dispersed by a monochromator and detected with a low-noise liquid nitrogen cooled CCD. All measurements were carried out at a sample temperature of 4.2 K.

The combined transport and optical characterization results are shown in Fig. 6. The interband transition wavelength (black) and the QW electron density (blue) are shown as a function of gate voltage. Circles (triangles) indicate the results of measurements done before (after) illumination of the sample with continuous wave (cw) lasers (with 815 and 830 nm center wavelength). Dashed lines show the corresponding simulation results from Fig. 4 for comparison. In the simulations all silicon dopants were assumed to be ionized, which is realized experimentally by sample illumination. Despite an increase by ~ 30% of the 2DES density to around 4.2×10^{11} cm^{-2}, upon illumination, the simulated and experimental results are in very good agreement with the predictions of the simulation. Consistently, the pinch-off gate voltage where the carrier density goes to zero is shifted to more negative values upon illumination as compared to the simulated pinch-off voltage. Repeated illumination of the sample did not introduce further significant changes in the 2DES density (half-filled triangles in Fig. 6), indicating a long-term stability of the 2DES density after the initial ionization of silicon dopants. The mobility of the 2DES was determined to be ~ 70,000 cm^2 V^{-1} s^{-1} within the entire gate voltage range above -1.5 V after sample illumination (data not shown).

Despite good agreement between simulations and experiment for the 2DES density, we found considerable discrepancy between expected and observed values for the wavelength of the optical transition that we monitored via PL. Figure 6 shows the wavelength of the PL peak as a function

© 2014 The Authors. *Phys. Status Solidi B* is published by WILEY-VCH Verlag GmbH & Co. KGaA, Weinheim

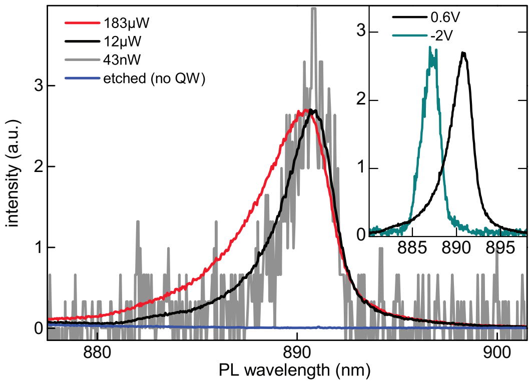

Figure 7 Photoluminescence spectra recorded for a Hall bar sample at 4.2 K with a QW thickness of 10 nm and incident excitation powers of $P_{\mathrm{exc}} = 183$ µW (red), 12 µW (black, main, and inset graph) and 43 nW (gray) scaled to maximum intensity values. The photoluminescence spectra were measured in the central Hall bar region at gate voltages of $V_{\mathrm{t}} = +0.6$ V (flatband) under cw excitation at a wavelength of 830 nm. The photoluminescence from an area where the QW was etched away is shown in blue for reference. Inset: photoluminescence spectra at two different gate voltages of +0.6 V (black) and −2.0 V (green) for incident excitation power of 300 nW.

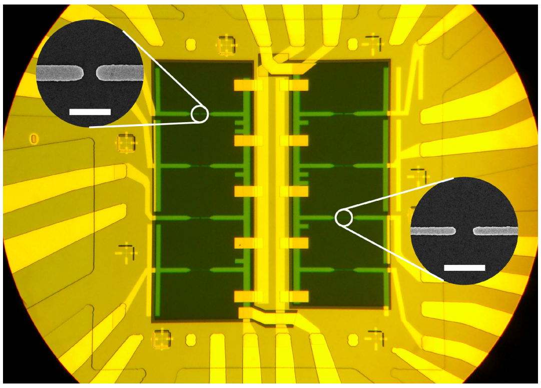

Figure 8 Optical microscope image of the sample layout with eight QPCs and two global top gates fabricated on the 10 nm InGaAs QW heterostructure. Optical and electron-beam lithography followed by gold deposition and lift-off were used to define gates (yellow) on top of a square mesa with an edge length of 160 µm. The QPCs are formed between the ends of finger-like gates (also shown as scanning-electron micrograph insets each including a horizontal scale bar corresponding to 1 µm length) of different geometries. On the top of the mesa two semitransparent rectangular gates were deposited which are electrically disconnected by cross-linked PMMA from all other gates used to define the QPCs.

of gate voltage recorded near the center of the Hall bar. Incident laser excitation powers were 7 µW in the voltage range between +0.6 and −1.0 V and 0.3 µW below −1.0 V, respectively. The excitation wavelength was set to 830 nm, close to the wavelength region of carbon impurity states in GaAs at 4.2 K [16]. The mean difference between the simulated and the measured optical transition wavelength is about 50 nm (83 meV) and a reversed energy dispersion as a function of gate voltage is observed (redshift in experiment vs. blueshift in simulations for increasing electron density). We speculate that the discrepancy partially arises from excitonic effects and the quantum confined Stark effect that were not accounted for in our simulations. Nevertheless, our main objective of the heterostructure design aiming at optical QW transition energies below the band gap of GaAs was successfully achieved.

Figure 7 shows the spectral characteristics of the PL. The spectra were measured with a confocal setup in the central Hall bar region at gate voltages of +0.6 V (flatband condition) for a cw laser excitation wavelength of 830 nm at 4.2 K. The PL exhibits an asymmetric profile reminiscent of Fermi edge singularity [17–19] even at lowest excitation powers down to ~ 40 nW (gray spectrum in Fig. 7). No PL was detected in the relevant spectral window from sample regions where the QW was etched away (blue spectrum in Fig. 7) indicating the QW to be the source of the PL. We find evidence of higher-energy shoulders at 883 and 885 nm that emerge with increasing excitation powers accompanied by a blue-shift of the PL maximum. These characteristics were consistently found at different spatial locations of the Hall bar structure where the QW was not etched away. We also found that the PL was sensitive to the gate voltage. The inset of Fig. 7 compares the PL spectra at $V_{\mathrm{t}} = +0.6$ and −2.0 V, showing a clear blue-shift of the PL resonance with more negative gate voltages that was accompanied by a gradual evolution of the PL line shape toward a symmetric Gaussian peak (fit not shown).

3.3 Outlook

The basic properties of the heterostructure described above represent a promising starting point for in-detail transport and optical studies of the 0.7-anomaly in QPCs. Figure 8 shows an optical micrograph of our present sample layout implemented on a heterostructure that contains a 2DES hosted by an InGaAs QW of 10 nm thickness. Gold gates defined by optical lithography (outer yellow pads) connect to inner gold gates processed by electron beam lithography (light yellow) across the mesa-edges (centered square and starlike surrounding connections). Eight QPCs of different widths and lengths of the gated constrictions between 200 and 500 nm are covered by layers of cross-linked poly methyl methacrylate (PMMA) (dark gray). The latter electrically isolates the QPC gates from the two semitransparent nickel–chromium top gates of 5 nm thickness (black rectangles on top of the PMMA in Fig. 8). They allow simultaneous optical access to the 2DES layer and tunability of carrier density. The insets in Fig. 8 show SEM pictures of two specific QPC geometries.

Figure 9 shows a series of conductance measurements on a specific QPC of the sample in Fig. 8 as function of the QPC gate voltage and a temperature of 4.2 K. Each pinch-off curve was measured at a top gate voltage V_{t} set equidistantly

© 2014 The Authors. *Phys. Status Solidi B* is published by WILEY-VCH Verlag GmbH & Co. KGaA, Weinheim

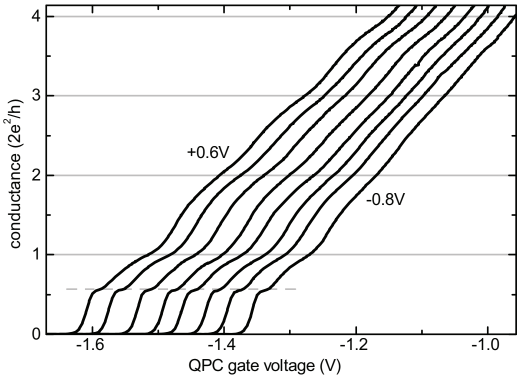

Figure 9 Conductance through a QPC of the sample in Fig. 8 measured at a setup temperature of 4.2 K. Shown are eight pinch-off curves as function of the QPC gate voltage, at various top gate voltages set between −0.8 and +0.6 V in steps of 0.2 V. Integer values of the spin-degenerate conductance quantum are highlighted by gray solid lines. A strongly pronounced kink is consistently visible at around 0.6 G_Q (dashed line).

between −0.8 and +0.6 V. A more positive voltage applied to the extended top gate increases the carrier density in the vicinity of the QPC, which shifts the QPC pinch-off to more negative voltages. Although thermally smeared out, four conductance plateaus are clearly visible at $V_t = +0.6$ V. Each emerging plateau becomes increasingly pronounced at higher 2DEG densities since the steeper lateral QPC confinement potential barriers raise the sublevel spacing within the constriction region. Additionally, a distinct kink occurs at about 0.6 G_Q throughout the whole top gate voltage range of 1.4 V (dashed line in Fig. 9). Its position as well as prominent appearance, compared to the QPC integer conductance plateaus at 4.2 K [4, 5], are indications of a 0.7-anomaly.

The next step will involve detailed transport experiments to study the 0.7-anomaly as a function of the QPC geometries in the accessible experimental parameter space. In opto-transport experiments we will then attempt to optically monitor the field dependence of the spin-up and spin-down densities in the vicinity of the QPC as a function of QPC gate voltage V_c and top gate voltage V_t. We will also aim to perform near-resonant injection of spin-polarized electrons in the vicinity of a QPC to observe spin-selective transport. We intend to exploit the full potential of the combined optical and transport setup in terms of position, energy and spin selective spectroscopy to shed light on the microscopic origin of the 0.7-anomaly.

Acknowledgements We thank J. P. Kotthaus for helpful discussions. We gratefully acknowledge funding by the Deutsche Forschungsgemeinschaft within the priority program "Semiconductor Spintronics" (SPP 1285) and the center of Excellence, Nanosystems Initiative Munich (NIM) as well as financial support from the Center for NanoScience (CeNS).

References

[1] B. J. van Wees, H. van Houten, C. W. J. Beenakker, J. G. Williamson, L. P. Kouwenhoven, D. van der Marel, and C. T. Foxon, Phys. Rev. Lett. **60**, 848 (1988).

[2] D. A. Wharam, T. J. Thornton, R. Newbury, M. Pepper, H. Ahmed, J. E. F. Frost, D. G. Hasko, D. C. Peacock, D. A. Ritchie, and G. A. C. Jones, J. Phys. C **21**, L209 (1988).

[3] M. Büttiker, Phys. Rev. B **41**, 7906 (1990).

[4] K. J. Thomas, J. T. Nicholls, M. Y. Simmons, M. Pepper, D. R. Mace, and D. A. Ritchie, Phys. Rev. Lett. **77**, 135 (1996).

[5] K. J. Thomas, J. T. Nicholls, N. J. Appleyard, M. Y. Simmons, M. Pepper, D. R. Mace, W. R. Tribe, and D. A. Ritchie, Phys. Rev. B **58**, 4846 (1998).

[6] N. J. Appleyard, J. T. Nicholls, M. Pepper, W. R. Tribe, M. Y. Simmons, and D. A. Ritchie, Phys. Rev. B **62**, R16275 (2000).

[7] S. M. Cronenwett, H. J. Lynch, D. Goldhaber-Gordon, L. P. Kouwenhoven, C. M. Marcus, K. Hirose, N. S. Wingreen, and V. Umansky, Phys. Rev. Lett. **88**, 226805 (2002).

[8] A. P. Micolich, J. Phys.: Condens. Matter **23**, 443201 (2011).

[9] F. Bauer, J. Heyder, E. Schubert, D. Borowsky, D. Taubert, B. Bruognolo, D. Schuh, W. Wegscheider, J. von Delft, and S. Ludwig, Nature **501**, 73 (2013).

[10] F. Bauer, J. Heyder, and J. von Delft, Phys. Rev. B **89**, 045128 (2014).

[11] C. Wetterich, Phys. Lett. B **301**, 90 (1993).

[12] W. Metzner, M. Salmhofer, C. Honerkamp, V. Meden, and K. Schönhammer, Rev. Mod. Phys. **84**, 299 (2012).

[13] V. Meden, W. Metzner, U. Schollwöck, and K. Schönhammer, Phys. Rev. B **65**, 045318 (2002).

[14] S. Andergassen, T. Enss, V. Meden, W. Metzner, U. Schollwöck, and K. Schönhammer, Phys. Rev. B **70**, 075102 (2004).

[15] http://www.nextnano.de/nextnano3.

[16] G. B. Stringfellow, W. Koschel, F. Briones, J. Gladstone, and G. Patterson, Appl. Phys. Lett. **39**, 581 (1981).

[17] G. D. Mahan, Phys. Rev. **153**, 882 (1967).

[18] P. Hawrylak, Phys. Rev. B **44**, 3821 (1991).

[19] C. L. Kane, K. A. Matveev, and L. I. Glazman, Phys. Rev. B **49**, 2253 (1994).

© 2014 The Authors. *Phys. Status Solidi B* is published by WILEY-VCH Verlag GmbH & Co. KGaA, Weinheim

Bibliography

Aharonov, Y. and D. Bohm, 1959: Significance of electromagnetic potentials in the quantum theory. *Phys. Rev.*, **115**(3), 485–491.

Altshuler, B. L., D. Khmel'nitzkii, A. I. Larkin, and P. A. Lee, 1980: Magnetoresistance and hall effect in a disordered two-dimensional electron gas. *Phys. Rev. B*, **22**, 5142–5153.

Appleyard, N. J., J. T. Nicholls, M. Pepper, W. R. Tribe, M. Y. Simmons, and D. A. Ritchie, 2000: Direction-resolved transport and possible many-body effects in one-dimensional thermopower. *Phys. Rev. B*, **62**, R16275–R16278.

Aryanpour, K. and J. E. Han, 2009: Ferromagnetic spin coupling as the origin of 0.7 anomaly in quantum point contacts. *Phys. Rev. Lett.*, **102**, 056805.

Bauer, F., J. Heyder, E. Schubert, D. Borowsky, D. Taubert, B. Bruognolo, D. Schuh, W. Wegscheider, J. von Delft, and S. Ludwig, 2013: Microscopic origin of the '0.7-anomaly' in quantum point contacts. *Nature*, **501**(7465), 73–78.

Bauer, F., J. Heyder, and J. von Delft, 2014: Functional renormalization group approach for inhomogeneous interacting fermi systems. *Phys. Rev. B*, **89**, 045128.

Birkholz, J. E., 2008: *Spin-orbit interaction in quantum dots and quantum wires of correlated electrons – A way to spintronics?* PhD thesis, Georg-August-Universität zu Göttingen.

Bohr, A. and B. Mottelson, 1998: *Nuclear Structure Vol. 2*. World Scientific.

Büttiker, M., 1990: Quantized transmission of a saddle-point constriction. *Phys. Rev. B*, **41**, 7906–7909.

Chen, T.-M., A. C. Graham, M. Pepper, I. Farrer, and D. A. Ritchie, 2008: Bias-controlled spin polarization in quantum wires. *Applied Physics Letters*, **93**(3), –.

Cronenwett, S. M., H. J. Lynch, D. Goldhaber-Gordon, L. P. Kouwenhoven, C. M. Marcus, K. Hirose, N. S. Wingreen, and V. Umansky, 2002: Low-temperature fate of the 0.7 structure in a point contact: A kondo-like correlated state in an open system. *Phys. Rev. Lett.*, **88**(22), 226805.

DiCarlo, L., Y. Zhang, D. T. McClure, D. J. Reilly, C. M. Marcus, L. N. Pfeiffer, and K. W. West, 2006: Shot-noise signatures of 0.7 structure and spin in a quantum point contact. *Physical Review Letters*, **97**(3), 036810.

Geim, A. K., 2009: Graphene: Status and prospects. *Science*, **324**(5934), 1530–1534.

Glazman, L. and M. Raikh, 1988: Resonant kondo transparency of a barrier with quasilocal impurity states. *Soviet Journal of Experimental and Theoretical Physics Letters*, **47**, 452–455.

Goulko, O., F. Bauer, J. Heyder, and J. von Delft, 2014: The effect of spin-orbit interactions on the 0.7-anomaly in quantum point contacts.

Güçlü, A. D., C. J. Umrigar, H. Jiang, and H. U. Baranger, 2009: Localization in an inhomogeneous quantum wire. *Phys. Rev. B*, **80**, 201302.

Heyder, J., 2014: Conductance formula for interacting fermi systems in keldysh formalism.

Heyder, J., F. Bauer, E. Schubert, D. Borowsky, D. Taubert, D. Schuh, W. Wegscheider, J. von Delft, and S. Ludwig, 2014: Geometric crossover between a quantum point contact and a kondo quantum dot.

Hikami, S., A. I. Larkin, and Y. Nagaoka, 1980: Spin-orbit interaction and magnetoresistance in the two dimensional random system. *Progress of Theoretical Physics*, **63**(2), 707–710.

Iqbal, M. J., R. Levy, E. J. Koop, J. B. Dekker, J. P. de Jong, J. H. M. van der Velde, D. Reuter, A. D. Wieck, R. Aguado, Y. Meir, and C. H. van der Wal, 2013: Odd and even kondo effects from emergent localization in quantum point contacts. *Nature*, **501**(7465), 79–83.

Jakobs, S. G., M. Pletyukhov, and H. Schoeller, 2010: Properties of multi-particle green's and vertex functions within keldysh formalism. *Journal of Physics A: Mathematical and Theoretical*, **43**(10), 103001.

Karrasch, C., 2006: Transport through correlated quantum dots – a functional renormalization group approach. Master's thesis, Georg-August Universität Göttingen. arXiv:cond-mat/0612329v1.

Karrasch, C., R. Hedden, R. Peters, T. Pruschke, K. SchÃűnhammer, and V. Meden, 2008: A finite-frequency functional renormalization group approach to the single impurity anderson model. *Journal of Physics: Condensed Matter*, **20**(34), 345205.

Koop, E. J., A. I. Lerescu, J. Liu, B. J. van Wees, D. Reuter, A. D. Wieck, and C. H. van der Wal, 2007: The influence of device geometry on many-body effects in quantum point contacts: Signatures of the 0.7 anomaly, exchange and kondo. *Journal of Superconductivity Incorporating Novel Magnetism*, **20**, 433.

Kouwenhoven, L., 2002: . private communication.

Landauer, R., 1957: Spatial variation of currents and fields due to localized scatterers in metallic conduction. *IBM Journal of Research and Development*, **1**(3), 223–231.

Laughlin, R., 1981: Quantized hall conductivity in two dimensions. *Phys. Rev. B* 5632–5633.

Lunde, A. M., A. D. Martino, A. Schulz, R. Egger, and K. Flensberg, 2009: Electron-electron interaction effects in quantum point contacts. *New Journal of Physics*, **11**(2), 023031.

Matveev, K. A., 2004: Conductance of a quantum wire at low electron density. *Phys. Rev. B*, **70**(24), 245319.

Meden, V., W. Metzner, U. Schollwöck, and K. Schönhammer, 2002: Scaling behavior of impurities in mesoscopic luttinger liquids. *Phys. Rev. B*, **65**, 045318.

Meir, Y., K. Hirose, and N. S. Wingreen, 2002: Kondo model for the "0.7 anomaly" in transport through a quantum point contact. *Phys. Rev. Lett.*, **89**(19), 196802.

Micolich, A. P., 2011: What lurks below the last plateau: experimental studies of the 0.7å ÌÑå 2 e 2 / h conductance anomaly in one-dimensional systems. *Journal of Physics: Condensed Matter*, **23**(44), 443201.

Nozieres, P., 1974: A “fermi-liquid” description of the kondo problem at low temperatures. *J. Low Temp. Phys.*, **17**, 31–42.

Oguri, A., 2001: Transmission probability for interacting electrons connected to reservoirs. *Journal of the Physical Society of Japan*, **70**(9), 2666–2681.

Pierret, R., 1983: *Field Effect Devices, Vol. IV of Modular Series on Solid State Devices*. Addison-Wesley.

Rejec, T. and Y. Meir, 2006: Magnetic impurity formation in quantum point contacts. *Nature*, **442**(7105), 900–903.

Ren, Y., W. W. Yu, S. M. Frolov, J. A. Folk, and W. Wegscheider, 2010: Zero-bias anomaly of quantum point contacts in the low-conductance limit. *Phys. Rev. B*, **82**, 045313.

Rokhinson, L. P., L. N. Pfeiffer, and K. W. West, 2006: Spontaneous spin polarization in quantum point contacts. *Phys. Rev. Lett.*, **96**(15), 156602.

Sarkozy, S., F. Sfigakis, K. Das Gupta, I. Farrer, D. A. Ritchie, G. A. C. Jones, and M. Pepper, 2009: Zero-bias anomaly in quantum wires. *Phys. Rev. B*, **79**, 161307.

Schubert, E., J. Heyder, F. Bauer, B. Waschneck, W. Stumpf, W. Wegscheider, J. von Delft, S. Ludwig, and A. Högele, 2014: Toward combined transport and optical studies of the 0.7-anomaly in a quantum point contact. *Phys. Status Solidi B* 1–7.

Sloggett, C., A. I. Milstein, and O. P. Sushkov, 2008: Correlated electron current and temperature dependence of the conductance of a quantum point contact. *The European Physical Journal B*, **61**(4), 427–432.

Smith, L. W., A. R. Hamilton, K. J. Thomas, M. Pepper, I. Farrer, J. P. Griffiths, G. A. C. Jones, and D. A. Ritchie, 2011: Compressibility measurements of quasi-one-dimensional quantum wires. *Phys. Rev. Lett.*, **107**, 126801.

Sommer, W. T., 1964: Liquid helium as a barrier to electrons. *Phys. Rev. Lett.*, **12**, 271–273.

Thomas, K. J., J. T. Nicholls, N. J. Appleyard, M. Y. Simmons, M. Pepper, D. R. Mace, W. R. Tribe, and D. A. Ritchie, 1998: Interaction effects in a one-dimensional constriction. *Phys. Rev. B*, **58**, 4846–4852.

Thomas, K. J., J. T. Nicholls, M. Y. Simmons, M. Pepper, D. R. Mace, and D. A. Ritchie, 1996: Possible spin polarization in a one-dimensional electron gas. *Phys. Rev. Lett.*, **77**(1), 135–138.

van der Wiel, W. G., S. D. Franceschi, T. Fujisawa, J. M. Elzerman, S. Tarucha, and L. P. Kouwenhoven, 2000: The kondo effect in the unitary limit. *Science*, **289**(5487), 2105–2108.

van Wees, B. J., H. van Houten, C. W. J. Beenakker, J. G. Williamson, L. P. Kouwenhoven, D. van der Marel, and C. T. Foxon, 1988: Quantized conductance of point contacts in a two-dimensional electron gas. *Phys. Rev. Lett.*, **60**(9), 848–850.

Wang, C.-K. and K.-F. Berggren, 1998: Local spin polarization in ballistic quantum point contacts. *Phys. Rev. B*, **57**, 4552–4556.

List of Publications

Microscopic Origin of the *0.7 anomaly* in Quantum Point Contacts
Florian Bauer*, Jan Heyder*, Enrico Schubert, David Borowsky, Daniela Taubert, Benedikt Bruognolo, Dieter Schuh, Werner Wegscheider, Jan von Delft, Stefan Ludwig
* equal contribution
Nature, **2013**, *501*, *73-78*

On the Relation between the *0.7 anomaly* and the Kondo effect: Geometric Crossover between a Quantum Point Contact and a Kondo Quantum Dot
Jan Heyder, Florian Bauer, Enrico Schubert, David Borowsky, Daniela Taubert, Dieter Schuh, Werner Wegscheider, Jan von Delft, and Stefan Ludwig
arXiv:1409.3415
to be submitted to *Phys. Rev. B*

Conductance Formula for Interacting Fermi Systems in Keldysh Formalism
Jan Heyder, Florian Bauer, Jan von Delft
to be submitted to *Phys. Rev. B*

Effect of Spin-Orbit Interactions on the 0.7 Anomaly in Quantum Point Contacts
Olga Goulko, Florian Bauer, Jan Heyder, Jan von Delft
Phys. Rev. Lett., **2014**, 113, 266402

Functional Renormalization Group Approach for Inhomogeneous Interacting Fermi-Systems
Florian Bauer, Jan Heyder, Jan von Delft
Phys. Rev. B, **2014**, 89, 045128

Toward combined transport and optical studies of the *0.7 anomaly* in a quantum point contact
Enrico Schubert, Jan Heyder, Florian Bauer, Bernd Waschneck, Wolfgang Stumpf, Werner Wegscheider, Jan von Delft, Stefan Ludwig, and Alexander Högele
Phys. Status Solidi B, 1-7, **2014**

Curriculum Vitae

Jan Heyder
born on April 29th 1982 in Frankfurt am Main

Education

Diploma, Ludwig-Maximilians-Universität München, 2010
Diploma Thesis: *Der Übergang vom Kondoeffekt im Quantendot zur 0.7 Leitwert-Anomalie im Quantenpunktkontakt*

Abitur (A-Levels), Maximiliansgymnasium München, 2001,
Main subjects: Mathematics, Physics

Danksagung

Meinem Doktorvater *Prof. Jan von Delft* danke ich für das in mich gesetzte fachliche Vertrauen, welches die Promotion an seinem Lehrstuhl ermöglichte. Er hat unser *0.7*-Projekt durchgehend mit viel Übersicht und großem Sachverstand geführt. Sein Vertrauen in meine mit der Zeit wachsende Fachkompetenz ermöglichte mir ein selbstständiges Arbeiten unter professioneller Führung, welches die Qualität meiner wissenschaftlichen Forschung durchwegs positiv beeinflusst hat. Seine Beharrlichkeit und wissenschaftliche Integrität sind alles andere als selbstverständlich und maßgeblich dafür verantwortlich, dass unsere Forschung es bis zu einer Veröffentlichung in NATURE gebracht hat.

Ich danke *Florian Bauer*, der zuerst ein Betreuer, später ein Kollege, immer aber schon ein guter Freund gewesen ist. Seine wissenschaftlichen Fähigkeiten erstrecken sich bemerkenswerterweise auf nahezu jeden Aspekt moderner physikalischer Forschung, womit ihm ein großer Anteil am Gelingen des *0.7*-Projekts zukommt. Insbesondere ist es der Zusammenarbeit mit ihm zuzuschreiben, dass die jahrelange Arbeit an dem NATURE-Paper mich nicht den Verstand gekostet hat.

Auf experimenteller Seite danke ich *Stefan Ludwig*. Seine hervorragende Arbeit ermöglichte eine besonders enge Zusammenarbeit zwischen Theorie und Experiment. Diese hat den wissenschaftlichen Stellenwert des gesamten *0.7*-Projekts enorm aufgewertet. Darüberhinaus verschaffte sie mir wichtige Einblicke in experimentelle Arbeitsweisen. Seine maßgebliche Mitarbeit während aller Phasen der Fertigstellung des Papers war von enormer Hilfe. Ich danke *David Borowski*, *Enrico Schubert* und *Daniela Taubert* für ihren jahrelangen unermüdlichen Einsatz beim Aufbau der Experimente, dem Durchführen der Messungen und deren Auswertung. Nicht zuletzt ihre große Leistung machte es möglich, dass wir von einer ausgezeichneten Kollaboration sprechen können.

Allen Mitgliedern des Lehrstuhls gilt mein großer Dank. In einer ausgesprochen guten Arbeitsatmosphäre, die sich in steter Hilfsbereitschaft und Rat, sowohl in fachlichen als auch privaten Fragen zeigte, fühlte ich mich gut eingebettet.

Ich danke *Anna*, deren Anwesenheit eine unglaubliche Bereicherung meines Lebens bedeutet. Ihre beharrliche Bestätigung meines Charakters, so rätselhaft sie mir auch erscheint, ist für mich eine enorme Quelle der Kraft und Inspiration.

Ich danke meinen Eltern *Regina* und *Joachim Heyder*. Ihre unermüdliche Fürsorge sowie ihr Glaube an meine Fähigkeiten förderten früh mein Selbstbewusstsein und erlaubten mir erst diesen Weg einzuschlagen. Ihr Anteil an dem Gelingen dieser Arbeit ist deshalb nicht hoch genug einzuschätzen.